Examining the metal selectivity of thiol rich *de novo* designed peptides as a strategy to make asymmetric alpha-helical protein assemblies

by

Catherine Suzanne Mocny

A dissertation submitted in partial fulfillment
of the requirements for the degree of
Doctor of Philosophy
(Chemistry)
in the University of Michigan
2016

Doctoral Committee:

Professor Vincent L. Pecoraro, Chair
Associate Professor Nicolai Lehnert
Associate Professor Bruce A. Palfey
Professor James E. Penner-Hahn

To my family

Acknowledgements

There are so many people whom I would like to gratefully thank for the roles they played during my graduate school career. First and foremost I wish to express my deepest thanks to my advisor, Vince. I have learned so much over the last five years working for him. Not only have I had the opportunity to learn multiple scientific techniques but I have also learned how to think critically, offer constructive criticism to coworkers, and how to simultaneously independently self-start and work in team environments. Your patience and guidance have been invaluable and I thank you so very much for taking the time to meet with me when I was in need of a third rotation and am so very thankful that I found my graduate school home in your lab.

In addition to my thesis advisor, I would also like to thank the rest of my thesis committee, Professors James Penner-Hahn, Nicolai Lehnert, and Bruce Palfey for their critical insights, helpful suggestions, and valuable time spent serving on my committee. I am also grateful for all of the collaborations I have had the opportunity to initiate and in which I could take part. This list includes: Professor James Penner-Hahn, Dr. Aniruddha Deb, Professor Nicolai Lehnert, Dr. Amy Speelman, Ashley McQuarters, Dr. Cédric Tard, Dr. Matteo Duca, Professor Brandon Ruotolo, Dr. Richard Kerr, and Dr. Toni Kuehl. I appreciate all of your help collecting, interpreting, and discussing all of our collaborative data.

I want to offer a very special thanks to my undergraduate mentor and advisor, Dr. Laura Lowe Furge. You have been both a professional and personal inspiration over the last (nearly) 10 years. You have been a much-appreciated source of encouragement through some very difficult times and decisions. I thank you very much for all of your support and all of the doors you have shown me, opened for me, and advised me to run-through.

I also need to extend many thanks to all of my labmates, past and present, in all of the labs that I have worked in over the past years. Not only have you offered continued support and critical discussions but also many of you have become some of my very dear friends. This list is lengthy and includes, but is not limited to: Fangting, Melissa, Ginny, Alison, Evan, Leela, David, Jeff, Tu, Jake, Tyler, Karl, and Audrey. Thank you for the parts you played in helping me fix things, training me on various different instruments, making things work, re-writing derivations for the thirtieth time, and, in general, for always having the time to chat.

To all of my friends, Chemistry-related, and not, you are all amazing. Graduate school was a long process and your continued support and friendship has been completely invaluable. A special thanks to Dr. Erik Guetschow and to Dr. Will Black, both who knew I belonged at the University of Michigan before I did. Thank you for your patience and your encouragement.

The biggest thank you to my family. While you may not have ever understood what I was doing, or saying, along this journey you have always supported me and have never doubted my abilities. To my parents, for their continued professional and academic support, and for their "let her finish school first" mentality. To my mother, who knew what needed to be done that day we walked onto Kalamazoo's campus, which I truly believe was the moment that set me on the path I still currently walk. To my siblings and their significant others, Tim & Christine, Jason & Jess, Kara & Tim, Sarah & Andy, Sarah Jo & Justin – you are all amazing. Thank you for everything you do, including making beautiful babies that I love to pieces. To my "in-laws", Jeff, Tina, Natalie and Stephanie – you are all awesome and I can't say how much you mean to me. A special thanks to Krysta, your motivation has been unparalleled during these last few years. Last, but certainly not least, I cannot thank you enough, Anthony, for all you have done and all the support you have provided during this journey. Your patience is inspirational and your confidence in me is uplifting. I would not have wanted to do this without you by my side.

Table of Contents

List of Tables

List of Figures

Abstract

The first preparation of metal-nucleated heterotrimers, asymmetric remote metal binding sites and Cu^{I}_{2} centers in *de novo* designed alpha-helical three-stranded coiled coils (3SCCs) is provided in this thesis. Peptides with Ala or Leu in the layer directly above a Cys_3 site, [sequence: Ac-GLKALEEK LKA**X**EEK CKALEEK $(LKALEEK)_2$G-NH_2], with X=A (peptide **A)** and X=L (peptide **B)** were mixed as 2(**A)** and 1(**B**), with Pb^{II} to form, Pb^{II}(**AAB)** heterotrimers over the pH range 7.4 to 9.4 with a distinct ^{207}Pb NMR chemical shift, (5600 ppm) compared to **AAA** (5575 ppm) and **BBB** Pb^{II}-homotrimers (5650 ppm). The coexistence of **AAB** and **AAA** chemical shifts in appropriate ratios confirms the formation of heterotrimers. The ability to make heterotrimeric 3SCCs removes previous restrictions due to the inherent self-association of the peptides, allowing for the design and analysis of asymmetric metal binding sites as observed in nature.

AAB aggregates containing a second metal binding site with 0-3 Asp residues above a His_3 site (Asp_XHis_3) are described for potential catalytic applications. Prior to this thesis work, only symmetric metal binding sites could be achieved within the 3SCC scaffold. An Asp residue may be added to the Leu/Cys or the Ala/Cys containing helix. UV-Vis, EPR and XAS analysis of Co^{II}-bound homotrimers reveal that 6-coordinate, highly symmetric Co^{II}-homotrimers are formed whereas less symmetric, 5-coordinate environments result for the Co^{II}-heterotrimers. The similarities between the heterotrimers and Co^{II}-substituted carboxypeptidase A support direct Co^{II}-Asp coordination in **AAB** systems. Zn^{II} XAS analysis indicates Zn^{II} is 4-coordinate in all Zn^{II}-homo- and heterotrimers, demonstrating that Co^{II} and Zn^{II} coordinate differently. The spectroscopic evidence confirms the first inclusion of asymmetric metal binding sites within 3SCCs.

Competition between Cu^{I} and Pb^{II} for Cys_3 reveals unprecedented Cu^{I}_{2} sites. XAS of Cu^{I}-peptides are consistent with Cu^{I}-Cu^{I} back-scatterering (2.66 Å) and 2 or 3 Cu^{I}-S distances (2.20 Å). UV-Vis studies confirm a 2:1 binding stoichiometry. Mixtures of Pb^{II} and Cu^{I} yield $Cu^{I}Pb^{II}Cys_3$ proteins. Preformed $Cu^{I}_{2}Cys_3$ inhibits binding of Pb^{II} while addition of one

equivalent of Cu^{I} to $Pb^{II}Cys_3$ does not displace Pb^{II} as $Cu^{I}Cys_3$ features develop. Excess Cu^{I} is required to displace Pb^{II}, indicating comparable Cu^{I} and Pb^{II} binding affinities.

Chapter 1. *De Novo* Protein Design as a Methodology for Synthetic Bioinorganic Chemistry

Introduction: A Synthetic Approach for Bioinorganic Chemistry

While metalloproteins have been known for nearly a century, it was only in the 1960's that inorganic chemists attempted to synthesize these fascinating biological co-factors. This successful approach often utilizes multidentate ligands containing relevant heteroatoms to bind metals in appropriate oxidation states and coordination numbers. A major strategic advantage was that small molecules were easy to crystalize, allowing well-defined complexes to be used as models for spectroscopy and reactivity of enigmatic metalloprotein sites. Through these studies, the mysteries of many interesting bioinorganic systems were revealed (*vide infra*).

While this chemical methodology was being practiced, major advances in biology were realized. This included the ability to isolate and manipulate genomes or individual strands of DNA, achieving selective mutations of proteins, crystalizing and structurally interrogating metalloproteins and developing automated synthesis, both at peptide and DNA levels, which allowed for the preparation of newly minted proteins. This ease of synthetic access to real proteins, with defined metal binding sites, which could now be defined at the same high resolution as small molecules, ushered in the field of *de novo* metalloprotein design. No longer was one restricted to ligands that were analogues of amino acids, no longer was chemistry often required to be completed in organic solvents to mimic a protein environment or confer stability on the metal site, no longer would one need to complete multi-step and tedious chemical syntheses to develop chirality around the metal center or probe second or third coordination sphere effects on spectroscopy and catalysis. In essence, bioinorganic chemistry was ready to be launched into the world of

synthetic biology. As defined by the European Union in a Report of a New and Emerging Science and Technology (NEST) High-Level Expert Group:

"Synthetic biology is the engineering of biology: the synthesis of complex, biologically based (or inspired) systems which display functions that do not exist in nature. This engineering perspective may be applied at all levels of the hierarchy of biological structures – from individual molecules to whole cells, tissues and organisms. In essence, synthetic biology will enable the design of 'biological systems' in a rational and systematic way."[1]

At the most reductionist level, *de novo* protein design, the process of using peptide sequences that are not existent in, but indeed inspired by nature, allows for the building of new function. The ultimate goal of this approach is to obtain stable peptide scaffolds with a desired functionality. Of particular interest to the Pecoraro laboratory is the utilization of α-helical proteins, such as the self-associating amphipathic α-helical coiled coils, to study metal binding in protein-like environments. The coiled-coil motif consists of amphipathic α-helices that undergo hydrophobic collapse when dissolved in aqueous solution resulting in a secondary structure stabilized by interior hydrophobic interactions and exterior electrostatic interactions.

The peptide sequences that result in such coiled-coils consist of heptad repeats, where a primary structure is repeated ever seven residues denoted ***abcdefg***. Within the heptad repeat, hydrophobic residues are found at the ***a*** and ***d*** positions and electrostatic residues at the ***e*** and ***g*** positions. The pitch of 3.6 residues per turn results in a misalignment of the ***a*** residues from one heptad repeat to the next, and the same is observed for the ***d*** residues, resulting in a super-coil of the α-helical structure.[2]

The identities of the residues located at both the hydrophobic positions and the hydrophilic positions have been shown to influence the oligiomeric preferences of the coiled-coil. The impact of the hydrophobic residues on the number of helices that associate directly relates to the different geometries of the ***a*** and ***d*** positions with respect to the helical backbone.[3,4] Combining Val residues at the ***a*** position with Leu residues at the ***d*** positions, provides a 3SCC; however, inclusion of a single Asn at the ***a*** position in

the one heptad, was shown to produce a two-stranded coiled coil (2SCC, Table 1-1).[5,6] Inclusion of Leu residues at the ***a*** positions and Ile at the ***d*** positions yields formation of a 4SCC, and Ile or Leu residues at both the ***a*** and ***d*** positions exclusively yields a 3SCC (Table 1-1).[7,8] Although Val is similar to Ile, inclusion of Leu residues at the ***a*** and Val residues at the ***d*** position results in a 3SCC, not a 4SCC as one might predict (Table 1-1).[7] Inversion to Ile residues in the ***a*** sites and Leu residues at the ***d*** sites provides 2SCCs.[7]

Table 1-1. Comparison of the number of self-associating helices as related to identity of the hydrophobic residues in positions ***a*** and ***d*** within the heptad repeat.

a position	***d*** position	#SCC	Notes	Reference
Ile	Leu	2		7
Ile	Ile	3		8
Leu	Leu	3		8
Leu	Ile	4		7
Leu	Val	3		7
Val	Leu	2	One Asn layer	5
Val	Leu	3		6

Coil-Ser, as designed by Lovejoy *et al.*, was based loosely off the previously reported Hodges peptide (a 2SCC) with five amino acid substitutions within the sequence to enhance helical formation and contained all Leu residues at the ***a*** and ***d*** residues (Table 1-1).[9] The system was originally designed to mimic a 2SCC; however, initial crystal structures provided an anti-parallel orientation of Coil-Ser with an up-up-down topology. Within the hydrophobic interior, eight Leu layers are observed composed of alternating ***d***, ***d'***, ***a''*** and ***a***, ***a'***, ***d''*** residues (where residues ***a*** and ***d***, ***a'*** and ***d'***, and ***a''*** and ***d''*** correspond to positions on helix 1, 2, and 3, respectively. Atomic solvation (hydrophobic) energy calculations (based on the method of Eisenberg and McLachlan and the atomic solvation parameters of Eisenberg *et al.*[10,11]) provided a net hydrophobic stabilization energy for both the parallel (-11.2 kcal/mol per helix) and antiparallel (-10.7 kcal/mol per helix) orientations of Coil-Ser. These energies, although very similar, support a more stable anti-parallel structure with a net energy difference compared to the parallel orientation of only 0.5 kcal/mol per helix. Additionally, repulsive interactions are observed when looking at the interhelical amino salt bridges resulting in salt bridges only

between helix 1 and 2. These results indicated that the hydrophobic collapse drives the formation of the antiparallel structure and presence of interhelical salt bridges are an indirect consequence, not a driving force, in the formation of coiled coils. Multiple subsequent crystal structures of substituted CoilSer have shown both parallel and anti-parallel orientations (vide infra).

Modification of the Coil-Ser sequence to include Val at the ***a*** positions resulted in a single, parallel homotrimer named V_aL_d, as determined by sedimentation equilibrium and X-ray crystallography.[6,12] In this sequence, eight hydrophobic layers are observed with alternating Val ***a***, ***a'***, ***a''*** and Leu ***d***, ***d'***, ***d''*** residues. Glu and Lys salt bridges are formed at each helical interface. A calculated atomic solvation energy of -18.4 kcal/mol per helix provides an increase in stability compared to both the parallel and anitparallel Coil-Ser peptide. Comparison of the Coil-Ser and V_aL_d crystal structures provides very similar structures when superimposing a monomer from each trimer; however, crystals of these systems grow in different space groups (P321 and $P2_12_12_1$ for V_aL_d and Coil-Ser, respectively).[9,12] Additionally, trimer stacking is observed for V_aL_d and not for Coil-Ser. These studies show that preferred packing of all Val residues in the ***a*** layers and all Leu residues in the ***d*** layers provides selective parallel 3SCC formation whereas all Leu residues in both *a* and *d* layers can result in either parallel or antiparallel orientations depending on experimental conditions and additional sequence perturbations.

The hydrophobicity of the residues flanking the ***a*** and ***d*** position has also been shown to influence the number of helices that associate within a coiled-coil peptide. For example, for both 2- and 3SCC, the ***e*** and ***g*** residues show electrostatic interactions; however, the ***b*** and ***c*** positions offer further contributions to the ionic interactions between the helices within 4SCC.[13,14] If polar groups are introduced into the ***a*** and ***d*** positions, the peptides show a preference for 2SCC to allow for partial solvation of the polar sidechains, as mentioned above where an Asn residue was included within the peptide sequence.

The Pecoraro laboratory has used these α-helical designed systems to generate well-defined secondary and tertiary protein structures capable of constraining metals into native-like structures or functions. Significant advances in understanding have allowed

for enhancement of the specificity and selectivity of metal binding. Designed three-helix bundles (3HB) are now being tested for practical applications as bioimaging agents (MRI contrast and luminescent probes) or for removal of uranyl ions from ocean water.[15,16]

Heavy Metal Binding to Designed 3SCC, Tris-Thiolate Sites

Many reviews have covered metalloprotein design and redesign with respect to inclusion and alterations of metal binding sites to obtain functional metalloproteins.[17–22] Our laboratory utilizes *de novo* designed three-stranded α-helical coiled coils (3SCC) and α-helical bundles to build, study and manipulate metal binding sites in pseudo-three-fold symmetric assemblies. Herein, I discuss how these peptides can impose uncommon coordination geometries, differentially recognize either the same metal in different geometries or different metals in different regions of the same scaffold, and then discuss how these insights have been used to generate catalytic systems capable of hydrolytic or redox transformations. I will also discuss the advances I have made during my dissertation work as they relate to three different facets of bioinorganic *de novo* design peptide chemistry.

In 1992, our laboratory initiated a collaboration with Bill DeGrado to study metal binding sites in *de novo* designed peptides. The **TRI** family of 3SCC was developed, that exploits a heptad repeat, a seven-amino acid sequence ($L_{\boldsymbol{a}}K_{\boldsymbol{b}}A_{\boldsymbol{c}}L_{\boldsymbol{d}}E_{\boldsymbol{e}}E_{\boldsymbol{f}}K_{\boldsymbol{g}}$),[23] containing hydrophobic Leu residues (***a*** and ***d***), charged residues capable of H-bonding and salt bridging (***e*** and ***g***), and fills the remaining locations (***b***, ***c***, and ***f***) with either helix-inducing or water solubilizing residues. Acetylated or amidated terminal glycine residues also induce the helical structure. Hydrophobic collapse drives the formation of coiled coils forming layers of leucine residues (alternating between ***a*** and ***d*** positions) along the interior of the coiled coil that may be substituted with metal binding residues. Depending on the pH, our **TRI** peptides can from either two-stranded (pH<4.5) or three-stranded (pH>5.5) coiled coils, consistent with the trends as outlined above (Figure 1-1).[24] Moving from N- to C-termini, there are three residues above (sequence ***d***XXX***a***) and two below (***a***XX***d***) an ***a*** layer within the alpha helical interior. This layer separation is reversed from

the ***d*** site perspective, resulting in changes of the side chain orientations between ***a*** and ***d*** site metal environments (Figure 1-2). The pattern between adjacent leucine layers becomes ***a***XX***d*** above and ***d***XXX***a*** below the ***d*** site. The **TRI** peptides have four heptad repeats with the sequence given in Table 1-2. This sequence can be truncated to 3-heptads (**BABY**) or elongated to 5-heptads (**GRAND**).

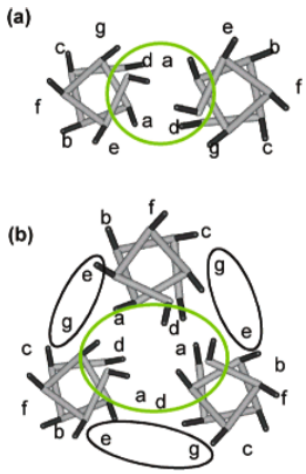

Figure 1-1. Helical wheel diagram for parallel (a) two, and (b) three-stranded coiled coils. Hydrophobic interactions are shown highlighted in green and electrostatic interactions are highlighted in black. Figure adapted from 24.

Extensive studies have demonstrated that these three-stranded coiled coils adopt native folds in aqueous solution rather than forming molten globules.[25] Analytical ultracentrifugation, HPLC analysis and diffusion based NMR techniques demonstrated that at pH ≥5.5 the **TRI** peptides form parallel 3SCC. Folding free energies indicated that these 3SCC were highly stable constructs that only denatured in the presence of multimolar guandinium chloride (i.e. ~2-4 mM GuHCl)[6,25]. Subsequently, numerous structures of apo **CoilSer** derivatives, a related sequence used in crystallographic studies, have appeared which confirm the parallel 3SCC assignment (Table 1-2).

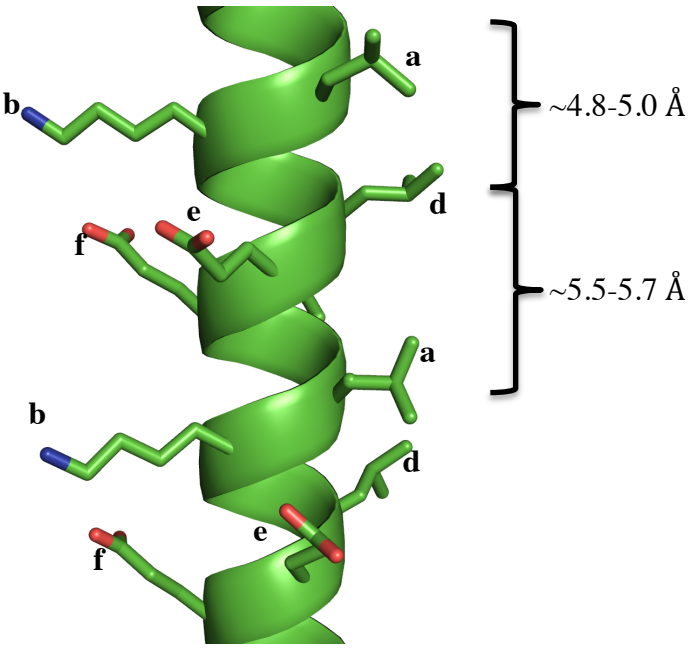

Figure 1-2. Side view of two-heptad repeats in one **TRI** helix showing the difference in distance between ***a***XX***d*** (4.8-5.0 Å) and ***d***XXX***a*** (5.5-5.7 Å).

Polyhedra for inorganic ions binding to proteinacious ligands provide coordination numbers from two to six and are generated through triangular structures. Trigonal environments are achieved by introducing a metal binding ligand into an ***a*** or ***d*** site, resulting in a three-fold symmetric binding site within the 3SCC (Figure 1-3).[26] Metal ion binding into the plane, or layer, of the three ligands provides a trigonal planar geometry, whereas displacing the metal up or down from such a plane generates trigonal pyramidal geometry. Pseudo tetrahedral and trigonal bipyramidal polyhedra are obtained by placing one or two ligands above (and below) trigonal planes, respectively. Octahedral structures can be realized by placing a second trigonal plane at a 60-degree angle above the first. The 3SCC motif was selected precisely because the C_3 symmetry accesses all of these polyhedra.

Designing a metal binding site into the **TRI** peptides is easily accomplished by substituting a Leu residue for a coordinating amino acid such as Cys (e.g., substitution of Leu to Cys in the 16th position gives **TRI**L16C, Table 1-2, Figure 1-4). While removing a Leu layer is destabilizing, subsequent metal binding provides sufficient stability to afford

well-folded metalloproteins. This cysteine substitution allows binding of heavy metals such as Hg^{II}, Pb^{II}, As^{III}, Cd^{II} and Bi^{III} (*vide infra*).[27]

Table 1-2. Peptide Sequences

Peptide	Sequence
	abcdefg
BABY	Ac-G LKALEEK LKALEEK LKALEEK G-NH_2
BABYL9C	Ac-G LKALEEK ***C***KALEEK LKALEEK G-NH_2
TRI	Ac-G LKALEEK LKALEEK LKALEEK LKALEEK G-NH_2
TRIL12C	Ac-G LKALEEK LKA***C***EEK LKALEEK LKALEEK G-NH_2
TRIL12AL16C	Ac-G LKALEEK LKA***A***EEK ***C***KALEEK LKALEEK G-NH_2
TRIL12$_D$LL16C	Ac-G LKALEEK LKA$_{D}$***L***EEK***C***KALEEK LKALEEK G-NH_2
TRIL16C	Ac-G LKALEEK LKALEEK ***C***KALEEK LKALEEK G-NH_2
TRIL2WL16C	Ac-G ***W***KALEEK LKALEEK ***C***KALEEK LKALEEK G-NH_2
TRIL16Pen	Ac-G LKALEEK LKALEEK $_{Pen}$KALEEKLKALEEK G-NH_2
TRIL9C	Ac-G LKALEEK ***C***KALEEK LKALEEK LKALEEK G-NH_2
TRIL9CL19C	Ac-G LKALEEK ***C***KALEEK LKA***C***EEK LKALEEK G-NH_2
TRIL9CL23H	Ac-G LKALEEK ***C***KALEEK LKALEEK ***H***KALEEK G-NH_2
TRIL9HL23C	Ac-G LKALEEK ***H***KALEEK LKALEEK ***C***KALEEK G-NH_2
TRIL23H	Ac-G LKALEEK LKALEEK LKALEEK ***H***KALEEK G-NH_2
TRIL9CL19TL23H	Ac-G LKALEEK ***C***KALEEK LKA***T***EEK ***H***KALEEK G-NH_2
TRIK22EL23HE27K	Ac-G LKALEEK LKALEEK LKALEE***E*** ***H***KAL***K***EK G-NH_2
GRAND	Ac-G LKALEEK LKALEEK LKALEEK LKALEEK LKALEEK G-NH_2
GRL16CL26TL30H	Ac-G LKALEEK LKALEEK ***C***KALEEK LKA***T***EEK ***H***KALEEK G-NH_2
GRL16CL26DL30H	Ac-G LKALEEK LKALEEK ***C***KALEEK LKA***D***EEK ***H***KALEEK G-NH_2
CoilSer	Ac-E WEALEKK LAALESK LQALEKK LEALEH G-NH_2
CSL9C	Ac-E WEALEKK ***C***AALESK LQALEKK LEALEH G-NH_2
CSL19C	Ac-E WEALEKK LAALESK LQA***C***EKK LEALEH G-NH_2
CSL16C	Ac-E WEALEKK LAALESK ***C***QALEKK LEALEH G-NH_2
CSL16Pen	Ac-E WEALEKK LAALESK $_{Pen}$QALEKKLEALEH G-NH_2
CSL9PenL23H	Ac-E WEALEKK $_{Pen}$AALESKLQALEKK ***H***EALEH G-NH_2
GRANDCoilSer	Ac-E WEALEKK LAALESK LQALEKK LQALEKK LEALEH G-NH_2
GRCSL12AL16C	Ac-E WEALEKK LAA***A***ESK ***C***QALEKK LQALEKK LEALEH G-NH_2
GRCSL16PenL26AL30C	Ac-E WEALEKK LAALESK $_{Pen}$QALEKKLQALEKK LEALEH G-NH_2
GRCSL16CL30H	Ac-E WEALEKK LAALESK ***C***QALEKK LQALEKK ***H***EALEH G-NH_2
α_3D	MGSWAEFKQRLAAIKTRLQALGGSEAELAAFEKEIAAFESELQA YKGKGNPEVELRKEAAAIRDELQAYRHN
α_3D**IV**	MGSWAEFKQRLAAIKTR***C***QALGGSEAE***C***AAFEKEIAAFESELQA YKGKGNPEVELRKEAAAIRDE***C***QAYRHN

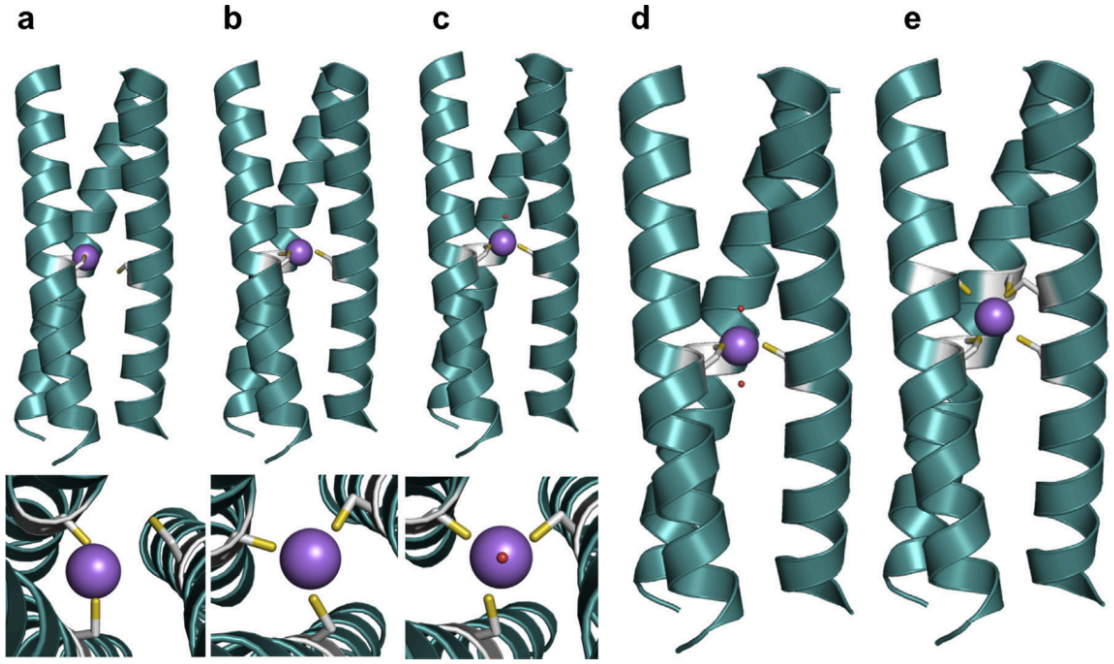

Figure 1-3. Pymol models of possible metal-binding geometries in a 3SCC. The metal-binding ligands are Cys residues and the metal is colored purple. (a) side-on view (top) and top-down view (bottom) of two-coordinate or linear geometry, (b) side-on view (top) and top-down view (bottom) of three-coordinate trigonal planar geometry, (c) side-on view (top) and top-down view (bottom) of four-coordinate tetrahedral geometry, (d) side-on view of five-coordinate trigonal bipyramidal geometry, and (e) side-on view of six-coordinate octahedral metal geometry. Models are generated using the crystal structure of $As^{III}_{S}(\mathbf{CS}L9C)_3$ PDB:2JGO.[28] Figure adapted from Ref 26.

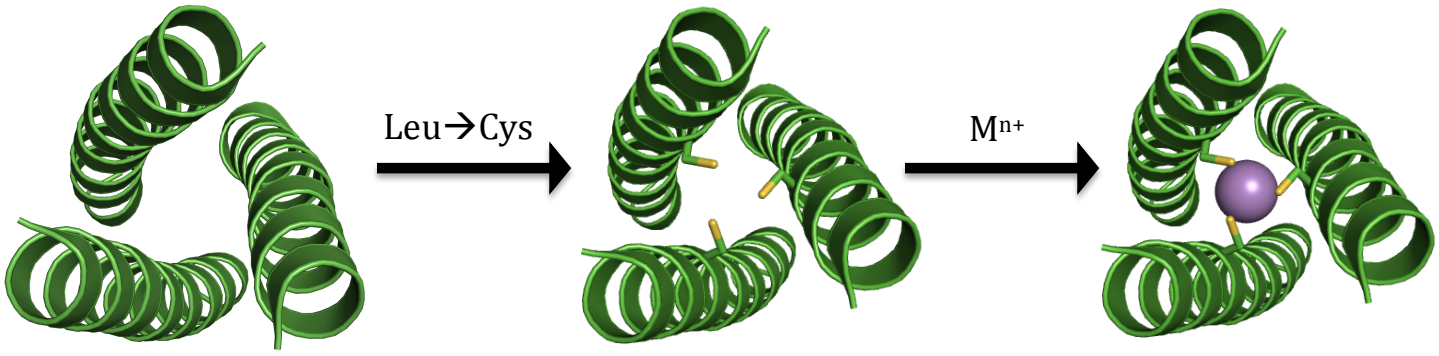

Figure 1-4. Pymol representation of the engineering of a tris-thiolate site within a 3SCC. Substitution of a Leu layer for Cys (middle) residues produces a tris-thiolate site for heavy metal binding (right). Figure adapted from Reference 29.

Initially, the Pecoraro laboratory chose Cys ligands for the hydrophobic interior as this amino acid is small, neutral and the metal ion preferences are distinctly different from the exterior carboxylate residues. Beyond the obvious objective (selective metal binding within a 3SCC), constraining metals in less common coordination geometries was desired. MerR, a metalloregulatory protein, is responsible for regulating the expression of the mer operon and binds to DNA in the presence (transcriptional activator) and absence (transcriptional repressor) of Hg^{II}, was proposed to bind Hg^{II} as a trigonal plane rather than the nearly ubiquitous linear Hg^{II} adducts observed in most proteins.[30–33] While trigonal Hg^{II} thiolate complexes had been crystallized from non-aqueous solution,[31,34,35] such structures were unstable in water, especially at the nanomolar concentrations where Hg^{II} was recognized by MerR. Thus, our first objective was to impose a third sulfur ligand onto Hg^{II} within a protein environment in aqueous solution.

A tris-Cys site was designed in **TRI** in an ***a*** position, generating **TRI**L9C and **TRI**L16C (Table 1-2). Studies determined that both linear and trigonal Hg^{II}-thiol coordination can be achieved. At pH <4.5, where the apo-peptide predominately forms a dimer, or conditions of 1:0.67 ratios of Hg^{II}:trimer (pH >5.5), spectroscopic features consistent with two-coordinate linear Hg^{II} complexes were observed (Table 1-3).[25,36,37]

Table 1-3. Comparison of Hg^{II}-bound MerR and **TRI** peptides

Sample	δ[a]	λ (Δε)[b]	Å[c]	ω (η)[d]
Hg^{II}MerR	-106[e]	242 (19.8)[f]	2.43[g]	1.19 (0.25)[h]
	-109 (DNA)[e]	260 (14.6)[f]		
		290 (6.45)[f]		
Hg^{II}(**TRI**LXC)$_2$	-834[i]	240 (2.7)[i]	2.30[i]	1.47 (0.13)[j]
Hg^{II}(**TRI**LXC)$_3^-$	-179 [i]	247 (19.2)[i]	2.41[i]	1.17 (0.25)[j,k]
		265 (11.9)[i]		
		295 (5.8) [i]		
Hg^{II}(Cys)$_4^{2-}$	-300 to -500[e,l]	280 (NR)[f]	2.54[g]	0.33 (0.0)[m]

TRILXC: X=9 or 16, both ***a*** site cysteine modifications. [a] δ given in ppm for ^{199}Hg NMR. [b] λ given in nm and Δε as $mM^{-1}cm^{-1}$. [c] Average Hg-S EXAFS bond lengths. [d] ω is given in rad/ns and η is a unitless quantity for ^{199m}Hg PAC. [e]Reference 6, pH 6.02. [f]Reference 30, pH 7.0. [g]Reference 27, pH 7.5. [h]Reference 31, pH NR. [i]Reference 34, pH 8.5. [j]Reference 35, pH 8.1, [k]pH 8.7. [l]Varied pH. [m]Reference 32, pH NR.

Between pH 5.5 and 8, with an excess of trimer to Hg^{II}, a 3SCC exists with a linear Hg^{II} and the third thiol uncoordinated. At pH >8 a three-coordinate, trigonal geometry was obtained with markedly different spectral features, closely matching Hg^{II}MerR (Table 1-3).[36,37] Thus, under conditions sufficient to deprotonate all three thiols, a trigonal planar geometry resulted.

Trigonal $Hg^{II}S_3$ sites are easily obtained when the thiol ligands are included at ***a*** positions. Higher pH values (pH ≥9) were required to obtain trigonal Hg^{II} in ***d*** sites as found in **TRI**L12C.[38] For structural studies, the **TRI** and **GR** peptides have yet to produce good 3-D crystals, and therefore we use **CoilSer** (**CS**) peptides as crystallographic analogs. The sequence of **CS** (found in Table 1-2) is similar to that of **TRI** and **GRCS** is similar to that of **GR**, with four or five, 7-residue heptad repeat units that promote helix formation, respectively. X-ray analysis of apo-**CS**L9C and **CS**L19C revealed that the preferred cysteine rotamers in ***a*** site peptides (e.g., **CS**L9C) positioned thiol groups into the helical interior, whereas cysteine sulfur atoms in **CS**L19C, a ***d*** site Cys_3, were oriented towards the helical interface (Figure 1-5), suggesting a significant rearrangement energy to form $Hg^{II}S_3$ at the ***d*** site.[25,39] X-ray analysis of Hg^{II}_3**CS**L12C has determined that at low pH conditions (pH 6.0), Hg^{II} binds to the **d** site in a linear fashion and the 3SCC crystallizes as an antiparallel 3SCC. This is only the second situation in which the **CS** peptides have been observed as antiparallel 3SCC (Unpublished data from Dr. Leela Ruckthong).[9]

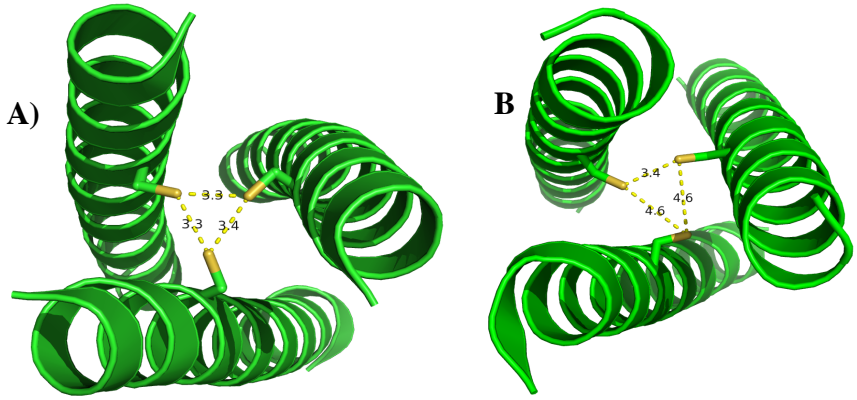

Figure 1-5. Pymol representations of the top-down view of the three-fold axis of X-ray structures of A) ***a*** site apo-(**CS**L9C)$_3$ (PDB: 3LJM), with S-S distances of 3.3, 3.3 and 3.4 Å. B) ***d*** site apo-(**CS**L19C)$_3$ (PDB: 2X6P), an enlarged metal binding site with S_γ-S_γ distances of 3.4, 4.6, and 4.6 Å.[39]

Recently, crystal structures of both apo-(**CS**L16C)$_3$ and $Hg^{II}_S Zn^{II}_N$(**GRCS**L16L30H)$_3$ were obtained and refined to 1.42 Å and 2.09 Å, respectively (Table 1-2, Figure 1-6).[29] It was determined that upon binding of Hg^{II} to the L16C site, that although it contains the requisite number of ligands for trigonal metal coordination, it requires significant rearrangement of the thiol side chains to support three-coordinate Hg^{II} ligation. In fact, the S_γ-S_γ distance must expand by nearly 0.9Å to accommodate Hg^{II} binding and the corresponding $\chi 1$ angles rotate from -69.20° to -151.88° (Table 1-4, Figure 1-6). This rearrangement required for metal ligation is defined as a *pre-disposed* Cys_3 site.* Notably, there is a water molecule located directly above the Hg^{II} ion at a distance of 2.79 Å (Figure 1-6C). This distance is too long for a direct Hg^{II}-OH_2 bond (estimated at ~2.2-2.3 Å) but is close enough at 3.39 Å to hydrogen bond with sulfur p-orbitals of the cysteine major conformer.

Introduction of an Ala "hole" (relating to the reduced steric bulk within the hydrophobic interior, as compared to the packing of three Leu residues) in layer above an **a** Cys_3 site does not greatly alter the geometry or coordination of Hg^{II}. Dr. Leela Ruckthong recently solved and refined the structure of Hg^{II}_S(**GRCS**L12AL16C)$_3$ to 1.92 Å (Figure 1-7).[29] Similar to $Hg^{II}_S Zn^{II}_N$(**GRCS**L16L30H)$_3$, the Cys_3 site is *pre-disposed* for Hg^{II} binding with a $\chi 1$ of -147.85 and a S_γ-S_γ distance 4.20 Å (Table 1-4). The primary coordination of Hg^{II} in the Cys_3 metal binding site is essentially identical within **GRCS**L12AL16C and **GRCS**L16L30H. One difference in the secondary coordination sphere of the Hg^{II} metal binding site is the presence of 3 additional water molecules, in addition to the water molecule observed in $Hg^{II}_S Zn^{II}_N$(**GRCS**L16L30H)$_3$ that is directly above the Hg^{II} metal ion (referred to from now on as the central H_2O). Introduction of the Ala residues allows for the central H_2O molecule, still located along the helical axis, to move away from the Hg^{II} to a distance of 3.56 Å, nearly 0.77 Å farther from the metal ion than in **GRCS**L16CL30H (Figure 1-7). This movement results in a distance too far

* A *pre-disposed* site is defined as the placement of the proper number and type of ligands at an appropriate layer within a 3SCC to bind a metal but significant rearrangement is required for the a proper geometry and metrical parameters of metal binding to occur. A *pre-organized* site is defined as not only the proper number and type of ligands within a layer, but in addition requires no, or very little perturbation, of the protein ligands to complex the desired metal in the proper geometry.[29]

from the sulfur atoms to form a hydrogen bonds, as was previously observed in $Hg^{II}_{S}Zn^{II}_{N}$(**GRCS**L16L30H)$_3$. However, the three additional water molecules, located near the helical interface, are only 2.63 Å from the central H_2O molecule and 3.25 Å from the sulfur atoms of the Cys ligands. These distances allow for an internal hydrogen-bonding network between the four water molecules as well as between the interface water molecules and the sulfur atoms of the Cys residues. This is the first instance in which a hydrogen-bonding network is observed within the hydrophobic interior of the **CS** family of 3SCC.

Concurrent with both L16C and L12AL16C $Hg^{II}Cys_3$ crystal structures, a structure of Zn^{II}_{S}(**GRCS**L12AL16C)$_3$ was also obtained and refined to 1.89Å.[29] Similarly to Hg^{II}_{S}(**GRCS**L12AL16C)$_3$, the χ1 angle of Zn^{II} bound to Cys_3 is -146.96° with a slightly shorter S_γ-S_γ distance of 3.94 Å, to accommodate the smaller Zn^{II} ion (Table 1-4, Figure 1-8). Unlike Hg^{II}, the Zn^{II} ion is observed to bind in a pseudo-tetrahedral geometry with three Cys ligands and direct coordination to one exogenous solvent molecule. Similarly to the Hg^{II} crystal structures, the changes required for metal binding result in a classification of the L16C site being *pre-disposed* for Zn^{II} chelation. Additionally, three non-coordinating water molecules are observed in the structure of Zn^{II}_{S}(**GRCS**L12AL16C)$_3$, very similar to those observed in Hg^{II}_{S}(**GRCS**L12AL16C)$_3$ (Figure 1-9). The waters located close to the helical interface are 3.65 Å from the Zn^{II} ion and 2.43 Å away from the central water molecule. An overlay of Zn^{II}_{S}(**GRCS**L12AL16C)$_3$ and Hg^{II}_{S}(**GRCS**L12AL16C)$_3$ show very similar locations of the water molecules that are close to the helical interface, but a significant discrepancy is observed for the location of the central water molecule, which can be explained by the direct coordination to the Zn^{II} ion but not to the Hg^{II} ion. These results indicate that regardless of ion, Zn^{II} or Hg^{II}, the space introduced in the layer above the Cys_3 site at the 16th position by an L12A substitution is very similar in size and capable of accommodating 4 water molecules.

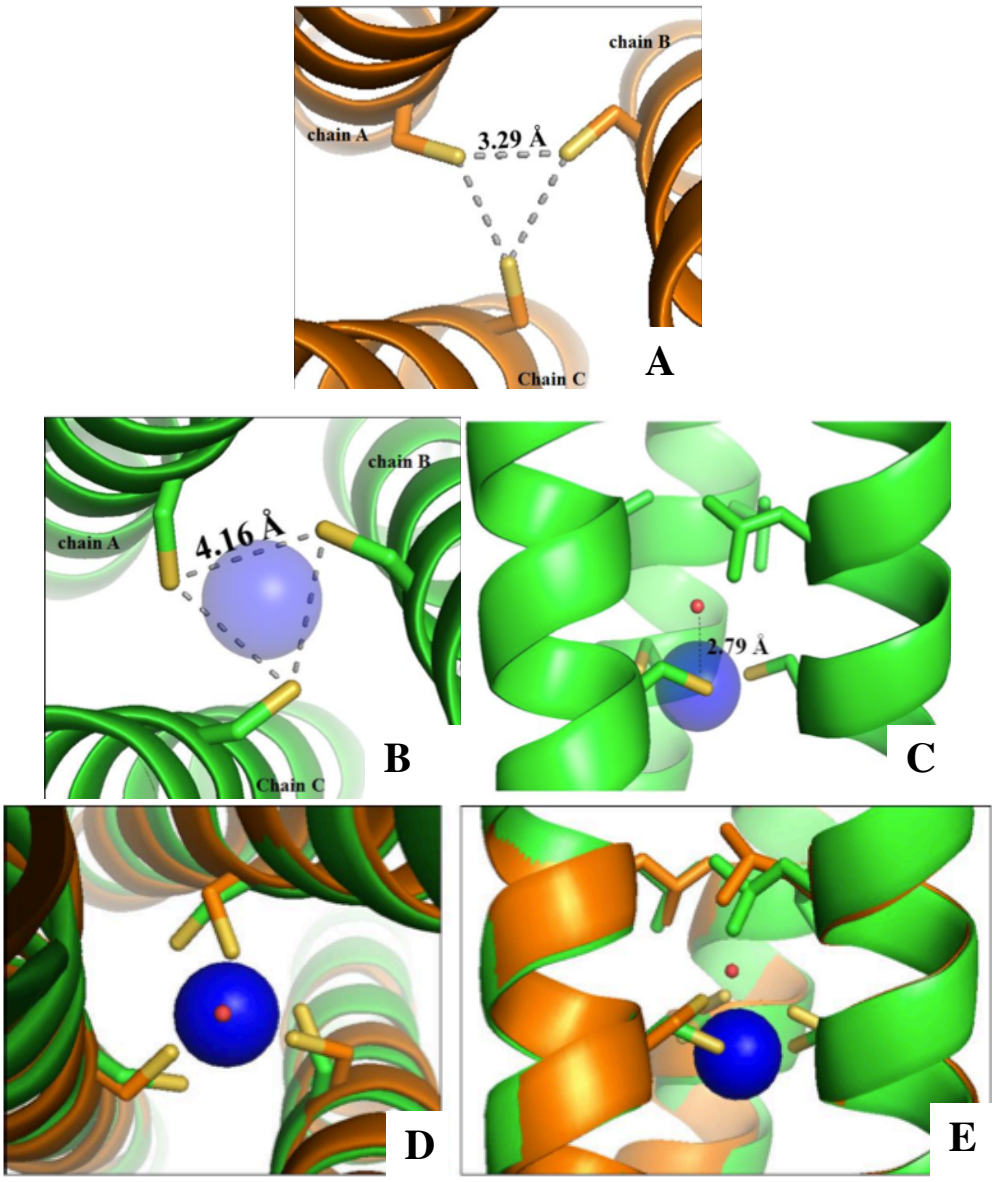

Figure 1-6. Pymol representations of the *pre-disposed* L16C site and resulting Cys_3 perturbations upon Hg^{II} binding. A) Top down view of the major conformers of Cys residues in apo-(**CS**L16C)$_3$. B) Top down and C) side view of the major, bound Cys residues of $Hg^{II}_{S}Zn^{II}_{N}$(**GRCS**L16CL30H)$_3^+$. D) Top and E) side view showing the overlay of apo-(**CS**L16C)$_3$ and $Hg^{II}_{S}Zn^{II}_{N}$(**GRCS**L16CL30H)$_3^+$. Main chains of $Hg^{II}_{S}Zn^{II}_{N}$(**GRCS**L16CL30H)$_3^+$ are shown in green and apo-(**CS**L16C)$_3$ in orange. Cysteine side chains are shown as sticks. Hg^{II} is represented as a blue sphere and the observed water molecule is shown in red. Figure adapted from Reference 29.

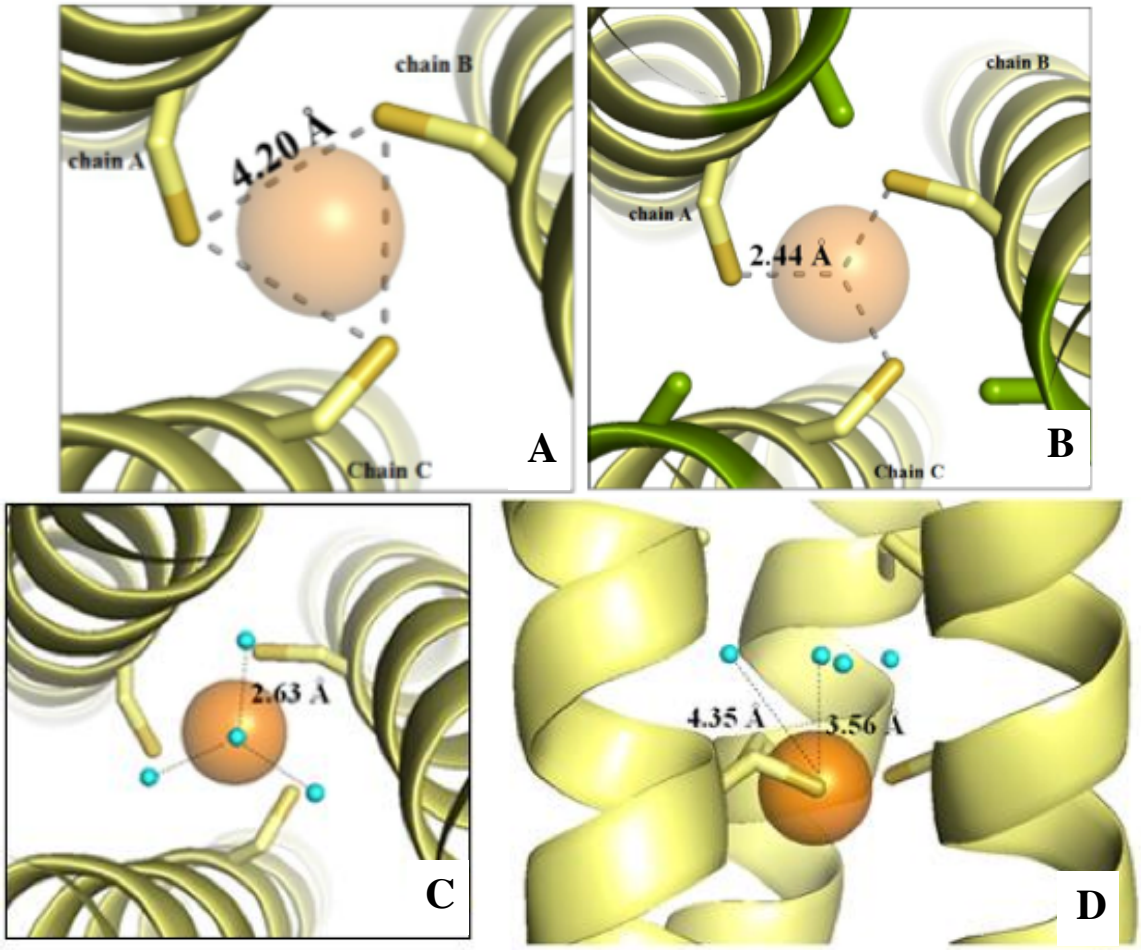

Figure 1-7. Pymol representations of Hg^{II} binding to **GRCS**L12AL16C. Top down view of the major Cys conformers of Hg^{II}_{S}(**GRCS**L12AL16C)$_3^-$ showing A) a 4.2 Å S_γ-S_γ distance and B) a 2.44 Å Hg^{II}-S distance. C) Top down and D) side on views of the water molecules that occupy the space introduced via the L12A substitution. Main chain helices are shown in pale yellow ribbons, 16Cys (sulfur = bright yellow) and 12Ala (green) side chains are present as sticks. The Hg^{II} ion is shown as an orange sphere and the uncoordinated water molecules are represented as blue spheres. Figure adapted from Reference 29.

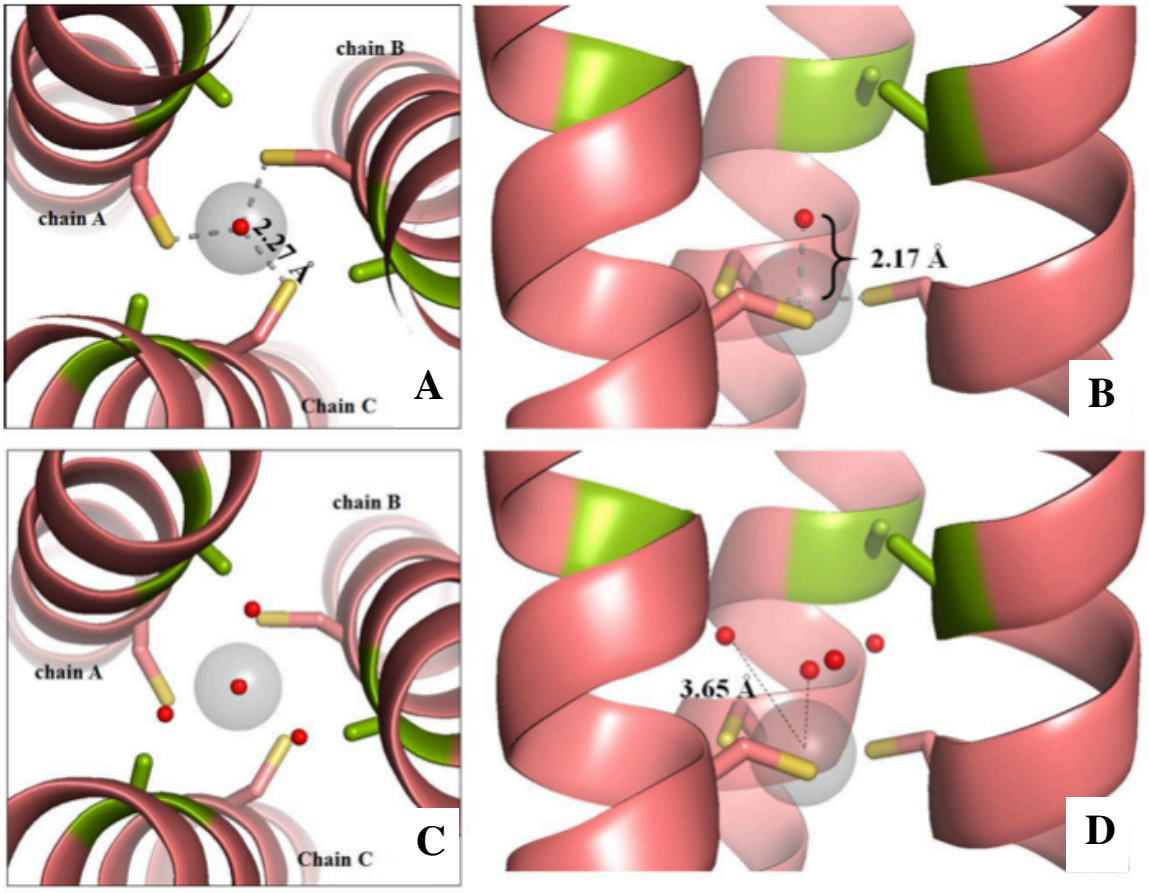

Figure 1-8. Pymol representations of Zn^{II} binding to **GRCS**L12AL16C. A) Top down and B) side on views of the first coordination sphere of the tetrahedral binding site. NOTE: The three uncoordinated waters present above the metal binding site in the crystal structure are omitted from panels A and B for clarity. All water molecules are included in the (C) top down and (D) side on views. Main chain helices are shown as light red ribbons, 16Cys (sulfur = bright yellow) and 12Ala (green) side chains are present as sticks. The Zn^{II} ion is shown as an grey sphere and the water molecules are represented as red spheres. Figure adapted from Reference 29.

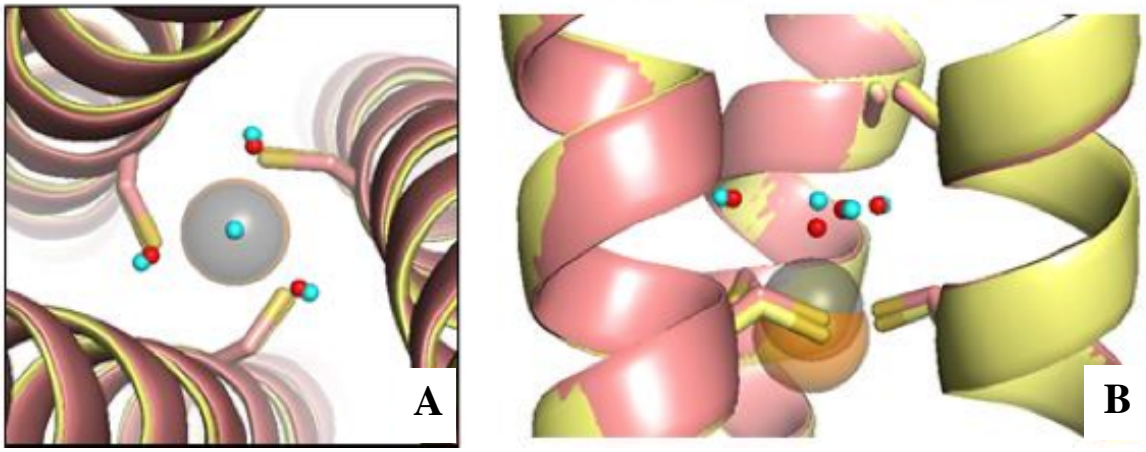

Figure 1-9. Pymol overlay representations comparing Zn^{II} and Hg^{II} binding and surrounding water molecules in **GRCS**L12AL16C. A) Top down and B) side on views of the overlay of Zn^{II}_S(**GRCS**L12AL16C)$_3^-$ and Hg^{II}_S(**GRCS**L12AL16C)$_3^-$ crystal structures (PDB codes not yet deposited). Main chain helices are shown in pale yellow and light red ribbons for the Hg^{II} and Zn^{II} structures, respectively. Sulfur atoms are shown in bright yellow. Cys and Ala residues are represented as sticks. Zn^{II} and Hg^{II} ions are shown in grey and orange, respectively. Water molecules are shown as red and blue for the Zn^{II}_S(**GRCS**L12AL16C)$_3^-$ and Hg^{II}_S(**GRCS**L12AL16C)$_3^-$ structures, respectively. Figure adapted from Reference 29.

Table 1-4. Comparison of apo- and Metallated Crystal Structure Metrical Parameters

	Metal Binding Site*							
	Cys_3				Pen_3		Ala_3/Cys_3	
	apo	Hg^{II}	Pb^{II}	As^{III}	apo	Hg^{II}	Hg^{II}	Zn^{II}
χ1 (°)	-69.20	-151.88	-68.38	-59.66	-49.85	-50.23	-147.85	-146.96
S_γ-S_γ (Å)	3.29	4.16	3.49	3.29	3.71	3.84	4.20	3.94
# of H_2O	-	1	0	0	-	0	4	1**
M-S distance (Å)	-	2.43	2.65	2.28	-	2.21	2.44	
S-M-S angle (°)	-	118.36	82.37		-	119.92	118.74	
Pre-disposed or Pre-organized		*Pre-disposed*	*Pre-organized*	*Pre-organized*		*Pre-organized*	*Pre-disposed*	*Pre-disposed*
Geometry		Trigonal pyramidal	Trigonal planar	Trigonal pyramidal		Trigonal planar	Trigonal planar	Tetrahedral

*All sites included in table are **a** sites. **H_2O molecules is directly coordinated to Zn^{II}. All data from Ref 29.

Interestingly, the preorganization of the metal site differs when comparing apo-(**CS**L16Pen)$_3$[29] to $Hg^{II}_S Zn^{II}_{N/O}$(**CS**L9PenL23H)$_3$[40] crystal structures. While one still observes trigonal coordination of the Hg^{II} ion, there is very little difference observed in the cysteine torsion angles upon binding Hg^{II} to penicillamine (Figure 1-10). In fact, only a slight elongation of the S_γ-S_γ distance of 0.13 Å and a small χ1 angle rotation from

-49.85° to -50.23° is required (Table 1-4). These minimal changes for Hg^{II} binding to a Pen_3 site shows that instead of simply being *pre-disposed*, we now have what is referred to as a *pre-organized* metal binding site. There is a difference in rigidity of the coordinating sulfur atoms between Cys and Pen ligands, likely due to the restriction imposed by the steric bulk of the γ-methyl groups on the rotation of the thiol group about the C_β atom. Indeed, differences are observed between the Hg^{II}-bound Cys_3 and Pen_3 sites. For example the bond distance of Hg^{II}-Pen_3 is 2.21 Å, a decrease in bond length of 0.22 Å when compared to Hg^{II}-Cys_3 (Table 1-4). This indicates that the bulk of the γ-methyl groups reduces the space available in comparison to the Cys_3 binding site. Additionally, the Hg^{II}-bound Pen_3 torsion angle of -50.23° varies drastically from that of Hg^{II}-bound Cys_3 at -151.88°. In all apo-(**CS**L16Pen)$_3$, $Hg^{II}_{S}Zn^{II}_{N/O}$(**CS**L9PenL23H)$_3$, and apo-(**CS**L16C)$_3$ are very similar in structure, but significant differences are observed between these three structures in comparison with $Hg^{II}_{S}Zn^{II}_{N/O}$(**GRCS**L16L30H)$_3$ (Figure 1-10). Therefore, the simple inclusion of methyl groups to Cys to form Pen results in a conversion from a *pre-disposed* to a *pre-organized* thiol-rich $Hg^{II}S_3$ binding site.

Cysteine substituted **GRAND** and **BABY** also bind Hg^{II} in an unprecedented trigonal geometry in water (experimental parameters are consistent with comparable **TRI** peptides).[38,41] The more stable **GRAND** peptides form trigonal Hg^{II} complexes at subnanomolar concentrations putting it on par with MerR. Studies with **BABY**L9C demonstrated how metals can nucleate protein folding.[42] At ten mM, pH 8.5, **BABY**L9C is unfolded. Addition of Hg^{II} associates the peptides forming Hg^{II} (**BABY**L9C)$_2$, matching the Hg^{II} linear structural preference. Because this system was designed to form a 3SCC, a third **BABY**L9C is recruited generating Hg^{II}(**BABY**L9C)$_3$, providing a three-coordinate Hg^{II} ion (Figure 1-11).[42] Thus, initially the metal induces its preferred structure, forcing an incorrect protein aggregation that ultimately rearranges to the desired 3SCC constraining the Hg^{II} into an uncommon geometry.

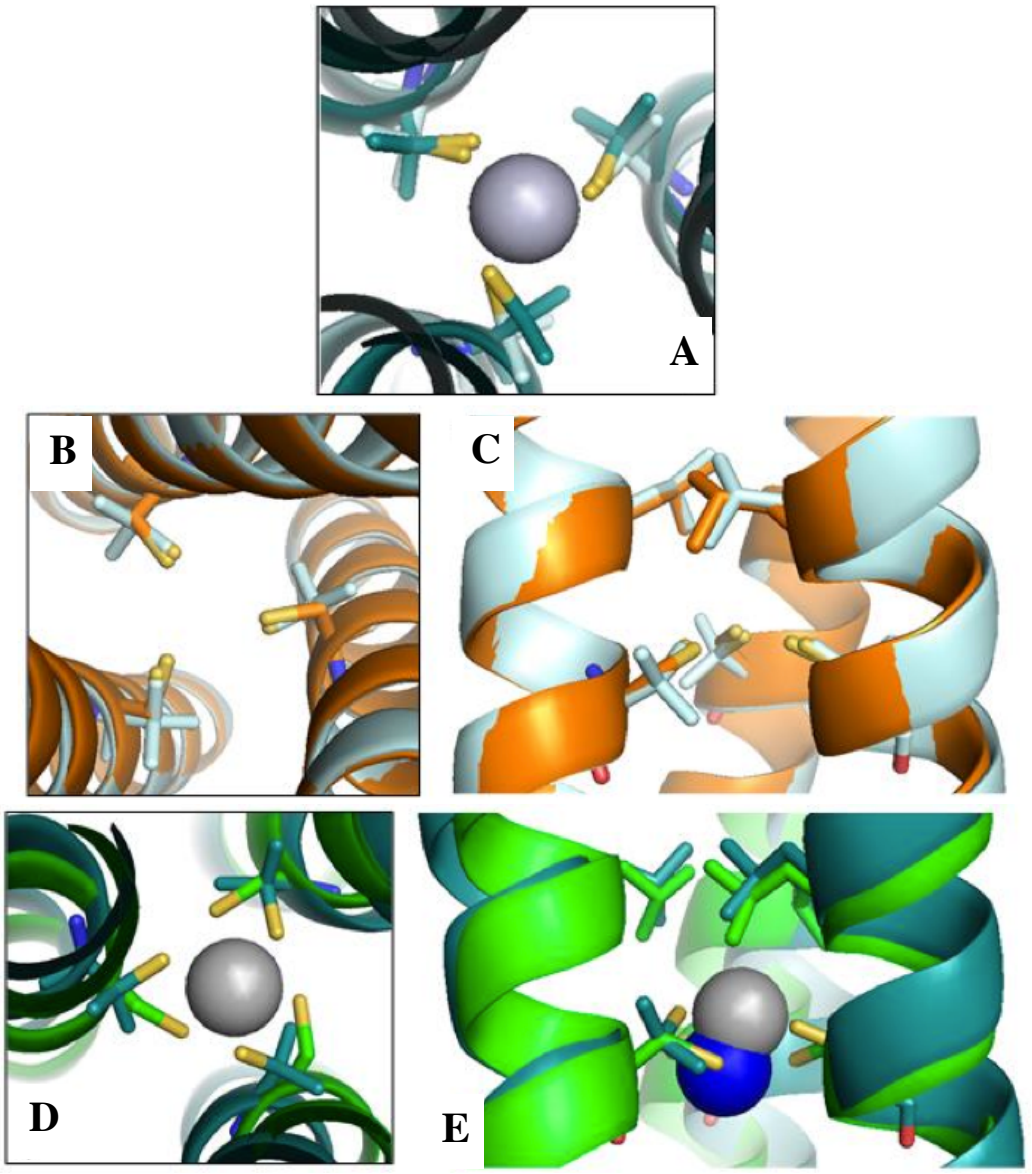

Figure 1-10. Pymol representations of the perturbations of a Pen_3 binding site upon Hg^{II} binding and comparison of Hg^{II} binding to **GRCS**L16CL30H and **CS**L9PenL23H. A) Top down view of an overlay of apo-**CS**L16Pen and $Hg^{II}{}_{S}Zn^{II}{}_{N/O}(OH_2)$(**CS**L9PenL23H)$_3{}^{n+}$.[40] Main atoms are shown as ribbon diagrams in which the apo-structure is in grey and metallated-structure is in cyan, Hg^{II} ion is shown in grey. B) Top down and C) side on view of the overlay of the Cys ligands from apo-(**CS**L16C)$_3$ (shown in orange) and Pen ligands from apo-(**CS**L16Pen)$_3$ (shown in light blue, PDB code: 3H5F).[43] D) Top down view and E) side on view comparing the trigonal structures of $Hg^{II}Cys_3$ from $Hg^{II}{}_{S}Zn^{II}{}_{N}$(**GRCS**L16CL30H)$_3{}^{+}$ (shown in green, Hg^{II} shown in blue) and $Hg^{II}Pen_3$ from $Hg^{II}{}_{S}Zn^{II}{}_{N/O}(OH_2)$(**CS**L9PenL23H)$_3{}^{n+}$ (shown in dark teal, Hg^{II} shown in grey) PDB: 3PBJ). Cys residues are represented as sticks with bright yellow sulfur atoms. Figure adapted from Reference 29.

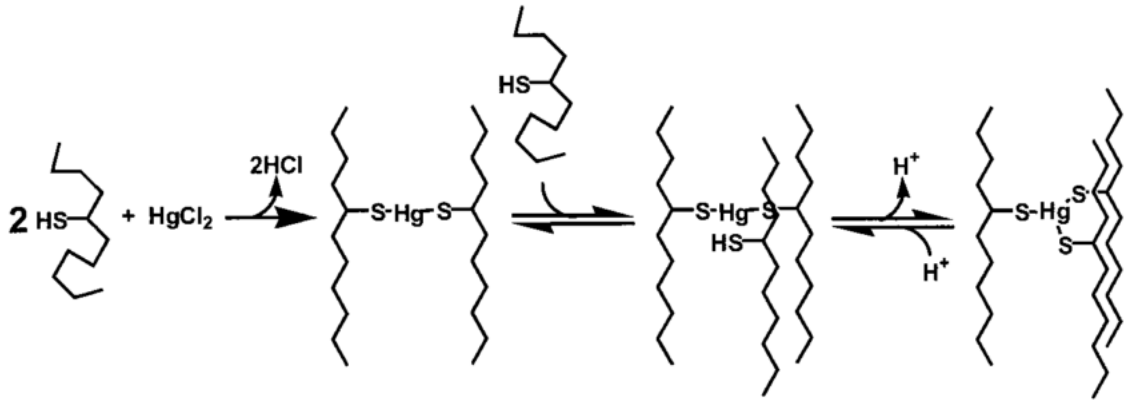

Figure 1-11. Schematic showing the proposed kinetic mechanism for cooperative folding of a three-stranded coiled coil around trigonal thiolato Hg(II) by an unstructured peptide (**Baby**L9C). Figure adapted from Reference 42.

The SmtB/ArsR families of metalloregulators represent an alternative set of multithiolate containing proteins that are responsible for controlling detoxification of heavy metals (e.g., Cd^{II}, As^{III}, and Pb^{II} in bacteria). CadC is a regulator for Cd^{II} detoxification (*Staphylococcus aureus*).[44] CadC has four cysteines that may sequester the metal.[45] Whether Cd^{II} binds to CadC as a tetrathiolate S_4 structure or as an S_3O site with an exogenously bound water has been discussed, providing another synthetic target for protein design. Furthermore, the copper metalloregulator CmtR might bind Cd^{II} in an unprecedented trigonal planar structure[46] providing our next objective, imposing a lower than desired coordination number.

Cd^{II} binding to **TRI**L16C and **TRI**L12C (Table 1-2) at pH 8.5 was explored via EXAFS, UV-Vis, ^{113}Cd NMR and ^{113m}Cd PAC spectroscopies. Similar complexes were formed with Cd^{II} in either ***a*** or ***d*** sites and, as was seen for Hg^{II}, the pK_a's for binding the third cysteine are different at 7.2 and 6.8 (**TRI**L12C and **TRI**L16C, respectively).[47] Because of the ***a*** and ***d*** site similarity, I will focus this discussion on the ***a*** site peptides with respect to Cd^{II} binding. ^{113}Cd NMR and ^{113m}Cd PAC spectroscopies are the most informative techniques for clarifying this system. One ^{113}Cd NMR signal was observed at 625 ppm for **TRI**L16C,[47] which is within the range of previously reported $Cd^{II}S_3$ and $Cd^{II}S_3O$ shifts. However, it was found using ^{113m}Cd PAC spectroscopy (Figure 1-12) that there were two Cd^{II} species present simultaneously, a $Cd^{II}S_3O$ complex (60%, $\omega_0 \approx 0.350$ rad/ns) and a $Cd^{II}S_3$ specie (40%, $\omega_0 \approx 0.450$ rad/ns). The apparently contradictory

speciation is a consequence of different experimental timescales. ^{113}Cd NMR probes the solution at millisecond intervals whereas ^{113m}Cd PAC interrogates the center on the nanosecond regime. Thus, it was concluded that the $Cd^{II}S_3O$ and $Cd^{II}S_3$ forms interconvert rapidly on the NMR, but not the PAC, timescales. Further examination of numerous derivatives, some of which are described below, led to a correlation using ^{113}Cd NMR to quantify the proportion of $Cd^{II}S_3O$ and $Cd^{II}S_3$ in a sample.[48] For ***a*** site peptides, Cd^{II} chemical shifts at ~575 ppm correspond to pure $Cd^{II}S_3O$, whereas $Cd^{II}S_3$ exhibits a single resonance at ~680-700 ppm. This ^{113}Cd NMR correlation allows us to assess whether a pure $Cd^{II}S_3O$ or $Cd^{II}S_3$ species or a mixture is prepared.

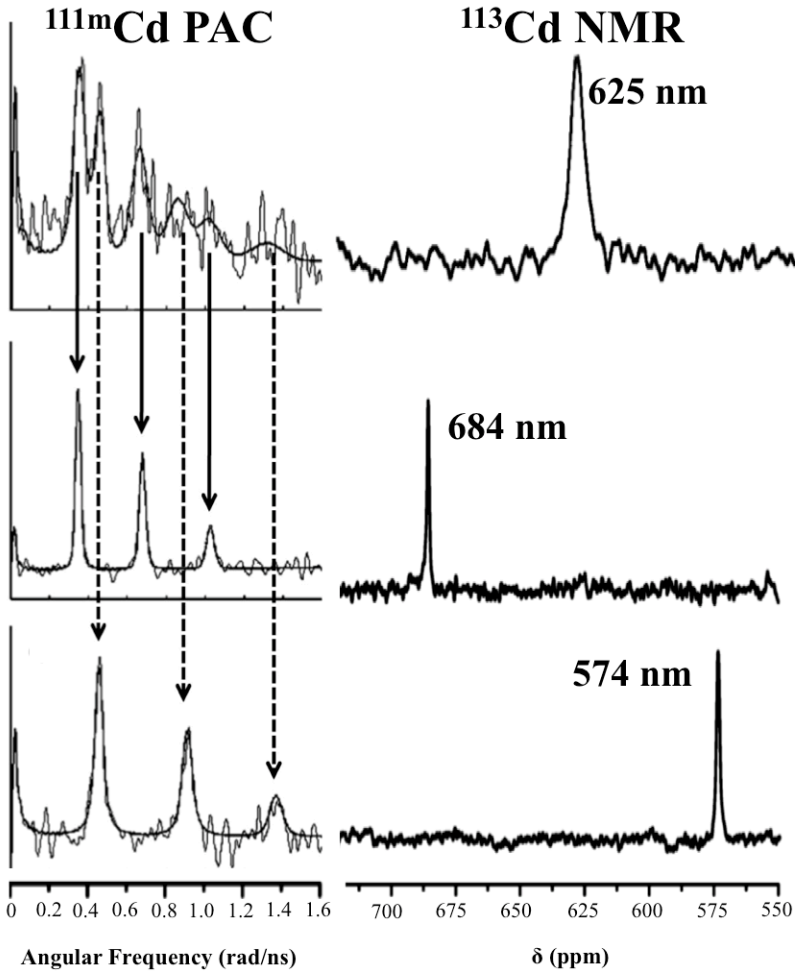

Figure 1-12. ^{111m}Cd PAC and ^{113}Cd NMR spectra of (top row) Cd^{II}_S(**C**SL16C)$_3^-$, (middle row) Cd^{II}_S(**C**SL12AL16C)$_3^-$, and (bottom row) Cd^{II}_S(**C**SL16Pen)$_3^-$. Lines correlate to the $Cd^{II}S_3O$ (solid) and $Cd^{II}S_3$ (dashed) species. Figure adapted from Reference 24.

It was reasoned that a pure $Cd^{II}S_3O$ center would result by removing the sterically constraining leucines in the layer above the cysteines (**TRI**L12AL16C, Table 1-2). The alanine substitution allowed water to enter the cavity above the metal, leading to a compound with 100% $\omega_0 \approx 0.340$ rad/ns and 574 ppm.[49]

Synthesizing the first water soluble $Cd^{II}S_3$ species was more challenging. Ultimately, two different strategies were successful. The first exploited the utilization of a penicillamine ligand, which is bulkier than cysteine, having methyl groups rather than protons at the C-β position (**TRI**L16Pen, Table 1-2). It was hypothesized that the methyl groups would block water from the hydrophobic region above the metal. Addition of Cd^{II} at pH 8.5 to **TRI**L16Pen gave Cd^{II}(**TRI**L16Pen)$_3$ a 100% $Cd^{II}S_3$ complex ($\omega_0 \approx 0.454$ rad/ns, 684 ppm).[49] Crystallographic analysis of apo-(**CS**L16Pen)$_3$ revealed that the geminal methyls on the β-C would not block the bound water.[43] The packing of the leucines in the 12th position also did not become perturbed, so other factors must lead to the desired structure.

Pure $Cd^{II}S_3$ was also achieved by exploiting D-amino acids using **TRI**L12DLL16C (Table 1-2). The reasoning here was that the leucine sidechain orientation shifted toward the metal binding site, blocking water access. Indeed, this hypothesis was correct forming a pure $Cd^{II}S_3$ complex ($\omega_0 \approx 0.456$ rad/ns, 697 ppm).[50] These two examples not only provide the only known synthetic cases where $Cd^{II}S_3$ can be prepared in water, but this was also the first application of using alternative chirality to modify the coordination geometry of a metal in a protein.

Having successfully designed both $Cd^{II}S_3O$ and $Cd^{II}S_3$ binding sites, a new peptide was designed with a single peptide with two distinct cysteine-binding sites capable of complexing Cd^{II} with different affinities or geometries. The relative affinities of Cd^{II} binding to peptides containing either ***a*** or ***d*** Cys sites predicted that the metal could be bound selectively first to the ***a*** position and then ***d***. Preparation of **TRI**L9CL19C confirmed this supposition as one equivalent of Cd^{II} bound exclusively to the L9C (***a*** site), while a second bound to the ***d*** site (Table 1-2, Figure 1-13).[51] Further success was realized when mixtures of Cd^{II} and Pb^{II} were shown to place Pb^{II} in the preferred ***d*** site while Cd^{II} occupied the ***a*** site.[52] From the perspective of molecular recognition and the

development of multicenter designed proteins, these observations were major advancements to the field.

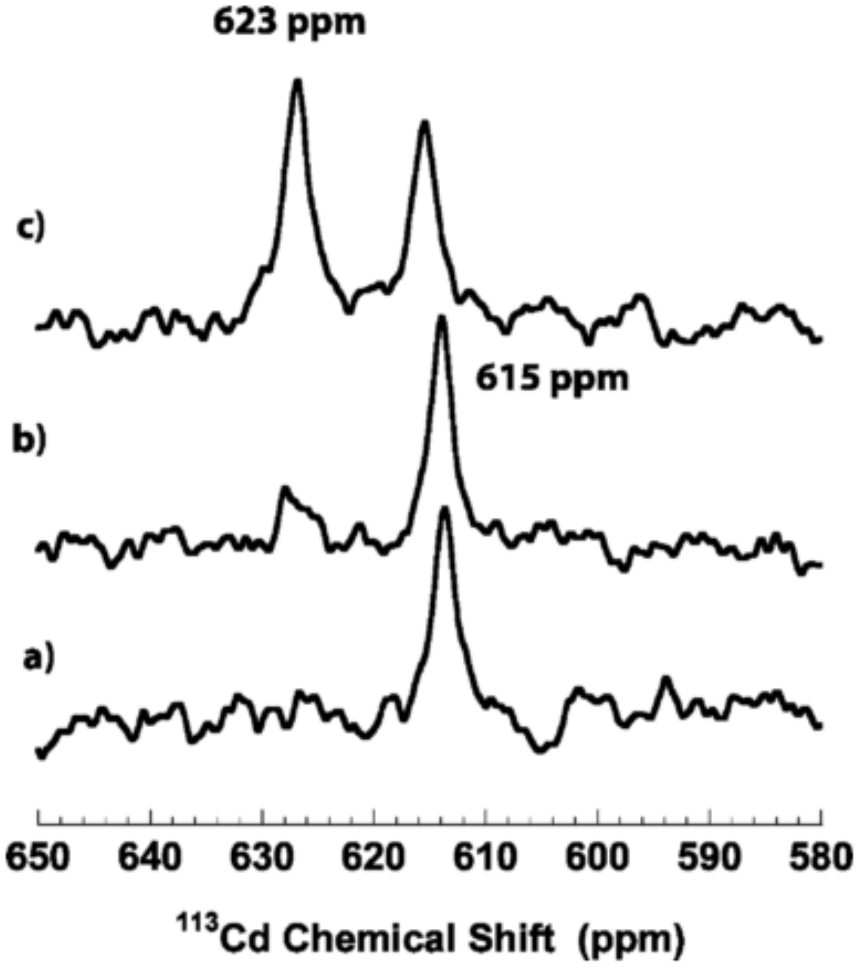

Figure 1-13. ^{113}Cd NMR spectra of 4 mM **TRI**L9CL19C at pH 8.5 with (a) 0.9, (b) 1.1 and (c) 2 equiv of $^{113}CdCl_2$. Figure adapted from Reference 51.

Peptides that could distinguish metals based on coordination number were our next targets. A sequence was designed that contained both an alanine/cysteine site as well as a penicillamine site in a peptide containing an extra heptad in order to retain sufficient aggregate stability. Addition of two equivalents of Cd^{II} to **GR**L16PenL26AL30C (Table 1-2) led to two ^{113}Cd NMR signals at 687 and 588 ppm correlating to the previously characterized $Cd^{II}S_3$ and $Cd^{II}S_3O$ sites.[53] The first equivalent of Cd^{II} bound exclusively to the pseudo-tetrahedral S_3O site, and occupation of the trigonal S_3 site only occurred with a second equivalent of Cd^{II} (Figure 1-14). Therefore, a 3SCC capable of sequestering Cd^{II}

simultaneously in two different geometries was designed exhibiting different affinities and physical properties.

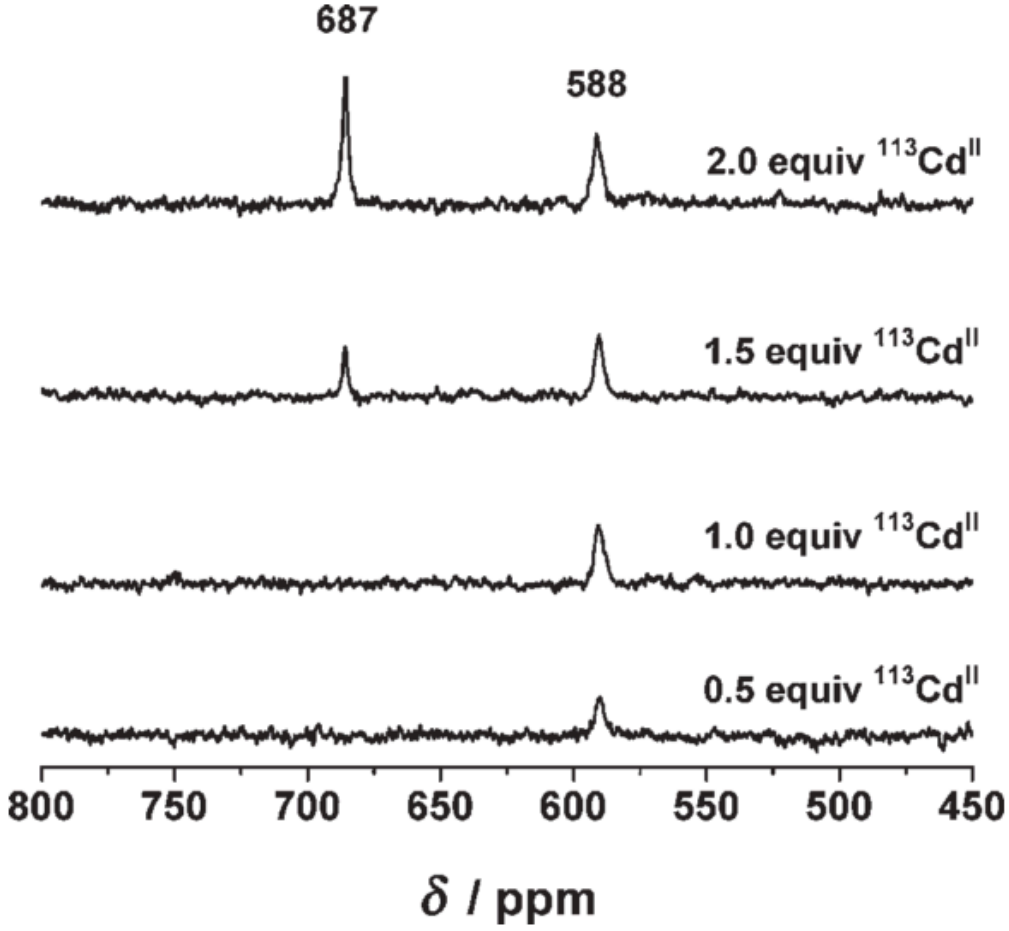

Figure 1-14. ^{113}Cd NMR spectra of solutions containing 2.6 mM trimer **GR**L16PenL26AL30C and different amounts of $^{113}Cd(NO_3)_2$ at pH 9.6. Figure adapted from Reference 53.

Unlike CadC, which forms three- and four-coordinate Cd^{II} structures, ArsR has three cysteine residues that bind As^{III} with three As-S bonds of 2.25Å in a proposed trigonal pyramidal geometry, however, structures of the proteins are unavailable.[54] The crystal structure of $As^{III}_S(\mathbf{CS}L9C)_3$ (1.8 Å resolution[28], Figure 1-15) revealed 2.28 Å As-S bond distances, in close agreement to As^{III}ArsR.[54] This first crystallographic report of $As^{III}S_3$ in a biologically relevant scaffold confirmed a trigonal pyramidal polyhedron, but in an unanticipated *endo*-isomer orienting the stereochemically active lone pair toward the C-terminus. Prior descriptions had assumed an *exo*-structure.[28]

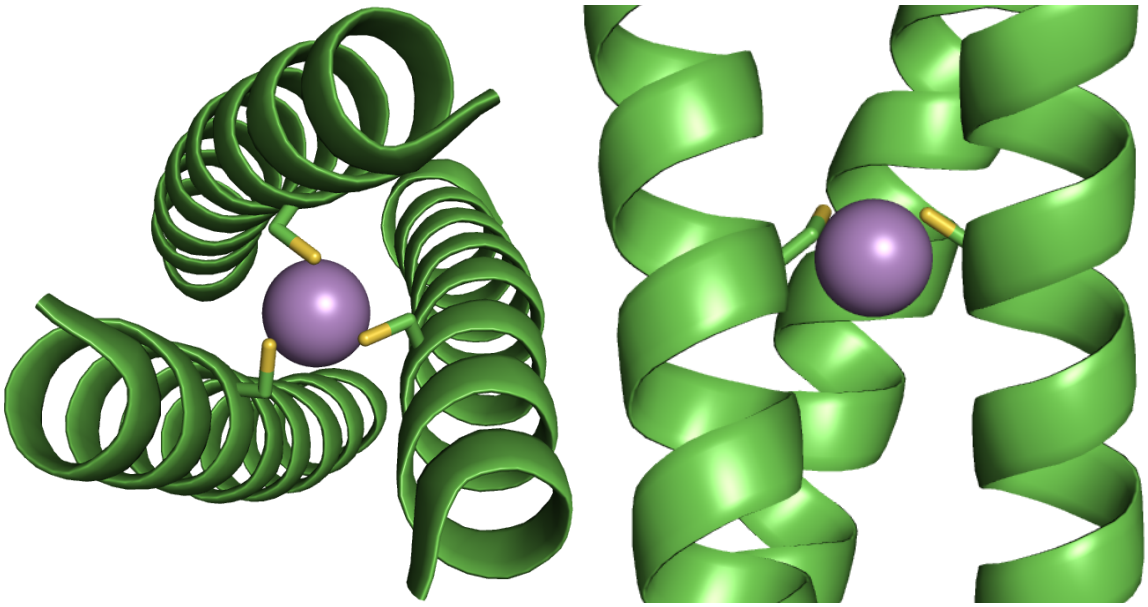

Figure 1-15. (A) Top down and (B) side-on view of pymol representations of trigonal pyramidal coordination in As^{III}_{S}(**CS**L9C)$_3$ (PDB: 2JGO).[28] Main chain atoms are shown as ribbon diagrams in green, cysteine residues are shown as sticks with sulfur ions in bright yellow. The As^{III} ion is shown as a purple sphere.

Lead^{II} can also form hemidirected trigonal pyramidal geometries in proteins such as aminolevulinic acid dehydratase.[55] Because Pb^{II} is larger than As^{III}, one might expect different coordination preferences within the **TRI** peptides. EXAFS analysis of Pb^{II}-**TRI** peptides yielded three 2.63 Å metal-sulfur distances.[56] Computational methods and experiments demonstrated that Pb^{II} prefers binding to ***d*** site cysteines, which provide more space in the interior of the 3SCC in comparison to the ***a*** site cysteines, and the pK_a of **TRI**L16C is higher (pK_a= 6.3) than **TRI**L12C (pK_a= 6.0).[27] This trend is in contrast to Cd^{II} and Hg^{II}. Thus, one can conceive of distinguishing metal sites based on differential cysteine substitution at the ***a*** or ***d*** layers. The first report of a ^{207}Pb NMR chemical shift for the $Pb^{II}(SR)_3$ chromophore was achieved using Pb^{II}-**TRI** peptides. This technique is astoundingly sensitive as changing the Cys residue from ***a*** to ***d*** sites or altering the sterics around the Pb^{II} results in NMR shifts of >200 ppm (Figure 1-16).[57]

Recently, a crystal structure of $Pb^{II}_{S}Zn^{II}_{N}$(**GRCS**L16CL30H)$_3$ was collected and refined to 2.17Å.[29] Comparison to apo-(**CS**L16C)$_3$ provides minimal expansion of the S_γ-S_γ distance of only 0.2Å and minimal rotation of the χ1 angles from -69.20° to -68.38° upon Pb^{II} binding, indicating the L16C site is *pre-organized* for Pb^{II} binding (Figure 1-

17, Table 1-4). Additionally, the Pb^{II} ion coordinates in a trigonal pyramidal geometry and the metal ion sits below the plane of the cysteine methyl groups (1.69Å) confirming an *endo*-configuration of Pb^{II} binding. This geometry and *endo*-configuration were previously observed with the $As^{III}_S(\mathbf{CS}L9C)_3$ crystal structure. In both cases the bulky and hemi-directed lone pairs of both As^{III} and Pb^{II} point down toward the C-terminus of the 3SCC. Closer examination of the As^{III} structure provides S_γ-S_γ distances of 3.29Å and χ1 angles -59.66°, similar to the values for apo-$(\mathbf{CS}L9C)_3$ of 3.22Å and -70.57° (Table 1-4). The larger discrepancy observed, when considering As^{III} binding in comparison to Pb^{II} binding, of the χ1 angles is assumed to be due to the smaller size of the As^{III} ion. However, in both cases, while As^{III} and Pb^{II} binding are not identical, these structures show that Cys_3 **a** sites (such as L16C and L9C) are *pre-organized* for the binding of trigonal pyramidal ions such as Pb^{II} and As^{III}. This observation is independent of ion charge or size.

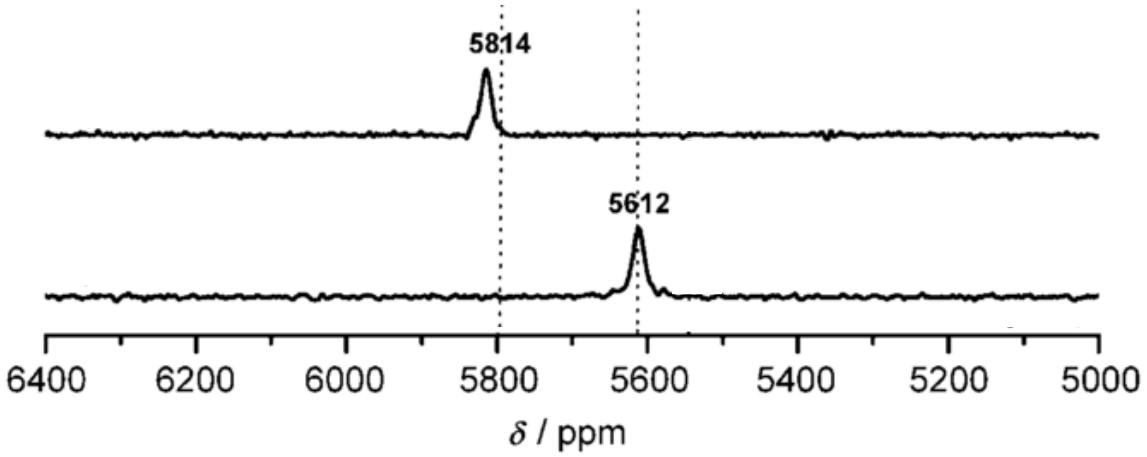

Figure 1-16. Natural-abundance ^{207}Pb NMR spectra (104.435 MHz) of Pb^{II}-bound three-stranded coiled coil peptides (10-12 mM); $Pb^{II}_S(\mathbf{CS}L12C)_3^-$ (top) and $Pb^{II}_S(\mathbf{CS}L16C)_3^-$ (bottom). Figure adapted from Reference 57.

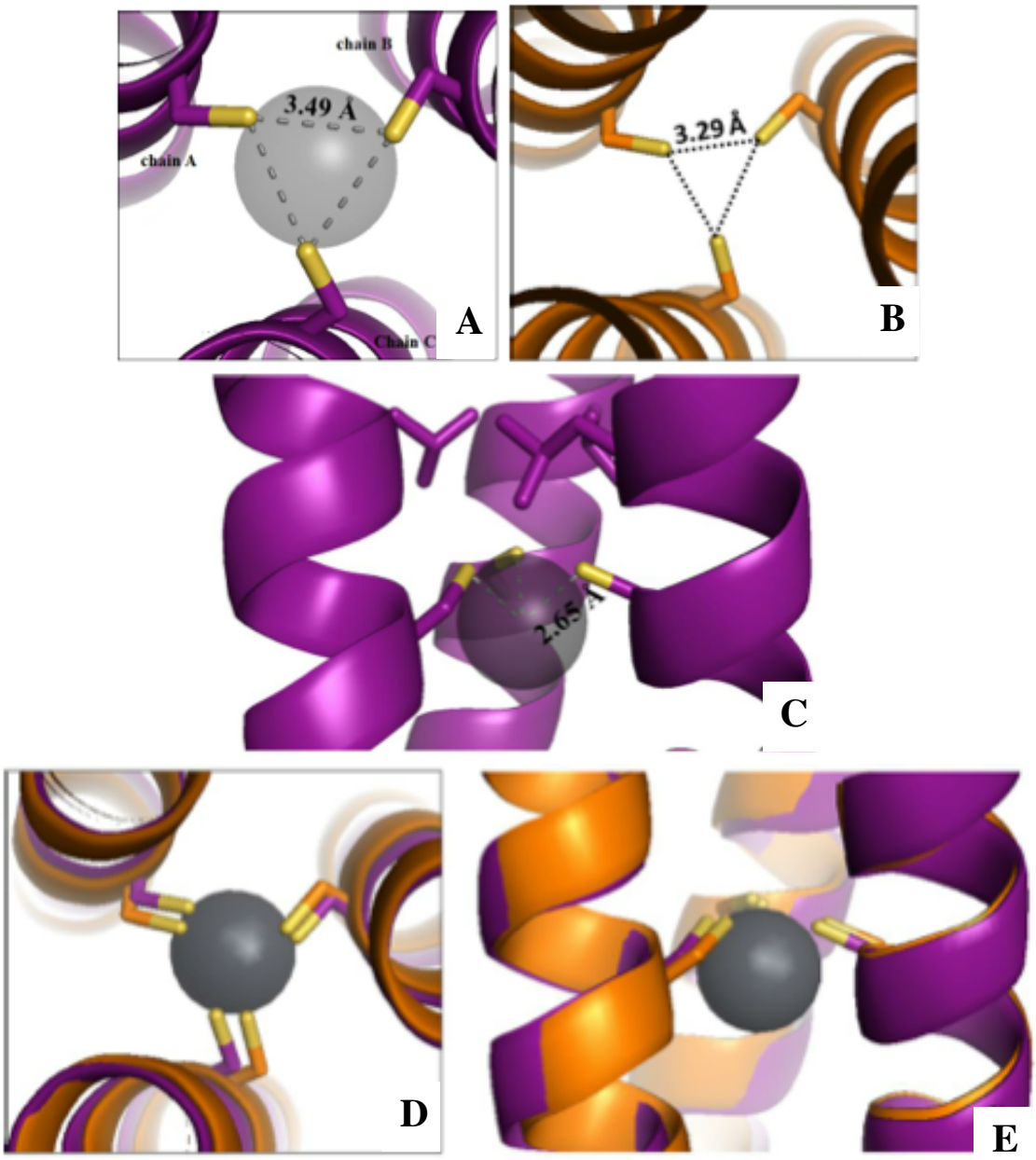

Figure 1-17. Pymol representation of trigonal pyramidal coordination in $Pb^{II}_{S}Zn^{II}_{N}$(**GRCS**L16CL30H)$_3^+$ and comparison with apo-(**CS**L16C)$_3$. Top down view from the N-termini of the $Pb^{II}Cys_3$ (A) and apo-Cys_3 (B) site showing a slight expansion of S_γ-S_γ distance from 3.29 to 3.49 Å upon Pb^{II} binding. C) Side on view of $Pb^{II}Cys_3$ showing endo-conformation and a Pb^{II}-S distance of 2.65 Å. D) Top down from the N-termini and E) side on view of the overly of $Pb^{II}_{S}Zn^{II}_{N}$(**GRCS**L16CL30H)$_3^+$ and apo-(**CS**L16C)$_3$ showing the *pre-organization* of L16C sites for Pb^{II} binding. Main chain atoms are shown as ribbon diagrams in purple (Pb^{II} structure) and orange (apo-structure), 12Leu and 16Cys side chains are shown as sticks with sulfur ions in bright yellow. The Pb^{II} ion is shown as a grey sphere. Figure adapted from Reference 29.

Therefore, Cys_3 sites within our 3SCC are pre-organized for Pb^{II} and As^{III} binding yet *pre-disposed* for binding of Zn^{II} or Hg^{II}. Considering the trend of atomic radii of As^{III} ~ Zn^{II} < Hg^{II} < Pb^{II}, it is clear that *pre-organization* or *pre-disposition* for metal binding is not dependent on metal ion size. However, it seems that *pre-organization* or *pre-disposition* for metal binding correlates, instead, to metal binding geometry. That is, when a metal binds in a trigonal pyramidal geometry as found with Pb^{II} and As^{III} to our Cys_3 sites, minimal perturbations are observed in the cysteine ligand torsion angles indicating that the apoprotein is *pre-organized for metal binding*. Interestingly, this is also observed when Hg^{II} binds to a Pen_3 site, suggesting that the packing of the extra methyl groups also influences the *pre-disposition* or *pre-organization* of the site. However, when metals bind to the Cys_3 site in a trigonal planar or pseudo-tetrahedral geometry, as with Hg^{II} and Zn^{II}, significant perturbations of the cysteine ligands are observed suggesting the site is *pre-disposed* for metals that bind with these geometries.

Water molecules are not observed in neither the case of $Pb^{II}_{S}Zn^{II}_{N}$(**GRCS**L16CL30H)$_3$ nor As^{III}_{S}(**CS**L9C)$_3$. Therefore, it appears that when the Cys_3 site is *pre-organized* for metal binding the structure does not contain an interior water molecule, but when the Cys_3 site is *pre-disposed* for metal binding the structure contains at least one water molecule. This indicates that the *pre-organized* orientation of the sulfur ligands results in less space between the 16Cys layer and the 12Leu layer as compared to the *pre-disposed* orientation of the Cys residues. This observation is again independent of ion charge or size.

However, there is a significant difference in the size of Pb^{II} vs As^{III}, and since this is not accommodated for in the layer above the Cys_3 binding site, it must be accommodated for in the layer below. Indeed, when the Leu packing is analyzed in the 19th position, the layer below the Cys_3 binding site, a change is observed between the Pb^{II} and As^{III} crystal structures (Figure 1-18). This is interesting since, as mentioned above, the space available between the 16th and 19th position (***a*** to ***d*** site) is smaller than that between the 12th and 16th position (***d*** to ***a*** site). This indicates that when a site is *pre-organized* for metal binding of a trigonal pyramidal geometry the energy requirement for rotating the Cys_3 ligands is greater than that required to alter the packing of the Leu

residues in the 19th position, ultimately resulting in the changing of the conformations of the Leu residues. For my dissertation work, $Pb^{II}Cys_3$ binding sites are incorporated into 3SCC in combination with steric matching of surrounding hydrophobic residues to obtain asymmetric 3SCC (*vide infra*).

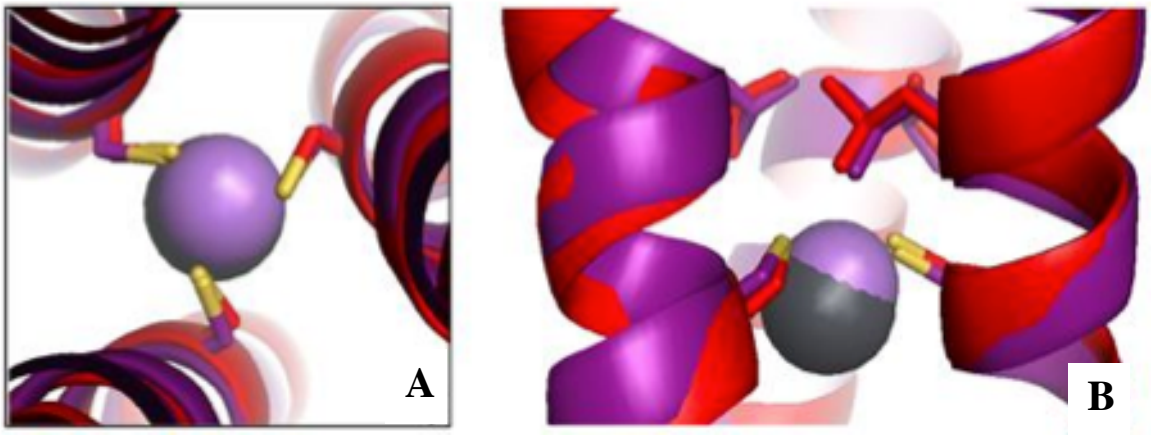

Figure 1-18. Pymol representations of the overlay of $Pb^{II}_{S}Zn^{II}_{N}$(**GRCS**L16CL30H)$_3^+$ and As^{III}_{S}(**CS**L9C)$_3$ (PDB: 2JGO).[28] A) Top down from the N-termini and B) side on view of the Cys_3 binding site. Main chains are shown in purple and red for the Pb^{II} and As^{III} structures, respectively. Pb^{II} and As^{III} ions are shown in grey and purple spheres, respectively. Cysteine residues are shown as sticks and sulfur atoms are shown in bright yellow. Figure adapted from Reference 29.

Clearly, significant understandings of factors that define protein-metal interactions were achieved using the **TRI** and **GR** peptides. Metal ions can be placed within environments that match their coordination preferences (Pb^{II}, As^{III}), or that impose higher (Hg^{II}) or lower (Cd^{II}) coordination numbers. Furthermore, one can now differentiate binding of metals at sites within a protein based on coordination preference, coordination number or ion type. However, a current and significant limitation of using the **TRI** and **GR** families of peptides is the inherent symmetry obtained by the self-assembling nature of the 3SCC. Therefore, the first goal of my dissertation, as detailed in Chapter 2, is to selectively obtain quantitatively asymmetric, or heterotrimeric, 3SCC using a $Pb^{II}Cys_3$ binding site in combination with steric matching of hydrophobic residues in the helical layers directly adjacent to the Pb^{II} binding site.

One strategy to incorporate asymmetry utilized in the Pecoraro lab is to employ a single polypeptide chain that can be site specifically mutated to generate channels or

acid-base catalysts. An appealing system is α_3D, a 3HB from the DeGrado laboratory.[58] α_3D (Table 1-2) was optimized to have a helix-turn-helix-turn-helix motif. Computational modeling suggested four sites where three cysteine residues could replace hydrophobes. The fourth model, a_3D**IV** (Table 1-2) was chosen as the test peptide to assess heavy metal binding (Figure 1-19). Comparison of the NMR structures of α_3D and α_3D**IV** reveal a *pre-disposed* metal binding site for Hg^{II} binding upon replacement of three leucines with cysteines with little perturbation of the scaffold (one cysteine residue must rearrange to bind Hg^{II}, Figure 1-19).[59,60] Metal complexation was strong and led to higher protein stability with Hg^{II} bound as a three coordinate complex, probably T-shaped, while Pb^{II} adopted a trigonal pyramidal geometry. Cd^{II} adopted two structures $Cd^{II}S_3O$ or $Cd^{II}S_3N$, with either coordinated water or His72, respectively.[60]

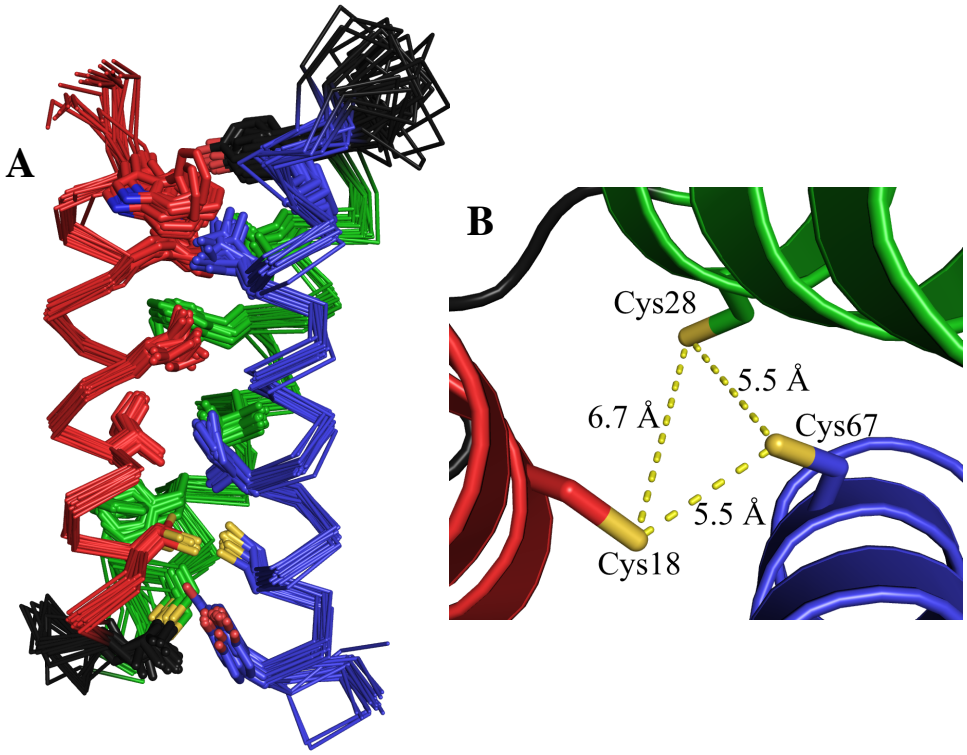

Figure 1-19: Pymol representation of a_3D**IV**. A) The twenty lowest energy NMR structures of α_3D**IV**, a single polypeptide chain 3HB and B) close up of the metal Cys_3 binding site in α_3D**IV**.[59]

Numerous attempts at obtaining selective and quantitative *parallel* asymmetric 3SCC have been reported. There are two possible heterotrimeric arrangements when forming asymmetric 3SCC, depending on the identities of the three independent helices. For instance, one helix can be changed to obtain a trimer with two of the same helices and one different, denoted as an AAB heterotrimer. Or, one could attempt to design a heterotrimer with all three helices being different, affording an ABC heterotrimer.

Nautiyal and Alber used a combination of positive and negative design principles to promote formation of heterotrimeric assemblies based solely on the ionic interactions at the helical interfaces.[61] The utilization of both positive and negative design promoted maximal complementary interhelical salt-bridging interactions in heterotrimeric scaffolds and would result in charge repulsion if symmetric homotrimers were formed. Jalan *et al.* also used both negative and positive design to form heterotrimeric assemblies with varying collagen peptides based on helical charge pairing based on register alignment (Figure 1-20).[62] Diss and Kennan used similar charge pairing between helicies as well as buried urea groups within the hydrophobic core of the 3SCC to promote formation of heterotrimers (Figure 1-20).[63] LeBruin *et al.* appended bidentate 2,2'-bipyridyl ligands to the end of collagen helices that induce heterotrimer formation upon octahedral binding of Ni^{II}.[64] All of these examples promoted formation of ABC heterotrimers (Figure 1-20).

ABB and ABC heterotrimers have been obtained in both the Keenan and Tanaka labs using a steric matching approach. Schnarr and Keenan initially obtained an AAB heterotrimer by pairing a bulky non-natural amino acid, cyclohexylanlanine (CHA) with small alanine residues. When only one layer is substituted, an AAB heterotrimer is formed but is not significantly more stable than the corresponding homotrimers.[65] When included in three alternating layers along the helical axis a selective ABC heterotrimer was obtained (Figure 1-21).[66] Concurrently, Tanaka and coworkers combined steric matching of one bulky tryptophan and two smaller alanine residues; however, when only this steric matching layer was utilized both the AAB heterotrimer and BBB homotrimer were observed.[67] To destabilize homotrimer formation and promote heterotrimer formation, they then combined the Ala_2Trp matching with electrostatic alterations on the exterior of the helices to obtain pure, and stable heterotrimeric mixtures.[68]

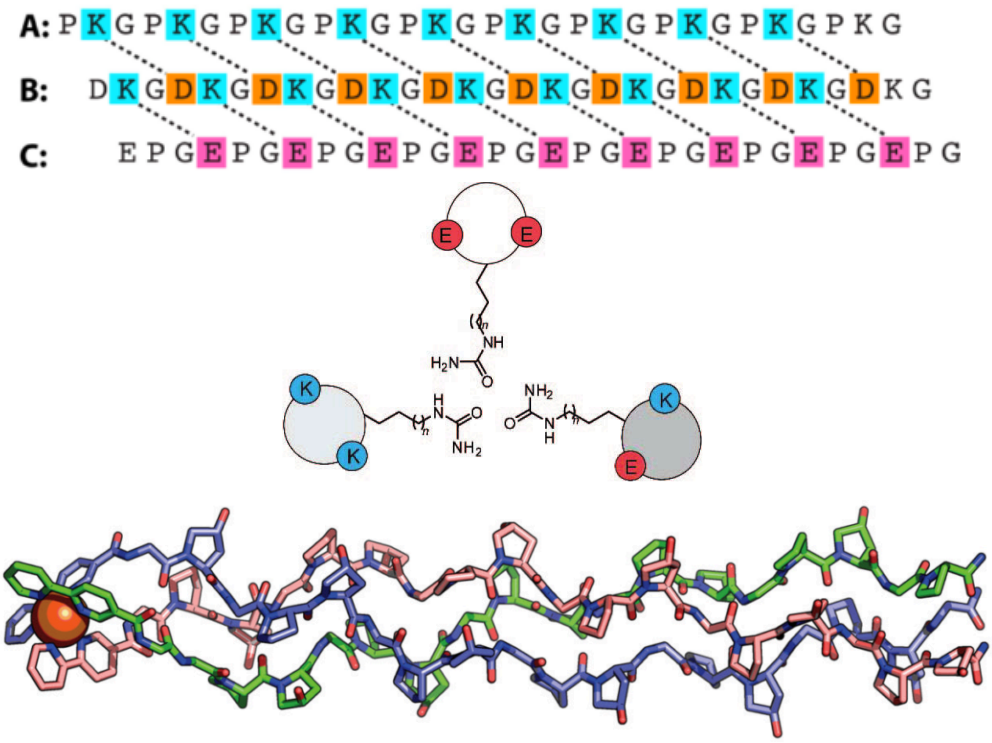

Figure 1-20. Schematics showing previous techniques for obtaining heterotrimeric 3SCC systems. Top: Schematic illustration of hydroxyproline-free ABC heterotrimer composed of $(PKG)_{10}$, $(DKG)_{10}$, and $(EPG)_{10}$ peptides electrostatically stabilized through multiple lysine-aspartate and lysine-glutamate salt bridges.[62] Schematic representing ABC heterotrimer with varying charged residues in the salt bridging positions to promote maximal ion pairing to form a parallel heterotrimer as well as the buried varying core polar residues.[63] Bottom: Computer-generated model of the Ni^{II}-assembled Ni:c1:c2:c3 heterotrimer. C1: bpy-GPOGPOGPOGPOGPOGPO-NH_2. C2: bpy-GGPOGPOGPOGPOGPOGPOGP-NH_2. C3: bpy-GOGPOGPOGPOGPOGPOG-NH_2.[64]

Thus far, interior bound metals have not been used to nucleate heterotrimeric formation. *Moreover, asymmetric scaffolds have never been used to generate asymmetric metal binding sites with potential catalytic activity.* Therefore, the primary goal of Chapter 2 of my dissertation is to combine steric matching of natural amino acids in combination with a Pb^{II} binding site to nucleate specific formation of a parallel A_2B type heterotrimer. This approach will require no changes in exterior residues or salt-bridging interactions and will only require two neighboring layers within the helices for selective formation, instead of altering layers throughout the entire scaffold, therefore leaving space within the scaffold for a second metal binding site. The ability to use an asymmetric scaffold to generate a second, asymmetric, and potentially catalytic, site will

be discussed more below. I will utilize multiple spectroscopic techniques to study the symmetry of the trimers with respect to the $Pb^{II}Cys_3$ binding site. I will discuss how the presence of a transition metal, for binding to a second metal binding site elsewhere in the scaffold, should have a lower affinity for the Cys_3 site than Pb^{II} as not to distrupt the heterotrimer specificity. Primarily, ^{207}Pb NMR will be used to analyze the difference between homotrimer and heterotrimer formation. I will also discuss how the identity of the heavy metal used to obtain heterotrimeric systems is important and how switching to Hg^{II} from Pb^{II} allows for formation of heterotrimeric systems with less than ideal selectivity.

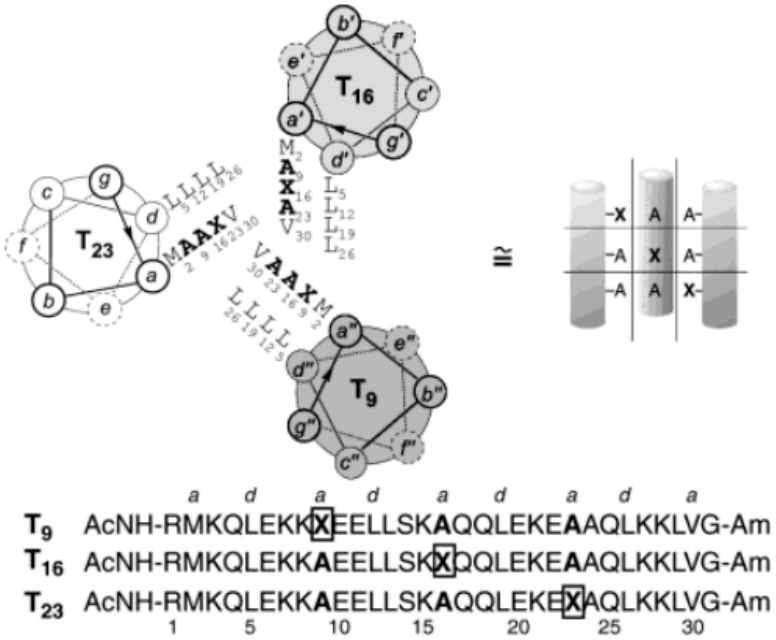

Figure 1-21. Helical wheel projection of the 1:1:1 $T_9/T_{16}/T_{23}$ complex (viewed down the helical axis from the N to C terminus), showing only core residues. The sequence of each peptide is also given. The tic-tac-toe arrangement of cyclohexylalanine residues (X) is depicted schematically at the right. Ac = acetyl and Am = amide. Figure adapted from Ref 62.

Concurrent with my thesis work, a crystal structure of Pb^{II}_S(**GRCS**L12AL16C)$_3^-$ was solved and refined by Dr. Leela Ruckthong. I will discuss the implications of how the metal binds within this structure in comparison to Pb^{II}_S(**GRCS**L16CL30H)$_3^-$, and how these observations may give shed some light onto the formation of Pb^{II}-bound heterotrimers and why different spectroscopic characteristics are observed. I will also

discuss how the location of the Ala/Leu pairing with respect to the Cys_3 binding site effects heterotrimer formation.

Transition Metal Binding to 3SCC, Spectroscopic Analysis of Second, Asymmetric Metal Binding Sites

After achieving control of heavy metal coordination chemistry, the Pecoraro laboratory embarked on defining the structure and environment surrounding transition metals with the intention of generating new catalysis and redox centers. Many non-heme metal centers in proteins utilize imidazole ligands. This presented a new concern for designing catalytic centers. Could far larger residues, such as histidine, be incorporated within the hydrophobic interior of 3SCC without disrupting the assembly? Our first system, **TRI**L9CL23H, exploited our ability to incorporate metals into 3SCC site selectively. At the N-terminal end of the construct, a high affinity binding site for Hg^{II} was designed using the existing cysteine methodology to confer additional aggregate stability. Guanidinium denaturation titrations demonstrated that $Hg^{II}Cys_3$ served this function.[25] A second substitution at Leu23 with histidine yielded a His_3 catalytic binding site offering a structural model of Carbonic Anhydrase (CA). The 23rd position was chosen since it was an ***a*** site that was located away from the center of the sequence to minimize steric disruption of the 3SCC, but not at the ends of the sequence to obtain a more structured binding site. CA has a His_3 coordination sphere in a b-sheet rich domain that binds Zn^{II} in a pseudo-tetrahedral environment with a fourth exogenous water ligand (Figure 1-22).[69]

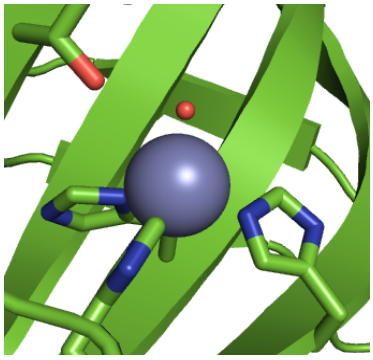

Figure 1-22. Pymol representation of the active site of Carbonic Anhydrase (PDB: 2CBA)[70] showing the primary His_3 Zn^{II}-binding site with an exogenous H_2O/OH^- ligand. Also shown is Thr199, a secondary sphere ligand shown to play an important role in catalysis.

The construct, $Hg^{II}_{S}Zn^{II}_{N/O}(OH_2)$(**TRI**L9CL23H)$_3$, allowed us to address two fundamental issues in bioinorganic chemistry. First, could a catalytic metal center found in a b-sheet structure be constructed within an entirely a-helical domain? Second, if such a structural match occurred, would such a center be competent to catalyze the native reaction? Spectroscopic studies (^{199}Hg NMR, UV-Vis) proved that a trigonal Hg^{II} was correctly formed. Ultimately, a crystal structure of $Hg^{II}_{S}Zn^{II}(OH_2)_{N/O}$(**CS**L9PenL23H)$_3^{n+}$ was obtained and refined to 2.2Å resolution (Figure 1-23). The model showed excellent overlay in the primary coordination sphere to the crystal structure of CA, with Zn-N and Zn-O distances within experimental error (Figure 1-24).[40] Therefore, imidazole is well accommodated within the 3SCC, Zn^{II} and Hg^{II} bind exclusively to their intended binding sites, Hg^{II} behaved as a structural site providing additional stability against denaturation and a CA like $Zn^{II}His_3$/water site was viable in a drastically different protein fold.

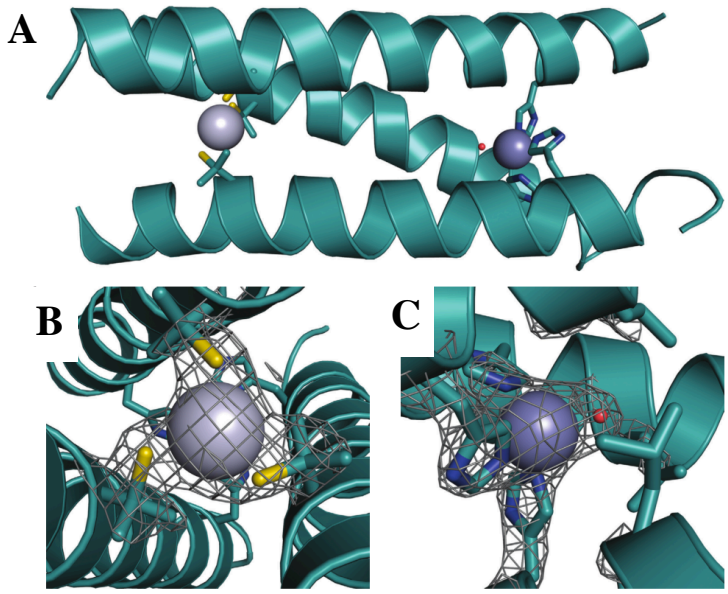

Figure 1-23. Ribbon diagrams of the $Hg^{II}_{S}Zn^{II}(OH_2)_{N/O}$(**C**S**L**9Pen**L**23H)$_3^{n+}$ parallel 3SCC (one of two different three-helix bundles present in the asymmetric unit) at pH 8.5. Shown are the main chain atoms represented as helical ribbons (cyan) and the Pen and His side chains in stick form (sulfur = yellow, nitrogen = blue, oxygen = red). **A**. One of two trimers found in the asymmetric unit of the crystal structure. **B**. Top-down view of the structural trigonal thiolate site, $Hg^{II}S_3$, confirming the proposed structure of Hg^{II} in Cys-containing **TRI** peptides. This metal site should mimic well the structural site in metalloregulatory protein MerR. **C**. Side view of the tetrahedral catalytic site, $Zn^{II}His_3O$, which closely mimics carbonic anhydrase and matrix metalloproteinase active sites. All figures shown are 2Fo-Fc electron density contoured at 1.5σ overlaid. Figure adapted from Ref 40.

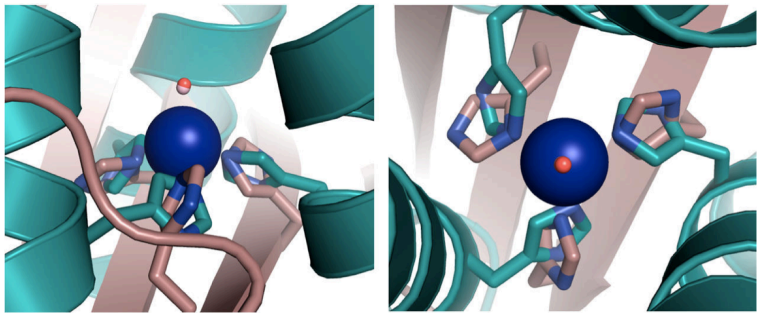

Figure 1-24. Overlay of the $Zn^{II}His_3O$ site in $Hg^{II}_{S}Zn^{II}(OH_2)_{N/O}$(**C**S**L**9Pen**L**23H)$_3^{n+}$ (teal, PDB: 3PBJ) with the active site of human CAII (tan, PDB: 2CBA). Left: Side-on view of the overlay with CAII. The solvent molecule (from PDB 3PBJ) is shown in red. Right: Top-down view of the overlay with CAII. The model displays an excellent structural overlay for the first coordination sphere atoms with CAII; however, the orientation of the imidazoles differs between the two proteins. Another subtle difference is that the present structure has three ε amino nitrogens bound to the Zn(II) ion, whereas CAII has a mixed two ε and one δ coordination sphere. Figure adapted from Ref 40.

The reaction catalyzed by CA is essentially diffusion limited hydration of CO_2 to bicarbonate and water.[71,72] Ester hydrolysis, via a similar mechanism as CO_2 hydration (Zn^{II}-OH nucelophilic attack), is often analyzed due to the significantly slower reaction times. When reported, $Hg^{II}_{S}Zn^{II}(OH)_{N/O}$(**TRI**L9CL23H)$_3$ was the fastest CA mimic of *p*-nitrophenolacetate *(p*NPA) hydrolysis with a k_{cat}/K_M of 23.3 $M^{-1}s^{-1}$ at pH 9.5, only ~100-fold slower than native CAII, and was a 550-fold increase over other small molecule mimics.[40,72,73] Access of small molecule substrates is viewed to be via breathing modes of the protein scaffold at the helical interface.[74] The pK_a=9.0 was two log units higher than that reported for CAII (pK_a = 6.8).[75,76] Two other designed Zn^{II} enzymes have since been reported that have faster *p*NPA hydrolysis rates.[77,78] However, to date *$Hg^{II}_{S}Zn^{II}(OH)_{N/O}$(**TRI**L9CL23H)$_3$ is still the fastest reported CA mimic for the native CO_2 hydration reaction with a rate of 1.8 x 10^5 $M^{-1}s^{-1}$ at pH 9.5*. This system is 430-fold faster than the best previously reported small molecule mimic reacting solely in water and only ~370-fold slower than the fastest CA, CAII.[71,72,79] Thus $Hg^{II}_{S}Zn^{II}(OH)_{N/O}$(**TRI**L9CL23H)$_3^{n+}$ is a fantastic structural model of CA and the first reported *de novo* designed peptide that rivaled the rates of catalysis of a native enzyme. This first generation construct sought to mimic only the first coordination sphere of CAII and did not provide residues to facilitate acid-base catalysis. Interestingly, CA mutants that delete a specific active site threonine have catalytic efficiencies 100-fold lower and a water pK_a ~8.8.[80,81] Our work clearly shows that, within 2 log units, the native protein fold is not essential for catalytic activity and that including an acid-base catalyst could confer the missing activity and altered pH dependence.

Dr. Melissa Zastrow determined whether the catalytic efficiency of our CA mimic depended on the position of the Zn^{II} site within the 3SCC. First, **TRI**L9CL23H was inverted to **TRI**L9HL23C (Table 1-2, Figure 1-25B), which yielded a *p*NPA activity of 15.5 $M^{-1}s^{-1}$, 67% of the $Hg^{II}_{S}Zn^{II}(OH)_{N/O}$(**TRI**L9CL23H)$_3^{n+}$ activity.[74] Next, she examined how changing from an ***a*** to a ***d*** His_3 site would affect the rates. The second peptide left the L9C position untouched but moved the His_3 to the 19th position (**TRI**L9CL19H, Table 1-2, Figure 1-25C). This peptide showed slightly less activity, 13.9 $M^{-1}s^{-1}$, 60% in comparison to $Hg^{II}_{S}Zn^{II}(OH)_{N/O}$(**TRI**L9CL23H)$_3^{n+}$. Finally, a peptide only containing Zn^{II} was prepared (**TRI**L23H, Table 1-2), which was stable and showed that

the Hg^{II} did not influence enzymatic activity. Additionally the kinetic pK_a's of these constructs were 9.2, a slight increase over the parent peptide (pK_a = 9.0). These studies show that Hg^{II} could be removed from the design and that the His_3 site can be relocated across the peptide scaffold without diminishing activity or altering pK_a's. Improvement on the current activity will require the design of second coordination sphere modifications, such as acid-base catalysts.

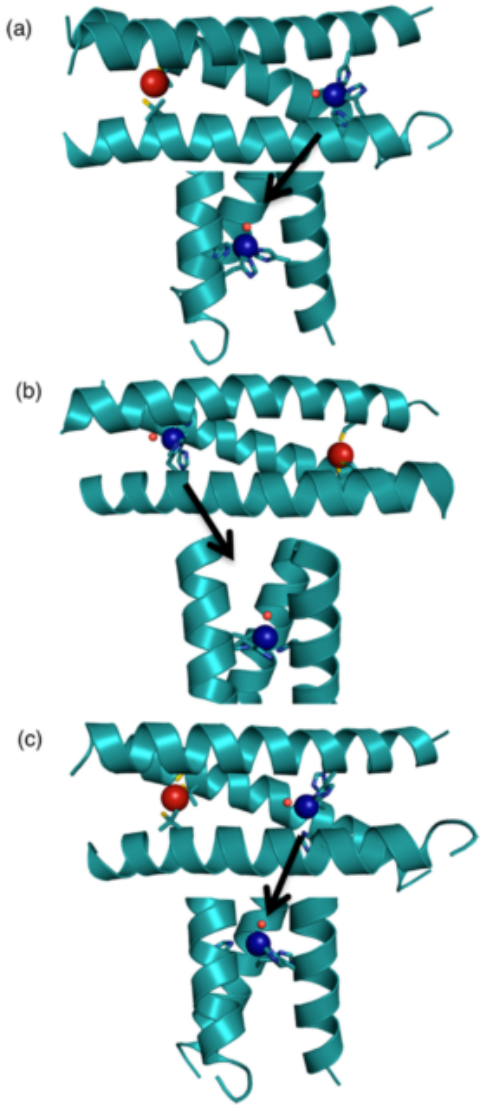

Figure 1-25. Comparison of the X-ray crystal structure of (a) $Hg^{II}_{S}Zn^{II}(OH_2)_{N/O}$(**CS**L9PenL23H)$_3^{n+}$ (PDB: 3PBJ) with Pymol models of (b) $Hg^{II}_{S}Zn^{II}(OH_2)_{N/O}$(**TRI**L9HL23C)$_3^{n+}$ based on the coordinates of 2JGO[28] and (c) $Hg^{II}_{S}Zn^{II}(OH_2)_{N/O}$(**CS**L9CL19H)$_3^{n+}$ based on the coordinates of 3PBJ.[40] Models were prepared in Pymol using the mutagenesis option and Pymol's rotamer library. Figure adapted from Ref 74.

Some of the most interesting bioinorganic systems complete redox catalysis. From a synthetic perspective, such a scaffold is far more difficult to prepare than for hydrolytic chemistry as one must control the coordination environment of the metal in at least two oxidation states. Copper nitrite reductase, CuNiR, contains a type 2 copper binding site where copper, not unlike Zn^{II} in CA, is coordinated to three histidine residues and an exogenous water molecule (Figure 1-26).[82] Once the crystal structure of $Hg^{II}_{S}Zn^{II}(OH_2)_{N/O}$(**CS**L9PenL23H)$_3^{n+}$ was obtained it was hypothesized that $Cu^{I/II}$ may bind in a similar fashion to offer a structural and functional model of CuNiR (Figure 1-27). Due to the potential redox sensitivity of thiols, **TRI**L23H was used since it was previously determined that $Hg^{II}S_3$ was not required for stability and did not influence catalysis (Table 1-2). Spectroscopic examination supports a five-coordinate Cu^{II} structure with three bound imidazoles.[83] The reduced Cu^{I} state has been interrogated by ^{1}H NMR and XAS, indicating that a trigonal planar Cu^{I} structure forms from pH 5.8-7.5. Thus, neither copper oxidation state fully reflects the present structural model for CuNiR.

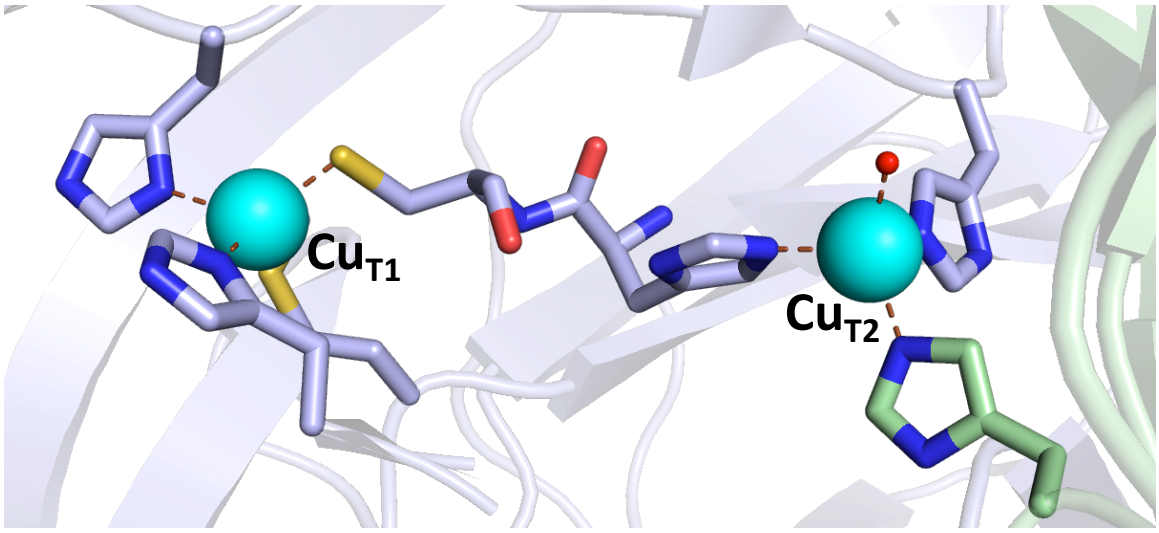

Figure 1-26. Active site of Copper nitrite reductase, CuNiR. CuNiR carries out the dissimilatory reduction of nitrite to nitric oxide and has both a type 1 and type 2 copper center in the active site. The Cu ion in the T2 center, where catalysis occurs, is coordinated by three histidine ligands and an exogenous water molecule. The Cu ion in the T1 center, where the electron transfer occurs, is coordinated by two histidine residues, one cysteine residue and one methionine residue. Figure adapted from Ref 84.

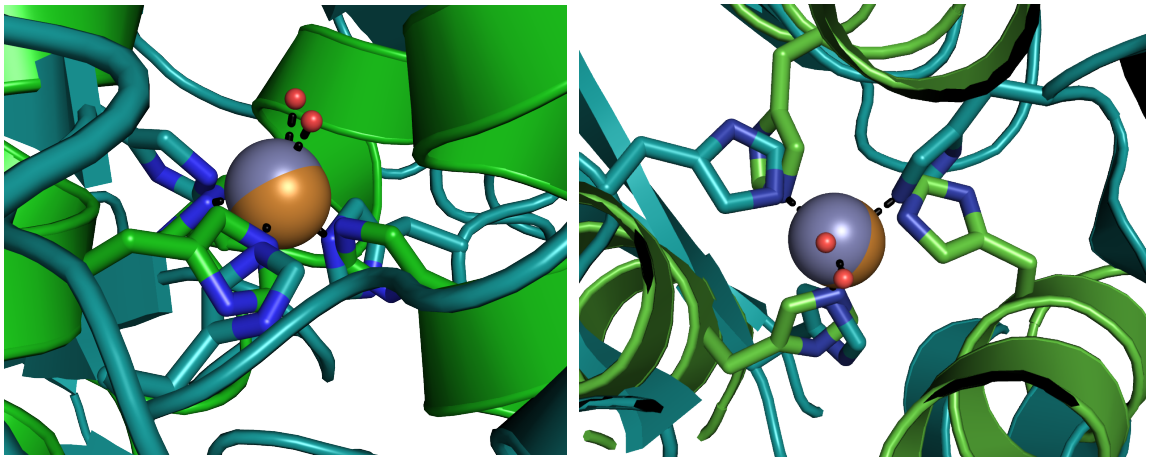

Figure 1-27. Overlay of the $Zn^{II}N_3O$ site in $Hg^{II}_SZn^{II}(OH_2)_{N/O}$(**CS**L9PenL23H)$_3^{n+}$ with the active site of Copper Nitrite Reductase (CuNiR, PDB: 2DY2).[85] $Hg^{II}_SZn^{II}_{O/N}$(**CS**L9PenL23H)$_3^{+}$ is shown in green (PDB 3PBJ)[40] and CuNiR in teal (PDB 2DY2). Left: Side-on view of the overlay with CuNiR. The solvent molecules are shown in red. Right: Top-down view of the overlay with CuNiR. The model displays an excellent structural overlay for the first coordination sphere atoms with CuNiR; however, the orientation of the imidazoles differs between the two proteins. Overlay was performed manually in Pymol.

An important parameter for any redox cofactor is its reduction potential. Using fluorescence quenching and UV-Vis spectroscopy, the binding affinities of both Cu^I and Cu^{II} to (**TRI**L23H)$_3$ were determined and then standard reduction potentials calculated. Values of ~400-500 mV were obtained, slightly higher than that reported for CuNiR (140-310 mV) suggesting that the trigonal planar Cu^I state stabilizes the reduced Cu^I(**TRI**L23H)$_3^{n+}$.[85] This system was quantitatively reduced from Cu^{II} to Cu^I by sodium ascorbate and produces NO when Cu^I is reacted with nitrite. Like CuNiR, the reaction is pH dependent with a maximal rate at pH 5.9 (5.2×10^{-4} s^{-1}). Although significantly less than CuNiR (~1,500 s^{-1} at pH 5.8), Cu^I(**TRI**L23H)$_3^{n+}$ is the only stable and most highly active aqueous, homogeneous mimic for the native enzyme.[86]

The electrostatics surrounding the metal binding site can greatly affect the center's redox potential. Dr. Fanging Yu re-designed $Cu^{I/II}$(**TRI**L23H)$_3$ to alter charged residues on the exterior of the 3SCC in hopes of optimizing both redox potential and catalytic efficiency (Figure 1-28). Inverting the K22 and E27 residues, (**TRI**K22EL23HE27K, Table 1-2), enhanced Cu^I affinity (100-fold) and a increased the rate 1.5-fold.[87] Additional peptides were designed keeping the K22E mutation but altered

other lysine or glutamate residues, changing the charge of the trimer from 0 to -3, -6, -9 and -12; however, all of these charge-modified peptides resulted in more positive reduction potentials (490-500 mV). These data demonstrated that surface mutations influence the reduction potential over a 100 mV range and the reaction rate by a factor of four. Recent studies show that altering the layer directly above the His_3 site from a Leu layer to an Ala layer, or an Ile layer, results in a 70-fold increase over the parent peptide (Figure 1-29).[88]

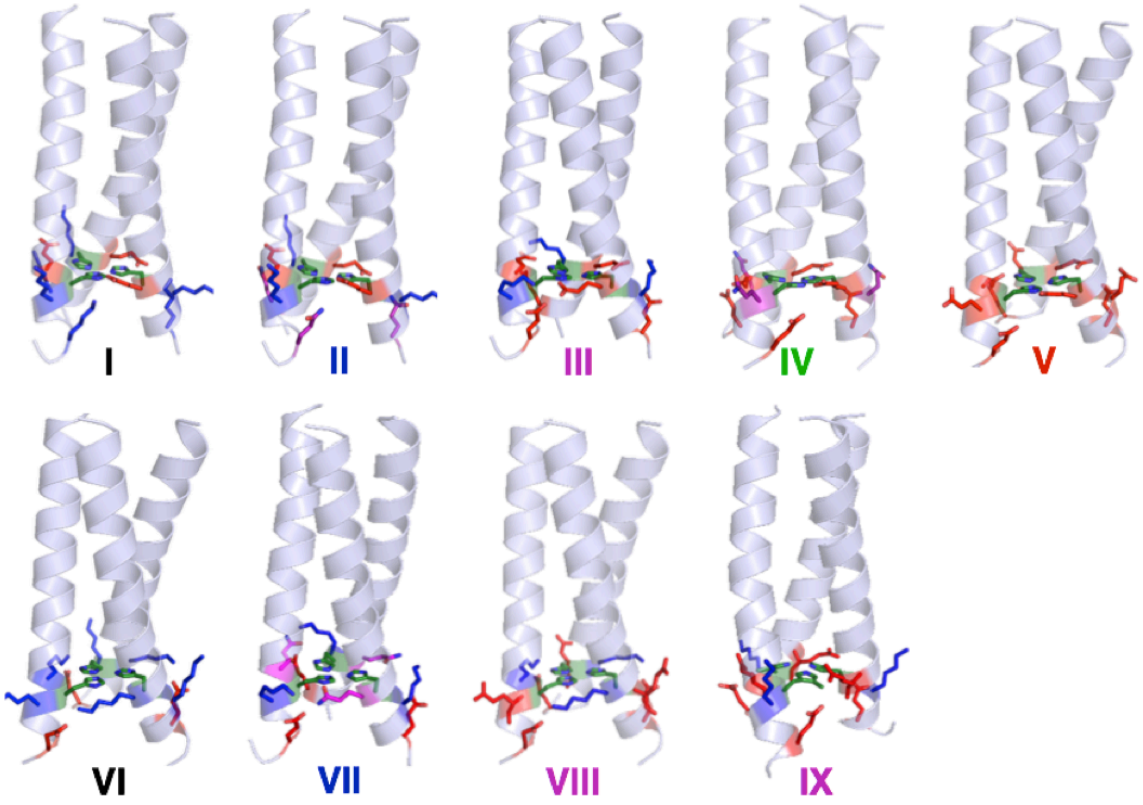

Figure 1-28. Pymol models of the re-designed $Cu^{I/II}$(**TRI**L23H)$_3^{n+}$ with altered exterior charged residues. I. **TRI**W-EHE27K; II. **TRI**W-EHE27Q; III. **TRI**W-EH; IV. **TRI**W-EHK24Q; V. **TRI**W-EHK24E; VI. **TRI**W-H; VII. **TRI**W-HK22Q; VIII. **TRI**W-HK24E; IX. **TRI**W-E_MH. These models are made based on the crystal structure of $Hg^{II}{}_SZn^{II}(OH_2)_{N/O}$(**CS**L9PenL23H)$_3^{n+}$ (PDB code: 3PBJ). Residues are color-coded by charge; red: negative, blue: positive, neutral: purple. The same color texts (I-IX) represent the same Δ_{charge}. Going from the left to right, Δ_{charge} is 0. -3. -6, -9, and -12 in a neutral pH range. Figure adapted from Ref 84.

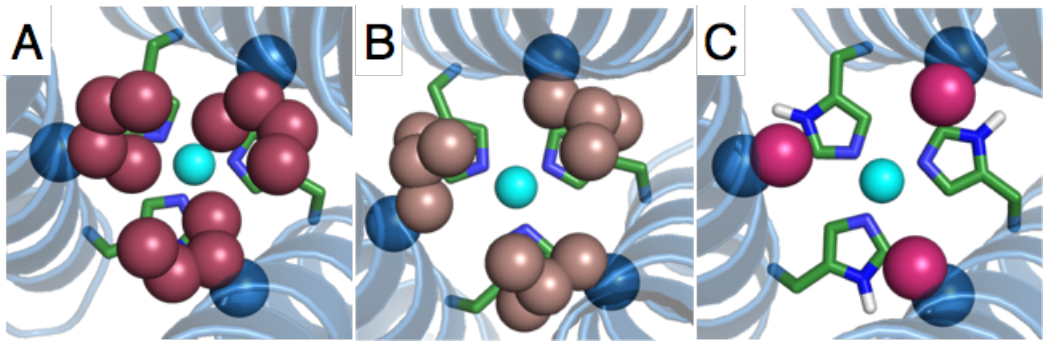

Figure 1-29. PyMol models of (A) ILE19, (B) LEU19, and (C) ALA19 showing the change of steric packing above the copper center. The PyMol models were made based on the crystal structure of $Zn^{II}_{N}Hg^{II}_{S}$(**CS**L9PenL23H)$_3^+$ (PDB code: 3PBJ)[40]. Cyan spheres: Cu^{I}. Peptide strands are represented by helices and His23 side chains are represented by sticks. Residues at the 19th position are shown in spheres to illustrate the space-filling above the copper center. Cu^{I} is represented in cyan spheres and nitrogen atoms are highlighted in blue. Figure adapted from Ref 88.

It can be concluded, from these catalytic studies, that major advances in preparing water soluble and stable catalysts can be realized using metalloprotein design. Furthermore, *metal coordination geometries can be recapitulated in dramatically different protein folds*. None-the-less, there are major challenges for further synthetic development. We must learn how to place acid-base catalysts in defined orientations within the helical assembly. In some cases, substrate, water and proton channels are important for catalysis, yet we still do not have a method to mimic such structures in these scaffolds. In order to broaden the range of catalytic sites, one must generate non-symmetric scaffolds that allow for mixed first and second coordination spheres.

As discussed above, CA and NiR, have symmetric primary coordination environments with pseudo 3-fold symmetry that fit nicely into the **TRI**/**GR** family of 3SCC. However, in both cases secondary coordination ligands, and residues even farther away (up to 15 Å in CAII)[89], play vital roles in functionality. In particular, CA has a secondary acid/base catalyst, Thr199, that when substituted for Ala results in a 100-fold decrease in activity.[80,81] A previous graduate student, Dr. Melissa Zastrow, designed a series of peptides in order to incorporate an acid/base catalyst in close proximity to the $Zn^{II}His_3$ site of $Hg^{II}_{S}Zn^{II}(OH)_{N/O}$(**TRI**L9CL23H)$_3^{n+}$ in hopes of mimicing the Thr199 ligand of CA. It should be reiterated that at this point all changes introduce into our **TRI** and **GR** peptides are introduced in a three-fold, symmetric fashion.

The first attempt to introduce an acid/base catalyst was to simply include a Thr residue in the layer directly above the His_3 site, yielding **TRI**L9CL19TL23H (Table 1-2). This peptide did not fold well even with the stabilizing $Hg^{II}Cys_3$ site, and only had a catalytic efficieny of 35% of the original, $Hg^{II}_{S}Zn^{II}(OH)_{N/O}$(**TRI**L9CL23H)$_3^{n+}$, mimic towards *p*NPA hydrolysis.[90] The sequence was then elongated to **GR**L16CL26TL30H (Table 1-2) to take advantage of the additional stability introduced by the longer **GR** peptide. This peptide showed much improved folding (~90% alpha-helical in the absence and presence of Hg^{II}). However, the catalytic efficiency of $Hg^{II}_{S}Zn^{II}(OH)_{N/O}$(**GR**L16CL26TL30H)$_3^{n+}$ is only 14.8 $M^{-1}s^{-1}$ (pH 9.5) for *p*NPA hydrolysis, 66% of the original mimic. This decrease in activity indicated that simply including a Thr residue within close proximity of the His_3 site didn't induce a positive change in the catalytic rate. It was hypothesized that this decrease in rate is actually due to the elongation of the peptide scaffold from **TRI** to **GR**, which is probably due to the slower breathing motion of the peptide and subsequent decreased substrate accessibility to the Zn^{II} binding site ($Hg^{II}_{S}Zn^{II}(OH)_{N/O}$(**GR**L2WL16CL30H)$_3^{n+}$ has a catalytic efficiency of 18.5 $M^{-1}s^{-1}$ at pH 9.5, approximately 80% of the original **TRI** mimic). The fact that the rate did not increase, even with the addition of the Thr residue in $Hg^{II}_{S}Zn^{II}(OH)_{N/O}$(**GR**L16CL26TL30H)$_3^{n+}$, is probably due to a less than ideal orientation of the Thr rotamers within the 3SCC, where the hydroxyl group may have rotated to the exterior of the helical interface with the methyl group facing the hydrophobic interior (Figure 1-30).

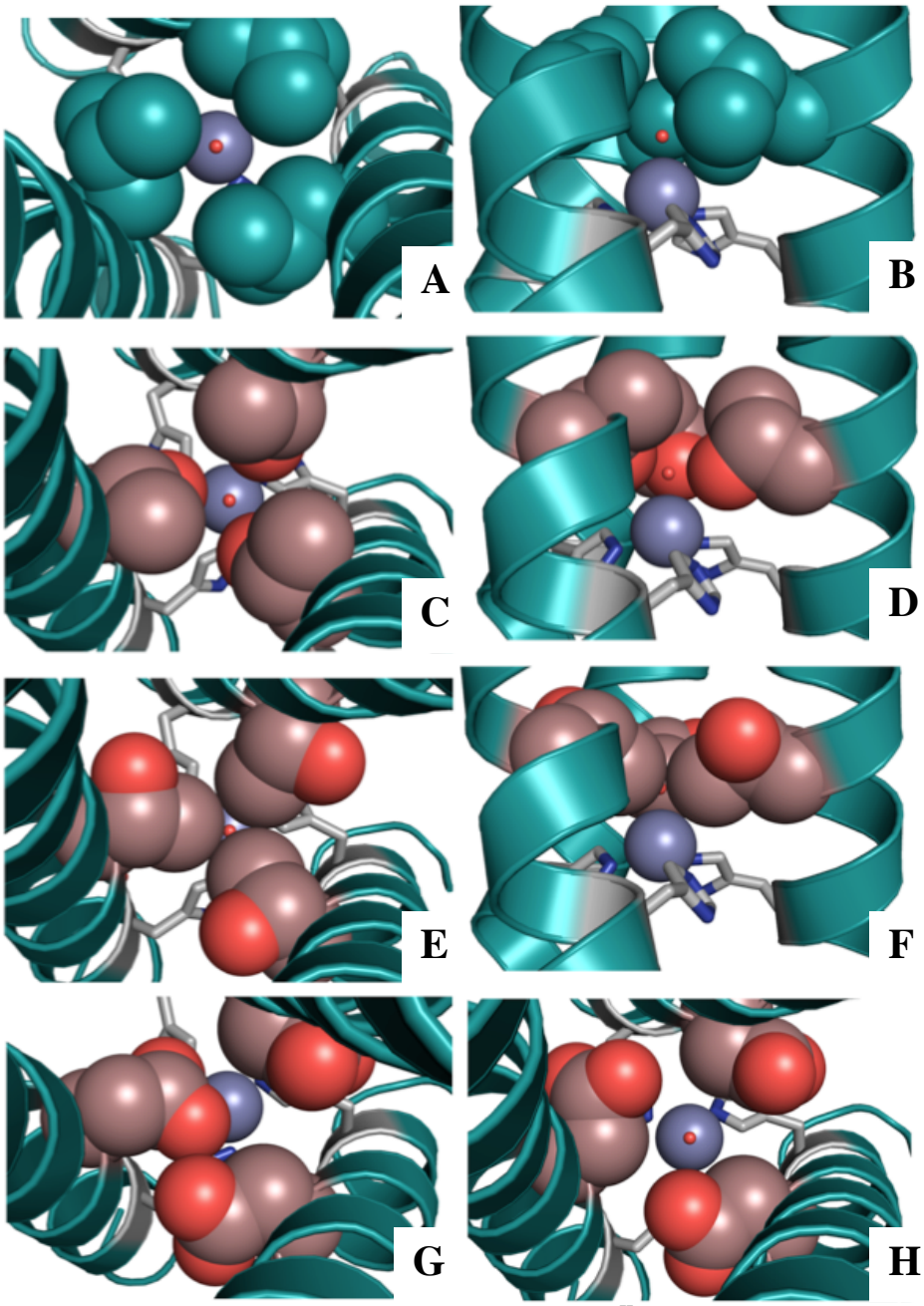

Figure 1-30. Comparison of the packing around the Zn^{II} site in the crystal structure of $Hg^{II}{}_{S}Zn^{II}(OH_2)_{N/O}$(**CS**L9PenL23H)$_3{}^{n+}$ (PDB: 3PBJ) and corresponding models including L19T or L19D mutations. **A**) and **B**) show the top down and side on views of the Zn^{II} site from $Hg^{II}{}_{S}Zn^{II}(OH_2)_{N/O}$(**CS**L9PenL23H)$_3{}^{n+}$ with space filling Leu19 spheres. **C**) and **D**) show top down and side on views, respectively, of the L19T variant with a rotamer that has the hydroxyl group pointing toward the Zn^{II} site. **E**) and **F**) show top down and side on views, respectively, of the L19T variant with a rotamer that has the hydroxyl group pointing toward the helical interface. **G**) and **H**) show side on views of the L26D variant, with two different rotamers, both which direct an oxygen atom toward the Zn^{II} site. The rotamers shown were chosen based on the minimum amount of potential steric clashing with surrounding residues. Figures adapted from Ref 90.

To eliminate the possibility of the hydroxyl group not pointing into the center of the trimer toward the $Zn^{II}His_3$ site in the acid/base substituted layer, the Thr residue was substituted to Asp, where the the carboxylate moiety would provide an oxygen atom to point toward the center of the helix regardless of the orientation (Figure 1-30). The resulting peptide, **GR**L16CL26DL30H (1-2) had a slightly lower alpha helical content in comparison to the Thr variant (~71-74% in the presence and absence of Hg^{II}) but provided a catalytic efficiency of 24.2 $M^{-1}s^{-1}$ for *p*NPA hydrolysis at pH 9.5, which is comparable to the original **TRI** mimic.[90] A kinetic pK_a for $Hg^{II}{}_SZn^{II}(OH)_{N/O}$(**GR**L16CL26DL30H)$_3{}^{n+}$ was determined to be 9.4, the highest pK_a yet observed for these mimics. Although these peptides were fantastic first-, and second-generation symmetric CA mimics, this previous work suggests that simply introducing a residue capable of acid/base chemistry in close proximity to the $Zn^{II}His_3$ site providing three new Thr or Asp residues is not enough to improve the catalytic efficiency of the original **TRI** system and, therefore, a single residue capable of secondary acid/base interactions needs to be introduced, per trimer, into the system, not per peptide (three per trimer), which previously resulted in a three-fold substitution.

At this particular point, all of the metal-binding sites our laboratory has engineered into our 3SCC have consisted of symmetric primary coordination sites. Thus far we do not have the means of including asymmetric primary coordination sites within our 3SCC. However, native systems, more often than not, *do* contain asymmetry in the first coordination sphere. Similar to CA, the Zn^{II} enzymes carboxypeptidase A (CPA) and thermolysin (TML) have histidine residues in close proximity to the metal binding site. Unlike CA, the peptidases CPA and TML only have two coordinating histidine ligands, a coordinated carboxylate residue (aspartate or glutamate) and varying numbers of coordinated solvent molecules (Figure 1-31). By developing a way to incorporate different ligands into the primary coordination sphere within our 3SCC the number of sites available for us to study within our systems will increase significantly.

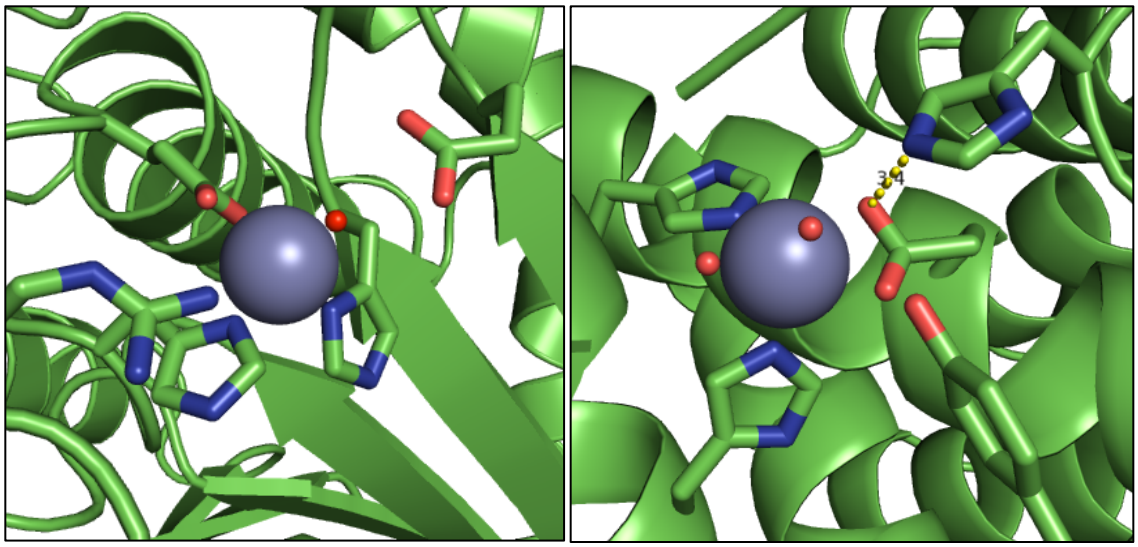

Figure 1-31. Active sites of carboxypeptidase A (CPA) and thermolysin (TML). Left: Zn^{II} bound to CPA (PDB: 1YME)[91] with direct ligation to two histidine residues, one carboxylic acid and an exogenous water molecule. Right: Zn^{II} bound TML (PDB: 1LNF)[92] showing a primary coordination sphere of two histidine residues, one carboxylate, and two water molecules. Of note, there is a third histidine residue within hydrogen bonding distance to the coordinating carboxylic acid group.

The second major goal of my dissertation is to evaluate whether metal induced steric matching of Ala/Leu in combition with $Pb^{II}Cys_3$ binding at one end of trimer can induce asymmetry to a second, remote metal binding site with first or second sphere asymmetric coordination geometry. In Chapter 3 I will discuss how I engineered a second metal binding site, in addition to the asymmetry-inducing $Pb^{II}Cys_3$ site, which contains both hisitidine and carboxylic acid residues within a 3SCC and will analyze the spectroscopic characteristics of these sites. . As discussed in Chapter 2, transition metal binding to a second site has a lower affinity for the Cys_3 site than Pb^{II}, and therefore does not distrupt the heterotrimer specificity, allowing for the study of transition metals in the second site with no concern for the integrity of the $Pb^{II}Cys_3$-induced heterotrimer. I will describe the spectroscopic parameters of the symmetric homotrimers (His_3 and $Carboxylate_3His_3$ sites) when bound to transition metals (Co^{II} and Zn^{II}) as well as the change in coordination environment as observed spectroscopically when carboxylic acid residues are included in close proximity of the His_3 binding site. In fact, when carboxylic acid residues are included in an asymmetric fashion in the layer directly above the His_3 site we no longer observe His_3 coordination, as evidenced by the similarities between

UV-Vis, EPR, and EXAFS data of my heterotrimers and asymmetric peptides such as CPA and TML ($His_2Carboxylate_{1,2}(H_2O)_Y$ Zn^{II}/Co^{II} binding). I will also address how the location of the carboxylic acid residues with respect to the His_3 binding site (above or below) effects Co^{II} binding. I will also discuss the implications of how the work in Chapter 3 impacts the broader discussion of the structure-function relationship between metal-binding ligands and secondary/tertiary protein folds, and how in the case of my heterotrimeric 3SCC Co^{II} may not be non-innocent spectrsocopic probe for Zn^{II}.

Comparative Metal Binding Studies to Cys_3 Sites: Discovery of an Unexpected Binuclear Cu_2Cys_3 Binding Site within a 3SCC

Essentially all aerobic organisms require trace amounts of copper to function; however, when it is not properly regulated copper becomes a toxin and, therefore, strict regulation of copper homeostasis is vital. Menkes syndrome and Wilson disease are the most common diseases due to copper deficiency in humans, and are both directly related to modifications of the human P_{1B}-type ATPase ATP7A and ATP7B, respectively.

Surface cell transporters, such as Ctr1, are responsible for the uptake and transport of copper ions but the mechanism of copper delivery, which is dependent on metallochaperones, is still debated. Multiple pathways, largely dependent on where the copper ion is being delivered, have been proposed; the Cox17, Atx1 and CCS pathways are delivery pathways to the mitochondria, the Golgi and to superoxide dismutase, respectively. Regardless of the differences between the proposed pathways, all of these copper metallochaperones contain similar thiol-rich copper binding sites with MXCXXC motifs within βαββαβ-folds (Figure 1-32). Considering our lab's previous success studying heavy metal binding (Pb^{II}, Cd^{II}, Hg^{II}, As^{III}, etc…) in three-fold symmetric Cys_3-containing environments within de novo designed 3SCC, the third major goal of my dissertation work, as discussed in Chapter 4, was to analyze the binding of Cu^{I} to our **TRI** and **GR** family of peptides, with the ultimate goal of obtaining relative affinities of Cu^{I} binding to Cys_3 binding sites with varying secondary coordination environments. Cu^{I}-bound **TRI** and **GR** peptides with different hydrophobes (Leu, Ala or d-Leu) in the layer

directly above the Cys_3 binding site were synthesized and analyzed using UV-Vis and EXAFS spectroscopy. Interestingly, the K-edge X-ray absorption spectroscopy of Cu^I-bound **TRI**L2WL16C (Table 1-2), at multiple pH conditions, has revealed a heavy back-scatterer consistent with a short Cu-Cu interaction with mixed two- and three-coordinate Cu-S environments. Additional analysis of the Cu-S charge transfer band via UV spectroscopy revealed a binding stoichiometry of two copper ions to one 3SCC. These data support a model where a binuclear Cu^I site coordinated with multiple sulfur atoms exists in this system, much like Cu^I binding to the repressor CopY.[93] This is the first time that a binuclear site has been observed within our Cys_3-containing **TRI**/**GR** peptides. Relative binding affinities of Cu^I to Cys_3 containing **TRI** and **GR** peptides were also analyzed using a competitive chelator, bathocuproine disulfonate (BCS^{2-}). The Cu^I binding affinities will be compared with respect to the changes in affinity based on secondary coordination environment.

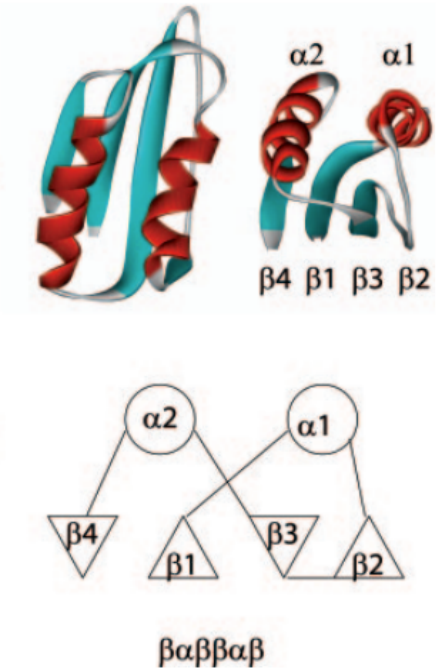

Figure 1-32. Schematic showing the common βαββαβ-folds, which contain the thiol-rich MXCXXC motifs to which copper binds in metallochaperones. Shown is a single ACT domain from E. coli D-3-phosphoglycerate dehydrogenase showing the βαββαβ-motif. In the diagram, the triangles point up or down to indicate the direction of the strand in the β-sheet. Numbers progress from N terminus to C terminus. Figure adapted from Ref 94.

As will be mentioned briefly in Chapter 2, competition has been observed between Cu^{I} and Pb^{II} for binding to the Cys_3 site within our 3SCC. Therefore, as I set out to determine the association constant for $Cu^{I}Cys_3$ in our peptides, one can imagine that an additional competition experiment between Pb^{II} and Cu^{I} could lead to a determination of the Pb^{II} association constant, a parameter we have previously been unable to measure due to the high affinity. Surprisingly, during attempts to determine $Pb^{II}Cys_3$ binding affinities, new spectroscopic data suggests the formation of another novel binuclear site, this time heteronuclear with one equivalent of Cu^{I} and one equivalent of Pb^{II}. I will discuss how the spectroscopic data suggest a kinetic model of $Cu^{I}_2Cys_3$ vs. $Cu^{I}Pb^{II}Cys_3$ formation as well as the perturbations to Pb^{II} spectrum in the presence of Cu^{I}. Additionally, I will describe the binding of Cu^{I} binding when a His_3 **a** site is present, in addition to a Cys_3 site, and what implications are observed for the preferential of Cu^{I} binding for two different binding sites within the same scaffold.

In Chapter 5 I will give a summary of the major results and achievements of my thesis work and I will propose future directions with respect to these projects.

References

(1) Synthetic Biology. Applying Engineering to Biology. *Report of a New and Emerging Science and Technology (NEST) High-Level Expert Group, European Commission*, 2005, *1*, 1–44.
(2) Boyle, A. L.; Woolfson, D. N. *Chem. Soc. Rev.* **2011**, *40*, 4295.
(3) Lupas, A. *Trends Biochem. Sci.* **1996**, *21*, 375.
(4) Betz, S. F.; Bryson, J. W.; DeGrado, W. F. *Curr. Opin. Struct. Biol.* **1995**, *5*, 457.
(5) O'Shea, E.; Klemm, J.; Kim, P.; Alber, T. *Science* **1991**, *254*, 539.
(6) Boice, J. A.; Dieckmann, G. R.; DeGrado, W. F.; Fairman, R. *Biochemistry* **1996**, *35*, 14480.
(7) Harbury, P.; Zhang, T.; Kim, P.; Alber, T. *Science* **1993**, *262*, 1401.
(8) Harbury, P. B.; Kim, P. S.; Alber, T. *Nature* **1994**, *371*, 80.
(9) Lovejoy, B.; Choe, S.; Cascio, D.; Mcrorie, D. K.; Degrado, W. F.; Eisenberg, D. *Science* **1993**, *259*, 1288.
(10) Eisenberg, D.; Wesson, M.; Yamashita, M. *Chem. Scr.* **1989**, *29A*.
(11) Eisenberg, D.; McLachlan, A. D. *Nature* **1986**, *319*, 199.
(12) Ogihara, N. L.; Weiss, M. S.; Degrado, W. F.; Eisenberg, D. *Protein Sci.* **1997**, *6*, 80.
(13) Myszka, D. G.; Chaiken, I. M. *Biochemistry* **1994**, *33*, 2363.
(14) Monera, O.; Zhou, N.; Kay, C.; Hodges, R. *J. Biol. Chem.* **1993**, *268*, 19218.
(15) Zhou, L.; Bosscher, M.; Zhang, C.; Ozçubukçu, S.; Zhang, L.; Zhang, W.; Li, C. J.; Liu, J.; Jensen, M. P.; Lai, L.; He, C. *Nat. Chem.* **2014**, *6*, 236.
(16) Berwick, M. R.; Lewis, D. J.; Jones, A. W.; Parslow, R. A.; Dafforn, T. R.; Cooper, H. J.; Wilkie, J.; Pikramenou, Z.; Britton, M. M.; Peacock, A. F. A. *J. Am. Chem. Soc.* **2014**, *136*, 1166.
(17) Yu, F.; Cangelosi, V. M.; Zastrow, M. L.; Tegoni, M.; Plegaria, J. S.; Tebo, A. G.; Mocny, C. S.; Ruckthong, L.; Qayyum, H.; Pecoraro, V. L. *Chem. Rev.* **2014**, *114*, 3495.
(18) Tebo, A. G.; Pecoraro, V. L. *Curr. Opin. Chem. Biol.* **2015**, *25*, 65.
(19) Plegaria, J. S.; Pecoraro, V. L. *Isr. J. Chem.* **2015**, *55*, 85.
(20) Peacock, A. F. A. *Curr. Opin. Chem. Biol.* **2013**, *17*, 934.
(21) Lu, Y.; Yeung, N.; Sieracki, N.; Marshall, N. M. *Nature* **2009**, *460*, 855.
(22) Dürrenberger, M.; Ward, T. R. *Curr. Opin. Chem. Biol.* **2014**, *19*, 99.
(23) Bryson, J. W.; Betz, S. F.; Lu, H. S.; Suich, D. J.; Zhou, H. X.; O'Neil, K. T.; DeGrado, W. F. *Science* **1995**, *270*, 935.
(24) Peacock, A. F. A.; Iranzo, O.; Pecoraro, V. L. *Dalton Trans.* **2009**, *9226*, 2271.
(25) Dieckmann, G. R.; McRorie, D. K.; Lear, J. D.; Sharp, K. A.; DeGrado, W. F.; Pecoraro, V. L. *J. Mol. Biol.* **1998**, *280*, 897.
(26) Zastrow, M. L.; Pecoraro, V. L. *Coord. Chem. Rev.* **2013**, *257*, 2565.
(27) Matzapetakis, M.; Ghosh, D.; Weng, T.-C.; Penner-Hahn, J. E.; Pecoraro, V. L. *J. Biol. Inorg. Chem.* **2006**, *11*, 876.
(28) Touw, D. S.; Nordman, C. E.; Stuckey, J. A.; Pecoraro, V. L. *Proc. Natl. Acad. Sci. USA* **2007**, *104*, 11969.
(29) Ruckthong, L. Crystallographic Comparison of Tris-Thiolate Sites in Designed Proteins to Control Metal Geometries, University of Michigan, 2016.
(30) Utschig, L.; Bryson, J.; O'Halloran, T. *Science* **1995**, *268*, 380.

(31) Gruff, E. S.; Koch, S. A. *J. Am. Chem. Soc.* **1990**, *112*, 1245.
(32) Watton, S. P.; Wright, J. G.; MacDonnell, F. M.; Bryson, J. W.; Sabat, M.; O'Halloran, T. V. *J. Am. Chem. Soc.* **1990**, *112*, 2824.
(33) Tröger, W. *Hyperfine Interact.* **1999**, *121*, 117.
(34) Butz, T.; Tröger, W.; Pöhlmann, T.; Nuyken, O. *Zeitschrift für Naturforsch. A* **1992**, *47*, 85.
(35) Wright, J. G.; Tsang, H.; Penner-hahn, J. E.; Halloran, T. V. O. *J. Am. Chem. Soc.* **1990**, *112*, 2434.
(36) Dieckmann, G. R.; McRorie, D. K.; Tierney, D. L.; Utschig, L. M.; Singer, C. P.; O'Halloran, T. V.; Penner-Hahn, J. E.; DeGrado, W. F.; Pecoraro, V. L. *J. Am. Chem. Soc.* **1997**, *119*, 6195.
(37) Iranzo, O.; Thulstrup, P. W.; Ryu, S.-B.; Hemmingsen, L.; Pecoraro, V. L. *Chemistry* **2007**, *13*, 9178.
(38) Ghosh, D.; Pecoraro, V. L. *Inorg. Chem.* **2004**, *43*, 7902.
(39) Chakraborty, S.; Touw, D. S.; Peacock, A. F. a; Stuckey, J.; Pecoraro, V. L. *J. Am. Chem. Soc.* **2010**, *132*, 13240.
(40) Zastrow, M. L.; Peacock, A. F. A.; Stuckey, J. A.; Pecoraro, V. L. *Nat. Chem.* **2012**, *4*, 118.
(41) Ghosh, D.; Lee, K.-H.; Demeler, B.; Pecoraro, V. L. *Biochemistry* **2005**, *44*, 10732.
(42) Farrer, B. T.; Harris, N. P.; Valchus, K. E.; Pecoraro, V. L. *Biochemistry* **2001**, *40*, 14696.
(43) Peacock, A. F. A.; Stuckey, J. A.; Pecoraro, V. L. *Angew. Chem. Int. Ed.* **2009**, *48*, 7371.
(44) Wang, Y.; Hemmingsen, L.; Giedroc, D. P. *Biochemistry* **2005**, *44*, 8976.
(45) Ye, J.; Kandegedara, A.; Martin, P.; Rosen, B. P. *J. Bacteriol.* **2005**, *187*, 4214.
(46) Banci, L.; Bertini, I.; Cantini, F.; Ciofi-Baffoni, S.; Cavet, J. S.; Dennison, C.; Graham, A. I.; Harvie, D. R.; Robinson, N. J. *J. Biol. Chem.* **2007**, *282*, 30181.
(47) Matzapetakis, M.; Farrer, B. T.; Weng, T.-C.; Hemmingsen, L.; Penner-Hahn, J. E.; Pecoraro, V. L. *J. Am. Chem. Soc.* **2002**, *124*, 8042.
(48) Iranzo, O.; Chakraborty, S.; Hemmingsen, L.; Pecoraro, V. L. *J. Am. Chem. Soc.* **2011**, *133*, 239.
(49) Lee, K.-H.; Cabello, C.; Hemmingsen, L.; Marsh, E. N. G.; Pecoraro, V. L. *Angew. Chem. Int. Ed.* **2006**, *45*, 2864.
(50) Peacock, A. F. A.; Hemmingsen, L.; Pecoraro, V. L. *Proc. Natl. Acad. Sci. USA* **2008**, *105*, 16566.
(51) Matzapetakis, M.; Pecoraro, V. L. *J. Am. Chem. Soc.* **2005**, *127*, 18229.
(52) Touw, D. Structural and Spectroscopic Studies of Heavy Metal Binding to de novo Designed Coiled Coil Peptides, University of Michigan, 2007.
(53) Iranzo, O.; Cabello, C.; Pecoraro, V. L. *Angew. Chem. Int. Ed.* **2007**, *46*, 6688.
(54) Shi, W.; Dong, J.; Scott, R. A.; Ksenzenko, M. Y.; Rosen, B. P. *J. Biol. Chem.* **1996**, *271*, 9291.
(55) Bergdahl, I. A.; Grubb, A.; Schütz, A.; Desnick, R. J.; Wetmur, J. G.; Sassa, S.; Skerfving, S. *Pharmacol. Toxicol.* **1997**, *81*, 153.
(56) Christou, G.; Folting, K.; Huffman, J. C. *Polyhedron* **1984**, *3*, 1247.
(57) Neupane, K. P.; Pecoraro, V. L. *Angew. Chem. Int. Ed.* **2010**, *49*, 8177.

(58) Walsh, S. T.; Cheng, H.; Bryson, J. W.; Roder, H.; DeGrado, W. F. *Proc. Natl. Acad. Sci. USA* **1999**, *96*, 5486.
(59) Plegaria, J. S.; Dzul, S.; Zuiderweg, E. R. P.; Stemmler, T. L.; Pecoraro, V. L. *Biochemistry* **2015**, *54*, 2858.
(60) Chakraborty, S.; Kravitz, J. Y.; Thulstrup, P. W.; Hemmingsen, L.; DeGrado, W. F.; Pecoraro, V. L. *Angew. Chem. Int. Ed.* **2011**, *50*, 2049.
(61) Nautiyal, S.; Alber, T. *Prot. Sci.* **1999**, *8*, 84.
(62) Jalan, A. A.; Demeler, B.; Hartgerink, J. D. *J. Am. Chem. Soc.* **2013**, *135*, 6014.
(63) Diss, M. L.; Kennan, A. J. *J. Org. Chem.* **2008**, *73*, 9752.
(64) Lebruin, L. T.; Banerjee, S.; O'Rourke, B. D.; Case, M. A. *Biopolymers* **2011**, *95*, 792.
(65) Schnarr, N. A.; Kennan, A. J. *J. Am. Chem. Soc.* **2001**, *123*, 11081.
(66) Schnarr, N. A.; Kennan, A. J. *J. Am. Chem. Soc.* **2002**, *124*, 9779.
(67) Kashiwada, A.; Hiroaki, H.; Kohda, D.; Nango, M.; Tanaka, T. *J. Am. Chem. Soc.* **2000**, *122*, 212.
(68) Kiyokawa, T.; Kanaori, K.; Tajima, K.; Kawaguchi, M.; Mizuno, T.; Oku, J.; Tanaka, T. *Chemistry* **2004**, *10*, 3548.
(69) Håkansson, K.; Wehnert, A.; Liljas, A. *Acta Crystallogr. D* **1994**, *50*, 93.
(70) Hakansson, K.; Wehnert, A. *J. Mol. Biol.* **1992**, *228*, 1212.
(71) Krebs, J. F.; Rana, F.; Dluhy, R. A.; Fierke, C. A. *Biochemistry* **1993**, *32*, 4496.
(72) Innocenti, A.; Scozzafava, A.; Parkkila, S.; Puccetti, L.; De Simone, G.; Supuran, C. T. *Bioorganic Med. Chem. Lett.* **2008**, *18*, 2267.
(73) Koerner, T. B.; Brown, R. S. *Can. J. Chem.* **2002**, *80*, 183.
(74) Zastrow, M. L.; Pecoraro, V. L. *J. Am. Chem. Soc.* **2013**, *135*, 5895.
(75) Lindskog, S. *Biochemistry* **1966**, *5*, 2641.
(76) Fierke, C.; Calderone, T.; Krebs, J. F. *Biochemistry* **1991**, *30*, 11054.
(77) Der, B. S.; Edwards, D. R.; Kuhlman, B. *Biochemistry* **2012**, *51*, 3933.
(78) Rufo, C. M.; Moroz, Y. S.; Moroz, O. V.; Stöhr, J.; Smith, T. A.; Hu, X.; DeGrado, W. F.; Korendovych, I. V. *Nat. Chem.* **2014**, *6*, 303.
(79) Slebocka-Tilk, H.; Cocho, J. L.; Frakman, Z.; Brown, R. S. *J. Am. Chem. Soc.* **1984**, *106*, 2421.
(80) Krebs, J. F.; Ippolito, J. A.; Christianson, D. W.; Fierke, C. A. *J. Biol. Chem.* **1993**, *268*, 27458.
(81) Liang, Z.; Xue, Y.; Behravan, G.; Jonsson, B. H.; Lindskog, S. *Eur. J. Biochem.* **1993**, *211*, 821.
(82) Averill, B. A. *Chem. Rev.* **1996**, *96*, 2951.
(83) Tegoni, M.; Yu, F.; Bersellini, M.; Penner-Hahn, J. E.; Pecoraro, V. L. *Proc. Natl. Acad. Sci. USA* **2012**, *109*, 21234.
(84) Yu, F. De novo designed metallopeptides with a type 2 copper center: a structural and functional model for copper nitrite reductase, Univeristy of Michigan, 2014.
(85) Jacobson, F.; Pistorius, A.; Farkas, D.; De Grip, W.; Hansson, Ö.; Sjölin, L.; Neutze, R. *J. Biol. Chem.* **2007**, *282*, 6347.
(86) Wijma, H. J.; Jeuken, L. J. C.; Verbeet, M. P.; Armstrong, F. A.; Canters, G. W. *J. Biol. Chem.* **2006**, *281*, 16340.
(87) Yu, F.; Penner-Hahn, J. E.; Pecoraro, V. L. *J. Am. Chem. Soc.* **2013**, *135*, 18096.
(88) Yu, F.; Stappen, C. Van; Tebo, A. G.; Penner-Hahn, J. E.; Vincent L. Pecoraro.

Angew. Chemie **2016**, *In Press*.
(89) Domsic, J. F.; Williams, W.; Fisher, S. Z.; Tu, C.; Agbandje-Mckenna, M.; Silverman, D. N.; McKenna, R. *Biochemistry* **2010**, *49*, 6394.
(90) Zastrow, M. De novo designed metalloenzymes: structural stabilization and hydrolytic catalysis in a family of α-helical coiled coils, University of Michigan, 2013.
(91) Greenblatt, H. M.; Feinberg, H.; Tucker, P. A.; Shoham, G. *Acta Crystallogr. Sect. D Biol. Crystallogr.* **1998**, *54*, 289.
(92) Holland, D. R.; Hausrath, A. C.; Juers, D.; Matthews, B. W. *Protein Sci.* **1995**, *4*, 1955.
(93) Cobine, P. A.; George, G. N.; Jones, C. E.; Wickramasinghe, W. A.; Solioz, M.; Dameron, C. T. *Biochemistry* **2002**, *41*, 5822.
(94) Grant, G. A. *J. Biol. Chem.* **2006**, *281*, 33825.

Chapter 2. Designing Heterotrimeric Three-Stranded Coiled Coils

Introduction

There are two primary approaches utilized to study the structure-function relationship of metalloenzyme active sites in designed systems, protein redesign and *de novo* protein design. Protein redesign consists of engineering artificial metalloenzymes via modifications to native scaffolds. Two examples of this approach include introduction of metal binding ligands as found in a native enzyme, or introduction of non-native cofactors into a preexisting well-folded and stable protein. The second approach, *de novo* protein design, consists of designing a peptide "from scratch", where the protein sequence is not derived from a native system. Both of these approaches offer bioinorganic chemists avenues to re-create and analyze known native metal centers within simplified peptidic environments to understand better what extent biological function is a consequence of biological structure. Our lab, as outlined in the previous chapter, has utilized *de novo* designed three-stranded coiled coils (3SCC) to study metal binding sites to clarify metal binding geometry, coordination and functionality within simplified constructs to elucidate metal binding behavior in native systems.

In particular, over the last several years our laboratory has utilized *de novo* peptide design of 3SCCs to obtain functional metalloenzymes capable of hydrolytic and redox catalysis.[1–4] While these systems offer the best catalytic efficiency, in aqueous solutions, for the native reactions of their corresponding metalloenzyme inspiration, we are currently limited by the inherent symmetry introduced by the self-assembling characteristics of our 3SCC scaffolds. This symmetry-related limitation has, therefore, lead to the inability to prepare asymmetric, or heterotrimeric, assemblies, selectively, that would be capable of providing mixed first coordination sphere metal binding environments or asymmetric second coordination sphere residues to mimic nearby acid-

base catalysts. While some native proteins contain three-fold symmetric primary binding sites, such as the $Zn^{II}His_3$ binding site of Carbonic Anhydrase (CA), the extended active sites contain extensive and essential hydrogen-bonding networks (Figure 2-1).[5,6] Attempts to introduce secondary interactions, such as hydrogen bonding donors, to the metal binding sites within 3SCCs results in triplicate modification, with one Thr per helix, due to the three-fold symmetric nature of the assembly.[1] Furthermore, current metal binding 3SCCs cannot model the vast number of native proteins that contain asymmetric primary coordination spheres, such as the common facial triad ($His_{2/3}$Carboxylate) metal binding sites found in alpha-ketoglutarate-dependent taurine deoxygenase (Figure 2-2A), and iron- or manganese-superoxide dismutases (Figure 2-2B), or the $His_2Carboxylate_X$ active sites of carboxypeptidase A and thermolysin (Figures 2-2C and 2-2D).[7–11] My goal is to lift the symmetry-related limitations by designing a peptide that combines steric matching of natural amino acids in close proximity to a tris-thiolate site that upon binding of Pb(II) provides selective formation of an A_2B heterotrimeric 3SCC.

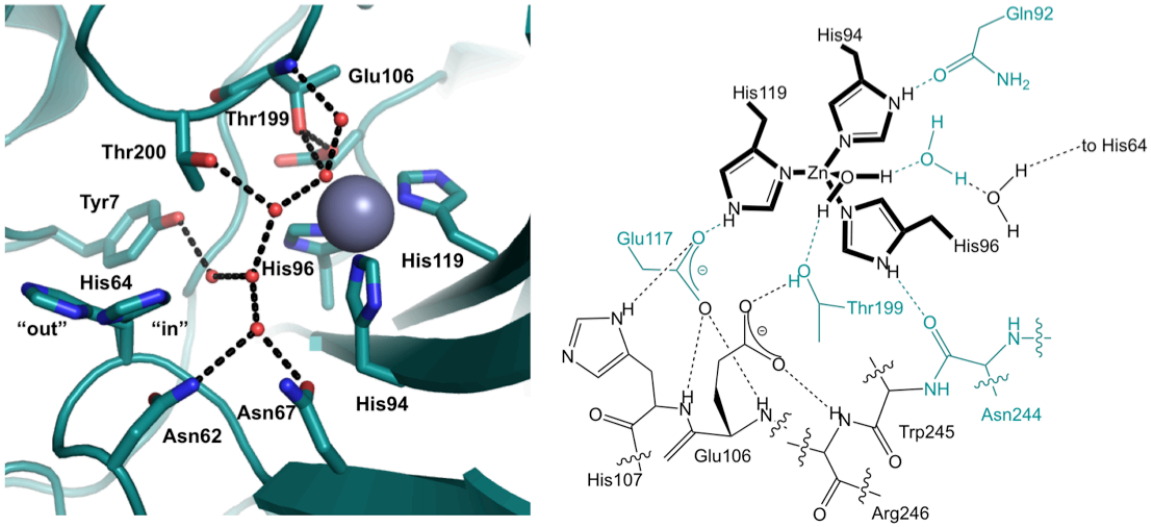

Figure 2-1. Structure of the active site of carbonic anhydrase II. Left panel: The extended active site of Human CAII showing the ordered water network (PDB: 3KS3).[46] Zn^{II} is represented by a gray sphere, and the oxygen atoms of water molecules are shown as smaller red spheres. The dotted lines represent presumed hydrogen bonds. Selected amino acids of the active site are shown as stick figures with both the inward and outward orientations of His64 (proton shuttle) shown. Right panel: ChemDraw scheme of the CAII primary and secondary Zn(II)-binding site. Figure adapted from Ref 47.

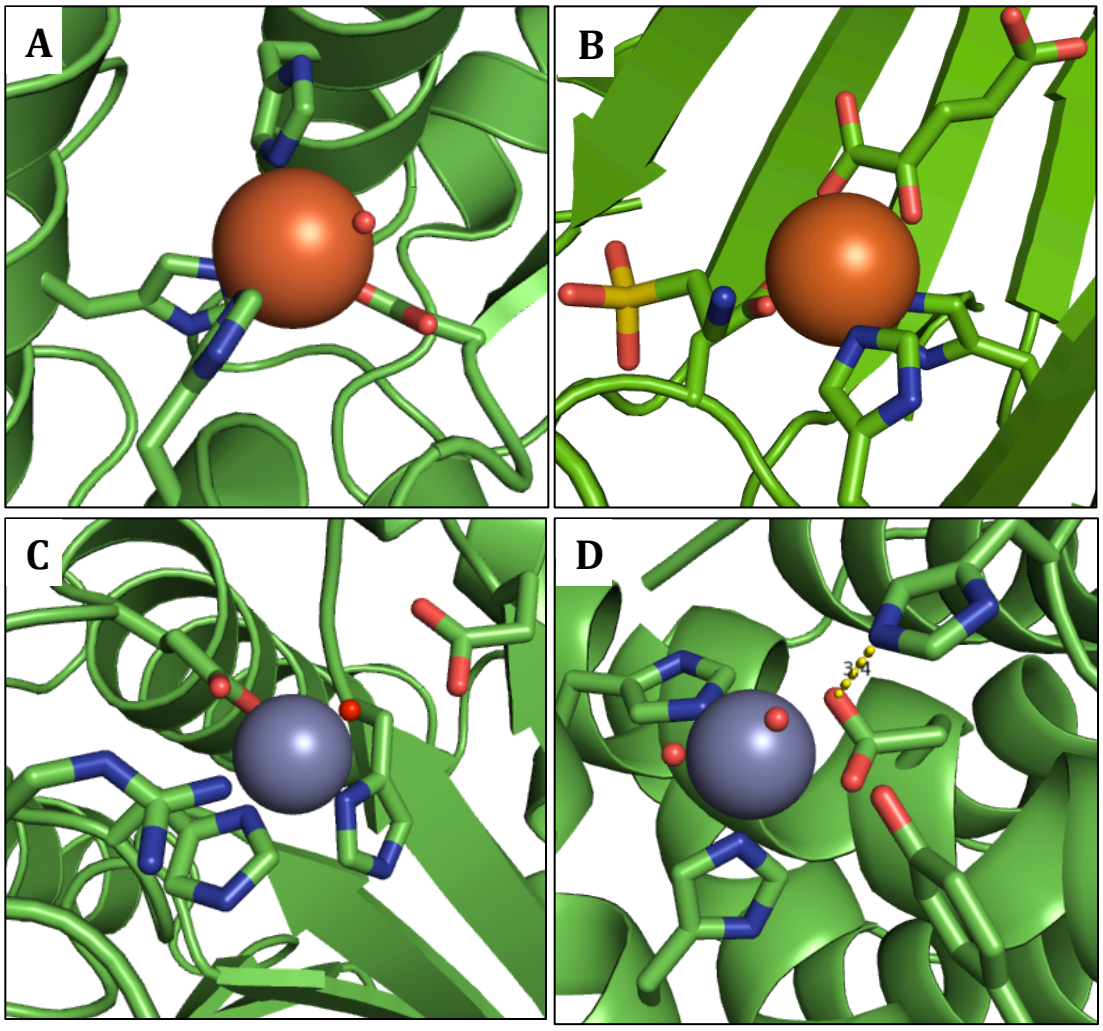

Figure 2-2. Asymmetric primary coordination spheres of A) alpha-ketoglutarate-dependent taurine deoxygenase (TauD, PDB: 1GY9),[7] B) iron- or manganese-superoxide dismutases (Fe/Mn SOD, PDB: 1ISB),[48] C) carboxypeptidase A (CPA, PDB: 1YME),[9] and D) thermolysin (TML, PDB: 1LNF).[10] Zn^{II} ions are shown as purple spheres and $Fe^{II/III}$ are shown as orange spheres. Selected amino acids of active site ligands are shown as stick figures where N atoms are highlighted in blue, oxygen in red and sulfur in yellow. Water molecules are shown as smaller red spheres.

There have been numerous reports of attempts to obtain *de novo* deigned heterotrimeric 3SCCs (Chapter 1).[12–15] In particular, Keenan and coworkers showed that steric matching of small, alanine, and bulky, cyclohexylalanine (CHA), residues allows for formation of ABC asymmetric 3SCC; however, to obtain pure heterotrimers three layers of alternating steric matching Ala_2CHA layers were required (Figure 2-3).[16] Tanaka and coworkers followed this work with a similar steric matching approach that required using two alanine residues and one tryptophan residue (Ala_2Trp), but also

included alterations to the salt bridging amino acids at the helical interfaces as well as modifications in the peptide sequence to the to destabilize undesired trimer formation.[17] Thus far, interior bound metals have not been used to nucleate heterotrimeric formation. *Moreover, asymmetric scaffolds have never been used to generate asymmetric metal binding sites, with potential catalytic activity.* I proposed combining steric matching of natural amino acids in combination with a $Pb^{II}Cys_3$ binding site to nucleate the specific formation of A_2B type heterotrimers. This approach would require no changes in exterior residues or salt-bridging interactions and would only require two neighboring layers within the helices for selective formation. This differs from previous constructs that required altering layers throughout the scaffold, therefore, leaving no space within the coiled coil for a second, catalytic or redox active metal binding site.

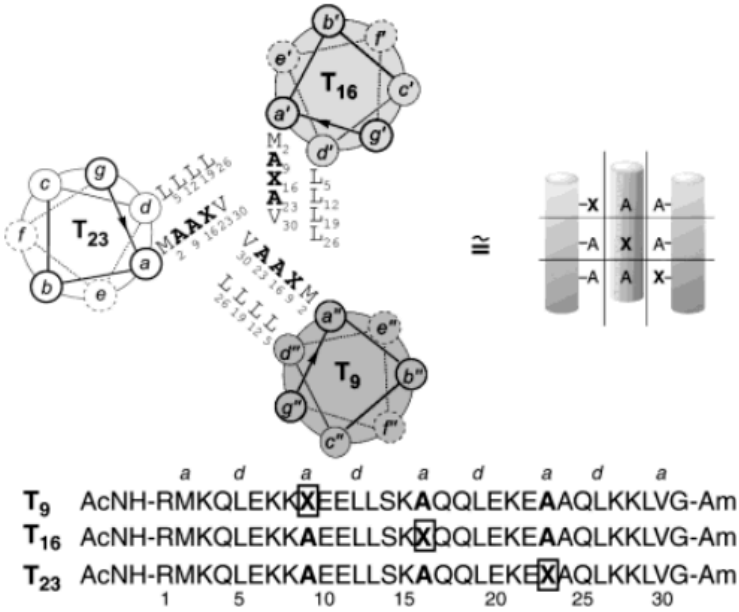

Figure 2-3. Helical wheel projection of the 1:1:1 $T_9/T_{16}/T_{23}$ complex (viewed down the helical axis from the N to C terminus), showing only core residues. The sequence of each peptide is also given. The tic-tac-toe arrangement of cyclohexylalanine residues (X) is depicted schematically at the right. Ac = acetyl and Am = amide. Figure adapted from Ref 16.

Lead interactions with cysteine rich environments have been previously characterized within the **TRI**/**GRAND** family of peptides, Ac-G(LKALEEK)$_{4/5}$G-NH_2 (Table 2-1). Our 3SCCs consist of amphipathic α-helical peptides that contain hydrophobic residues at the first (**a**) and fourth (**d**) positions of a heptad repeat (**abcdefg**).

Hydrophobic collapse and electrostatic interactions between the **e** and **g** positions result in the self-assembly of the 3SCCs. Metal binding sites, as mentioned above, can be engineered into the construct by substituting a hydrophobic layer with a coordinating ligand. Substitution of a single leucine by cysteine, in each strand, has generated sulfur rich $M^{n+}Cys_3$ sites that associate with toxic heavy metals to form protein complexes.[18–22]

Table 2-1. Peptide Sequences

Peptide	Sequence
	abcdefg
BABY	Ac-G LKALEEK LKALEEK LKALEEK G-NH_2
BABYL12C	Ac-G LKALEEK LKA***C***EEK LKALEEK G-NH_2
TRI	Ac-G LKALEEK LKALEEK LKALEEK LKALEEK G-NH_2
TRIL12AL16C	Ac-G LKALEEK LKA***A***EEK ***C***KALEEK LKALEEK G-NH_2
TRILWL12AL16C	Ac-G ***W***KALEEK LKA***A***EEK ***C***KALEEK LKALEEK G-NH_2
TRIL2WL16C	Ac-G ***W***KALEEK LKALEEK ***C***KALEEK LKALEEK G-NH_2
GRAND	Ac-G LKALEEK LKALEEK LKALEEK LKALEEK LKALEEK G-NH_2
GRL12AL16CL26C	Ac-G LKALEEK LKA***A***EEK ***C***KALEEK LKA***C***EEK LKALEEK G-NH_2
GRL2WL16C	Ac-G ***W***KALEEK LKALEEK ***C***KALEEK LKALEEK LKALEEK G-NH_2
GRL2WL12AL16L30H	Ac-G ***W***KALEEK LKA***A***EEK ***C***KALEEK LKALEEK ***H***KALEEK G-NH_2
GRL2WL16CL19AL30H	Ac-G ***W***KALEEK LKALEEK ***C***KA***A***EEK LKALEEK ***H***KALEEK G-NH_2
GRL2WL16CL30H	Ac-G ***W***KALEEK LKALEEK ***C***KALEEK LKALEEK ***H***KALEEK G-NH_2
CoilSer	Ac-E WEALEKK LAALESK LQALEKK LEALEH G-NH_2
CSL9C	Ac-E WEALEKK ***C***AALESK LQALEKK LEALEH G-NH_2
CSL12C	Ac-E WEALEKK LAA***C***ESK LQALEKK LEALEH G-NH_2
CSL16C	Ac-E WEALEKK LAALESK ***C***QALEKK LEALEH G-NH_2
CSL12AL16C	Ac-E WEALEKK LAA***A***ESK ***C***QALEKK LEALEH G-NH_2
GRANDCoilSer	Ac-E WEALEKK LAALESK LQALEKK LQALEKK LEALEH G-NH_2
GRCSL12AL16C	Ac-E WEALEKK LAA***A***ESK ***C***QALEKK LQALEKK LEALEH G-NH_2
GRCSL16CL30H	Ac-E WEALEKK LAALESK ***C***QALEKK LQALEKK ***H***EALEH G-NH_2

A particularly sensitive technique employed to analyze $Pb^{II}Cys_3$ environments is ^{207}Pb NMR. Historically, ^{207}Pb NMR has been used to study multiple Pb^{II}-coordination environments in small molecules with mixed S/O, S/N and N/O coordinating ligands; however, until recently, only one example was reported using this technique to characterize metalloproteins.[23–28] In 1996, Aramini *et al.* published a study utilizing ^{207}Pb NMR to analyze Pb^{II}-substituted calmodulin and other calcium binding proteins ($Pb^{II}O_7$).[29] Regardless of the high affinity of Pb^{II} for thiol-rich metal binding sites, it was not until 2011 that Neupane *at al.* located the $^{207}Pb^{II}S_3$ chemical shift, in a peptidic environment.[30] This was largely due to the difficulty in identifying where a $Pb^{II}S_3$ signal

would appear in the very wide chemical shift range of 16000 ppm (compared to ~200 ppm for ^{13}C, or ~900 ppm for ^{113}Cd).[29] The technique has proved indispensible for studying Pb^{II} binding to **GR** and **TRI** peptides that contain Cys_3 metal binding sites. Indeed, a simple change from an **a** to **d** site Cys_3 results in NMR shifts of >200 ppm.[30]

In this chapter, I will describe the design, preparation and spectroscopic characterization (with emphasis on heteronuclear NMR) of heterotrimeric *de novo* designed 3SCCs. My approach will combine steric matching of Ala and Leu residues in the layer directly above a Cys_3 metal binding site with Pb^{II} binding to the Cys_3 binding site. I will discuss how NMR and UV-Vis analysis support formation of a new species that is not due to coalescence and is not simply a combination of two homotrimeric peptides. I will address how the Pb^{II} site is not affected by the presence of an additional transition metal, such as Co^{II} or Zn^{II}. I will also consider the specifications required to form selective heterotrimeric 3SCCs such as how Hg^{II}, another thiolphilic metal that binds tightly to our 3SCCs, is not able to induce selective heterotrimer formation and how Ala/Leu pairings in the layer below the Cys_3 site, with respect to the N-terminus, does not (yet) lead to obvious 3SCC formation. Finally, I will examine how a recently refined Pb^{II}-bound homotrimeric crystal structures by Dr. Leela Ruckthong may provide insight into why heterotrimers form in the presence of Pb^{II} and use this information to assess whether the basis for the initial design strategy was correct.

Materials and Methods

Peptide Synthesis and Purification. Peptides were synthesized on one of two instruments: an Applied Biosystems 433A synthesizer or a Biotage Initiator+Alstra synthesizer on a Rink Amide Methylbenzhydrylamine (MBHA) resin using standard Fmoc-*t*Bu-based protection protocols (HBTu/HOBt coupling).[31] Crude peptides were cleaved from the resin using trifluoroacetic acid (TFA), ethanedithiol, anisole, and thioanisole (90:3:2:5), dissolved in doubly distilled water and lyophilized to dryness. Purified peptides were isolated using Waters 600 HPLC on a reverse phase C18 column (flow rate: 20 mL/min, solvent A: 0.1% TFA in water and B:0.1% TFA in 90:10 CH-

$_3$CN:H_2O. A linear gradient was used starting at 70:30, A:B and increasing to 20:80 over 35 min.). ESI-MS was used to confirm the mass of purified peptide and collections were lyophilized to yield pure, white powder. Concentrations of all peptides were determined by tryptophan absorbance at 280 nm (ε = 5500 $M^{-1}cm^{-1}$).[32]

Circular Dichroism (CD) and Ultraviolet-Visible (UV-Vis) Spectroscopy. CD spectra were collected on an AVIV 62DS spectrometer or a Jasco CD-Spectropolarimeter in a 1-cm quartz cuvette at 25 °C. Guanidine hydrochloride (GuaHCl) titrations were carried out at pH 8.0 using an automated titrator with a syringe pump as described previously.[33] Fittings of the free energy change from folded to unfolded for **GR**-ACH and **GR**-CH were determined as previously described.[34] All other peptides do not show enough stability of the folded state to fit the data to a two-step model and will therefore be compared via estimated midpoint for GuaHCl denaturation titrations. UV-Vis spectra were recorded in quartz cuvettes at room temperature on a Cary 100 Bio UV/Vis spectrometer.

Pb(II)-binding titrations. Titrations of Pb^{II} into peptide were performed at room temperature and monitored via UV-Vis spectroscopy in a 1-cm quartz cuvette. $Lead^{II}$ titrations were completed in 50 mM TRIS buffer at pH 8.5 at a peptide concentration of 30 μM 3SCC. TRIS adjustments were made using small aliquots of concentrated KOH and HCl. Aliquots of a $Pb^{II}(NO_3)_2$ stock solution, standardized using inductively coupled plasma-optical emission spectroscopy (ICP-OES, Perkin-Elmer Optima 2000 DV with Winlab software) were titrated into the peptide solution. For all titrations, the difference spectra were obtained by subtracting the background spectrum of the peptide under identical conditions but in the absence of metal.

pH Titrations. Lead was bound to the peptide and diluted to a concentration of 60 μM trimer in water. The pH was titrated by adding small aliquots of KOH to the solution. The pH was monitored and allowed to stabilize before analysis of the $Pb^{II}Cys_3$ band ($\varepsilon\approx$345 nm) was conducted. The data was fitted to three different deprotonation models, all-corresponding to deprotonation of thiol to thiolate in the presence of bound Pb^{II}. The three models correspond to different deprotonation equilibrium including (I) 1-proton release, (II) 2-proton simultaneous release, and (III) 2-proton released step-wise. $MPep_3^-$,

$MPep_3H$, and $MPep_3H^+$ correspond to completely deprotonated, singly protonated and doubly protonated Metal (M, where M is Pb^{II} in these studies) bound trimer (Pep_3). $[Pep_3]_{TOT}$ is the total concentration of trimer in solution, and $[H^+]$ is the concentration of protons in solution, which is directly related to the pH (the independent variable of the experiment).

Model (I). This scenario corresponds to an equilibrium associated with the apparent pK_a value for the metal-chelation deprotonation of a one-proton release model, which can be expressed by Equation 1.

$$MPep_3H \rightleftharpoons H^+ + MPep_3^- \qquad \text{Equation 1}$$

The apparent association constant for the 1-proton deprotonation model can be expressed using Equation 2.

$$K_a = \frac{[H^+][MPep_3^-]}{[MPep_3H]} \qquad \text{Equation 2}$$

Rearrangement of Equation 2 gives Equation 3.

$$[MPep_3H] = \frac{[H^+][MPep_3^-]}{K_a} \qquad \text{Equation 3}$$

The mass balance equation for $[Pep_3]_T$ is expressed in Equation 4.

Mass Balance Equation:

$$[Pep_3]_{TOT} = [MPep_3H] + [MPep_3^-] \qquad \text{Equation 4}$$

Substitution of Equation 3 into Equation 4 gives Equation 6.

$$[Pep_3]_{TOT} = \frac{[H^+][MPep_3^-]}{K_a} + [MPep_3^-] \qquad \text{Equation 5}$$

$$= [MPep_3^-]\left(\frac{[H^+]}{K_a} + 1\right) \qquad \text{Equation 6}$$

This equation can then be directly related to the absorbance observed at ~345 nm by substituting $[P_3]_{TOT}$ from Equation 7 (where *b* is the path length of the cuvette) into Equation 6.

$$\text{Absorbance}^{345\ nm} = \varepsilon^{345\ nm} * [Pep_3]_{TOT} * b \qquad \text{Equation 7}$$

Rearrangement of Equation 5 can then be used to fit the titration data at Abs 345 nm using Prism 5 (GraphPad Software)[35] to yield the apparent pK_a value for a one-proton deprotonation step.

Model (II). The scenario corresponding to the equilibrium associated with the apparent pK_{a1} and pK_{a2} values for the metal-chelation deprotonation of a stepwise deprotonation of two protons can be expressed by Equation 8.

$MP_3H_2^+ \rightleftharpoons H^+ + MP_3H \rightleftharpoons H^+ + MP_3^-$ Equation 8

The apparent association constants for each deprotonation step can be expressed using Equations 9 and 10.

$$K_{a1} = \frac{[H^+][MPep_3H]}{[MPep_3H_2^+]}$$ Equation 9

$$K_{a2} = \frac{[H^+][MPep_3^-]}{[MPep_3H]}$$ Equation 10

Rearrangement of Equation 10 gives Equation 11.

$$[MPep_3H] = \frac{[H^+][MPep_3^-]}{K_{a2}}$$ Equation 11

Substitution of $[MPep_3H]$ into Equation 9 gives Equation 12.

$$K_{a1} = \frac{[H^+]^2[MPep_3^-]}{[MPep_3H_2^+]K_{a2}}$$ Equation 12

Rearrangement of Equation 12 gives Equation 13.

$$[MPep_3H_2^+] = \frac{[H^+]^2[MPep_3^-]}{K_{a1}K_{a2}}$$ Equation 13

The mass balance equation for $[Pep_3]_{TOT}$ is expressed in Equation 14.

Mass Balance Equation:

$[Pep_3]_{TOT} = [MPep_3H_2^+] + [MPep_3H] + [MPep_3^-]$ Equation 14

Substitution of Equation 11 and Equation 13 into Equation 14 gives Equation 16.

$$[Pep_3]_{TOT} = \frac{[H^+]^2[MPep_3^-]}{K_{a1}K_{a2}} + \frac{[H^+][MPep_3^-]}{K_{a2}} + [MPep_3^-]$$ Equation 15

$$= [MPep_3^-]\left(\frac{[H^+]^2}{K_{a1}K_{a2}} + \frac{[H^+]}{K_{a2}} + 1\right)$$ Equation 16

This equation can then be directly related to the absorbance observed at ~345 nm by substituting $[Pep_3]_{TOT}$ from Equation 7 (where *b* is the path length of the cuvette) into Equation 16. Rearrangement of Equation 16 can then be used to fit the titration data at Abs 345 nm using Prism 5 (GraphPad Software)[35] to yield the apparent pK_{a1} and pK_{a2} values for the deprotonation associated with a stepwise 2-proton metal-chelation deprotonation of $Pb^{II}Cys_3$.

Model (III). The equilibrium associated with the apparent pK_{a2} value for the metal-chelation deprotonation of a simultaneous deprotonation of two protons can be expressed by Equation 17.

$$MPep_3H_2^+ \rightleftharpoons 2\ H^+ + MPep_3^- \qquad \text{Equation 17}$$

The apparent association constant for the simultaneous 2-proton deprotonation step can be expressed using Equation 18.

$$K_{a2} = \frac{[H^+]^2[MPep_3^-]}{[MPep_3H_2^+]} \qquad \text{Equation 18}$$

Rearrangement of Equation 18 gives Equation 19.

$$[MPep_3H_2^+] = \frac{[H^+]^2[MPep_3^-]}{K_{a2}} \qquad \text{Equation 19}$$

The mass balance equation for $[Pep_3]_{TOT}$ is expressed in Equation 20.

Mass Balance Equation:

$$[Pep_3]_{TOT} = [MPep_3H_2^+] + [MPep_3^-] \qquad \text{Equation 20}$$

Substitution of Equation 19 into Equation 20 gives Equation 22.

$$[Pep_3]_{TOT} = \frac{[H^+]^2[MPep_3^-]}{K_{a2}} + [MPep_3^-] \qquad \text{Equation 21}$$

$$= [MPep_3^-]\left(\frac{[H^+]^2}{K_{a2}} + 1\right) \qquad \text{Equation 22}$$

This equation can then be directly related to the absorbance observed at ~345 nm by substituting $[Pep_3]_{TOT}$ from Equation 7 (where *b* is the path length of the cuvette) into Equation 22. Rearrangement of Equation 22 can then be used to fit the titration data at Abs 345 nm using Prism 5 (GraphPad Software)[35] to yield the apparent pK_{a2} value.

Fitting the data using all three models gives a consistent pK_{a1} value from both the single-deprotonation model and the simultaneous 2-proton release model. Best fits for each titration are discussed below.

NMR Spectroscopy. NMR samples were prepared by dissolving pure, lyophilized peptide in 10% D_2O. Metallopeptides were prepared by addition of isotopically enriched $^{207}Pb(NO_3)_2$ or $^{199}Hg(NO_3)_2$ (92.4%, Oak Ridge National Laboratory, TN) to non-buffered solutions of 3-5 mM peptide trimer. All samples were adjusted to the desired pH using small aliquots of concentrated KOH or HCl. ^{207}Pb NMR spectra were recorded at a frequency of 145.9 MHz on a Varian 700 MHz spectrometer at 25 °C with spin = 0, 0.20 ms relaxation time, and 20 ms acquisition time. ^{199}Hg NMR spectra were recorded at a frequency of 125.3 MHz on a Varian 700 MHz spectrometer at 25° C with spin = 0, 0.005 ms relaxation time, and 10 ms acquisition time. Linear predictions (10-30 points) were performed to remove noise, and the real FID was determined as previously described.[30,36,37] The data were processed with an exponential line broadening of 400-600 Hz using MestRe-C software.[38] The ^{207}Pb NMR shifts are reported as the observed signal plus ~2986 ppm, as reference by tetramethyllead (δ=0 ppm; toluene) using 1 M $Pb(NO_3)_2$ in D_2O (natural abundance salt, δ=-2986 ppm) as an external standard. The external standard was run after each experimental collection to adjust for any shifting of the magnetic field.

Results and Discussion

Pb^{II}-Nucleated Heterotrimers with Ala/Leu Pairings "above"

The story of preparing metal nucleated heterotrimeric 3SCCs starts with preliminary work completed by a previous post-doctoral researcher, Dr. Kosh Neupane, who spent a great deal of time analyzing the difference in selectivity between **a** and **d** Cys_3 site binding of Pb^{II}, the specificity of where a lead ion binds first, and if the sterics around the site influence the metal binding preference. After locating the $Pb^{II}S_3$ signal, he

showed that the length of the peptides used did not influence the ^{207}Pb NMR signal, as evidenced via analysis of Pb^{II}(**Baby**L12C)$_3^-$ and Pb^{II}(**CS**L12C)$_3^-$ (Table 2-1),* both yielding chemical shifts of ~5800 ppm (Figure 2-4). At the same time, he discovered that when Pb^{II} is bound to a peptide containing cysteine substitution at a **d** site, the ^{207}Pb NMR signal observed was nearly ~200 ppm downfield with respect to a corresponding **a** site modified peptide (Figure 2-4).[30] Additionally, if one peptide contained both an **a** and a **d** site cysteine, such as **GR**L12AL16CL26C (Table 2-1), the first equivalent of Pb^{II} would bind exclusively to the **a** site and occupation of the **d** site was observed only upon addition of a second equivalent of Pb^{II} (Figure 2-4). Removing some of the hydrophobic packing around an **a** site to produce a Cys_3 site with a "hole", **TRI**L12AL16C (Table 2-1), provided an additional upfield shift, by nearly 100 ppm, from the original unaltered **a** site of **CS**L9C (Table 2-1, Figure 2-5).[37]

* The nomenclature used to describe the metal complexes studied herein is as follows: When Pb^{II} is bound to the Cys_3 site, the peptide, for example **TRI**-C, will be referred to as: $Pb^{II}{}_S$(**TRI**-C)$_3^-$, where '$_S$' represents the atom that coordinates the Pb^{II} ion. When a second metal, M^{n+}, is introduced to bind to the His_3 site, a subscript of '$_N$' will be included to denote His binding. The charge of the complex corresponds to the sum of the oxidation states of the metals, minus the charge of the coordinated ligands. In the case of a $Pb^{II}Cys_3$ site, the charge is ($^-$), from Pb^{II} and three thiol ligands. When M^{2+} is included the total charge will be ($^+$) from two divalent metals and three deprotonated thiolate ligands, for example: $Pb^{II}{}_S Zn^{II}{}_N$(**GRCS**L16CL30H)$_3^+$.

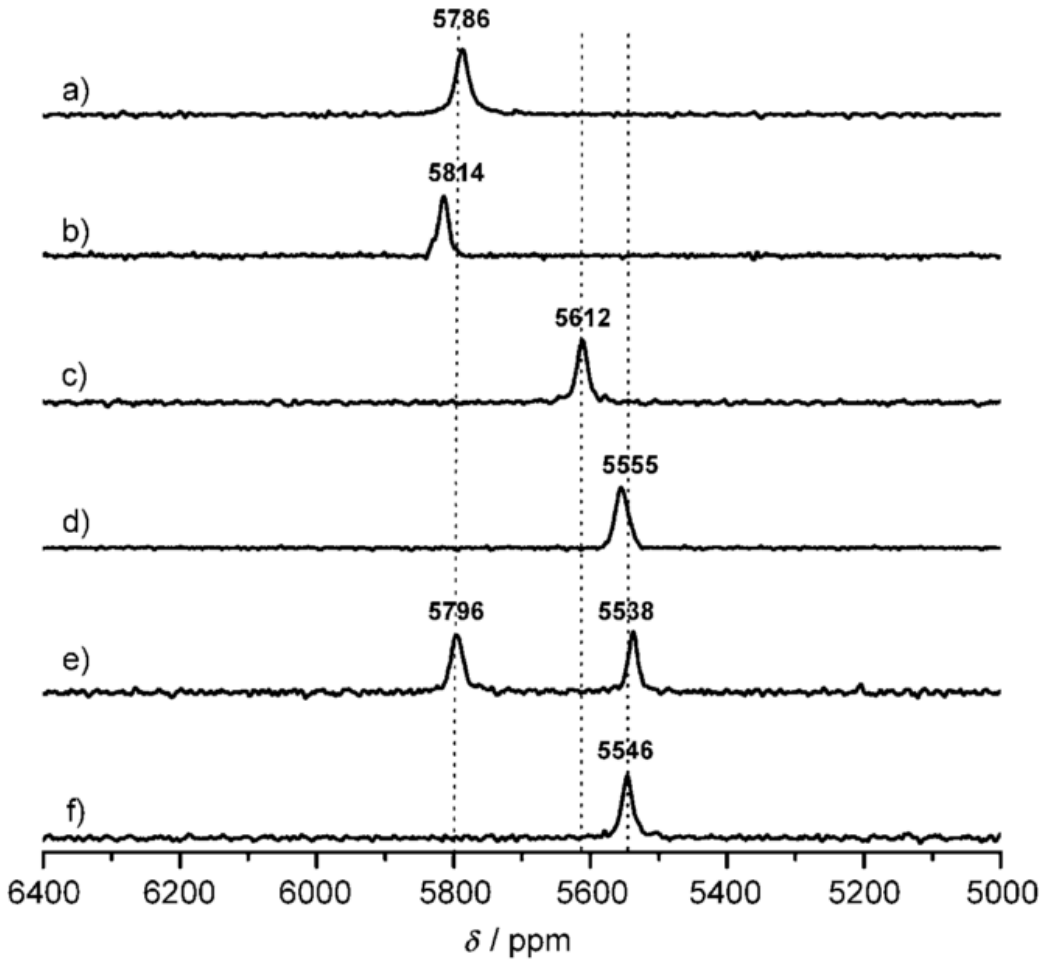

Figure 2-4. ^{207}Pb NMR spectra of Pb^{II}-bound 3SCC peptides. a) Pb^{II}(**BABY**L12C)$_3^-$, b) Pb^{II}(**CS**L12C)$_3^-$, c) Pb^{II}(**CS**L16C)$_3^-$, d) Pb^{II}(**CS**L12AL16C)$_3^-$, e) Pb^{II}_2(**GR**L12AL16L26C)$_3^{2-}$, f) Pb^{II}(**GR**L12AL16CL26C)$_3^{4-}$. All spectra were recorded for 10–12 h using natural- abundance $Pb(NO_3)_2$, (^{207}Pb=22.6%), pH 7.35, at 25 °C. Figure adapted from Ref 30.

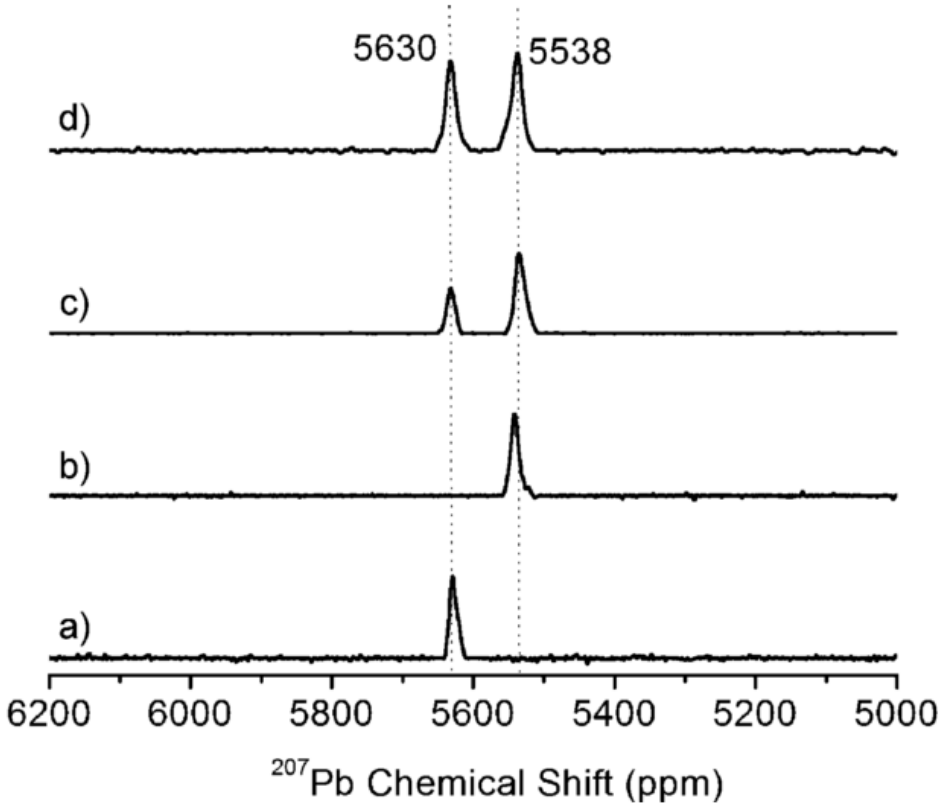

Figure 2-5. ^{207}Pb NMR Spectra of Pb^{II} bound peptides showing the selective binding of Pb^{II} to the peptide with a hole above the metal binding site. a) Pb^{II}(**CS**L9C)$_3^-$, b) Pb^{II}(**TRI**L12AL16C)$_3^-$, c) Equimolar ratio of **CS**L9C and **TRI**L12AL16C with 1 equivalent of $Pb^{II}(NO_3)_2$, d) Equimolar ratio of **CS**L9C and **TRI**L12AL16C with 2 equivalent of $Pb^{II}(NO_3)_2$. The concentration of metallopeptides used is approximately 5 mM. All spectra were recorded at room temperature (25 °C) for 2 hr using isotopically enriched $Pb^{II}(NO_3)_2$, pH 7.45. Figure adapted from Ref 49.

It was at this point that we started to ask the question – can the high-affinity $Pb^{II}Cys_3$ site be combined with the steric matching of Ala and Leu residues to make heterotrimers? In order to exploit the steric matching concept mentioned above the leucine layer at the 12th position were substituted for an alanine layer. The bulky amino acid to be used, and paired with two alanine-containing helices, was leucine. In Kennan's work, smaller hydrophobes substituted for cyclohexylalanine, such as cyclopropylalanine (isostructural to leucine), were insufficient to generate a single, stable heterotrimeric aggregate. Thus, one might predict that access to such parallel heterotrimeric systems using leucine as the bulky residue, in the **TRI** or **GR** peptides, should be difficult. However, both experimental and computational studies, as mentioned above, indicated

that Pb^{II} binding to cysteine substituted **TRI** and **GR** peptides was sensitive to the steric constraints of the second coordination sphere, presumably due to the metal's large size and bulky lone pair.[37] Additionally, substitution of the leucine layers within the 3SCCs has been determined to destabilize the peptide scaffold as layers of hydrophobic packing residues within the helical core are removed. Therefore, the peptide scaffold itself is most stable with Leu residues over Ala residues, but the Pb^{II} ion is expected to bind better in the presence of an Ala layer. Based on these considerations, the subsequent question was could mixed assemblies containing peptides with either leucine, **TRI**L2WL16C, or alanine, **TRI**L2WL12AL16C (already biased toward heterotrimer formation based on the steric matching approach, Table 2-1), be stabilized by combining helical stability (from the Leu residues) as well as exploiting the Pb^{II} steric preference (allowing space via Ala substitutions to accommodate the bulky metal ion)?

It has been shown that ^{207}Pb NMR is particularly powerful for discerning Pb^{II} binding to homoleptic (a metal binding environment with identical ligands), Cys_3 sites in designed proteins as demonstrated by the approximately 75 ppm chemical shift separation of Pb^{II}_S(**TRI**L2WL12AL16C)$_3^-$, designated Pb^{II}_S(**TRI**-AC)$_3^-$, and Pb^{II}_S(**TRI**L2WL16C)$_3^-$, designated Pb^{II}_S(**TRI**-C)$_3^-$ (Figure 2-6). Above pH 6, these peptides have been shown to form well-behaved parallel three stranded coiled-coils with characteristic circular dichroism and guanadinium chloride denaturation isotherms characteristic of cooperative unfolding in the presence and absence of metals.[19,33,39] These resonances represent the upper and lower limits that would be expected in subsequent experiments involving heterotrimeric species.[30] ^{207}Pb NMR was then used to analyze mixtures of these peptides.

When adding two equivalents of the Pb^{II}_S(**TRI**-C)$_3^-$ and one equivalent of Pb^{II}_S(**TRI**-AC)$_3^-$ in the presence of one equivalent $Pb^{II}(NO_3)_2$, two peaks are observed at new chemical shifts (δ= 5631 and 5604 ppm), with a clear dominance of the more downfield shifted species (Figure 2-6b). However, switching the stoichiometry to two equivalents of Pb^{II}_S(**TRI**-AC)$_3^-$ and one equivalent of Pb^{II}_S(**TRI**-C)$_3^-$ resulted in only one observed resonance, corresponding to the smaller of the two peaks found with the opposite stoichiometry (δ=5604 ppm, Figure 2-6c). From these results I deduce that

mixing together two equivalents of Pb^{II}_S(**TRI**-AC)$_3^-$ and one equivalent of Pb^{II}_S(**TRI**-C)$_3^-$ selectively provides a new heterotrimeric 3SCC, here on referred to as the Pb^{II}_S[(**TRI**-AC)$_2$(**TRI**-C)$_1$]$^-$. However, when analyzing the stoichiometric mixture of Pb^{II}_S[(**TRI**-AC)$_1$(**TRI**-C)$_2$]$^-$, it appears that a mixture of both the Pb^{II}_S(**TRI**-AC)$_1$(**TRI**-C)$_2^-$ and Pb^{II}_S[(**TRI**-AC)$_2$(**TRI**-C)$_1$]$^-$ heterotrimers are formed. These results suggest that mixtures of Pb^{II}_S[(**TRI**-AC)$_n$(**TRI**-C)$_{3-n}$]$^-$ where n=2 provides selective heterotrimeric formation whereas n=1 does not. The stoichiometery is consistent with that used by both the Kennan and Tanaka labs.

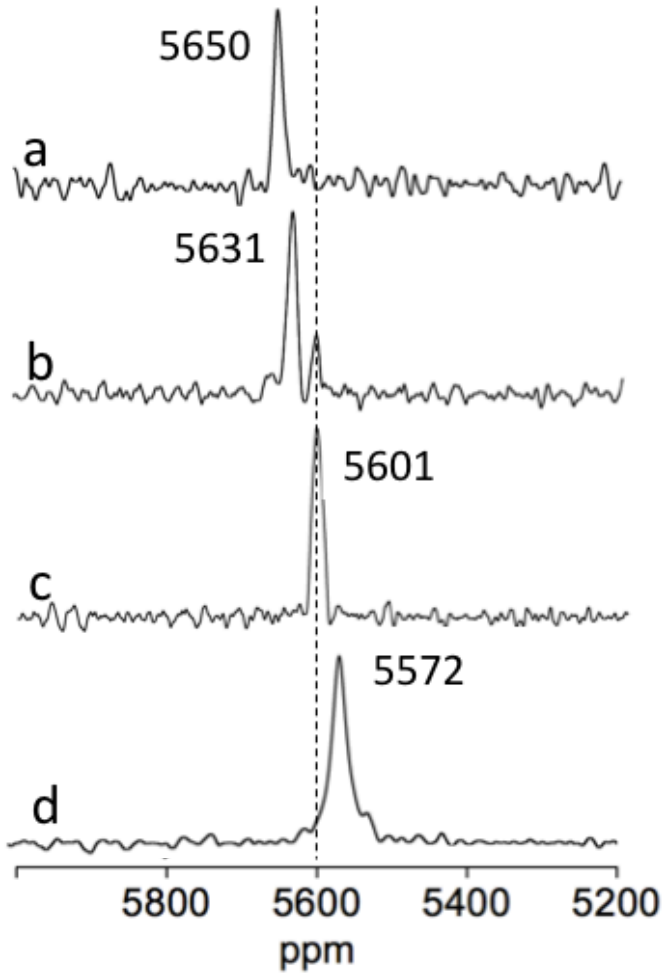

Figure 2-6. ^{207}Pb NMR spectra of a) Pb^{II}_S(**TRI**-C)$_3^-$, b) Pb^{II}_S[(**TRI**-C)$_2$(**TRI**-AC)$_1$]$^-$, c) Pb^{II}_S[(**TRI**-C)$_1$(**TRI**-AC)$_2$]$^-$, and d) Pb^{II}_S(**TRI**-AC)$_3^-$. All spectra were recorded at room temperature (25 °C) for 5 hr using isotopically enriched $Pb^{II}(NO_3)_2$, pH 7.4.

One can imagine three limiting scenarios when stoichiometrically mixing peptides with alanines (**TRI**-AC, **A**) and leucines (**TRI**-C, **B**) in the 12-position to one equivalent of Pb^{II}. For consideration of statistical distributions, Pb^{II}_S(**TRI**-AC)$_3^-$ and Pb^{II}_S(**TRI**-C)$_3^-$ are referred to as $\mathbf{A}_3$ and $\mathbf{B}_3$, respectively. We consider the scenario where two equivalents of **A** are mixed with one equivalent of **B**. One could imagine that metallated homotrimeric species $\mathbf{A}_3$ and $\mathbf{B}_3$ were thermodynamically preferred for the first model, yielding a 2:1 ratio of these species. The second possibility is that there is no preference. In this case, one would expect a statistical peptide distribution based on the initial peptide stoichiometries, yielding $\mathbf{A}_3$ (8/27), $\mathbf{A}_2\mathbf{B}$ (12/27), $\mathbf{AB}_2$ (6/27) and $\mathbf{B}_3$ (1/27). The final possibility is that one heterotrimeric species is preferred, which in this case would yield 100% $\mathbf{A}_2\mathbf{B}$.

The NMR spectra that would be observed for these conditions will depend on whether the system is on the slow or fast exchange time regime. If slow, individual resonances from each species should be observed, whereas if fast, coalescence of the ^{207}Pb NMR signals between the species is expected with a new peak observed at an intermediary distance between the two homotrimeric peaks dependent on the ratios of $\mathbf{A}_3$, $\mathbf{A}_2\mathbf{B}$, $\mathbf{AB}_2$ and $\mathbf{B}_3$ aggregates present. For the first scenario where there is predicted to be a 2:1 ratio of $\mathbf{A}_3$ and $\mathbf{B}_3$, one would expect either two resonances at 5575 and 5650 ppm with ratios of 2:1, respectively, for slow exchange, or a broadened single resonance at 5600 ppm (fast exchange). In the second case, slow exchange would lead to four peaks that are dependent on the chemical shifts of heterotrimeric species in a ratio of 8:12:6:1, while fast exchange would again yield a value at ~5600 ppm. Finally, if a single heterotrimeric species is formed one would expect to see a single resonance consistent with an $\mathbf{A}_2\mathbf{B}$ species.

Examination of Figure 2-6 allows two of these five possibilities to be eliminated. Pure $\mathbf{A}_3$, Pb^{II}_S(**TRI**-AC)$_3^-$, and $\mathbf{B}_3$, Pb^{II}_S(**TRI**-C)$_3^-$, yield resonances at 5572 ppm and 5650 ppm, respectively. When the ratio of **A**:**B** is varied to 1:2 or 2:1 a single resonance is observed with chemical shift value of 5631 ppm and 5601 ppm, respectively. These spectra are consistent either with *fast exchange* for the first two scenarios described above or for the existence of a single $\mathbf{AB}_2$ or $\mathbf{A}_2\mathbf{B}$. However, the data are inconsistent

with *slow* exchange spectra with either a statistical distribution of $\mathbf{A}_3$, $\mathbf{A}_2\mathbf{B}$, $\mathbf{AB}_2$ and $\mathbf{B}_3$ aggregates or a 2:1 mixture of $\mathbf{A}_3$ and $\mathbf{B}_3$ peptides. An important hint to the behavior of this system is provided by careful inspection of Figure 2-6b where a minor resonance is observed at 5601 ppm. If this resonance is real, it indicates that the system cannot be at the fast exchange limit, as under these conditions only one resonance should be observed (*vide infra*).

To test this hypothesis, I examined the binding of two equivalents of Pb^{II} to a mixture of five equivalents of the Ala/Cys_3 peptide ($\mathbf{A}_3$) and one equivalent of the Leu/Cys_3 peptide ($\mathbf{B}_3$). Concurrently, I hypothesized that I could take advantage of this selective heterotrimer formation using a Pb^{II} binding "structural site" to introduce asymmetry into other parts of the peptide. For example, a second asymmetric metal binding site could be engineered into the scaffold for functional applications (See Chapter 3). I used the more stable **GR** peptides for this purpose.[40,41] To test these hypotheses, two new peptides were synthesized: **GR**L2WL12AL16CL30H (designated **GR**-ACH, or $\mathbf{A}_3$) and **GR**L2WL16CL30H (designated **GR**-CH, or $\mathbf{B}_3$, Table 2-1).

It had been previously determined that the inclusion of a Trp substitution in the 2nd position of our **TRI** and **GR** peptides allows for a simple and straightforward method for determining peptide concentration and does not cause significant disruption of the hydrophobic packing or destabilization of the packing.[42] However, even considering the lack of concern regarding stability with the Leu→Trp substitution, **GR**-ACH still contains three substitutions and the folding and stabilities of the peptides were, therefore, determined using CD spectroscopy and guanidine hydrochloride (GuaHCl) denaturation titrations. The folding of both **GR**-ACH and **GR**-CH were examined at pH 8.0 (Figure 2-7). A characteristic CD spectrum of an alpha-helical coiled coil yields a double well with minima at 208 and 222 nm. The spectra for **GR**-ACH and **GR**-CH show well-folded alpha-helical folding with molar ellipticity [Θ] (-34865 and -33785 deg $dmol^{-1}$ cm^2, respectively), which is >95% folding for each peptide, compared to an ideal, fully folded alpha-helical structure. As observed in Figure 2-7, the midpoint of **GR**-CH is slightly higher than that of **GR**-ACH indicating a slight decrease in stability, as one might expect, when an additional substitution, in this case, L12A, is introduced into the sequences. The

midpoints for **GR**-ACH and **GR**-CH were fit to 1.83 ± 0.06 and 2.28 ± 0.03 M GuaHCl, respectively, and fits of the denaturation curves reveals a ΔG of unfolding of 1.96 ± 0.4 and 3.04 ± 0.6 kcal/mol, respectively.[34] These data confirm a decrease in stability of ~1 kcal/mol and a ~0.5 M decrease in midpoint when Ala is substituted for Leu in these peptides.

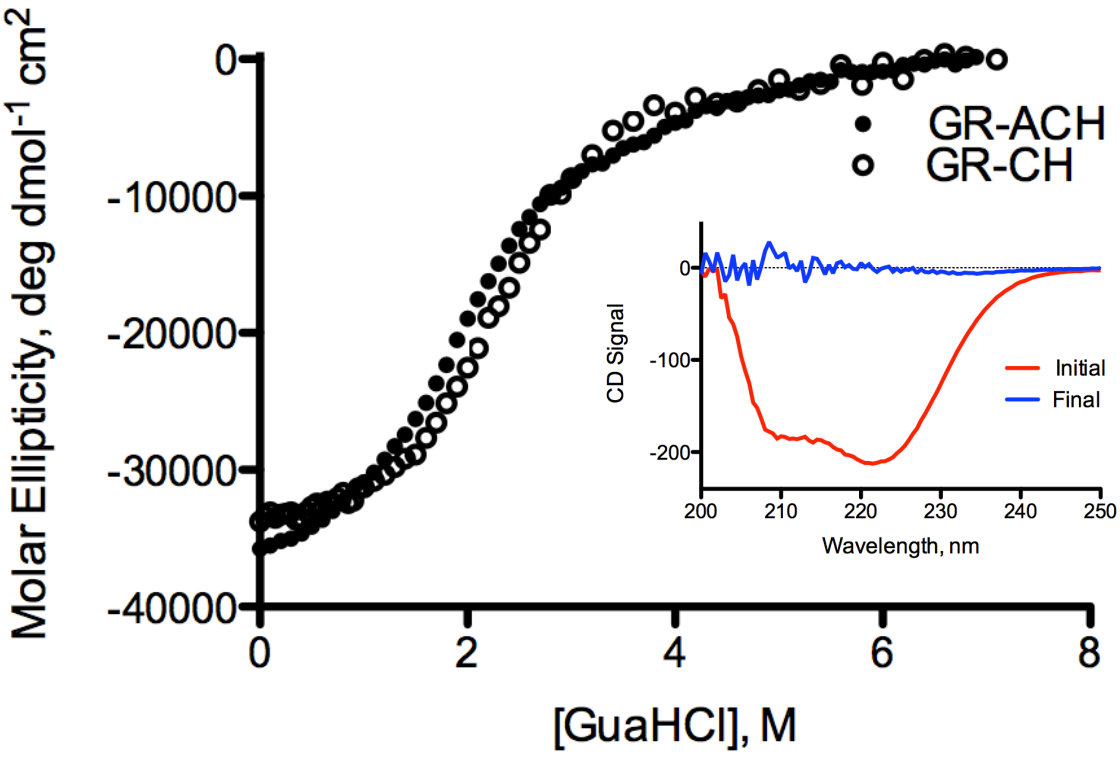

Figure 2-7. Overlay of guanidine hydrochloride denaturation titration data of **GR**-ACH (closed circle) and **GR**-CH (open circle) in 10 mM Phosphate buffer at pH 8.0. Inset: CD spectra of **GR**-ACH before (red) and after (blue) the addition of 7 M GuaHCl.

As this was the first time **GR**-ACH and **GR**-CH were being used to bind Pb^{II}, I also analyzed the binding of Pb^{II} to the Cys_3 sites via UV-Vis spectroscopy. Aliquots of Pb^{II}, as either nitrate or chloride salt solutions, were added to a solution of 60 μM **GR**-ACH or **GR**-CH, resulting in 20 μM 3SCC, in 100 mM TRIS buffer at pH 8.5. As the peptides complex Pb^{II}, an increase in absorbance at 340-350 nm is observed, characteristic of $Pb^{II}Cys_3$ binding (Figures 2-8A and 2-8C).[19,30] For both peptides, analysis of the spectra determines a maximal absorbance is reached at one equivalent of

Pb^{II} added. The immediate flattening out of the traces, as observed in Figures 2-8B and 2-8D, indicates that Pb^{II} binds extremely tightly to the Cys_3 sites and association constants cannot be directly measured via this technique as no equilibrium is observed between free and bound Pb^{II} in the presence of our peptides. Linear regression analysis of the data at ~345 nm provided molar extinction coefficients of 3630 and 3520 $M^{-1}cm^{-1}$ for **GR**-CH and **GR**-ACH, respectively, which is comparable to previously reported $Pb^{II}Cys_3$ sites.[19,36,43,44]

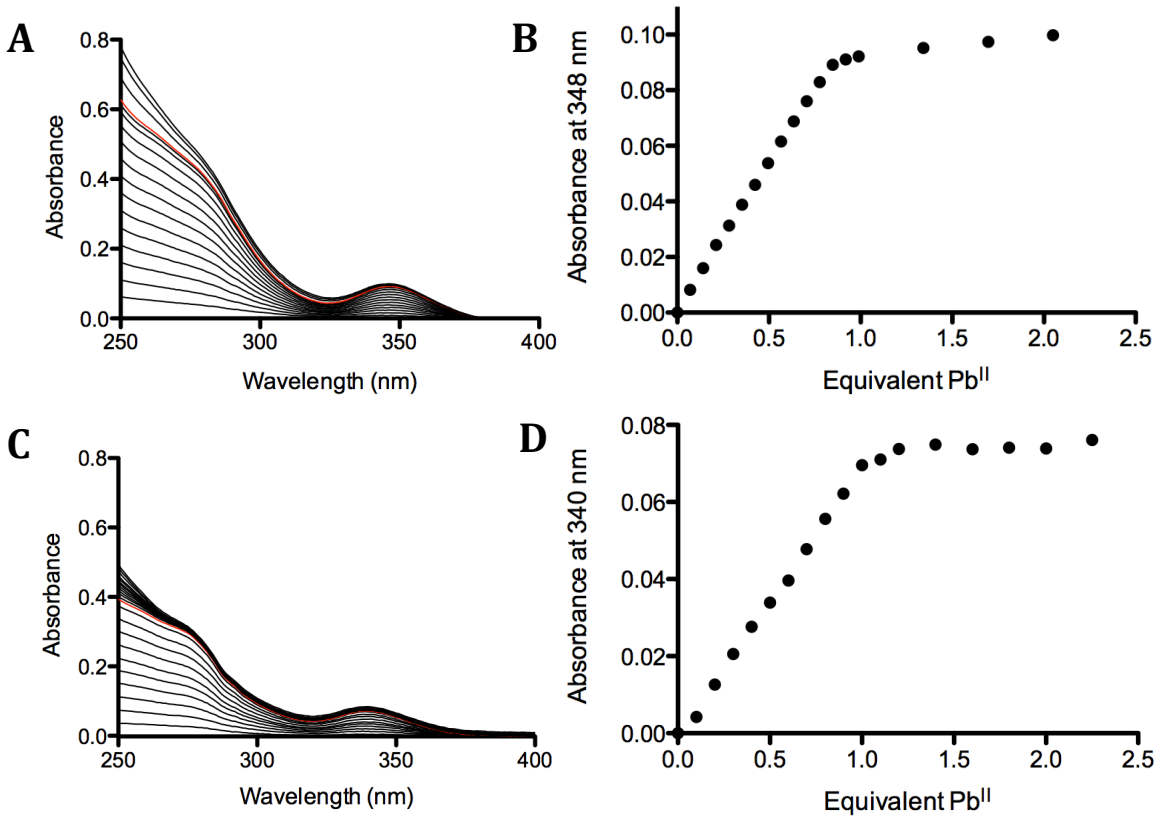

Figure 2-8. Titration spectra of Pb^{II} into a solution of A) **GR**-CH and C) **GR**-ACH at pH 8.5 in 50 mM TRIS Buffer. Corresponding titration curves showing the 1:1 binding stoichiometry of equivalent of Pb^{II} added with respect to 3SCC at 348 and 340 nm for B) **GR**-CH and D) **GR**-ACH.

Closer analysis of the spectra at ~345 nm demonstrates that there is indeed a difference in the maximal absorbance between Pb^{II}_S(**GR**-ACH)$_3^-$ and Pb^{II}_S(**GR**-CH)$_3^-$, observed at 340 and 348 nm, respectively. Therefore, mixtures of the two peptides, in 2:1 and 1:2 ratios, were also analyzed. The resulting mixtures, Pb^{II}_S[(**GR**-ACH)$_2$(**GR**-CH)$_1$]$^-$ and Pb^{II}_S[(**GR**-ACH)$_1$(**GR**-CH)$_2$]$^-$, show absorbance maxima at intermediate distances

between the two homotrimeric peptides at 342 and 345 nm, respectively (Figure 2-9A). However, when calculated spectra are determined by adding ⅔ and ⅓ of the respective homotrimeric spectra, the calculated spectra overlay nearly exactly with that of the data obtained for the mixtures of $Pb^{II}_{S}[(\mathbf{GR}\text{-ACH})_2(\mathbf{GR}\text{-CH})_1]^-$ and $Pb^{II}_{S}[(\mathbf{GR}\text{-ACH})_1(\mathbf{GR}\text{-CH})_2]^-$ (Figure 2-9B). This indicates that analysis via UV-Vis of the $Pb^{II}Cys_3$ peak cannot distinguish between a new, heterotrimeric peptide and a mixture of the homotrimeric peptides.

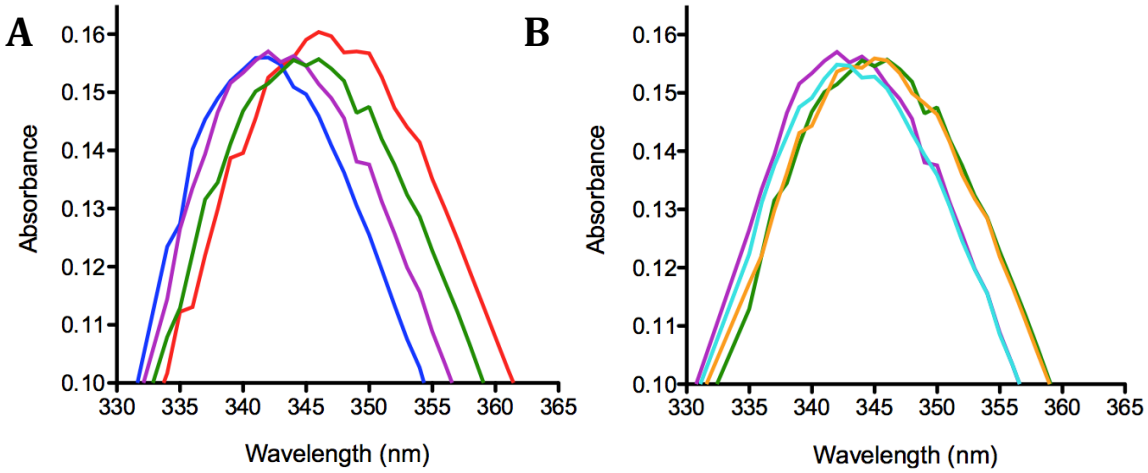

Figure 2-9. Overlay of UV-Vis analysis comparing A) experimental $Pb^{II}S_3$ LMCT bands of Pb^{II}-bound homo- and heterotrimeric 3SCC and B) calculated heterotrimeric spectra from the experimental homotrimeric data. A) Experimental UV-Vis spectra of blue: $Pb^{II}_{S}(\mathbf{GR}\text{-ACH})_3^-$, purple: $Pb^{II}_{S}[(\mathbf{GR}\text{-ACH})_2(\mathbf{GR}\text{-CH})_1]^-$, green: $Pb^{II}_{S}[(\mathbf{GR}\text{-ACH})_1(\mathbf{GR}\text{-CH})_2]^-$, and red: $Pb^{II}_{S}(\mathbf{GR}\text{-CH})_3^-$. B) Experimental heterotrimeric mixtures shown in purple: $Pb^{II}_{S}[(\mathbf{GR}\text{-ACH})_2(\mathbf{GR}\text{-CH})_1]^-$, and green: $Pb^{II}_{S}[(\mathbf{GR}\text{-ACH})_1(\mathbf{GR}\text{-CH})_2]^-$, and calculated mixtures of homotrimers shown in light blue: $⅔[Pb^{II}_{S}(\mathbf{GR}\text{-ACH})_3^-] + ⅓[Pb^{II}_{S}(\mathbf{GR}\text{-CH})_3^-]$ and yellow: : $⅓[Pb^{II}_{S}(\mathbf{GR}\text{-ACH})_3^-] + ⅔[Pb^{II}_{S}(\mathbf{GR}\text{-CH})_3^-]$.

Previously, **a** and **d** site Cys_3 peptides were shown to have different ^{207}Pb NMR shifts as well as slight differences in their apparent pK_a values.[19,30] Since different ^{207}Pb NMR shifts are observed for the **a** site peptides with and without Ala substitutions, as well as the Ala/Leu peptide mixtures, I wanted to assess the difference in the pH dependencies for the metal chelate deprotonation of the Ala containing peptide, **TRI**-AC, as well as the heterotrimeric mixtures.

Pb^{II} binding to **TRI** and **GR** peptides has a significant pH dependence, as evidenced by the absence of the ~350 nm $Pb^{II}Cys_3$ LMCT band at low pH, and the

presence of this band at higher pH (generally > pH 5).[19] There are two models for thiol deprotonation to consider when analyzing the pH dependence of Pb^{II}-bound 3SCC complexes. The equilibrium for cysteine deprotonation can be seen in Scheme 1, where the thiol is deprotonated before the metal associates with the ligand.

$$Pb^{II} + P_3\text{-}SH \rightleftharpoons Pb^{II} + P_3\text{-}S^- + H^+ \rightleftharpoons Pb^{II}\text{-}S\text{-}P_3 \qquad \text{Scheme 1}$$

P_3-SH, P_3-S^-, and Pb^{II}-S-P_3 correspond to the protonated thiol with no associated metal ion, deprotonated thiolate with no metal associated and metal-thoilate complex, respectively. This model represents a thiol pK_a where the Pb^{II} ion is not associated with the ligand until after deprotonation of the thiol ligand has occurred. In this situation, the deprotonation of the thiol ligand is associated with metal complexation, but deprotonation is required before complexation can occur.

The second model for thiol deprotonation is described in Scheme 2, where the metal ion is associated with the neutral thiol before deprotonation.

$$Pb^{II} + HS\text{-}P_3 \rightleftharpoons Pb^{II}\text{-}HSP_3 \rightleftharpoons Pb^{II}\text{-}S\text{-}P_3 + H^+ \qquad \text{Scheme 2}$$

HS-P_3, Pb^{II}-HSP_3, and Pb^{II}-S-P_3 correspond to protonated thiol before metal association, metal-associated neutral thiol, and metal associated thiolate, respectively. In this scenario, the presence of the Pb^{II} ion perturbs the thiol pK_a because the ligands are already associated with the metal ion before deprotonation. In this case, the sulfur binds to the Pb^{II} as either a thiol or thiolate. In both cases the final species, Pb^{II}-S-P_3, is the complex that provides the LMCT band at ~340 nm and, therefore, we cannot spectroscopically distinguish between the two models.

Additionally, it should be noted that although Scheme 1 and Scheme 2 show only one proton being released, the deprotonation step may indeed correlate to a multiple proton step. To distinguish between a 1 and 2 proton step, all of the pH titration data discussed below are fit to three different fitting equations, as derived in the Materials and Methods section. The first fit considers only one proton being released (Equation 7). The second and third fitting models consider two protons being released in a step-wise (Equation 16) or simultaneous (Equation 22) fashion.

Ultimately, we may learn multiple things from the analysis of pK_a values for these Pb^{II}-bound peptides. First, determining the pK_a values of these metallated peptides is essential in order to establish the pH conditions required to form, completely, the $Pb^{II}S_3$ species. Considering that Pb^{II} binding is the key component controlling nucleation of the heterotrimeric peptides, these titrations define the useful pH range for these heterotrimeric complexes. Additionally, if the pK_a values of the heterotrimers are sufficiently different from those of the homotrimers, then these analyses could offer another confirmation that a new species is indeed being made when Ala/Cys and Leu/Cys peptides are mixed together.

The pH of a solution containing 180 μM (60 μM 3SCC) **TRI**-AC, [(**TRI**-AC)$_2$(**TRI**-C)$_1$], [(**TRI**-AC)$_1$(**TRI**-C)$_2$] or **TRI**-C (pK_a previously reported for **TRI**-C but repeated here for internally consistency) and 30 μM $Pb^{II}(NO_3)_2$ was increased from approximately pH 3 to 9 with small aliquots of KOH. The formation of the trigonal pyramidal $Pb^{II}S_3$ complex, as evidenced by the growth of the characteristic LMCT $Pb^{II}S_3$ at ~345 nm, was observed to be complete by pH 7 for all four samples (Figure 2-10). The steepness of the curves of these titrations is directly related to the number of protons released upon metal binding. Generally speaking, the pH titration curves for Pb^{II}_S(**TRI**-C)$_3^-$ and Pb^{II}_S[(**TRI**-AC)$_1$(**TRI**-C)$_2$]$^-$ are less steep than those for Pb^{II}_S(**TRI**-AC)$_3^-$ and Pb^{II}_S[(**TRI**-AC)$_2$(**TRI**-C)$_1$]$^-$, supporting a multi-proton release associated occurring for both Pb^{II}_S(**TRI**-C)$_3^-$ and Pb^{II}_S[(**TRI**-AC)$_1$(**TRI**-C)$_2$]$^-$. Table 2-2 shows the pKa values for each experiment for each fitting model (1H$^+$, stepwise 2H$^+$, and simultaneous 2H$^+$).

Table 2-2. pK_a values for Pb^{II}_S(**TRI**-C)$_3^-$, Pb^{II}_S(**TRI**-AC)$_3^-$, Pb^{II}_S[(**TRI**-AC)$_2$(**TRI**-C)$_1$]$^-$, and Pb^{II}_S[(**TRI**-AC)$_1$(**TRI**-C)$_2$]$^-$ fit to 1-proton, 2-proton stepwise and 2-proton simultaneous models.

Peptide	1 H$^+$	2 H$^+$, Simultaneous	2 H$^+$, Step-wise	
	pK_{a1}	pK_{a2}	pK_{a1}	$_pK_{a2}$
Pb^{II}_S(**TRI**-C)$_3^-$,	5.91 ± 0.05	11.72 ± 0.03	5.62 ± 0.26	11.33 ± 0.50
Pb^{II}_S(**TRI**-AC)$_3^-$	5.43 ± 0.02	10.83 ± 0.04	-	-
Pb^{II}_S[(**TRI**-AC)$_2$(**TRI**-C)$_1$]$^-$	5.27 ± 0.04	10.47 ± 0.06	-	-
Pb^{II}_S[(**TRI**-AC)$_1$(**TRI**-C)$_2$]$^-$	5.51 ± 0.10	10.99 ± 0.16	-	-

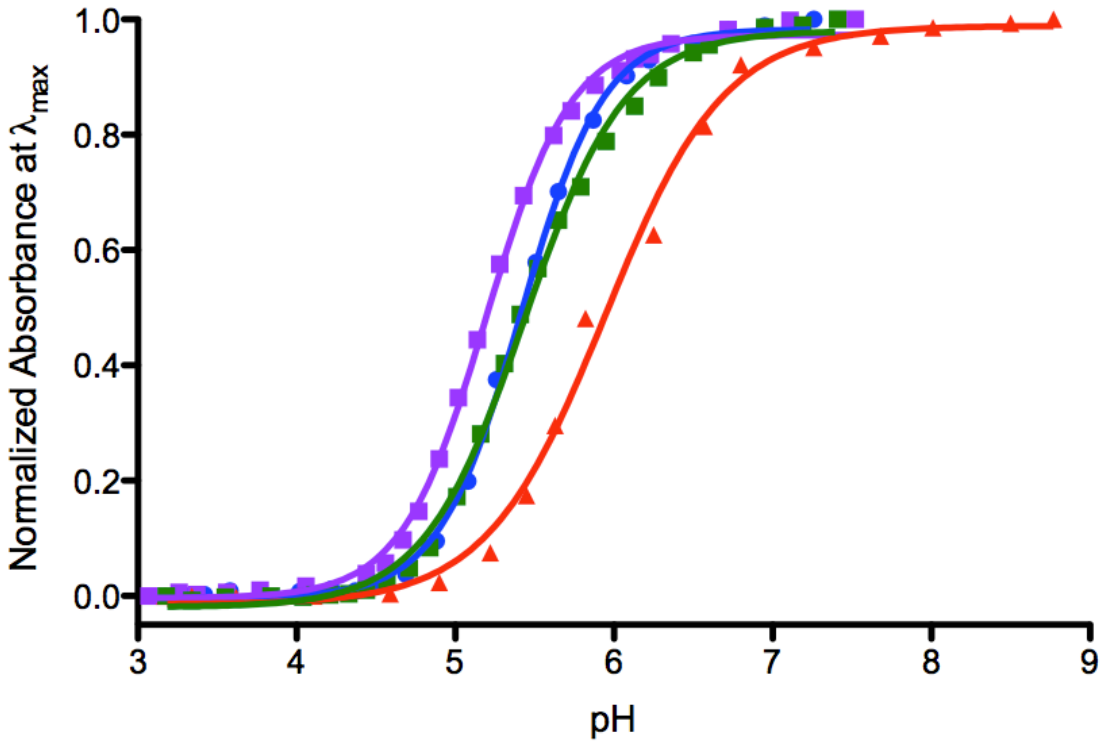

Figure 2-10. pH titration curves of $Pb^{II}Cys_3$ at λ_{max} for homo- and heterotrimers. Data fitted to Equation 22, Blue circles: pK_{a2} = 10.83 ± 0.04 for Pb^{II}_S(**TRI**-AC)$_3^-$, purple squares: pK_{a2} = 10.47 ± 0.06 for Pb^{II}_S[(**TRI**-AC)$_2$(**TRI**-C)$_1$]$^-$, green squares: pK_{a2} = 10.99 ± 0.03 for Pb^{II}_S[(**TRI**-AC)$_1$(**TRI**-C)$_2$]$^-$, and red triangles: pK_{a2} = 11.33 ± 0.04 for Pb^{II}_S(**TRI**-C)$_3^-$.

The most basic pK_a observed, for all three fitting equations, is for Pb^{II}_S(**TRI**-C)$_3^-$, with a best fit obtained using the two-proton step-wise model (pK_{a1} = 5.62 ± 0.26, pK_{a2} = 11.33 ± 0.50, Table 2-2); however, within error, these values are not different indicating the process may indeed be simultaneous. The opposite homotrimer, Pb^{II}_S(**TRI**-AC)$_3^-$ shows a more acidic pK_a and fits best to a simultaneous 2 H^+ model (pK_{a2} = 10.8 ± 0.04, Table 2-2). These data indicate that the identity of the residue in the layer above the Cys_3 binding site doesn't perturb the number of protons released during the pH titration of the Pb^{II}-Pep_3 solutions. Interestingly, Pb^{II}_S(**TRI**-C)$_3^-$ is the only peptide that provided a statistically good fit for a two-proton stepwise model, with the other three peptides providing ambiguous fits.

The titration curve of heterotrimer Pb^{II}_S[(**TRI**-AC)$_2$(**TRI**-C)$_1$]$^-$, which is pure via ^{207}Pb NMR analysis, fits best to a 2 H^+ simultaneous model (pK_{a2} = 10.47 ± 0.06, Table

2-2). The other heterotrimer, $Pb^{II}_S[(\mathbf{TRI}\text{-}AC)_1(\mathbf{TRI}\text{-}C)_2]^-$ is similar to that of the homotrimer $Pb^{II}_S(\mathbf{TRI}\text{-}AC)_3^-$, and statistically fits best to a 1 H^+ model (pK$_a$ = 5.51 ± 0.10, Table 2-2). The discrepancy observed for the best fits of $Pb^{II}_S[(\mathbf{TRI}\text{-}AC)_1(\mathbf{TRI}\text{-}C)_2]^-$ may be a direct consequence of the corresponding pK$_a$ related to the association of 3SCC from 2SCC, which occurs at pH ~5.5.[33] It is possible that there is some ambiguity in the fit of $Pb^{II}_S[(\mathbf{TRI}\text{-}AC)_2(\mathbf{TRI}\text{-}C)_1]^-$ because we are observing a concurrent formation of the folded peptide as well as deprotonation of the thiols to for the $Pb^{II}S_3$ complex. For direct comparison, considering the relatively comparable goodness of fits between the models for all the peptides, the pK$_{a2}$ value for $Pb^{II}_S[(\mathbf{TRI}\text{-}AC)_1(\mathbf{TRI}\text{-}C)_2]^-$ was fit to 10.99 ± 0.03 (Table 2-2). Considering a 2 H^+ step for each sample a general trend can be determined for relative pK$_{a2}$ values of $Pb^{II}_S(\mathbf{TRI}\text{-}C)_3^- > Pb^{II}_S(\mathbf{TRI}\text{-}AC)_3^- \approx Pb^{II}_S[(\mathbf{TRI}\text{-}AC)_1(\mathbf{TRI}\text{-}C)_2]^- > Pb^{II}_S[(\mathbf{TRI}\text{-}AC)_2(\mathbf{TRI}\text{-}C)_1]^-$. In all of these cases full complexation of the completely deprotonated $Pb^{II}S_3$ system is obtained by pH 7 indicating that all experiments conducted at or above pH 7 should not be influenced by the pK$_a$ of Pb^{II}-bound thiolate ligands.

Additionally, when considering the pK$_a$ values of the heterotrimers we see that the values obtained cannot simply be the sum of a combination of the homotrimeric traces. As seen in Figure 2-11, when a calculation is performed, to add two equivalents of $Pb^{II}_S(\mathbf{TRI}\text{-}AC)_3^-$ and one equivalent of $Pb^{II}_S(\mathbf{TRI}\text{-}C)_3^-$, a trace is obtained with a pK$_{a2}$ of ~11.13. The calculation for the opposite mixture one equivalents of $Pb^{II}_S(\mathbf{TRI}\text{-}AC)_3^-$ and two equivalent of $Pb^{II}_S(\mathbf{TRI}\text{-}C)_3^-$ provides a pK$_a$ value of ~11.50. In both cases these values are more basic than the values fitted to the experimental data for $Pb^{II}_S[(\mathbf{TRI}\text{-}AC)_1(\mathbf{TRI}\text{-}C)_2]^-$ (pK$_{a2}$ = 10.99) and $Pb^{II}_S[(\mathbf{TRI}\text{-}AC)_2(\mathbf{TRI}\text{-}C)_1]^-$ (pK$_{a2}$ = 10.47). Again, a combination of homotrimers in solution would not produce the values observed for the heterotrimer samples. These data support a model that when mixing the Ala/Cys and Leu/Cys peptides together we are not simply getting a mixture of the homotrimeric species but are indeed obtaining new, heterotrimeric 3SCCs. This data, in combination with the ^{207}Pb NMR data, supports formation of heterotrimeric 3SCC, nucleated by the binding of Pb^{II} to Cys_3 sites with a mixed Ala/Leu layer above the metal binding site.

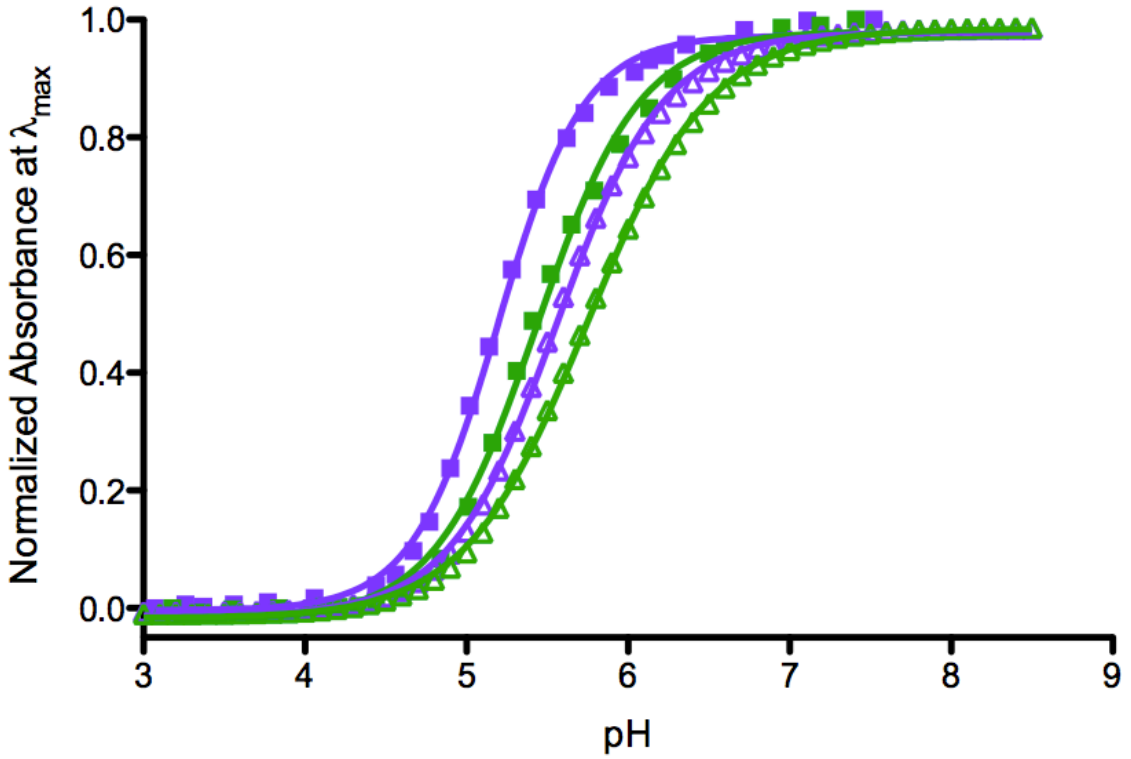

Figure 2-11. Overlay of experimental pH titration curves of $Pb^{II}Cys_3$ at λ_{max} for heterotrimers with calculated heterotrimeric spectra from the experimental homotrimeric data. Experimental heterotrimeric mixtures shown in closed purple squares: $Pb^{II}_S[(\mathbf{TRI}\text{-}AC)_2(\mathbf{TRI}\text{-}C)_1]^-$, and closed green squares: $Pb^{II}_S[(\mathbf{TRI}\text{-}AC)_1(\mathbf{TRI}\text{-}C)_2]^-$, and calculated mixtures of homotrimers shown in open purple triangles: $\frac{2}{3}[Pb^{II}_S(\mathbf{TRI}\text{-}AC)_3^-] + \frac{1}{3}[Pb^{II}_S(\mathbf{TRI}\text{-}C)_3^-]$ and open green triangles: : $\frac{1}{3}[Pb^{II}_S(\mathbf{TRI}\text{-}AC)_3^-] + \frac{2}{3}[Pb^{II}_S(\mathbf{TRI}\text{-}C)_3^-]$. Data fitted to Equation 19 provides pK_{a2} values of 11.3 and 11.5 for $Pb^{II}_S[(\mathbf{TRI}\text{-}AC)_2(\mathbf{TRI}\text{-}C)_1]^-$ and $Pb^{II}_S[(\mathbf{TRI}\text{-}AC)_1(\mathbf{TRI}\text{-}C)_2]^-$, respectively.

We then turned to ^{207}Pb NMR to evaluate whether the longer, more stable **GR** peptides exhibited the same behavior as seen for the **TRI** peptides. ^{207}Pb NMR of $Pb^{II}_S(\mathbf{GR}\text{-}ACH)_3^-$ and $Pb^{II}_S(\mathbf{GR}\text{-}CH)_3^-$, 3-5 mM 3SCC with one equivalent enriched $^{207}Pb^{II}(NO_3)_2$ adjusted to pH 7.4 with small aliquots of KOH, exhibited similar resonances as the analogous **TRI** peptides (Figures 2-12a and 2-12d). Additionally, the mixed peptide systems, $Pb^{II}_S[(\mathbf{GR}\text{-}ACH)_1(\mathbf{GR}\text{-}CH)_2]^-$ and $Pb^{II}_S[(\mathbf{GR}\text{-}ACH)_2(\mathbf{GR}\text{-}CH)_1]^-$, also resulted in similar ^{207}Pb NMR resonances as seen with the **TRI** peptides (Figures 2-12b and 2-12c). Interestingly, the same minor resonance at 5597 ppm appeared in the $Pb^{II}_S[(\mathbf{GR}\text{-}ACH)_1(\mathbf{GR}\text{-}CH)_2]^-$ spectrum (Figure 2-12b). When considering the 5:1 peptide ratio, as mentioned above, if the system is under the fast exchange regime, one should

observe a single broad resonance at ~5585 ppm, whereas under slow exchange conditions two resonances at ~5575 and ~5600 ppm should be present. Clearly, it is the second possibility that results (Figure 2-13). Unlike previous designs, this stoichiometric control can be achieved using a single layer of Ala/Leu matching directly above a $Pb^{II}Cys_3$ layer, allowing for a separate asymmetric functionalization of the scaffold toward the C-terminus.

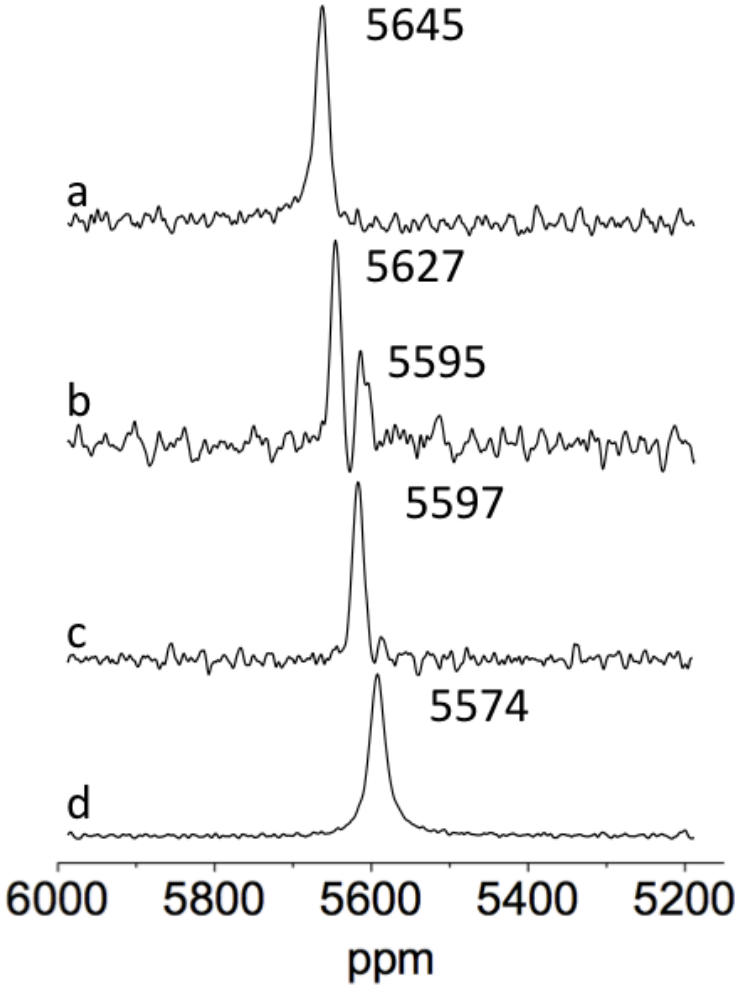

Figure 2-12. ^{207}Pb NMR spectra of a) Pb^{II}_S(**GR**-CH)$_3^-$, b) Pb^{II}_S[(**GR**-CH)$_2$(**GR**-ACH)$_1$]$^-$, c) Pb^{II}_S[(**GR**-CH)$_1$(**GR**-ACH)$_2$]$^-$, d) Pb^{II}_S(**GR**-ACH)$_3^-$. All spectra were recorded at room temperature (25 °C) for 5 hr using isotopically enriched $Pb^{II}(NO_3)_2$, pH 7.4.

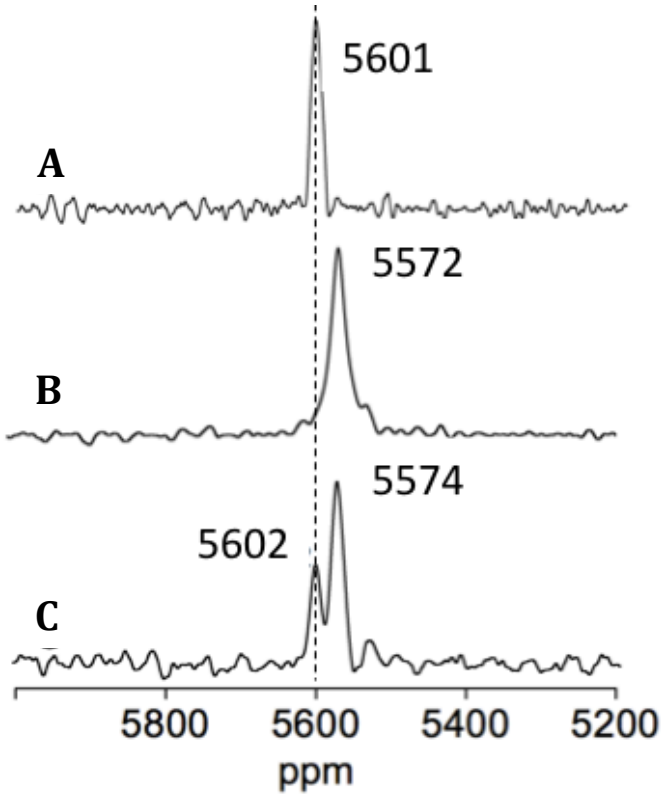

Figure 2-13. ^{207}Pb NMR of A) $Pb^{II}_S[(\textbf{TRI}\text{-}C)_1(\textbf{TRI}\text{-}AC)_2]^-$, B) $Pb^{II}_S(\textbf{TRI}\text{-}AC)_3^-$ and five equivalents of **GR**-ACH and one equivalent of **GR**-CH in the presence of 2 equivalents enriched $Pb^{II}(NO_3)_2$. All spectra were recorded at room temperature (25 °C) for 5 hr using isotopically enriched $^{207}Pb^{II}(NO_3)_2$, pH 7.4.

These studies are fundamentally interesting in the design community as they demonstrate 1) how to prepare controllably **A_2B** type systems using a metal as a template and 2) confer this asymmetric selectively using two adjacent layers of the coiled coils rather than requiring modification along the entire peptide sequence. This second achievement is critical for attaining the ultimate goal of producing selective heterotrimeric 3SCCs in order to obtain a scaffold that contains a second, distinct metal binding site that may lead to a functional asymmetric redox or catalytically active site. This objective requires that the binding of a metal different from Pb^{II} occurs at the second, functional site rather than being competitive with Pb^{II} for the heterotrimeric nucleating Cys_3 site. Similarly, the second site should have a lower affinity for Pb^{II} than the primary Cys_3 site. Thus, it was necessary to determine the relative binding affinities of metals to the nucleating site $Pb^{II}Cys_3$ and the redox/catalytic site $M^{n+}His_3$.

The analysis of competition of other metals with Pb^{II} for the primary structural site with thiolate ligands was assessed using **GR**L2WL16C, designated **GR**-C (Table 2-1). A second metal, such as $Co^{II}SO_4$, was added in a 1:1 metal:trimer ratio, producing a possible $Co^{II}_S(\mathbf{GR}\text{-}C)_3^-$ complex, at 30 μM metallated 3SCC in 100 mM TRIS buffer, pH 8.0. Pb^{II} was then titrated into the solution and the Pb-S LMCT absorption at 346 nm was monitored to track whether Pb^{II} displaced the transition metal. The Pb^{II} easily displaces Co^{II} as these titration curves can be overlaid with the tight binding curves observed for the formation of $Pb^{II}_S(\mathbf{GR}\text{-}C)_3^-$ in the absence of transition metals (Figure 2-14). The experiment was also completed in the presence of $Zn^{II}SO_4$ and $[Cu^{I}(CH_3CN)_4]BF_4$. Similarly to Co^{II}, addition of Pb^{II} easily displaces Zn^{II} as the titration curve can be overlaid with the tight $Pb^{II}_S(\mathbf{GR}\text{-}C)_3^-$ binding curve (Figure 2-14); however, competition is observed for $Pb^{II}Cys_3$ binding when Cu^{I} is present.

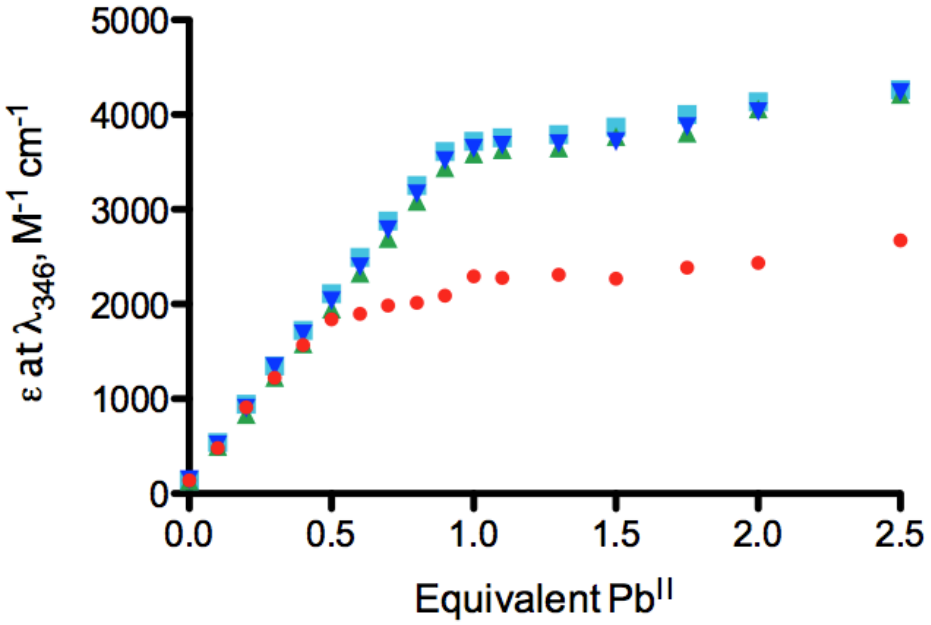

Figure 2-14. UV-Vis titration curves of transition metal displacement via equivalent of Pb^{II} added, with respect to 3SCC, to **GR**-C (no transition metal: dark blue inverted triangle, Co^{II}: light blue square, Zn^{II}: green triangle, and Cu^{I}: red circles) at pH 8.5 in 100 mM Tris-HCl buffer.

The relative affinity of Pb^{II} for a cysteine sulfur vs. imidazole nitrogen metal binding site within the same peptide has been determined by the exclusive and quantitative binding of Pb^{II} to the sulfur site forming $Pb^{II}_S(\mathbf{GR}\text{-}CH)_3^-$ as observed via both

UV-Vis and ^{207}Pb NMR spectroscopies. There was no evidence of Pb^{II} binding to the His_3 site, indicating that minimally, Pb^{II} binds preferentially, and possibly exclusively, to the sulfur site. It has been reported that Cu^{I} has a picomolar affinity for a His_3 site in the **TRI** peptides[45] suggesting that Pb^{II} might go exclusively to the sulfur site while Cu^{I} could be complexed at the histidine site. This behavior is indeed observed when Pb^{II} is titrated into Cu^{I}(**GR**-CH)$_3^{2-}$; no competition is observed between Pb^{II} and Cu^{I} at the cysteine site (Figure 2-15). This result indicates that when His_3 and Cys_3 sites are present, Pb^{II} binding to the Cys_3 site is not inhibited in the presence of Cu^{I}.

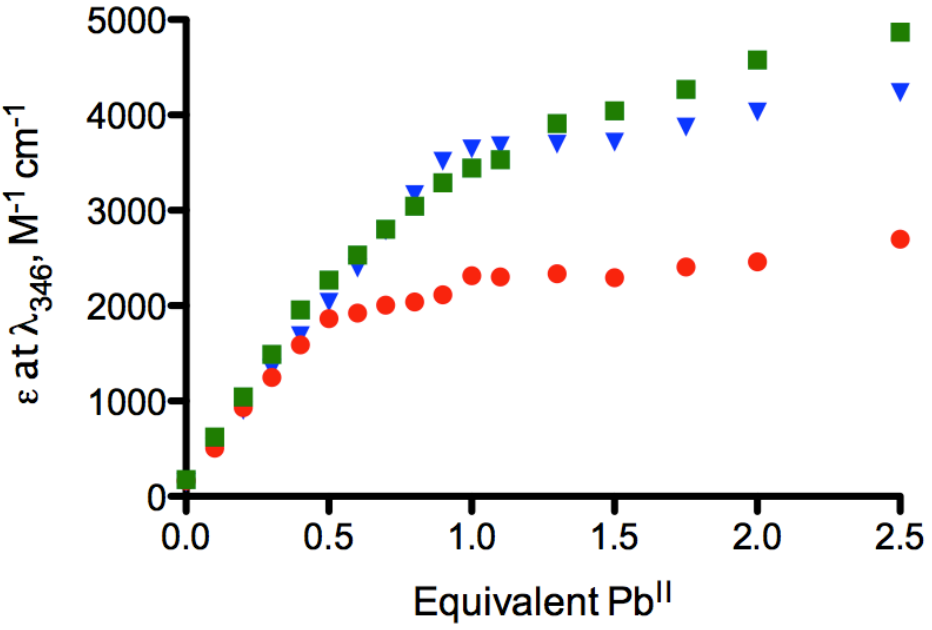

Figure 2-15. UV-Vis titration curves comparing the competition of Cu^{I} and Pb^{II} for a Cys_3 site in the presence and absence of an additional His_3 site within the same peptide. Equivalents of Pb^{II} added, with respect to 3SCC, to **GR**-C, in the absence and presence of Cu^{I} is shown in blue inverted triangles and red circles, respectively. Pb^{II} addition to **GR**-CH in the presence of Cu^{I} is shown in green squares. All data collected at pH 8.5 in 100 mM Tris-HCl buffer.

Pb^{II}-Heterotrimers with Remote Transition Metal Binding Sites

To assess the influence on the $Pb^{II}Cys_3$ from a second metal binding to a remote His_3, site, I also analyzed the ^{207}Pb NMR of $Pb^{II}{}_S M^{II}{}_N$(**GR**-ACH)$_3^+$, $Pb^{II}{}_S M^{II}{}_N$[(**GR**-ACH)$_2$(**GR**-CH)$_1$]$^+$, $Pb^{II}{}_S M^{II}{}_N$[(**GR**-ACH)$_1$(**GR**-CH)$_2$]$^+$, and $Pb^{II}{}_S M^{II}{}_N$(**GR**-CH)$_3^+$, where

M^{II} is $Co^{II}SO_4$ or $Zn^{II}SO_4$. As seen in Figure 2-16, addition of either Co^{II} or Zn^{II} does not cause a perturbation of the $Pb^{II}Cys_3$ site with the second metal present.† The distance between the $Pb^{II}Cys_3$ site and the $M^{II}His_3$ site is ~20 Å, far enough for the paramagnetic characteristics of Co^{II} not to influence the NMR spectra originating from the $Pb^{II}Cys_3$ site.

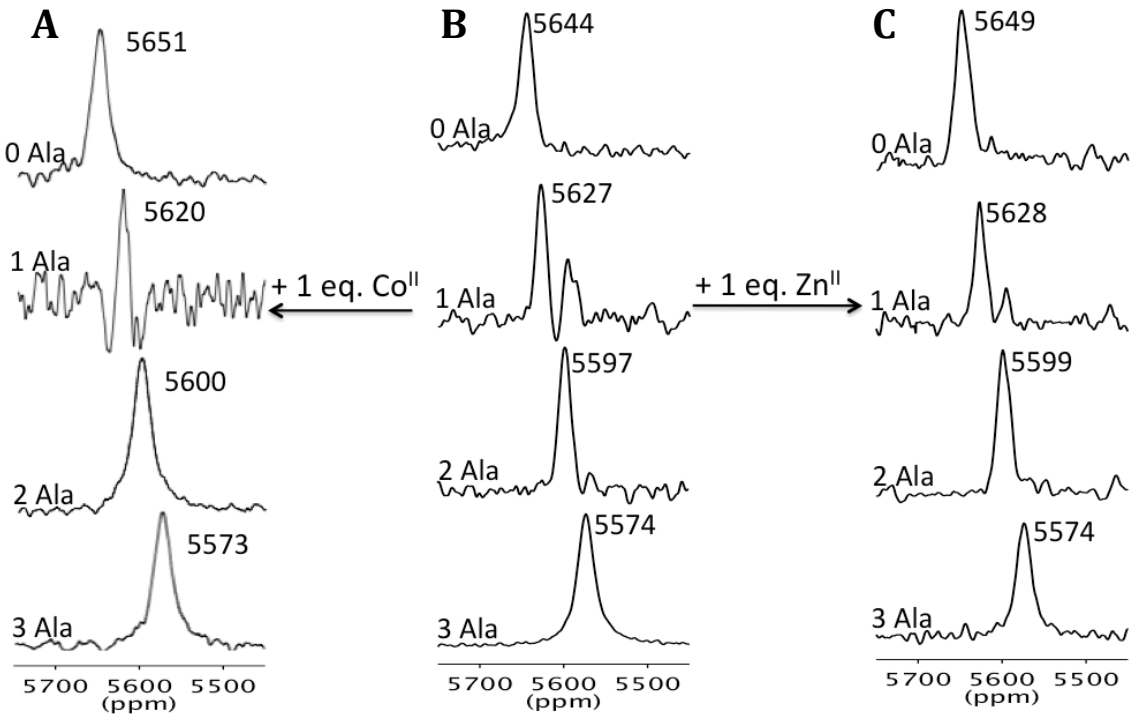

Figure 2-16. ^{207}Pb NMR spectra of Pb^{II} bound homo- and heterotrimers in the absence (B) and presence of a transition metal, Co^{II} (A) or Zn^{II}(C). 0 Ala: $Pb^{II}_SM^{II}_{N/O}$(**GR**-CDH)$_3^{n+}$, 1 Ala: $Pb^{II}_SM^{II}_{N/O}$[(**GR**-CDH)$_2$(**GR**-ACH)$_1$]$^{n+}$, 2 Ala: $Pb^{II}_SM^{II}_{N/O}$[(**GR**-CDH)$_1$(**GR**-ACH)$_2$]$^{n+}$, 3 Ala: $Pb^{II}_SN^{II}_{N/O}$(**GR**-ACH)$_3^{n+}$, collected at pH 8.5.

Previous catalytic studies with the **TRI** and **GR** peptides examined metal binding behavior over a wide pH range, therefore, it was necessary to assess whether our new heterotrimers would retain their composition in neutral and basic solution. The ^{207}Pb NMR resonances for Pb^{II}_S(**GR**-ACH)$_3^-$, Pb^{II}_S(**GR**-CH)$_3^-$, Pb^{II}_S[(**GR**-ACH)$_2$(**GR**-CH)$_1$]$^-$, and Pb^{II}_S[(**GR**-ACH)$_1$(**GR**-CH)$_2$]$^-$ combinations at pH 8.4 and 9.4 matched exactly those observed at pH 7.4 demonstrating that this metal nucleation strategy can be applied broadly (Figure 2-17).

† ^{207}Pb NMR in the presence of both Pb^{II} and Co^{II} was completed with peptides that contain Asp residues in the layer directly above the His_3 site with respect to the N-termini. These peptides will be discussed, at length, in Chapter 3.

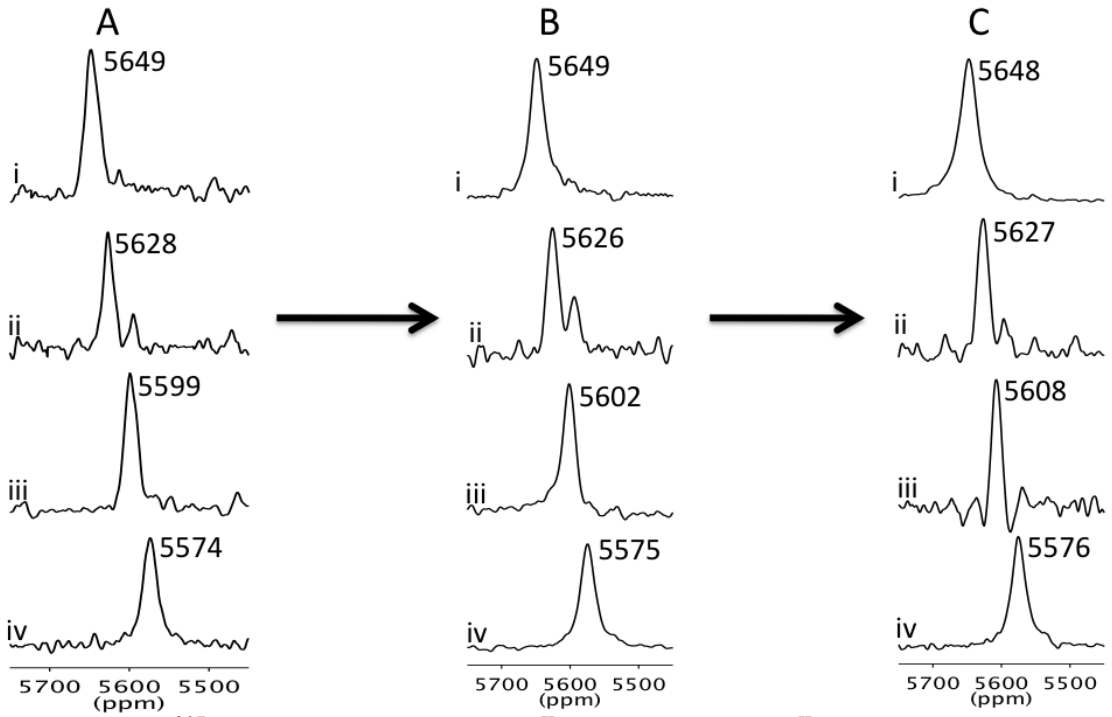

Figure 2-17. ^{207}Pb NMR spectra of i) $Pb^{II}_S(\mathbf{GR}\text{-}CH)_3^-$, ii) $Pb^{II}_S[(\mathbf{GR}\text{-}CH)_2(\mathbf{GR}\text{-}ACH)_1]^-$, iii) $Pb^{II}_S[(\mathbf{GR}\text{-}CH)_1(\mathbf{GR}\text{-}ACH)_2]^-$, iv) $Pb^{II}_S(\mathbf{GR}\text{-}ACH)_3^-$ at pH 7.4 (panel A), pH 8.4 (panel B) and pH 9.4 (panel C).

Analysis of Hg^{II}-Nucleated Heterotrimers

Due to the observed competition between Cu^I and Pb^{II} for sulfur binding (see Chapter 4 for an in depth analysis of Cu^I and Pb^{II} competition for a Cys_3 site), and the attractiveness of being able to include an additional cysteine residue within our peptide scaffolds, for example, to introduce a Cupredoxin-like second metal binding site, I next assessed the ability of Hg^{II} to promote selective heterotrimer formation, instead of Pb^{II}. As said in Chapter 1, Hg^{II} binds tightly to our 3SCCs in both stoichiometric and pH dependent fashions. When 3 equivalents of peptide to one equivalent of Hg^{II} are mixed above pH 7.5, a 3-coordinate $Hg^{II}Cys_3$ species is obtained. Analysis via ^{199}Hg NMR of a standard **a**-site, such as **TRI**L2WL16C (Figure 2-18a) results in a chemical shift at -184 ppm, similar to other aliphatic three-coordinate Hg^{II}-thiolate complexes. Similarly to Pb^{II}, when an Ala substitution is introduced in the layer above the Cys_3 binding site an upfield shift to -244 ppm is observed (Figure 2-18d). This is the most upfield shift ever observed in our **TRI** peptides for an **a** site Cys_3 peptide.

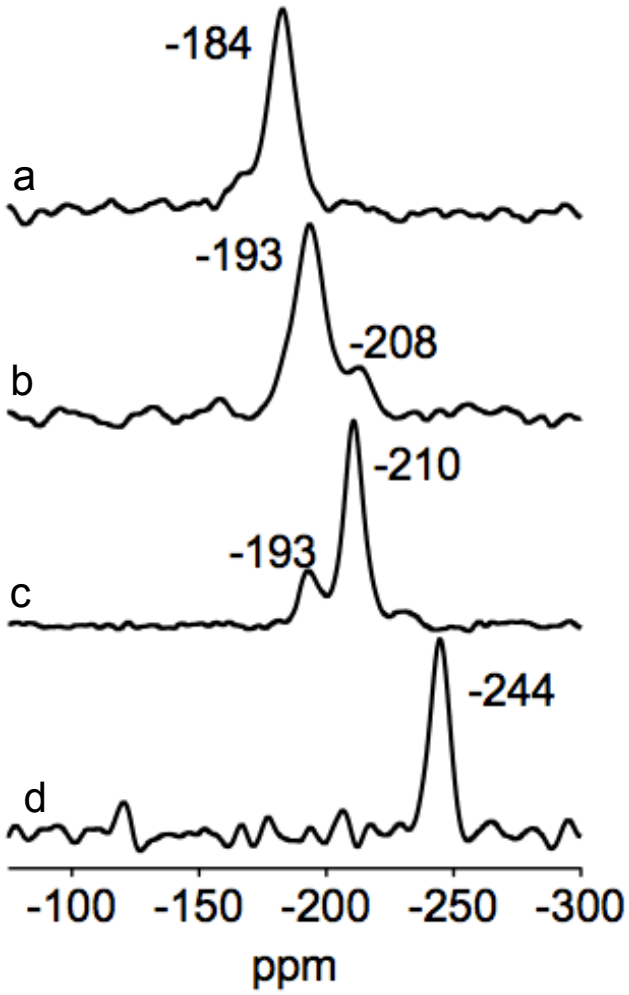

Figure 2-18. ^{199}Hg NMR spectra of a) Hg^{II}_S(**TRI**-C)$_3^-$, b) Hg^{II}_S[(**TRI**-C)$_2$(**TRI**-AC)$_1$]$^-$, c) Hg^{II}_S[(**TRI**-C)$_1$(**TRI**-AC)$_2$]$^-$, d) Hg^{II}_S(**TRI**-AC)$_3^-$. All spectra were recorded at room temperature (25 °C) for 5 hr using isotopically enriched $Hg^{II}(NO_3)_2$, pH 8.5.

When 2:1 and 1:2 ratios of **TRI**-AC and **TRI**-C are mixed at pH 8.5, in the presence Hg^{II}, as previously was done with Pb^{II}, peaks at intermediate chemical shifts were observed for both Hg^{II}_S[(**TRI**-AC)$_2$(**TRI**-C)$_1$]$^-$ and Hg^{II}_S[(**TRI**-AC)$_1$(**TRI**-C)$_2$]$^-$ mixtures (Figures 2-18b and 2-18c). For Hg^{II}_S[(**TRI**-AC)$_1$(**TRI**-C)$_2$]$^-$, a dominant peak is observed, slightly upfield, at -193 ppm with a smaller peak even further upfield at -210 ppm (Figure 2-18b). The opposite heterotrimeric mixture, Hg^{II}_S[(**TRI**-AC)$_2$(**TRI**-C)$_1$]$^-$, showed the same two peaks as the first heterotrimeric mixture, however, the dominance has been shifted to the most upfield shift resonance at -210 ppm with the smaller peak observed at -193 ppm (Figure 2-18c). The shifting observed for the ^{207}Pb NMR was

consistent with a shift of ~25 ppm between each species. Interestingly, we do not see this same equidistance difference for the Hg-bound systems (Figure 2-18). Instead, from the most downfield to the most upfield 3SCC we see shifts of ~10, ~17 and ~34 ppm. Therefore, ^{199}Hg NMR showed similar heterotrimer production in the presence of Hg^{II} bound to mixed peptide systems; however, when Hg^{II} is the nucleating metal, the expected heterotrimer was dominant, but not exclusive, as the opposite heterotrimer was also present. Hence, at pH 8.5, Hg^{II} binding does promote heterotrimer formation but does not allow for *selective* heterotrimer formation as was observed in the case of $Pb^{II}_S[(\mathbf{TRI}\text{-AC})_2(\mathbf{TRI}\text{-C})_1]^-$. Future studies to determine how the pK_a values of the metal-chelation deprotonation of Hg^{II} bound **TRI**-AC and heterotrimers are necessary to determine if a similar decrease in pK_a is observed for the Hg^{II}-bound heterotrimers in comparison to the Hg^{II}-homotrimers.

A second approach for using Hg^{II} instead of Pb^{II} to nucleate the formation of selective heterotrimers was to exploit the preference of Hg^{II} to bind only two sulfurs in a linear fashion. Previous studies had shown that ratios of 2:1 peptide monomer:Hg^{II} exploited the preference of Hg^{II} to bind in a linear fashion, driving the formation of a 2SCC. Addition of more peptide results in the conversion of $Hg(pep)_2$ to $Hg(pep)_3^-$ as the ratio of peptide monomer: Hg^{II} increases. Therefore, I wanted to determine if forming a homodimer of **TRI**-AC and then adding one equivalent of **TRI**-C would provide a pure Hg^{II}-bound heterotrimer. First, I added $^{199}Hg(NO_3)_2$ in a 1:2 ratio with **TRI**-AC and observed only one peak via ^{199}Hg NMR analysis at -867.8 ppm (Figure 2-19). In attempt to form a heterotrimer, I then added one equivalent of **TRI**-C, with respect to the concentration of **TRI**-AC. The NMR spectrum then showed the presence of both heterotrimers at -195 and -211 ppm (in addition to residual 2SCC at -867 ppm, Figure 2-19). These results indicate that Hg^{II} is not capable of nucleating the formation of heterotrimeric 3SCC regardless of the order of addition (**TRI**-AC + **TRI**-C, then add Hg^{II} OR **TRI**-AC + Hg, then add **TRI**-C). These data also confirm that we are accessing the true thermodynamic speciation of the heterotrimers rather than kinetically trapping a distribution of mixed 3SCCs.

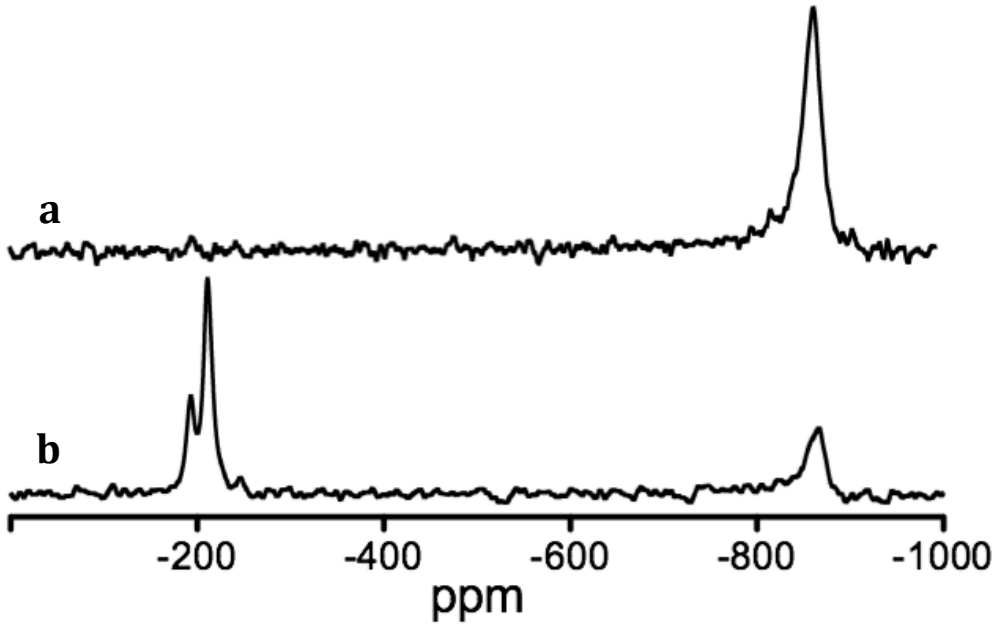

Figure 2-19. ^{199}Hg NMR spectra of a) Hg^{II}_{S}(**TRI**-AC)$_2$, and b) Hg^{II}_{S}(**TRI**-AC)$_2$ + 1 equivalent of **TRI**-C. All spectra were recorded at room temperature (25 °C) for 5 hr using isotopically enriched $^{199}Hg^{II}(NO_3)_2$, pH 8.5.

Pb^{II}-Heterotrimers with Ala/Leu Pairings "below"

Next, I wanted to address the question of whether heterotrimeric Pb^{II} 3SCCs could be obtained, selectively, if the Ala/Leu steric pairing was in the layer directly below the Cys_3 binding site. To do so, I synthesized **GR**L2WL16CL19AL30H (**GR**-CAH, Table 2-1). Pb^{II} binding to Cys_3 was confirmed via analysis of UV-Vis spectroscopy. Aliquots of $Pb^{II}(NO_3)_2$ were added to a solution of 60 μM **GR**-CAH, 20 μM 3SCC, in 100 mM TRIS buffer at pH 8.5. A peak characteristic of a $Pb^{II}S_3$ LMCT, with a maximal absorption observed at 345 nm, grew in until one equivalent of Pb^{II} was reached, followed by an immediate halt in the increase in absorption. This pattern is again indicative of very tight $Pb^{II}S_3$ binding (Figure 2-20). A linear regression analysis of the data at 345 nm provided a molar extinction coefficient of only 2595 $M^{-1}cm^{-1}$, a 25% decrease from the lower limit of what is normally observed for PbS_3 binding in the **TRI** and **GR** peptides.

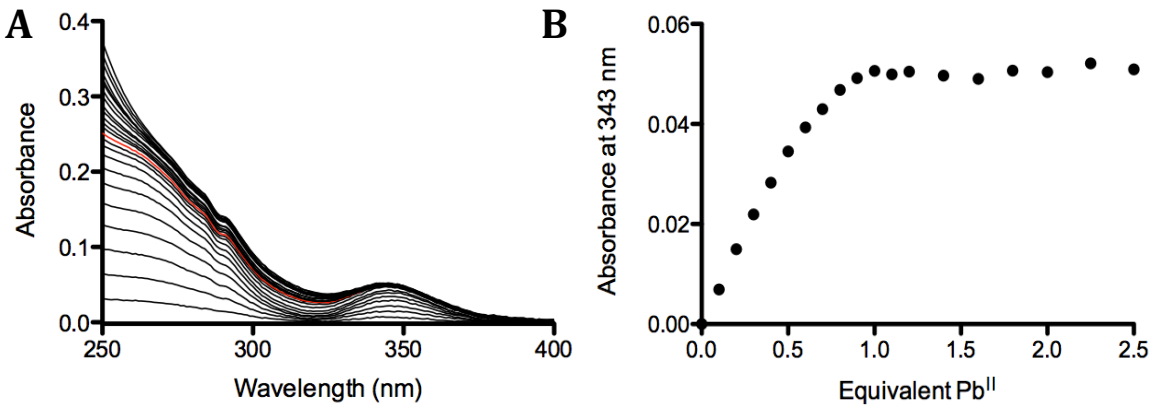

Figure 2-20. Titration spectra of Pb^{II} into a solution of A) **GR**-CAH and B) the corresponding titration curves showing the 1:1 binding stoichiometry of equivalent of Pb^{II} added with respect to 3SCC at 343 nm. Data collected at pH 8.5 in 50 mM TRIS Buffer.

To determine if the decreased extinction coefficient was due to poor peptide folding, the folding and stability of **GR**-CAH was determined at pH 8.0 using CD spectroscopy and a guanidine hydrochloride (GuaHCl) denaturation titration. A characteristic CD spectrum of an alpha-helical coiled coil yields a double well with minima at 208 and 222 nm, but the molar ellipiticity [Θ] was determined to be only -25922 deg $dmol^{-1}$ cm^2, only ~73% folded (Figure 2-21). This indicates that a simple change in design from the Ala substitution being above the Cys_3 layer to below the binding site results in a nearly 20% loss of initial folding in the apo-peptide. As observed in Figure 2-21, the midpoint of **GR**-CAH is difficult to determine since the peptide denatures immediately upon addition of GuaHCl and no stable well folded initial state is observed; however, the midpoint can be estimated to be, at most, only 1 M GuaHCl. This is ~0.8 M lower than the midpoint of **GR**-ACH indicating the inclusion of an Ala residue below the Cys_3 layer results in a less stable peptide compared to an Ala substitution above the Cys_3 site, both of which are less stable than the corresponding **GR**-CH peptide.

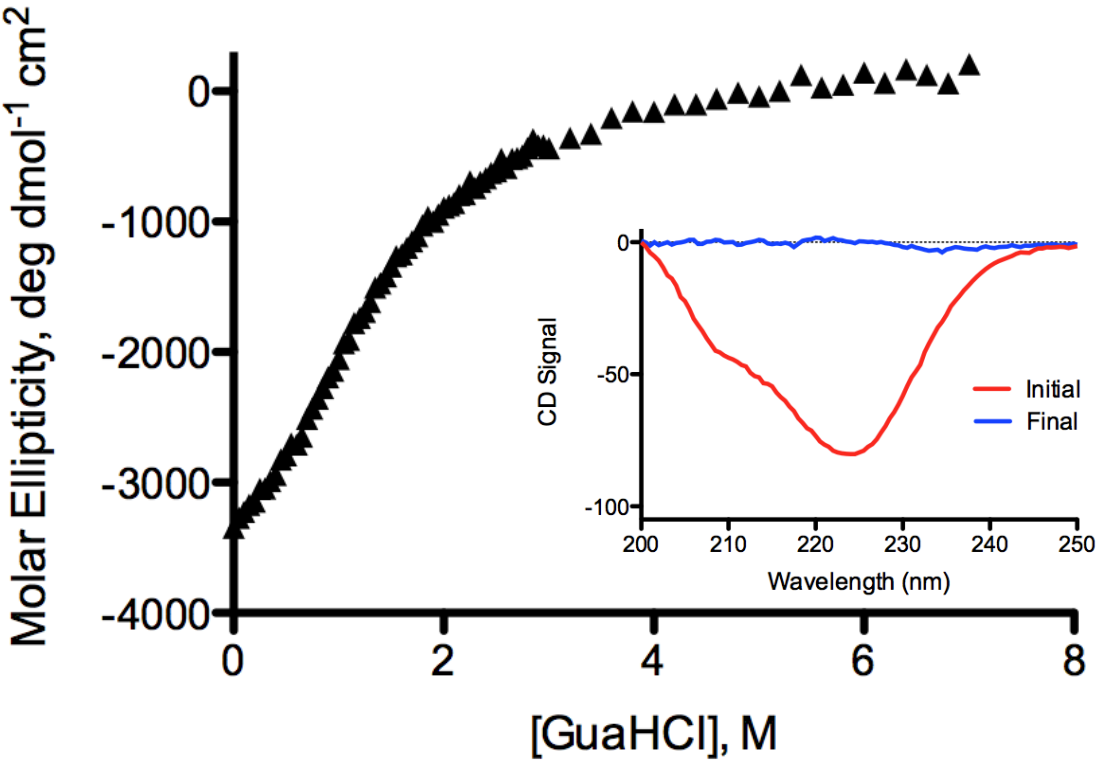

Figure 2-21. Guanidine hydrocholoride denaturation titration data of **GR**-CAH in 10 mM Phosphate buffer at pH 8.0. Inset: CD spectra of **GR**-CAH before (red) and after (blue) the addition of 7 M GuaHCl.

I next turned to ^{207}Pb NMR to further characterize Pb^{II} binding to **GR**-CAH. In the presence of one equivalent $^{207}Pb^{II}$ at pH 7.4, a chemical shift was observed at 5712 ppm (Figure 2-22). This is, to date, the most downfield shifted peak observed for a $Pb^{II}S_3$ environment in an **a** Cys_3 site by approximately 65 ppm. Previously, we saw that introduction of an Ala layer directly above an **a** site Cys_3 resulted in an 75 ppm upfield shift (5575 ppm) from the corresponding Leu/Cys peptide at 5650 ppm. Indeed, these results indicate that inclusion of an Ala layer below the Cys_3 site, with respect to the N-terminus, does not produce a similar upfield shift but actually produces an opposite result with a downfield chemical shift. All subsequent attempts to obtain a heterotrimeric 3SCC by mixing **GR**-CH and **GR**-CAH in the presence of $^{207}Pb^{II}$ does not produce a PbS_3 chemical shift under the reported experimental conditions.

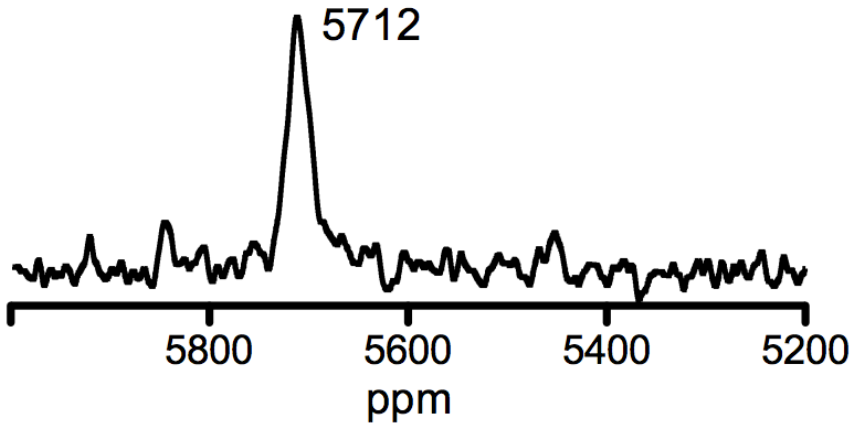

Figure 2-22. ^{207}Pb NMR of Pb^{II}_{S}(**GR**-CAH)$_3^-$. Spectrum was recorded at room temperature (25 °C) for 5 hr using isotopically enriched $Pb^{II}(NO_3)_2$, pH 7.4.

One possibility that $Pb^{II}_{S}[(\mathbf{GR}\text{-CAH})_{3-n}(\mathbf{GR}\text{-CH})_n]^-$ heterotrimers are not observed is that Pb^{II} nucleates heterotrimers from a mixture of **GR**-CH and **GR**-CAH but that the resulting chemical shift is perturbed so much that we do not see it within the normal range (5590-6200 ppm) scanned for $Pb^{II}S_3$ **TRI** and **GR** systems. This possibility seems unlikely, given the behavior of the trend observed for the original heterotrimers where the chemical shifts of $Pb^{II}_{S}[(\mathbf{GR}\text{-ACH})_2(\mathbf{GR}\text{-CH})_1]^-$ and $Pb^{II}_{S}[(\mathbf{GR}\text{-ACH})_1(\mathbf{GR}\text{-CH})_2]^-$ fall between the chemical shifts of the corresponding $Pb^{II}_{S}(\mathbf{GR}\text{-ACH})_3^-$ and $Pb^{II}_{S}(\mathbf{GR}\text{-CH})_3^-$ homotrimers. Considering the range of Pb NMR signals (>16,000 ppm),[30] locating a peak that appears in a different chemical shift region may be a non-trivial task.

A second possibility is that a $Pb^{II}_{S}[(\mathbf{GR}\text{-CAH})_{3-n}(\mathbf{GR}\text{-CH})_n]^-$ heterotimer behaves differently than the $Pb^{II}_{S}[(\mathbf{GR}\text{-ACH})_{3-n}(\mathbf{GR}\text{-CH})_n]^-$ mixtures, with respect to the relaxation time of the Pb^{II} nucleus, in a way that causes the $Pb^{II}Cys_3$ signal to no longer be detectable. It is also possible that there is rapid exchange of the peptides, considering the destabilization observed in the GuaHCl denaturation titration, causing the peptide to dissociate or resulting in multiple, interconverting, cysteine conformations. Any of these processes could result in the broadening of the $^{207}Pb^{II}Cys_3$ signal to the point of being undetectable.

A last consideration is that a statistical distribution is obtained when mixing the **GR**-CAH and **GR**-CH peptides, in the presence of Pb^{II} does not result in selectivity. If

this scenario occurs, then it is unlikely that any of the species is populated enough to result in a resolvable ^{207}Pb NMR signal, due to decreased concentration of any particular species. UV-Vis analysis does confirm the presence of a $Pb^{II}Cys_3$ chromophore when Pb^{II} is added to a solution of **GR**-CAH, which suggests that Pb^{II} is most likely binding in the $Pb^{II}_S[(\mathbf{GR}\text{-CAH})_{3-n}(\mathbf{GR}\text{-CH})_n]^-$ mixes; however, thus far a ^{207}Pb NMR signal has remained elusive.

I next measured the pK$_a$ corresponding to the metal-chelation deprotonation for Pb^{II}-bound **GR**-CAH, and the corresponding $Pb^{II}_S[(\mathbf{GR}\text{-CAH})_{3-n}(\mathbf{GR}\text{-CH})_n]^-$ heterotrimers, to determine if a the pH value used for the NMR analysis was appropriate. The pH of a solution containing 180 μM (60 μM 3SCC) peptide and 30 μM $Pb^{II}(NO_3)_2$ was increased from approximately pH 3 to pH 9 with small aliquots of concentrated KOH. Pb^{II} binding to Cys_3 was analyzed via increasing absorbance at 345 nm and was complete by pH 8.0 (Figure 2-23). All of the data sets were fit to the single proton release, the simultaneous two-proton release and the step-wise two-proton release models as described above.

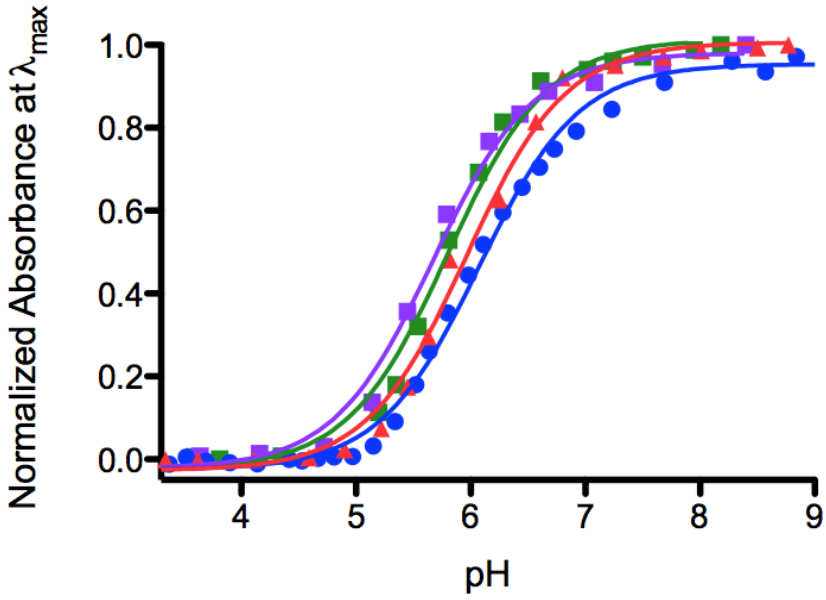

Figure 2-23. pH titration curves of $Pb^{II}Cys_3$ at λ_{max} for homo- and heterotrimers with Ala/Leu pairings below the Cys_3 site. Data fitted to Equation 22, Blue circles: pK$_{a2}$ = 12.06 ± 0.06 for $Pb^{II}_S(\mathbf{GR}\text{-CAH})_3^-$, purple squares: pK$_{a2}$ = 11.43 ± 0.29 for $Pb^{II}_S[(\mathbf{GR}\text{-CAH})_2(\mathbf{GR}\text{-CH})_1]^-$, green squares: pK$_{a2}$ = 11.49 ± 0.05 for $Pb^{II}_S[(\mathbf{GR}\text{-CAH})_1(\mathbf{GR}\text{-CH})_2]^-$, and red triangles: pK$_{a2}$ = 11.72 ± 0.04 for $Pb^{II}_S(\mathbf{TRI}\text{-C})_3^-$.

The pH titration curves for $Pb^{II}_S[(\mathbf{GR}\text{-}CAH)_2(\mathbf{GR}\text{-}CH)_1]^-$ and $Pb^{II}_S[(\mathbf{GR}\text{-}CAH)_1(\mathbf{GR}\text{-}CH)_2]^-$ provide more acidic pK$_a$ values than either of the homotrimers, $Pb^{II}_S(\mathbf{GR}\text{-}CAH)_3^-$ and $Pb^{II}_S(\mathbf{TRI}\text{-}C)_3^-$ (Figure 2-22). Table 2-3 shows the pK$_a$ values for each peptide using all three fitting models. For $Pb^{II}_S(\mathbf{GR}\text{-}CAH)_3^-$, the data is statistically best fit to a one proton step with a pK$_a$ of 6.07 ± 0.03 (Table 2-3). $Pb^{II}_S[(\mathbf{GR}\text{-}CAH)_2(\mathbf{GR}\text{-}CH)_1]^-$ and $Pb^{II}_S[(\mathbf{GR}\text{-}CAH)_1(\mathbf{GR}\text{-}CH)_2]^-$ titrations are best fit to a step-wise two-proton deprotonation model with pK$_{a1}$ = 5.56 ± 0.02 and pK$_{a2}$ =10.91 ± 0.21 and 11.05 ± 0.12, respectively (Table 2-3). An overlay of the normalized titrations shows that both heterotrimers have more acidic transitions than either of the homotrimers (Figure 2-23). In all of these cases full complexation of the completely deprotonated $Pb^{II}S_3$ system is obtained by pH 7 indicating that all experiments conducted at or above pH 7 should not be influenced by the pK$_a$ of the thiolate associated with the Pb^{II} ion. These data suggest that the lack of ^{207}Pb NMR signal for either the $Pb^{II}_S[(\mathbf{GR}\text{-}CAH)_2(\mathbf{GR}\text{-}CH)_1]^-$ or the $Pb^{II}_S[(\mathbf{GR}\text{-}CAH)_1(\mathbf{GR}\text{-}CH)_2]^-$ heterotrimeric mixtures is probably not due to the pH value of the analyzed solutions. The similarities in the pK$_a$ values, compared to the original heterotrimers with the Ala/Leu pairing above the Cys_3 site, do not indicate that a significantly perturbed ^{207}Pb NMR signal should be expected.

Table 2-3. pK$_a$ values for $Pb^{II}_S(\mathbf{TRI}\text{-}C)_3^-$, $Pb^{II}_S(\mathbf{GR}\text{-}CAH)_3^-$, $Pb^{II}_S[(\mathbf{GR}\text{-}CAH)_2(\mathbf{GR}\text{-}CH)_1]^-$, and $Pb^{II}_S[(\mathbf{GR}\text{-}CAH)_1(\mathbf{GR}\text{-}CH)_2]^-$ fit to 1-proton, 2-proton stepwise and 2-proton simultaneous models.

Peptide	1 H^+	2 H^+, Simultaneous	2 H^+, Step-wise	
	pK$_{a1}$	pK$_{a2}$	pK$_{a1}$	$_p$K$_{a2}$
$Pb^{II}_S(\mathbf{TRI}\text{-}C)_3^-$,	5.91 ± 0.05	11.72 ± 0.03	5.62 ± 0.26	11.33 ± 0.50
$Pb^{II}_S(\mathbf{GR}\text{-}CAH)_3^-$	6.07 ± 0.03	12.06 ± 0.06	-	-
$Pb^{II}_S[(\mathbf{GR}\text{-}CAH)_2(\mathbf{GR}\text{-}CH)_1]^-$	5.76 ± 0.14	11.43 ± 0.29	5.60 ± 0.12	10.91 ± 0.21
$Pb^{II}_S[(\mathbf{GR}\text{-}CAH)_1(\mathbf{GR}\text{-}CH)_2]^-$	5.78 ± 0.02	11.49 ± 0.05	5.56 ± 0.02	11.05 ± 0.12

While crystal structures of Pb^{II} nucleated heterotrimers have been elusive, Dr. Leela Ruckthong has recently solved and refined the structures of $Pb^{II}_S(\mathbf{GRCS}L16CL30H)_3^-$ and $Pb^{II}_S(\mathbf{GRCS}L12AL16C)_3^-$ (Table 2-1). Therefore, I will use the crystal structures of the homotrimers corresponding to the Ala/Cys (**GRCS**L12AL16C) and Leu/Cys (**GRCS**L16CL30H) peptides to explore possible

explanations for the formation of heterotrimeric species in the presence of Pb^{II} and Hg^{II} (admittedly, non-selectively).

As discussed in Chapter 1, a comparison of apo-(**CS**L16C)$_3$ to the crystal structures of $Hg^{II}_{S}Zn^{II}_{N}$(**GRCS**L16L30H)$_3^+$, Hg^{II}_{S}(**GRCS**L12AL16C)$_3^-$, and Zn^{II}_{S}(**GRCS**L12AL16C)$_3^-$ has revealed that a Cys_3 site in an **a** position, within our 3SCCs, is *pre-disposed*, meaning it contains the correct number of ligands but requires significant rearrangement of the ligands for metal binding in either trigonal planar or tetrahedral geometries (Figure 2-24). Additionally, comparing apo-(**CS**L16C)$_3$ to the crystal structures of As^{III}_{S}(**CS**L9C)$_3$ and to $Pb^{II}_{S}Zn^{II}_{N}$(**GRCS**L16CL30H)$_3^+$ has shown that an **a** Cys_3 site is *pre-organized,* meaning that the correct number of binding ligands are present and they require no or very little rearrangement, for metal binding in a trigonal pyramidal geometry (Figures 2-24C and 2-24D). This trend has been determined to be dependent on metal binding geometry and is independent of metal ion size.

Additionally, *pre-disposed* metal binding to a Cys_3 site and the subsequent rearrangement of the sulfur ligands results in enough room between the Cys_3 layer and the layer directly above it (the 12th position) for a water molecule to either directly bind to the metal, as is observed in Zn^{II}_{S}(**GRCS**L12AL16C)$_3^-$ or to hydrogen bond to the p-orbitals of the sulfur ions, as is observed in $Hg^{II}_{S}Zn^{II}_{N}$(**GRCS**L16L30H)$_3^+$. In the case of Hg^{II}_{S}(**GRCS**L12AL16C)$_3^-$, not only does the rearrangement of the *pre-disposed* site allow for a water directly above the Hg^{II} ion, but it also allows for three other water molecules to situate near the helical interface. These water molecules hydrogen bond both to the central water molecule and the p-orbitals of the sulfur ions. Water molecules, thus far, have not been observed in any cases where metal binding is *pre-organized*, although this could be due to the symmetry of the unit cell and therefore could correlate to a crystallographic artifact and not necessarily the lack of existence of a central water molecule. However, to account for an increase in size, from As^{III} to Pb^{II} for example, the changes observed in the peptidic structure occur in the in hydrophobic packing of the Leu layer below the Cys_3 binding site (the 19th position) rather than cause reorganization of the Cys_3 site, as observed in the *pre-disposed* situations (Figure 2-25).

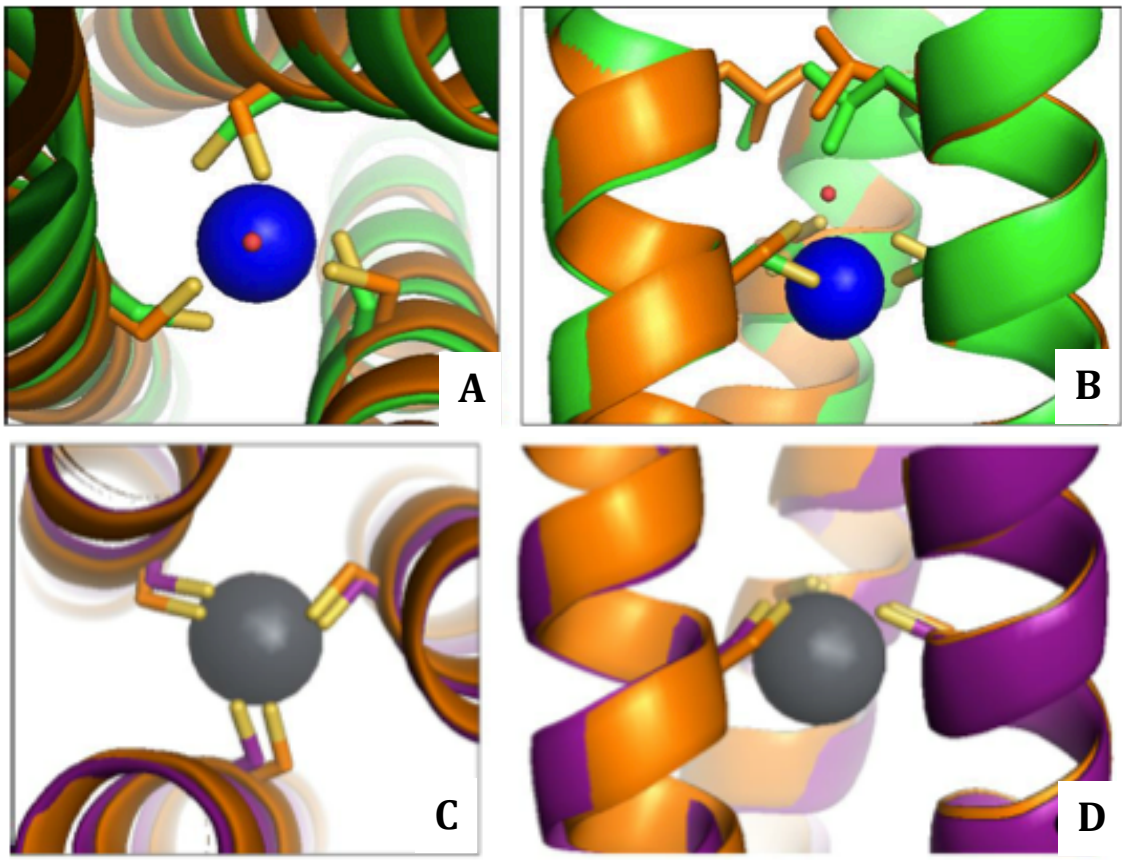

Figure 2-24. Pymol representation of the overlay of apo-(**CS**L16C)$_3$ with $Hg^{II}_{S}Zn^{II}_{S}$(**GRCS**L16CL30H)$_3^{n+}$ (A and B) and apo-(**CS**L16C)$_3$ with $Pb^{II}_{S}Zn^{II}_{N}$(**GRCS**L16CL30H)$_3^{n+}$ showing the difference between metal binding and *pre-organized* metal binding, respectively. A) Top and B) side view showing the overlay of apo-(**CS**L16C)$_3$ and $Hg^{II}_{S}Zn^{II}_{N}$(**GRCS**L16CL30H)$_3^{n+}$. C) Top and D) side on views of the overlay of $Pb^{II}_{S}Zn^{II}_{N}$(**GRCS**L16CL30H)$_3^{n+}$ and apo-(**CS**L16C)$_3$.Main chains of $Hg^{II}_{S}Zn^{II}_{N}$(**GRCS**L16CL30H)$_3^{n+}$ are shown in green, apo-(**CS**L16C)$_3$ in orange, and $Pb^{II}_{S}Zn^{II}_{N}$(**GRCS**L16CL30H)$_3^{n+}$ in purple. Cysteine side chains are shown as sticks. Hg^{II} is represented as a blue sphere, Pb^{II} is represented as a grey sphere. 12Leu and 16Cys side chains are shown as sticks with sulfur ions in bright yellow. Figure adapted from Ref 50.

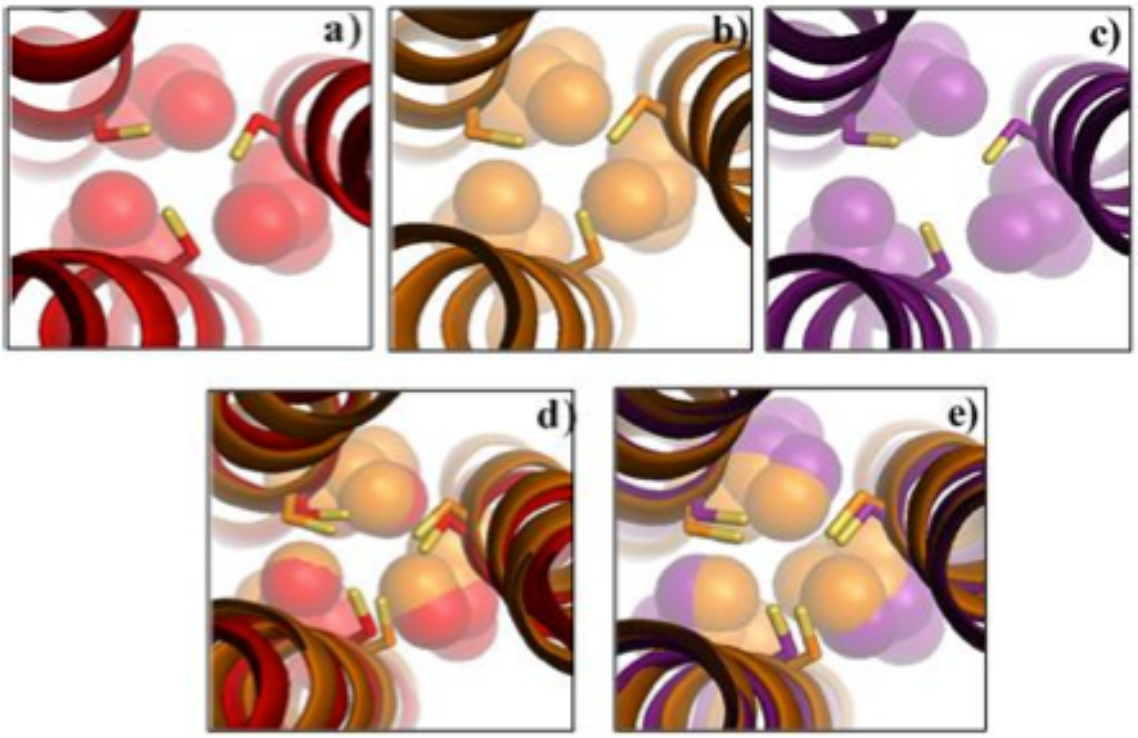

Figure 2-25. Packing of Leu residues (shown as spheres) demonstrating the hydrophobic packing below the trigonal pyramidal binding site compared to the apo-structure. Top panels: From top down view of the N-termini, representing the packing of a) 12Leu below the 9Cys layer in As^{III}_{S}(**CS**L9C)$_3$ (PDB: 2JGO),[42] b) 19Leu below the 16Cys in apo-(**CS**L16C)$_3$ and c) 19Leu below the 16Cys in $Pb^{II}_{S}Zn^{II}_{N}$(**GRCS**L16CL30H)$_3^{n+}$. Bottom panels: Representing in f) the packing comparison between a) and b). In e) an overlay between b) and c) Main atoms of $Pb^{II}_{S}Zn^{II}_{N}$(**GRCS**L16CL30H)$_3^{n+}$, apo-(**CS**L16C)$_3$ and As^{III}(**CS**L9C)$_3$ are represented as purple, orange and red ribbon diagrams, respectively. Cys side chains are present as sticks in which the thiols are yellow. Leu residues are shown as spheres indicating the packing. Pb(II) and As(III) ions are omitted for clarity. Figure adapted from Ref 50.

However, analysis of Pb^{II}_{S}(**GRCS**L12AL16C)$_3^-$ shows a combination of these two situations. The structure (currently under refinement) provides a trigonal pyramidal $Pb^{II}Cys_3$ metal binding site with an endo-configuration, a Pb-S distance of 2.64 Å, a S_γ-S_γ distance of 3.45 Å, and a χ_1 angle of -57.69° (Figure 2-26). These values are similar to those of both apo-**CS**L16C and $Pb^{II}_{S}Zn^{II}_{N}$(**GRCS**L16CL30H)$_3^{n+}$ (Pb-S= 2.64 Å, S_γ-S_γ = 3.29 and 3.49 Å, χ1 = -69.20 and -68.38°, respectively) and support the assignment that **GRCS**L12AL16C is *pre-organized* for Pb^{II} binding (Figure 2-26). In fact, Pb^{II} binding to Cys_3 sites of both **GRCS**L12AL16C and **GRCS**L16CL30H are nearly identical in the first coordination sphere (Figure 2-27). However, upon introduction of the Ala layer at the

12th position, water molecules are now observed in the space provided by the Ala substitution in Pb^{II}_{S}(**GRCS**L12AL16C)$_3^-$. No central water is observed on the helical axis above the Pb^{II} ion, similar to what was not observed in the Hg^{II} and Zn^{II} structures; however, similar to the waters observed in Hg^{II}_{S}(**GRCS**L12AL16C)$_3^-$, Pb^{II}_{S}(**GRCS**L12AL16C)$_3^-$ has three water molecules that are near to the helical interface in between the helices (Figure 2-28). The water molecules are 3.37 Å from the sulfur ion of the coordinating Cys ligands and, therefore, form hydrogen bonds with the p-orbitals of the sulfur ions (Figure 2-28).

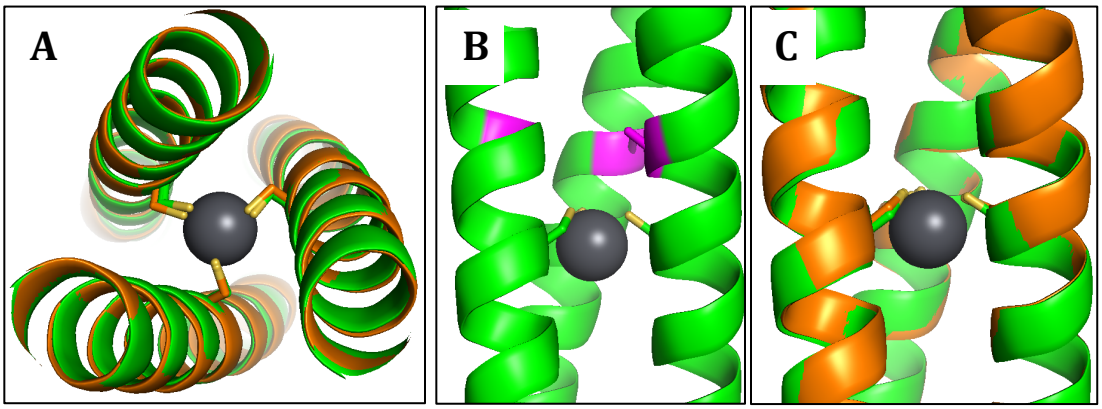

Figure 2-26. Pymol representation of trigonal pyramidal coordination in Pb^{II}_{S}(**GRCS**L12A16C)$_3^-$ and comparison with apo-(**CS**L16C)$_3$. A) Top down view from the N-termini of the overlay of Pb^{II}_{S}(**GRCS**L12A16C)$_3^-$ and apo-(**CS**L16C)$_3$ site showing a slight expansion of S_γ-S_γ distance from 3.29 to 3.45 Å upon Pb^{II} binding. B) Side on view of Pb^{II}_{S}(**GRCS**L12A16C)$_3^-$ showing endo-conformation with Pb^{II} ion directed toward the C-terminus, away from the L12A substitution, with a Pb^{II}-S distance of 2.68 Å. C) Side on view of the overly of Pb^{II}_{S}(**GRCS**L12A16C)$_3^-$ and apo-(**CS**L16C)$_3$ showing the *pre-organization* of L12AL16C sites for Pb^{II} binding. Main chain atoms are shown as ribbon diagrams in green (Pb^{II} structure) and orange (apo-structure), 12Ala (in panel B) and 16Cys side chains are shown as sticks with sulfur ions in bright yellow, Ala sticks are shown in purple. The Pb^{II} ion is shown as a dark grey sphere. Figure adapted from Ref 50.

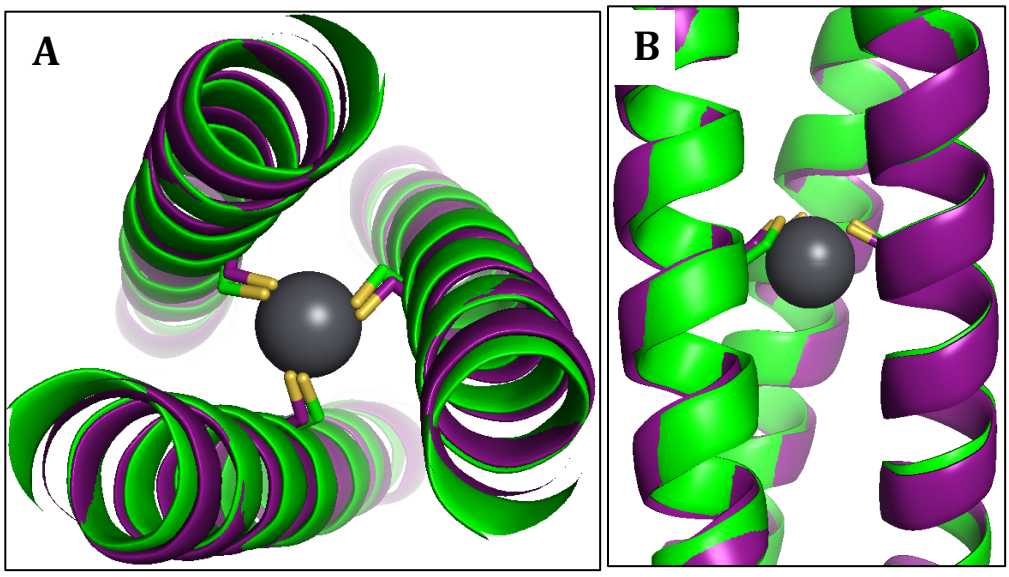

Figure 2-27. Pymol representations of the overlay of $Pb^{II}_{S}Zn^{II}_{N}$(**GRCS**L16CL30H)$_3^+$ and Pb^{II}_{S}(**GRCS**L12AL16C)$_3^-$. A) Top down from the N-termini and B) side on view of the Cys_3 binding site. Main chains are shown in purple and green for the L16C and L12AL16C structures, respectively. Pb^{II} ions are shown in grey spheres. Cysteine residues are shown as sticks and sulfur atoms are shown in bright yellow. Figure adapted from Ref 50.

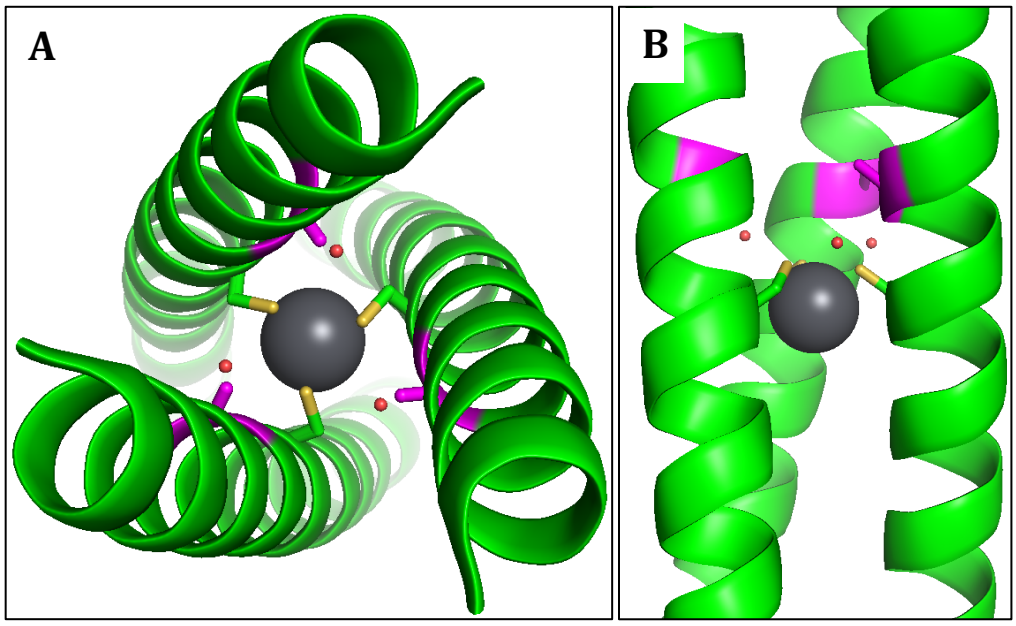

Figure 2-28. Pymol overlay representations showing the surrounding water molecules in Pb^{II}_{S}(**GRCS**L12AL16C)$_3^-$. A) Top down and B) side on views of the Pb^{II}_{S}(**GRCS**L12AL16C)$_3^-$ crystal structure. Main chain helices are shown in green. Sulfur atoms are shown in bright yellow. Cys and Ala residues are represented as sticks. Pb^{II} ions are shown in grey spheres. Water molecules are shown as small red spheres. Figure adapted from Ref 50.

As mentioned above, previous computational analysis determined that $Pb^{II}Cys_3$ binding is very sensitive to steric influences of the secondary coordination sphere. DFT analysis was conducted on two model peptide systems, one that coupled a Leu/Cys combination and one that coupled an Ala/Cys combination. The lowest energy structure corresponded to the Ala/Cys peptide, and also that the lowest energy system was an *exo*-confirmer.[37] Therefore, we originally hypothesized that perhaps when Pb^{II} bound to a Leu/Cys homotrimer, such as **TRI**-C, the Leu residues in the layer above forced an unfavorable *endo*-confirmer, and that **TRI**-AC would better accommodate the bulky lone pair of Pb^{II}, allowing for an *exo*-configuration. If this were true, one could consider that a mixture of **TRI**-C and **TRI**-AC, say $(\textbf{TRI}\text{-AC})_2(\textbf{TRI}\text{-C})_1$, could form an even more energetically favorable environment for $Pb^{II}Cys_3$ binding.

However, we now know from the crystal structures of both $Pb^{II}_{S}Zn^{II}_{N}(\textbf{GRCS}\text{L16CL30H})_3^{n+}$ and $Pb^{II}_{S}(\textbf{GRCS}\text{L12AL16C})_3^{-}$ that Pb^{II} binds to an **a** site Cys_3 in the *endo*-configuration,‡ with the metal oriented below the sulfur plane toward the C-terminus, regardless of the identity of the residue in the layer directly above the metal binding site. This directly negates the original hypothesis, supported by the DFT results, that the Pb^{II} would be bound in the *exo*-conformation with the Pb^{II} ion oriented towards the N-terminus. It is possible that the difference in the structural predictions and the DFT calculations could be due to the lack of water molecules included in the DFT models therefore not allowing for hydrogen-bonding interactions to the sulfur ions. Additionally, the calculations did not consider the constraints imposed upon the cysteine rotamers as would be observed in an α-helix. Inclusion of both hydrogen-bonds as well as secondary structural restrictions would most definitely influence the energies associated with the predicted states and could skew the relative energies enough to result in a different lowest energy model that might agree better with the structural predictions.

‡ Endo-configuration is assigned because the β-carbon of the cysteine residue and the metal ion are observed on the same plane, with respect to the coordinating sulfur ion. This configuration could occur with the metal ion, and the β-carbon oriented toward the N-terminus, pointing "up" in the 3SCC, or toward the C-terminus, pointing "down" in the 3SCC. In the cases of the peptides discussed in this study all endo-configurations correlate to the latter where the Pb^{II} and As^{III} ions are located below the Cys_3 plane closer to the 19Leu residues than the 12Ala/Leu residues.

Thus, instead of a heterotrimer better accommodating the bulky lone pair of Pb^{II} as originally hypothesized, I now believe that the selective formation of heterotrimeric species may instead be a direct consequence of the water molecules being able to interact with the sulfur p-orbitals of the Cys ligands as observed when an Ala substitution is included in the layer directly above the Cys_3 binding site, in combination with the hydrophobic packing of the lone Leu residue. The *endo*-confirmation, in addition to the direction in which the Pb^{II} ion "points" down (toward the C-terminus), confirms that the initial idea that the large Pb^{II} ion was better accommodated within the hydrophobic interior of the 3SCC upon addition of Ala residues, introduced symmetrically or asymmetrical, above the Cys_3 binding site, was indeed incorrect. Rearrangement of these sulfur residues to bind a trigonal pyramidal ion such as Pb^{II} or As^{III} in the exo configuration would result in a significant energy penalty.

If the selectivity for heterotrimer formation is indeed due to hydrogen-bonding stabilization introduced via the L12A substitution in combination with the pre-organized Cys_3 site for Pb^{II} binding then one would expect that Pb^{II} binding to an Ala/Cys homotrimer would be the most stable. This is contradictory to the CD spectroscopic analysis of peptide stability as described above where the Leu/Cys peptide is ~1 kcal/mol more stable than the Ala/Cys peptide; however, the denaturation studies are for the apo-proteins and do not consider how the stability of the peptides might change upon $Pb^{II}Cys_3$ binding. It is possible that although the peptide is most stable with all Leu residues in the layer above the Cys_3 site, and that, upon addition of the bulky Pb^{II} the Leu/Cys peptide is destabilized. Therefore, one could imagine that a compromise is reached upon the combination of a mixed Ala_2Leu peptide in the presence of Pb^{II}, where the stability of the apo-peptide is pacified by the inclusion of a Leu residue but the Pb^{II} site is satisfied with the asymmetric hydrogen bonding now possible with the 2Ala residues present.

The crystal structures of $Pb^{II}{}_SZn^{II}{}_N$(**GRCS**L16CL30H)$_3^{n+}$ and $Pb^{II}{}_S$(**GRCS**L12AL16C)$_3^-$, and the differences observed in the spectroscopic analyses, allow for one to imagine that the combination of Ala/Cys and Leu/Cys peptides, in the presence of Pb^{II}, could result in a heterotrimeric peptide that contains an intermediate number of water molecules (with respect to the number of water molecules observed in

the crystal structures of the homotrimeric peptides) occupying the space introduced by the Ala residues. Figure 2-29 shows a top down view of $Pb^{II}_{S}Zn^{II}_{N}$(**GRCS**L16CL30H)$_3^{n+}$ and Pb^{II}_{S}(**GRCS**L12AL16C)$_3^{-}$ and models of the 2:1 and 1:2 mixtures of these peptides. This figure shows how the space introduced in the layer above the Cys_3 site is greatest, as one would expect, for the Ala/Cys homotrimer and smallest, essentially non-existent, for the Leu/Cys homotrimer. The heterotrimeric models have intermediate amounts of space available that could presumably be occupied by either one or two water molecules, while still retaining some hydrophobic packing characteristics due to the presence of the Leu residue. The change in symmetry of the hydrogen-bonding network between the water molecules and the sulfur ions could explain the changes in the spectroscopic parameters observed for the heterotrimeric species. One could also imagine that the introduction and alterations of a hydrogen bonding network near the $Pb^{II}Cys_3$ site proposed here could explain the perturbed pK_a values observed for Pb^{II}_{s}[(**TRI**-AC)$_{3-n}$(**TRI**-C)$_n$]$^-$ heterotrimers.

The lack of spectroscopic evidence for heterotrimer formation when the Ala residues are introduced below the Cys_3 binding site could also support this new hypothesis. The structural data show that the Pb^{II} ion points down toward the C-terminus, where the L19A substitution occurs. In this scenario, the orientation of the Pb^{II} ion could result in the exclusion of water molecules, even with the inclusion of the Ala residues below the Cys_3 site, resulting in a peptide that looks comparable to the Leu/Cys peptide. If the hydrogen bonding introduced via the L12A substitution is indeed required for heterotrimer formation then I would not expect to form discrete heterotrimers with the **GR**-CAH peptide since this peptide would not offer any hydrogen-bonding stabilization.

Ultimately, crystal structures of the Pb^{II} heterotrimers are required to confirm this hypothesis. Given the trend observed for water molecules in the Ala/Cys and Leu/Cys homotrimeric crystal structures, the notion that selective Pb^{II}-nucleated A_2B heterotrimeric 3SCC formation could be a direct consequence of favorable energetics obtained from the resulting asymmetric hydrogen bonding interactions due to asymmetric inclusion of water molecules within the structures is appealing.

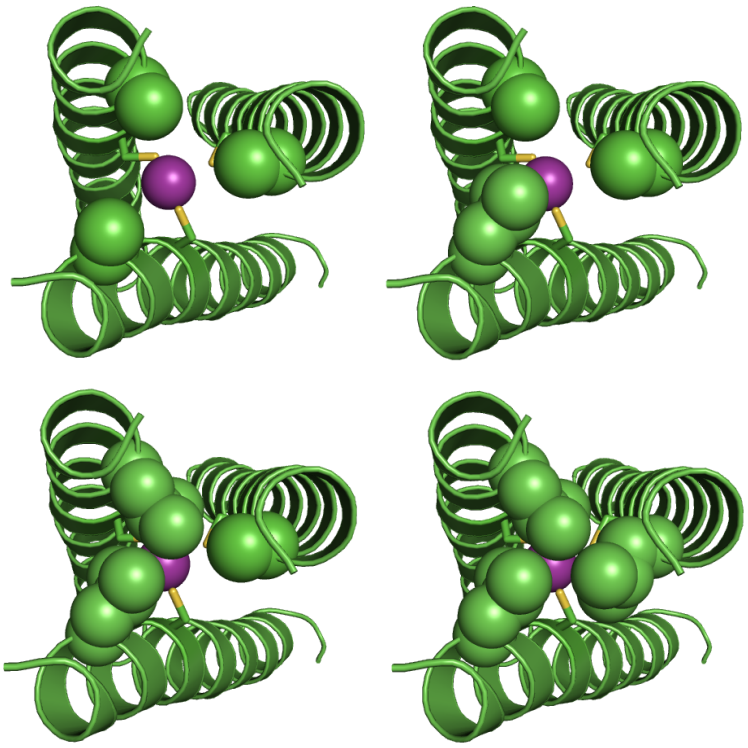

Figure 2-29. Top down views of A) Pb^{II}_{S}(**GRCS**L12AL16C)$_3^-$ and D) $Pb^{II}_{S}Zn^{II}_{S}$(**GRCS**L16CL30H)$_3^{n+}$ and models of heterotrimeric mixtures, B) Pb^{II}_{S}[(**GR**-CH)$_1$(**GR**-ACH)$_2$]$^-$ and C) Pb^{II}_{S}[(**GR**-CH)$_2$(**GR**-ACH)$_1$]$^-$. Main chain helices are shown in green. Cys residues are represented as sticks with sulfur atoms shown in bright yellow. Pb^{II} ions are shown in purple spheres. Leu12 and Ala12 residues are shown in green space filling spheres. (A) and (D) are Pymol representations from the crystal structures reported in Ref 50. (B) and (C) models were prepared in Pymol using the mutagenesis option and Pymol's rotamer library and the PDB of $Pb^{II}_{S}Zn^{II}_{S}$(**GRCS**L16CL30H)$_3^{n+}$ (PDB code not deposited yet).

I also turned to Hg^{II}-bound crystal structures to address the lack of selectivity of heterotrimer formation observed when Hg^{II} is used as the nucleating metal. As discussed in Chapter 1, introduction of Ala residues at the 12th position (Hg^{II}_{S}(**GRCS**L12AL16C)$_3^-$) resulted in four water molecules to occupy the space above the Hg^{II} ion. One could imagine that the hydrogen-bonding network obtained between the central H_2O molecule and the three water molecules nearer to the helical interface, and between these three water molecules and the p-orbitals of the sulfur ions of the Cys resides, could offer added stability to the structure when compared to the single central water molecule of $Hg^{II}_{S}Zn^{II}_{N}$(**GRCS**L16CL30H)$_3^{n+}$. However, similarly to the discussion above, the apo-

peptide itself is most stable when the layer above the Cys_3 site is well packed with Leu residues.

In the case of the Hg^{II}_S(**GRCS**L12AL16C)$_3^-$ structure there are six hydrogen bonding interactions total, two per water molecule located near the helical interface: one to the p-orbital of the closest sulfur ion, and one to the central water molecule. In the opposite homotrimer, $Hg^{II}_S Zn^{II}_N$(**GRCS**L16CL30H)$_3^{n+}$, the central water molecule is close enough to hydrogen bond to the p-orbitals of the sulfur ions, resulting in three hydrogen-bonding interactions.

Assuming that the number of water molecules observed in the interior of the 3SCC correlates to the number of Ala residues present in the layer above the Cys_3 site, plus one additional central water molecule, consistent with both of the Hg^{II}_S(**GRCS**L12AL16C)$_3^-$ and Hg^{II}_S(**GRCS**L12AL16C)$_3^-$ crystal structures, one could imagine, that an intermediate number of water molecules (two or three) is likely in both heterotrimeric scaffolds. It is also possible that the location of the central water ion is directly related to the number of Leu residues present, closest with three Leu residues and farthest away with three Ala residues. Therefore the hydrogen-bonding capacity of the central water molecule could be modulated depending on the heterotrimeric mixture (2Leu or 1Leu). The combination of the number of helical waters present as well as the fluctuation in the location of the central water molecule could therefore provide a comparable number of hydrogen bonds in either the Ala_2Leu or $AlaLeu_2$ heterotrimer, therefore explaining the lack of selectivity with Hg^{II}-nucleation.

For example, a system containing one Ala and two Leu residues in the layer above the $Hg^{II}Cys_3$ site would have two water molecules present, where one is at the helical interface (directly correlated to the single Ala residues in the 12th layer), and the two Leu residues would cause the central water molecule to be pushed closer to the Hg^{II} ion. In this scenario, the helical water molecule will likely hydrogen bond to both the central water molecule and the closest sulfur ion, and the proximity of the central water molecule may be such that it can hydrogen bond to the remaining two sulfur ions, resulting in a total of four hydrogen-bonding interactions. Conversely, for the system

containing two Ala residues and one Leu residue, the central water molecule may not be close enough to hydrogen bond to the sulfur atoms but would likely hydrogen bond to two water molecules at the helical interfaces, which in turn both hydrogen bond to the sulfur ions on the nearest two Cys residues. This, again, provides four hydrogen bonds within the network. The comparable number of hydrogen bonds could explain why a mixture of Ala_2Leu_1 and Ala_1Leu_2 heterotrimers are observed in both the 1:2 and 2:1 peptide mixtures. This does not contradict the above argument for the stability compromise between the presence of a hydrogen-bonding network between both the central and helical interface water molecules in addition to peptide stability provided by the included Leu residues.

In all, the original hypothesis that heterotrimers were formed, selectively, due to the inclusion of Ala residues to better accommodate the bulky size of a Pb^{II} ion has been proven false. However, the Ala/Leu pairing in the layer above the metal Cys_3 binding site seems instead to allow for a hydrogen bonding network between water molecules accommodated within the space provided by the smaller Ala hydrophobes and the p-orbital of the cysteine residues. It seems that the stability of the peptide scaffold is due to a compromise in hydrophobic packing between Leu residues and the stability introduced via hydrogen bonding networks. In the case of Pb^{II}, with no evidence of a central water molecule, the Ala_2Leu heterotrimer is formed selectively, perhaps due to maximal stability of the hydrogen bonding network in the presence of 2Ala residues; however, in the case of Hg^{II}, where a central water molecule is present, the hydrogen bonding network introduced in either the Ala_2Leu or $AlaLeu_2$ matchings could be comparable therefore removing any selectivity.

Conclusions

In this chapter I have presented evidence for the successful, selective formation of heterotrimeric $\mathbf{A_2B}$ 3SCCs via methodologies that combine heavy metal nucleation with steric matching of natural amino acids (alanine and leucine residues), which is hypothesized to result in the inclusion of hydrogen-bonding networks near the metal

nucleation site. This design allows for the use of simple, self-assembling α-helices containing only coded amino acids to form an asymmetric helical scaffold with space in the same construct to incorporate a second metal binding site. Systems that combine Ala/Leu pairings in the layer above the Cys_3 binding site are on the slow exchange regime as determined by ^{207}Pb NMR and do not show coalescence. New ^{207}Pb NMR peaks are observed for heterotrimeric mixtures and pK_a determination of Pb^{II} binding to the $\mathbf{A_2B}$ heterotrimer provides the lowest pK_a value for Pb^{II} binding to Cys_3 sites in our peptides to date. Considering that the pK_a values of both homotrimers are more basic than the $\mathbf{A_2B}$ heterotrimer, this provides additional evidence that a new species is formed and that we are not simply observing a mixture of the two, homotrimeric species. Elongation from **TRI** to **GR** peptides, addition of a second metal binding site toward the C-termini of the 3SCC, and varied pH conditions (pH 7.4-9.4) have proven not to perturb the specificity of heterotrimer formation. The presence of Co^{II} or Zn^{II} does not inhibit Pb^{II} binding and do not influence the ^{207}Pb NMR shifts observed for either the homotrimers or heterotrimers. There is no evidence that inclusion of the Ala/Leu pairing in the layer below the Cys_3 binding site allows for heterotrimer formation. This is the first example of an asymmetric 3SCC scaffold with interior metal binding sites and all natural amino acids. With this methodology in hand, one may now use the asymmetry induced at the $Pb^{II}Cys_3$ site to expand asymmetry to other metal binding sites in the same scaffold and study more complex metalloenzyme active sites that either have mixed first coordination sphere environments or asymmetric 2^{nd}-coordination spheres which provide electrostatic or hydrogen binding residues in close proximity to a catalytic center.

References

(1) Zastrow, M. L.; Pecoraro, V. L. *J. Am. Chem. Soc.* **2013**, *135*, 5895–5903.
(2) Zastrow, M. L.; Peacock, A. F. A.; Stuckey, J. A.; Pecoraro, V. L. *Nat. Chem.* **2012**, *4*, 118–123.
(3) Tegoni, M.; Yu, F.; Bersellini, M.; Penner-Hahn, J. E.; Pecoraro, V. L. *Proc. Natl. Acad. Sci. U. S. A.* **2012**, *109*, 21234–21239.
(4) Yu, F.; Penner-Hahn, J. E.; Pecoraro, V. L. *J. Am. Chem. Soc.* **2013**, *135*, 18096–18107.
(5) Kiefer, L. L.; Paterno, S. A.; Fierke, C. A. *J. Am. Chem. Soc.* **1995**, *117*, 6831–6837.
(6) Krebs, J. F.; Ippolito, J. A.; Christianson, D. W.; Fierke, C. A. *J. Biol. Chem.* **1993**, *268*, 27458–27466.
(7) Elkins, J. M.; Ryle, M. J.; Clifton, I. J.; Dunning Hotopp, J. C.; Lloyd, J. S.; Burzlaff, N. I.; Baldwin, J. E.; Hausinger, R. P.; Roach, P. L. *Biochemistry* **2002**, *41*, 5185–5192.
(8) Kerfeld, C. A.; Yoshida, S.; Tran, K. T.; Yeates, T. O.; Cascio, D.; Bottin, H. H.; Berthomieu, C.; Sugiura, M.; Boussac, A. *J. Biol. Inorg. Chem.* **2003**, *8*, 707–714.
(9) Greenblatt, H. M.; Feinberg, H.; Tucker, P. A.; Shoham, G. *Acta Crystallogr. Sect. D Biol. Crystallogr.* **1998**, *54*, 289–305.
(10) Holland, D. R.; Hausrath, A. C.; Juers, D.; Matthews, B. W. *Protein Sci.* **1995**, *4*, 1955–1965.
(11) Holden, H. M.; Matthews, B. W. *J. Biol. Chem.* **1988**, *263*, 3256–3260.
(12) Nautiyal, S.; Woolfson, D. N.; King, D. S.; Alber, T. *Biochemistry* **1995**, *34*, 11645–11651.
(13) Diss, M. L.; Kennan, A. J. *J. Org. Chem.* **2008**, *73*, 9752–9755.
(14) Lebruin, L. T.; Banerjee, S.; O'Rourke, B. D.; Case, M. A. *Biopolymers* **2011**, *95*, 792–800.
(15) Jalan, A. A.; Demeler, B.; Hartgerink, J. D. *J. Am. Chem. Soc.* **2013**, *135*, 6014–6017.
(16) Schnarr, N. A.; Kennan, A. J. *J. Am. Chem. Soc.* **2002**, *124*, 9779–9783.
(17) Kiyokawa, T.; Kanaori, K.; Tajima, K.; Kawaguchi, M.; Mizuno, T.; Oku, J.; Tanaka, T. *Chemistry* **2004**, *10*, 3548–3554.
(18) Matzapetakis, M.; Farrer, B. T.; Weng, T.-C.; Hemmingsen, L.; Penner-Hahn, J. E.; Pecoraro, V. L. *J. Am. Chem. Soc.* **2002**, *124*, 8042–8054.
(19) Matzapetakis, M.; Ghosh, D.; Weng, T.-C.; Penner-Hahn, J. E.; Pecoraro, V. L. *J. Biol. Inorg. Chem.* **2006**, *11*, 876–890.
(20) Farrer, B. T.; McClure, C. P.; Penner-Hahn, J. E.; Pecoraro, V. L. *Inorg. Chem.* **2000**, *39*, 5422–5423.
(21) Dieckmann, G. R.; McRorie, D. K.; Tierney, D. L.; Utschig, L. M.; Singer, C. P.; O'Halloran, T. V.; Penner-Hahn, J. E.; DeGrado, W. F.; Pecoraro, V. L. *J. Am. Chem. Soc.* **1997**, *119*, 6195–6196.
(22) Iranzo, O.; Cabello, C.; Pecoraro, V. L. *Angew. Chem. Int. Ed.* **2007**, *46*, 6688–6691.
(23) Arsenault, J.; Dean, P. *Can. J. Chem.* **1983**, *61*, 1516–1523.
(24) Dean, P.; Vittal, J.; Payne, N. *Inorg. Chem.* **1984**, *23*, 4232–4236.
(25) Briand, G. G.; Smith, A. D.; Schatte, G.; Rossini, A. J.; Schurko, R. W. *Inorg.*

Chem. **2007**, *46*, 8625–8637.
(26) Andersen, R. J.; DiTargiani, R. C.; Hancock, R. D.; Stern, C. L.; Goldberg, D. P.; Godwin, H. A. *Inorg. Chem.* **2006**, *45*, 6574–6576.
(27) Rupprecht, S.; Langemann, K.; Lügger, T.; McCormick, J. M.; Raymond, K. N. *Inorganica Chim. Acta* **1996**, *243*, 79–90.
(28) Claudio, E. S.; ter Horst, M. A.; Forde, C. E.; Stern, C. L.; Zart, M. K.; Godwin, H. A. *Inorg. Chem.* **2000**, *39*, 1391–1397.
(29) Aramini, J. M.; Hiraoki, T.; Yazawa, M.; Yuan, T.; Zhang, M.; Vogel, H. J. *J. Biol. Inorg. Chem.* **1996**, *1*, 39–48.
(30) Neupane, K. P.; Pecoraro, V. L. *Angew. Chem. Int. Ed.* **2010**, *49*, 8177–8180.
(31) Chan, W. C.; White, P. D. *Fmoc Solid Phase Peptide Synthesis: A Practical Approach*; Chan, W.; White, P., Eds.; Oxford Univ Press, New York, 2000.
(32) *The Protein Protocols Handbook*; Walker, J. M., Ed.; 2nd Editio.; Humana Press Inc.: Totowa, NJ, 2002.
(33) Dieckmann, G. R.; McRorie, D. K.; Lear, J. D.; Sharp, K. A.; DeGrado, W. F.; Pecoraro, V. L. *J. Mol. Biol.* **1998**, *280*, 897–912.
(34) Pace, C. N.; Scholtz, J. M. In *Protein Structure: A Practical Approach*; Creighton, T. E., Ed.; Oxford Univ Press, Tokyo, 1997; pp. 299–321.
(35) GraphPad Prism version 5.00 for Mac, GraphPad Software, San Diego California USA, www.graphpad.com.
(36) Neupane, K. P.; Pecoraro, V. L. *J. Inorg. Biochem.* **2011**, *105*, 1030–1034.
(37) Zampella, G.; Neupane, K. P.; De Gioia, L.; Pecoraro, V. L. *Chem. Eur. J.* **2012**, *18*, 2040–2050.
(38) Cobas, C.; Cruces, J.; Sardina, F.; MestRe-C version 2.3, Universidad de Santiago de Compostela, S. MestRe-C version 2.3, Universidad de Santiago de Compostela, Spain, 2000.
(39) Farrer, B. T.; Harris, N. P.; Valchus, K. E.; Pecoraro, V. L. *Biochemistry* **2001**, *40*, 14696–14705.
(40) Ghosh, D.; Lee, K.-H.; Demeler, B.; Pecoraro, V. L. *Biochemistry* **2005**, *44*, 10732–10740.
(41) Su, J. Y.; Hodges, R. S.; Kay, C. M. *Biochemistry* **1994**, *33*, 15501–15510.
(42) Touw, D. S.; Nordman, C. E.; Stuckey, J. A.; Pecoraro, V. L. *Proc. Natl. Acad. Sci. USA* **2007**, *104*, 11969–11974.
(43) Busenlehner, L. S.; Cosper, N. J.; Scott, R. A.; Rosen, B. P.; Wong, M. D.; Giedroc, D. P. *Biochemistry* **2001**, *40*, 4426–4436.
(44) Mah, V.; Jalilehvand, F. *Inorg. Chem.* **2012**.
(45) Tegoni, M.; Yu, F.; Bersellini, M.; Penner-Hahn, J. E.; Pecoraro, V. L. *Proc. Natl. Acad. Sci. USA* **2012**, *109*, 21234–21239.
(46) Avvaru, B. S.; Arenas, D. J.; Tu, C.; Tanner, D. B.; McKenna, R.; Silverman, D. N. *Arch. Biochem. Biophys.* **2010**, *502*, 53–59.
(47) Zastrow, M. De novo designed metalloenzymes: structural stabilization and hydrolytic catalysis in a family of α-helical coiled coils, University of Michigan, 2013.
(48) Lah, M. S.; Dixon, M. M.; Pattridge, K. A.; Stallings, W. C.; Fee, J. A.; Ludwig, M. L. *Biochemistry* **1995**, *34*, 1646–1660.
(49) Zampella, G.; Neupane, K. P.; De Gioia, L.; Pecoraro, V. L. *Chem. - A Eur. J.*

2012, *18*, 2040–2050.
(50) Ruckthong, L. Crystallographic Comparison of Tris-Thiolate Sites in Designed Proteins to Control Metal Geometries, University of Michigan, 2016.

Chapter 3. Characterization of Symmetric and Asymmetric Transition Metal Binding Sites within *de Novo* Designed Three-Stranded Coiled Coils

Introduction

While metal induced heterotrimers, as introduced and characterized in Chapter 2, are unprecedented in the literature, the *ultimate* goal of my thesis work was to obtain heterotrimeric peptides with a second, also asymmetric, metal binding site capable of binding transition metals with potential catalytic or redox-active properties. Once Pb^{II}-nucleated heterotrimers were obtained, my next objective was to build, and characterize, a second metal binding site within the same scaffold. I rationalized that once selective heterotrimer formation was obtained via Pb^{II} nucleation at the Cys_3 site, then asymmetry could be extended to a second metal binding site in either the primary or secondary coordination sphere.

My initial objective was to expand upon the Carbonic Anhydrase (CA) mimic designed and characterized by Dr. Melissa Zastrow, which provided an excellent structural model of the primary coordination sphere of CA and catalytic rates for the native substrate that were only 400-fold slower than the fastest isozyme, HCAII.[1–3] Previously, all attempts to introduce secondary coordination sphere residues resulted in symmetric, three-fold inclusion into the 3SCC. For example, in the secondary coordination sphere of Zn^{II} in CA there is a Thr residue that participates in catalysis, and when substituted for Ala results in a 100-fold decrease in functionality. Due to the symmetry previously imposed upon our 3SCCs due to self-association, inclusion of a Thr residue into our scaffolds provided a Thr_3His_3 environment, a system that does not offer increased catalytic efficiency over the original His_3 model.[4] Additionally, as outlined in the introduction of Chapter 2, asymmetric primary coordination spheres for transition metal binding are currently not attainable within our symmetric 3SCCs.

In this chapter, I will describe how I used the Pb^{II}-nucleated heterotrimer to design a transition metal binding site, with a nearby Asp residue, with the hope of introducing an acid/base catalyst in close proximity to a Zn^{II}-bound water molecule in a His_3 site. The Co^{II} ion was used extensively as a spectroscopic probe to characterize the new, asymmetric metal binding site. I will explore how Co^{II} UV-Vis, EPR, and XAS spectroscopic data support a 6-coordinate Co^{II} site in homotrimeric samples and a 5-coordinate Co^{II} site. These structures will be compared to Co^{II}-substituted native metalloenzymes including CA, carboxypeptidase A (CPA), thermolysin (TML), and VanX. Strong evidence of direct coordination of the metal to the new Asp residue, in the heterotrimeric peptides, will be presented. Interestingly, Zn^{II} EXAFS of the heterotrimeric peptides show little difference from the homotrimeric data indicating two things: 1) The addition of the Asp residue does not seem to perturb significantly the coordination number of Zn^{II}-binding when compared to the homotrimeric samples. Secondly, the data suggest that Co^{II} may be a non-innocent probe for this site when compared to Zn^{II} binding. Initial kinetics experiments on the new Zn^{II}-bound heterotrimeric systems will be explored, with special comment made on the unexpected contributions to esterase activity from the heterotrimer-nucleating $Pb^{II}Cys_3$ site.

I will consider the perturbations of the secondary coordination sphere around the binding site and how they affect heterotrimer formation as well as Co^{II} binding. One such perturbation consists of altering the sequence of the peptide in order to place the Asp residue in the same peptide that contains the Ala substitution. Another point of discussion will be the perturbation on Co^{II} spectral properties upon the addition of excess Pb^{II} to peptides containing multiple aspartate residues. The spectroscopic data support a hetero-binuclear $Pb^{II}Co^{II}$ site at the end of the peptide away from the nucleating $Pb^{II}{}_SCys_3$ center. Other substitutions consist of changing the sterics around the His_3 binding site. In particular, introduction of a $_D$Leu residue in the layer above the His_3 site results in the first observed difference in Co^{II} binding between **TRI** and **GR** peptides with the same coordinating ligands in comparable positions within the sequence.

Materials and Methods

Peptide Synthesis and Purification. Peptides were synthesized on one of two instruments: an Applied Biosystems 433A synthesizer or a Biotage Initiator+Alstra synthesizer on a Rink Amide Methylbenzhydrylamine (MBHA) resin using standard Fmoc-*t*Bu-based protection protocols (HBTu/HOBt coupling).[5] Crude peptides were cleaved from the resin using trifluoroacetic acid (TFA), ethandithiol, anisole, and thioanisole (90:3:2:5), dissolved in double distilled water and lyophilized to dryness. Purified peptides were isolated using a Waters 600 HPLC on a reverse phase C18 column (flow rate: 20 mL/min, solvent A: 0.1% TFA in water and B:0.1% TFA in 90:10 $CH_3CN:H_2O$. A linear gradient was used starting at 70:30, A:B and increasing to 20:80 over 35 min.). ESI-MS was used to confirm the mass of purified peptide and collections were lyophilized to yield pure, white powder. Concentrations of all peptides were determined by tryptophan absorbance at 280 nm ($\varepsilon = 5500\ M^{-1}cm^{-1}$).[6]

Circular Dichroism (CD) and Ultraviolet-Visible (UV-Vis) Spectroscopy. CD spectra were collected on an AVIV 62DS spectrometer or a Jasco CD-Spectropolarimeter in a 1-cm quartz cuvette at 25 °C. Guanidine hydrochloride (GuaHCl) titrations were carried out at pH 8.0 using an automated titrator with a syringe pump as described previously.[7] UV-Vis spectra were recorded in quartz cuvettes at room temperature on a Cary 100 Bio UV/Vis spectrometer.

Pb(II)-binding titrations. Titrations of Pb^{II} into peptide were performed at room temperature and monitored via UV-Vis spectroscopy in a 1-cm quartz cuvette. $Lead^{II}$ titrations were completed in 50 mM TRIS buffer at pH 8.5 at a peptide concentration of 30 μM. TRIS adjustments were made using small aliquots of concentrated KOH and HCl. Aliquots of a $Pb^{II}(NO_3)_2$ stock solution (standardized using inductively coupled plasma-optical emission spectroscopy ICP-OES, Perkin-Elmer Optima 2000 DV with Winlab software) were titrated into the peptide solution. For all titrations, the difference spectra were obtained by subtracting the background spectrum of the peptide under identical conditions but in the absence of metal. After the addition of each aliquot, the solutions were stirred for ten minutes to allow for equilibration before recording the absorbance spectrum.

Co^{II}-binding titrations.

I) Direct Co^{II} binding. Titrations of Co^{II} into peptide solutions were performed at room temperature and monitored via Vis spectroscopy in a 1-cm quartz cuvette. $Cobalt^{II}$ titrations were completed in 50 mM HEPES buffer (pH 7.5) at a peptide concentration of 0.3-0.6 mM peptide trimer. HEPES adjustments were made using small aliquots of concentrated KOH or HCl. Aliquots of $Co^{II}SO_4$ stock solution (standardized using ICP-OES, Perkin-Elmer Optima 2000 DV with Winlab software) were titrated into the peptide solution and absorbance spectra were recorded from 400-800 nm. For all titrations, the difference spectra were obtained by subtracting the background spectrum of the peptide in the absence of Co^{II}. After the addition of each aliquot, the solutions were stirred for five minutes to allow for equilibration before recording the absorbance spectrum.

The titration curves were fitted to a non-linear least squares algorithm using Prism 5 (GraphPad Software) with the data plotted as a function of absorbance (at the appropriate λ_{max} for each peptide) versus total concentration of Co^{II} added. Equation 1 describes the binding equilibrium for these experiments.

$$Co + Pep_3 \rightleftharpoons CoPep_3 \qquad \text{Equation 1}$$

The apparent dissociation constant, $K_{d,CoPep3}$, was calculated using Equation 2.

$$K_{d,CoPep3} = \frac{[Pep_3]_f[Co]_f}{[CoPep_3]} \qquad \text{Equation 2}$$

For the titration, aliquots of Co^{II} were titrated into a solution of Pep_3. The absorption band between 400 and 700 nm, due to the d-d transitions of Co^{II}-bound to Pep_3, was monitored and increased as Co^{II} is complexed at the Asp_XHis_3 site. Mass balance equations for $[Co]_T$ and $[Pep]_T$ can be defined and related to $[Co]_f$ and $[Pep_3]_f$ as seen in Equations 4 and 6. Subscript '$_T$' indicates total concentrations as detailed in the experimental conditions.

Mass Balance Equations:

$$[Co]_T = [Co]_f + [CoPep_3] \qquad \text{Equation 3}$$

$$[Co]_f = [Co]_T - [CoPep_3] \quad \text{Equation 4}$$

$$[Pep_3]_T = [CoPep_3] + [Pep_3]_f \quad \text{Equation 5}$$

$$[Pep_3]_f = [Pep_3]_T - [CoPep_3] \quad \text{Equation 6}$$

Substituting Equations 4 and 6 into Equation 2 yields Equation 7

$$K_d = \frac{([Pep_3]_T - [CoPep_3])([Co]_T - [CoPep_3])}{[CoPep_3]} \quad \text{Equation 7}$$

The K_d value can be directly related to the absorbance observed at λ_{max} for each peptide (between 400-700 nm) by substituting $[CoPep_3]$ from Equation 8 (where *b* is the path length of the cuvette) into Equation 7.

$$\text{Absorbance}^{\lambda max} = \varepsilon^{\lambda max} * [CoPep_3] * b \quad \text{Equation 8}$$

Rearrangement of Equation 7, in terms of $\text{Absorbance}^{\lambda max}$, can then be used to fit the titration data at λ_{max} using Prism 5 (GraphPad Software)[8] to yield the K_d of Co^{II}-binding. $\varepsilon^{\lambda max}$ was determined as part of the least squares analysis.

II) Co^{II}-binding pH Titrations. Co^{II} was added to a solution of peptide and diluted to a concentration of 0.43 mM Pb^{II}(**GR**L2WL12AL16CL30H)$_3^-$ in water. The pH was titrated by adding small aliquots of 5M KOH to the solution. The pH was monitored and allowed to stabilize before analysis of the $Co^{II}Asp_XHis_X$ band ($\lambda \approx 560$ nm) was conducted.

NMR Spectroscopy. NMR samples were prepared by dissolving pure, lyophilized peptide in 10% D_2O. Metallopeptides were prepared by addition of isotopically enriched $^{207}Pb(NO_3)_2$ (92.4%, Oak Ridge National Laboratory, TN) to non-buffered solutions of 3-5 mM peptide trimer. All samples were adjusted to the desired pH using small aliquots of concentrated KOH or HCl. ^{207}Pb NMR spectra were recorded at a frequency of 145.9 MHz on a Varian 700 MHz spectrometer at 25 °C with spin = 0, 0.20 ms relaxation time, and 20 ms acquisition time. Linear predictions (0-30 points) were performed to remove noise, and the real FID was determined as previously described.[9–11] The data were processed with an exponential line broadening of 400-600 Hz using MestRe-C

software.[12] The ^{207}Pb NMR shifts are reported as the observed signal plus ~2986 ppm, and referenced by tetramethyllead (δ=0 ppm; toluene) using 1 M $Pb(NO_3)_2$ in D_2O (natural abundance salt, δ=-2986 ppm) as an external standard. The external standard was run after each experimental collection to adjust for any shifting of the magnetic field.

Electron Paramagnetic Resonance (EPR) Spectroscopy. EPR spectra were recorded using a Bruker X-band EMX electron spin resonance spectrometer with an Oxford Instruments liquid helium cryostat at ~7 K. All samples were prepared at ~1mM $CoSO_4$, with 0.5 equivalents of Co^{II} with respect to peptide trimer to ensure minimal free Co^{II} was present. All samples were prepared in pH 7.5 HEPES buffer (final concentration ~30 mM) with pH adjusted using small aliquots of concentrated KOH and H_2SO_4. Glycerol was added (25-50%) as a glassing agent. All EPR parameters were obtained via the fitting of collected spectra to obtain simulated spectra using EPR data fitting software (SpinCount).[13]

X-ray Absorption Spectroscopy (XAS). Solutions of 1.0 mM $Pb^{II}_{S}M^{n+}_{N/O}$(3SCC) were prepared with 30-50 mM HEPES buffer at pH 7.5. An excess of peptide (1.0 mM apo-3SCC) was present to ensure the free Zn^{II} or Co^{II} concentration was minimal (<0.01%). The samples were pH adjusted then mixed with 50% glycerol (glassing agent) and loaded into a sample cell and frozen in liquid nitrogen for transport and analysis. All XAS measurements were performed at Stanford Synchrotron Radiation Lightsource, SSRL, (Beam line: 7-3). A Si(220) double crystal monochromator was utilized, with a flat Rh-coated vertically collimating harmonic rejection mirror. Data were collected with a beam size of 1 x 9 mm^2 and the X-ray energy was calibrated by collecting the absorption spectrum of a Co, or Zn, foil as a reference, placed between two ionization chambers situated after the sample, at the same time as the fluorescence data were collected, with the first infection point assigned as 7709.5 and 9670 eV, for Co^{II} and Zn^{II} data, respectively. The samples during data acquisition were maintained at a temperature of ~7-9 K, and the data were measured in fluorescence mode with a 30-element energy resolving Ge detector. The data were collected using 10 eV steps in the pre-edge region, 0.25 eV for the edge region, and 0.05 $Å^{-1}$ increments for the extended x-ray absorption

fine structure (EXAFS) region up to k=13 $Å^{-1}$, with integration times of 1 s in the pre-edge and edge regions and 1-20 s (k^3 weighted) in the EXAFS region for a total scan time of ~40 min. The raw data were examined for glitches and the fluorescence from the good channels was then utilized for averaging. The EXAFS data were analyzed using the EXAFSPAK[14] suite of programs, where the theoretical amplitude and phase parameters used were calculated using FEFF 9[15] using two metal-ligand distances, the Debye-Waller factors for the Zn-O or Co-O and Zn-N_{His} or Co-N_{His} shells and E_0 as the only adjustable parameters. For the remaining histidine distances, for the our shell scattering, assuming a rigid imidazole ring with distances and angles that equals to the average Co-histidine or Zn-histidine models found in the Cambridge Crystallographic data base, the imidazole Debye-Waller factors were defined taking into consideration that the σ^2 value for each of these scattering paths will increase proportionally, were taken and used from the previous calculated data by Bunker et *al.*[16] for an ordered imidazole.

Magnetic Circular Dichroism (MCD) Spectroscopy. All MCD data collection and analysis was done in collaboration with Dr. Amy Speelman and Ashely McQuarters of Nicolai Lehnert's laboratory at the University of Michigan. Solutions of ~2.0 mM $Pb^{II}_{S}M^{n+}_{N/O}$(3SCC) were prepared with 30-50 mM HEPES buffer at pH 7.5. An excess of peptide (2.0 mM apo-3SCC) was present to ensure the free Co^{II} concentration was minimal (<0.01%). The samples were pH adjusted then mixed with 50% ethylene glycol (glassing agent) and loaded into a sample cell and frozen in liquid nitrogen for transport and analysis. The MCD setup employs an Oxford SM4000 cryostat and a JASCO J-815 CD spectrometer. The SM4000 cryostat consists of a liquid helium-cooled superconducting magnet providing horizontal magnetic fields of 0-7 T. The J-815 spectrometer uses a gaseous nitrogen-cooled xenon lamp and a detector system consisting of two interchangeable photomultiplier tubes in the UV-Vis and NIR range. The samples were loaded into a 1.5-00 K variable temperature insert (VTI), which offers optical access to the sample via four optical windows made from Suprasil B quartz. The MCD spectra were measured in [θ] = mdeg and converted to Δε ($M^{-1}cm^{-1}T^{-1}$) using the conversion factor $\Delta\varepsilon=\theta/(32980 \bullet cdB)$, where *c* is the concentration, *B* is the magnetic field, and *d* is the path length. The product *cd* can be substituted by $A_{MCD}/\varepsilon_{UV\text{-}vis}$, where A is the

absorbance of the sample measured by the CD spectrometer. The spectra were recorded at 2 K in a magnetic field of 7 T.

Competitive Zn^{II}-binding Titrations. The apparent Zn^{II}-binding constants were determined using a primary standard competition with the colormetric Zn^{II} chelator, Zincon (2-carboxy-2'-hydroxy-5'-(sulfoformazyl)benzene). Zn^{II} forms a 1:1 complex with Zincon (Zi) that offers a distinct absorption band at 620 nm (ε~16,000 $M^{-1}cm^{-1}$) at pH 9.0 and an apparent dissociation constant ($K_{d,app}$) of 3.5 x 10^{-8} M (consistent with reported $K_{d,app}$ for $Zn^{II}Zi$ at pH 9.0).[17–19] The parameters were evaluated at pH 9.0 (50 mM CHES, 0.1 M Na_2SO_4) by titrating aliquots of Zn^{II} (stock solutions were standardized using ICP-OES, Perkin-Elmer Optima 2000 DV with Winlab software) into a solution of 10 μM Zi. A 5 cm pathlength cell was used for the calibration titration of Zn-Zi binding at pH 9.0. For experiments involving removal of Zn^{II} from ZnZi by peptide, an excess of Zi over $ZnSO_4$ was used to ensure complete Zn^{II} binding to Zi (10 μM Zi and 5 μM Zn^{II}). For the opposite titration, where Zn^{II} is bound to the peptide and removed via addition of Zi, the peptide was in excess (2 μM Pep_3 and 1 μM Zn^{II}). Both approaches should give similar apparent binding constants for $Zn^{II}Pep_3$, indicating equilibrium has been reached. The binding equilibrium for this competition can be expressed by Equation 9.

$$ZnPep_3 + Zi \rightleftharpoons Pep_3 + ZnZi \qquad \text{Equation 9}$$

The apparent dissociation constant of $ZnPep_3$, $K_{d,ZnPep3}$, can be calculated using Equation 10, where $[Pep_3]_f$ and $[Zi]_f$ are free trimer and Zi, respectively.

$$K_{comp} = \frac{K_{d,ZnPep3}}{K_{d,\,ZnZi}} = \frac{[Pep_3]_f[ZnZi]}{[ZnPep_3][Zi]_f} \qquad \text{Equation 10}$$

The forward reaction, defined as Zi titrated into $Zn^{II}Pep_3$, results in an absorption band at 620 nm that increases as Zi is added to the $Zn^{II}Pep_3$ solution as a result of complexation of Zn^{II} to form the ZnZi complex. The mass balance equations for $[Zi]_f$ and $[Pep_3]_f$ can be described and related to $[Zn]_f$ and $[Pep_3]_f$ as seen in Equations 12 and 14. Subscript '$_T$' indicates total concentrations as detailed in the experimental conditions.

Mass Balance Equations:

$$[Zi]_T = [Zi]_f + [ZnZi] \qquad \text{Equation 11}$$

$$[Zi]_f = [Zi]_T - [ZnZi] \quad \text{Equation 12}$$

$$[Pep_3]_T = [ZnPep_3] + [Pep_3]_f \quad \text{Equation 13}$$

$$[Pep_3]_f = [Pep_3]_T - [ZnPep_3] \quad \text{Equation 14}$$

Substituting Equations 12 and 14 into Equation 10 yields Equation 15.

$$\frac{K_{d,ZnPep3}}{K_{d,\,ZnZi}} = \frac{([Pep_3]_T - [ZnPep_3])[ZnZi]}{[ZnPep_3]([Zi]_T - [ZnZi])} \quad \text{Equation 15}$$

This equation can then be directly related to the absorbance observed at 620 nm by substituting [ZnZi] from Equation 16 (where *b* is the path length of the cuvette) into Equation 15.

$$\text{Absorbance}^{620\text{ nm}} = \varepsilon^{620\text{nm}} * [ZnZi] * b \quad \text{Equation 16}$$

Rearrangement of Equation 15 can then be used to fit the titration data at Abs 620 using Prism 5 (GraphPad Software)[8] to yield the apparent $K_{d,ZnPep3}$ of Zn^{II}-binding. An analogous approach was used for the reverse titration, defined as Pep_3 titrated into a solution of ZnZi. $\varepsilon^{\lambda max}$ was determined as part of the least squares analysis.

Esterase Activity Assays. The esterase activities of Zn^{II}-bound peptides (homotrimer Pb^{II}_S(**GR**L2WL12AL16CL30H)$_3^-$ and heterotrimers Pb^{II}_S[(**GR**-ACH)$_2$(**GR**-CH)]$^-$, Pb^{II}_S[(**GR**-ACH) $_2$(**GR**-CDH)]$^{n+}$, and Pb^{II}_S[(**GR**-ACH)$_2$(**GR**-CTH)] $^{n+}$) were determined spectrophometrically with *p*NPA (*p*-nitrophenol acetate) substrate (0.3-6.0 M) at room temperature in a 1-cm quartz cuvette. Data were collected at 348 nm, the isosbestic point for *p*-nitrohenol and *p*-nitropholate anion (ε = 5000 $M^{-1}cm^{-1}$).[20] The observed activities were corrected for background ester hydrolysis in the absence of enzyme. The control reaction, $Zn^{II}SO_4$ in the presence of substrate and absence of enzyme, did not exhibit any activity above that of the blank (*p*NPA in buffer). Activities were determined at pH 9.5, 50 mM CHES, 0.1 M Na_2SO_4. The substrate solution was prepared fresh daily in acetonitrile (3.0 mM *p*NPA). A cuvette containing 50 mM buffer, water, 6% acetonitrile (for consistency across substrate concentrations, due to solubility of the substrate), and *p*NPA was used as a background absorbance followed by addition of peptide (10 μM

$ZnSO_4$ and 50 μM peptide, to ensure all Zn^{II} was bound) to measure esterase activity. The increase in absorption at 348 nm was measured every 25 seconds for a minimum of 10 min, and longer for the slower rates. Initial rates for each substrate concentration were determined from linear fits of product formation versus elapsed time. These slopes, the initial rates, ν, were then plotted as function of substrate concentration ([*p*NPA]) and fitted to the Michaelis-Menten equation (Prism 5, GraphPad Software)[8], from which k_{cat}/K_M, k_{cat} and K_M values, with errors, were determined. Control experiments in the absence of the His_X, Asp_XHis_X, and Thr_XHis_X, for $Pb^{II}_S[(\mathbf{GR}\text{-AC})_2(\mathbf{GR}\text{-C})]^-$, were completed to determine the esterase activity of the $Pb^{II}S_3$ site in the **GR** peptides, which was measured as non-negligible and will be discussed below.

CO_2 Hydration Activity Assays. Initial rates of CO_2 hydration were measured at 25 °C on an OLIS RSM Stopped-Flow Spectrophotometer. CO_2 itself does not have spectral properties that can be monitored, so a pH-indicator method was utilized to track the reactions. A buffer/indicator combination of CHES/thymol blue (pH 9.5, λ_{max} = 590 nm, ε= 40,500 $M^{-1}cm^{-1}$)[21] was used with an ionic strength of 0.1 M Na_2SO_4. Saturated solutions of CO_2 were prepared by bubbling CO_2 gas (Matheson Tri-Gas, Inc., Research Grade) through doubly distilled water for at least 20 minutes. Dilutions were made using gas-tight glass syringes and a final check of substrate concentration was determined during each concentration point as previously reported.[4,21,22] Substrate concentrations ranged from 2-20 mM CO_2. The substrate solution was mixed by the stopped-flow with either a catalyst solution (contains: buffer, indicator, $Pb^{II}_SZn^{II}_{N/O}(\mathbf{GR}\text{-ACH})_3^+$, and apo-**GR**-ACH or control solution (contains: buffer, indicator and apo-**GR**-ACH). Each shot contained 50 mM buffer, 25 μM indicator, and 0.1 M Na_2SO_4. Control shots contained 88 μM apo-**GR**-ACH and catalyst shots contained 88 μM $Pb^{II}_S(\mathbf{GR}\text{-ACH})_3^-$ and 40 μM $ZnSO_4$, ensuring final $Pb^{II}_SZn^{II}_{N/O}(\mathbf{GR}\text{-ACH})_3^+$ concentration of 40 μM. The experimental buffer factors were close to those that were calculated theoretically, as previously reported.[1,4,21,22] Several seconds worth of absorbance data was collected upon rapid mixing of the substrate solution with the buffer/indicator solution by the stopped-flow apparatus. Initial rates were determined from the initial portion of the reaction (generally less than 10% of the reaction observed). At least 6 replicates at each substrate

concentration were averaged and the rate for the control was subtracted from that of the corresponding catalyst reaction. The difference, resulting in the initial rate of the Zn^{II}-catalyst, was plotted as a function of CO_2 concentration and fitted using the Michaelis-Menten equation in Prism 5 (GraphPad Software).[8]

Results and Discussion

Design of a Heterotrimeric 3SCC

Armed with the ability to use Pb^{II} binding and steric matching to obtain heterotrimeric assemblies, I examined whether it would be possible to add a single acid/base catalyst in the layer above the His_3 site. I used the **GR** family of peptides to mitigate the decreased stability caused by disrupting a third leucine layer. Because of the ambiguity for the location of the hydroxyl group presented by threonine, as discussed in Chapters 1 & 2, I instead inserted an aspartatic acid in the 26th position, as either orientation of the carboxylate would present an oxygen atom toward the His_3 metal binding site (Figure 3-1). The resulting peptide was **GR**L2WL16CL26DL30H, designated **GR**-CDH (Table 3-1). An aspartate was chosen over glutamate to ensure that the Zn^{II} could not simultaneously bind to the three histidine residues as well as the carboxylate moeity, which would be reminiscient of an $M(His)_3(Carboxylate)_X(H_2O)_Y$ site found in iron/manganese superoxide dismutases. Models showed that the aspartate should form a hydrogen bond with the Zn^{II} bound water, with a nearest oxygen-Zn^{II} distance of 3.6 Å, compared to a metal-carboxylate distance of 1.8 Å with a modeled Glu (Figures 3-1A and 3-1B). Therefore, the first generation of heterotrimeric 3SCCs would conatin two metal binding sites. The first is used to nucleate the formation of the asymmetric scaffold via binding of Pb^{II}, and the second is used to bind transition metals. These heterotrimers would be obtained by mixing **GR**-ACH and **GR**-CDH in the presence of Pb^{II} to provide $Pb^{II}_S[(\mathbf{GR}\text{-ACH})_2(\mathbf{GR}\text{-CDH})_1]^{n+}$ and $Pb^{II}_S[(\mathbf{GR}\text{-ACH})_1(\mathbf{GR}$-

$CDH)_2]^{n+}$ (Table 1).* Protein stability and folding of **GR**-ACH and Pb^{II} binding to **GR**-ACH is disucssed in Chapter 2. These results will be compared to **GR**-CDH below.

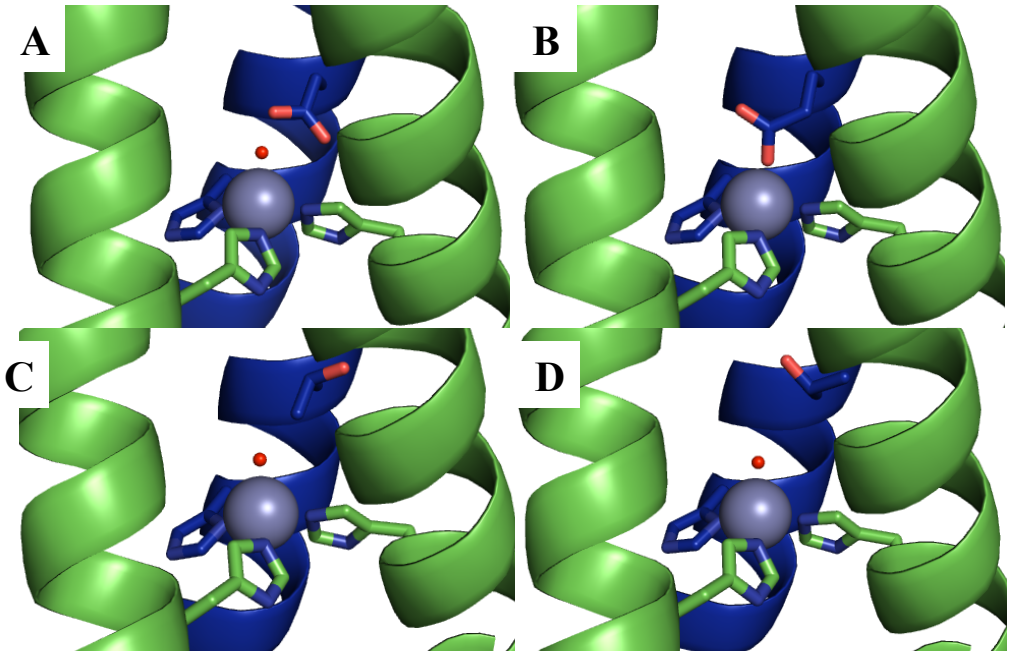

Figure 3-1. Pymol models of possible hydrogen-bonding residues in the layer directly above a His_3 transition metal binding site in a 3SCC. The metal-binding ligands are His residues and the hydrogen-bonding residues contain hydroxyl (Thr) or carboxylic acid (Asp or Glu) moieties with nitrogen atoms in blue and oxygen atoms in red. Metal ions are colored grey. The heterotrimeric assembly is emphasized by two green helices and one blue helix. (A) Side-on view of a modeled Asp_1His_3 site (Asp-Zn^{II} distance of 3.6 Å). (B) Side-on view of a modeled Glu_1His_3 site (Glu-Zn^{II} distance of 1.8 Å). Side-on views of modeled Thr_1His_3 sites with the hydroxyl group rotated (C) "out" toward the helical interface and (D) "in" toward the hydrophobic core (Thr-OH_2 "in" distance is 4.3 Å). Models are generated using the crystal structure of $Hg^{II}{}_SZn^{II}{}_{N/O}$(**CS**L9PenCL23H)$_3^{n+}$ (PDB: 3PBJ).[1]

* The nomenclature used to describe the metal complexes studied herein is as follows: When Pb^{II} is bound to the Cys_3 site, the peptide, for example **GR**-CH, will be referred to as: $Pb^{II}{}_S$(**GR**-CH)$_3^-$, where '$_S$' represents the atom that coordinates the Pb^{II} ion. When Co^{II} or Zn^{II} are bound to a Asp_XHis_3 site, there is a presumed mixed coordination sphere of nitrogen atoms from the His ligands and oxygen atoms from either the Asp carboxylic acid moieties or exogenous solvent molecules. $Zn^{II}{}_{N/O}$ or $Co^{II}{}_{N/O}$ will be used to indicate transition metal binding at the Asp_XHis_3 site with an expected mixed primary N/O coordination sphere. The charge of the complex corresponds to the sum of the oxidation states of the metals, minus the charge of the coordinated ligands. In the case of a $Pb^{II}Cys_3$ site, the charge is (-), from Pb^{II} and three thiol ligands. When Asp residues are included in the sequence an (n+) charge is assigned due to the ambiguity of both of the protonation state of the Asp ligands in the presence of a transition metal as well as the coordination environment of the transition metal, for example: $Pb^{II}{}_SCo^{II}{}_{N/O}$(**GR**-CDH)$_3^{n+}$. In the absence of a transition metal, Pb^{II} binding to an Asp containing peptide will still be charged as (n+) due to the ambiguity of the protonation state of the Asp ligands in the hydrophobic protein environment, such as $Pb^{II}{}_S$(**GR**-CDH)$_3^{n+}$.

Table 3-1. Peptide Sequences

Peptide	Abbr.	Sequence
		abcdefg
TRI		Ac-G LKALEEK LKALEEK LKALEEK LKALEEK G-NH_2
TRIL2W		Ac-G ***W***KALEEK LKALEEK LKALEEK LKALEEK G-NH_2
TRIL9CL23H		Ac-G LKALEEK ***C***KALEEK LKALEEK ***H***KALEEK G-NH_2
TRIL16C		Ac-G LKALEEK LKALEEK ***C***KALEEK LKALEEK G-NH_2
TRIL12A16C		Ac-G LKALEEK LKA***A***EEK ***C***KALEEK LKALEEK G-NH_2
TRIL12$_D$L16C		Ac-G LKALEEK LKA$_D$***L***EEK***C***KALEEK LKALEEK G-NH_2
TRIL16Pen		Ac-G LKALEEK LKALEEK***Pen***KALEEK LKALEEK G-NH_2
TRIL2WL23H		Ac-G ***W***KALEEK LKALEEK LKALEEK ***H***KALEEK G-NH_2
TRIL9CL23H		Ac-G LKALEEK LKALEEK ***C***KALEEK ***H***KALEEK G-NH_2
TRIL2WL19$_D$LL23H	**TRI**-$_D$LH	Ac-G ***W***KALEEK LKALEEK LKA$_D$**L**EEK***H***KALEEK G-NH_2
GRAND	**GR**	Ac-G LKALEEK LKALEEK LKALEEK LKALEEK LKALEEK G-NH_2
GRL2WL16C	**GR**-C	Ac-G LKALEEK LKALEEK ***C***KALEEK LKALEEK LKALEEK G-NH_2
GRL2WL12AL16C	**GR**-AC	Ac-G LKALEEK LKA***A***EEK ***C***KALEEK LKALEEK LKALEEK G-NH_2
GRL2WL16CL26DL30H	**GR**-CDH	Ac-G LKALEEK LKA***A***EEK ***C***KALEEK LKA***D***EEK ***H***KALEEK G-NH_2
GRL2WL12AL16CL30H	**GR**-ACH	Ac-G LKALEEK LKA***A***EEK ***C***KALEEK LKALEEK ***H***KALEEK G-NH_2
GRL2WL16CL30HL33D	**GR**-CHD	Ac-G LKALEEK LKA***A***EEK ***C***KALEEK LKADEEK ***H***KA***D***EEK G-NH_2
GRL2WL12AL16CL26DL30H	**GR**-ACDH	Ac-G LKALEEK LKA***A***EEK ***C***KALEEK LKALEEK ***H***KA***D***EEK G-NH_2
GRL2WL16CL26TL30H	**GR**-CTH	Ac-G LKALEEK LKA***A***EEK ***C***KALEEK LKA***T***EEK ***H***KALEEK G-NH_2
GRL2WL16CL30H	**GR**-CH	Ac-G LKALEEK LKA***A***EEK ***C***KALEEK LKADEEK ***H***KALEEK G-NH_2
GRL2WL16CL26$_D$LL30H	**GR**-C$_D$LH	Ac-G LKALEEK LKA***A***EEK ***C***KALEEK LKA$_D$***L***EEK***H***KALEEK G-NH_2
CoilSer		Ac-E WEALEKK LAALESK LQALEKK LEALEH G-NH_2
CSL9PenL23H		Ac-E WEALEKK**Pen**AALESK LQALEKK ***H***EALEH G-NH_2

The stability of **GR**-CDH was investigated because three hydrophobic layers have been perturbed. CD spectroscopy and guanidine hydrochloride (GuaHCl) denaturation titrations were used to determine the folding and stability of **GR**-CDH (Figure 3-2). A characteristic CD spectrum with a double well with minima at 208 and 222 nm was observed, indicative of alpha-helical coiled coil structure. The spectrum for **GR**-CDH showed relatively good folding with a molar ellipticity [Θ] of -26046 deg $dmol^{-1}$ cm^2, which corresponds to ~74% initial folding compared to an ideal, fully folded alpha-helical structure. This model cannot be fit to a two step denaturation curve due to the lack of a defined folded state before addition of GuaHCl, but analysis of Figure 3-2 shows a midpoint at approximately 1 M for the denaturation of **GR**-CDH. The **GR**-CDH shows ~20% less α-helical content, in the absence of denaturant, as compared to **GR**-ACH and has a lower midpoint (~1 M compared to ~2 M for **GR**-ACH).

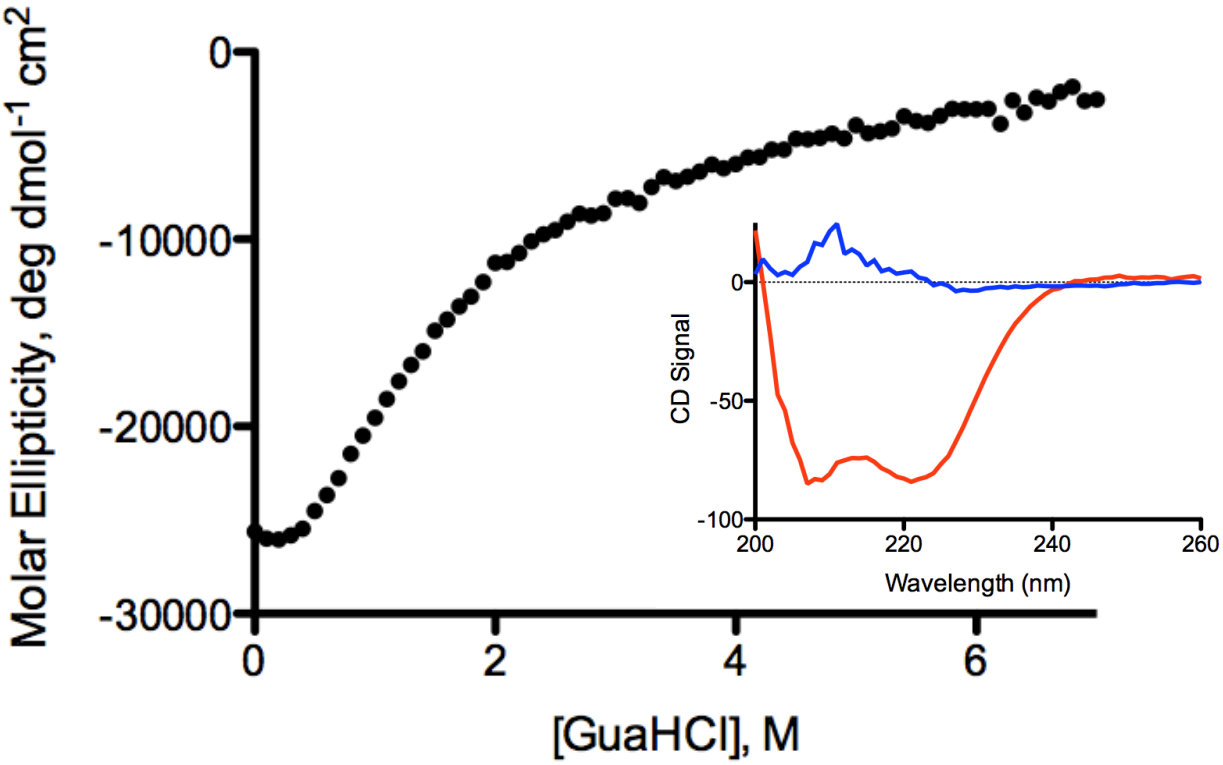

Figure 3-2. Guanidine hydrochloride denaturation titration data of 8 μM 3SCC **GR**-CDH in 10 mM Phosphate buffer at pH 8.0. Inset: CD spectra of **GR**-CDH before (red) and after (blue) the addition of 7 M GuaHCl.

Pb^{II} binding to **GR**-CDH was analyzed via UV-Vis spectroscopy to determine if the presence of Asp/His combined mutations affected the binding of Pb^{II} to the Cys_3 site. Aliquots of $Pb^{II}(NO_3)_2$ were added to a solution of 60 μM **GR**-CDH, resulting in 20 μM 3SCC, in 100 mM TRIS buffer at pH 8.5. As the peptides complex Pb^{II}, an increase in absorbance at 348 nm is observed, characteristic of $Pb^{II}Cys_3$ binding[9,11,23,24] and consistent with Pb^{II} binding to **GR**-CH (Figure 3-3A). Analysis of the spectra determines a maximal absorbance is reached at one equivalent of Pb^{II} added. The immediate leveling out of the titration curve at one equivalent of Pb^{II} added, as observed in Figure 3-3B, indicates that Pb^{II} binding is extremely tight to the Cys_3 sites and association constants cannot be directly measured via this technique as no equilibrium is observed between free and bound Pb^{II} in the presence of our peptides, which again is consistent with **GR**-ACH. Linear regression analysis of the data at 348 nm provided molar extinction coefficients of 3470 $M^{-1}cm^{-1}$, which is comparable to previously reported $Pb^{II}Cys_3$ sites (3520 $M^{-1}cm^{-1}$ for **GR**-ACH from Chapter 2). Therefore, I have determined that Pb^{II} binds preferentially

to the Cys_3 site in the homotrimeric aggregate even in the presence of an L26D subsitution, leaving open the posibility of adding a transition metal to the aspartate/histidine site.

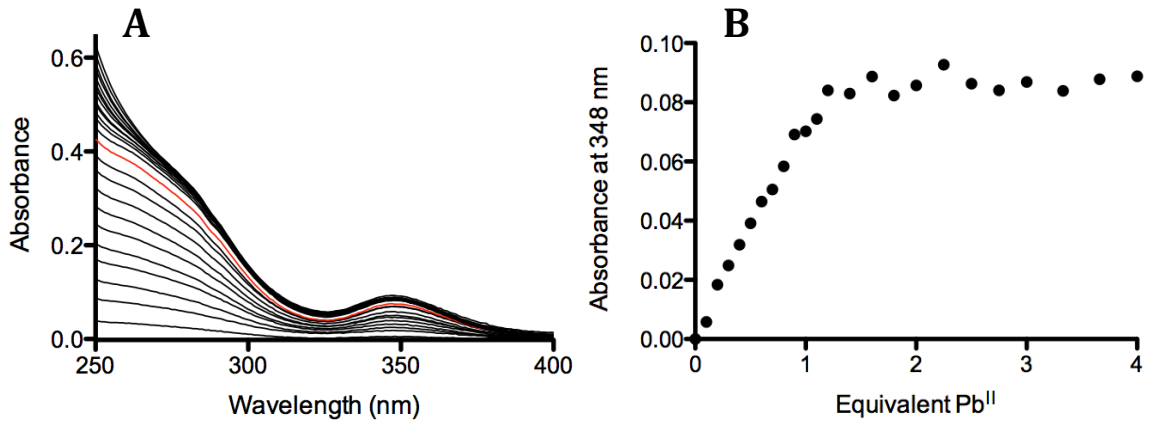

Figure 3-3. UV titration spectra of the addition of Pb^{II} into a solution of A) 20 μM (3SCC) **GR**-CDH and B) the corresponding titration curve showing the 1:1 binding stoichiometry of equivalents of Pb^{II}, added with respect to 3SCC, at 348 nm. Data collected at pH 8.5 in 50 mM TRIS Buffer.

Spectroscopic Characterization of Co^{II}-Bound Homotrimers

Because Zn^{II} is spectroscopically silent, Co^{II} is often added to biomolecules to act as a spectroscopic probe to elucidate metal site structure.[25–29] Here, I used Co^{II} UV-Vis, EPR, and XAS spectroscopies to monitor Co^{II}-binding to the second metal binding site included in the homo- and heterotrimeric constructs. Perturbations of the Co^{II} spectroscopy in these heterotrimeric constructs, nucleated via Pb^{II} binding to the Cys_3 site with a neighboring Ala/Leu steric matching layer, should allow for distinction between symmetric and asymmetric second metal binding sites. I started with analysis of the Co^{II} site of two homotrimeric systems, which are expected to structurally resemble both CA and our previously studied 3SCC CA mimic $(Hg^{II}{}_{S}Zn^{II}(OH_X)_{N/O}(\mathbf{TRI}L9CL23H)_3)^{n+}$, discussed in Chapter 1, Table 3-1)[1].

Aliquots of $Co^{II}SO_4$ were added to solutions of **GR**-ACH and **GR**-CDH, in 50 mM HEPES at pH 7.5. One equivalent of $Pb^{II}(NO_3)_2$ was also present in both solutions. Upon addition of Co^{II} to the homotrimeric $Pb^{II}{}_{S}(\mathbf{GR}\text{-ACH})_3^-$, a broad peak at 517 nm (ε =

30 M^{-1} cm^{-1}) was observed (Figure 3-4) and attributed to Co^{II} binding to the His_3 site. The homotrimeric spectrum, resulting from the asprtate modified peptide, Pb^{II}_S(**GR**-CDH)$_3^{n+}$, displayed a red-shifted peak at 543 nm (ε = 83 M^{-1} cm^{-1}) after Co^{II} addition (Figure 3-4). Thus, to understand the structure, it is worthwhile considering the spectroscopic behavior of Co^{II}.

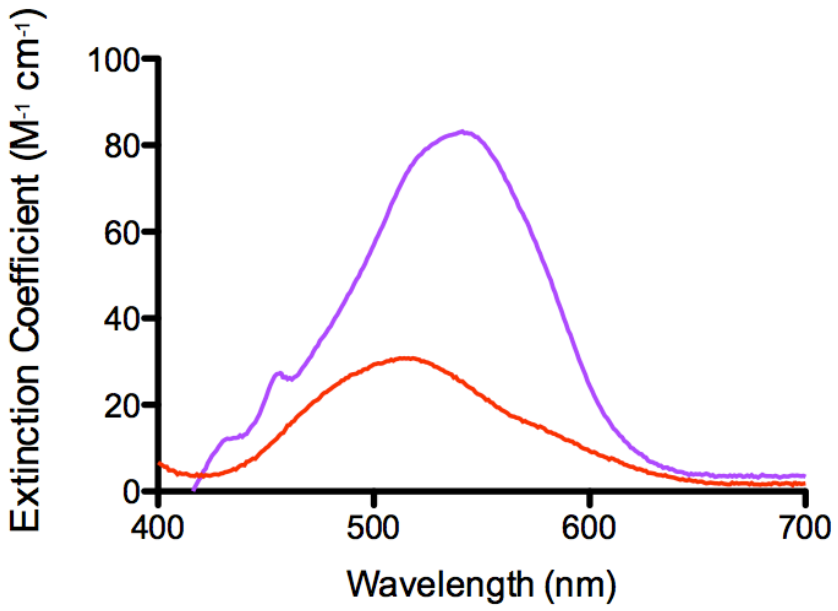

Figure 3-4. UV-Vis overlay of $Pb^{II}_S Co^{II}_{N/O}$(**GR**-CH)$_3^{n+}$, in red, and $Pb^{II}_S Co^{II}_{N/O}$(**GR**-CDH)$^{n+}$, in purple at pH 7.5 in 50 mM HEPES buffer. Data are plotted as molar extinction coefficient (determined using Co^{II} concentration) versus wavelength.

In general, Co^{II} geometry is separated into three groups, which may be distinguished by the extinction coefficients of the d-d transitions of these systems. First, octahedral Co^{II} complexes usually do not exceed extinction coefficients of ~50 $M^{-1}cm^{-1}$.[30,31] Conversely, tetrahedral Co^{II} complexes can have extinction coefficients of 300 $M^{-1}cm^{-1}$ or greater.[26] Five-coordinate Co^{II} complexes generally fall between these two extremes with extinction coefficients of 50-250 $M^{-1}cm^{-1}$. However, ambiguity is often encountered due to distortion of the Co^{II} coordination geometry. Therefore, assigning coordination number based on UV-Vis characteristics is a non-trivial task; however, in the case of both $Pb^{II}_S Co^{II}_N$(**GR**-ACH)$_3^+$ and $Pb^{II}_S Co^{II}_N$(**GR**-CDH)$_3^{n+}$, the low extinction coefficients (ε ~ 30-80 M^{-1} cm^{-1}, Table 3-2) and broad single peaks of these

spectra indicate relatively high symmetry at the Co^{II} binding site, and probably octahedral coordination geometry.

Table 3-2. Electronic absorption values for Co^{II} bound complexes

Complex	Solvent	λ_{max}, nm (ε, $M^{-1}cm^{-1}$)
$Pb^{II}{}_{S}Co^{II}{}_{N/O}$(**GR**-ACH)$_3^{+}$	HEPES Buffer (pH 7.5)	517 (30)
$Pb^{II}{}_{S}Co^{II}{}_{N/O}$(**GR**-CDH)$_3^{n+}$	HEPES Buffer (pH 7.5)	543 (83)
$Pb^{II}{}_{S}Co^{II}{}_{N/O}$(**GR**-CHD)$_3^{n+}$	HEPES Buffer (pH 7.5)	517 (30)
$Hg^{II}{}_{S}Co^{II}{}_{N/O}$(**GR**-CDH)$_3^{n+}$	HEPES Buffer (pH 7.5)	543 (83)
$Co^{II}{}_{N/O}$(**TRI**L2WL23H)$_3^{2+}$	HEPES Buffer (pH 7.5)	517 (35)
$Pb^{II}{}_{S}Co^{II}{}_{N/O}$[(**GR**-ACH)$_2$(**GR**-CDH)$_1$)]$^{n+}$	HEPES Buffer (pH 7.5)	517 (147), 545 (155), 590 (124), 628 (~35)
$Pb^{II}{}_{S}Co^{II}{}_{N/O}$[(**GR**-ACH)$_1$(**GR**-CDH)$_2$)]$^{n+}$	HEPES Buffer (pH 7.5)	517 (152), 547 (173), 583 (133)
⅔($Pb^{II}{}_{S}Co^{II}{}_{N/O}$(**GR**-ACH)$_3^{+}$)+ ⅓ ($Pb^{II}{}_{S}Co^{II}{}_{N/O}$(**GR**-CDH)$_3^{n+}$) - calc	HEPES Buffer (pH 7.5)	523 (48)
⅓($Pb^{II}{}_{S}Co^{II}{}_{N/O}$(**GR**-ACH)$_3^{+}$)+ ⅔($Pb^{II}{}_{S}Co^{II}{}_{N/O}$(**GR**-CDH)$_3^{n+}$) - calc	HEPES Buffer (pH 7.5)	540 (83)
$Co^{II}{}_{N/O}$[(**GR**-ACH)$_2$(**GR**-CDH)$_1$)]$^{n+}$	HEPES Buffer (pH 7.5)	519 (130), 545 (144), 590 (112)
$Co^{II}{}_{N/O}$[(**GR**-ACH)$_1$(**GR**-CDH)$_2$)]$^{n+}$	HEPES Buffer (pH 7.5)	519 (117), 545 (131), 590 (~80)
$Pb^{II}{}_{S}Co^{II}{}_{N/O}$[(**GR**-ACH)$_2$(**GR**-CHD)$_1$)]$^{n+}$	HEPES Buffer (pH 7.5)	515 (58), 590 (~30)
$Pb^{II}{}_{S}Co^{II}{}_{N/O}$[(**GR**-ACH)$_1$(**GR**-CHD)$_2$)]$^{n+}$	HEPES Buffer (pH 7.5)	513 (47), 590 (~18)
$Pb^{II}{}_{S}Co^{II}{}_{N/O}$(**GR**-ACDH)$_3^{n+}$	HEPES Buffer (pH 7.5)	543 (110)
$Pb^{II}{}_{S}Co^{II}{}_{N/O}$[(**GR**-ACDH)$_2$(**GR**-CH)$_1$)]$^{n+}$	HEPES Buffer (pH 7.5)	517 (200), 544 (215), 586 (167), 626 (~60)
$Pb^{II}{}_{S}Co^{II}{}_{N/O}$[(**GR**-ACDH)$_1$(**GR**-CH)$_2$)]$^{n+}$	HEPES Buffer (pH 7.5)	524 (152), 544 (165), 592 (120)
$Pb^{II}{}_{S}Co^{II}{}_{N/O}$[(**GR**-ACDH)$_2$(**GR**-C)$_1$)]$^{n+}$	HEPES Buffer (pH 7.5)	543 (68)
$Pb^{II}{}_{S}Co^{II}{}_{N/O}$(**TRI**-$_D$LH)$_3^{4+}$	HEPES Buffer (pH 7.5)	517 (~59), 541 (62), 588 (~33)
$Pb^{II}{}_{S}Co^{II}{}_{X}$(**GR**-C$_D$LH)$_3^{n+}$	HEPES Buffer (pH 7.5)	507 (~11)
$Co^{II}{}_{X}$(**TRI**L2W)	HEPES Buffer (pH 7.5)	505 (~9)
[Co^{II}(BPZG)Cl][38]	CH_2Cl_2	504 (133), 546 (~150), 593 (255), 615 (~100)
Co^{II}-CPA[27]	TRIS Buffer (pH 7.0)	505 (120), 550 (155), 585 (160)
Co^{II}-Thermolysin[28]	HEPES Buffer (pH 7.0)	495 (60), 550 (80)
Co^{II}-VanX[48]	TRIS Buffer (pH 7.6)	515 (110), 550 (110), 595 (~83)
Co^{II}-HCAII[30]	H_2O, pH 7.1	513 (180), 556 (250), 615 (190), 641 (200)
CoII(tris-pyrazolyl)[30]	H_2O, ≤7.8	507 (40)
Co^{II} (tris-pyrazolyl)[30]	H_2O, ≥8.0	460 (sh), 478 (45), 615 (20), 641 (25)

Figure 3-5 shows an overlay of the visible spectra of $Pb^{II}{}_{S}Co^{II}{}_{N}$(**GR**-ACH)$_3^{+}$ and $Pb^{II}{}_{S}Co^{II}{}_{N/O}$(**GR**-CDH)$_3^{n+}$ with $Hg^{II}{}_{S}Co^{II}{}_{N/O}$(**GR**-CDH)$_3^{n+}$ and $Co^{II}{}_{N/O}$(**TRI**L2WL23H)$_3^{2+}$ (data for both peptides without Pb^{II} were collected by Dr. Melissa Zastrow, Table 1). Nearly identical spectra between 400-700 nm are observed for $Pb^{II}{}_{S}Co^{II}{}_{N/O}$(**GR**-ACH)$_3^{+}$ and $Co^{II}{}_{N/O}$(**TRI**L2WL23H)$_3^{2+}$, indicating that elongation of the peptide sequence from **TRI** to **GR** does not effect the Co^{II} binding to a His_3 **a**-site. It also supports the assumption that the presence of the $Pb^{II}Cys_3$ site does not perturb Co^{II} binding to a His_3 site. The similarity observed between $Pb^{II}{}_{S}Co^{II}{}_{N}$(**GR**-CDH)$_3^{n+}$ and $Hg^{II}{}_{S}Co^{II}{}_{N/O}$(**GR**-CDH)$_3^{n+}$ shows that the identity of the heavy metal bound to the Cys_3 site does not influence the $Co^{II}His_3$ visible spectrum.

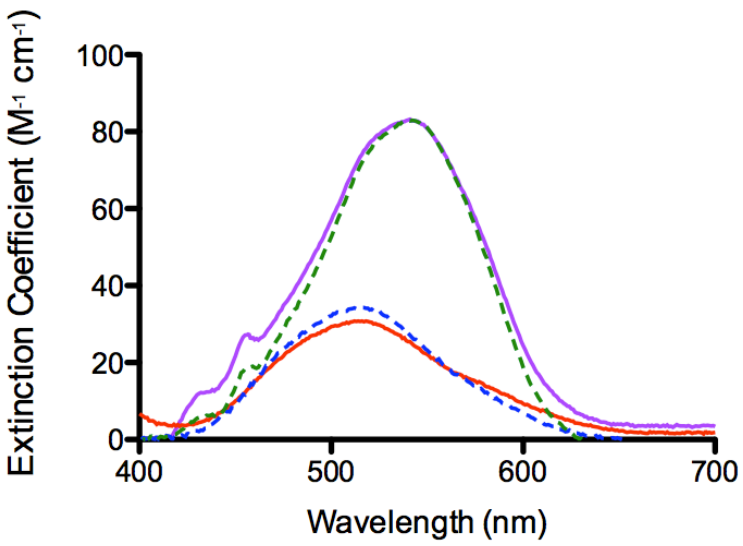

Figure 3-5. UV-Vis overlay of $Pb^{II}_{S}Co^{II}_{N/O}$(**GR**-CH)$_3^{n+}$ (red), $Pb^{II}_{S}Co^{II}_{N/O}$(**GR**-CDH)$_3^{n+}$ (purple), $Hg^{II}_{S}Co^{II}_{N/O}$(**GR**-CDH)$_3^{n+}$ (dashed green), and $Co^{II}_{N/O}$(**TRI**L2WL23H)$_3^{n+}$ (dashed blue) at pH 7.5 in 50 mM HEPES buffer. Data are plotted as molar extinction coefficient (determined using Co^{II} concentration) versus wavelength.

Apparent dissociation constants, $K_{d,CoPep3}$, for Co^{II} binding to the His_3 site, with and without an Asp_3 mutation in the layer directly above the metal binding site (with respect to the N-termini) were determined using a non-linear least square fitting analysis (Equation 7). Titration data at λ_{max} = 517 and 543 nm, for **GR**-ACH and **GR**-CDH, respectively, were plotted as a function of Co^{II} concentration, adjusting for any non-specific binding of Co^{II} and fitted as derived in the Methods Section.[4] The binding affinities of Co^{II} obtained for **GR**-ACH and **GR**-CDH, at pH 7.5, are K_d = 40.9 ± 6.2 and 49.5 ± 7.7 μM, respectively (Figure 3-6, Table 3-3). The value obtained for Co^{II} binding to a His_3 site is the same within error as that reported previously by Dr. Melissa Zatrow for a His_3 site in a comparable **TRI** peptide (K_d = 35 ± 4).[4] The Asp_3His_3 value is only slightly elevated in comparison to the reported value (K_d = 25 ± 9)[4] but is still within the experimental error. These results are particularly interesting because concurrent experiments have shown that Cu^{I} binding affinities to Cys_3 and His_3 sites are dependent on the length of the peptide analyzed (See Chapter 4). This indicates that relative metal binding affinities appear to be dependent on the metal and the metal binding site/peptide analyzed. Furthermore, within error, the dissociation constant for Co^{II} binding to a His_3 and Asp_3His_3 site are the same.

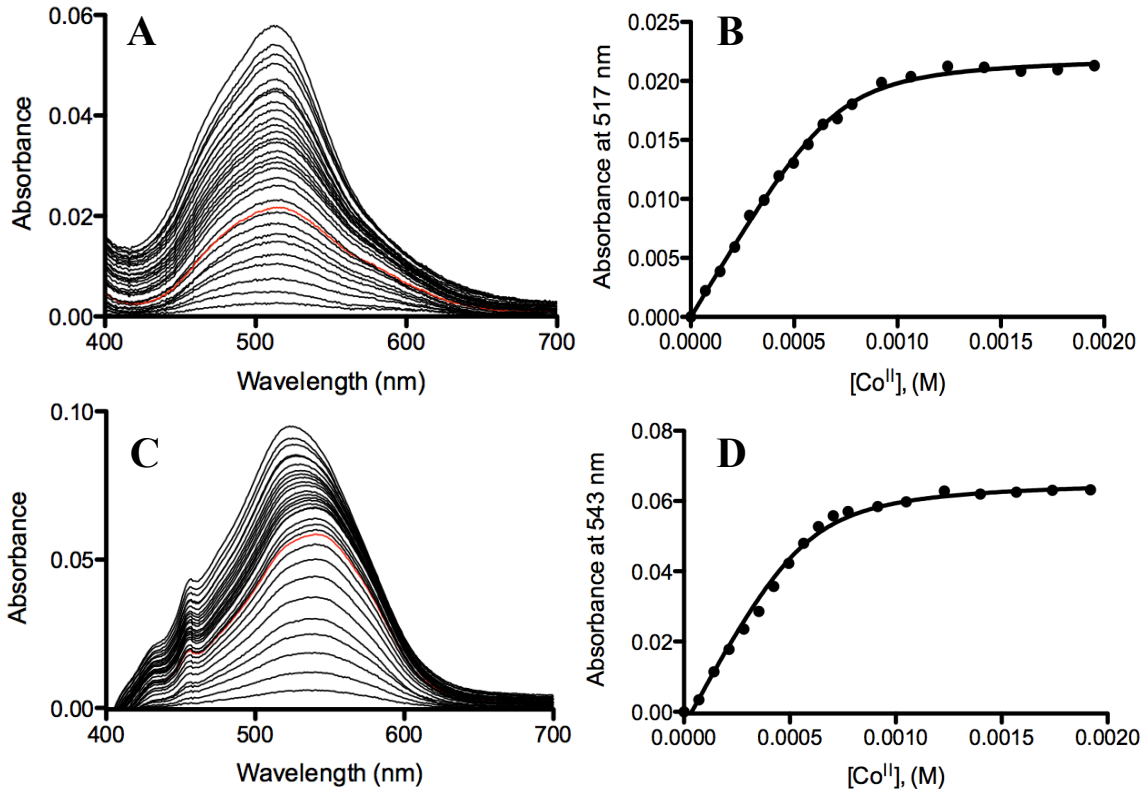

Figure 3-6. UV-Vis titration and titration curves of $Co^{II}SO_4$ added to a solution of 1.73 mM Pb^{II}_S(**GR**-CH)$_3^-$ (A and B) and 2.13 mM Pb^{II}_S(**GR**-CDH)$_3^{n+}$ (C and D) at pH 7.5 in 50 mM HEPES buffer. The titration data (A and C) are plotted as absorbance versus wavelength and the titration curves (B and D) are plotted as absorbance at λ_{max} versus [Co^{II}]. The trace that correlates to one equivalent of [Co^{II}] added, with respect to 3SCC, is shown in red. The black circles represent the raw data and the non-linear best-fit curve is shown as a black line (Equation 7, as described in the Materials and Methods section).

Dr. Melissa Zastrow previously determined that Co^{II} binds to the His_3 site of **TRI**L2WL23H (Table 3-1) with analogous spectral features observed between pH 5.5 to pH 9.8.[4] Comparison of the UV-Vis traces of the Co^{II} d-d bands of $Pb^{II}_SCo^{II}_{N/O}$(**GR**-ACH)$_3^+$ and $Hg^{II}_SCo^{II}_{N/O}$(**TRI**L9CL23H)$_3^+$ revealed that elongation of the peptide from **TRI** to **GR** did not alter the UV-Vis features of a $Co^{II}His_3$ site (Figure 3-5). Additionally, the metal bound at the Cys_3 site, Hg^{II} or Pb^{II}, made no difference in terms of the Co^{II}-binding UV-Vis data. I confirmed the similarities of Co^{II} binding to His_3 sites in **GR** and **TRI** peptides again by analyzing the pH dependence of $Pb^{II}_SCo^{II}_{N/O}$(**GR**-ACH)$_3^+$ where Co^{II} binding is observed starting at pH ~5.5 and the spectral trace is essentially unchanged until pH ~9.0 (Figure 3-7). The primary goal of this pH titration was to determine if Co^{II} binding to a His_3 site in a **GR** peptide is the similar to the same site in a

TRI peptide, and whether at pH of 7.5 was appropriate for analyzing Co^{II}-bound homo- and heterotrimers. The data reported here confirm that complete complexation of Co^{II} is observed before pH 7.5 and that the spectra look identical between **GR** and **TRI** $Co^{II}His_3$ sites.

Table 3-3. Apparent dissociation constants for Co^{II} binding to Asp_XHis_3 sites in the **TRI** and **GR** peptides at pH 7.5.

Peptide	$K_{d, app}$ (μM)
$Pb^{II}{}_SCo^{II}{}_{N/O}$(**GR**-ACH)$_3{}^+$	41 ± 6
$Pb^{II}{}_SCo^{II}{}_{N/O}$(**GR**-CDH)$_3{}^{n+}$	50 ± 8
$Pb^{II}{}_SCo^{II}{}_{N/O}$(**GR**-CHD)$_3{}^{n+}$	350 ± 80
$Hg^{II}{}_SCo^{II}{}_{N/O}$(**GR**-CDH)$_3{}^{n+}$	35 ± 4*
$Co^{II}{}_{N/O}$(**TRI**L2WL23H)$_3{}^{2+}$	25 ± 4*
$Pb^{II}{}_SCo^{II}{}_{N/O}$[(**GR**-ACH)$_2$(**GR**-CDH)$_1$)]$^{n+}$	20 ± 2
$Pb^{II}{}_SCo^{II}{}_{N/O}$[(**GR**-ACH)$_1$(**GR**-CDH)$_2$)]$^{n+}$	7.9 ± 3.9
$Pb^{II}{}_SCo^{II}{}_{N/O}$[(**GR**-ACH)$_2$(**GR**-CHD)$_1$)]$^{n+}$	10 ± 6
$Pb^{II}{}_SCo^{II}{}_{N/O}$[(**GR**-ACH)$_1$(**GR**-CHD)$_2$)]$^{n+}$	18 ± 8
$Pb^{II}{}_SCo^{II}{}_{N/O}$[(**GR**-ACH)$_2$(**GR**-CTH)$_1$)]$^{n+}$	13 ± 2
$Pb^{II}{}_SCo^{II}{}_{N/O}$(**GR**-ACDH)$_3{}^{n+}$	11 ± 3
$Pb^{II}{}_SCo^{II}{}_{N/O}$[(**GR**-ACDH)$_2$(**GR**-CH)$_1$)]$^{n+}$	11 ± 1
$Pb^{II}{}_SCo^{II}{}_{N/O}$[(**GR**-ACDH)$_1$(**GR**-CH)$_2$)]$^{n+}$	22 ± 2
$Pb^{II}{}_SCo^{II}{}_{N/O}$[(**GR**-ACDH)$_2$(**GR**-C)$_1$)]$^{n+}$	25 ± 10
$Pb^{II}{}_SCo^{II}{}_{N/O}$(**TRI**-$_D$LH)$_3{}^{4+}$	39 ± 9

*Data collected by Dr. Melissa Zastrow.[4]

I then looked to Co^{II}-substituted native enzymes to help elucidate the metal environment in our homotrimeric systems. Bertini *et al.* has extensively studied both Co^{II}-substituted CA as well as small molecule CA mimics with complexes that retain enzymatic activity.[29,32] In the cases of both the small molecule mimics and the native enzyme there are significant pH-dependencies of these systems, ascribed to the acid-base properties of the active site. The UV-Vis spectrum of Co^{II}CA provides a maximal extinction coefficient of 300 $M^{-1}cm^{-1}$, indicative of a probable four-coordinate, tetrahedral metal environment. The extreme decrease in extinction coefficient observed in both homotrimeric systems, $Pb^{II}{}_SCo^{II}{}_{N/O}$(**GR**-ACH)$_3{}^+$, and $Pb^{II}{}_SCo^{II}{}_{N/O}$(**GR**-CDH)$_3{}^{n+}$, suggests both higher symmetry and higher coordination number.

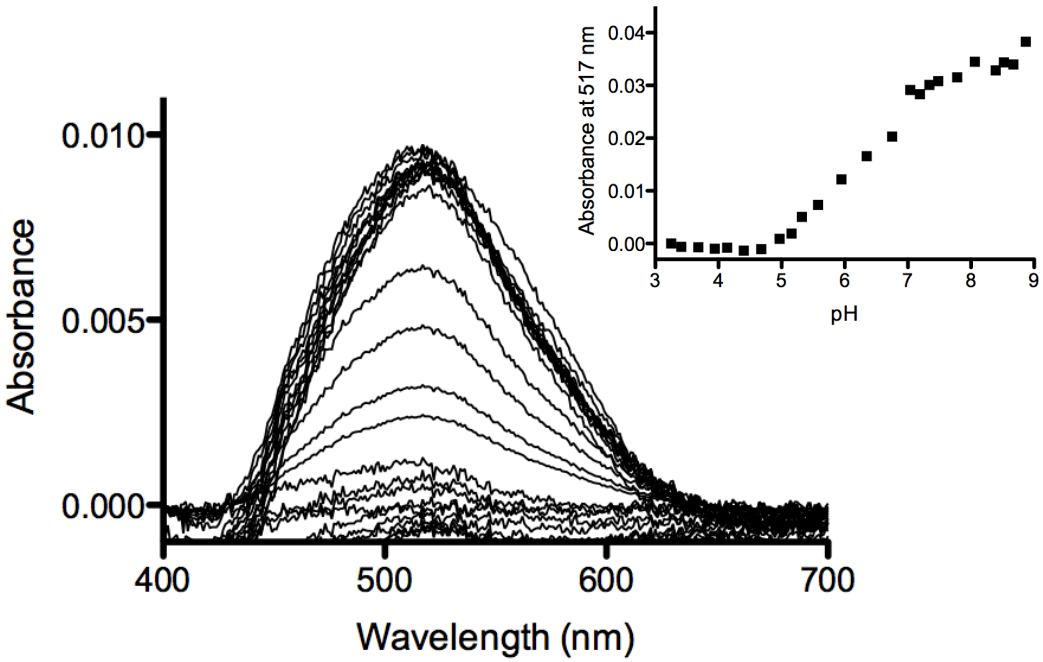

Figure 3-7. UV-Vis spectra representing the pH titration of 0.43 mM $Pb^{II}_{S}Co^{II}_{N/O}$(**GR**-ACH)$_3^{n+}$ with inset: the corresponding titration curve at 517 nm. The spectral data are plotted as absorbance versus wavelength and the titration data are plotted as absorbance at 517 nm versus pH. The pH titration was initiated at low pH and increased using small aliquots of concentrated KOH. The black circles represent the raw absorbance data at 517 nm.

Interestingly, when comparing to Co^{II}[tris-(3,5-dimethyl-1-pyrazolylmethyl)amine] hydrate, a CA small molecule mimic with approximate trigonal bipyramidal geometry and N_4O coordination, at pH ~7.7-8.0, we see a very similar trace when compared to $Pb^{II}_{S}Co^{II}_{N/O}$(**GR**-ACH)$_3^{+}$ (Figure 3-8, Table 3-2).[33,34] Conversely, when the pH of the pyrazolylmethyl complex is increased, the trace looks more like the $Pb^{II}_{S}Co^{II}_{N/O}$(**GR**-CDH)$_3^{n+}$ homotrimer (Table 3-2). The spectra of Co^{II}[tris-(3,5-dimethyl-1-pyrazolylmethyl)amine] hydrate is different at high and low pH, presumably due to a transition from Co^{II}-OH_2 to Co^{II}-OH. The similarities between the lower pH spectra with $Pb^{II}_{S}Co^{II}_{N/O}$(**GR**-ACH)$_3^{+}$ (at pH 7.5) and the similarities between the higher pH spectra with $Pb^{II}_{S}Co^{II}_{N/O}$(**GR**-CDH)$_3^{n+}$ (at pH 7.5) could indicate that the negative environment introduced by the Asp_3His_3 peptide could promote deprotonation of a bound water molecule at lower pH than the corresponding His_3 containing peptide.

It has been reported that Co^{II}-bound CA yields octahedral geometries upon oxidation to Co^{III}.[35] To address the possibility of air-oxidation of Co^{II} to Co^{III}, the above experiments were repeated anaerobically. Samples were prepared identically to aerobic

samples with the exception of being in an inert atmosphere glove box using oxygen-free buffer solution, water, peptide stocks and metal stocks. In the cases of both Pb^{II}_{S}(**GR**-ACH)$_3^-$ and Pb^{II}_{S}(**GR**-CDH)$_3^{n+}$, addition of $Co^{II}SO_4$ in an anaerobic environment resulted in identical UV-Vis spectra as the aerobic experiment (Figure 3-9). These results indicate that our Co^{II}-bound systems are not air sensitive and oxidation from Co^{II} to Co^{III} is not observed. Future studies will address the changes of the d-d absorption bands following the chemical oxidation of Co^{II} to Co^{III}.

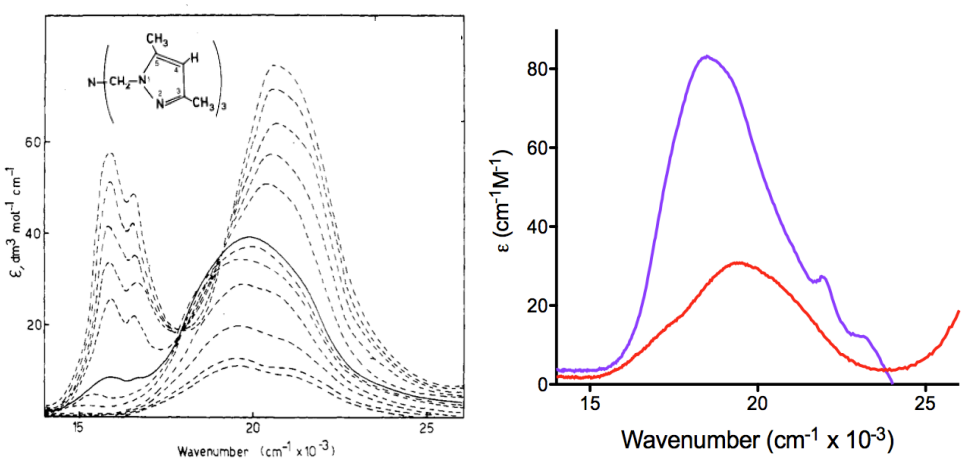

Figure 3-8. (A) pH dependence of the electronic spectra of the Co^{II}[tris-(3,5-dimethyl-1-pyrazolylmethyl)amine] hydrate complex in water shown as ε ($dm^3mol^{-1}cm^{-1}$) vs. Wavenumber (cm^{-1} x 10^{-3}). From the top, pH 9.55, 9.3, 9.15, 8.9, 8.7, 8.3, 7.9, 7.7, 7.6, 7.2, 6.2, 5.0. The pH of the solid line (8.3) is that resulting from dissolving the complex in water at 10^{-3} mol dm^{-3} concentration. Panel A adapted from Ref 32. (B) UV-Vis overlay of $Pb^{II}_{S}Co^{II}_{N/O}$(**GR**-CH)$_3^{n+}$, in red, and $Pb^{II}_{S}Co^{II}_{N/O}$(**GR**-CDH)$^{n+}$, in purple at pH 7.5 in 50 mM HEPES buffer. Data are plotted as molar extinction coefficient (determined using Co^{II} concentration) versus wavenumber (cm^{-1} x 10^3).

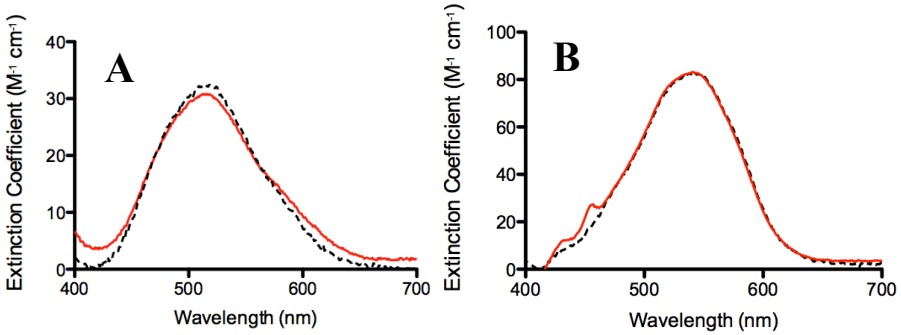

Figure 3-9. UV-Vis overlay of (A) $Pb^{II}_{S}Co^{II}_{N/O}$(**GR**-CH)$_3^{n+}$ and (B) $Pb^{II}_{S}Co^{II}_{N/O}$(**GR**-CDH)$_3^{n+}$ collected aerobically (red lines) and anaerobically (black dashed lines) at pH 7.5 in 50 mM HEPES buffer. Data are plotted as molar extinction coefficient (determined using Co^{II} concentration) versus wavelength.

In order to obtain metrical parameters for the Co^{II} coordination environment, X-ray absorption spectroscopy (XAS) was used to analyze Co^{II} bound homotrimers. Samples consisted of ~2 mM Pb^{II}-bound 3SCC, 0.5 equivalents of $Co^{II}SO_4$, ~30-50 mM buffer and ~50% glycerol. Data was collected at ~7-11 K. XAS data were collected and processed in collaboration with Dr. Aniruddha Deb of the Penner-Hahn Laboratory (University of Michigan). Examination of the X-ray absorption near edge structure (XANES) shows a pre-edge feature at 7710 eV consistent with a Co^{II} 1s-3d transition (Figure 3-10). This transition is symmetry forbidden and is more intense as the symmetry around the metal center is relaxed; therefore, a correlation can be drawn between the intensity of this peak and the coordination number of the Co^{II} complex. In particular, the area under the peak, as well as the number obtained by dividing the height of the pre-edge peak by the main edge height, can then be compared to values determined from complexes with known coordination numbers and geometries. For $Pb^{II}{}_SCo^{II}{}_{N/O}$(**GR**-ACH)$_3^+$ the values for both the area under the pre-edge peak, in percentage, and the ratio of the pre-edge:edge peaks are 5.8 and 2.0, respectively (Table 3-4). The addition of the Asp mutation provides an increase in the pre-edge peak area to 7.6, but a slight decrease in the ratio of the pre-edge:edge peaks to 1.9. These values, for both of these peptides, are consistent with with 5-coordinate Co^{II} small molecules complexes (Cambridge Structural Database).[36]

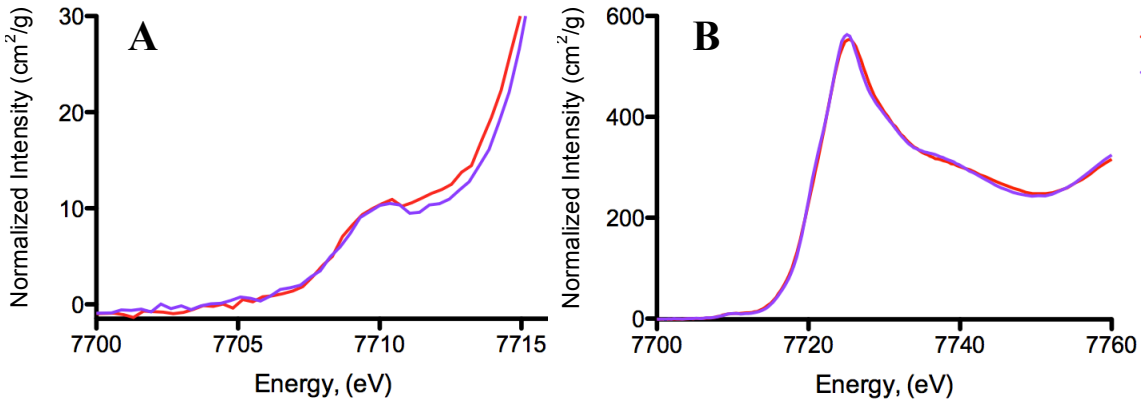

Figure 3-10. XANES spectra of the Co^{II} (A) pre-edge and (B) edge of homotrimers: 1.0 mM $Pb^{II}{}_SCo^{II}{}_{N/O}$(**GR**-ACH)$_3^{n+}$ (red) and 1.0 mM $Pb^{II}{}_SCo^{II}{}_{N/O}$(**GR**-CDH)$_3^{n+}$ (purple) at pH 7.5 in 30 mM HEPES.

Table 3-4. Co^{II} XANES pre-edge:edge height area and pre-edge area for Co^{II} binding to Asp_XHis_3 sites in homo- and heterotrimeric **GR** peptides at pH 7.5.

Peptide	Pre-edge Area (%)	Pre-edge:Edge Ratio
$Pb^{II}{}_SCo^{II}{}_{N/O}$(**GR**-ACH)$_3{}^+$	6.0	2.0
$Pb^{II}{}_SCo^{II}{}_{N/O}$(**GR**-CDH)$_3{}^{n+}$	7.6	1.9
$Pb^{II}{}_SCo^{II}{}_{N/O}$(**GR**-CHD)$_3{}^{n+}$	5.5	2.2
$Pb^{II}{}_SCo^{II}{}_{N/O}$[(**GR**-ACH)$_2$(**GR**-CDH)$_1$)]$^{n+}$	5.8	2.0
$Pb^{II}{}_SCo^{II}{}_{N/O}$[(**GR**-ACH)$_1$(**GR**-CDH)$_2$)]$^{n+}$	9.4	2.8
$Pb^{II}{}_SCo^{II}{}_{N/O}$(**GR**-ACDH)$_3{}^{n+}$	6.6	2.0
$Pb^{II}{}_SCo^{II}{}_{N/O}$[(**GR**-ACDH)$_2$(**GR**-CH)$_1$)]$^{n+}$	10.3	3.5
$Pb^{II}{}_SCo^{II}{}_{N/O}$[(**GR**-ACDH)$_1$(**GR**-CH)$_2$)]$^{n+}$	15.4	6.3

A nearest-neighbor peak, typical of scattering observed by direct nitrogen and/or oxygen metal coordination, dominates the extended X-ray absorption fine structure (EXAFS) data and is best fit with a single nitrogen/oxygen shell at ~2.10 Å (Table 3-5 and Figure 3-11). There is also evidence in both homotrimer samples of outer shell scattering typical of histidine coordination (Figures 3-11A and 3-11C, $2.5 < R < 4$ Å). Multiple models with varying numbers of imidazole and oxygen ligands were used to fit these data, but the best fit was determined to be six oxygen/nitrogen ligands with an average Co^{II}-N/O distance of 2.115 Å for both $Pb^{II}{}_SCo^{II}{}_{N/O}$(**GR**-ACH)$_3{}^+$ and $Pb^{II}{}_SCo^{II}{}_{N/O}$(**GR**-CDH)$_3{}^{n+}$, with DW: 1.5 & 7.6, F=404 and DW: 2.2 & 6.6, F=291, respectively, where DW is the Debeye Waller factor and F is the goodness of fit (Table 3-5).

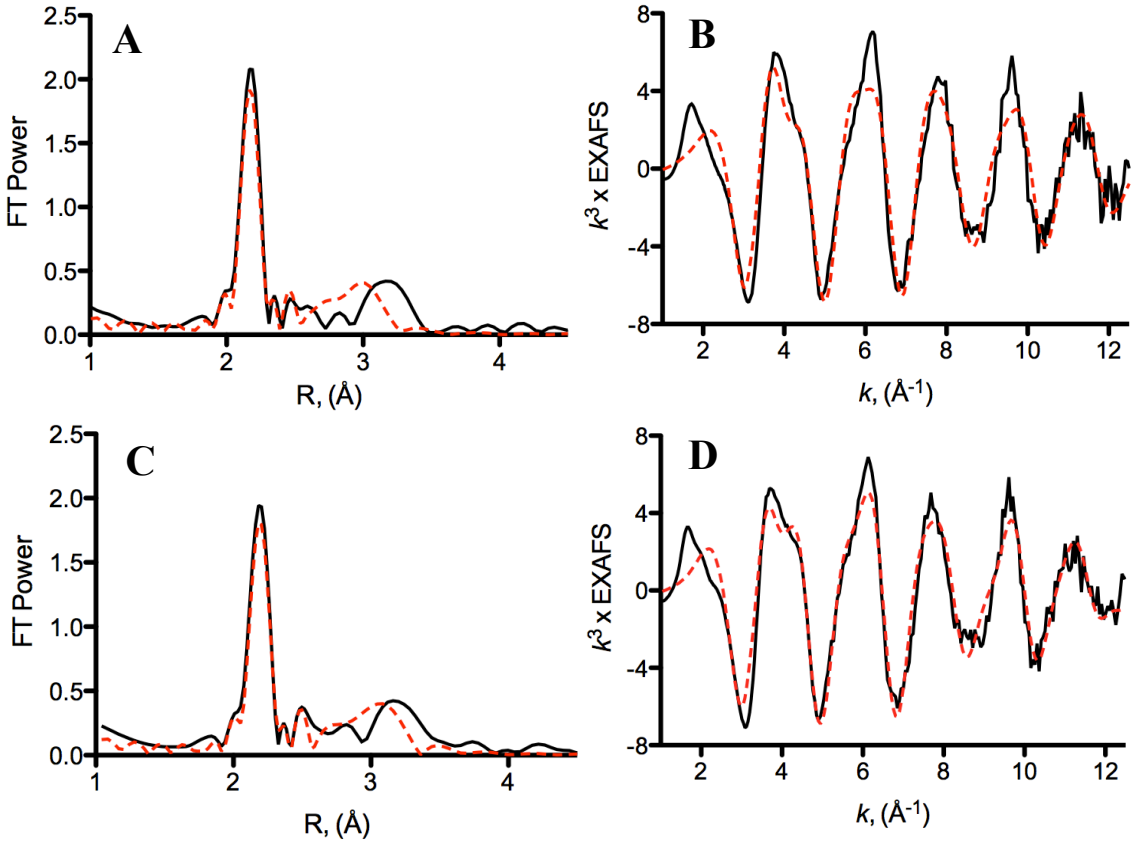

Figure 3-11. Fourier transform of Co^{II} EXAFS of (A) 1.0 mM $Pb^{II}_{S}Co^{II}_{N/O}$(**GR**-ACH)$_3^{n+}$ and (C) 1.0 mM $Pb^{II}_{S}Co^{II}_{N/O}$(**GR**-CDH)$_3^{n+}$ at pH 7.5 in 30 mM HEPES. Co^{II} EXAFS (B) $Pb^{II}_{S}Co^{II}_{N/O}$(**GR**-ACH)$_3^{n+}$ and (D) $Pb^{II}_{S}Co^{II}_{N/O}$(**GR**-CDH)$_3^{n+}$. Experimental data is shown in black and best fits for N_3O_3 Co^{II}-coordination are shown in red dashed lines.

Table 3-5. EXAFS fitting parameters for Co^{II} binding to Asp_XHis_3 sites in homo- and heterotrimeric GR peptides at pH 7.5.

Peptide	Co^{II}-L distance (Single), Å	CN*	Multi-scattering shell	Co^{II}-L distance (Multi), Å	DW (Multi)	F
$Pb^{II}_SCo^{II}_{N/O}$(**GR**-ACH)$_3^+$	2.10	6	N_3O_3	2.115	1.5, 7.6	404
			N_2O_4	2.103	3.4, 6.3	316
$Pb^{II}_SCo^{II}_{N/O}$(**GR**-CDH)$_3^{n+}$	2.10	6	N_3O_3	2.115	2.2, 6.6	291
			N_2O_4	2.101	4.9, 5.7	269
$Pb^{II}_SCo^{II}_{N/O}$(**GR**-CHD)$_3^{n+}$	2.08⌘	-	-	-	-	344
$Pb^{II}_SCo^{II}_{N/O}$[(**GR**-ACH)$_2$(**GR**-CDH)$_1$)]$^{n+}$	2.07	5 or 6	N_3O_2	2.075	1.3, 9.2	573
			N_2O_3	2.070	2.0, 10	434
			N_3O_3	2.085	2.8, 9.0	474
			N_2O_4	2.085	4.0, 7.7	377
$Pb^{II}_SCo^{II}_{N/O}$[(**GR**-ACH)$_1$(**GR**-CDH)$_2$)]$^{n+}$	2.07	5 or 6	N_3O_2	2.080	5.0, 9.0	248
			N_3O_3	2.085	2.8, 9.0	226
$Pb^{II}_SCo^{II}_{N/O}$(**GR**-ACDH)$_3^{n+}$	2.09	6	N_3O_3	2.105	3.7,8.8	281
			N_2O_4	2.093	5.3,6.4	277
$Pb^{II}_SCo^{II}_{N/O}$[(**GR**-ACDH)$_2$(**GR**-CH)$_1$)]$^{n+}$	2.05⌘	-	-	-	-	226
$Pb^{II}_SCo^{II}_{N/O}$[(**GR**-ACDH)$_1$(**GR**-CH)$_2$)]$^{n+}$	1.98	4	N_2O_2	1.995	4.2, 9.4	218
			N_3O_1	1.995	5.1, 6.0	278

Single indicates fits of direct N/O ligands only. Multi indicates fits considering backscattering of His and Asp residues. *CN is coordination number used for the multi-scattering fits. For $Pb^{II}_SCo^{II}_{N/O}$[(**GR**-ACH)$_1$(**GR**-CDH)$_2$)]$^{n+}$, the data would not fit to N_2O_4 or N_2O_3 primary coordination spheres. DW and F correspond to Debye Waller factors and goodness of fit parameters, respectively. ⌘Samples indicative of mixed Co^{II} coordination numbers, therefore fits with multi-scattering secondary spheres were not conducted.

Interpretation of the Co^{II} XAS data has proven non-trivial. The EXAFS bond distances are simply too long, when compared to small model complexes, to correlate to five-coordinate, or lower, binding sites. However, the EXAFS bond distances contradict the data obtained via analysis of the pre-edge/edge ratios and the pre-edge area values, which support a Co^{II} coordination number of five. With data that supported both 6- (EXAFS distances) and 5-coordinate (XANES analysis), I wanted to address the possibility of a mixed 6- and 4-coordinate environment. If indeed the samples were comprised of mostly 6-coordinate Co^{II} ligation but a small amount of 4-coordinate ligation, this could explain why the pre-edge/edge ratios and the pre-edge area values are slightly higher than 6-coordinate complexes, while the EXAFS data are dominated by the longer 6-coordinate species. Therefore, I analyzed whether a mixture of 4- and 6-coordinate distances would provide two peaks, resolvable via fitting of the EXAFS data. Simulated mixtures of two average bond distances were analyzed, the shorter bond distance was set at 1.98 Å, consistent with a Co-N/O bond distance in a tetrahedral complex, and the second bond length, correlating to the 6-coordinate Co^{II} species, was

varied from 2.10 to 2.19 Å at 0.02-0.03 Å intervals (Figure 3-12). At the smallest difference in distance between the two distances only one peak is observed in the EXAFS; however, an increase of the long distance from 2.10 Å to 2.13 Å provided a simulated spectrum with a visible shoulder, correlating to the 1.98 Å distance scatterer (Figure 3-12, green trace). As the difference between the distances increases, the peaks become more resolved. The EXAFS data, with best-fit distances of 2.115 Å, correlates to a difference of 0.135 Å when compared to a 4-coordinate distance of 1.98 Å. Therefore, if the homotrimer samples contained both 4- and 6-coordinate Co^{II} species we might expect to see a shoulder correlating to the lower coordination species. Both homotrimer samples show very symmetric peaks and, therefore, do not obviously support the presence of a 4-coordinate species in the sample; however, this possibility cannot be completely ruled out at this time.

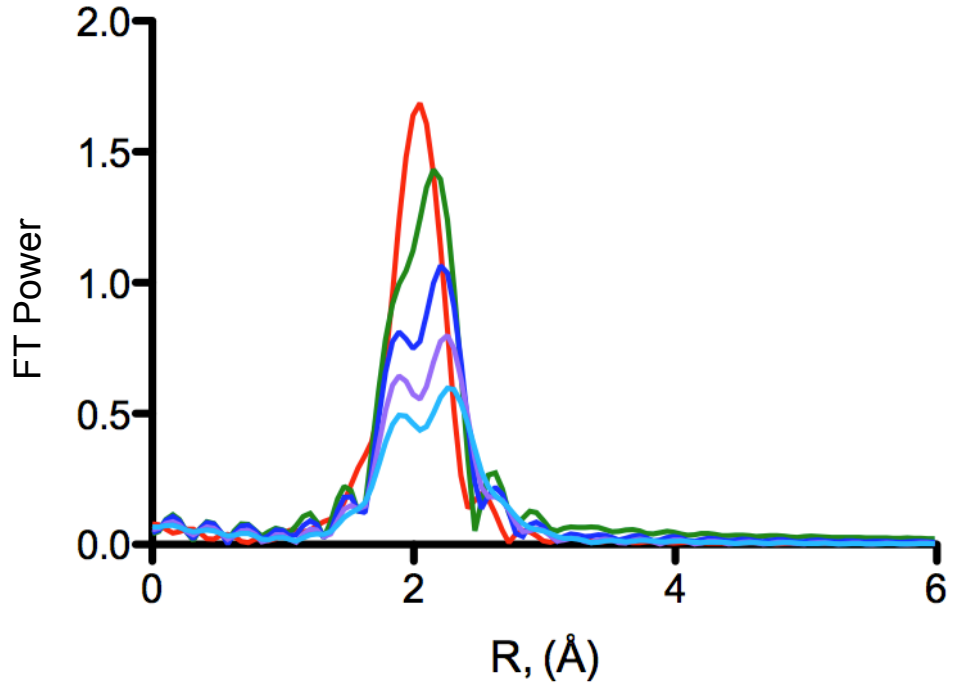

Figure 3-12. Overlay of simulated Fourier Transform traces for fits of mixed four- and six-coordinate Co^{II} complexes with varying Co^{II}-ligand 6-coordinate distances. All traces have four-coordinate distances set at 1.98 Å with varied six-coordinate distances from 2.10 Å (red), 2.13 Å (green), 2.15 Å (dark blue), 2.17 Å (purple) and 2.19 Å (light blue).

X-band EPR spectra were collected for both the $Pb^{II}_{S}Co^{II}_{N/O}$(**GR**-ACH)$_3^+$ and $Pb^{II}_{S}Co^{II}_{N/O}$(**GR**-CDH)$_3^{n+}$ homotrimers at 4K. Samples were prepared analogously to the XAS samples. Both homotrimeric peptides produced two relatively axial signals similar to each other and to that of Co^{II}-substituted CA (Figure 3-13).[33,37] Grell and Bray suggest a 4-coordinate environment for the similarly axial signal for Co^{II}CA.[37] However, considering both the very low extinction coefficients as determined by UV-Vis spectroscopy, for both of the homotrimers, and the EXAFS fits providing bond distances that are too long to be consistent for either 4- or 5-coordinate Co^{II} environments, I propose that both $Pb^{II}_{S}Co^{II}_{N/O}$(**GR**-CDH)$_3^-$ and $Pb^{II}_{S}Co^{II}_{N/O}$(**GR**-ACH)$_3^+$ are 6-coordinate Co^{II} species. The similarities in the EPR data are most likely due to both tetrahedral and octahedral coordination environments having cubic symmetry, both of which result in quartet ground states and, therefore, the similar EPR spectra.

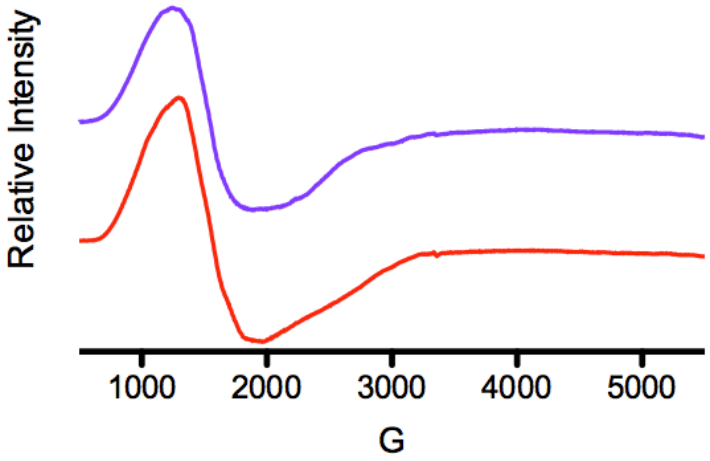

Figure 3-13. X-Band EPR spectra of 1.0 mM $Pb^{II}_{S}Co^{II}_{N/O}$(**GR**-ACH)$_3^{n+}$ (red) and 1.0 mM $Pb^{II}_{S}Co^{II}_{N/O}$(**GR**-CDH)$_3^{n+}$ (purple) at pH 7.5 in 30 mM HEPES, collected at 10 K.

At this time, the differences between the XANES and EXAFS data have proven difficult to explain. However, the majority of the spectroscopic data including the low extinction coefficients observed via UV-Vis analysis, the relatively axial spectra obtained via EPR analysis and the long 2.115 Å distances obtained from EXAFS fits support highly symmetric, and probably 6-coordinate, Co^{II} centers in both $Pb^{II}_{S}Co^{II}_{N/O}$(**GR**-ACH)$_3^+$ and $Pb^{II}_{S}Co^{II}_{N/O}$(**GR**-CDH)$_3^{n+}$. The perturbations observed in the UV-Vis spectra support different coordination ligands between the Asp_3His_3 and His_3 sites. The Co^{II} site

in (**GR**-ACH)$_3$ is mostly likely made up of three histidine residues and three oxygen atoms, presumably from coordinated water molecules. The Co^{II} center of (**GR**-CDH) is most likely still 6-coordinate but could have one less histidine ligand and a direct Asp ligand, such as $Co^{II}N_2Carboxylate_1(OH_2)_3$; however, at this time I cannot rule out a $N_3(OH_2)_3$ environment in which the bound molecules are perturbed by hydrogen-bonding to the nearby Asp_3 layer.

In collaboration with the laboratory of Nicolai Lehnert, I also analyzed $Pb^{II}_SCo^{II}_{N/O}$(**GR**-ACH)$_3^+$ and $Pb^{II}_SCo^{II}_{N/O}$(**GR**-CDH)$_3^{n+}$ via Magnetic Circular Dichorism (MCD) Spectroscopy. Samples were prepared similarly to the EPR and XAS samples with the exception of using ethylene glycol as a glassing agent instead of glycerol. $Pb^{II}_SCo^{II}_{N/O}$(**GR**-ACH)$_3^+$ provided an MCD spectra with a negative signal centered at 593 nm and a positive signal at 550 nm (Figure 3-14A). $Pb^{II}_SCo^{II}_{N/O}$(**GR**-CDH)$_3^{n+}$ exhibited only one strong negative band at 490 nm (Figure 3-14B).

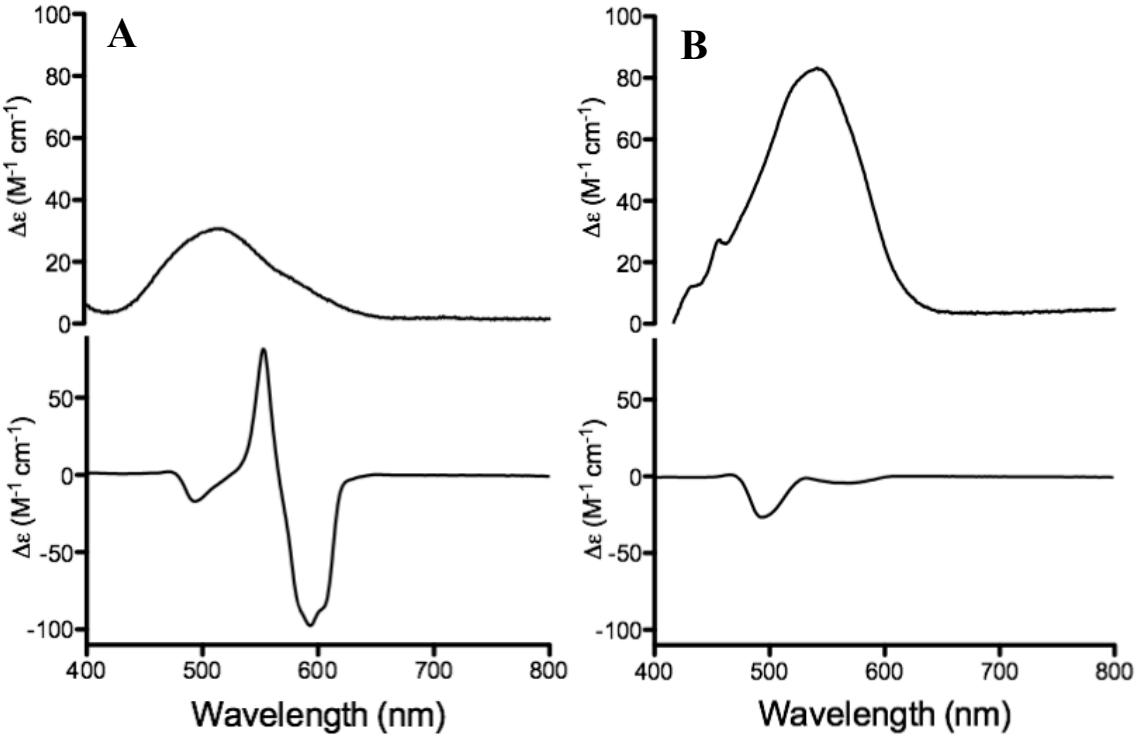

Figure 3-14. Absorbance (top) and MCD (bottom) spectra of ~2.0 mM $Pb^{II}_SCo^{II}_{N/O}$(**GR**-ACH)$_3^{n+}$ (A) and $Pb^{II}_SCo^{II}_{N/O}$(**GR**-CDH)$_3^{n+}$ (B) at pH 7.5 in 50 mM HEPES, collected at RT (Absorbance) and 2K (MCD).

According to Kaden *et al.* there are three general groups used to characterize the overall fingerprint of Co^{II} MCD spectra, dependent on the coordination geometry of the metal ion. Octahedral systems exhibit an absorption maximum of low intensity centered near 500 nm (Figure 3-15A).[38] Tetrahedral Co^{II} complexes exhibit a significant negative band at low frequency (~600-700 nm) with a smaller positive band at higher frequency (~500-600 nm, Figure 3-15B). For intermediate pentacoordinate Co^{II} complexes, the spectra general show multiple bands of negative ellipticity ranging in energy from 500-700 nm, and sometimes a positive band is also observed at higher energy (~500 nm Figure 3-15C). Following these general guidelines, $Pb^{II}_{S}Co^{II}_{N/O}$(**GR**-ACH)$_3^{+}$ and $Pb^{II}_{S}Co^{II}_{N/O}$(**GR**-CDH)$_3^{n+}$ show tetrahedral and octahedral characteristics, respectively.

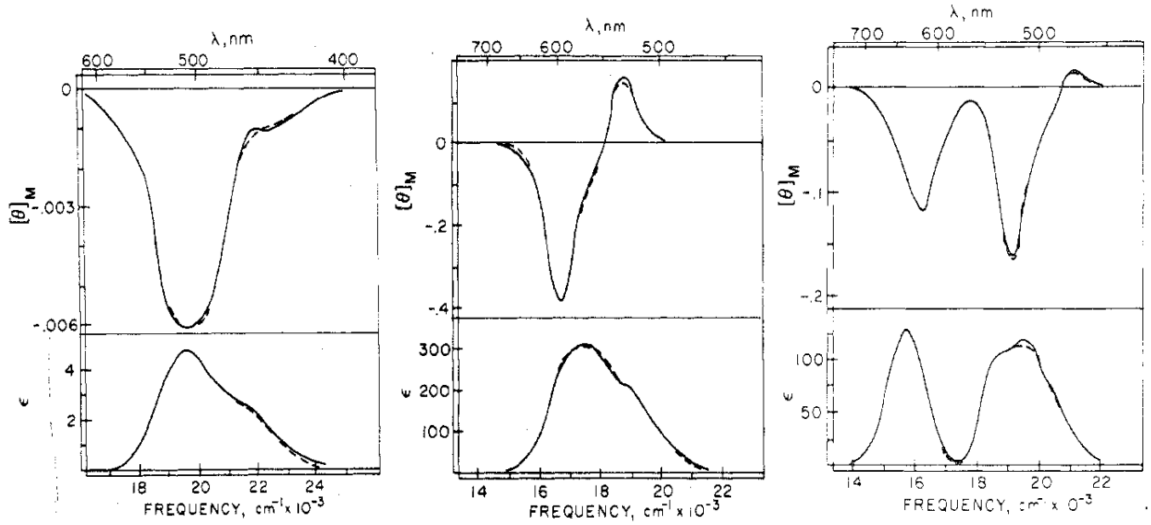

Figure 3-15. Absorbance (top) and MCD (bottom) spectra of octahedral $Co(H_2O)_6^{2+}$ (A), tetrahedral $Co(hisH\_1)_2^{2-}$ (B), and penta-coordinate $Co(Me_6tren)Br_2$ in $CHCl_3$ (C). Figure adapted from Ref XX.[38]

To address the subtle spectroscopic differences observed between the two homotrimers a new peptide was synthesized, **GR**L2WL16CL30HL33D (**GR**-CHD, Table 3-1). This peptide is similar to the **GR**-CDH peptide in that they both contain 3-fold Asp substitutions, however the Asp layer has been moved from the N-terminal side of the His_3 binding site in **GR**-CDH to below the metal on the C-terminal side providing **GR**-CHD.

The stability and initial folding of **GR**-CHD were analyzed via CD spectroscopy and GuaHCl denaturation titrations. The double well feature of an alpha-helical bundle was once again observed (Figure 3-16) providing a molar ellipticity [Θ] of -18816 deg

dmol^{-1} cm^2, which corresponds to only ~53% initial folding, compared to an ideal, fully folded alpha-helical structure. The decrease observed in folding may be due to the close proximity of the Asp residues with respect to the C-termini of the coiled coil, perhaps resulting in more fraying of the peptide in attempt to solvate the charged Asp residues. Fits of the data to a two-step denaturation provide a $\Delta G°_{unfolding}$ of 2.4 ± 0.9 kcal/mol and a midpoint of denaturation is observed at about 2.5 M GuaHCl. These data indicate that although the initial folding is only about 50% the peptide itself is relatively stable to denaturation via addition of GuaHCl as observed by an increased midpoint compared to **GR**-ACH or **GR**-CDH (2.0 and 1.0 M, respectively).

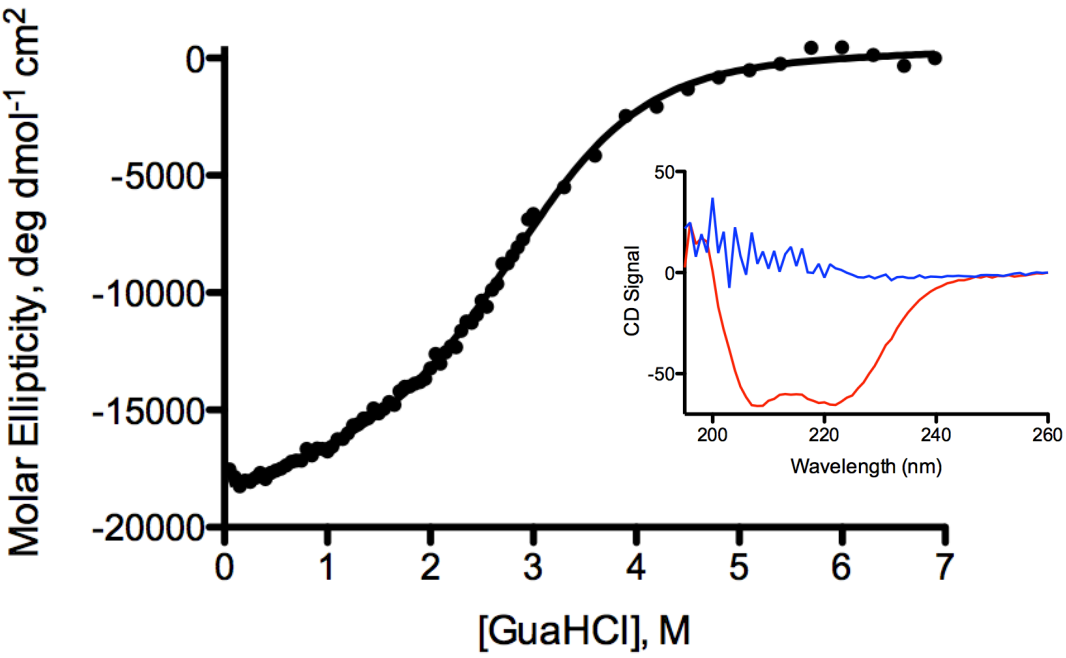

Figure 3-16. Guanidine hydrochloride denaturation titration data of **GR**-CHD (10 μM 3SCC) in 10 mM Phosphate buffer at pH 8.0. Inset: CD spectra of **GR**-CHD before (red) and after (blue) the addition of 7 M GuaHCl.

Aliquots of $Co^{II}SO_4$ were added to a solution of 1.05 mM **GR**-CHD, yielding 0.35 mM 3SCC, in 50 mM HEPES at pH 7.5, with one equivalent of $Pb^{II}(NO_3)_2$ also present. UV-Vis analysis of $Pb^{II}{}_SCo^{II}{}_{N/O}$(**GR**-CHD)$_3{}^{n+}$ revealed a trace identical to that of $Pb^{II}{}_SCo^{II}{}_{N/O}$(**GR**-ACH)$_3{}^+$ and *not* $Pb^{II}{}_SCo^{II}{}_{N/O}$(**GR**-CDH)$_3{}^{n+}$ with an absorbance maximum at 543 nm (ε= 33 M^{-1}cm^{-1}) (Figure 3-17, Table 3-2). This indicates that when the Asp residues are introduced below the His_3 site they do not effect Co^{II} binding, conversely to

what was observed for the $Pb^{II}_{S}Co^{II}_{N/O}$(**GR**-CDH)$_3^{n+}$ homotrimer. The Co^{II} dissociation constant was determined for $Pb^{II}_{S}Co^{II}_{N/O}$(**GR**-CHD)$_3^{n+}$, using Equation 7, to be 350 ± 80 μM, which is the weakest binding of Co^{II} to a His_3 site by 10-fold (Figure 3-18, Table 3-3). EPR analysis of $Pb^{II}_{S}Co^{II}_{N/O}$(**GR**-CHD)$_3$ shows that the Co^{II} ion exhibits a comparable axial signal (Figure 3-19) as seen with the previous two homotrimers.

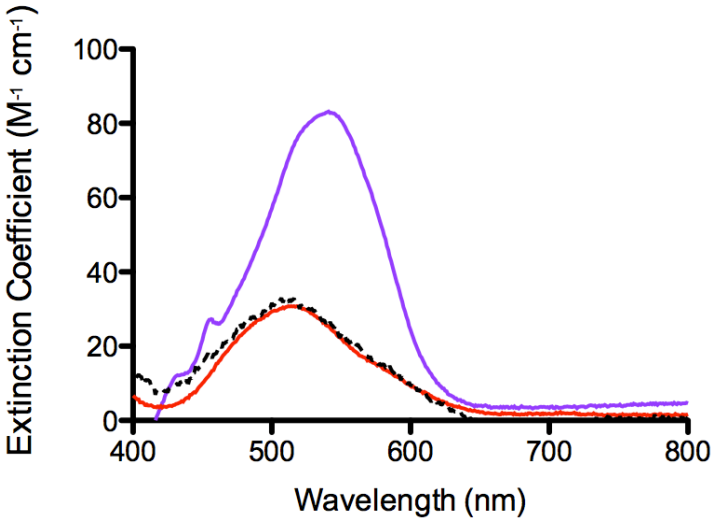

Figure 3-17. UV-Vis overlay of $Pb^{II}_{S}Co^{II}_{N/O}$(**GR**-CH)$_3^{n+}$ (red), and $Pb^{II}_{S}Co^{II}_{N/O}$(**GR**-CDH)$_3^{n+}$ (purple), and $Pb^{II}_{S}Co^{II}_{N/O}$(**GR**-CHD)$_3^{n+}$ (black dashed) at pH 7.5 in 50 mM HEPES buffer. Data are plotted as molar extinction coefficient (determined using Co^{II} concentration) versus wavelength.

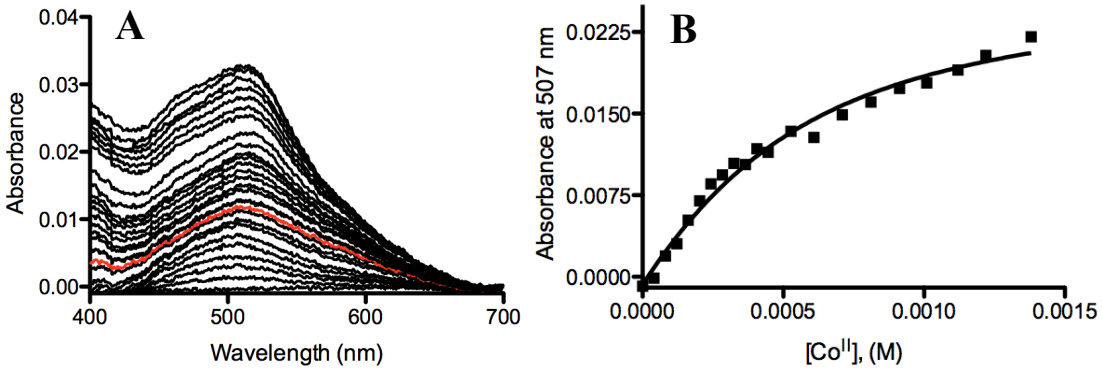

Figure 3-18. UV-Vis titration (A) and titration curve (B) of $Co^{II}SO_4$ added to a solution of 0.35 mM Pb^{II}_{S}(**GR**-CHD)$_3^-$ at pH 7.5 in 50 mM HEPES buffer. The titration data are plotted as absorbance versus wavelength and the titration curve is plotted as absorbance at 507 nm versus [Co^{II}]. The trace that correlates to one equivalent of [Co^{II}] added, with respect to 3SCC, is shown in red. The black circles represent the raw data and the non-linear best-fit curve is shown as a black line (Equation 7, as described in the Materials and Methods section).

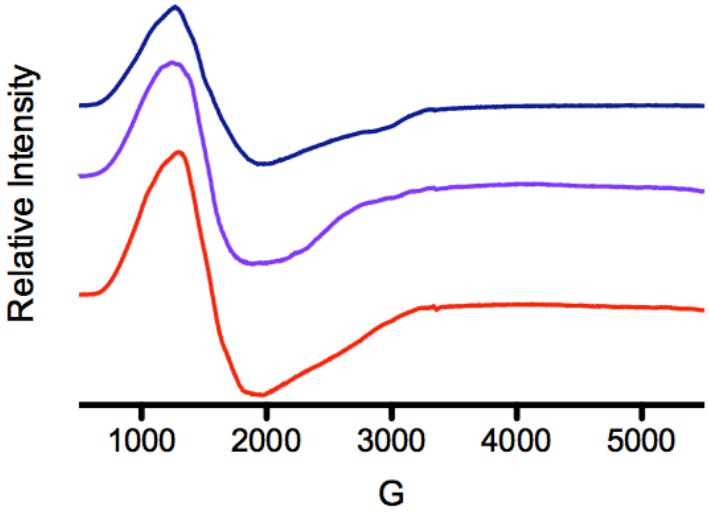

Figure 3-19. X-Band EPR spectra of 1.0 mM $Pb^{II}_{S}Co^{II}_{N/O}$(**GR**-ACH)$_3^{n+}$ (red), 1.0 mM $Pb^{II}_{S}Co^{II}_{N/O}$(**GR**-CDH)$_3^{n+}$ (purple), and 1.0 mM $Pb^{II}_{S}Co^{II}_{N/O}$(**GR**-CHD)$_3^{n+}$ (dark blue), at pH 7.5 in 30 mM HEPES, collected at 10 K.

Analysis of the XANES for $Pb^{II}_{S}Co^{II}_{N/O}$(**GR**-CHD)$_3^{n+}$ reveals a pre-edge/edge peak ratio of 2.0, which is consistent with both the $Pb^{II}_{S}Co^{II}_{N/O}$(**GR**-ACH)$_3^{+}$ and $Pb^{II}_{S}Co^{II}_{N/O}$(**GR**-CDH)$_3^{n+}$ homotrimers, and the pre-edge area falls between those of the homotrimers with a value of 6.6 (Figure 3-20, Table 3-4). The edge peak is slightly lower in intensity when compared to the $Pb^{II}_{S}Co^{II}_{N/O}$(**GR**-ACH)$_3^{+}$ and $Pb^{II}_{S}Co^{II}_{N/O}$(**GR**-CDH)$_3^{n+}$ homotrimers, perhaps indicating some mixture is obtained at the site with a lower coordination number (Figure 3-20). Due to the possible mixed coordination as evidenced by the XANES data, only a single-shell fit was conducted for $Pb^{II}_{S}Co^{II}_{N/O}$(**GR**-CHD)$_3^{n+}$ revealing an average Co^{II}-N/O distance of 2.08 Å (4.9 DW, F= 344, Table 3-5, Figure 3-21). This distance is 0.02 Å shorter than those determined for the first-shell fits of the $Pb^{II}_{S}Co^{II}_{N/O}$(**GR**-ACH)$_3^{+}$ and $Pb^{II}_{S}Co^{II}_{N/O}$(**GR**-CDH)$_3^{n+}$ homotrimers (Figure 3-21, Table 3-5).

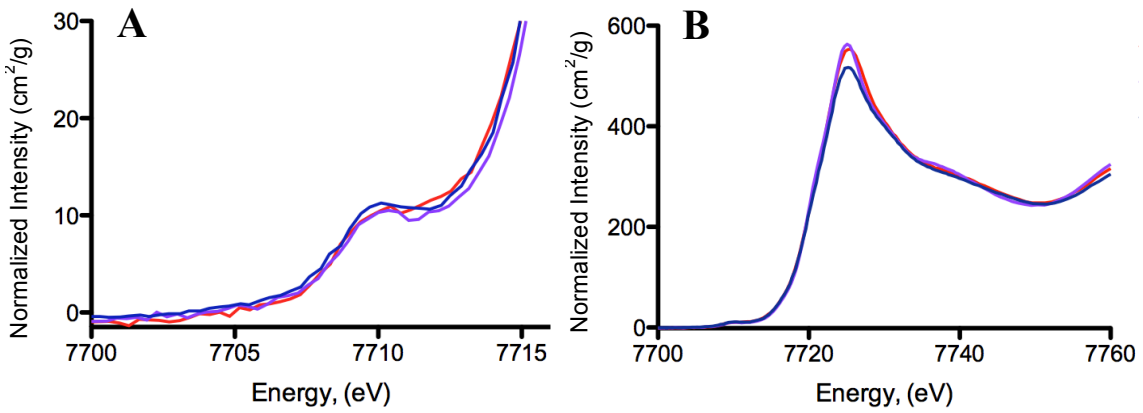

Figure 3-20. XANES spectra of the Co^{II} (A) pre-edge and (B) edge of homotrimers: 1.0 mM $Pb^{II}_{S}Co^{II}_{N/O}$(**GR**-ACH)$_3^{n+}$ (red), 1.0 mM $Pb^{II}_{S}Co^{II}_{N/O}$(**GR**-CDH)$_3^{n+}$ (purple), and 1.0 mM $Pb^{II}_{S}Co^{II}_{N/O}$(**GR**-CHD)$_3^{n+}$ (dark blue) at pH 7.5 in 50 mM HEPES buffer.

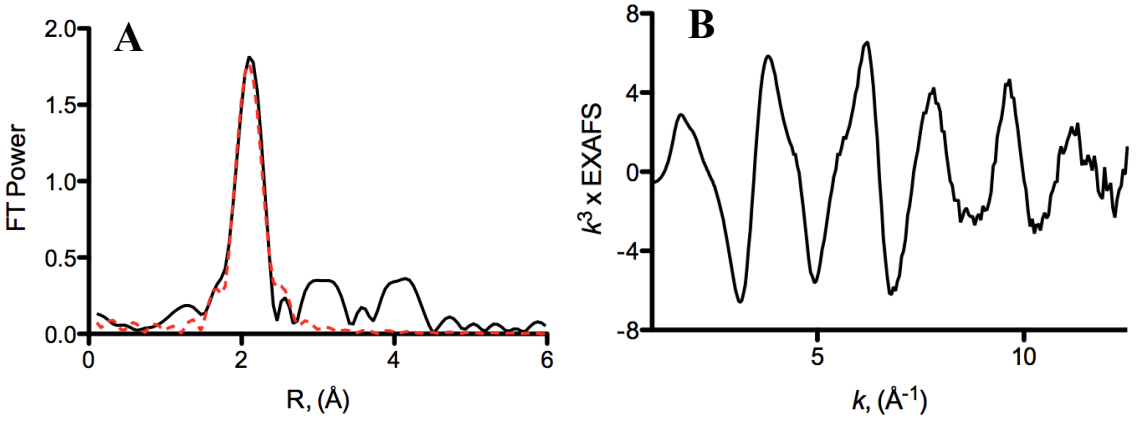

Figure 3-21. Fourier transform of Co^{II} EXAFS of (A) 1.0 mM $Pb^{II}_{S}Co^{II}_{N/O}$(**GR**-CHD)$_3^{n+}$ at pH 7.5 in 50 mM HEPES. Co^{II} EXAFS (B) 1.0 mM $Pb^{II}_{S}Co^{II}_{N/O}$(**GR**-CHD)$_3^{n+}$. Experimental data is shown in black and single shell fitting is shown for the Fourier transform as a dashed red line.

In combination, these data support a model that the spectroscopic signatures for the Asp_3 peptides above the His_3 site are not perturbed solely by the introduction of negative charge in close proximity to the metal binding site; however, the subtle spectral differences observed between the **GR**-CDH and **GR**-ACH homotrimers could arise from the Co^{II} interacting directly with the Asp ligands in the $Pb^{II}_{S}Co^{II}_{N/O}$(**GR**-CDH)$_3^{n+}$ homotrimer. Another possibility is that the three aspartic acid residues orient in a way that perturbs the hydrogen bonding of the Co^{II}-bound water molecules, I cannot yet distinguish between these possibilities spectroscopically. The UV-Vis spectrum of

$Pb^{II}_{S}Co^{II}_{N/O}$(**GR**-CHD)$_3^{n+}$ suggests similar coordination to $Pb^{II}_{S}Co^{II}_{N/O}$(**GR**-ACH)$_3^{+}$, but there are inconsistencies between the $Pb^{II}_{S}Co^{II}_{N/O}$(**GR**-CHD)$_3^{n+}$ and $Pb^{II}_{S}Co^{II}_{N/O}$(**GR**-ACH)$_3^{+}$ Co^{II} apparent dissociation constants (350 and 41 μM, respectively) and EXAFS average Co^{II}-N/O distances (2.08 and 2.10 Å, respectively, for single shell fits only, Table 3-5). It is possible that the Asp_3 residues below the His_3 site provide hydrogen-bonding interactions to bound-Co^{II} water molecules but are too far to directly coordinate to the metal ion, resulting in some perturbations to the Co^{II} site that are not completely consistent with either $Pb^{II}_{S}Co^{II}_{N/O}$(**GR**-ACH)$_3^{+}$ or $Pb^{II}_{S}Co^{II}_{N/O}$(**GR**-CDH)$_3^{n+}$ homotrimer.

Spectroscopic Characterization of Co^{II}-Bound Heterotrimers

While homotrimeric dual site peptides are interesting as they further demonstrate the ability to differentiate metal binding positions in proteins, the major innovation of these studies is to generate asymmetric metal environments within a simple, otherwise highly symmetric scaffold. To evaluate whether Pb^{II}-nucleated heterotrimer formation affords a remote metal binding site with first or second sphere asymmetric coordination geometry, I probed the binding of Co^{II} to Pb^{II}_{S}(**A$_{3-n}$B$_n$**) type heterotrimers, where n=1 and 2. When Co^{II} is added to a mixture of two equivalents of **GR**-ACH and one equivalent of **GR**-CDH in the presence of one equivalent of Pb^{II} one would expect to produce the hetereotrimeric Pb^{II}_{S}[(**GR**-ACH)$_2$(**GR**-CDH)$_1$]$^{n+}$ peptide. However, I can predict the spectral behavior if the two peptides instead form 2:1 mixtures of homotrimers. If I simply look at a calculated mixture of the two homotrimeric UV-Vis spectra, simulated by adding the two homotrimeric spectra together in the appropriate stoichiometry (Ala_2Leu_1 or Ala_1Leu_2), the prediction is that a peak at 523 nm (ε = 48 M^{-1} cm^{-1}, Figure 3-22, Table 3-2) would result for the Ala_1Leu_2 whereas the Ala_2Leu_1 mixture should result in a peak at 540 nm (ε = 83 M^{-1} cm^{-1}, Figure 3-22, Table 3-2).

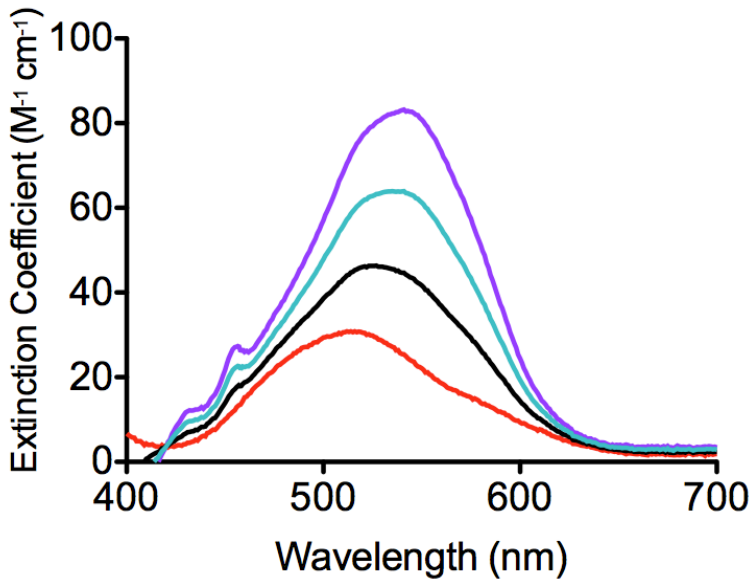

Figure 3-22. UV-Vis of $Pb^{II}_{S}Co^{II}_{N/O}$(**GR**-CH)$_3^{n+}$ (red) and $Pb^{II}_{S}Co^{II}_{N/O}$(**GR**-CDH)$_3^{n+}$ (purple) at pH 7.5 in 50 mM HEPES buffer overlaid with calculated spectra for ⅔[$Pb^{II}_{S}Co^{II}_{N/O}$(**GR**-CH)$_3^{n+}$] + ⅓[$Pb^{II}_{S}Co^{II}_{N/O}$(**GR**-CDH)$_3^{n+}$] (black) and ⅔[$Pb^{II}_{S}Co^{II}_{N/O}$(**GR**-CDH)$_3^{n+}$] + ⅓[$Pb^{II}_{S}Co^{II}_{N/O}$(**GR**-CH)$_3^{n+}$] (light blue). Experimental data (red and purple) and calculated spectra (black and light blue) are plotted as molar extinction coefficients (determined using Co^{II} concentration) versus wavelength.

Addition of $Co^{II}SO_4$ to solutions of Pb^{II}_{S}[(**GR**-ACH)$_2$(**GR**-CDH)$_1$]$^{n+}$ or Pb^{II}_{S}[(**GR**-ACH)$_1$(**GR**-CDH)$_2$]$^{n+}$, in and 50 mM HEPES at pH 7.5, resulted in a significantly different spectrum than the calculated spectrum mentioned above. Indeed, four peaks at 517 nm (ε = 147 M^{-1} cm^{-1}), 545 nm (ε = 155 M^{-1} cm^{-1}), 590 nm (ε = 124 M^{-1} cm^{-1}) and 628 nm (ε = 35 M^{-1} cm^{-1}) were observed for $Pb^{II}_{S}Co^{II}_{N/O}$[(**GR**-ACH)$_2$(**GR**-CDH)$_1$]$^{n+}$ (Figure 3-23, Table 3-5). Similarly, when Co^{II} was added to the opposite heterotrimeric mixture, Pb^{II}_{S}[(**GR**-ACH)$_1$(**GR**-CDH)$_2$]$^{n+}$, a similar spectrum was observed with three peaks at 517, 547, and 583 nm with slightly increased extinction coefficients of 152, 173 and 133 $M^{-1}cm^{-1}$, respectively (Figure 3-23, Table 3-5). The shoulder at 628 nm is not as prominent in the Pb^{II}_{S}[(**GR**-ACH)$_1$(**GR**-CDH)$_2$]$^{n+}$ sample. The increased extinction coefficients and increased number of features in both of these spectra indicate a decrease in symmetry due to the d-d Co^{II} transition becoming less forbidden, therefore, supporting a decrease in Co^{II} coordination number and/or a change in symmetry in comparison to the homotrimeric sites. Co^{II} dissociation constants were also determined by non-linear fits of the titration data to be 19.7 ± 1.9 and 7.9 ± 3.9 μM for Pb^{II}_{S}[(**GR**-ACH)$_2$(**GR**-CDH)$_1$]$^{n+}$

and $Pb^{II}_{S}[(\mathbf{GR}\text{-ACH})_1(\mathbf{GR}\text{-CDH})_2]^{n+}$, respectively (Figure 3-24, Table 3-3). These dissociation constants are 2-4-fold higher than the homotrimers, indicating slightly tighter binding of Co^{II} to a site that contains one or two Asp residues.

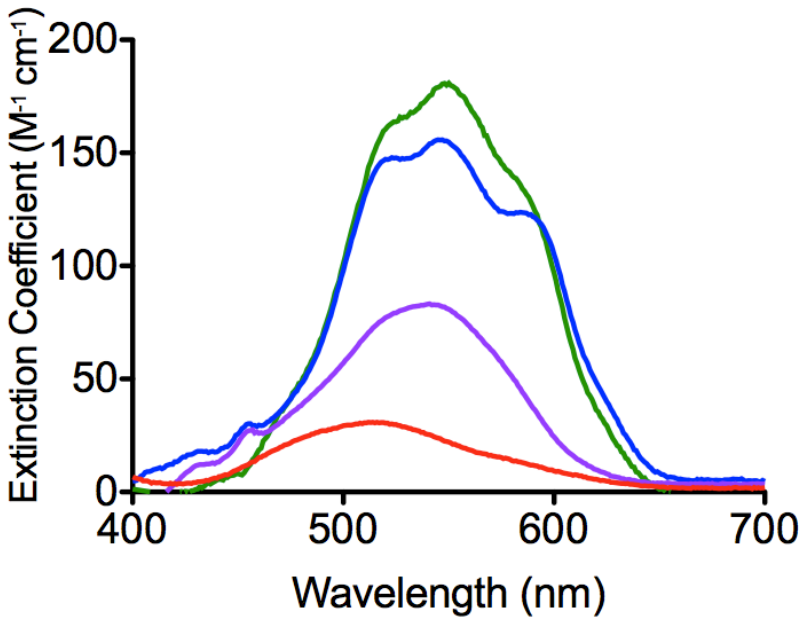

Figure 3-23. UV-Vis overlay of homotrimers $Pb^{II}_{S}Co^{II}_{N/O}(\mathbf{GR}\text{-CH})_3^{n+}$ (red) and $Pb^{II}_{S}Co^{II}_{N/O}(\mathbf{GR}\text{-CDH})_3^{n+}$ (purple) and heterotrimers: $Pb^{II}_{S}Co^{II}_{N/O}[(\mathbf{GR}\text{-ACH})_2(\mathbf{GR}\text{-CDH})_1]^{n+}$ (blue) and $Pb^{II}_{S}Co^{II}_{N/O}[(\mathbf{GR}\text{-ACH})_1(\mathbf{GR}\text{-CDH})_2]^{n+}$ (green) at pH 7.5 in 50 mM HEPES buffer. Data are plotted as molar extinction coefficients (determined using Co^{II} concentration) versus wavelength.

To address whether I was observing induced heterotrimeric selectivity due to Pb^{II} or simply just seeing a statistical distribution of the mixed peptides, I also analyzed Co^{II} binding to the heterotrimeric peptide mixtures in the absence of Pb^{II}. These mixtures, $[(\mathbf{GR}\text{-ACH})_2(\mathbf{GR}\text{-CDH})_1]^{n+}$ and $[(\mathbf{GR}\text{-ACH})_1(\mathbf{GR}\text{-CDH})_2]^{n+}$ showed similar spectra with peaks at 517 and 545 nm and a peak/shoulder at 590 nm (Figure 3-25A), with decreased extinction coefficients. When a statistical spectrum was calculated (where A = **GR**-ACH and B = **GR**-CDH), and the mixture contained $\mathbf{A}_3$ (8/27), $\mathbf{A}_2\mathbf{B}$ (12/27), $\mathbf{AB}_2$ (6/27) and $\mathbf{B}_3$ (1/27), (Figure 3-25B), the spectrum for the heterotrimer $[(\mathbf{GR}\text{-ACH})_2(\mathbf{GR}\text{-CDH})_1]^{n+}$ overlays very well with the experimental $Co^{II}_{N/O}[(\mathbf{GR}\text{-ACH})_2(\mathbf{GR}\text{-CDH})_1]^{n+}$ spectrum. This observation indicates that in the absence Pb^{II} the distribution of species is indeed statistical, but when Pb^{II} was present one sees metal-induced selectivity of a heterotrimeric species as evidenced by the multiple transitions, increase in extinction

coefficients and slight change in peak ratios. Therefore, in the absence of Pb^{II}, heterotrimer formation is observed as a statistical distribution that contains both heterotrimeric and both homotrimers species. This confirms that Pb^{II} is necessary for *singular and selective* formation of the heterotrimer peptides.

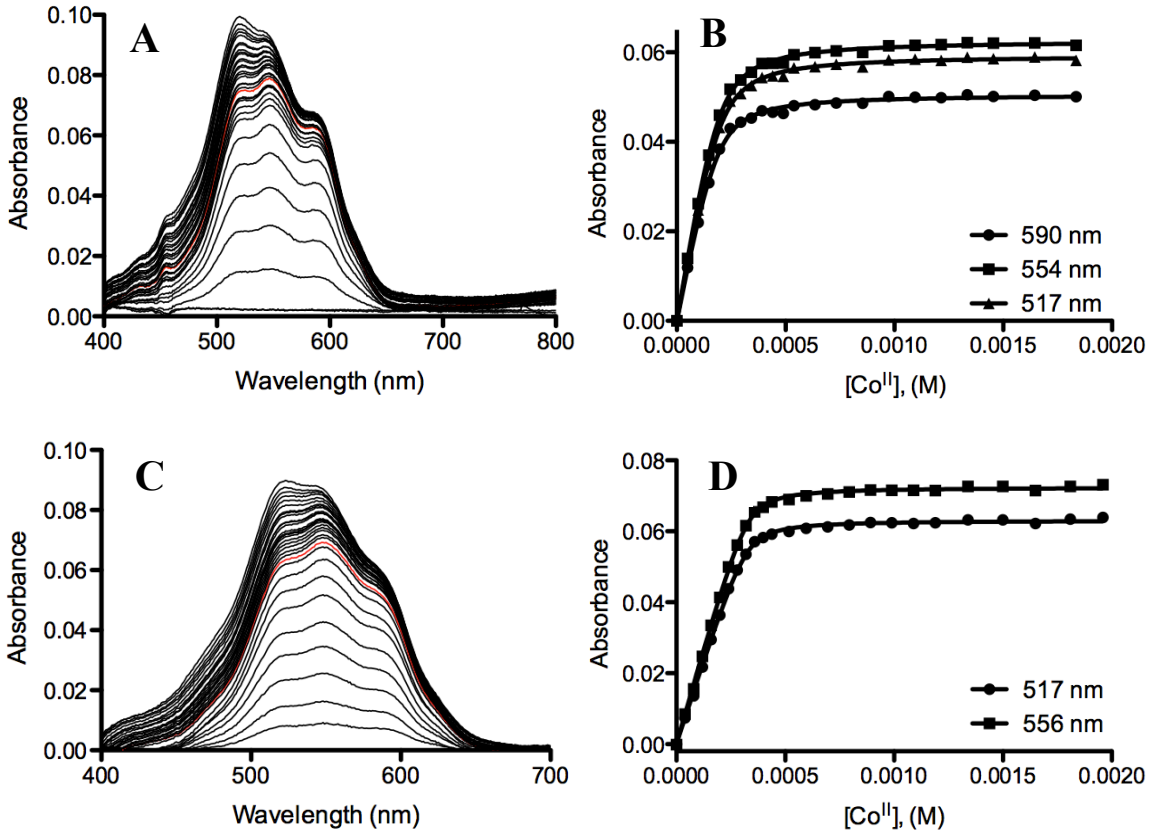

Figure 3-24. UV-Vis titration and titration curves of $Co^{II}SO_4$ added to a solution of 0.52 mM $Pb^{II}{}_SCo^{II}{}_{N/O}[(\mathbf{GR}\text{-ACH})_2(\mathbf{GR}\text{-CDH})_1]^{n+}$ (A and B) and 0.41 mM $Pb^{II}{}_SCo^{II}{}_{N/O}[(\mathbf{GR}\text{-ACH})_1(\mathbf{GR}\text{-CDH})_2]^{n+}$ (C and D) at pH 7.5 in 50 mM HEPES buffer. The titration data (A and C) are plotted as absorbance versus wavelength and the titration curves (B and D) are plotted as absorbance at λ_{max} versus $[Co^{II}]$. The trace that correlates to one equivalent of $[Co^{II}]$ added, with respect to 3SCC, is shown in red. The black circles represent the raw data and the non-linear best-fit curve is shown as a black line (Equation 7, as described in the Materials and Methods section).

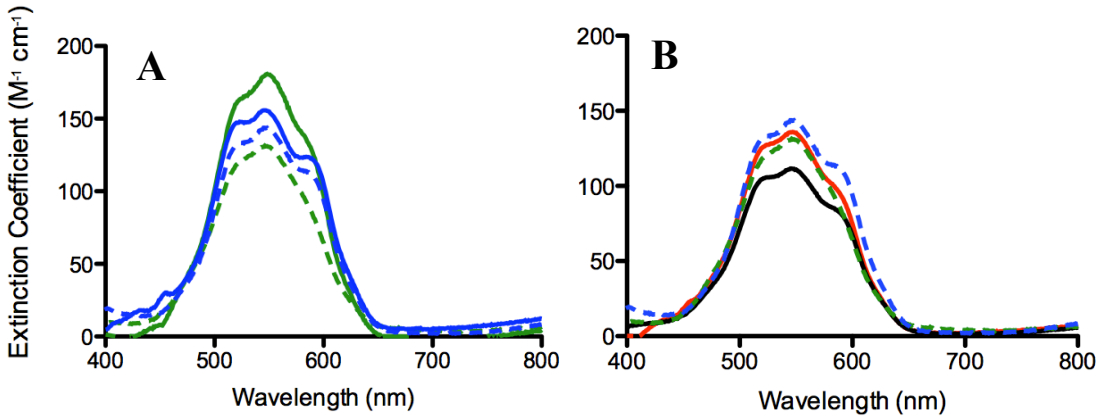

Figure 3-25. (A) UV-Vis overlay of Co^{II} binding to heterotrimers in the presence of Pb^{II}: $Pb^{II}_{S}Co^{II}_{N/O}[(\mathbf{GR}\text{-ACH})_2(\mathbf{GR}\text{-CDH})_1]^{n+}$ (blue) and $Pb^{II}_{S}Co^{II}_{N/O}[(\mathbf{GR}\text{-ACH})_1(\mathbf{GR}\text{-CDH})_2]^{n+}$ (green) and in the absence of Pb^{II}: $Co^{II}_{N/O}[(\mathbf{GR}\text{-ACH})_2(\mathbf{GR}\text{-CDH})_1]^{n+}$ (dashed blue) and $Co^{II}_{N/O}[(\mathbf{GR}\text{-ACH})_1(\mathbf{GR}\text{-CDH})_2]^{n+}$ (dashed green). (B) UV-Vis overlay of Co^{II} binding to heterotrimers in the absence of Pb^{II}: $Co^{II}_{N/O}[(\mathbf{GR}\text{-ACH})_2(\mathbf{GR}\text{-CDH})_1]^{n+}$ (dashed blue), and $Co^{II}_{N/O}[(\mathbf{GR}\text{-ACH})_1(\mathbf{GR}\text{-CDH})_2]^{n+}$ (dashed green), and the corresponding UV-Vis traces for calculated statistical mixture of $(\mathbf{GR}\text{-ACH})_2(\mathbf{GR}\text{-CDH})_1$ (black) and $(\mathbf{GR}\text{-ACH})_2(\mathbf{GR}\text{-CDH})_1$ (red) as determined from the experimental Co^{II} homo- and heterotrimers (See Chapter 2 for discussion of the statistical distribution). All experimental and calculated spectra are plotted as molar extinction coefficient (determined using Co^{II} concentration) versus wavelength.

I also looked at Co^{II}-binding to Asp_1 and Asp_2 heterotrimeric mixtures where the Asp residues are located below the His_3 binding site. In the presence of Pb^{II}, 2:1 and 1:2 mixtures of **GR**-ACH and **GR**-CHD would provide $Pb^{II}_{S}[(\mathbf{GR}\text{-ACH})_2(\mathbf{GR}\text{-CHD})_1]^{n+}$ and $Pb^{II}_{S}[(\mathbf{GR}\text{-ACH})_1(\mathbf{GR}\text{-CHD})_2]^{n+}$, respectively. Addition of Co^{II} to these mixtures (0.5 mM 3SCC each) resulted in traces that more closely resembled the Co^{II}-bound homotrimers than the Co^{II}-heterotrimers with the Asp residues above the His_3 layer. Co^{II} binding to $Pb^{II}_{S}[(\mathbf{GR}\text{-ACH})_2(\mathbf{GR}\text{-CHD})_1]^{n+}$ resulted in a peak at 515 nm with a shoulder at 590 nm (ε = 58 and 32 M^{-1} cm^{-1}, respectively, Figure 3-26, Table 3-2). The opposite heterotrimer, $Pb^{II}_{S}[(\mathbf{GR}\text{-ACH})_1(\mathbf{GR}\text{-CHD})_2]^{n+}$ produced a similar spectrum upon binding Co^{II} with a λ_{max} at 513 nm and a similar shoulder at 590 nm with slightly decreased extinction coefficients (ε = 47 and 18 M^{-1} cm^{-1}, respectively, Figure 3-26, Table 3-2). These extinction coefficient values are comparable to $Pb^{II}_{S}Co^{II}_{N/O}(\mathbf{GR}\text{-ACH})_3^{+}$ and $Pb^{II}_{S}Co^{II}_{N/O}(\mathbf{GR}\text{-CDH})_3^{n+}$, suggesting similarly high symmetry of the Co^{II} center and probable high coordination number.

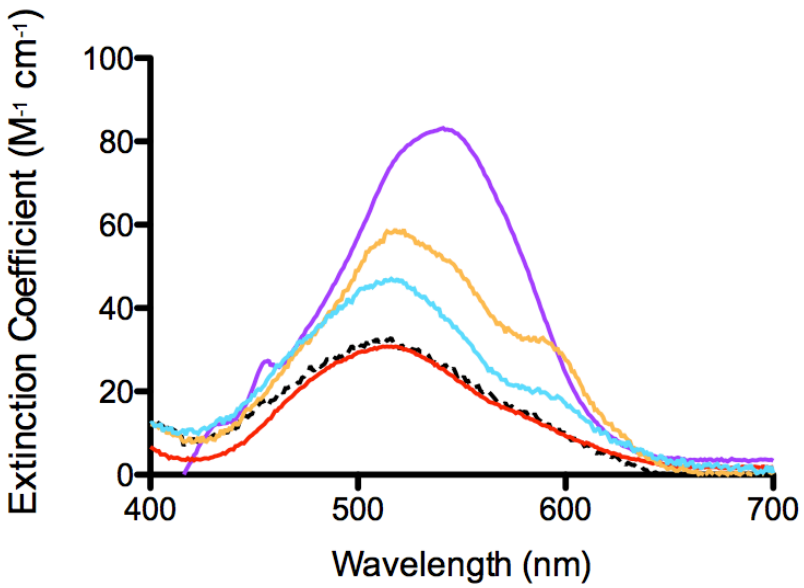

Figure 3-26. UV-Vis overlay of homotrimers $Pb^{II}_{S}Co^{II}_{N/O}$(**GR**-CH)$_3^{n+}$ (red), $Pb^{II}_{S}Co^{II}_{N/O}$(**GR**-CDH)$_3^{n+}$ (purple), and $Pb^{II}_{S}Co^{II}_{N/O}$(**GR**-CHD)$_3^{n+}$ (dashed black) and heterotrimers: $Pb^{II}_{S}Co^{II}_{N/O}$[(**GR**-ACH)$_2$(**GR**-CHD)$_1$]$^{n+}$ (orange) and $Pb^{II}_{S}Co^{II}_{N/O}$[(**GR**-ACH)$_1$(**GR**-CHD)$_2$]$^{n+}$ (blue). Data are plotted as molar extinction coefficient (determined using Co^{II} concentration) versus wavelength.

Co^{II} apparent dissociation constants were also determined by non-linear fits of the titration data to be 10.1 ± 5.6 and 17.5 ± 7.7 μM for $Pb^{II}_{S}Co^{II}_{N/O}$[(**GR**-ACH)$_2$(**GR**-CHD)$_1$]$^{n+}$ and $Pb^{II}_{S}Co^{II}_{N/O}$[(**GR**-ACH)$_1$(**GR**-CHD)$_2$]$^{n+}$, respectively (Equation 7, Figures 3-27A, Table 3-3). The apparent dissociation constants for these two heterotrimeric mixtures, with one or two aspartic acid residues below the His_3 site, are 10-fold tighter than the $Pb^{II}_{S}Co^{II}_{N/O}$(**GR**-CHD)$_3^{n+}$ homotrimer and are comparable to the original heterotrimers: Pb^{II}_{S}[(**GR**-ACH)$_2$(**GR**-CDH)$_1$]$^{n+}$ and Pb^{II}_{S}[(**GR**-ACH)$_1$(**GR**-CDH)$_2$]$^{n+}$. This could be due to Asp residues introduced asymmetrically below the His_3 site preferring rotamers that can interact with the Co^{II} site differently in comparison to when the Asp residues are introduced symmetrically where three negatively charged residues in close proximity to the Co^{II} site may be less favorable. However, I do not expect direct coordination to the Co^{II} ion due to the dissimilarities between the Pb^{II}_{S}[(**GR**-ACH)$_{3-n}$(**GR**-CDH)$_n$]$^{n+}$ and Pb^{II}_{S}[(**GR**-ACH)$_{3-n}$(**GR**-CHD)$_n$]$^{n+}$ heterotrimers. In all, the sites produced by the heterotrimers where the Asp residue is included in the layer below the His_3 site provided significantly smaller perturbations to the UV-Vis spectra in comparison to the heterotrimers that contain the Asp substitution in the layer above the His_3 site. The

coordination geometry of Co^{II}, when bound to $Pb^{II}_S[(\mathbf{GR}\text{-ACH})_2(\mathbf{GR}\text{-CHD})_1]^{n+}$ and $Pb^{II}_S[(\mathbf{GR}\text{-ACH})_1(\mathbf{GR}\text{-CHD})_2]^{n+}$, is probably relatively symmetric, as evidenced by the relatively low extinction coefficients.

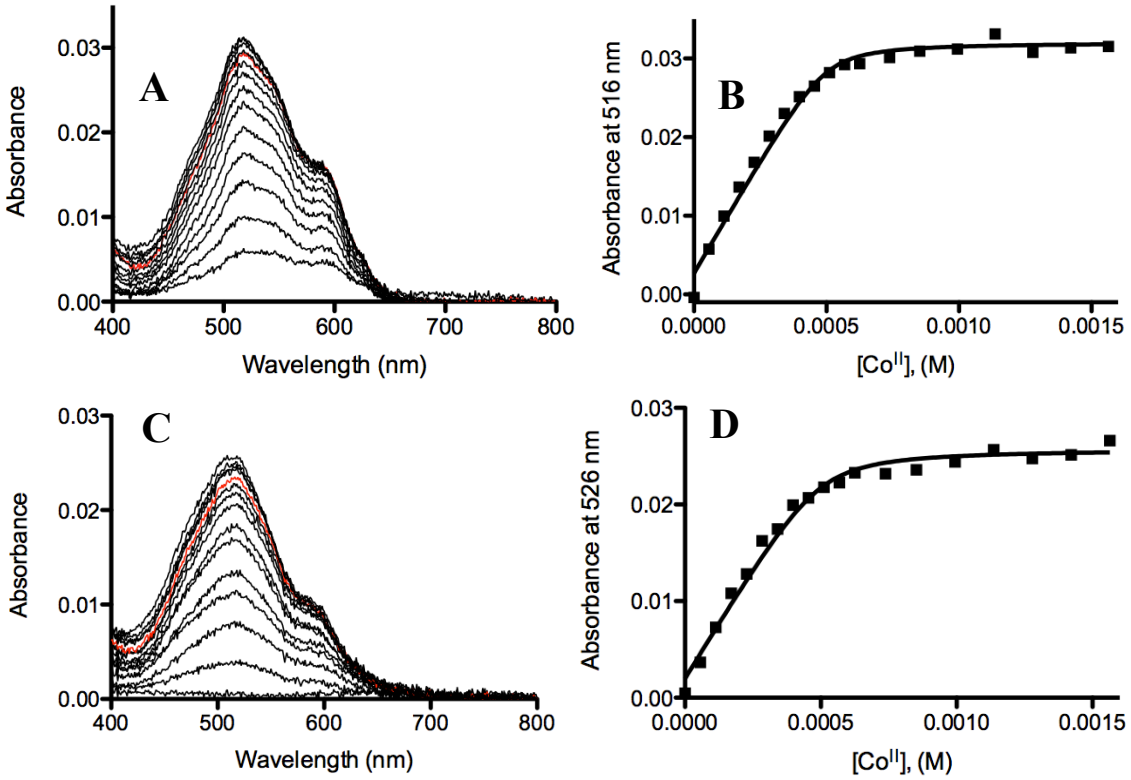

Figure 3-27. UV-Vis titration and titration curves of $Co^{II}SO_4$ added to a solution of 0.5 mM $Pb^{II}_S Co^{II}_{N/O}[(\mathbf{GR}\text{-ACH})_2(\mathbf{GR}\text{-CHD})_1]^{n+}$ (A and B) and 0.5 mM $Pb^{II}_S Co^{II}_{N/O}[(\mathbf{GR}\text{-ACH})_1(\mathbf{GR}\text{-CHD})_2]^{n+}$ (C and D) at pH 7.5 in 50 mM HEPES buffer. The titration data (A and C) are plotted as absorbance versus wavelength and the titration curves (B and D) are plotted as absorbance at λ_{max} versus $[Co^{II}]$. The trace that correlates to one equivalent of $[Co^{II}]$ added, with respect to 3SCC, is shown in red. The black circles represent the raw data and the non-linear best-fit curve is shown as a black line (Equation 7, as described in the Materials and Methods section).

XAS was used to analyze Co^{II} bound heterotrimers. Analysis of the XANES at both the pre-edge and edge show that the when only one Asp residue is introduced into the system, as in $Pb^{II}_S Co^{II}_{N/O}[(\mathbf{GR}\text{-ACH})_2(\mathbf{GR}\text{-CDH})_1]^{n+}$, the trace looks very similar to the homotrimeric peptides (Figure 3-28). Indeed the pre-edge/edge ratio is 2.0 and the area under the pre-edge peak is 6.0 (Table 3-4). However, when analyzing the opposite heterotrimer, $Pb^{II}_S Co^{II}_{N/O}[(\mathbf{GR}\text{-ACH})_1(\mathbf{GR}\text{-CDH})_2]^{n+}$, with two Asp residues in close proximity to the His_3 site, the pre-edge peak is more intense and the edge peak is less

intense (ratio of 2.8, Table 3-4) and the pre-edge peak area is elevated to 9.4 (Table 3-4) – evidence which all supports the symmetry around the Co^{II} site being lessened, which in turn supports a lower coordination environment in comparison to the homotrimeric samples.

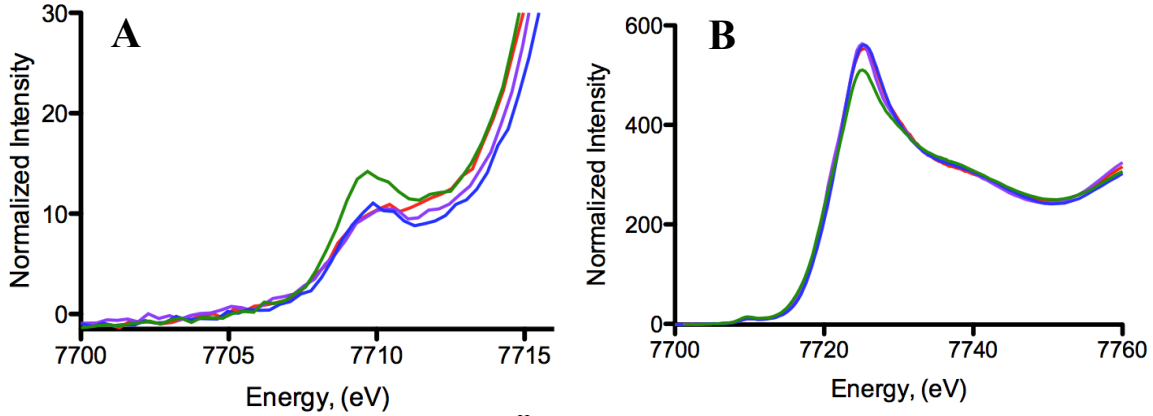

Figure 3-28. XANES spectra of the Co^{II} (A) pre-edge and (B) edge of homotrimers: 1.0 mM $Pb^{II}{}_{S}Co^{II}{}_{N/O}$(**GR**-ACH)$_3{}^{n+}$ (red) and 1.0 mM $Pb^{II}{}_{S}Co^{II}{}_{N/O}$(**GR**-CDH)$_3{}^{n+}$ (purple) and heterotrimers: 1.0 mM $Pb^{II}{}_{S}Co^{II}{}_{N/O}$[(**GR**-ACH)$_2$(**GR**-CDH)$_1$]$^{n+}$ (blue) and 1.0 mM $Pb^{II}{}_{S}Co^{II}{}_{N/O}$[(**GR**-ACH)$_1$(**GR**-CDH)$_2$]$^{n+}$ (green) at pH 7.5 in 50 mM HEPES buffer.

As was the case with the homotrimers, the EXAFS data show a similar dominate peak in both $Pb^{II}{}_{S}Co^{II}{}_{N/O}$[(**GR**-ACH)$_1$(**GR**-CDH)$_2$]$^{n+}$ and $Pb^{II}{}_{S}Co^{II}{}_{N/O}$[(**GR**-ACH)$_2$(**GR**-CDH)$_1$]$^{n+}$ at ~2.07 Å. Both samples show evidence of outer shell histidine scattering patterns (Figure 3-29, 2.5 < R < 4 Å). Multiple models with varying numbers of imidazole nitrogen atoms and other oxygen ligands (water or carboxylate) were used to fit these data, but the best fit was determined to be five oxygen/nitrogen ligands with an average Co^{II}-N/O distance of 2.08 Å (1.3 & 9.3 DW, F=573, Table 3-5) for $Pb^{II}{}_{S}Co^{II}{}_{N/O}$[(**GR**-ACH)$_2$(**GR**-CDH)$_1$]$^{n+}$ and a slightly shorter distance of 2.075 Å for $Pb^{II}{}_{S}Co^{II}{}_{N/O}$[(**GR**-ACH)$_1$(**GR**-CDH)$_2$]$^{n+}$ (5.0 & 9.0 DW, F=248, Table 3-5). Contrary to both $Pb^{II}{}_{S}Co^{II}{}_{N/O}$(**GR**-ACH)$_3{}^{+}$ and $Pb^{II}{}_{S}Co^{II}{}_{N/O}$(**GR**-CDH)$_3{}^{n+}$ homotrimers, the best distances obtained via fitting of the heterotrimer EXAFS data are consistent with a 5-coordinate Co^{II}-coordination. The XANES trace of the $Pb^{II}{}_{S}Co^{II}{}_{N/O}$[(**GR**-ACH)$_2$(**GR**-CDH)$_1$]$^{n+}$, where one Asp is included in the Co^{II} binding site, looks very similar to the proposed 6-coordinate homotrimers, but it has EXAFS best fit distances that are shorter and more comparable to those of the $Pb^{II}{}_{S}Co^{II}{}_{N/O}$[(**GR**-ACH)$_1$(**GR**-CDH)$_2$]$^{n+}$ heterotrimer. The decrease observed in bond distances from 2.115 Å to ~2.08 Å is consistent with a

one integer decrease in coordination number from the homotrimer (proposed 6-coordinate) to heterotrimer peptides, resulting in probable 5-coordinate environments.

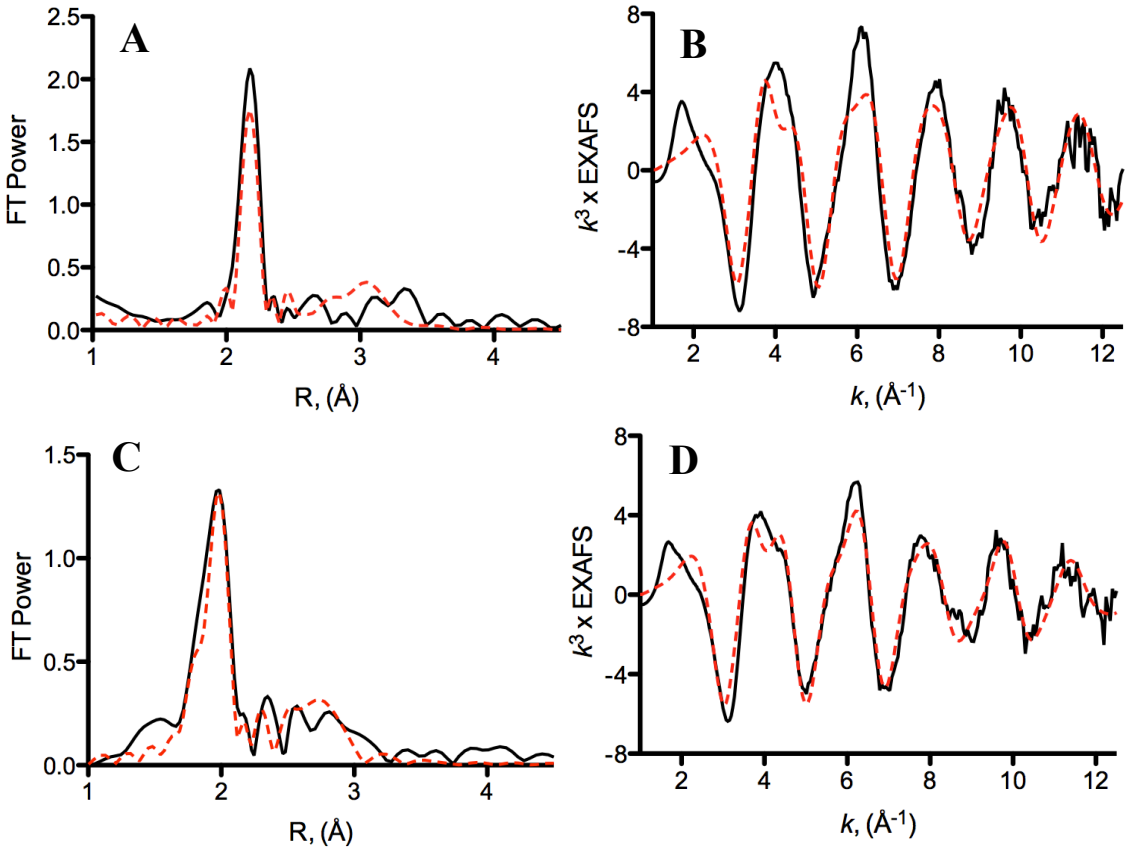

Figure 3-29. Fourier transform of Co^{II} EXAFS of (A) $Pb^{II}{}_{S}Co^{II}{}_{N/O}[(\mathbf{GR}\text{-ACH})_2(\mathbf{GR}\text{-CDH})_1]^{n+}$ and (C) $Pb^{II}{}_{S}Co^{II}{}_{N/O}[(\mathbf{GR}\text{-ACH})_1(\mathbf{GR}\text{-CDH})_2]^{n+}$ at pH 7.5 in 50 mM HEPES buffer. Co^{II} EXAFS (B) 1.0 mM $Pb^{II}{}_{S}Co^{II}{}_{N/O}[(\mathbf{GR}\text{-ACH})_2(\mathbf{GR}\text{-CDH})_1]^{n+}$ and (D) 1.0 mM $Pb^{II}{}_{S}Co^{II}{}_{N/O}[(\mathbf{GR}\text{-ACH})_1(\mathbf{GR}\text{-CDH})_2]^{n+}$. Experimental data is shown in black and best fits for N_3O_2 Co^{II}-coordination are shown in dashed red lines.

The combination of XANES and EXAFS data suggests that the $Pb^{II}{}_{S}Co^{II}{}_{N/O}[(\mathbf{GR}\text{-ACH})_2(\mathbf{GR}\text{-CDH})_1]^{n+}$ heterotrimer is probably a mixture of mostly 5- and some 6-coordinate Co^{II} species and the $Pb^{II}{}_{S}Co^{II}{}_{N/O}[(\mathbf{GR}\text{-ACH})_2(\mathbf{GR}\text{-CDH})_1]^{n+}$ heterotrimer is a more pure 5-coordinate Co^{II} species. The best derived distances from the EXAFS fits correspond well with reported values for five-coordinate Co^{II} small molecule complexes, as reported by the Cambridge Structural Database (4-coordinate ≈ 1.996 Å, 5-coordinate ≈ 2.065 Å, 6-coordinate ≈ 2.13 Å).[36] The increased bond distances and overall lower pre-edge:edge ratio of the homotrimers, in comparison to the heterotrimers, further supports higher coordination of Co^{II}-bound homotrimeric peptides.

Furthermore, Co^{II} X-band EPR spectra collected at 4K of the heterotrimer systems show very similar spectra to each other, which vary dramatically in comparison to the homotrimer systems. Heterotrimeric EPR samples were prepared identically to homotrimeric samples at 2 mM total peptide trimer with 1 mM Co^{II} in ~50 mM HEPES, pH 7.5, with ~50% glycerol. The EPR of both $Pb^{II}_{S}Co^{II}_{N/O}[(\mathbf{GR}\text{-ACH})_1(\mathbf{GR}\text{-CDH})_2]^{n+}$and $Pb^{II}_{S}Co^{II}_{N/O}[(\mathbf{GR}\text{-ACH})_2(\mathbf{GR}\text{-CDH})_1]^{n+}$ produce spectra with slightly more rhombic characteristics with turning points at $g_{eff(x,y,z)}$ = 5.3, 3.4 and 2.0 (Figure 3-30). Simulations of the $Pb^{II}_{S}Co^{II}_{N/O}[(\mathbf{GR}\text{-ACH})_2(\mathbf{GR}\text{-CDH})_1]^{n+}$heterotrimer were obtained using SpinCount (Figure 3-31).[13] The discrepancies between the data of $Pb^{II}_{S}Co^{II}_{N/O}[(\mathbf{GR}\text{-ACH})_2(\mathbf{GR}\text{-CDH})_1]^{n+}$and the EPR simulation could be due to a mixture of Co^{II} environments present in the sample, as supported by the XAS data. Regardless, the heterotrimers are more rhombic in character than the axial homotrimeric signals.

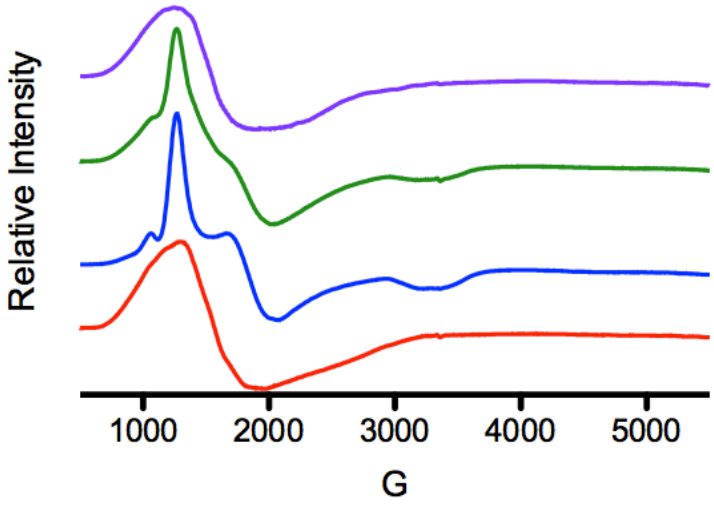

Figure 3-30. X-Band EPR spectra of homotrimers: 1.0 mM $Pb^{II}_{S}Co^{II}_{N/O}(\mathbf{GR}\text{-ACH})_3^{n+}$ (red) and 1.0 mM $Pb^{II}_{S}Co^{II}_{N/O}(\mathbf{GR}\text{-CDH})_3^{n+}$ (purple) and heterotrimers: 1.0 mM $Pb^{II}_{S}Co^{II}_{N/O}[(\mathbf{GR}\text{-ACH})_2(\mathbf{GR}\text{-CDH})_1]^{n+}$ (blue) and 1.0 mM $Pb^{II}_{S}Co^{II}_{N/O}[(\mathbf{GR}\text{-ACH})_1(\mathbf{GR}\text{-CDH})_2]^{n+}$ (green) at pH 7.5 in 30 mM HEPES buffer, collected at 10 K.

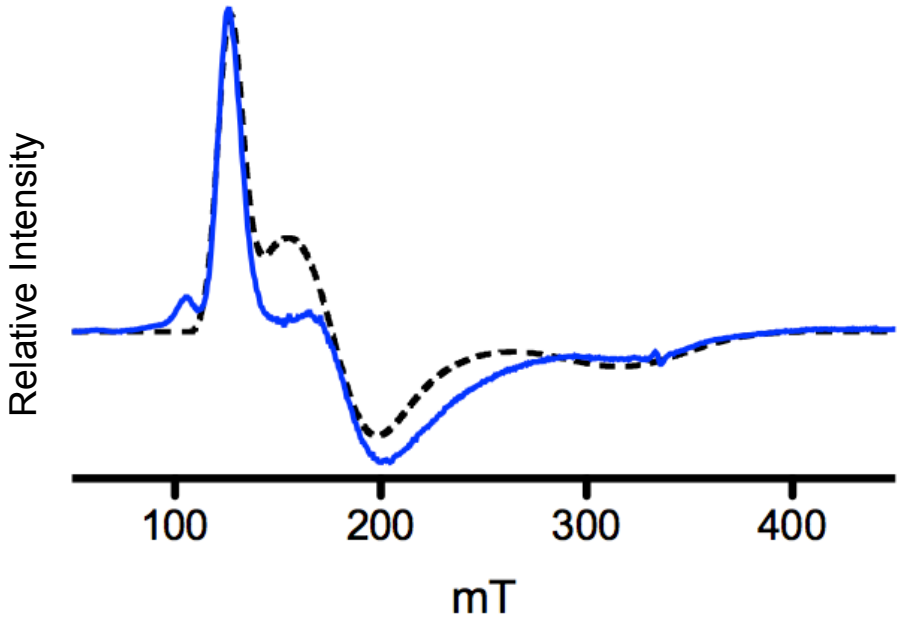

Figure 3-31. X-Band EPR spectra of 1.0 mM $Pb^{II}_{S}Co^{II}_{N/O}[(\mathbf{GR}\text{-ACH})_2(\mathbf{GR}\text{-CDH})_1]^{n+}$ at pH 7.5 in 30 mM HEPES buffer, collected at 4 K. Blue spectrum: data, black dashed line: simulation.

The MCD spectra of $Pb^{II}_{S}Co^{II}_{N/O}[(\mathbf{GR}\text{-ACH})_1(\mathbf{GR}\text{-CDH})_2]^{n+}$ and $Pb^{II}_{S}Co^{II}_{N/O}[(\mathbf{GR}\text{-ACH})_2(\mathbf{GR}\text{-CDH})_1]^{n+}$ provide similar traces to on another with multiple intense negative bands (542, 553, and 570 nm for $Pb^{II}_{S}Co^{II}_{N/O}[(\mathbf{GR}\text{-ACH})_1(\mathbf{GR}\text{-CDH})_2]^{n+}$and 539 and 577 nm for $Pb^{II}_{S}Co^{II}_{N/O}[(\mathbf{GR}\text{-ACH})_2(\mathbf{GR}\text{-CDH})_1]^{n+}$, Figures 3-32A and 3-32B, respectively). As mentioned above, multiple negative bands observed in the MCD spectra are consistent with less symmetric, 5-coordinate Co^{II} environments. A decrease in symmetry from a d^7 O_h symmetry (ground state: $^4T_{1g}$) to a pentacoordinate Co^{II} species would result in a new ground state of either $^4E'_g$ or $^4A_2$ for D_{3h} or C_{4v} symmetry, respectively. The difference in the singly or doubly degenerate ground state would show different MCD terms; however, without explicit assignments of the observed transitions I cannot yet assign the coordination geometry of the proposed 5-coordiante heterotrimeric species.

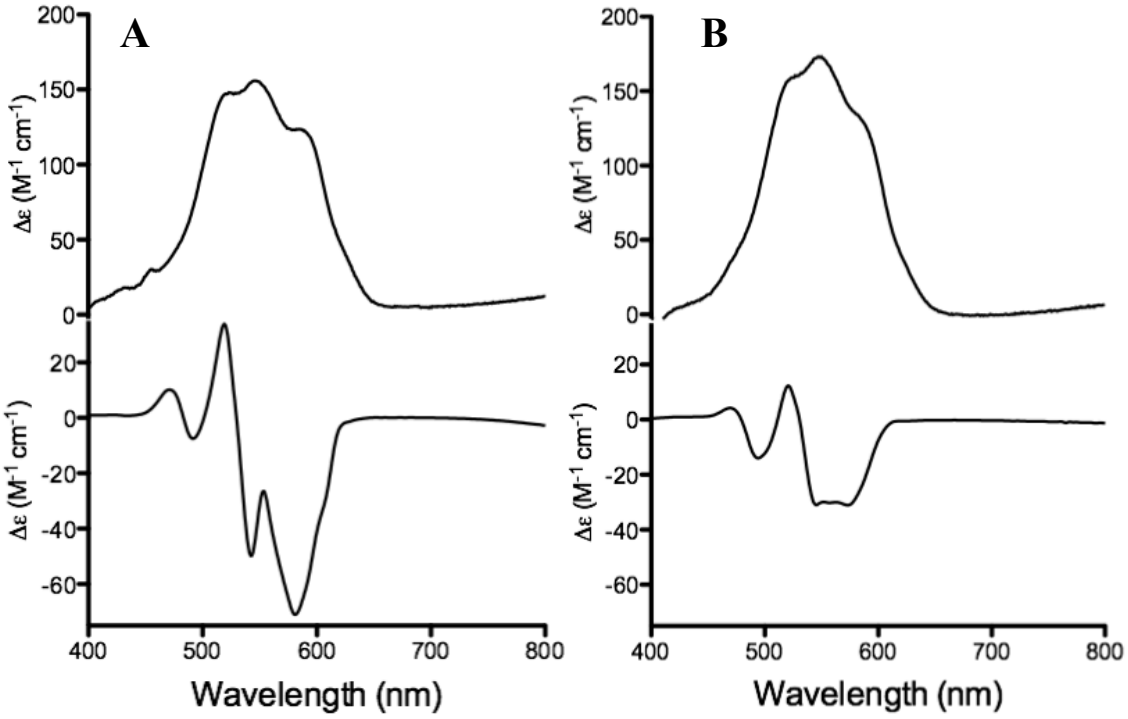

Figure 3-32. Absorbance (top) and MCD (bottom) spectra of ~2.0 mM $Pb^{II}_{S}Co^{II}_{N/O}[(\mathbf{GR}\text{-ACH})_2(\mathbf{GR}\text{-CDH})_1]^{n+}$ (A) and $Pb^{II}_{S}Co^{II}_{N/O}[(\mathbf{GR}\text{-ACH})_1(\mathbf{GR}\text{-CDH})_2]^{n+}$ (B) at pH 7.5 in 50 mM HEPES, collected at RT (Absorbance) and 2K (MCD).

In all, these MCD data are in agreement with the EPR and XAS data, further confirming lower symmetry and lower coordination number in the Co^{II}-bound heterotrimers compared to the Co^{II}-homotrimers. The MCD data of both homotrimers and both heterotrimers are relatively simple, and, especially in the case of the homotrimers (Figure 3-14A and 3-14B), therefore support that only one species is present in the samples. Unfortunately, the literature on biological samples with Co^{II} bound is quite muddled and not nearly as plentiful as one might expect considering the frequency of how often Co^{II} is used as a probe for Zn^{II}-metalloenzymes. Further studies to determine the coordination geometry is necessary to further elucidate the identities of the specific transitions observed.

Clearly, no combination of the spectra of the homotrimers, as obtained via UV-Vis, EPR, MCD, or XAS can reproduce the spectra of the heterotrimeric Co^{II} complexes. This strongly suggests that the asymmetry of the heterotrimer, induced by the Pb^{II} binding, can be extended to a second, asymmetric transition metal binding site as

confirmed by the perturbed physical properties observed upon Co^{II} binding. ^{207}Pb NMR analysis of the homotrimers, $Pb^{II}_{S}Co^{II}_{N/O}$(**GR**-ACH)$_3^{+}$ and $Pb^{II}_{S}Co^{II}_{N/O}$(**GR**-CDH)$_3^{n+}$, and the heterotrimers, $Pb^{II}_{S}Co^{II}_{N/O}$[(**GR**-ACH)$_2$(**GR**-CDH)$_1$]$^{n+}$ and $Pb^{II}_{S}Co^{II}_{N/O}$[(**GR**-ACH)$_1$(**GR**-CDH)$_2$]$^{n+}$, afforded no change in the chemical shifts (Figure 3-33), further confirming that the addition of Co^{II} does not alter the $Pb^{II}Cys_3$ environment of these species.

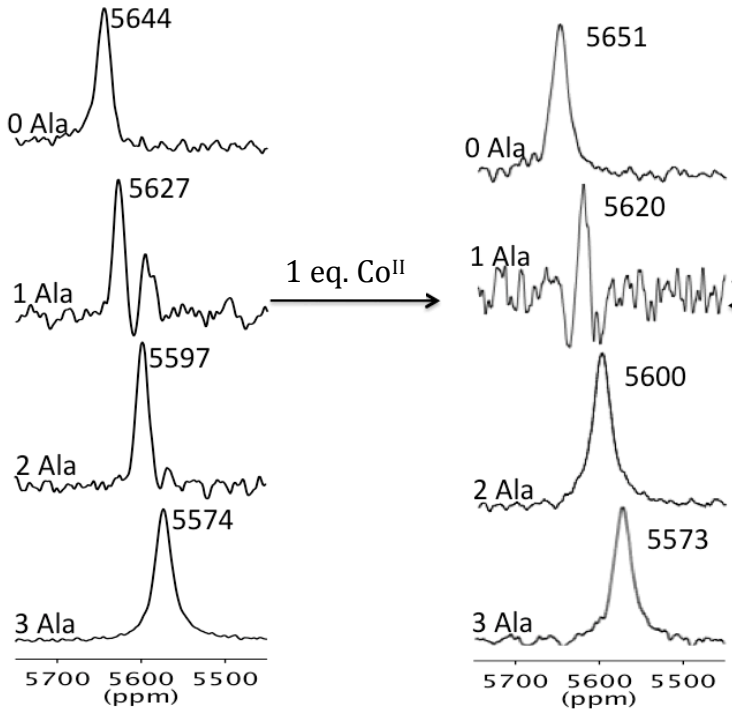

Figure 3-33. ^{207}Pb NMR spectra of 3-5 mM Pb^{II} bound homo- and heterotrimers in the absence (left) and presence (right) of Co^{II}. 0 Ala: $Pb^{II}_{S}M^{II}_{N/O}$(**GR**-CDH)$_3^{n+}$, 1 Ala: $Pb^{II}_{S}M^{II}_{N/O}$[(**GR**-CDH)$_2$(**GR**-ACH)$_1$]$^{n+}$, 2 Ala: $Pb^{II}_{S}M^{II}_{N/O}$[(**GR**-CDH)$_1$(**GR**-ACH)$_2$]$^{n+}$, 3 Ala: $Pb^{II}_{S}N^{II}_{N/O}$(**GR**-ACH)$_3^{n+}$, collected at pH 8.5.

To summarize the coordination preferences of the homo- and heterotrimers, EXAFS analysis supports average Co^{II}-N/O bond distances consistent with 6-coordinate metal binding sites for the homotrimers, mostly 5-coordinate for $Pb^{II}_{S}Co^{II}_{N/O}$[(**GR**-ACH)$_1$(**GR**-CDH)$_2$] and a probable mixed 5/6-coordinate Co^{II} site in $Pb^{II}_{S}Co^{II}_{N/O}$[(**GR**-ACH)$_2$(**GR**-CDH)$_1$]. Concurrently, the EPR and UV-Vis data show similarities among the heterotrimers and similarities among the homotrimers, but there is a stark difference between the traces from the symmetric and asymmetric scaffolds.

Small molecules with similar coordinating ligands have been previously synthesized and characterized with bound Co^{II}. Scarpellini *et al.* prepared a family of compounds that contain a tris-amine scaffold that contains one carboxylate oxygen moiety.[39] The [Co^{II}(BPZG)(OAc)] complex was found to have five ligands with a first coordination sphere consisting of two substituted pyrazole ligands, a tripodal nitrogen, a solvent molecule and a monodentate coordinating carboxylate group (Figure 3-34). This five-coordinate complex afforded a very similar visible spectrum to the [$Pb^{II}_{S}Co^{II}_{N/O}$(**GR**-ACH)$_2$(**GR**-CDH)$_1$]$^{n+}$ heterotrimer with four peaks at 504, 546, 593, and 615 nm with extinction coefficients of 133, ~150, 255, and ~100 $M^{-1}cm^{-1}$, respectively (Table 3-2). Additionally, reports by Jacobsen *et al.* and Kunz *et al.* using pyrazolyl and substituted imidazole, respectively, show spectra related to this heterotrimer complex with energy and extinction coefficients consistent with a five-coordinate environment (Figure 3-34, Table 3-2).[40,41]

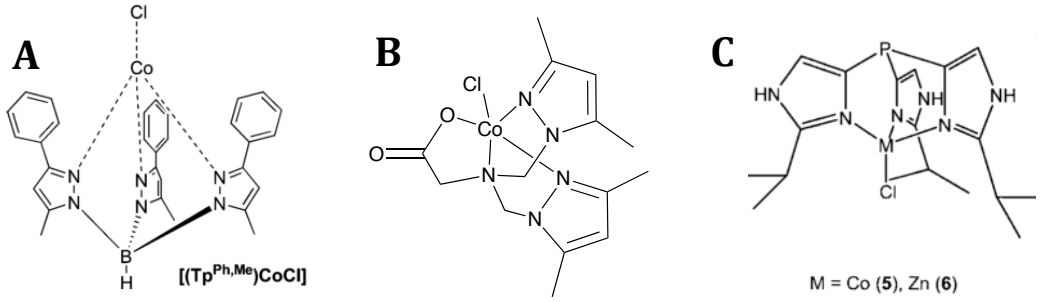

Figure 3-34. Schematic representations of (A) [(4-TI^{PhMe})Co^{II}Cl]Cl, (B) [Co^{II}(BPZG)(OAc)], and (C) [(4-TI^{PiPr})Co^{II}Cl]Cl. Figure adapted from Ref 69, 70, and 71.

Initially, the aspartate residues introduced at the 26th position was engineered with the intention of providing an acid-base catalyst in close proximity to the His_3 site. However, due to the significant perturbations in spectral fingerprints between the Co^{II}-bound homo- and heterotrimers we were forced to consider the possibility of direct oxygen coordination to the Co^{II} when aspartate residues are present in an asymmetric fashion. The binding sites of Carboxypeptidase A (CPA), a Zn^{II}-metalloenzyme that catalyzes endopeptidase and C-terminal exoesterase reactions, and thermolysin (TML), a Zn^{II}-metalloproteinase, offer similar metal-binding environments with $His_2Carboxylate_X(OH_2)_Y$ motifs (the number of coordinating oxygen atoms from the carboxylate moiety (X) and waters molecules (Y) is dependent on the study referenced,

Figure 3-35).[42–44] Indeed, the Co^{II} UV-Vis traces of both CPA and TML look strikingly similar to our Co^{II}-bound heterotrimers with similar energies and extinction coefficients (Table 3-2).[28,45] The EPR of Co^{II}-substituted CPA shows a similarly rhombic signal to the reported heterotrimers with g-$values_{eff}$ of 5.40, 2.84 and 1.90.[46]

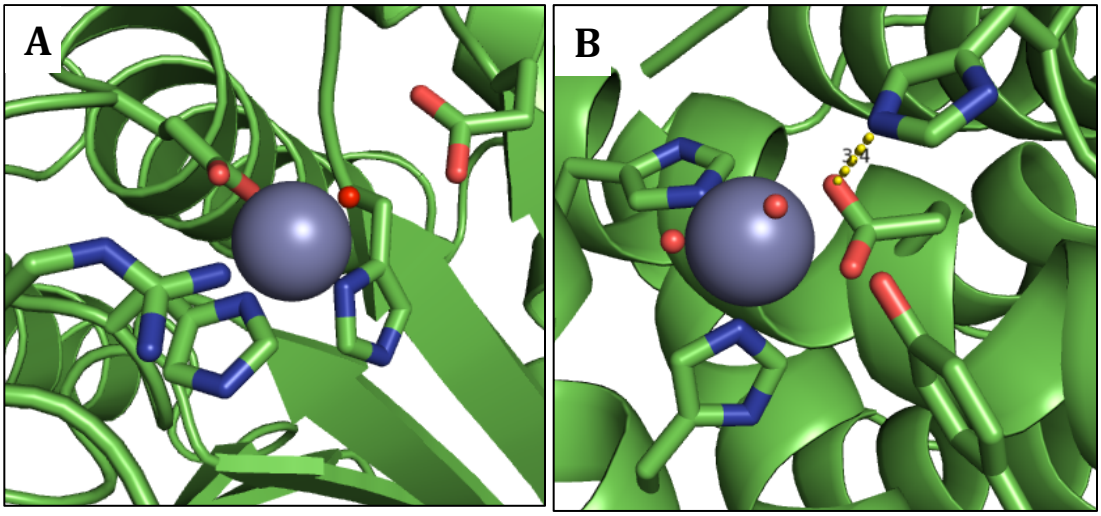

Figure 3-35. Coordination spheres of A) carboxypeptidase A (CPA, PDB: 1YME)[43] and B) thermolysin (TML, PDB: 1LNF).[42] Zn^{II} ions are shown as grey spheres. Selected amino acids of active site ligands are shown as stick figures where N atoms are highlighted in blue and oxygen in red. Water molecules are shown as smaller red spheres and hydrogen bonds are shown as dashed yellow lines.

VanX, an essential gene product for vancomycin resistance in bacteria, is a monomeric Zn^{II}-binding protein with a metal binding site that coordinates Zn^{II} in a tetrahedral fashion to two His residues, one Asp residue, and an exogenous solvent molecule (Figure 3-36).[47,48] Co^{II}-substituted VanX produces a UV-Vis spectrum with molar absorptivities of ~100 $M^{-1}cm^{-1}$ with absorbance maxima at ~510, 550 and 590 nm, similar to my Co^{II}-bound heterotrimers (Table 3-2).[49] Additionally, Co^{II} EPR provided a similarly rhombic-like spectrum with $g_{eff(x,y,z)}$ values of 1.92, 3.71, and 5.64. These data support a 5-coordinate environment for Co^{II}-bound VanX. Interestingly, the EXAFS fits for Co^{II}-VanX provide best fits values for 5-coordinate environments of ~2.0 Å, a value that seems to better correlate to a 4-coordinate Co^{II} site. Regardless, the similarities between my Co^{II}-bound heterotrimers, and Co^{II}-substituted CPA, VanX, and TML support the conclusion that direct carboxylate coordination is occurring when Co^{II} is introduced to a His_3 site with either one or two Asp residues in close proximity.

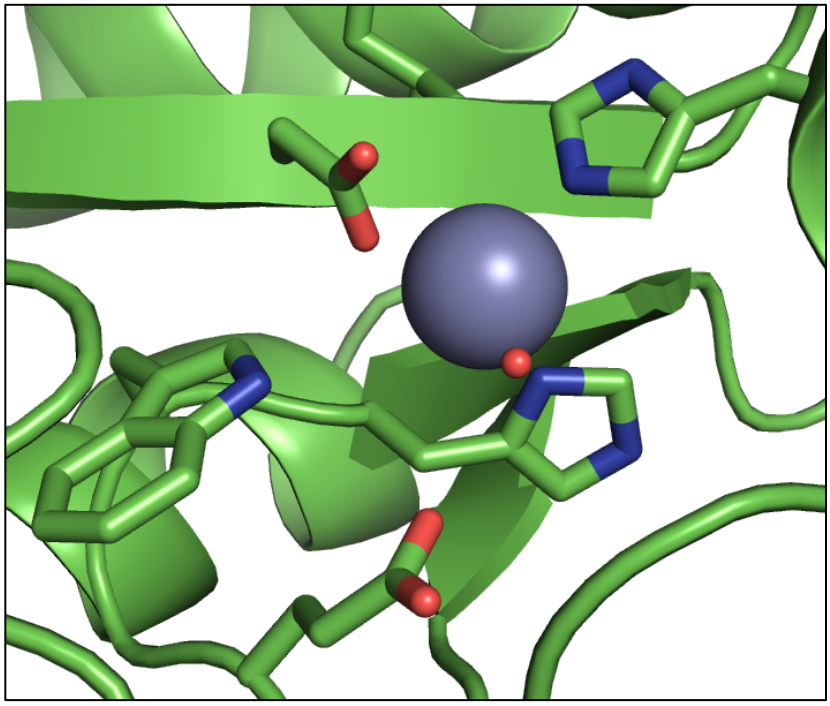

Figure 3-36. Primary coordination sphere of VanX (PDB: 1R44).[48] Zn^{II} ion is shown as a grey sphere. Selected amino acids of active site ligands are shown as stick figures where N atoms are highlighted in blue and oxygen in red. Water molecules are shown as smaller red spheres.

At this point, an analysis of the interior of the 3SCC provided from the previously reported $ZnHis_3OH_2$ crystal structure ($Hg^{II}_{S}Zn^{II}_{N/O}$(**CS**-L9PenCL23H)$_3^{n+}$, PDB: 3PBJ)[1] was warranted to determine if manipulation of the Co^{II} binding site could accommodate a $His_2O_XOH_2$-like coordination. Using the molecular modeling program COOT,[50] an aspratate was mutated into the layer above the His_3 site to mimic the [$Pb^{II}_{S}Co^{II}_{N/O}$(**GR**-ACH)$_2$(**GR**-CDH)$_1$]$^{n+}$ heterotrimeric system. Rotation of the imidazole rings and aspartate residue, as well as movement of the metal ion closer to the N-terminus of the 3SCC, afforded metal-His distances of 1.98 and 2.0 Å, metal-O distances for the aspartate oxygen atoms of 2.2 and 2.0 Å and a metal-OH_2 distance of 1.95 Å (Figure 3-37). These distances are comparable to those observed in CPA, TML, and VanX, and only slightly shorter than the distances obtained from the EXAFS fittings for my heterotrimers (Model average N/O: 2.03 Å vs. EXAFS average: 2.075 Å, Table 3-5).[42,43,48]

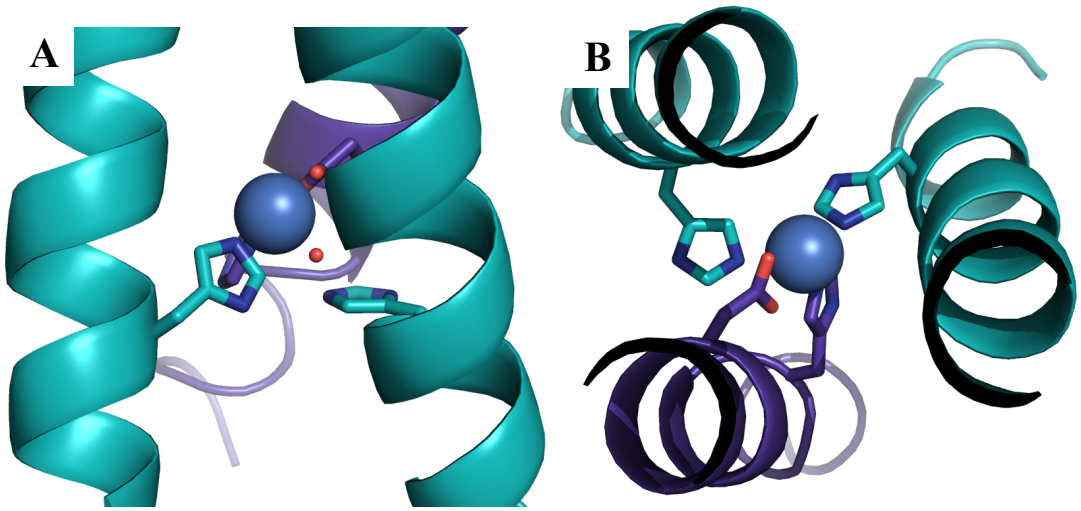

Figure 3-37. (A) Side-on and (B) top down views of a Pymol model with a $His_2Asp_1OH_2$ primary coordination sphere in a heterotrimeric 3SCC. The metal-binding ligands are His and Asp residues with nitrogen atoms in blue and oxygen atoms in red. The metal ion is colored blue and the potential water molecule as a red sphere. The heterotrimeric assembly is emphasized by two teal helices and one purple helix. A third, un-coordinated His residue is also shown. Models are generated using the crystal structure of $Hg^{II}{}_SZn^{II}{}_{N/O}(\mathbf{CS}L9PenCL23H)_3{}^{n+}$ (PDB: 3PBJ).[1]

When the metal ion is moved up toward the N-termini and toward the helical interface to offer direct coordination to two His and the Asp residues, this results in a metal-His distance to the third histidine residue of 4.0 Å. This distance is too far for metal coordination and supports the assignment that the direct Asp metal- coordination requires the third His residue to become uncoordinated (although it could form a hydrogen bond with a coordinated water). Closer examination of the crystal structure of TML reveals a third His residue in close proximity to the binding site at a distance of 4.2 Å (Figure 3-35B).[42] This histidine is proposed to offer hydrogen-bonding properties to the Zn-bound water (2.3 Å from Zn^{II} and 2.7 Å from the uncoordinated His residue). Therefore, in COOT I also modeled in a water molecule in between the metal and the uncoordinated His residue (2.0 Å from the Zn^{II} ion and 2.2 Å from the uncoordinated His residue). I also overlaid the crystal structure of the $Zn^{II}His_3$ site from $Hg^{II}{}_SZn^{II}(OH)_{N/O}(\mathbf{CS}L9PenCL23H)_3{}^+$ with the COOT His_2AspOH_2 model to obtain a displacement of the Zn^{II} ion of 1.4 Å (Table 3-1, Figure 3-38).[1] Although this is just a model and a crystal structure of the heterotrimer is necessary to confirm the structural parameters, I feel this image is a good first estimate of how Co^{II} could be coordinated in

the heterotrimeric peptides. This model is consistent with all spectral data and demonstrates that an asymmetric primary $His_2O_X(OH_2)_Y$ coordination environment is possible within the heterotrimers without significant interruption of the trimer packing or folding.

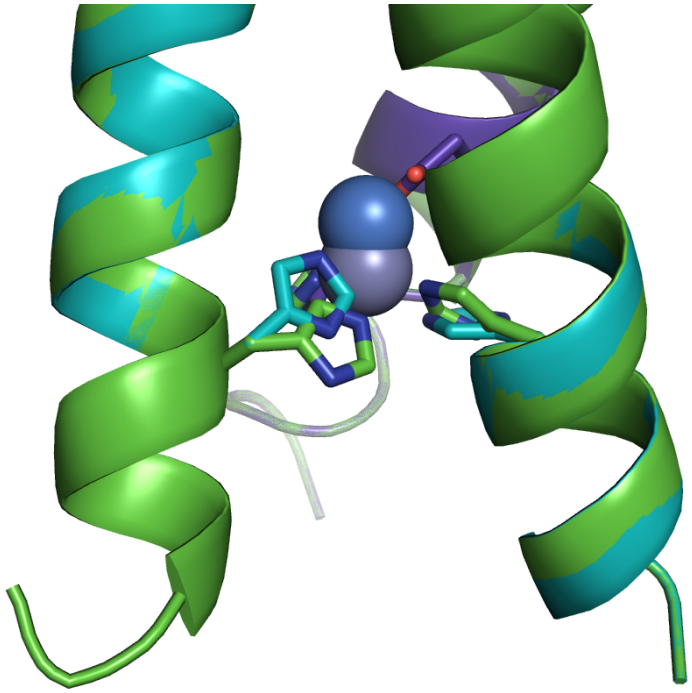

Figure 3-38. Overlay side-on view of $Hg^{II}_{S}Zn^{II}_{N/O}$(**CS**L9PenCL23H)$_3^{n+}$ (green helices and grey metal ion sphere) and a Pymol model with a $His_2Asp_1OH_2$ primary coordination sphere in a 3SCC (teal and purple helices, blue metal ion sphere). The metal-binding ligands are His and Asp residues with nitrogen atoms in blue and oxygen atoms in red. The movement of the metal ion of 1.4 Å toward the Asp residue in the pymol model is shown. Models are generated using the crystal structure of $Hg^{II}_{S}Zn^{II}_{N/O}$(**CS**L9PenCL23H)$_3^{n+}$ (PDB: 3PBJ).[1]

This data shows that the primary objective of preparing a transition metal in an asymmetric first coordination environment using non-covalent, self-assembling, heterotrimeric, α-helical 3SCCs, has been achieved. The primary goal of obtaining an asymmetric secondary coordination sphere for a potential catalytic site by introduction of an aspartate in close proximity to a His_3 site is not supported by comparison of the Co^{II}-bound spectral data. However, arguably more interestingly, the spectral data is more consistent with a change in the primary coordination sphere resulting in a less-symmetric, five-coordinate $N_2O_X(OH_2)$ binding site.

Indeed, when the T199 of CA is mutated to Asp, the Zn^{II}-bound hydroxide is displaced and direct carboxylate ligation is observed, essentially abolishing catalytic activity.[51] The coordination of a carboxylate residue, while still coordinating all three histidine residues, requires significant conformational changes in the polypeptide backbone of CA. Although our 3SCCs have previously provided an excellent scaffold to mimic CA, both structurally in the first coordination sphere and kinetically, this sort of substantial conformational change is not possible within the rigid alpha-helical structure of our scaffolds. I propose that a Co^{II} metal ion can bind to either all three histidine residues or a combination of two histidine residues and an Asp residue, but the 3SCC structure cannot accommodate the conformational changes required for direct $Co^{II}His_3Asp$ coordination. Future studies will analyze the perturbations on this transition-metal binding site by incorporating residues that are less likely to coordinate directly to the metal and, therefore, better fulfill the roll of an acid base catalysis model (Thr or Ser instead of Asp, See Chapter 5).

Testing the Versatility of Heterotrimer Formation: Combined Ala/Asp Mutations

As discussed in Chapter 2, ^{207}Pb NMR analysis of a 1:2 ratio of Ala:Leu containing peptides indicates that $Pb^{II}_S[(\mathbf{GR}\text{-ACH})_1(\mathbf{GR}\text{-CH})_2]^-$ as well as $Pb^{II}_S[(\mathbf{GR}\text{-ACH})_2(\mathbf{GR}\text{-CH})_1]^-$ are formed as indicated by the presence of two peaks at ~5600 and ~5625 ppm. In the opposite configuration, a 2:1 ratio of Ala:Leu containing peptides, such as, yields only a single peak for $Pb^{II}_S[(\mathbf{GR}\text{-ACH})_2(\mathbf{GR}\text{-CH})_1]^-$ with a chemical shift of ~5600 ppm, indicating formation of a single heterotrimeric 3SCC. However, Co^{II} EXAFS analysis of the $M^{n+}His_3$ site that binds transition metals suggests that $Pb^{II}_SCo^{II}_{N/O}[(\mathbf{GR}\text{-ACH})_1(\mathbf{GR}\text{-CDH})_2]^-$ provides a more pure 5-coordinate Co^{II} environment than $Pb^{II}_S[(\mathbf{GR}\text{-ACH})_2(\mathbf{GR}\text{-CDH})_1]^-$, which looks like it may contain a mixture of 5- and 6-coordinate Co^{II}. This observation lead me to ask three questions, first, could I obtain a pure heterotrimer, via ^{207}Pb NMR, while including the Ala and the Asp substitution within the same peptide? Second, would a peptide containing four substitutions, Ala, Cys, Asp, and His, be well folded and stable? And lastly, would the

Co^{II} EXAFS of this new heterotrimeric mixture provide a pure 5-coordinate Co^{II} site, supporting a wholly pure species at both the Pb^{II} site and the Co^{II} site?

First, I synthesized and characterized **GR**L2WL12AL16CL26DL30H, or **GR**-ACDH (Table 3-1). For heterotrimer formation, **GR**-ACDH will be mixed, in the presence of Pb^{II}, with **GR**-CH, which was characterized in Chapter 2. CD spectroscopy and GuaHCl denaturation titrations were used to determine the folding and stability of **GR**-ACDH (Figure 3-39). The CD spectrum showed a peak at 222 nm, indicative of alpha-helical colied coil structure, but the second feature at 208 nm was not well resolved. Additionally, **GR**-ACDH showed very poor folding with a molar ellipticity [Θ] of -16056 deg $dmol^{-1}$ cm^2, which corresponds to only ~48% initial folding compared to an ideal, fully folded alpha-helical structure, compared to ~95% folding for the complimentary **GR**-CH peptide (See Chapter 2). This model cannot be fit to a two step denaturation curve due to the lack of a defined folded state before the addition of GuaHCl, but analysis of Figure 3-36 shows a midpoint of less than 1 M for the denaturation of **GR**-ACDH. **GR**-ACDH, therefore, folds ~30% less compared to **GR**-CDH and ~50% less compared to **GR**-ACH. A progressive decrease in denaturation mid-point can be observed from 2.28 M for **GR**-CH, 1.83 M for **GR**-ACH to ~1M for **GR**-CDH and less than 1M for **GR**-ACDH (Figure 3-40).

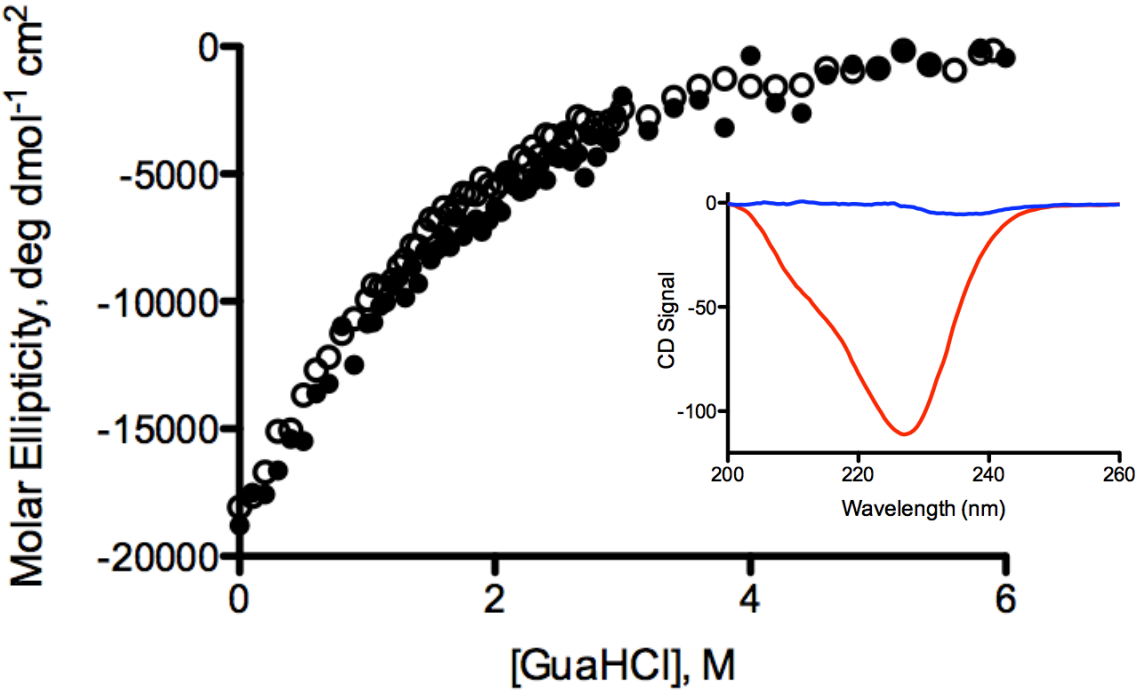

Figure 3-39. Guanidine hydrochloride denaturation titration data of **GR**-ACDH in the absence (open circle) and presence (closed circles) of Pb^{II} and Co^{II}, yielding $Pb^{II}_{S}Co^{II}_{N/O}$(**GR**-ACDH)$_3^{n+}$, in 10 mM Phosphate buffer at pH 8.0, [3SCC] = 8 μM. Inset: CD spectra of **GR**-ACDH before (red) and after (blue) the addition of 6 M GuaHCl.

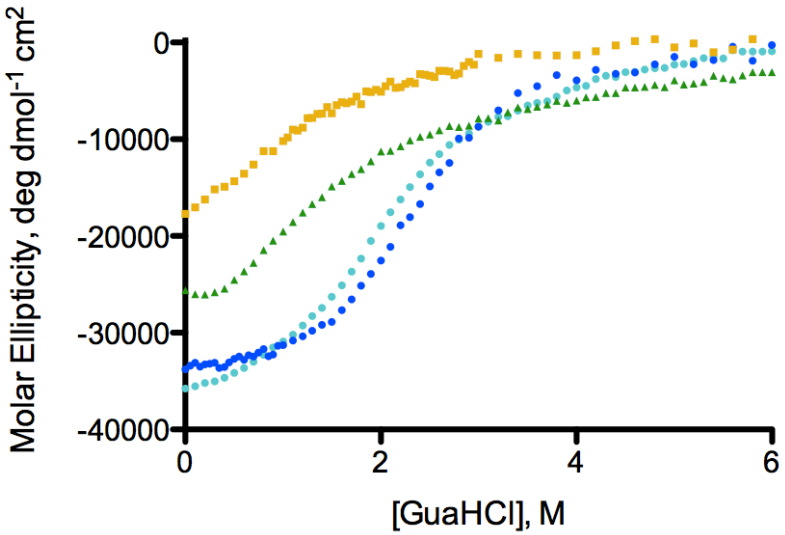

Figure 3-40. Overlay of guanidine hydrochloride denaturation titration data of **GR**-ACH (light blue circle), **GR**-CH (dark blue circle), **GR**-CDH (green triangle), and **GR**-ACDH (orange square) in 10 mM Phosphate buffer at pH 8.0.

Pb^{II} binding to **GR**-ACDH was analyzed via UV-Vis spectroscopy where aliquots of $Pb^{II}(NO_3)_2$ were added to a solution of 20 μM (3SCC) **GR**-ACDH in TRIS buffer at pH 8.5 (Figure 3-41). The peptide complexed Pb^{II}, as observed in the previous peptides, with a characteristic LMCT band at 341 nm. Saturation of the Cys_3 site is observed at one equivalent of Pb^{II} and linear regression analysis of the increase in absorbance as a function of total Pb^{II} added provided a molar extinction coefficient of 2902 $M^{-1}cm^{-1}$. This confirms that Pb^{II} binds comparably to **GR**-ACDH, even when four mutations are contained within the peptide sequence, and the corresponding lower initial folding.

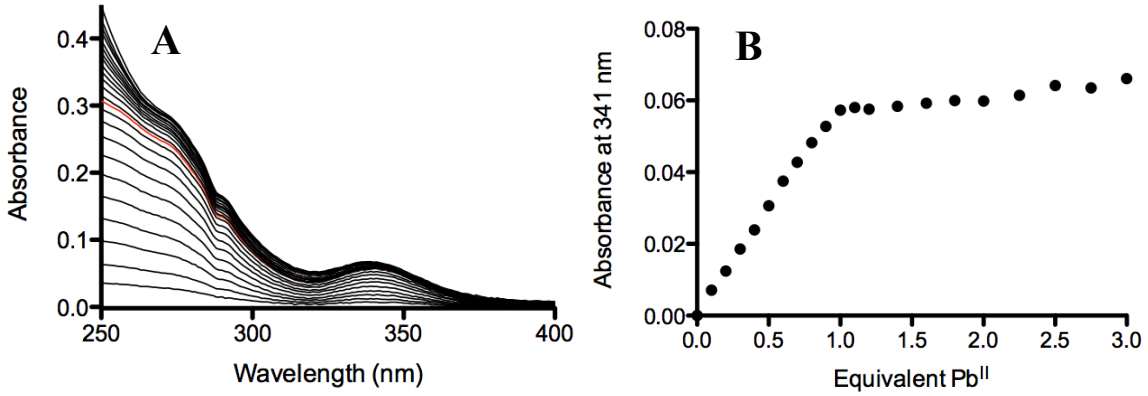

Figure 3-41. Titration spectra of Pb^{II} into a solution of A) 20 μM **GR**-ACDH and B) the corresponding titration curves showing the 1:1 binding stoichiometry of equivalent of Pb^{II} added with respect to 3SCC at 341 nm. Data collected at pH 8.5 in 50 mM TRIS Buffer.

Previously, heavy metals, such as Hg^{II}, have been shown to offer increased stability to the 3SCCs when bound to a Cys_3 site. I therefore waned to determine if the presence of Pb^{II}, in addition to Co^{II}, would offer some increased stability and folding for **GR**-ACDH. Interestingly, the addition of Co^{II} and Pb^{II} offer no increased stability as evidenced in the CD spectrum of $Pb^{II}{}_S Co^{II}{}_{N/O}$(**GR**-ACDH)$_3{}^{n+}$ having a molar ellipticity [Θ] of -16578 deg $dmol^{-1}$ cm^2, corresponding to only ~49% initial folding (Figure 3-39). This indicates that even when two metal ions are bound to **GR**-ACDH there is still no significant increase in initial folding or added stability toward GuaHCl denaturation.

However, since I saw evidence of Pb^{II} binding via UV-Vis, I decided to try to analyze this new, albeit relatively unstable, peptide via ^{207}Pb NMR, in hopes that the stability offered by the opposite peptide required to form the desired heterotrimer (**GR**-

CH) would offer enough stability to compensate for the **GR**-ACDH peptide. In the presence of both Pb^{II} and Co^{II} the same chemical shifts are observed for $Pb^{II}_{S}Co^{II}_{N/O}$(**GR**-ACDH)$_3^{n+}$, $Pb^{II}_{S}Co^{II}_{N/O}$[(**GR**-CH)$_1$(**GR**-ACDH)$_2$]$^{n+}$, and $Pb^{II}_{S}Co^{II}_{N/O}$[(**GR**-CH)$_2$(**GR**-ACDH)$_1$]$^{n+}$, indicating that even though the stability of **GR**-ACDH is low the heterotrimer formation at the Pb^{II} site is not hindered by including the Ala and Asp residues on the same peptide.

Next, I wanted to determine if the inclusion of the Ala and Asp residues on the same peptide offered any changes to the UV-Vis spectra of the Co^{II} d-d bands of the homotrimer, $Pb^{II}_{S}Co^{II}_{N/O}$(**GR**-ACDH)$_3^{n+}$, and both heterotrimers, $Pb^{II}_{S}Co^{II}_{N/O}$[(**GR**-CH)$_1$(**GR**-ACDH)$_2$]$^{n+}$, and $Pb^{II}_{S}Co^{II}_{N/O}$[(**GR**-CH)$_2$(**GR**-ACDH)$_1$]$^{n+}$. Aliquots of $Co^{II}SO_4$ were added to homotrimeric and heterotrimeric solutions with ~0.5-0.75 mM 3SCC, and one equivalent of $Pb^{II}(NO_3)_2$, in 50 mM HEPES buffer at pH 7.5. Consistent with the original peptides as outlined above, Co^{II} binding to the homotrimer $Pb^{II}_{S}Co^{II}_{N/O}$(**GR**-ACDH)$_3^{n+}$ resulted in one, broad peak at 543 nm with an elevated extinction coefficient (ε = 110 M^{-1} cm^{-1}, Figure 3-42, Table 3-2). This value is slightly greater in comparison to 6-coordinate Co^{II} complexes and on the low end of the range of 5-coordinate Co^{II} complexes. A slightly tighter apparent dissociation constant of 10.5 ± 3.1 μM was determined by fitting the Co^{II} titration data to Equation 7 (5-times tighter than that of $Pb^{II}_{S}Co^{II}_{N/O}$(**GR**-CDH)$_3^{n+}$, Figures 3-43A and 3-43B, Table 3-3).

A similar increase, of about 20%, in extinction coefficient is observed upon the addition of Co^{II} to Pb^{II}_{S}[(**GR**-CH)$_1$(**GR**-ACDH)$_2$]$^{n+}$, the heterotrimer that offers a pure ^{207}Pb NMR spectrum (Figure 3-40C). The overall trace is very similar to that observed for $Pb^{II}_{S}Co^{II}_{N/O}$[(**GR**-ACH)$_1$(**GR**-CDH)$_2$]$^{n+}$ with three peaks at 517 nm (ε = 200 M^{-1} cm^{-1}), 544 nm (ε = 215 M^{-1} cm^{-1}), 586 nm (ε = 167 M^{-1} cm^{-1}) and a shoulder at 626 nm (ε ~ 60 M^{-1} cm^{-1}, Figure 3-43C, Table 3-2). In the case of $Pb^{II}_{S}Co^{II}_{N/O}$[(**GR**-CH)$_1$(**GR**-ACDH)$_2$]$^{n+}$, more peak definition is observed at 586 nm. Interestingly, the same overall trace is observed, but with only a very small increase in extinction coefficient in comparison to the original heterotrimers, when Co^{II} is added to the opposite heterotrimeric mixture, $Pb^{II}_{S}Co^{II}_{N/O}$[(**GR**-CH)$_2$(**GR**-ACDH)$_1$]$^{n+}$. Three peaks were observed at 524 nm (ε = 152

M^{-1} cm^{-1}), 544 nm (ε = 165 M^{-1} cm^{-1}), 592 nm (ε = 120 M^{-1} cm^{-1}, Figure 3-43E, Table 3-2).

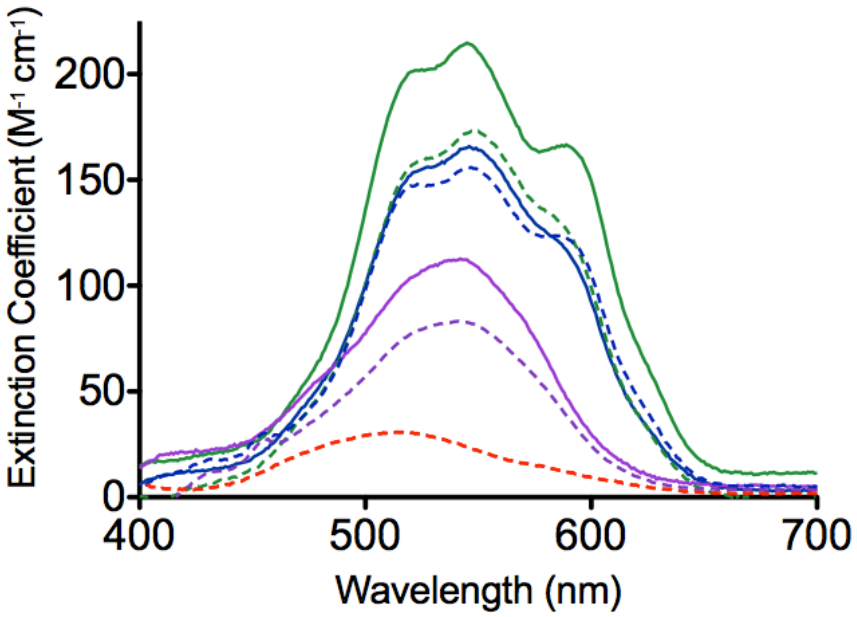

Figure 3-42. UV-Vis overlay of original homotrimers $Pb^{II}_{S}Co^{II}_{N/O}$(**GR**-CH)$_3^{n+}$ (dashed red) and $Pb^{II}_{S}Co^{II}_{N/O}$(**GR**-CDH)$_3^{n+}$ (dashed purple) and original heterotrimers: $Pb^{II}_{S}Co^{II}_{N/O}$[(**GR**-ACH)$_2$(**GR**-CDH)$_1$]$^{n+}$ (dashed blue) and $Pb^{II}_{S}Co^{II}_{N/O}$[(**GR**-ACH)$_1$(**GR**-CDH)$_2$]$^{n+}$ (dashed green). The new homotrimer $Pb^{II}_{S}Co^{II}_{N/O}$(**GR**-ACDH)$_3^{n+}$ (purple) and new heterotrimers: $Pb^{II}_{S}Co^{II}_{N/O}$[(**GR**-CH)$_2$(**GR**-ACDH)$_1$]$^{n+}$ (blue) and $Pb^{II}_{S}Co^{II}_{N/O}$[(**GR**-CH)$_1$(**GR**-ACDH)$_2$]$^{n+}$ (green) are also shown. All data were collected at pH 7.5, 50 mM HEPES buffer. Data are plotted as molar extinction coefficient (determined using Co^{II} concentration) versus wavelength.

The apparent Co^{II} dissociation constants were determined by fitting the titration data to be 11.2 ± 1.2 and 21.8 ± 2.4 μM, for $Pb^{II}_{S}Co^{II}_{N/O}$[(**GR**-CH)$_1$(**GR**-ACDH)$_2$]$^{n+}$ and $Pb^{II}_{S}Co^{II}_{N/O}$[(**GR**-CH)$_2$(**GR**-ACDH)$_1$]$^{n+}$, respectively (Equation 7, Figures 3-43D and 3-43E, Table 3-3). These dissociation constants, unlike the case of $Pb^{II}_{S}Co^{II}_{N/O}$(**GR**-ACDH)$_3^{n+}$, are essentially the same as those obtained for the original heterotrimeric mixtures. The increase in extinction coefficient of $Pb^{II}_{S}Co^{II}_{N/O}$[(**GR**-CH)$_1$(**GR**-ACDH)$_2$]$^{n+}$, while not observed for $Pb^{II}_{S}Co^{II}_{N/O}$[(**GR**-CH)$_2$(**GR**-ACDH)$_1$]$^{n+}$, could support the original hypothesis that including the Ala and Asp substitutions on the same peptide could provide a pure heterotrimer, as evidenced by ^{207}Pb NMR, as well as a more pure 5-coordinate Co^{II} site, as indicated by the UV-Vis data, presumably related to an even less symmetric and less octahedral-like site.

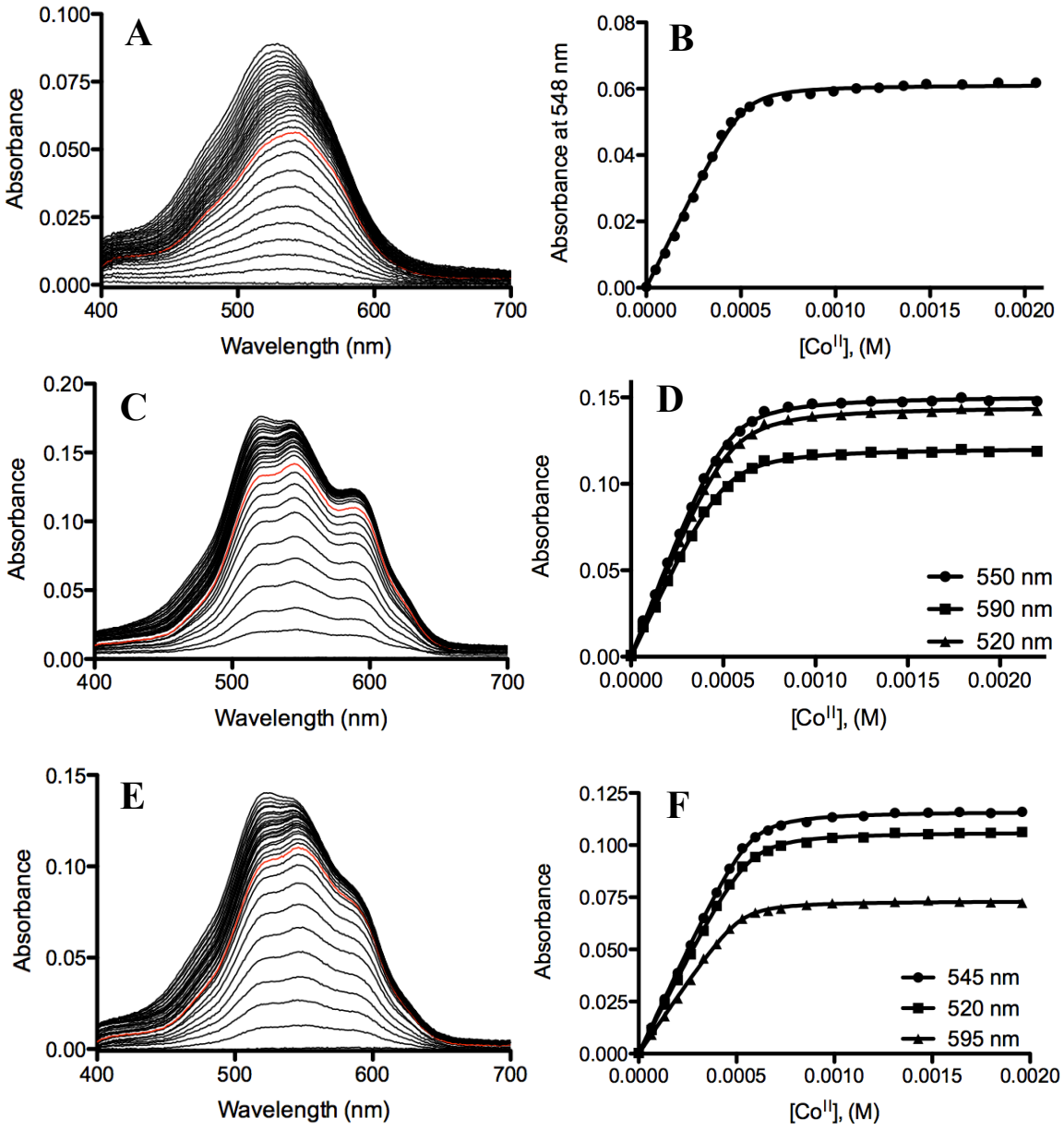

Figure 3-43. UV-Vis titration and titration curves of $Co^{II}SO_4$ added to a solution of 0.53 mM $Pb^{II}_{S}Co^{II}_{N/O}$(**GR**-ACDH)$_3^{n+}$ (A and B), 0.50 mM $Pb^{II}_{S}Co^{II}_{N/O}$[(**GR**-ACDH)$_1$(**GR**-CH)$_2$]$^{n+}$ (C and D), and 0.50 mM $Pb^{II}_{S}Co^{II}_{N/O}$[(**GR**-ACDH)$_2$(**GR**-CH)$_1$]$^{n+}$ (E and F) at pH 7.5 in 50 mM HEPES buffer. The titration data (A, C and E) are plotted as absorbance versus wavelength and the titration curves (B, D, and F) are plotted as absorbance at λ_{max} versus [Co^{II}]. The trace that correlates to one equivalent of [Co^{II}] added, with respect to 3SCC, is shown in red. The black circles represent the raw data and the non-linear best-fit curve is shown as a black line (Equation 7, as described in the Materials and Methods section).

Co^{II} X-band EPR spectra were collected, at ~10 K, for $Pb^{II}_{S}Co^{II}_{N/O}$(**GR**-ACDH)$_3^{n+}$, $Pb^{II}_{S}Co^{II}_{N/O}$[(**GR**-CH)$_1$(**GR**-ACDH)$_2$]$^{n+}$, and $Pb^{II}_{S}Co^{II}_{N/O}$[(**GR**-CH)$_2$(**GR**-ACDH)$_1$]$^{n+}$. Samples were prepared identically to the previous EPR and XAS samples. Little difference was observed between the original homo- and heterotrimers and the new mixtures, where the Ala and Asp substitutions were contained within the same peptide. The homotrimeric sample, $Pb^{II}_{S}Co^{II}_{N/O}$(**GR**-ACDH)$_3^{n+}$, showed similar axial behavior as the original homotrimers and the new heterotrimers showed comparably more rhombic signals, as previously observed and described (Figure 3-44). These data suggest that the spectroscopic fingerprints, as analyzed via UV-Vis and EPR, are very similar from homotrimer to homotrimer, regardless of which helix contains the Ala or Asp residues. The same can be said for the striking similarities observed between the heterotrimeric samples.

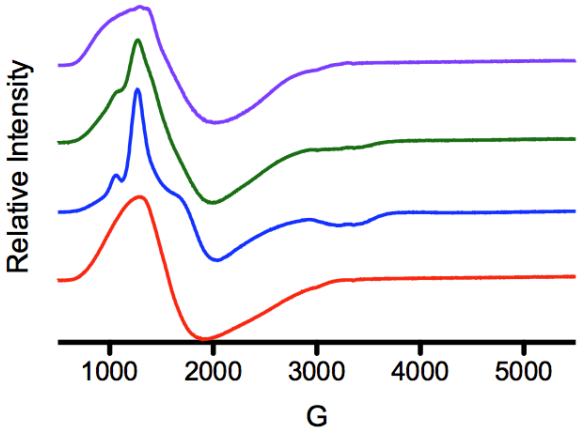

Figure 3-44. X-band EPR spectra of homotrimers: 1.0 mM $Pb^{II}_{S}Co^{II}_{N/O}$(**GR**-ACH)$_3^{n+}$ (red) and 1.0 mM $Pb^{II}_{S}Co^{II}_{N/O}$(**GR**-ACDH)$_3^{n+}$ (purple) and new heterotrimers: 1.0 mM $Pb^{II}_{S}Co^{II}_{N/O}$[(**GR**-ACDH)$_1$(**GR**-CH)$_2$]$^{n+}$ (blue) and 1.0 mM $Pb^{II}_{S}Co^{II}_{N/O}$[(**GR**-ACDH)$_2$(**GR**-CH)$_1$]$^{n+}$ (green) at pH 7.5 in 30 mM HEPES, collected at 10 K.

The biggest variation observed between the original heterotrimers (where Ala and Asp substitutions are on different peptides) and the new heterotrimers, $Pb^{II}_{S}Co^{II}_{N/O}$[(**GR**-CH)$_1$(**GR**-ACDH)$_2$]$^{n+}$, and $Pb^{II}_{S}Co^{II}_{N/O}$[(**GR**-CH)$_2$(**GR**-ACDH)$_1$]$^{n+}$, was observed when comparing the Co^{II} XAS data. First, I looked to the XANES spectrum for the homotrimeric $Pb^{II}_{S}Co^{II}_{N/O}$(**GR**-ACDH)$_3^{n+}$ sample (all samples for homo- and heterotrimers containing **GR**-ACDH were prepared analogously to the EPR and XAS

samples above). Analysis of the XANES at both the pre-edge and edge show that when the Ala and Asp residues are included on the same helix the trace looks very similar to the original homotrimeric peptides (Figure 3-45), with only a slight decrease in intensity observed at the edge peak (Table 3-4). The pre-edge/edge ratio is still 2.0 and the area under the pre-edge peak is 6.6 (Table 3-4). The EXAFS data show similar features as described above with a dominate peak at ~2.1 Å and evidence of outer shell histidine scattering patterns (Figure 3-43, 2.5 < R < 4 Å). Similar models as described above were used to fit the data, with two equally good best fits determined to be six oxygen/nitrogen ligands (3His and 3 oxygen atoms, or 2His and 4 oxygen atoms) with an average Co^{II}-N/O distances of ~2.1 Å (3.7-5.3 & 6.4-8.8 DW, F= 277-281, Table 3-5, Figures 3-46A and 3-46B). This primary coordination distance is only slightly shorter than the best fits for the $Pb^{II}{}_{S}Co^{II}{}_{N/O}$(**GR**-ACH)$_3{}^{+}$ and $Pb^{II}{}_{S}Co^{II}{}_{N/O}$(**GR**-CDH)$_3{}^{n+}$ samples (2.115 Å, Table 3-5) suggesting similar coordination number and geometry between all three homotrimers.

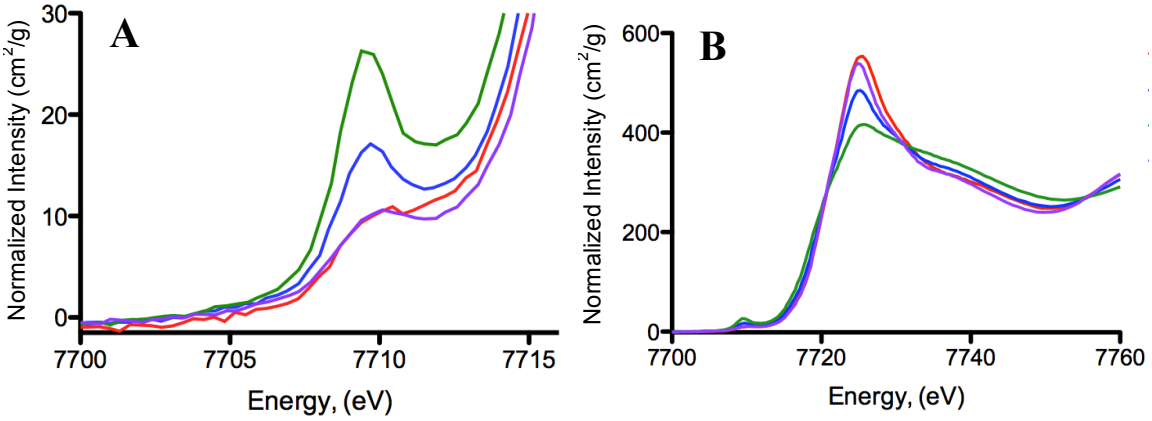

Figure 3-45. XANES spectra of the Co^{II} (A) pre-edge and (B) edge of homotrimers: 1.0 mM $Pb^{II}{}_{S}Co^{II}{}_{N/O}$(**GR**-ACH)$_3{}^{n+}$ (red) and 1.0 mM $Pb^{II}{}_{S}Co^{II}{}_{N/O}$(**GR**-ACDH)$_3{}^{n+}$ (purple) and heterotrimers: 1.0 mM $Pb^{II}{}_{S}Co^{II}{}_{N/O}$[(**GR**-ACDH)$_2$(**GR**-CH)$_1$]$^{n+}$ (blue) and 1.0 mM $Pb^{II}{}_{S}Co^{II}{}_{N/O}$[(**GR**-ACDH)$_1$(**GR**-CH)$_2$]$^{n+}$ (green) at pH 7.5 in 50 mM HEPES.

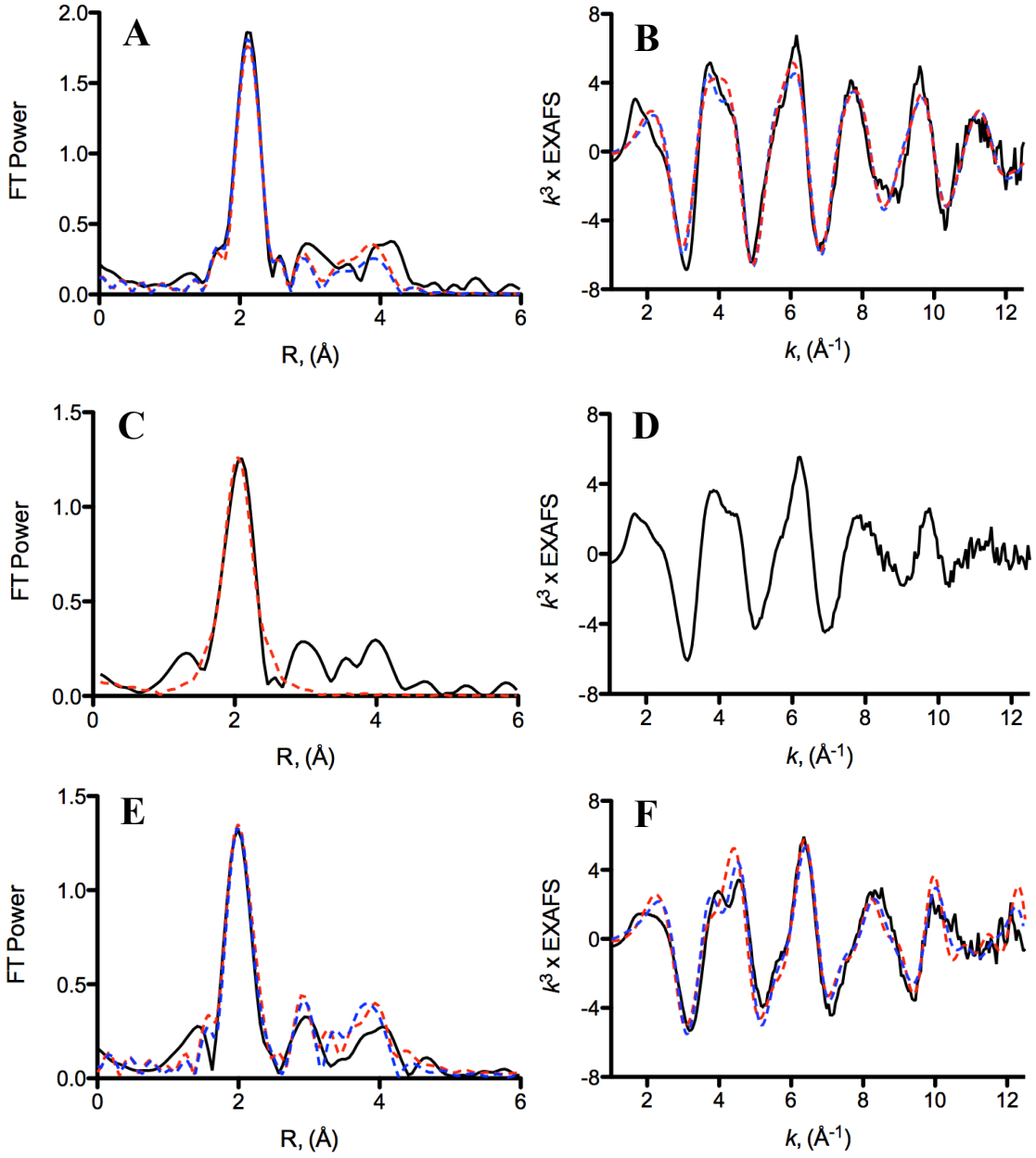

Figure 3-46. Fourier transform of Co^{II} EXAFS of (A) $Pb^{II}_{S}Co^{II}_{N/O}$(**GR**-ACDH)$_3^{n+}$, (C) $Pb^{II}_{S}Co^{II}_{N/O}$[(**GR**-ACDH)$_2$(**GR**-CH)$_1$]$^{n+}$, and (E) $Pb^{II}_{S}Co^{II}_{N/O}$[(**GR**-ACDH)$_1$(**GR**-CH)$_2$]$^{n+}$ at pH 7.5 in 50 mM HEPES buffer. Co^{II} EXAFS (B) 1.0 mM $Pb^{II}_{S}Co^{II}_{N/O}$(**GR**-ACDH)$_3^{n+}$, (D), 1.0 mM $Pb^{II}_{S}Co^{II}_{N/O}$[(**GR**-ACDH)$_2$(**GR**-CH)$_1$]$^{n+}$, and (F) 1.0 mM $Pb^{II}_{S}Co^{II}_{N/O}$[(**GR**-ACDH)$_1$(**GR**-CH)$_2$]$^{n+}$. Experimental data is shown in black and best fits for N_3O_3 (red) and N_2O_4 (blue) shells are shown in dashed lines for $Pb^{II}_{S}Co^{II}_{N/O}$(**GR**-ACDH)$_3^{n+}$. Single sphere fit is shown in a dashed red line for $Pb^{II}_{S}Co^{II}_{N/O}$[(**GR**-ACDH)$_2$(**GR**-CH)$_1$]$^{n+}$. Best fits for N_3O_2 (red) and N_2O_3 (blue) shells are shown in dashed lines for $Pb^{II}_{S}Co^{II}_{N/O}$[(**GR**-ACDH)$_1$(**GR**-CH)$_2$]$^{n+}$.

However, when I analyzed the heterotrimers, $Pb^{II}_{S}Co^{II}_{N/O}[(\mathbf{GR}\text{-}CH)_1(\mathbf{GR}\text{-}ACDH)_2]^{n+}$, and $Pb^{II}_{S}Co^{II}_{N/O}[(\mathbf{GR}\text{-}CH)_2(\mathbf{GR}\text{-}ACDH)_1]^{n+}$, the differences were much more apparent. First, the XANES of $Pb^{II}_{S}Co^{II}_{N/O}[(\mathbf{GR}\text{-}CH)_1(\mathbf{GR}\text{-}ACDH)_2]^{n+}$ showed a lower edge peak intensity and a higher pre-edge peak intensity, which correlates to a decrease in symmetry at the Co^{II} site, with a calculated pre-edge/edge ratio of 3.5 and a pre-edge peak are of 10.3 (Table 3-4). A similar EXAFS trace is once again observed (Figure 3-46C) with obvious outer-sphere scattering; however, because the XANES data support a possible mixed coordination number Co^{II}-complex (seemingly in between four- and five-coordinate), only a single-shell fit was conducted revealing an average Co^{II}-N/O distance of 2.048 Å (9.2 DW, F= 226, Table 3-5, Figures 3-46C and 3-46D). This is the shortest distance (by 0.035 Å) yet measured within these systems, again supporting a decrease in coordination to a five-coordination Co^{II} center. Thus far, the spectroscopic evidence suggests this heterotrimer is the most pure in terms of the formation of the heterotrimeric scaffold (^{207}Pb NMR) and has the most 5-coordinate like Co^{II} center (UV-Vis and EPR), and, the XAS supports the lowest symmetry at the Co^{II} center and is most consistent with a 5-coordinate environment.

Then, I analyzed the opposite heterotrimer, $Pb^{II}_{S}Co^{II}_{N/O}[(\mathbf{GR}\text{-}CH)_2(\mathbf{GR}\text{-}ACDH)_1]^{n+}$ and the differences were even more surprising. According to the UV-Vis, this heterotrimer looks very similar, with respect to the energy of the observed transitions and the extinction coefficients, to the original $Pb^{II}_{S}Co^{II}_{N/O}[(\mathbf{GR}\text{-}ACH)_1(\mathbf{GR}\text{-}CDH)_2]^{n+}$ heterotrimer. The EPR also looks very similar to that of the original 1:2 Ala:Leu heterotrimer. However, the XAS data tell a different story. The XANES data show a significant decrease in edge height as well as a significant increase in the pre-edge height, indicating an even bigger change in the symmetry around the Co^{II} site in comparison to any of the previously analyzed peptides. In fact, the pre-edge/edge ratio was determined to be 6.3 and the pre-edge area was measured at 15.4, a 50% increase in both values over the $Pb^{II}_{S}Co^{II}_{N/O}[(\mathbf{GR}\text{-}CH)_1(\mathbf{GR}\text{-}ACDH)_2]^{n+}$ heterotrimer. Fits of the EXAFS data provide average Co^{II}-N/O distances of 1.995 Å (4.2-5.1 & 9.4-6.0 DW, F=218-278, Figures 3-46E and 3-46F, Table 3-5). The two best fits were for four primary coordinated ligands, with equally good fits for N_2O_2 and N_3O environments (Table 3-5). The decrease in average bond length from 2.085 to 1.995 Å is consistent with a decrease in coordination

number from five- to four-coordinate; however, the UV-Vis and EPR data are consistent and comparable with the previously assigned 5-coordinate samples. Therefore, collection of another set of XAS data is required to determine if this sample is actually best described as a four-coordinate Co^{II} center or if this reported XAS data set is an anomaly.

Although there is some ambiguity in the reliability of the $Pb^{II}{}_{S}Co^{II}{}_{N/O}[(\mathbf{GR}\text{-}CH)_2(\mathbf{GR}\text{-}ACDH)_1]^{n+}$ XAS sample, the spectroscopic analysis of this new set of peptides, where the Ala and Asp residues are included on the same helix, have provided some very important insights. It appears that the **GR**-ACDH homotrimer is considerably destabilized in comparison to **GR**-ACH, **GR**-CDH and **GR**-CH, but this decreased stability has not shown a significant effect on Pb^{II} binding via either UV-Vis or NMR analysis. Additionally, the decrease in average Co^{II}-N/O distance in combination with the elevated extinction coefficients for the $Pb^{II}{}_{S}Co^{II}{}_{N/O}[(\mathbf{GR}\text{-}CH)_1(\mathbf{GR}\text{-}ACDH)_2]^{n+}$ heterotrimer support that the primary hypothesis of this section has be achieved, which was to obtain a heterotrimer that is pure at both the Pb^{II} and Co^{II} sites.

Armed with the **GR**-ACDH peptide, I also wanted to determine how Co^{II} binding would be affected if one of the His residues was removed from the binding site, in agreement with an uncoordinated third His ligand in TML as well as the lack of a third His_3 ligand in CPA (see discussion above). To study this sort of binding site I used a heterotrimeric mixture where the Ala, Asp and His residues were included in the same peptide, **GR**-ACDH, and a complimentary peptide sequence were no ligands are available at the Co^{II} binding site, **GR**L2WL16C, or **GR**-C (Table 3-1). The resulting heterotrimer, $Pb^{II}{}_{S}Co^{II}{}_{N/O}[(\mathbf{GR}\text{-}ACDH)_2(\mathbf{GR}\text{-}C)_1]^{n+}$ showed Co^{II} binding via UV-Vis analysis with a maximum absorbance at 543 nm (ε = 68 $M^{-1}cm^{-1}$), which looks very similar in shape to the $Pb^{II}{}_{S}Co^{II}{}_{N/O}(\mathbf{GR}\text{-}CDH)_3{}^{n+}$ and $Pb^{II}{}_{S}Co^{II}{}_{N/O}(\mathbf{GR}\text{-}ACDH)_3{}^{n+}$ homotrimers, but does have a lower extinction coefficient (Table 3-2, Figure 3-47). Indeed, even the Co^{II} dissociation constant is intermediate at 24.6 ± 11.5 μM (compared to 11.4 and 49.5 μM for $Pb^{II}{}_{S}Co^{II}{}_{N/O}(\mathbf{GR}\text{-}ACDH)_3{}^{n+}$ and $Pb^{II}{}_{S}Co^{II}{}_{N/O}(\mathbf{GR}\text{-}CDH)_3{}^{n+}$, respectively, Table 3-2). Multiplying the spectra obtained from $Pb^{II}{}_{S}Co^{II}{}_{N/O}(\mathbf{GR}\text{-}ACDH)_3{}^{n+}$ by ⅔, because the $Pb^{II}{}_{S}Co^{II}{}_{N/O}[(\mathbf{GR}\text{-}ACDH)_2(\mathbf{GR}\text{-}C)_1]^{n+}$ heterotrimer is ⅔ **GR**-ACDH, provides a UV-Vis spectra nearly identical to that obtained when adding Co^{II} to the $Pb^{II}{}_{S}[(\mathbf{GR}\text{-}ACDH)_2(\mathbf{GR}\text{-}C)_1]^{n+}$ mixture (Figure 3-44). Therefore, it appears that when Co^{II} is added to $Pb^{II}{}_{S}[(\mathbf{GR}\text{-}$

ACDH)$_2$(**GR**-C)$_1$]$^{n+}$ I may actually be obtaining 100% Co^{II} binding to Pb^{II}_S(**GR**-ACDH)$_3^{n+}$. Further analysis is necessary to distinguish between a Co^{II}-bound $Pb^{II}_SCo^{II}_{N/O}$[(**GR**-ACDH)$_2$(**GR**-C)$_1$]$^{n+}$ heterotrimer and Co^{II} binding to the Pb^{II}_S(**GR**-ACDH)$_3^{n+}$ component of the mixture.

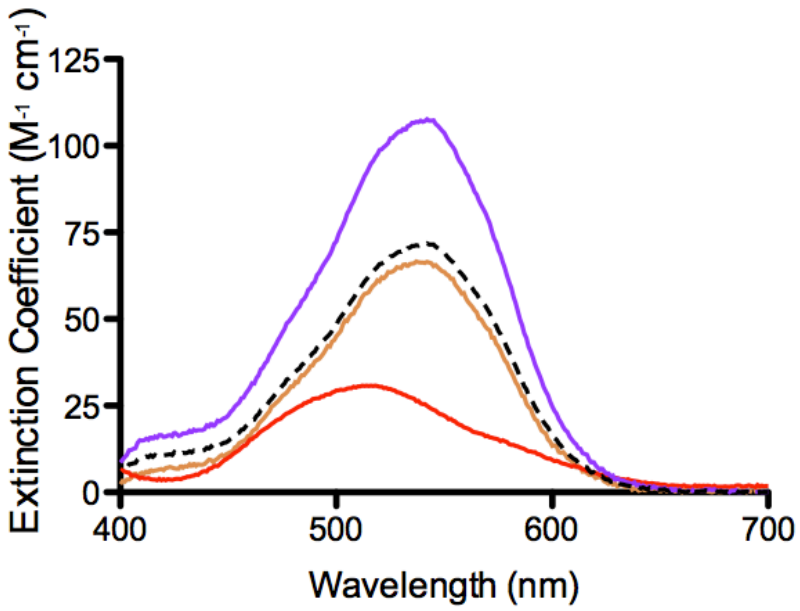

Figure 3-47. UV-Vis overlay of homotrimers $Pb^{II}_SCo^{II}_{N/O}$(**GR**-CH)$_3^{n+}$ (red), and $Pb^{II}_SCo^{II}_{N/O}$(**GR**-CDH)$_3^{n+}$ (purple), with heterotrimer: $Pb^{II}_SCo^{II}_{N/O}$[(**GR**-ACDH)$_2$(**GR**-C)$_1$]$^{n+}$ (orange) at pH 7.5 in 50 mM HEPES buffer. The calculated spectra of ⅔[$Pb^{II}_SCo^{II}_{N/O}$(**GR**-ACDH)$_3^{n+}$] is shown in dashed black. Experimental and calculated spectra are plotted as molar extinction coefficient (determined using Co^{II} concentration) versus wavelength.

These data indicate that complete removal of this His residue from the binding site does not provide the same Co^{II} binding environment as observed in the $Pb^{II}_SCo^{II}_{N/O}$[(**GR**-ACH)$_n$(**GR**-CDH)$_{3-n}$]$^{n+}$ or the $Pb^{II}_SCo^{II}_{N/O}$[(**GR**-ACDH)$_n$(**GR**-CH)$_{3-n}$]$^{n+}$ heterotrimers. It is possible that the Co^{II} coordinates to Asp and His residues on different helices within the trimer and, therefore, removing all coordinating ligands from one strand does not provide the proper ligand geometry to provide the CPA/TML-type of Co^{II} center.

However, even though complete removal of one His residue does not provide a CPA/TML $His_2O_x(H_2O)_Y$ type of site, the mixture still binds Co^{II}, with a UV-Vis spectrum that supports a relatively symmetric environment (as evidenced by the low

extinction coefficient) with comparable dissociation constants as seen in the $Pb^{II}_{S}Co^{II}_{N/O}$(**GR**-ACDH)$_3^{n+}$ and $Pb^{II}_{S}Co^{II}_{N/O}$(**GR**-CDH)$_3^{n+}$ homotrimers (Table 3-3). EPR, XAS and/or crystallography analysis is necessary to further elucidate Co^{II}-binding in $Pb^{II}_{S}Co^{II}_{N/O}$[(**GR**-ACDH)$_2$(**GR**-C)$_1$]$^{n+}$. Additionally, inclusion of the Asp and His residues on opposite helices, such as making a heterotrimer with peptides such as two equivalents of **GR**-ACH and one equivalent of and Asp-only peptide (**GR**L2WL16CL26D) could offer more insight into the necessity of the third His residue in close proximity to the binding site.

Effect of Excess Pb^{II} on the Transition Metal Binding Site

Previously, the addition of excess Pb^{II} to 3SCCs, homo- or heterotrimeric, with only a Cys_3 substitution in the peptide sequence, showed no perturbation on the formation of the intended heterotrimeric scaffold. Next, I wanted to determine how excess Pb^{II} would affect the Co^{II} binding to peptides with a second, remote binding site. To do so, aliquots of $Pb^{II}(NO_3)_2$ were added to a solution of 0.66 mM $Pb^{II}_{S}Co^{II}_{N/O}$(**GR**-ACH)$_3^{+}$ or 0.5 mM $Pb^{II}_{S}Co^{II}_{N/O}$(**GR**-CDH)$_3^{n+}$, and the Co^{II} d-d transitions at ~500-600 nm were observed for perturbations. In the case of $Pb^{II}_{S}Co^{II}_{N/O}$(**GR**-ACH)$_3^{+}$, the addition of three equivalents of Pb^{II}, in addition to the equivalent bound to the Cys_3 site, provided no change in the spectra (Figure 3-48A). However, when excess Pb^{II} was added to $Pb^{II}_{S}Co^{II}_{N/O}$(**GR**-CDH)$_3^{n+}$, a decrease in the peak intensity is observed as well as a blue-shift in the peak maxima from 543 nm to 517 nm (Figure 3-48B).

A continuous decrease in the absorbance at 543 nm was observed from 0-1 equivalents as a function of excess added Pb^{II}. Afterwards, no further change was seen upon an additional equivalent of excess Pb^{II} was added (Figure 3-48C). The spectrum of the new blue-shifted species observed with one equivalent of excess Pb^{II} is nearly identical to that of $Pb^{II}_{S}Co^{II}_{N/O}$(**GR**-ACH)$_3^{+}$ with a maximum absorbance at 517 nm and an extinction coefficient of 33 $M^{-1}cm^{-1}$ (Figure 3-48B). These data suggest that excess Pb^{II} does not perturb Co^{II} when coordinated to a His_3 site; however, when Asp residues are present, as in $Pb^{II}_{S}Co^{II}_{N/O}$(**GR**-CDH)$_3^{n+}$, the addition of excess Pb^{II} alters the Co^{II}

environment. This results in a UV-Vis trace similar to $Pb^{II}_{S}Co^{II}_{N/O}$(**GR**-ACH)$_3^+$, supporting similar Co^{II} behavior.

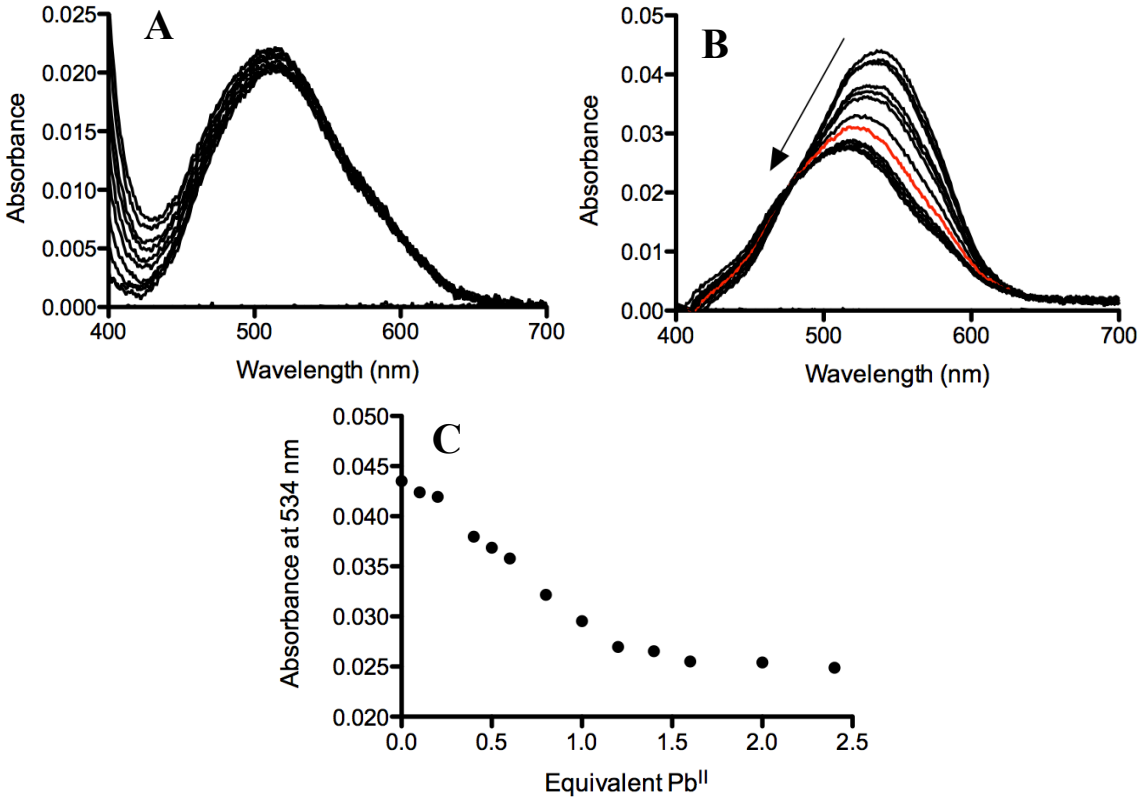

Figure 3-48. Titration spectra of excess Pb^{II} into a solution of (A) 0.66 mM $Pb^{II}_{S}Co^{II}_{N/O}$(**GR**-ACH)$_3^{n+}$, and (B) 0.5 mM $Pb^{II}_{S}Co^{II}_{N/O}$(**GR**-CDH)$_3^{n+}$. The trace that correlates with one equivalent of additional Pb^{II} is shown in red. (C) The corresponding titration curve to (B), showing the 1:1 binding stoichiometry of one additional equivalent of Pb^{II} added with respect to 3SCC at 543 nm. Data collected at pH 7.5 in 50 mM HEPES Buffer.

Pb^{II} is known to bind to oxygen-rich environments, such as the Ca^{2+} binding sites of calmodulin.[52–54] Therefore, I suspect that the excess equivalent of Pb^{II} is interacting with the Asp residues near the $Co^{II}His_3$ site. This, in turn, prevents the previous Co^{II}-Asp interactions, whether it is prohibiting the direct coordination of the Asp residues to the Co^{II} or disrupting hydrogen bonding between the Asp residues and water ions bound to the Co^{II}. At this time we cannot spectroscopically differentiate between these scenarios.

These experiments offer two new considerations. First, excess Pb^{II} should be avoided in samples of $Pb^{II}_{S}Co^{II}_{N/O}$(**GR**-CDH)$_3^{n+}$ because it could interfere with the Co^{II} environment leading to perturbed spectra. Second, and most exciting, these data suggest

that we may be seeing evidence of one peptide scaffold, with two metal binding sites, that is capable of binding three metal ions. This is the first of two scenarios where the spectroscopy presented in my thesis work supports a hetero-binuclear site forming within a single metal binding site within a 3SCC (See Chapter 4 for the discussion of a potential $Pb^{II}Cu^{I}$ hetero-binuclear site). A crystal structure and/or XAS analysis is required to further explore a potential Pb^{II}-Co^{II} interaction.

Co^{II}-binding to His_3 sites with Perturbed Secondary Spheres.

I have described multiple scenarios in which the secondary sphere around the Co^{II} binding site has been altered and the spectroscopic changes that resulted. Introduction of an Asp_3 layer directly above the His_3 site provides a slightly different UV-Vis trace, but relatively comparable EPR and XAS data, when compared to the $Co^{II}His_3$ site. Introducing this Asp_3 site below the His_3 site provides even less spectroscopic perturbations on Co^{II} binding, when compared to the $Pb^{II}{}_{S}Co^{II}{}_{N/O}$(**GR**-ACH)$_3{}^{+}$ homotrimer. Addition of an extra equivalent of Pb^{II} to $Pb^{II}{}_{S}Co^{II}{}_{N/O}$(**GR**-CDH)$_3{}^{n+}$ changes the UV-Vis trace to reveal a spectrum similar to that of $Pb^{II}{}_{S}Co^{II}{}_{N/O}$(**GR**-ACH)$_3{}^{+}$. In these scenarios, the most perturbation is observed when the layer above the His_3 site is altered.

As discussed in Chapter 1, altering the sterics around a $Cd^{II}Cys_3$ site allows for control over the Cd^{II} coordination number. Cd^{II}(**TRI**L2WL16C)$_3{}^{-}$ provides a mixture of three- and four-coordinate species (Table 3-1).[55] Cd^{II}(**TRI**L12AL16C)$_3$ provides space for a water molecule to coordinate to the Cd^{II} ion resulting in a pure four-coordinate site (Table 3-1).[56] Conversely, added hydrophobic bulkiness, as provided in both Cd^{II}(**TRI**L16Pen)$_3{}^{-}$ and Cd^{II}(**TRI**L12$_D$LL16C)$_3{}^{-}$ completely blocks the access of water to the site providing pure three-coordinate environments (Table 3-1).[56,57] Due to the heterotrimers discussed above providing evidence of mixed Co^{II} environments, I wanted to introduce a $_D$Leu layer above the His_3 site in hopes of enforcing a single coordination number, analogously to the $Cd^{II}S_3$ example. Therefore, I wanted to see how inclusion of a $_D$Leu layer would perturb the Co^{II} binding to a His_3 site. So, I analyzed Co^{II} binding to **TRI**L2WL19$_D$LL23H, **TRI**-$_D$LH (Table 3-1). Aliquots of $Co^{II}SO_4$ were added to a

solution of 0.5 mM **TRI**-$_D$LH (3SCC) at pH 7.5 and analyzed via UV-Vis spectroscopy from 400-800 nm. Upon complexation of Co^{II} to **TRI**-$_D$LH, a broad peak at 541 nm (ε = 62 M^{-1} cm^{-1}) was observed with two shoulders at 517 nm (ε = 59 M^{-1} cm^{-1}) and 588 nm (ε = 33 M^{-1} cm^{-1}, Figure 3-49, Table 3-2). Interestingly, these energies correspond to the transitions observed in the heterotrimeric $Pb^{II}_SCo^{II}_{N/O}$[(**GR**-ACH)$_1$(**GR**-CDH)$_2$]$^{n+}$ and $Pb^{II}_SCo^{II}_{N/O}$[(**GR**-ACH)$_2$(**GR**-CDH)$_1$]$^{n+}$ peptides; however, the extinction coefficients associated with these transitions are significantly decreased (less than 50% of the heterotrimers) and are consistent with the intensities observed in the $Pb^{II}_SCo^{II}_{N/O}$(**GR**-ACH)$_3^+$ and $Pb^{II}_SCo^{II}_{N/O}$(**GR**-CDH)$_3^{n+}$ homotrimers.

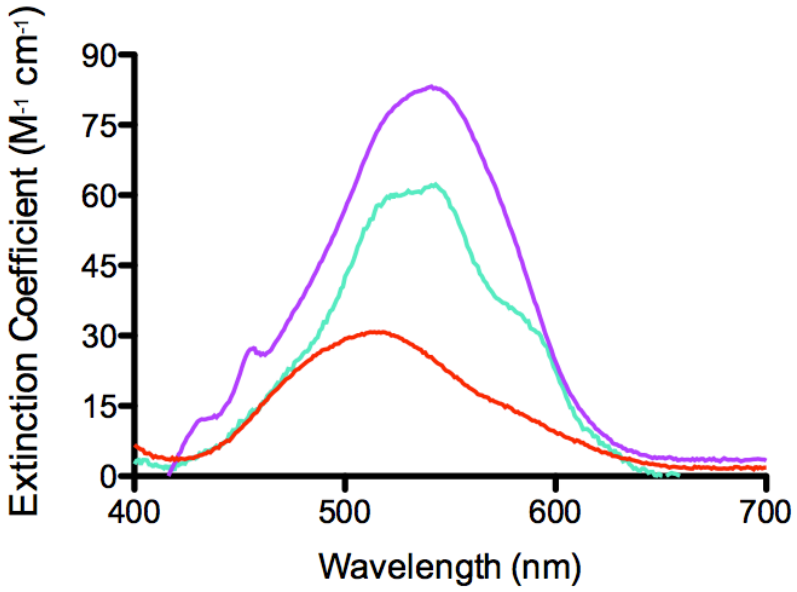

Figure 3-49. UV-Vis overlay of homotrimers $Pb^{II}_SCo^{II}_{N/O}$(**GR**-CH)$_3^{n+}$ (red), and $Pb^{II}_SCo^{II}_{N/O}$(**GR**-CDH)$_3^{n+}$ (purple), with $Pb^{II}_SCo^{II}_{N/O}$(**TRI**-$_D$LH)$_3^{n+}$ (teal) at pH 7.5 in 50 mM HEPES buffer. Experimental data are plotted as molar extinction coefficient (determined using Co^{II} concentration) versus wavelength.

The dissociation constant for Co^{II} binding to the $_D$LeuHis$_3$ site was determined using a non-linear least squares fitting analysis (Equation 7) in Prism 5 (GraphPad Software).[8] Titration data at λ = 600 nm were plotted as a function of Co^{II} concentration, adjusting for non-specific Co^{II} binding, and fitted as described in the Methods Section. The binding affinity obtained for $Co^{II}_{N/O}$(**TRI**-$_D$LH)$_3^{2+}$ at pH 7.5 is 38.3 ± 8.7 μM (Figure 3-50, Table 3-3). This value is very similar to the Co^{II} dissociation constants for

$Pb^{II}_{S}Co^{II}_{N/O}$(**GR**-ACH)$_3^{+}$ and $Pb^{II}_{S}Co^{II}_{N/O}$(**GR**-CDH)$_3^{n+}$, indicating that the $_D$Leu substitution does not appear to alter the ability of Co^{II} to bind to the His_3 site.

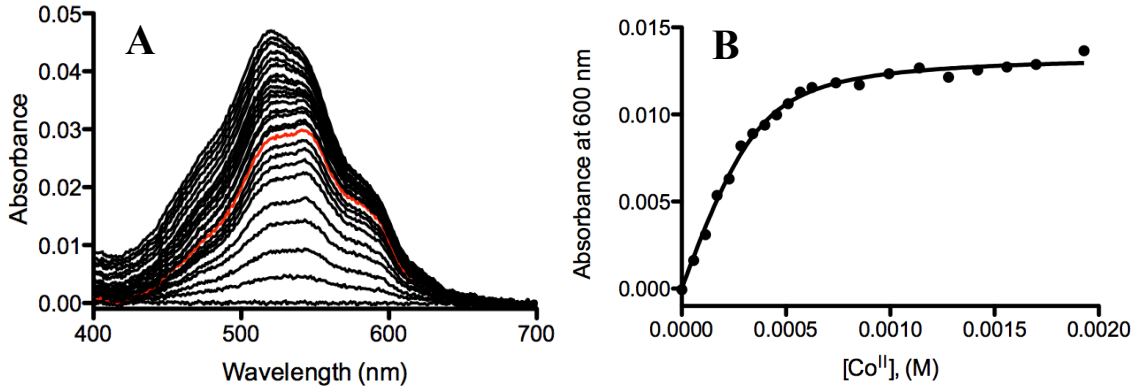

Figure 3-50. UV-Vis titration and titration curves of $Co^{II}SO_4$ added to a solution of 0.5 mM 3SCC **TRI**-$_D$LH (A) at pH 7.5 in 50 mM HEPES buffer. The titration data (A) are plotted as absorbance versus wavelength and the titration curves (B) are plotted as absorbance at $\lambda_{600\ nm}$ versus [Co^{II}]. The trace that correlates to one equivalent of [Co^{II}] added, with respect to 3SCC, is shown in red. The black circles represent the raw data and the non-linear best-fit curve is shown as a black line (Equation 7, as described in the Materials and Methods section).

An X-band EPR spectrum was collected for $Co^{II}_{N/O}$(**TRI**-$_D$LH)$_3^{n+}$ at 4K. The EPR spectrum for this sample is very different than any of the previously discussed samples. In fact, this sample looked very much like Co^{II}-coordinated to tris[2-(dimethylamino)ethyl]amine, Me_6TREN,[†] which is known to from a trigonal bipyramidal Co^{II}-complex (Figure 3-51).[58] The similarity observed between $Co^{II}_{N/O}$(**TRI**-$_D$LH)$_3^{n+}$ and Co^{II}(Me_6TREN)X (where X is a bound Cl^- or Br^-) suggest that when a $_D$Leu layer is introduced in the layer above the His_3 site, Co^{II} adopts a trigonal-bipyramidal geometry, with relatively high symmetry around the metal ion (due to the low extinction coefficients as determined via UV-Vis).

[†] Data collected at the University of Michigan for Feng Shao, a visiting scholar from the lab of Talal Mallah (Institut de Chimie Moléculaire et des Matériaux d'Orsay, CNRS, Université Paris Sud 11, 91405 Orsay Cedex, France.) Feng synthesized the Co^{II}-bound complex and I collected the EPR data.

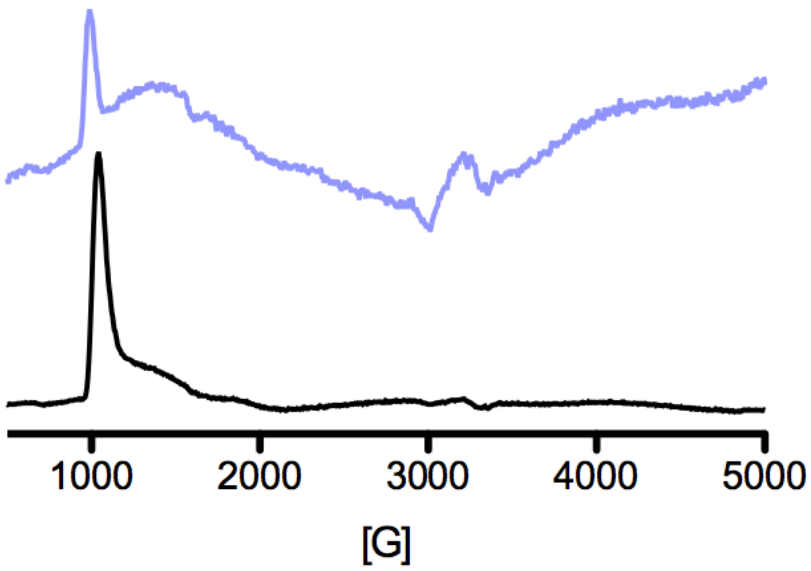

Figure 3-51. X-band EPR spectra of 1.0 mM $Co^{II}_{N/O}$(**TRI**-$_D$LH)$_3^{n+}$ (black) and 0.4 mM $Co^{II}_{N/X}$(Me_6Tren)X (purple) at pH 7.5 in 50 mM HEPES, collected at 4K.

Then, I inserted the $_D$LeuHis$_3$ binding site into a **GR** peptide, **GR**L2WL16CL26$_D$LL30H, or **GR**-C$_D$LH (Table 3-1), with the ultimate goal of utilizing Pb^{II}-nucleated heterotrimers to study the perturbed environment of Co^{II} sites consisting of varied numbers of $_D$Leu residues (comparable to the Asp$_X$His$_3$ studies above). However, when Co^{II}-binding studies via UV-Vis spectroscopy revealed that Co^{II} binds to the homotrimer, Pb^{II}_S(**GR**-C$_D$LH)$_3^{n+}$, non-specifically (Figure 3-52).[4] This is the first scenario in which elongating from a **TRI** peptide to a **GR** peptide resulted in the inability to bind Co^{II}. Therefore, future studies will be necessary to determine conditions where the desired heterotrimer can be formed with **GR** peptides or one may need to revert to forming heterotrimers with the **TRI** peptides.

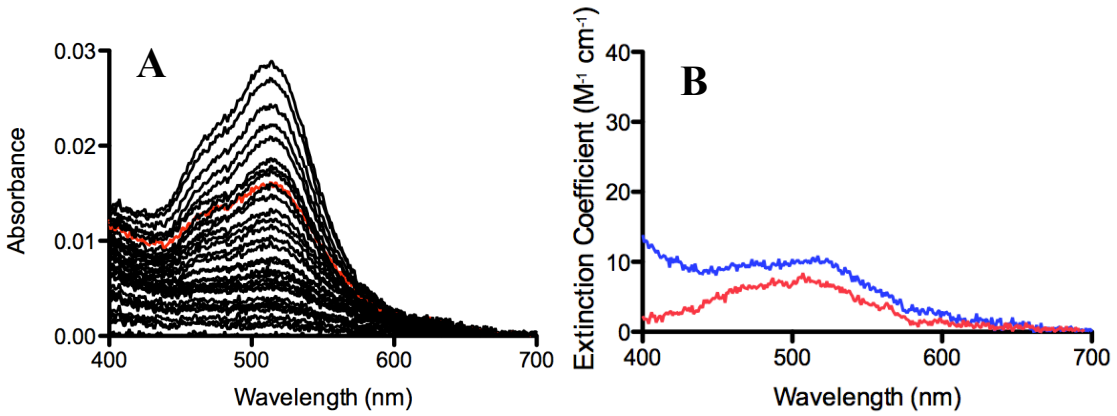

Figure 3-52. (A) UV-Vis titration of $Co^{II}SO_4$ added to a solution of 1.48 mM Pb^{II}_S(**GR**-C_DLH)$_3^{n+}$ at pH 7.5 in 50 mM HEPES buffer. The titration data are plotted as absorbance versus wavelength. The trace that correlates to one equivalent of [Co^{II}] added, with respect to 3SCC, is shown in red. (B) UV-Vis overlay $Pb^{II}_S Co^{II}_{N/O}$(**GR**-C_DLH)$_3^{n+}$ (blue) and Co^{II}_X(**TRI**L2W)$_3^{n+}$ (red). Experimental data are plotted as molar extinction coefficient (determined using Co^{II} concentration) versus wavelength.

Spectroscopic Comparison of Zn^{II} Heterotrimers to Co^{II} Heterotrimers

In comparison to Co^{II}, many spectroscopic techniques are unavailable to Zn^{II} due to the d^{10} electronic configuration, which makes it difficult to analyze the difference between Zn^{II}-bound homo- and heterotrimers. Additionally, crystal structures of Zn^{II}-bound to heterotrimers as well as Zn^{II}-bound to a symmetric Asp_3His_3 site, have proven elusive. However, some meterical parameters can be obtained via Zn^{II} XAS. The goal of this study was to determine if a similar change in coordination number is observed between the Zn^{II}-bound homo- and heterotrimers as observed in the Co^{II}-bound samples, which should be evidenced by both the XANES edge as well as the distances observed from the EXAFS best fits.

Samples consisted of 2 mM Pb^{II}-bound 3SCC, 1 mM $Zn^{II}SO_4$, ~30-50 mM buffer (HEPES, pH 7.5 and CHES, pH 9.5) and ~50% glycerol; all data were collected at ~7-11K. In general, the XANES spectra for all homo- and heterotrimers at both pH 7.5 and 9.5 are quite similar, indicating the overall coordination number and geometry of the Zn^{II} centers do not change significantly upon addition of aspartate residues or a change in pH between the samples (Figures 3-53A and 3-53B, respectively). However some variation

is observed at the different pH values in the relative intensities and peak energies (Figures 3-53C and 3-53D). Analysis of the edge peak at ~9667 eV, for the pH 7.5 samples, reveals that when one aspartic acid or no aspartic acid residues are present, very similar edge intensities are observed. In contrast, the presence of two or three aspartic acid residues results in systematic increases in the edge intensities (Figure 3-53D). This trend, increasing edge intensity with respect to the number of aspartic acid residues present, is observed at pH 9.5 as well. The only exception is the $Pb^{II}_{S}Zn^{II}_{N/O}[(\mathbf{GR}\text{-ACH})_1(\mathbf{GR}\text{-CDH})_2]^{n+}$ sample with two aspartic acid residues, which shows the lowest edge intensity (Figure 3-53C). The samples trend to higher edge energy with increasing numbers of aspartic acid residues available in the binding site for both pH values (Figure 3-53D).

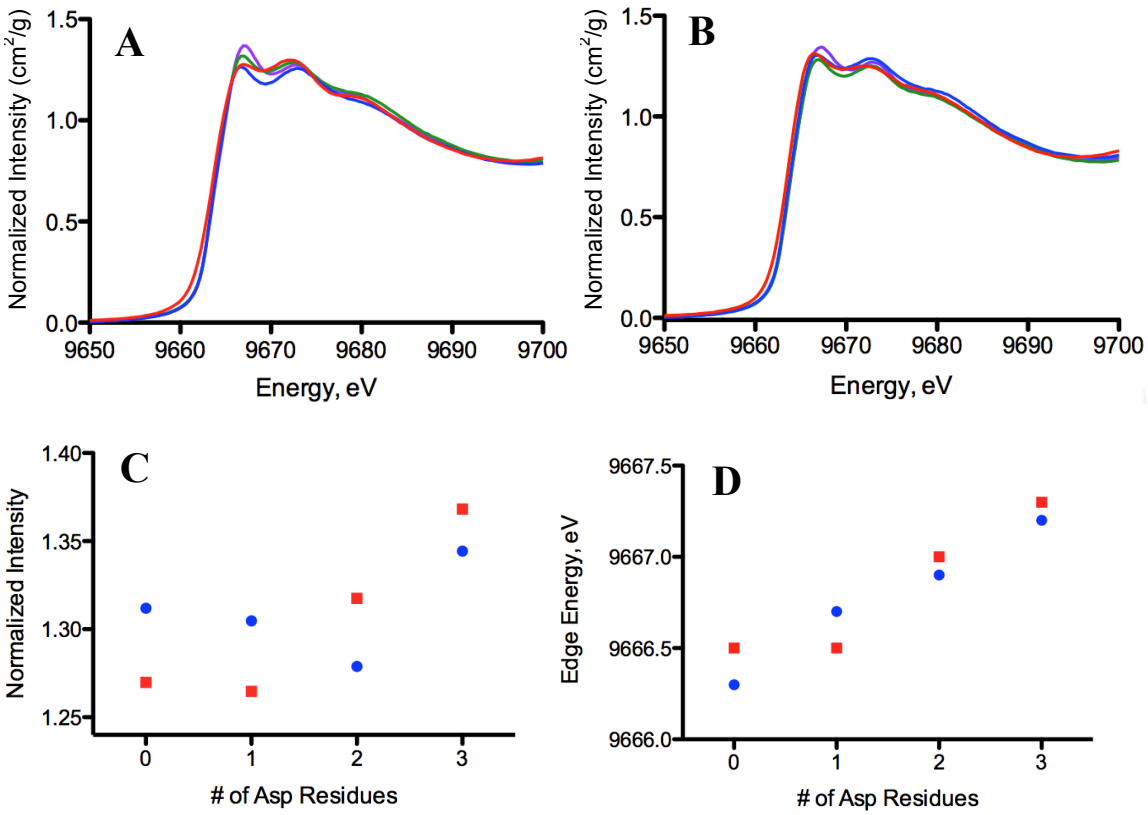

Figure 3-53. Overlay of XANES spectra showing the difference of the Zn^{II} edge at pH 7.5 (A) and 9.5 (B) of homotrimers: 1.0 mM $Pb^{II}_{S}Co^{II}_{N/O}(\mathbf{GR}\text{-ACH})_3^{n+}$ (red) and 1.0 mM $Pb^{II}_{S}Co^{II}_{N/O}(\mathbf{GR}\text{-CDH})_3^{n+}$ (purple) and heterotrimers: 1.0 mM $Pb^{II}_{S}Co^{II}_{N/O}[(\mathbf{GR}\text{-ACH})_2(\mathbf{GR}\text{-CDH})_1]^{n+}$ (blue) and 1.0 mM $Pb^{II}_{S}Co^{II}_{N/O}[(\mathbf{GR}\text{-ACH})_1(\mathbf{GR}\text{-CDH})_2]^{n+}$ (green). Figures (C) and (D) show the correlation of normalized edge intensity and edge energy verses the number of Asp residues in the Zn^{II} binding site, respectively, at pH 7.5 (red squares) and pH 9.5 (blue circles).

Overlaying the XANES spectra for each sample at the two pH values provides nearly identical spectra for both $Pb^{II}_{S}Zn^{II}_{N/O}$(**GR**-CDH)$_3^{n+}$ and $Pb^{II}_{S}Zn^{II}_{N/O}$[(**GR**-ACH)$_1$(**GR**-CDH)$_2$]$^{n+}$; however, subtle yet apparent differences are observed for $Pb^{II}_{S}Zn^{II}_{N/O}$(**GR**-ACH)$_3^{+}$ and $Pb^{II}_{S}Zn^{II}_{N/O}$[(**GR**-ACH)$_2$(**GR**-CDH)$_1$]$^{n+}$ (Figure 3-54). The similarities observed in the general traces indicate the same coordination number and geometry; however, observed differences may correlate to different coordinating ligands,[59] say N_2O_2 versus N_3O, or perhaps can be attributed to different protonation states of a presumed Zn^{II}-bound water molecule. Introduction of potential hydrogen bonding residues, such as the aspartate residues in my case, could result in perturbations to the pK_a of the Zn^{II}-bound water, and this could be the reason for the slight changes observed in the edge region.

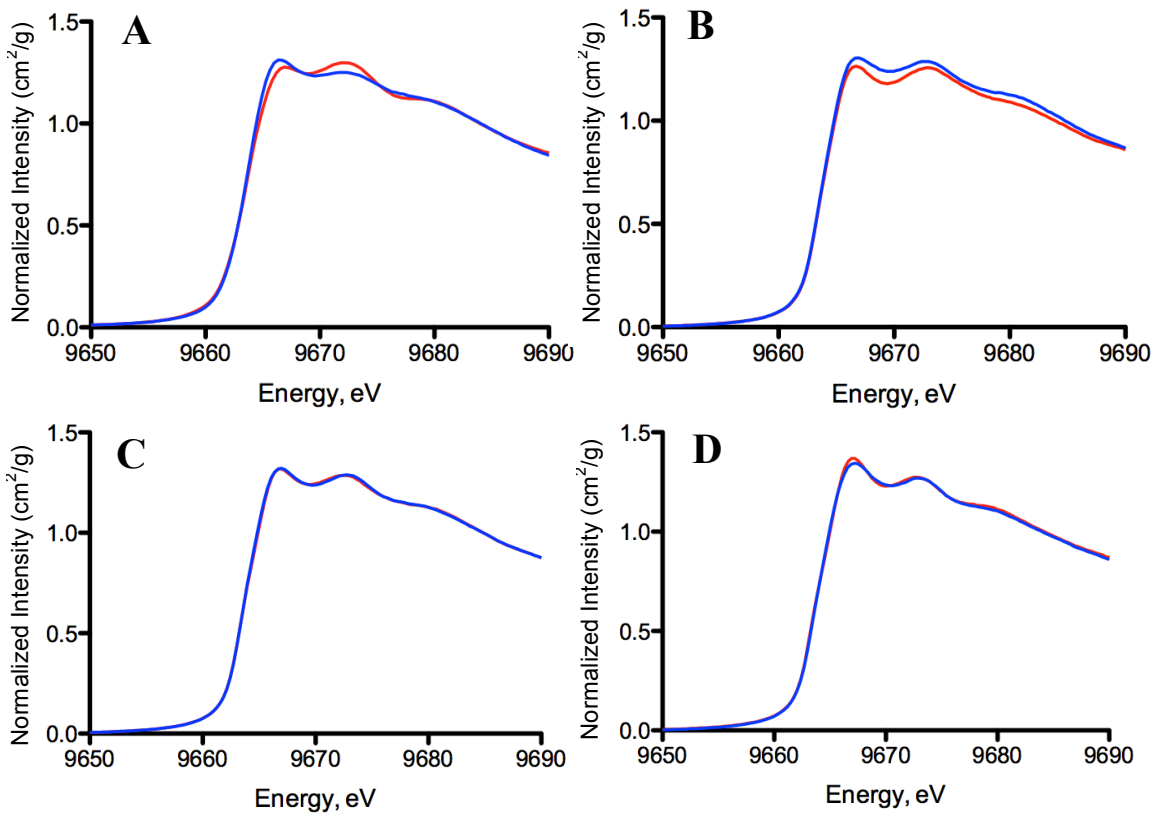

Figure 3-54. Overlay of XANES spectra showing the different of the Zn^{II} edge from pH 7.5 (red) and 9.5 (blue) for $Pb^{II}_{S}Co^{II}_{N/O}$(**GR**-ACH)$_3^{n+}$ (A), $Pb^{II}_{S}Co^{II}_{N/O}$[(**GR**-ACH)$_2$(**GR**-CDH)$_1$]$^{n+}$ (B), $Pb^{II}_{S}Co^{II}_{N/O}$[(**GR**-ACDH)$_1$(**GR**-CDH)$_2$]$^{n+}$ (C) and $Pb^{II}_{S}Co^{II}_{N/O}$(**GR**-CDH)$_3^{n+}$ (D), all samples are at 1.0 mM.

Similarly to what was observed for the Co^{II} samples, a nearest-neighbor peak, typical of scattering observed by direct nitrogen and/or oxygen metal coordination, dominates the EXAFS data and is best fit with a single nitrogen/oxygen shell at ~2.00 Å (Table 3-6 and Figure 3-55). There is also evidence in all of the Zn^{II}-bound homo- and heterotrimer samples, at pH 7.5 and 9.5, for outer shell scattering typical of histidine coordination (Figures 3-55, 3-56, 3-57, 3-58, 3-59, 3-60, 3-61, and 3-62, 2.5 < R < 4 Å). Multiple models with varying numbers of imidazole and oxygen ligands were used to fit these data including 4-, 5-, and 6-coordinate environments. In the case of every sample, at both pH values, the best-fit data correlated to a 4-coordinate environment (Table 3-6). Unfortunately, EXAFS fitting does not allow for the distinction between N_3O and N_2O_2 fits. In the cases of $Pb^{II}_{S}Zn^{II}_{N/O}[(\mathbf{GR}\text{-ACH})_2(\mathbf{GR}\text{-CDH})_1]^{n+}$ at pH 7.5 and $Pb^{II}_{S}Zn^{II}_{N/O}(\mathbf{GR}\text{-ACH})_3^{+}$ at pH 9.5, the fits for N_3O are not good (indicated by the very large goodness of fit values, Table 3-6). This latter point contradicts numerous crystal structures (e.g., of $Hg^{II}_{S}Zn^{II}(OH)_{N/O}(\mathbf{TRI}L9CL23H)_3^{+}$) that definitively show a tetrahedral $Zn^{II}His_3(OH_2)$ polyhedron.

Table 3-6. EXAFS fitting parameters for Zn^{II} binding to Asp_XHis_3 sites in homo- and heterotrimeric **GR** peptides at pH 7.5 and 9.5.

Peptide	Shell	pH	Zn^{II}-L distance, Å	DW	F
$Pb^{II}_{S}Zn^{II}_{N/O}(\mathbf{GR}\text{-ACH})_3^{+}$	N_2O_2	7.5	1.969	6.2, 4.5	71
		9.5	1.973	7.9, 2.3	58
	N_3O_1	7.5	1.969	7.6, 1.2	67
$Pb^{II}_{S}Zn^{II}_{N/O}(\mathbf{GR}\text{-CDH})_3^{n+}$	N_2O_2	7.5	1.964	5.0, 2.1	74
		9.5	1.966	4.1, 3.5	47
	N_3O_1	9.5	1.965	5.7, 0.5	54
$Pb^{II}_{S}Zn^{II}_{N/O}[(\mathbf{GR}\text{-ACH})_2(\mathbf{GR}\text{-CDH})_1)]^{n+}$	N_2O_2	7.5	1.969	4.7, 2.5	83
		9.5	1.965	4.1, 3.7	71
	N_3O_1	9.5	1.965	5.5, 1.1	80
$Pb^{II}_{S}Zn^{II}_{N/O}[(\mathbf{GR}\text{-ACH})_1(\mathbf{GR}\text{-CDH})_2)]^{n+}$	N_2O_2	7.5	1.960	5.0, 3.8	80
		9.5	1.967	4.7, 3.7	77
	N_3O_1	7.5	1.961	6.8, 1.2	86
		9.5	1.967	6.0, 1.0	83

All fits include multi-scattering parameters for His residues. N_3O_1 fits for $Pb^{II}_{S}Zn^{II}_{N/O}(\mathbf{GR}\text{-ACH})_3^{+}$ at pH 9.5, $Pb^{II}_{S}Zn^{II}_{N/O}(\mathbf{GR}\text{-CDH})_3^{n+}$ at pH 7.5, and $Pb^{II}_{S}Zn^{II}_{N/O}[(\mathbf{GR}\text{-ACH})_2(\mathbf{GR}\text{-CDH})_1)]^{n+}$ at pH 7.5 resulted in unreasonable Zn^{II}-L distances of >2.4 Å or negative DW factors and have therefore been omitted. DW and F correspond to Debye Waller factors and goodness of fit parameters, respectively.

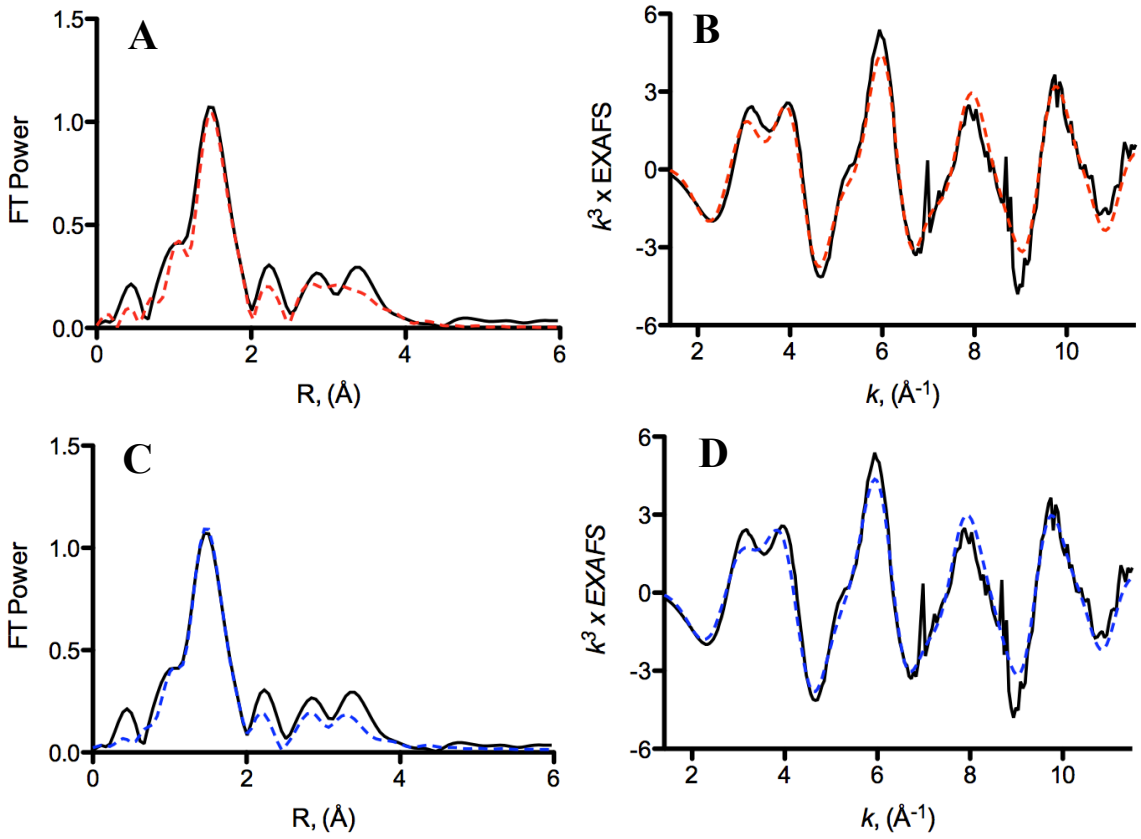

Figure 3-55. Fourier transform of Zn^{II} EXAFS of 1.0 mM $Pb^{II}_{S}Zn^{II}_{N/O}$(**GR**-ACH)$_3^{n+}$ (A, C) and the Zn^{II} EXAFS (B, D) at pH 7.5. Experimental data is shown in black and the equally good fits for N_3O_1 for the FT and EXAFS are shown in A and B (red dashed line) and for N_2O_2 are shown in C and D (blue dashed line).

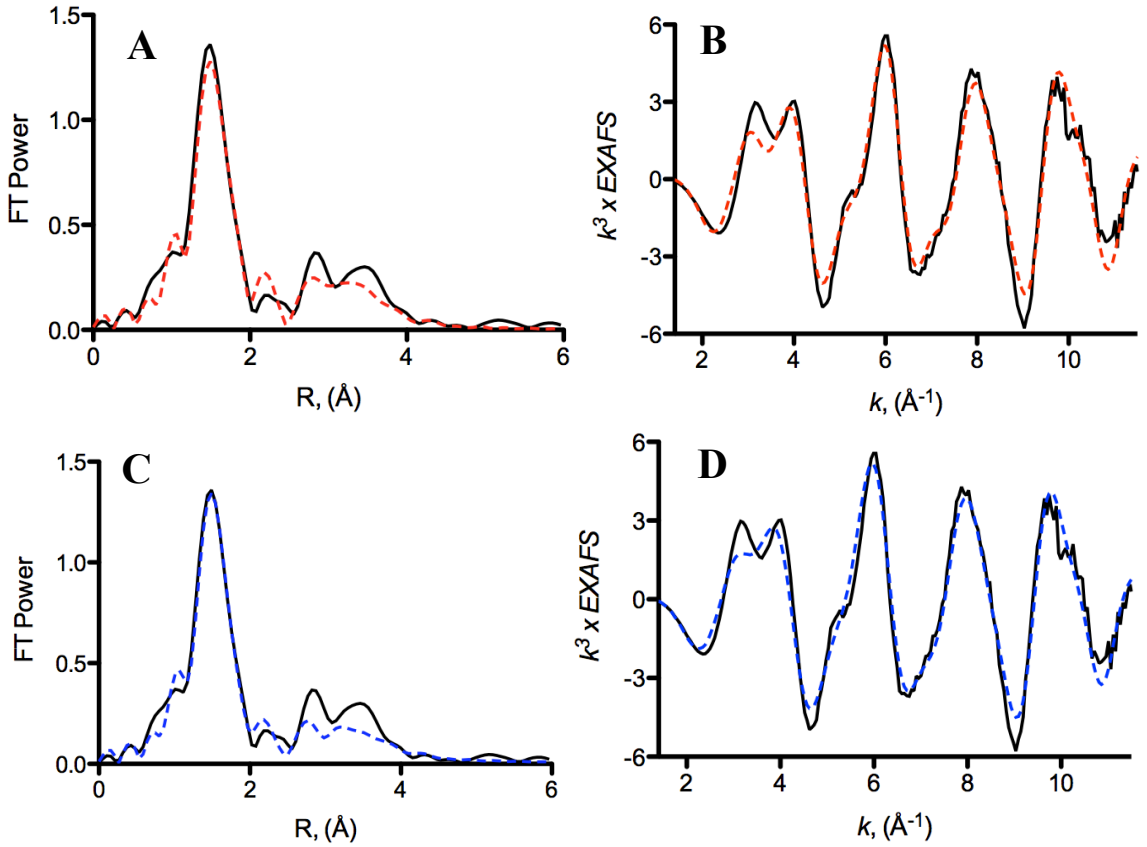

Figure 3-56. Fourier transform of Zn^{II} EXAFS of 1.0 mM $Pb^{II}_{S}Zn^{II}_{N/O}$[(**GR**-ACH)$_2$(**GR**-CDH)$_1$]$^{n+}$ (A, C) and the Zn^{II} EXAFS (B, D) at pH 7.5. Experimental data is shown in black and the equally good fits for N_3O_1 for the FT and EXAFS are shown in A and B (red dashed line) and for N_2O_2 are shown in C and D (blue dashed line).

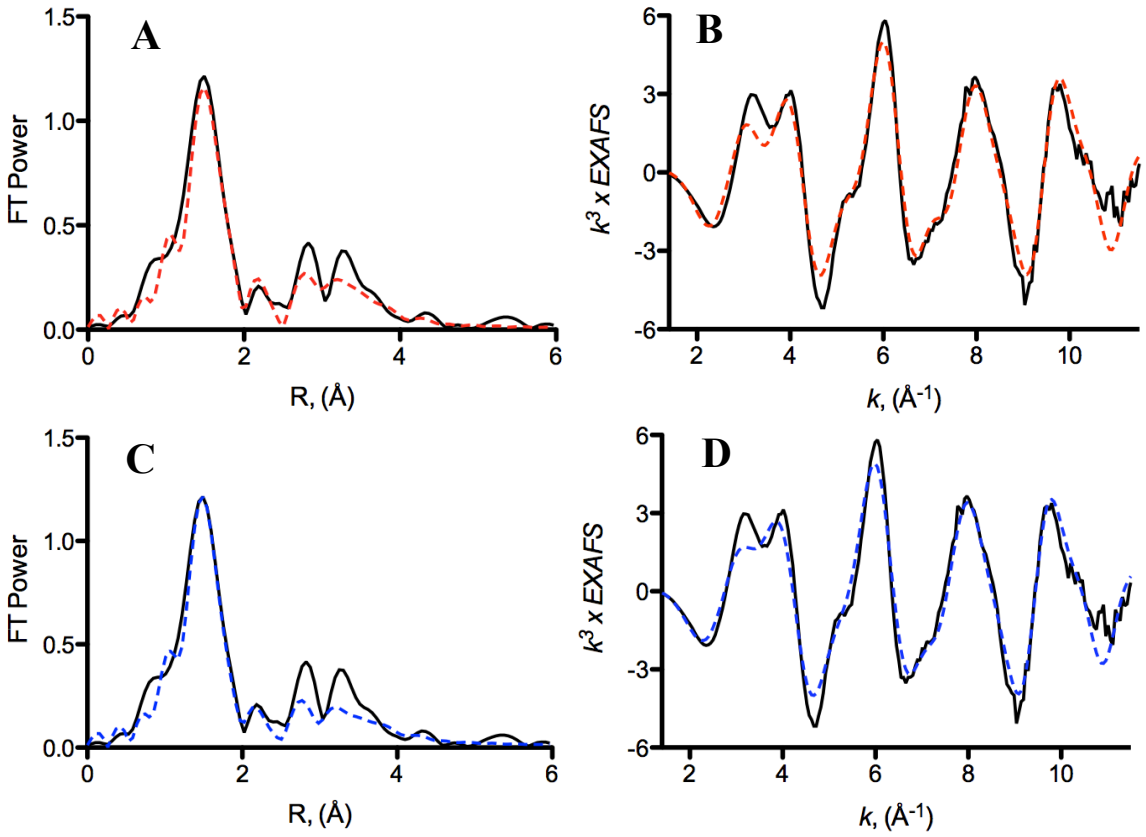

Figure 3-57. Fourier transform of Zn^{II} EXAFS of 1.0 mM $Pb^{II}_{S}Zn^{II}_{N/O}[(\mathbf{GR}\text{-ACH})_1(\mathbf{GR}\text{-CDH})_2]^{n+}$ (A, C) and the Zn^{II} EXAFS (B, D) at pH 7.5. Experimental data is shown in black and the equally good fits for N_3O_1 for the FT and EXAFS are shown in A and B (red dashed line) and for N_2O_2 are shown in C and D (blue dashed line).

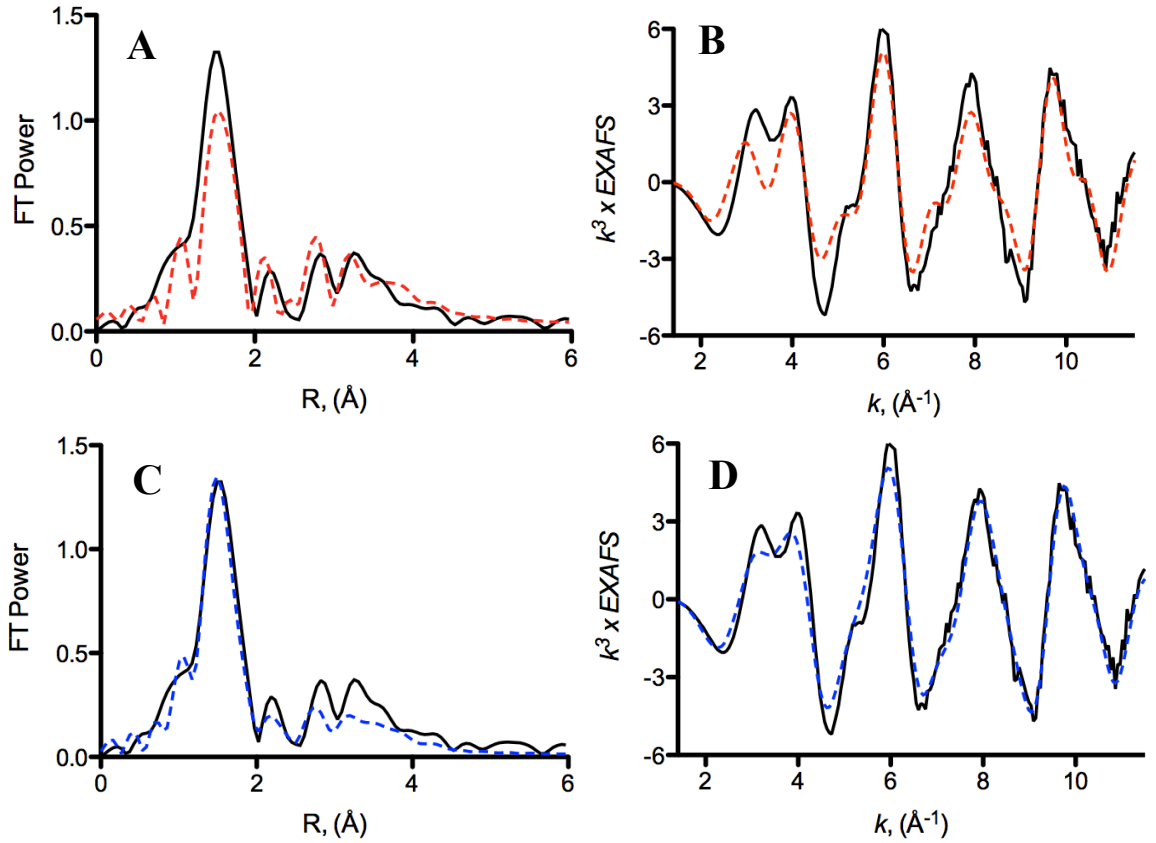

Figure 3-58. Fourier transform of Zn^{II} EXAFS of 1.0 mM $Pb^{II}_{S}Zn^{II}_{N/O}$(**GR**-CDH)$_3^{n+}$ (A, C) and the Zn^{II} EXAFS (B, D) at pH 7.5. Experimental data is shown in black and the equally good fits for N_3O_1 for the FT and EXAFS are shown in A and B (red dashed line) and for N_2O_2 are shown in C and D (blue dashed line).

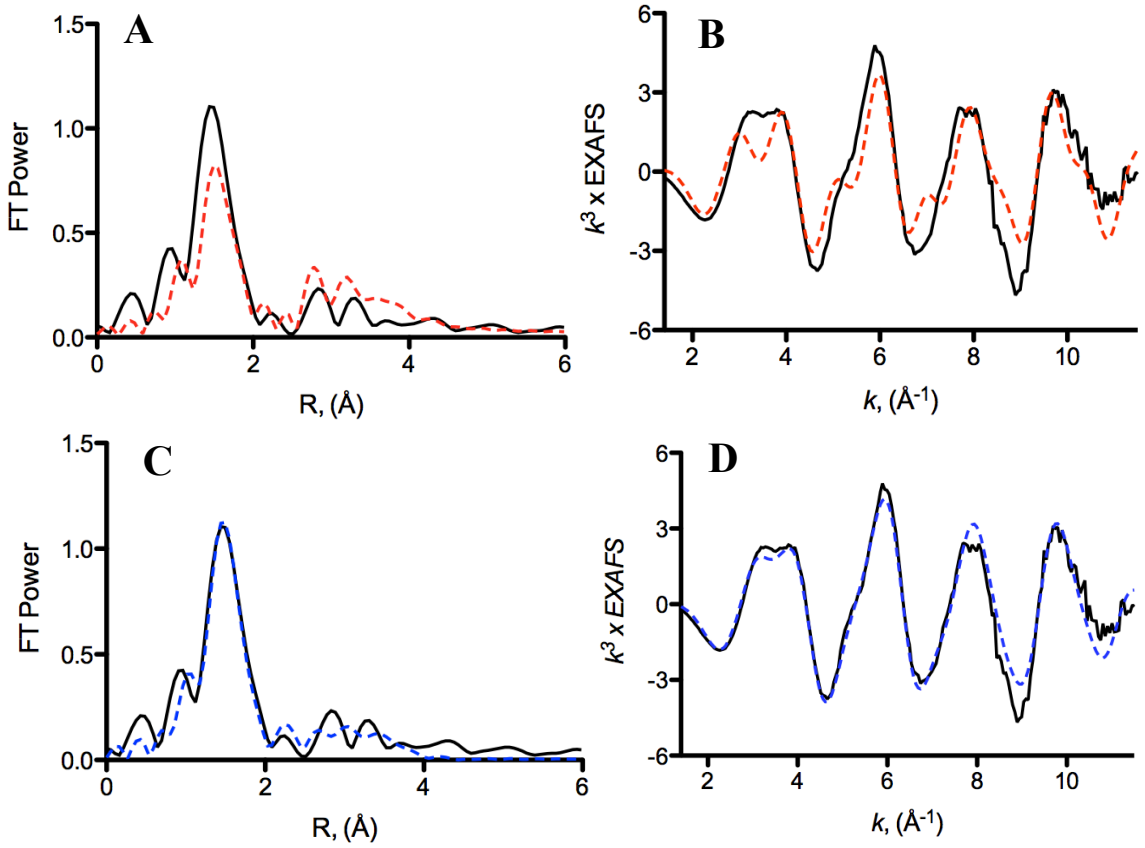

Figure 3-59. Fourier transform of Zn^{II} EXAFS of 1.0 mM $Pb^{II}_{S}Zn^{II}_{N/O}$(**GR**-ACH)$_3^{n+}$ (A, C) and the Zn^{II} EXAFS (B, D) at pH 9.5. Experimental data is shown in black and the equally good fits for N_3O_1 for the FT and EXAFS are shown in A and B (red dashed line) and for N_2O_2 are shown in C and D (blue dashed line).

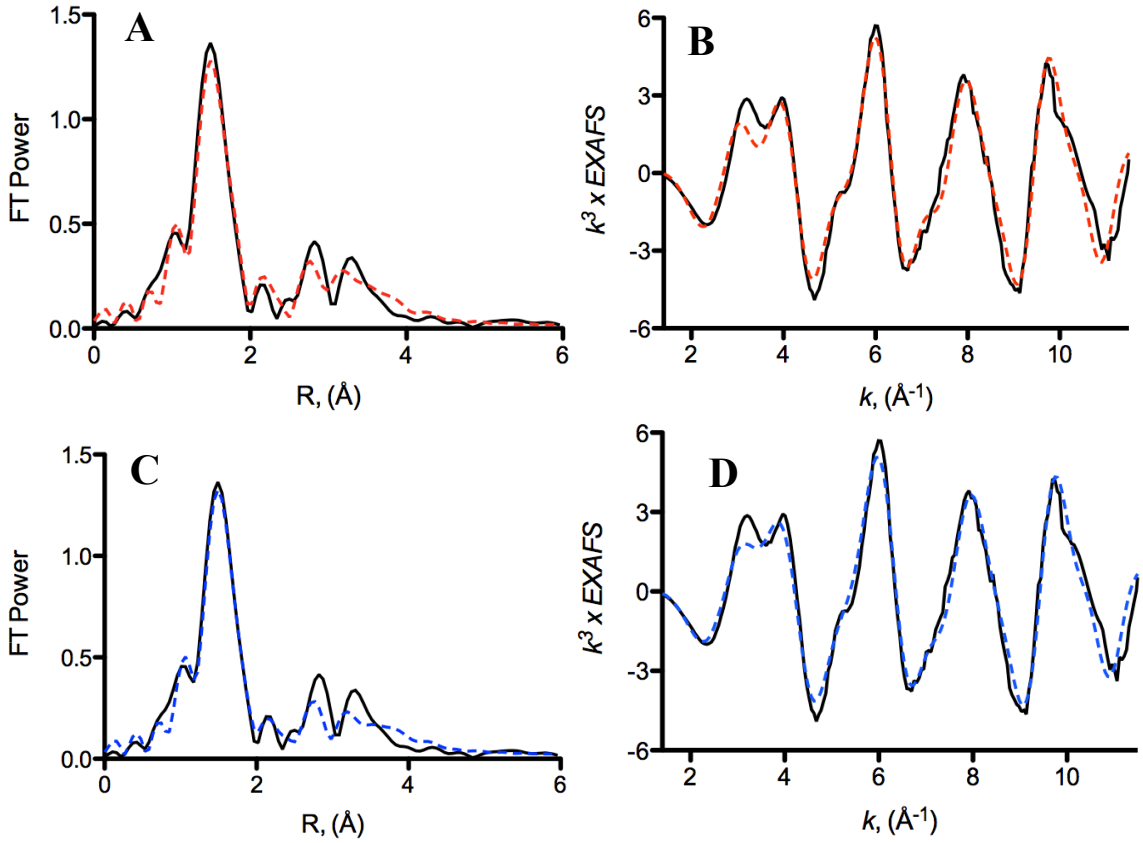

Figure 3-60. Fourier transform of Zn^{II} EXAFS of 1.0 mM $Pb^{II}_{S}Zn^{II}_{N/O}[(\mathbf{GR}\text{-ACH})_2(\mathbf{GR}\text{-CDH})_1]^{n+}$ (A, C) and the Zn^{II} EXAFS (B, D) at pH 9.5. Experimental data is shown in black and the equally good fits for N_3O_1 for the FT and EXAFS are shown in A and B (red dashed line) and for N_2O_2 are shown in C and D (blue dashed line).

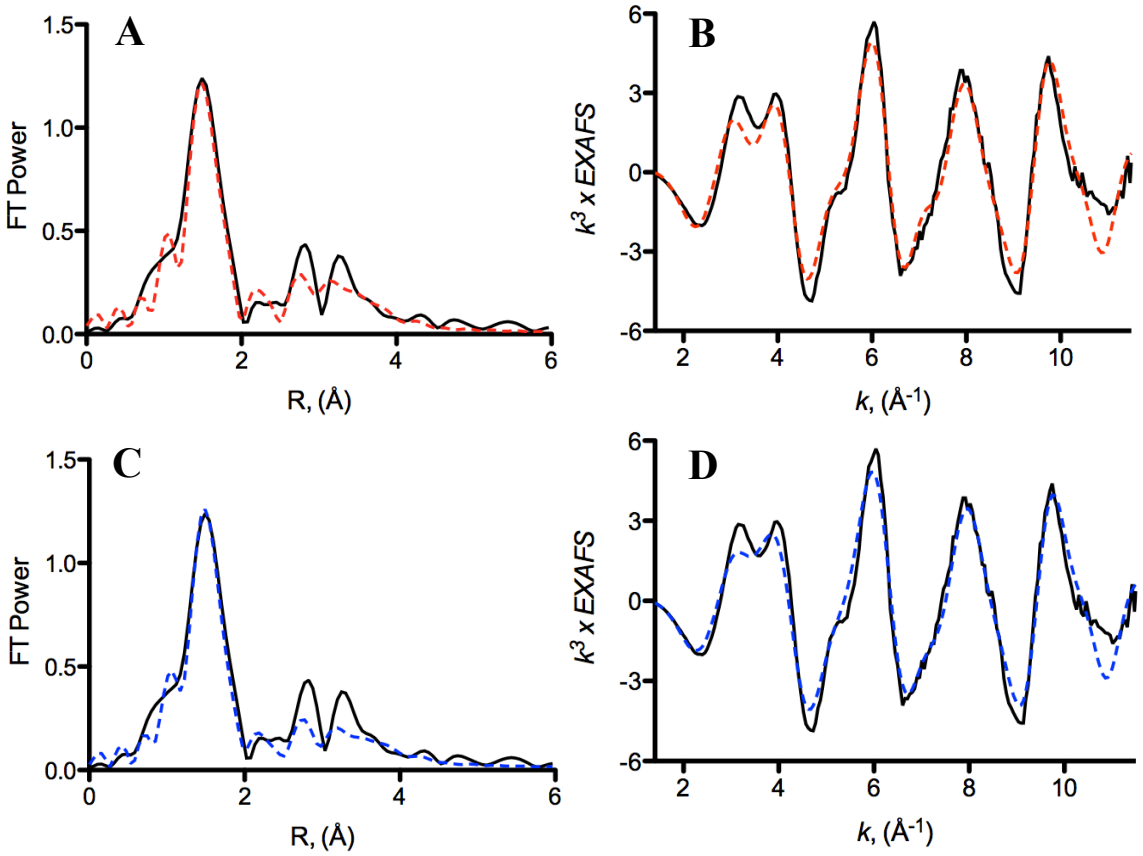

Figure 3-61. Fourier transform of Zn^{II} EXAFS of 1.0 mM $Pb^{II}_{S}Zn^{II}_{N/O}$[(**GR**-ACH)$_1$(**GR**-CDH)$_2$]$^{n+}$ (A, C) and the Zn^{II} EXAFS (B, D) at pH 9.5. Experimental data is shown in black and the equally good fits for N_3O_1 for the FT and EXAFS are shown in A and B (red dashed line) and for N_2O_2 are shown in C and D (blue dashed line).

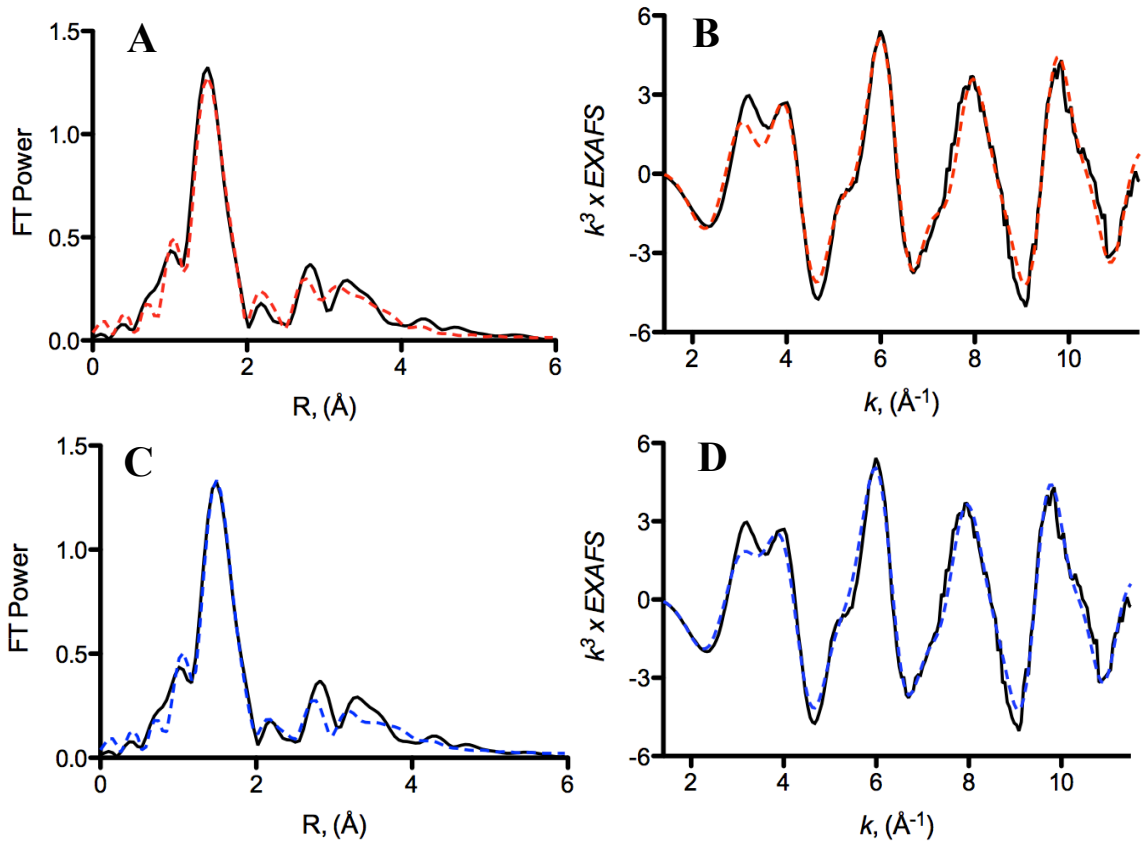

Figure 3-62. Fourier transform of Zn^{II} EXAFS of 1.0 mM $Pb^{II}_{S}Zn^{II}_{N/O}$(**GR**-CDH)$_3^{n+}$ (A, C) and the Zn^{II} EXAFS (B, D) at pH 7.5. Experimental data is shown in black and the equally good fits for N_3O_1 for the FT and EXAFS are shown in A and B (red dashed line) and for N_2O_2 are shown in C and D (blue dashed line).

As shown in Table 3-6, the change in bond distances and goodness of fits from N_2O_2 to N_3O fitting parameters is negligible (except in the cases of $Pb^{II}_{S}Zn^{II}_{N/O}$[(**GR**-ACH)$_2$(**GR**-CDH)$_1$]$^{n+}$ at pH 7.5 and $Pb^{II}_{S}Zn^{II}_{N/O}$(**GR**-ACH)$_3^{+}$ at pH 9.5), indicating two things. First, these similarities indicate that the identities of the coordinating ligands cannot be elucidated from the EXAFS fits to help explain the difference in the XANES spectra; however, with bond distances of 1.96 ± 0.1Å, the EXAFS fits do corroborate a four-coordinate Zn^{II} environment for all of the peptide samples. Second, when compared to reported four-coordinate small molecule Zn^{II} complexes (Table 3-7), we see that all of the distances provided from the fits are only slightly shorter, again supporting a 4-coordinate environment in all of my Zn^{II}-bound homo- and heterotrimers.

Table 3-7. Zn^{II}-N/O bond distances for relevant $Zn^{II}N_3O$ small molecule complexes

Complex	$R(Zn^{II}\text{-}N)_{avg}$, Å	$R(Zn^{II}\text{-}O)$, Å	Reference
$\{[Pim^{iPr,tBu}]ZnOH\}(ClO_4)$	2.082	1.860[a]	73
$[(TriMIm)Zn^{II}(OH_2)](BF_4)_2$	2.129	2.003[b]	75
$[L1Zn^{II}(OH_2)(BNPP)_2 \bullet 6H_2O$	2.028	1.984[b]	74
$[L1Zn^{II}(OH)]ClO_4 \bullet 1.5H_2O$	2.015	2.046[a]	74

[a]Zn-O ligand is (OH). [b]Zn^{II}-O ligand is (OH_2).

Ultimately, crystal structures are required to characterize the identities of the coordinating ligands within the Zn^{II}-bound systems further. It is of great significance to note the difference in coordination number, obtained via XAS analysis, and supported via EPR and UV-Vis spectroscopy for the Co^{II} species, between the Zn^{II} and Co^{II} systems. At this point, a 5- or 6-coordinate environment best characterizes all but one of the Co^{II}-bound peptides but ALL of the Zn^{II} XAS data suggest 4-coordinate Zn^{II} environments. This is very interesting to note since it supports the contention that in all the cases of my homo- and heterotrimeric peptide scaffolds that Co^{II} is a non-innocent spectroscopic probe for Zn^{II}. As mentioned above, Co^{II} is regularly used as a spectroscopic probe for Zn^{II} but Co^{II} is also commonly used because when substituted in Zn^{II}-metalloenzymes significant activity is often retained.[25,60,61] However, studies have indicated that Co^{II} has a tendency to adopt higher coordination numbers when substituted for Zn^{II} in both small molecules and native metalloenzymes.[26,35,62–64] Indeed, Co^{II}-substituted CA has been reported to adopt four-,[26,63,65] five-,[26,35,63] and six-coordinate[35,64] geometries. The work presented here is a clear indication of a case when Co^{II}-coordination does not necessarily offer a good picture for what is happening with Zn^{II}.

To characterize the properties of Zn^{II} binding further, I used the colorimetric chelator, Zincon (Zi), in competitive binding titrations, to measure the apparent dissociation constants of Zn^{II} to both homo- and heterotrimeric peptides at pH 9.0. First, I determined the Zn^{II} binding to $Pb^{II}_S(\mathbf{GR}\text{-}CH)_3^-$ to determine if the metal bound to the Cys_3 site had any influence on the Zn^{II}-His_3 binding. An apparent dissociation constant of 0.17 ± 0.09 μM was obtained from the fit from Equation 15 using Prism 5 (GraphPad Software)[8] and is comparable to the value obtained, by Dr. Melissa Zastrow, of 0.11 ± 0.05 μM for $Hg^{II}_S Zn^{II}_{N/O}(\mathbf{GR}\text{-}CH)_3^{n+}$ (Figure 3-63, Table 3-8).[4] This supports the

assumption that the Zn^{II} binding affinity is independent of the metal bound the Cys_3 structural (Hg^{II}) or nucleation (Pb^{II}) site.

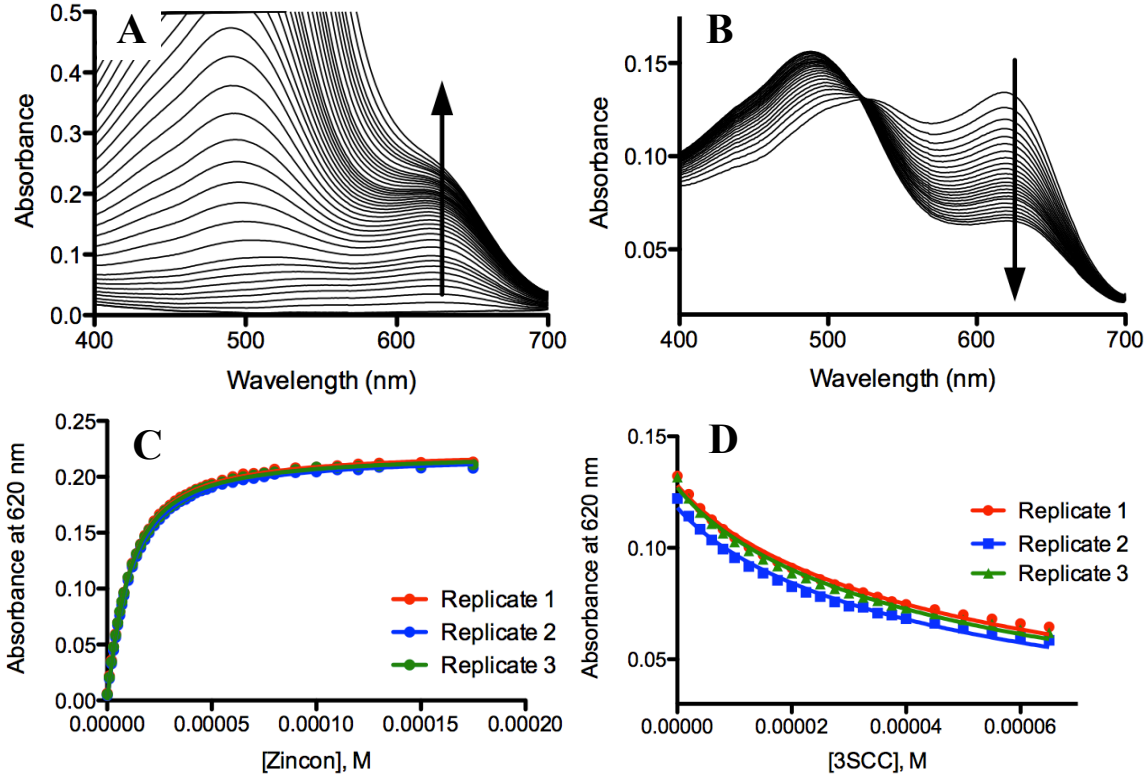

Figure 3-63. Competitive Zn^{II}-binding titrations versus Zincon at pH 9.0 for Pb^{II}_S(**GR**-CH)$_3^-$ in the forward (10 μM $Pb^{II}_SZn^{II}_{N/O}$(**GR**-CH)$_3^{n+}$ + Zi) and reverse (5 μM Zn^{II}Zi + Pb^{II}_S(**GR**-CH)$_3^{n+}$) direction. Representative UV-Vis spectra for the titration in the A) forward and B) reverse directions. C) Titration curve of Abs at 620 nm as a function of [Zi] for the forward titration and D) Titration curve of Abs at 620 nm as a function of [3SCC] for the reverse titration.

Table 3-8. Apparent dissociation constants for Zn^{II} binding to Asp_XHis_3 sites in the **TRI** and **GR** peptides at pH 9.0.

Peptide	$K_{d,\ app}$ (μM)
$Pb^{II}_SZn^{II}_{N/O}$(**GR**-ACH)$_3^+$	0.17 ± 0.10
$Hg^{II}_SZn^{II}_{N/O}$(**GR**-CDH)$_3^{n+}$	0.0031 ± 0.0010*
$Hg^{II}_SZn^{II}_{N/O}$(**GR**-CTH)$_3^{n+}$	0.0023 ± 0.0014*
$Hg^{II}_SZn^{II}_{N/O}$(**GR**-CH)$_3^{n+}$	0.11 ± 0.05*
$Pb^{II}_SZn^{II}_{N/O}$[(**GR**-ACH)$_2$(**GR**-CDH)$_1$)]$^{n+}$	1.10 ± 0.60
$Pb^{II}_SZn^{II}_{N/O}$[(**GR**-ACH)$_2$(**GR**-CTH)$_1$)]$^{n+}$	0.71 ± 0.30

*Data collected by Dr. Melissa Zastrow.[4]

Then, I determined the apparent dissociation constant of Zn^{II} to the heterotrimer, $Pb^{II}_S[(\mathbf{GR}\text{-ACH})_2(\mathbf{GR}\text{-CDH})_1]^{n+}$, to be 1.1 ± 0.6 μM (Figure 3-64A and 3-64B, Table 3-8). This value is a factor of ten larger than the corresponding homotrimers, perhaps due to the preference of Zn^{II} to bind the nitrogen atoms of the His_3 layer more so than the Asp ligands as introduced in the heterotrimer. A second, and perhaps more likely possibility, is that the introduction of only one Asp residue introduces a hydrogen bonding interaction to a Zn^{II}-bound water molecule resulting in a perturbation of the Zn^{II} binding affinity. Future studies of the Zn^{II} binding affinity for the opposite heterotrimer, $Pb^{II}_S[(\mathbf{GR}\text{-ACH})_1(\mathbf{GR}\text{-CDH})_2]^{n+}$, may help determine a trend in Zn^{II} binding preferences.

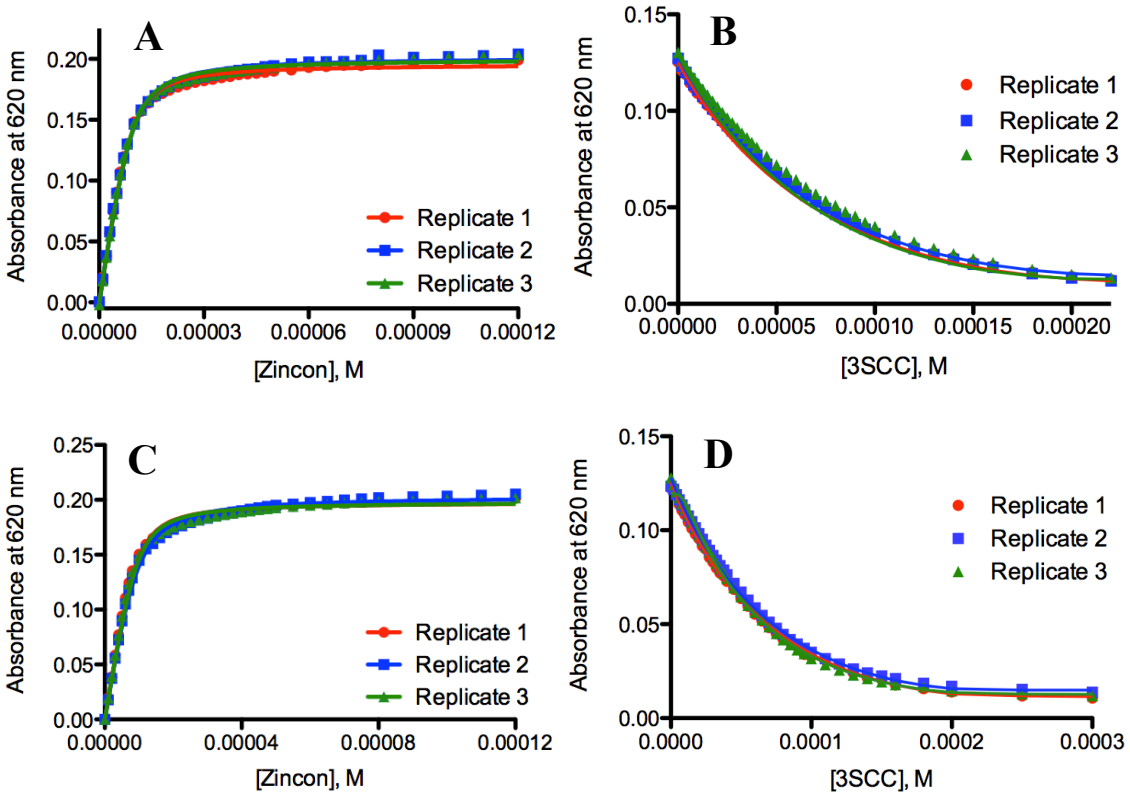

Figure 3-64. Competitive Zn^{II}-binding titrations versus Zincon, in the forward (10 μM $Zn^{II}Pep_3$ + Zi) and reverse (5 μM $Zn^{II}Zi$ + 3SCC) directions at pH 9.0 for heterotrimers with asymmetric second metal binding sites. Plots show titration data of Abs at 620 nm vs [Zi] or [3SCC] for $Pb^{II}_S[(\mathbf{GR}\text{-ACH})_2(\mathbf{GR}\text{-CDH})_1]^-$ (A: forward, B: reverse) and for $Pb^{II}_S[(\mathbf{GR}\text{-ACH})_2(\mathbf{GR}\text{-CTH})_1]^-$ (C: forward, D: reverse).

At this particular point, I was also curious about the possibility of placing one Thr residue in close proximity to the His_3 site, which would directly mimic CA. I analyzed Zn^{II} binding to $Pb^{II}_S[(\mathbf{GR}\text{-ACH})_2(\mathbf{GR}\text{-CTH})_1]^{n+}$, where **GR**-CTH is

GRL2WL16CL26TL30H (Table 3-1). This mixture provided a dissociation constant of 0.71 ± 0.30 μM (Figures 3-64C and 3-64D, Table 3-8), comparable to the $Pb^{II}_{S}[(\mathbf{GR}\text{-ACH})_2(\mathbf{GR}\text{-CDH})_1]^{n+}$ heterotrimer. In the cases of both Thr and Asp heterotrimers we see dissociation constants that are weaker than the corresponding homotrimers by a factor of ~200-fold (0.0031 ± 0.0005 μM and 0.0023 ± 0.0014 μM for $Hg^{II}_{S}Zn^{II}_{N/O}(\mathbf{GR}\text{-CDH})_3^{n+}$ and $Hg^{II}_{S}Zn^{II}_{N/O}(\mathbf{GR}\text{-CTH})_3^{n+}$, respectively, Table 3-8). The weaker Zn^{II} binding to the heterotrimers, in comparison to the homotrimers, is opposite of what was observed for Co^{II} binding to the same peptides. (Co^{II} binding to $Pb^{II}_{S}[(\mathbf{GR}\text{-ACH})_2(\mathbf{GR}\text{-CTH})_1]^{n+}$ produces an apparent dissociation constant of 12.5 ± 2.3 μM, Table 3-3). The differences in the dissociation constants between Zn^{II} and Co^{II} may be a direct consequence of the different coordination environments as suggested by the EXAFS analyses. A second explanation for the opposite trends observed between metals is that when an oxygen containing ligand is introduced, asymmetrically, the propensity of the Co^{II} to bind to it, and therefore uncoordinating one His ligand, is more likely than that for Zn^{II}, which may prefer to stay bound to all three His residues regardless of the secondary coordination sphere changes.

In general, Co^{II} binds to the peptides in this study with apparent dissociation constants of 8-50 uM (at pH 7.5, with the exception of $Pb^{II}_{S}Co^{II}_{N/O}(\mathbf{GR}\text{-CHD})_3^{n+}$), whereas Zn^{II} binds tighter with apparent dissociation constants of 3 nm – 1 μM (at pH 9.0). This trend is consistent with that observed in native metalloenzymes, such as CA and CPA, where Zn^{II} binding is ~10^3 tighter than Co^{II} binding. Zn^{II} binding is also ~10^{-3} M tighter in CA (K_d = 4.0 pm) compared to the reported values here, but is on the same order of magnitude when compared to Zn^{II}-CPA (K_d = 4.7 nM).[66,67] This trend is also consistent with Co^{II} binding, where Co^{II}-binds to CA with an apparent dissociation constant of 20 nM (10^{-3} M tighter than my systems) and to CPA with K_d = 1.5 μM (comparable to my systems).[67,68] These data support that whether the site is N_2O_2 or N_3O, like CPA or CA, respectively, that Zn^{II} binds tigther than Co^{II}, as is also observed in nature. Future studies at comparable pH values should be conducted (current studies for Co^{II} binding are at pH 7.5 and Zn^{II} are at 9.0) before further comparisons between Co^{II} and Zn^{II} binding affinities are made.

Preliminary Kinetics Studies of Zn^{II}-bound heterotrimers

As mentioned in Chapter 1, Dr. Melissa Zastrow determined that elongation from $Hg^{II}_{S}Zn^{II}_{N/O}$(**TRI**L9CL23H)$_3^{n+}$ to $Hg^{II}_{S}Zn^{II}_{N/O}$(**GR**-CH)$_3^{n+}$ resulted in a 20% decrease in catalytic efficiency from 23.3 ± 0.3 $M^{-1}s^{-1}$ to 18.5 ± 0.6 $M^{-1}s^{-1}$ for *p*NPA hydrolysis (Table 3-9).[4] Addition of a Thr residue, resulting in the homotrimeric 3-fold substituted $Hg^{II}_{S}Zn^{II}_{N/O}$(**GR**-CTH)$_3^{n+}$ peptide, resulted in a slightly decreased catalytic efficiency of 14.8 $M^{-1}sec^{-1}$ (Table 3-9). Conversely, when she included an Asp residue, resulting in the $Hg^{II}_{S}Zn^{II}_{N/O}$(**GR**-CDH)$_3^{n+}$ homotrimer, she observed a catalytic efficiency comparable to the original **TRI** peptide of 24.2 ± 2.5 $M^{-1}s^{-1}$ (Table 3-9). Although the work done for this chapter focused heavily on the spectroscopic characterization of heterotrimeric peptides, I also wanted to present preliminary kinetic data to determine if the heterotrimeric peptides offered any improvement over the catalytic efficiencies provided by the homotrimeric scaffolds.

Table 3-9. Kinetic parameters for hydrolysis of *p*NPA by homo- and heterotrimeric **TRI** and **GR** peptides at pH 9.5.

Peptide	k_{cat}/K_M, $M^{-1}s^{-1}$	k_{cat}, s^{-1}	K_M, mM
$Hg^{II}_{S}Zn^{II}_{N/O}$(**TRI**L9CL23H)$_3^{n+}$	23.3 ± 0.3	0.040 ± 0.012	1.5 ± 0.5
$Hg^{II}_{S}Zn^{II}_{N/O}$(**GR**-CH)$_3^{n+}$	18.5 ± 0.6	0.064 ± 0.007	3.5 ± 0.5
$Hg^{II}_{S}Zn^{II}_{N/O}$(**GR**-CDH)$_3^{n+}$	24.2 ± 2.5	0.024 ± 0.004	1.0 ± 2.0
$Hg^{II}_{S}Zn^{II}_{N/O}$(**GR**-CTH)$_3^{n+}$	14.8 ± 1.4	0.056 ± 0.026	3.8 ± 2.1
Hg^{II}_{S}(**TRI**L9C)$_3^{-}$	1.9 ± 0.3	-	-
$Pb^{II}_{S}Zn^{II}_{N/O}$[(**GR**-ACH)$_2$(GR-CH)$_1$]$^{n+}$	23.5 ± 1.9	0.011 ± 0.001	0.5 ± 0.1
$Pb^{II}_{S}Zn^{II}_{N/O}$[(**GR**-ACH)$_2$(**GR**-CDH)$_1$)]$^{n+}$	25.1 ± 2.5	0.021 ± 0.003	0.8 ± 0.2
$Pb^{II}_{S}Zn^{II}_{N/O}$[(**GR**-ACH)$_2$(**GR**-CTH)$_1$)]$^{n+}$	20.6 ± 2.1	0.030 ± 0.007	1.5 ± 0.7
Pb^{II}_{S}[(**GR**-AC)$_2$(GR-C)$_1$]$^{n+}$	11.2 ±1.6	0.740 ± 0.025	6.8 ± 3.0

Data for all peptide catalysts with Hg^{II} bound were collected by Dr. Melissa Zastrow.[4]

To achieve this objective, I evaluated $Pb^{II}_{S}Zn^{II}_{N/O}$[(**GR**-ACH)$_2$(**GR**-CTH)$_1$]$^{n+}$ and $Pb^{II}_{S}Zn^{II}_{N/O}$[(**GR**-ACH)$_2$(**GR**-CDH)$_1$]$^{n+}$ for their hydrolytic activity towards *p*NPA. Both $Pb^{II}_{S}Zn^{II}_{N/O}$[(**GR**-ACH)$_2$(**GR**-CDH)$_1$]$^{n+}$ and $Pb^{II}_{S}Zn^{II}_{N/O}$[(**GR**-ACH)$_2$(**GR**-CTH)$_1$]$^{n+}$ show saturation kinetics for *p*NPA hydrolysis at pH 9.5 (Figures 3-65A and 3-65B). The catalytic efficiencies are 20.6 ± 2.1 and 25.1 ± 2.5 $M^{-1}s^{-1}$ (Table 3-9), both of which are within error of the rates determined for the original $Hg^{II}_{S}Zn^{II}_{N/O}$(**TRI**L9CL23H)$_3^{+}$ system. The rates for these systems are 0.030 ± 0.007 and 0.021 ± 0.003 sec^{-1}, respectively for $Pb^{II}_{S}Zn^{II}_{N/O}$[(**GR**-ACH)$_2$(**GR**-CTH)$_1$]$^{n+}$ and $Pb^{II}_{S}Zn^{II}_{N/O}$[(**GR**-ACH)$_2$(**GR**-CDH)$_1$]$^{n+}$,

compared to 0.04 s^{-1} for the original model (Table 3-9). The K_M values are both slightly lower than the original mimic (~2 mM) at 1.5 ± 0.5 and 0.8 ± 0.2 mM for $Pb^{II}_{S}Zn^{II}_{N/O}[(\mathbf{GR}\text{-ACH})_2(\mathbf{GR}\text{-CTH})_1]^{n+}$ and $Pb^{II}_{S}Zn^{II}_{N/O}[(\mathbf{GR}\text{-ACH})_2(\mathbf{GR}\text{-CDH})_1]^{n+}$, respectively (Table 3-9). The lower K_M rates suggest that even though the Zn^{II} binding is weaker, there is better substrate access to the Zn^{II} site. At this point it seemed as though the heterotrimers offer comparable rates when compared to the original $Hg^{II}_{S}Zn^{II}_{N/O}(\mathbf{TRI}\text{L9CL23H})_3^{n+}$ and $Hg^{II}_{S}Zn^{II}_{N/O}(\mathbf{GR}\text{-CDH})_3^{n+}$ homotrimers.

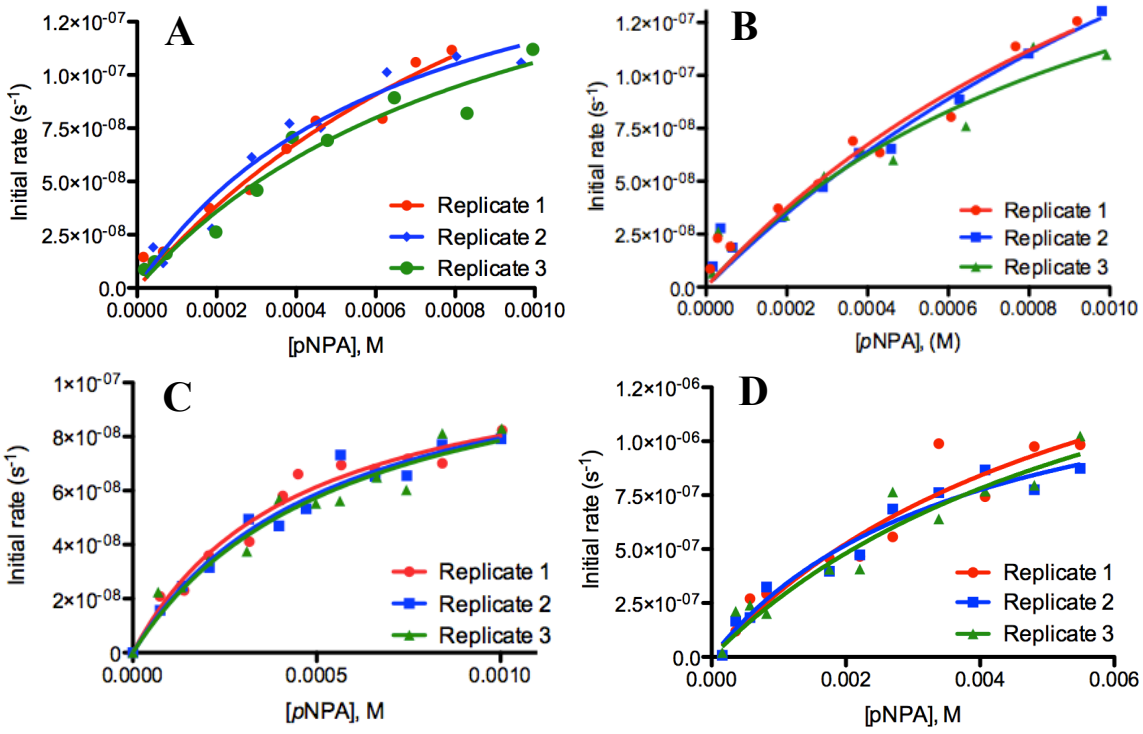

Figure 3-65. *p*NPA hydrolysis by (A) 10 μM $Pb^{II}_{S}Zn^{II}_{N/O}[(\mathbf{GR}\text{-ACH})_2(\mathbf{GR}\text{-CDH})_1]^{n+}$, (B) 10 μM $Pb^{II}_{S}Zn^{II}_{N/O}[(\mathbf{GR}\text{-ACH})_2(\mathbf{GR}\text{-CTH})_1]^{n+}$, (C) 10 μM $Pb^{II}_{S}Zn^{II}_{N/O}[(\mathbf{GR}\text{-ACH})_2(\mathbf{GR}\text{-CH})_1]^{n+}$ and (D) 10 μM $Pb^{II}_{S}[(\mathbf{GR}\text{-AC})_2(\mathbf{GR}\text{-C})_1]^{n+}$ at pH 9.5 in 50 mM CHES buffer, 0.1 M Na_2SO_4. Plots show the initial rates at pH 9.5 vs [pNPA] and the corresponding fits, for three replicates, as fitted to the Michaelis-Menten equation.

Next, I wanted to determine if the catalytic efficiency of a Pb^{II}-bound heterotrimer with a symmetric $Zn^{II}His_3$ binding site, $Pb^{II}_{S}Zn^{II}_{N/O}[(\mathbf{GR}\text{-ACH})_2(\mathbf{GR}\text{-CH})_1]^{n+}$, was comparable to a similar $Zn^{II}His_3$ in $Hg^{II}_{S}Zn^{II}_{N/O}(\mathbf{GR}\text{-CH})_3^{+}$. $Pb^{II}_{S}Zn^{II}_{N/O}[(\mathbf{GR}\text{-ACH})_2(\mathbf{GR}\text{-CH})_1]^{n+}$ showed saturation kinetics for *p*NPA hydrolysis at pH 9.5 with a catalytic efficiency of 23.5 ± 1.9 $M^{-1}s^{-1}$ (Figure 3-65C, Table 3-9). The rate and K_M for this peptide were determined to be 0.011 ± 0.001 s^{-1} and 0.51 ± 0.08 M (Table 3-9). This rate

is nearly 30% higher than the Hg^{II}-bound homotrimer. The values determined for the rate and K_M are the lowest reported for any **TRI** or **GR** system, indicating very good substrate access and also a very slow rate (resulting in a comparable catalytic efficiency). These values indicate that something else, other than just catalysis at the $Zn^{II}His_3$ site, is likely occurring within this scaffold to contribute to *p*NPA hydrolysis.

This observation led me to analyze the hydrolysis of *p*NPA by $Pb^{II}_S[(\mathbf{GR}\text{-}AC)_2(\mathbf{GR}\text{-}C)_1]^-$ (where **GR**-AC is **GR**L2WL12AL16C and **GR**-C is **GR**L2WL16C, Table 3-1) to determine the contribution to catalysis due to the $Pb^{II}Cys_3$ site. Interestingly, in the absence of the His_3 site, I still observed saturation kinetics for *p*NPA hydrolysis at pH 9.5 (Figure 3-65D). The catalytic rate obtained is 11.2 ± 1.6 $M^{-1}s^{-1}$ with a rate of 0.074 ± 0.025 s^{-1} and a K_M of 6.8 ± 3.0 M (Table 3-9). This is a significantly elevated K_M indicating that the substrate has much poorer access to the active site, which is now the $Pb^{II}Cys_3$ site; however, the rate is quite high in comparison to those reported for the $Zn^{II}His_3$ rates (Table 3-9).[1,4]

Interestingly, this is not the first report of Pb^{II} catalyzing Zn^{II} reactions. Berreau and coworkers characterized the catalysis of amide cleavage reactions by a Pb^{II}-bound small molecule mimic, the design of which was inspired by mononuclear Zn^{II} centers, in comparison to a comparable Zn^{II}-bound complex.[69] Although DFT calculations suggest that the reaction pathways differ between Zn^{II}- and Pb^{II}-bound complexes, the same amide methanolysis product is observed for both catalysts. In fact, at a given temperature, the Pb^{II}-bound mimic provided an observed rate of amide methanolysis that was ~10-fold faster than the corresponding Zn^{II} mimic.[70] These results indicate that the hydrolysis of *p*NPA by the $Pb^{II}Cys_3$ site in my scaffolds is not completely unprecedented.

Therefore the discovery of *p*NPA hydrolysis via the $Pb^{II}Cys_3$ site has multiple implications. First, direct comparison of my Pb^{II} systems to Melissa's reported Hg^{II} systems is not a straightforward process, as the $Hg^{II}Cys_3$ site was found not to contribute to catalysis (Table 3-9).[1] Second, determination of the contribution of $Pb^{II}Cys_3$ catalysis vs. the $Zn^{II}Aaa_XHis_3$ (where Aaa is Asp or Thr) catalysis is a non-trivial determination, as the Zn^{II} rate is not simply the difference in the total rate from the $Pb^{II}Cys_3$ rate. Therefore, I have determined that although my constructs are indeed catalytically active toward

*p*NPA hydrolysis, there are new and non-trivial contributions to the reaction to consider. Thus, direct comparison of the Zn^{II}-bound Pb^{II}-heterotrimeric and Hg^{II}-homotrimeric systems is elusive.

It should be noted that if the primary coordination sphere of the Zn^{II} ion has been modified, such as N_2O_2, then these heterotrimers will not be good CA mimics, regardless of the ambiguity due to contribution to *p*NPA hydrolysis from the $Pb^{II}Cys_3$ site. An N_2O_2 site may instead be more appropriate mimic for CPA or TML, which catalyze peptidase chemistry.[42–44,71] In CA, mutation of a primary coordinating His ligands to a carboxyamide can sometimes retain catalytic activity toward *p*NPA hydrolysis, but it is always greatly diminished.[72] In the case of mutations from His ligands to carboxylate residues (H94D, H94E, H199D, or H199E), which could presumably provide an N_2O_2 primary coordination sphere, *p*NPA hydrolysis is, maximally, 30% of wild-type CA.[72] Therefore, it is possible that my heterotrimers have provided a primary coordination sphere that is not conducive for esterase activity at the Zn^{II} site.

Considering the ability of the $Pb^{II}Cys_3$ site to catalyze *p*NPA hydrolysis, I also conducted one single kinetic experiment to determine if such a contribution would also be observed for CO_2 hydration. $Pb^{II}{}_SZn^{II}{}_{N/O}$(**GR**-ACH)$_3^+$ exhibits saturation kinetics for CO_2 hydration at pH 9.5 (Figure 3-66). A catalytic efficiency of 7.4 x 10^4 $M^{-1}s^{-1}$ with a rate of 310 s^{-1} and K_M of 4.3 mM were obtained. Errors are not included since the experiment was not repeated in triplicate. These values correlate well to those reported for $Hg^{II}{}_SZn^{II}{}_{N/O}$(GR-CH)$_3^+$ of k_{cat}/K_M = 7.4 ± 3.4 x 10^4 $M^{-1}s^{-1}$, k_{cat} = 730 ± 290 s^{-1}, and K_M = ~9.8 mM. These data indicate that $Pb^{II}{}_SZn^{II}{}_{N/O}$(**GR**-ACH)$_3^+$ and $Hg^{II}{}_SZn^{II}{}_{N/O}$(**GR**-CH)$_3^{n+}$ have the same kinetic parameters. Since Hg^{II} was found not to contribute to CO_2 hydration, we can make the preliminary conclusion that a $Pb^{II}Cys_3$ site will also not likely contribute to the hydration of CO_2, since the Zn^{II} sites should be comparable between the two samples. These data, in tandem with the *p*NPA rates, suggest that while the Pb^{II}-nucleated heterotrimers may result in a very convoluted comparisons within the *p*NPA hydrolysis reaction kinetics, that the CO_2 hydration kinetics might be a straightforward comparison between homotrimeric and heterotrimeric peptides with potential asymmetric Zn^{II} binding sites. Such a conclusion is gratifying as the CO_2 hydration chemistry is the

naturally evolved reaction for CA and represents, ultimately, the most stringent test for designed metalloprotein hydratases.

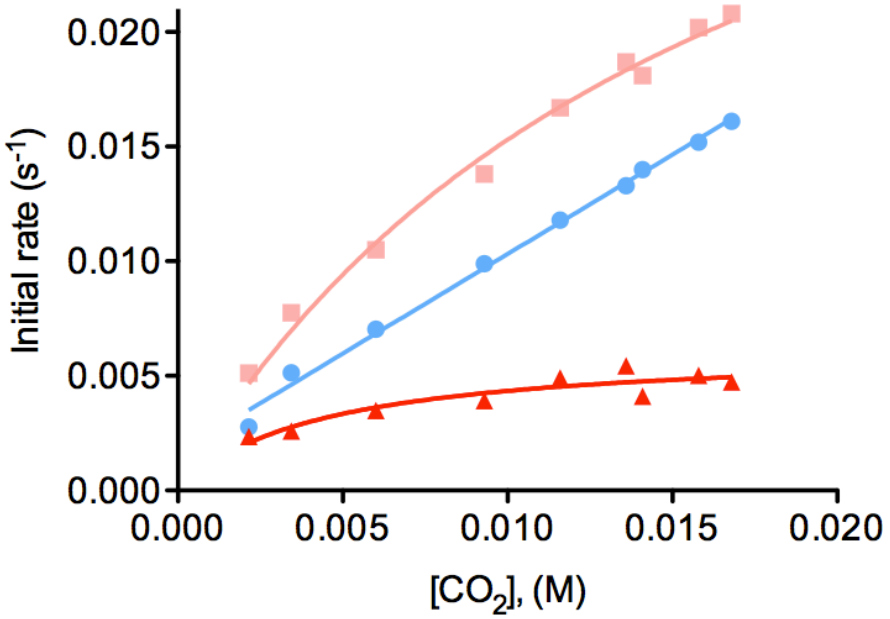

Figure 3-66. CO_2 hydration by 10 μM $Pb^{II}_{S}Zn^{II}_{N/O}[(\mathbf{GR}\text{-ACH})_2(\mathbf{GR}\text{-CH})_1]^{n+}$ at pH 9.25 in 50 mM CHES buffer, 0.1 M Na_2SO_4. The initial rates vs. $[CO_2]$ are fitted to the Michaelis-Menten equation. Catalyst rates is shown in light pink squares, blank rates are shown in blue circles, and the difference rates are shown in red triangles.

Conclusions

Herein I have presented the first steps at characterizing transition metal binding to symmetric and asymmetric binding sites within Pb^{II}-nucleated heterotrimeric scaffolds. Inspired by the acid/base Thr residue in CA, T199, which provides a hydrogen-bonding interaction to the native Zn^{II}-bound solvent molecule, I introduced an Asp residue into the peptide sequence in the layer directly above the His_3 binding site, with respect to the N-terminus, of a *de novo* designed 3SCC. Applying the methodology introduced in Chapter 2, Pb^{II}-nucleated heterotrimers with one, or two, Asp residues in close proximity to the His_3 transition metal binding site were then obtained. Co^{II} was used as a spectroscopic probe to characterize the resulting homo- and heterotrimeric systems with varying numbers of Asp residues near the active site. Co^{II} spectroscopy of the symmetric peptides, $Pb^{II}_{S}Co^{II}_{N/O}(\mathbf{GR}\text{-ACH})_3^{+}$ and $Pb^{II}_{S}Co^{II}_{N/O}(\mathbf{GR}\text{-CDH})_3^{n+}$, provide UV-Vis, EPR and XAS

data comparable to that of Co^{II}-substituted CA and CA small molecule mimics. The first generation of heterotrimeric peptides with asymmetric transition metal binding sites, $Pb^{II}_{S}Co^{II}_{N/O}[(\mathbf{GR}\text{-ACH})_2(\mathbf{GR}\text{-CDH})_1]^{n+}$ and $Pb^{II}_{S}Co^{II}_{N/O}[(\mathbf{GR}\text{-ACH})_1(\mathbf{GR}\text{-CDH})_2]^{n+}$, provided Co^{II} spectroscopic data comparable to that of Co^{II}-substituted CPA, TML, or VanX. Indeed, the spectroscopic data support direct carboxylate coordination within the heterotrimeric peptides as well as a lower coordination number, probably 5-coordinate, for the heterotrimers as compared to the homotrimers (more consistent with 6-coordinate Co^{II} complexes). The Co^{II} site appears more 5-coordinate in the $Pb^{II}_{S}Co^{II}_{N/O}[(\mathbf{GR}\text{-ACH})_1(\mathbf{GR}\text{-CDH})_2]^{n+}$ heterotrimer, where two Asp residues are in close proximity to the His_3 site.

Inclusion of the Asp residues below the His_3 binding site, in both symmetric and asymmetric fashions, provided spectroscopic data similar to that of the homotrimeric $Pb^{II}_{S}Co^{II}_{N/O}(\mathbf{GR}\text{-ACH})_3^{+}$ system. This supports a model with comparable 6-coordination of the Co^{II} environments in $Pb^{II}_{S}Co^{II}_{N/O}(\mathbf{GR}\text{-CHD})_3^{-}$, $Pb^{II}_{S}Co^{II}_{N/O}[(\mathbf{GR}\text{-ACH})_2(\mathbf{GR}\text{-CHD})_1]^{n+}$ and $Pb^{II}_{S}Co^{II}_{N/O}[(\mathbf{GR}\text{-ACH})_1(\mathbf{GR}\text{-CHD})_2]^{n+}$. These data demonstrate that simple inclusion of negative charge from carboxylate moieties in close proximity of the His_3 site is not responsible for the subtle differences observed between the $Pb^{II}_{S}Co^{II}_{N/O}(\mathbf{GR}\text{-ACH})_3^{+}$ and $Pb^{II}_{S}Co^{II}_{N/O}(\mathbf{GR}\text{-CDH})_3^{-}$ homotrimers. These data also indicate that the inclusion of the Asp residues has geometric restrictions required to form the asymmetric Co^{II} centers comparable to those in $Pb^{II}_{S}Co^{II}_{N/O}[(\mathbf{GR}\text{-ACH})_2(\mathbf{GR}\text{-CDH})_1]^{n+}$ and $Pb^{II}_{S}Co^{II}_{N/O}[(\mathbf{GR}\text{-ACH})_1(\mathbf{GR}\text{-CDH})_2]^{n+}$.

The initial goal of including an Asp residue to provide hydrogen-bonding interactions for a metal-bound water molecule is not supported by Co^{II} spectroscopic analysis. Instead of perturbations to the second coordination sphere to mimic the Zn^{II} binding site of CA, I have actually modified the primary coordination sphere, providing spectroscopic characteristics that support direct Co^{II}-carboxylate coordination, resulting in a likely N_2O_3 ligation similar to CPA and TML. This is likely a direct consequence due to the propensity of Co^{II} to bind to the oxyanion provided by the Asp ligand. Additionally, it is very likely that a chelate effect occurred when the DXXH sequence was employed to introduce an Asp ligand in the layer above the His_3 site.

Similar conclusions can be made for the second generation of Co^{II}-bound homo- and heterotrimers in which the Ala and Asp residues are included on the same helix within the 3SCC. This alteration was made to optimize the purity of both the heterotrimer formation (2:1 Ala/Leu pairing at the $Pb^{II}Cys_3$ site confirmed by ^{207}Pb NMR) as well as the Co^{II} site (supported via analysis of Co^{II} spectroscopy). The Co^{II} UV-Vis and EPR data of $Pb^{II}_{S}Co^{II}_{N/O}$(**GR**-ACDH)$_3^{n+}$, $Pb^{II}_{S}Co^{II}_{N/O}$[(**GR**-ACDH)$_2$(**GR**-CH)$_1$]$^{n+}$, and $Pb^{II}_{S}Co^{II}_{N/O}$[(**GR**-ACH)$_1$(**GR**-CH)$_2$]$^{n+}$ are consistent with the corresponding first-generation peptides. The XAS data for $Pb^{II}_{S}Co^{II}_{N/O}$(**GR**-ACDH)$_3^{n+}$ and $Pb^{II}_{S}Co^{II}_{N/O}$[(**GR**-ACDH)$_1$(**GR**-CH)$_2$]$^{n+}$ again support 6- and 5-coordinate Co^{II} environments, respectively. In fact the $Pb^{II}_{S}Co^{II}_{N/O}$[(**GR**-ACH)$_1$(**GR**-CH)$_2$]$^{n+}$ data is consistent with a pure Pb^{II} site as well as a more 5-coordinate-like Co^{II} complex at the Asp_2His_3 site. However, XAS parameters are more consistent with a 4-coordinate Co^{II} center were observed for $Pb^{II}_{S}Co^{II}_{N/O}$[(**GR**-ACDH)$_2$(**GR**-CH)$_1$]$^{n+}$.

Zn^{II} XAS analysis of $Pb^{II}_{S}Zn^{II}_{N/O}$(**GR**-ACH)$_3^{+}$, $Pb^{II}_{S}Zn^{II}_{N/O}$(**GR**-CDH)$_3^{n+}$ and the corresponding heterotrimers provides consistent evidence at pH 7.5 and 9.5, for four-coordinate Zn^{II} environments in all of the homo- and heterotrimer samples. Although the exact identity of the four ligands cannot be determined via XAS, these data indicate that Co^{II} binds with a different geometry and coordination number, in all cases, when compared to Zn^{II}; therefore, Co^{II} appears to be a non-innocent probe for Zn^{II} binding within these constructs. Initial kinetic experiments indicate that the $Pb^{II}Cys_3$ site is catalytically active toward *p*NPA hydrolysis; however, CO_2 hydration by $Pb^{II}_{S}Zn^{II}_{N/O}$(**GR**-ACH)$_3^{+}$ is comparable to $Hg^{II}_{S}Zn^{II}_{N/O}$(**GR**-CH)$_3^{n+}$, indicating that future direct comparison can be made for the CO_2 kinetic parameters.

Overall, this work suggests that the goal of obtaining Pb^{II}-nucleated heterotrimeric 3SCCs with asymmetric transition metal binding sites has been reached when binding Co^{II} and Zn^{II}. The Co^{II} spectroscopy supports the formation of an asymmetric primary coordination sphere. These asymmetric Co^{II} bound peptides share many spectral characteristics with Co^{II}-substituted CPA, TML and VanX. This is the first report of asymmetric transition metal binding sites within self-associating 3SCCs. Zn^{II} binding was also observed within the heterotrimeric peptides, and although at this time I

cannot say whether or not the primary coordination sphere has been altered, the modifications included in the peptide sequence, either the first or second coordination sphere, must be different than the corresponding homotrimers.

Additionally, due to the differences in the coordination numbers between Co^{II} and Zn^{II}, supported by XAS analysis, it is possible that the inclusion of an Asp residue in the layer directly above the His_3 site provided the intended asymmetric Zn^{II} secondary environment, as inspired by the T199 residue of CA. The Zn^{II} XAS data support 4-coordinate Zn^{II} centers at both neutral and high pH, which could correspond to His_3OH_2 environments with a nearby Asp residue. If the primary coordination sphere was indeed altered for Zn^{II} binding, then the site would no longer be the intended CA mimic, as discussed above. However, if the Zn^{II} coordination is indeed His_3O, as evidenced by X-ray crystallography and generally comparably good XAS fits (compared to N_2O_2), it is possible that the Asp (or Thr) residue has provided an asymmetric secondary coordination sphere. Inclusion of an acid/base catalyst in the 26th position could hydrogen bond with the presumed Zn^{II}-bound water molecule, as observed in CA.

Initial kinetic studies indicate that the $Pb^{II}Cys_3$ site is not active toward CO_2 hydration, which could allow for future studies to determine, straightforwardly, if the Zn^{II}-bound heterotrimers, with Asp nearby residues, offer improved catalytic activity or perturbed kinetic pK_a values for the Zn^{II} bound water.

References

(1) Zastrow, M. L.; Peacock, A. F. A.; Stuckey, J. A.; Pecoraro, V. L. *Nat. Chem.* **2012**, *4*, 118.
(2) Krebs, J. F.; Ippolito, J. A.; Christianson, D. W.; Fierke, C. A. *J. Biol. Chem.* **1993**, *268*, 27458.
(3) Liang, Z.; Xue, Y.; Behravan, G.; Jonsson, B. H.; Lindskog, S. *Eur. J. Biochem.* **1993**, *211*, 821.
(4) Zastrow, M. De novo designed metalloenzymes: structural stabilization and hydrolytic catalysis in a family of α-helical coiled coils, University of Michigan, 2013.
(5) Chan, W. C.; White, P. D. *Fmoc Solid Phase Peptide Synthesis: A Practical Approach*; Chan, W.; White, P., Eds.; Oxford Univ Press, New York, 2000.
(6) *The Protein Protocols Handbook*; Walker, J. M., Ed.; 2nd ed.; Humana Press Inc.: Totowa, NJ, 2002.
(7) Dieckmann, G. R.; McRorie, D. K.; Lear, J. D.; Sharp, K. A.; DeGrado, W. F.; Pecoraro, V. L. *J. Mol. Biol.* **1998**, *280*, 897.
(8) GraphPad Prism version 5.00 for Mac, GraphPad Software, San Diego California USA, www.graphpad.com.
(9) Neupane, K. P.; Pecoraro, V. L. *Angew. Chem. Int. Ed.* **2010**, *49*, 8177.
(10) Neupane, K. P.; Pecoraro, V. L. *J. Inorg. Biochem.* **2011**, *105*, 1030.
(11) Zampella, G.; Neupane, K. P.; De Gioia, L.; Pecoraro, V. L. *Chem. Eur. J.* **2012**, *18*, 2040.
(12) Cobas, C.; Cruces, J.; Sardina, F.; MestRe-C version 2.3, Universidad de Santiago de Compostela, S. MestRe-C version 2.3, Universidad de Santiago de Compostela, Spain, 2000.
(13) Hendrich, M. SpinCount.
(14) George, G.N., Pickering, I. J. EXAFSPAK, 2000.
(15) Rehr, J. J.; Kas, J. J.; Vila, F. D.; Prange, M. P.; Jorissen, K. *Phys. Chem. Chem. Phys.* **2010**, *12*, 5503.
(16) Dimakis, N.; Bunker, G. *Phys. Rev. B* **2002**, *65*, 1.
(17) Shaw, C. F.; Laib, J. E.; Savas, M. M.; Petering, D. H. *Inorg. Chem.* **1990**, *29*, 403.
(18) Mekmouche, Y.; Coppel, Y.; Hochgräfe, K.; Guilloreau, L.; Talmard, C.; Mazarguil, H.; Faller, P. *ChemBioChem* **2005**, *6*, 1663.
(19) Säbel, C. E.; Neureuther, J. M.; Siemann, S. *Anal. Biochem.* **2010**, *397*, 218.
(20) Verpoorte, J. A.; Mehta, S.; Edsall, J. T. *J. Biol. Chem.* **1967**, *242*, 4221.
(21) Khalifah, R. G. *J. Biol. Chem.* **1971**, *246*, 2561.
(22) Cangelosi, V. M.; Deb, A.; Penner-Hahn, J. E.; Pecoraro, V. L. *Angew. Chem. Int. Ed.* **2014**, *53*, 7900.
(23) Magyar, J. S.; Weng, T.-C.; Stern, C. M.; Dye, D. F.; Rous, B. W.; Payne, J. C.; Bridgewater, B. M.; Mijovilovich, A.; Parkin, G.; Zaleski, J. M.; Penner-Hahn, J. E.; Godwin, H. A. *J. Am. Chem. Soc.* **2005**, *127*, 9495.
(24) Matzapetakis, M.; Ghosh, D.; Weng, T.-C.; Penner-Hahn, J. E.; Pecoraro, V. L. *J. Biol. Inorg. Chem.* **2006**, *11*, 876.
(25) Maret, W.; Vallee, B. L. *Methods Enzym.* **1993**, *226*, 52.
(26) Werth, M. T.; Grazyna, S. T.; Michael, F. *Inorg. Chem.* **1995**, *34*, 218.
(27) Holmquist, B.; Kaden, T. A.; Vallee, B. L. *Biochem.* **1975**, *14*, 1454.

(28) Horrocks, W. D.; Ishley, J. N.; Holmquist, B.; Thompson, J. S. *J. Inorg. Biochem.* **1980**, *12*, 131.
(29) Bertini, I.; Luchinat, C. *Acc. Chem. Res.* **1983**, *115*, 272.
(30) Coleman, J. E. *Annu. Rev. Biochem.* **1992**, *61*, 897.
(31) Bertini, I.; Luchinat, C. *Ann. N.Y. Acad.* **1984**, *429*, 89.
(32) Bertini, I.; Canti, G.; Luchinat, C.; Mani, F. *Inorg. Chem.* **1981**, 1670.
(33) Bencini, A.; Bertini, I.; Canti, G.; Gatteschi, D.; Luchinat, C. *J. Inorg. Biochem.* **1981**, *14*, 81.
(34) Benelli, C.; Bertini, I.; Di Vaira, M.; Mani, F. *Inorg. Chem.* **1984**, *23*, 1422.
(35) Avvaru, B. S.; Arenas, D. J.; Tu, C.; Tanner, D. B.; McKenna, R.; Silverman, D. N. *Arch. Biochem. Biophys.* **2010**, *502*, 53.
(36) C. R. Groom, I. J. Bruno, M. P. Lightfoot and S. C. Ward, Acta Cryst. (2016). B72, 171-179; F. H. Allen, Acta Cryst., B58, 380-388, 2002. The Cambridge Structural Database.
(37) Grell, E.; Bray, R. C. *Biochim. Biophys. Acta* **1971**, *236*, 503.
(38) Kaden, T. A.; Holmquist, B.; Vallee, B. L. *Inorg. Chem.* **1974**, *13*, 2585.
(39) Scarpellini, M.; Wu, A. J.; Kampf, J. W.; Pecoraro, V. L. *Inorg. Chem.* **2005**, *44*, 5001.
(40) Jacobsen, F. E.; Breece, R. M.; Myers, W. K.; Tierney, D. L.; Cohen, S. M. *Inorg. Chem.* **2006**, *45*, 7306.
(41) Kunz, P. C.; Reiß, G. J.; Frank, W.; Kläui, W. *Eur. J. Inorg. Chem.* **2003**, *2003*, 3945.
(42) Holland, D. R.; Hausrath, A. C.; Juers, D.; Matthews, B. W. *Protein Sci.* **1995**, *4*, 1955.
(43) Greenblatt, H. M.; Feinberg, H.; Tucker, P. A.; Shoham, G. *Acta Crystallogr. Sect. D Biol. Crystallogr.* **1998**, *54*, 289.
(44) Holden, H. M.; Matthews, B. W. *J. Biol. Chem.* **1988**, *263*, 3256.
(45) Kaden, T. A.; Holmquist, B.; Vallee, B. L. *Biochem. Biophys. Res. Comm.* **1972**, *46*, 1654.
(46) Martinelli, R. A.; Hanson, G. R.; Thompson, J. S.; Holmquist, B.; Pilbrow, J. R.; Auld, D. S.; Vallee, B. L. *Biochemistry* **1989**, *28*, 2251.
(47) Walsh, C. *Science* **1999**, *284*, 442.
(48) Bussiere, D. E.; Pratt, S. D.; Katz, L.; Severin, J. M.; Holzman, T.; Park, C. H. *Mol. Cell* **1998**, *2*, 75.
(49) Breece, R. M.; Costello, A.; Bennett, B.; Sigdel, T. K.; Matthews, M. L.; Tierney, D. L.; Crowder, M. W. *J. Biol. Chem.* **2005**, *280*, 11074.
(50) Emsley, P.; Cowtan, K. *Acta Crystallogr. Sect. D Biol. Crystallogr.* **2004**, *60*, 2126.
(51) Ippolito, J. A.; Baird, T. T.; McGee, S. A.; Christianson, D. W.; Fierke, C. A. *Proc. Natl. Acad. Sci. U. S. A.* **1995**, *92*, 5017.
(52) Ouyang, H.; Vogel, H. J. *BioMetals* **1998**, *11*, 213.
(53) Simons, T. J. *Neurotoxicology* **1993**, *14*, 77.
(54) Aramini, J. M.; Hiraoki, T.; Yazawa, M.; Yuan, T.; Zhang, M.; Vogel, H. J. *J. Biol. Inorg. Chem.* **1996**, *1*, 39.
(55) Matzapetakis, M.; Farrer, B. T.; Weng, T.-C.; Hemmingsen, L.; Penner-Hahn, J. E.; Pecoraro, V. L. *J. Am. Chem. Soc.* **2002**, *124*, 8042.
(56) Lee, K.-H.; Matzapetakis, M.; Mitra, S.; Marsh, E. N. G.; Pecoraro, V. L. *J. Am.*

Chem. Soc. **2004**, *126*, 9178.
(57) Peacock, A. F. A.; Stuckey, J. A.; Pecoraro, V. L. *Angew. Chem. Int. Ed.* **2009**, *48*, 7371.
(58) Ruamps, R.; Batchelor, L. J.; Guillot, R.; Zakhia, G.; Barra, A.-L.; Wernsdorfer, W.; Guihéry, N.; Mallah, T. *Chem. Sci.* **2014**, *5*, 3418.
(59) Kuzmin, A.; Chaboy, J. *IUCrJ* **2014**, *1*, 571.
(60) Bertini, I.; Luchinat, C. *Adv. Inorg. Biochem.* **1984**, *6*, 71.
(61) Bennett, B. In *Metals in Biology*; 2010; Vol. 29, pp. 345–370.
(62) Kremer-Aach, A.; Kläui, W.; Bell, R.; Strerath, A.; Wunderlich, H.; Mootz, D. *Inorg. Chem.* **1997**, *36*, 1552.
(63) Crawford, P. A.; Yang, K.; Sharma, N.; Bennett, B.; Crowder, M. W. *Biochemistry* **2005**, *44*, 5168.
(64) Kleifeld, O.; Rulísek, L.; Bogin, O.; Frenkel, A.; Havlas, Z.; Burstein, Y.; Sagi, I. *Biochemistry* **2004**, *43*, 7151.
(65) Håkansson, K.; Wehnert, A.; Liljas, A. *Acta Crystallogr. D* **1994**, *50*, 93.
(66) Kiefer, L. L.; Krebs, J. F.; Paterno, S. A.; Fierke, C. A. *Biochemistry* **1993**, *32*, 9896.
(67) Coleman, J. E.; Vallee, B. L. *J. Biol. Chem.* **1960**, *235*, 390.
(68) Hunt, J. A.; Ahmed, M.; Fierke, C. A. *Society* **1999**, 9054.
(69) Elton, E. S.; Zhang, T.; Prabhakar, R.; Arif, A. M.; Berreau, L. M. *Inorg. Chem.* **2013**, *52*, 11480.
(70) Ingle, G. K.; Makowska-Grzyska, M. M.; Szajna-Fuller, E.; Sen, I.; Price, J. C.; Arif, A. M.; Berreau, L. M. *Inorg. Chem.* **2007**, *46*, 1471.
(71) Auld, D. S.; Galdes, A.; Geoghegan, K. F.; Holmquist, B.; Martinelli, R. A.; Vallee, B. L. *Proc. Natl. Acad. Sci. U. S. A.* **1984**, *81*, 5041.
(72) Lesburg, C. A.; Huang, C.; Christianson, D. W.; Fierke, C. A. *Biochemistry* **1997**, *36*, 15780.
(73) Kimblin, C.; Allenb, W. E.; Parkin, G.; Hill, C.; Hill, C.; H, C. **1995**, *1*, 1813.
(74) Echizen, T.; Ibrahim, M. M.; Nakata, K.; Izumi, M.; Ichikawa, K.; Shiro, M. *J. Inorg. Biochem.* **2004**, *98*, 1347.
(75) Voo, J. K.; Incarvito, C. D.; Yap, G. P. A.; Rheingold, A. L.; Riordan, C. G. *Polyhedron* **2004**, *23*, 405.

Chapter 4. *De Novo* Designed Metallopeptides: Unexpected homo- and hetero-binuclear Cu^{I} Cys_3 Sites

Introduction

Copper is an important trace metal that is indispensible for essentially all organisms. The hallmark of copper reactivity in biological systems is its redox property, which leads to a variety of copper proteins that catalyze oxidoreductase and mono/dioxygenase reactions or carry out electron transfer.[1–11] These reactions are critical for many cellular functions; however, copper is a potential toxin if not regulated properly. Free copper ions carry out Fenton-type reactions that produce deleterious reactive oxygen species, which can cause lipid, nucleic acid, and protein damage.[12,13] These effects demand a tight homeostatic regulation of copper acquisition, distribution and use. For example, the most common copper related disorders in humans are Menkes and Wilson diseases, which are related to defects of the human P_{1B}-type ATPases (ATP7A and ATP7B, respectively).[14–19] Too much copper can result in Wilson's disease, where the brain and liver are overloaded with copper and, because of copper's proficiency at redox chemistry, can lead to negative effects such as the production of unwanted hydroxyl radicals in the body. Clinical symptoms of excessive copper overload can range from liver failure to neurological defects. Conversely, in Menkes Disease too little copper is transported across the gut, causing insufficient loading of copper into copper-dependent enzymes. This deficiency can result in symptoms ranging from neurological defects, delayed development and ultimately death. Therefore, strict regulation of copper homeostasis is vital.

The uptake and transport of copper ions involve cell surface transporters (Ctr1)[20] and copper chaperones. Three pathways with three distinct metallochaperones have been proposed to deliver copper to the mitochondria (Cox17 pathway), the Golgi (Atx1 pathway), and the cytosolic superoxide dismutase (CCS pathway).[21–24] Intracellular

copper trafficking is achieved through ligand exchange of these metallochaperones with their delivery target via thermodynamic and kinetic control. The mechanistic details of transfer, however, are not completely understood on the molecular level. Over the years, two- and three-coordinate copper-thiol/thiolate species have been proposed to be key intermediates.[23–26] Regardless of the differences between the proposed pathways, all of these copper metallochaperones contain similar *thiol-rich copper S_n* binding sites.

As summarized in Chapter 1, the Pecoraro lab has demonstrated that *de novo*[27–32] designed Cys_3 containing peptides provide binding environments amenable for Hg^{II}, Pb^{II}, Cd^{II}, and As^{III} binding to address heavy metal selectivity, specificity and coordination preference in a protein environment.[33–47] In Chapter 2 I described how a Cys_3 site can be used to bind Pb^{II}, with varied steric matching in the secondary coordination environment to provide space for a stabilizing hydrogen bonding network, to provide heterotrimeric 3SCC. Additionally, a past group member, Dr. Fangting Yu, extensively studied many systematically designed structural and functional models of the $Cu^{I}His_3$ type-2 copper center of native CuNiR (see Chapter 1 for a brief summary).[48–50] Considering the extensive work previously conducted in the Pecoraro lab regarding heavy metal homeostasis with thiolphilic metals such as Hg^{II}, Pg^{II}, As^{III}, etc…, in combination with the thiolphilicity of Cu^{I}, it was surprising that no one had yet analyzed Cu^{I} binding to a Cys_3 site within the **TRI** and **GR** families of 3SCC.

In this chapter, I will describe how the investigation of Cu^{I} binding to Cys_3 sites within *de novo* designed 3SCCs, under physiologically relevant pH conditions, provides an unexpected binuclear Cu^{I} site as supported via UV-Vis and XAS spectroscopy. The association constants of the $Cu^{I}_2Cys_3$ centers within peptides that have different secondary coordination spheres have been determined using a primary standard competition titration with bathocuproinedisulfonate (BCS^{2-}). Additionally, previously measured $Cu^{I}His_3$ binding constants can be used to confirm the combined association constants by observing Cu^{I} competition for binding in a peptide that contains both a Cys_3 and a His_3 binding site. The similarities observed between Cu^{I} binding to Cys_3 sites within the **TRI/GR** peptides and Cu^{I} metallochaperones will be discussed as well as the

resulting implications of the structure-function relationship of binuclear Cu^{I} binding sites in thiol-rich binding pockets.

Furthermore, I hoped to use the Cu^{I} affinities to determine the ever-elusive $Pb^{II}Cys_3$ binding affinities via competition between Cu^{I} and Pb^{II} for the same Cys_3 site. However, UV-Vis titrations of such competition experiments reveal data that support Cu^{I} binding to a Cys_3 environment in the presence of Pb^{II}, therefore, suggesting formation of a heterobinuclear $Cu^{I}Pb^{II}Cys_3$ metal center. Such a site is both unexpected and unprecedented within our **TRI** and **GR** families of 3SCCs and has never been reported in biology.

Materials and Methods

General Procedures. All samples containing Cu^{I} were prepared and handled in an inert atmosphere glove box using oxygen-free buffer, water, and acetonitrile. A stock Cu^{I} solution was prepared in degassed acetonitrile using $[Cu(CH_3CN)_4]BF_4$ salt. Stock Cu^{I} concentrations of 100-200 mM were determined by spectrophotometric titrations using 2,9-dimethyl-1,10-phenanthroline, DMP.[51]

Peptide Synthesis and Purification. Peptides were synthesized on one of two instruments: an Applied Biosystems 433A synthesizer or a Biotage Initiator+Alstra synthesizer on a Rink Amide Methylbenzhydrylamine (MBHA) resin using standard Fmoc-*t*Bu-based protection protocols (HBTu/HOBt coupling).[52] Crude peptides were cleaved from the resin using trifluoroacetic acid (TFA), ethandithiol, anisole, and thioanisole (90:3:2:5), dissolved in double distilled water and lyophilized to dryness. Purified peptides were isolated using Waters 600 HPLC on a reverse phase C18 column (flow rate: 20 mL/min, solvent A: 0.1% TFA in water and B: 0.1% TFA in 90:10 CH_3CN:H_2O. A linear gradient was used starting at 70:30, A:B and increasing to 20:80 over 35 min.). ESI-MS was used to confirm the mass of purified peptide and collections were lyophilized to yield pure, white powder. Concentrations of all peptides were determined by tryptophan absorbance at 280 nm (ε = 5,500 $M^{-1}cm^{-1}$).[53]

Ultraviolet-Visible (UV-Vis) Spectroscopy. UV-Vis spectra were recorded in 1-cm quartz cuvettes at room temperature on a Cary 100 Bio UV/Vis spectrometer.

Pb^{II}-binding titrations. Titrations of Pb^{II} into peptide were performed at room temperature and monitored via UV-Vis spectroscopy in a 1-cm quartz cuvette. $Lead^{II}$ titrations were completed in 50 mM TRIS buffer at pH 8.5 at a peptide concentration of 30 μM. TRIS adjustments were made using small aliquots of concentrated KOH and HCl. Aliquots of $Pb^{II}(NO_3)_2$ or $PbCl_2$ stock solutions (standardized using inductively coupled plasma-optical emission spectroscopy) were titrated into the peptide solution. For all titrations, a background spectrum of buffer and water were subtracted from the peptide and metallated samples.

Competitive Cu^{I}-binding titrations.

BCS^{2-} and Pep_3 competition for Cu^{I} binding. A competitive chelation assay was used to determine the affinity of Cu^{I} to Cys_3-containing **TRI** or **GR** peptides. Bathocuproinedisulfonate, BCS^{2-}, is a well-defined Cu^{I} chelator, binds Cu^{I} in a 2:1 ratio providing a colored $[Cu(BCS)_2]^{3-}$ species (λ_{max} = 483 nm; $\varepsilon^{483\ nm}$ = 13,300 $M^{-1}cm^{-1}$; log β_2 = 19.8).[54] A solution of 40 μM Cu^{I} and 80 μM peptide (50 mM buffer: MES, pH 6.5, HEPES, pH 7.5, or CHES, pH 9.0) was prepared in a 1-cm quartz anaerobic cuvette in an inert atmosphere glove box and titrated with an ~6 mM BCS^{2-} solution. The increase in absorbance at 483 nm was followed using UV-Vis spectroscopy. All titration additions were carried out in the glovebox. Prism 5 (GraphPad Software)[55] was used to fit the spectrophotometric data taking into account the protonation equilibrium of BCS^{2-} (pK_a = 5.7).[54]

Four models were considered to derive fitting equations for the determination of the binding affinities of Cu^{I} to Cys_3 containing peptides. The first model addresses the formation of a mononuclear $Cu^{I}Pep_3$ species, as shown below in Model 1. If the data fits to this model then weak binding of the second equivalent of Cu^{I} to the peptide is expected, as it supports the formation of 100% mononuclear $Cu^{I}Pep_3$ before any binuclear $Cu^{I}_2Pep_3$ is formed.

Model 1. The binding equilibrium for the first scenario, where Cu^{I} binds to apo-peptide to form $Cu^{I}Cys_3$, can be expressed by Equation 1.

$$Cu + 2\ BCS^{2-} \rightleftharpoons [Cu(BCS)_2]^{3-} + Pep_3 \qquad \text{Equation 1}$$

The apparent association constant of $Cu^{I}Pep_3$ can be calculated using Equation 2.

$$K_{comp} = \frac{K_{BCS}}{K_{CuCys3}} = \frac{[Cu(BCS)_2][Pep_3]_f}{[BCS^{2-}]_f^2[CuPep_3]} \qquad \text{Equation 2}$$

Where K_{CuCys3}, the association constant of one equivalent of Cu^{I} binding to a 3SCC, is to be fit and K_{BCS} is a known value.[54] Mass balance equations for $[Cu]_T$, $[Pep_3]_T$, and $[BCS^{2-}]_T$ can be as seen in Equations 3-5.

Mass Balance Equations:

$$[Pep_3]_T = [Pep_3]_f + [CuPep_3]$$

$$[Pep_3]_f = [Pep_3]_T - [CuPep_3] \qquad \text{Equation 3}$$

$$[Cu]_T = [CuPep_3] + [Cu(BCS)_2] + [Cu]_f$$

$$[CuPep_3] = [Cu]_T - [Cu(BCS)_2] \qquad \text{Equation 4}$$

$$[BCS^{2-}]_T = [BCS^{2-}]_f + [HBCS^{-}]_f + 2[Cu(BCS)_2] \qquad \text{Equation 5}$$

Where:

$$HBCS^{-} \rightleftharpoons BCS^{2-} + H^{+} \qquad \text{Equation 6}$$

$$K_a = \frac{[BCS^{2-}]_f[H^{+}]}{[HBCS^{-}]_f}$$

$$[HBCS^{-}]_f = \frac{[BCS^{2-}]_f[H^{+}]}{K_a} \qquad \text{Equation 7}$$

Therefore:

$$[BCS^{2-}]_T = [BCS^{2-}]_f + \frac{[BCS^{2-}]_f[H^{+}]}{K_a} + 2[Cu(BCS)_2]$$

$$[BCS^{2-}]_f = \frac{[BCS^{2-}]_T - 2[Cu(BCS)_2]}{(1 + ([H^{+}]/K_a)} \qquad \text{Equation 8}$$

Substituting Equations 3, 4 and 8 into Equation 2 yields Equation 9.

$$K_{comp} = \frac{[Cu(BCS)_2]([Pep_3]_T - [Cu]_T + [Cu(BCS)_2])}{([Cu]_T - [Cu(BCS)_2])(([BCS]_T - [Cu(BCS)_2])/(1+([H^+]/Ka)))} \quad \text{Equation 9}$$

The K_{CuCys3} value can be directly related to the absorbance observed at 483 nm by substituting $[Cu(BCS)_2]$ from Equation 10 (where *b* is the path length of the cuvette) into Equation 9.

$$\text{Absorbance}^{483\ nm} = \varepsilon^{483\ nm} * [Cu(BCS)_2] * b \quad \text{Equation 10}$$

The data does not converge to Equation 9 as derived from Model 1. This supports that a model in which one equivalent of Cu^I binds to all Pep_3 before any binuclear $Cu^I_2Pep_3$ is formed is not correct. This is supported by the presence of a $Cu^I_2Pep_3$ species at low concentrations of Cu^I as observed in the XAS data (see below).

Model 2. An alternative approach addresses an independent step-wise model where first a Cu^IPep_3 species is formed followed by a $Cu^I_2Pep_3$ species upon addition of excess Cu^I (greater than one equivalent) as expressed in Equation 11.

$$Cu^I + Pep_3 \rightleftharpoons Cu^IPep_3 + Cu^I \rightleftharpoons Cu^I_2Pep_3 \quad \text{Equation 11}$$

However, this model is under parameterized and I cannot write an analytical equation to evaluate the individual stepwise constants.

Model 3. Since I cannot write an equation to analyze the independent stepwise model (Model 2), I attempted to simplify the data into two regions corresponding to the competition of BCS^{2-} with each independent equivalent of Cu^I. This model assumes that all of the peptide is loaded with Cu^I to form the mononuclear Cu^IPep_3 species before the second equivalent of Cu^I binds to form the binuclear $Cu^I_2Pep_3$ species; however, the fitting is done by splitting the data into two regions corresponding to $0 \leq Cu \leq 1$ and $1 \leq Cu \leq 2$. Cu^I binding can be expressed by Equations 12 and 13.

$$Cu^I + Pep_3 \rightleftharpoons Cu^IPep_3 \quad \text{Equation 12}$$

$$Cu^IPep_3 + Cu^I \rightleftharpoons Cu^I_2Pep_3 \quad \text{Equation 13}$$

The data corresponding to the first equivalent of Cu^I binding corresponds to Model 1 and will be fitted with Equation 9. The corresponding BCS^{2-} competition model for the fitting

the second half of the equation to Equation 13 can be seen in Equation 14 and the derivation is as follows.

$$Cu_2Pep_3 + 4\ BCS^{2-} \rightleftharpoons 2[Cu(BCS)_2]^{3-} + Pep_3 \qquad \text{Equation 14}$$

The apparent association constant of $Cu^I{}_2Cys_3$ can be calculated using Equation 15.

$$K_{comp} = \frac{K_{BCS}}{K_{Cu+CuCys3}} = \frac{[Cu(BCS)_2][CuPep_3]_f}{[BCS^{2-}]_f^2[Cu_2Pep_3]} \qquad \text{Equation 15}$$

Where $K_{Cu+CuCys3}$, the association constant of one equivalent of Cu^I binding to a pre-formed mononuclear Cu^I-Pep_3 species, is to be fit and K_{BCS} is a known value.[54] New mass balance equations for $[Cu]_T$ and $[Pep_3]_T$ can be seen in Equations 17 and 18. The same mass balance for $[BCS^{2-}]_T$ from Equation 8 is still appropriate here.

Mass Balance Equations:

$$[Pep_3]_T = [CuPep_3] + [Cu_2P_3]$$

$$[CuPep_3] = [Pep_3]_T - [Cu_2Pep_3] \qquad \text{Equation 16}$$

$$[Cu]_T = [Pep_3] + [Cu(BCS)_2] + [Cu_2Pep_3]$$

$$[Cu_2Pep_3] = [Cu]_T - [Pep_3]_T - [Cu(BCS)_2] \qquad \text{Equation 17}$$

Substituting Equations 16, 17 and 8 into Equation 15 yields Equation 18.

$$K_{comp} = \frac{[Cu(BCS)_2](2[Pep_3]_T - [Cu]_T + [Cu(BCS)_2])}{([Cu]_T-[Pep_3]-[Cu(BCS)_2])(([BCS^{2-}]_T-2[Cu(BCS)_2])/(1+([H^+]/Ka)))^2} \qquad \text{Equation 18}$$

The $K_{Cu+CuCys3}$ value can be directly related to the absorbance observed at 483 nm by substituting $[Cu(BCS)_2]^{3-}$ from Equation 10 (where *b* is the path length of the cuvette) into Equation 18.

This allows for the first data region to be analyzed with Equation 9 and the second half of the data to be fitted to Equation 18; however, attempts to fit each set of truncated data to Equations 9 and 18, respectively, results, once again, in nonconvergence.

Model 4. A fourth scenario, where Cu^I binds to apo-protein to form $Cu^I{}_2Cys_3$ (with no mononuclear Cu^ICys_3 species) can be expressed by Equation 19.

$$Cu_2Pep_3 + 4\ BCS^{2-} \rightleftharpoons 2[Cu(BCS)_2]^{3-} + Pep_3 \qquad \text{Equation 19}$$

The apparent association constant of $Cu^I_2Cys_3$ can be calculated using Equation 20.

$$K_{comp} = \frac{(K_{BCS})^2}{K_{Cu2Cys3}} = \frac{[Cu(BCS)_2]^2[Pep_3]_f}{[BCS^{2-}]_f^4[Cu_2Pep_3]} \qquad \text{Equation 20}$$

Where $K_{Cu2Cys3}$, the association constant of Cu^I binding to apo-peptide to form a binuclear $Cu^I_2Cys_3$ site, is to be fit and K_{BCS} is a known value.[54] New mass balance equations for $[Cu]_T$ and $[Pep_3]_T$ can be seen in Equations 21 and 22. The same mass balance for $[BCS^{2-}]_T$ from Equation 8 is still appropriate here.

Mass Balances:

$$[Cu]_T = 2[Cu_2Pep_3] + [Cu(BCS)_2] + [Cu]_f$$

$$[Cu_2Pep_3] = \tfrac{1}{2}([Cu]_T - [Cu(BCS)_2]) \qquad \text{Equation 21}$$

$$[Pep_3]_T = [Cu_2Pep_3] + [Pep_3]_f$$

$$[Pep_3]_f = [Pep_3]_T - [Cu_2Pep_3] \qquad \text{Equation 22}$$

Substituting Equations 8, 21 and 22 into Equation 20 yields Equation 23.

$$K_{comp} = \frac{[Cu(BCS)_2]^2([Pep_3]_T - (\tfrac{1}{2}([Cu]_T - [Cu(BCS)_2])))}{([BCS^{2-}]_f + [BCS^{2-}][H^+](1/K_a) + 2[Cu(BCS)_2])^4(\tfrac{1}{2}([Cu]_T - [Cu(BCS)_2]))} \qquad \text{Equation 23}$$

The $K_{Cu2Cys3}$ value can be directly related to the absorbance observed at 483 nm by substituting $[Cu(BCS)_2]^{3-}$ from Equation 10 (where *b* is the path length of the cuvette) into Equation 23.

For the experiment, where aliquots of BCS^{2-} are titrated into a solution of Cu^I-bound Pep_3, an absorption band at 483 nm is due to the $[Cu^I(BCS)_2]^{3-}$ complex, and increases as Cu^I is complexed by BCS^{2-}. Analysis of a decrease in Cu^I-Pep complex at 266 nm is convoluted due to absorbance in the UV region by the $[Cu^I(BCS)_2]^{3-}$ complex. The titration data at Abs 483 were fit by rearranging Equation 9, Equations 9 and 18, for their respective regions of titration data, and Equation 23, alone in Prism 5 (GraphPad Software).[55] The data would not converge to either Equation 9 or a combination of Equations 9 and 18.

The data will fit to Equation 23, but there are too many unknown parameters to fit to Model 2. Subsequently, I will present XAS data at pH 7.5 that suggests at very low Cu^I concentration a significant amount of a $Cu^I_2Pep_3$ species is observed. If Model 4 is indeed correct, then this suggests that the binding affinity for Cu^I to Pep_3 to form the mononuclear site is comparable to the second equivalent of Cu^I binding to Cu^IPep_3 to form the dinuclear $Cu^I_2Pep_3$ species.

Direct Cu^I-binding titrations. Titrations of Cu^I into peptide were performed at room temperature and monitored via UV-Vis spectroscopy in a 1-cm quartz anaerobic cuvette. Cu^I titrations were completed in 50 mM degassed potassium phosphate (KPhos) buffer at pH 8.0 at a peptide concentration of ~50-150 μM (17-50 μM 3SCC). KPhos adjustments were made using small aliquots of concentrated KOH and HCl. Aliquots of a $[Cu(CH_3CN)_4]BF_4$, dissolved in degassed acetonitrile and diluted in degassed H_2O, were titrated into the peptide solution. For all titrations, a background spectrum of buffer and water were subtracted from the peptide and metallated samples.

Equation 24 can express the binding equilibrium for the competition experiment of Cu^I binding to a peptide with both Cys_3 and His_3 sites, **GR**L2WL16CL30H. Similarly to the BCS^{2-} titrations, it is assumed that no free Cu^I is present in solution during these titrations. Additionally, due to the non-convergence of Equations 9 and 18, in addition to the 2:1 binding stoichiometry observed in the direct Cu^I binding experiments, it is assumed that no mononuclear Cu^I species is formed. A final assumption is that the binding affinity of Cu^I to a His_3 site does not influence the affinity of Cu^I binding to a Cys_3 site in the same peptide scaffold, and vice versa.

$$2CuHis_3 + Cys_3 \rightleftharpoons Cu_2Cys_3 + 2His_3 \qquad \text{Equation 24}$$

The competition constant for Cu^I binding to the Cys_3 and His_3 sites can be calculated using Equation 25.

$$K_{comp} = \frac{K_{Cu2Cys3}}{(K_{CuHis3})^2} = \frac{[Cu_2Cys_3][His_3]_f^2}{[Cys_3]_f[CuHis_3]^2} \qquad \text{Equation 25}$$

Where $K_{Cu2Cys3}$ is the association constant to be fit, K_{CuHis3} is the association constant determined from Cu^I binding to a His_3 site in the absence of a Cys_3 site and K_{BCS} is a

known value.[54] A value of 5.0 x 10^{12} M^{-1} is used for K_{CuHis3}, as previously reported for **TRI**L2WL23H of 5.0 x 10^{12} M^{-1}.[56] For the titration, where aliquots of Cu^{I} are titrated into a solution of **GR**L2WL16CL30H, an absorption band at 266 nm is due to the Cu_2Cys_3 complex, and increases as Cu^{I} is complexed at the Cys_3 site. Mass balance equations for $[Cu]_T$, $[Cys_3]_T$, and $[His_3]_T$ can be defined and related to $[Pep_3]_T$ as seen in Equations 23, 24, 25, and 26.

Mass Balance Equations:

$$[Cu]_T = [CuHis_3] + 2[Cu_2Cys_3] + [Cu]_f$$

$$[CuHis_3] = [Cu]_T - 2[Cu_2Cys_3] \qquad \text{Equation 23}$$

$$[Pep_3]_T = [His_3]_T = [Cys_3]_T \qquad \text{Equation 24}$$

$$[His_3]_T = [CuHis_3] + [His_3]_f$$

$$[His_3]_f = [His_3]_T - [CuHis_3] \qquad \text{Equation 25}$$

$$[Cys_3]_T = [Cu_2Cys_3] + [Cys_3]_f$$

$$[Cys_3]_f = [Cys_3]_T - [Cu_2Cys_3] \qquad \text{Equation 26}$$

Substituting Equations 23-26 into Equation 21 yields Equation 27.

$$\frac{K_{Cu2Cys3}}{(K_{CuHis3})^2} = \frac{[Cu_2Cys_3]([Pep_3]_T - [Cu]_T + 2[Cu_2Cys_3])^2}{([Pep_3]_T - [Cu_2Cys_3])([Cu]_T - 2[Cu_2Cys_3])^2} \qquad \text{Equation 27}$$

The $K_{Cu2Cys3}$ value can be directly related to the absorbance observed at 266 nm by substituting $[Cu_2Cys_3]$ from Equation 28 (where *b* is the path length of the cuvette) into Equation 27.

$$\text{Absorbance}^{266\text{ nm}} = \varepsilon^{266\text{ nm}} * [Cu_2Cys_3] * b \qquad \text{Equation 28}$$

Unfortunately, the number of variables in this equation can not be reduced sufficiently to be inputted properly into Prism 5 (GraphPad Software)[55]; however, the equation can be manually used to individually determine K_{comp} for each titration point (*vide infra*). A discussion of the associated assumptions made for this model, listed above, can be found below.

Cu^{I} and Pb^{II} competition for Cys_3 binding. Cu^{I} and Pb^{II} competition experiments were

conducted at room temperature and monitored via UV-Vis spectroscopy in a 1-cm quartz anaerobic cuvette. Competition experiments were performed in 50 mM degassed TRIS buffer at pH 7.5 or 8.5 at a peptide concentration of 30 μM. Aliquots of Pb^{II} or Cu^{I} were titrated into the peptide solution and competition was analyzed via increases or decreases in the $Pb^{II}S_3$ LMCT band at ~340 nm, indicating binding or displacement of Pb^{II} by Cu^{I}, respectively. $Pb^{II}Cys_3$ and $Cu^{I}Cys_3$ sites both show features at ~266 nm and therefore straightforward analysis of the competition at this wavelength is non-trivial. For all titrations, the difference spectra were obtained by subtracting the background spectrum of the peptide under identical conditions but in the absence of metal.

^{207}Pb NMR Spectroscopy. NMR samples were prepared, anaerobically, by dissolving pure, lyophilized peptide in degassed 10% D_2O in an inert atmosphere box. Metallopeptides were prepared by addition of isotopically enriched $^{207}Pb(NO_3)_2$ (92.4%, Oak Ridge National Laboratory, TN) and Cu^{I} from a stock solution of $[Cu(CH_3CN)_4]BF_4$ dissolved in acetonitrile, to non-buffered solutions of 3-5 mM peptide trimer. All samples were adjusted to the desired pH using small aliquots of concentrated KOH or HCl. ^{207}Pb NMR spectra were recorded at a frequency of 145.9 MHz on a Varian 700 MHz spectrometer at 25 °C with spin = 0, 0.20 ms relaxation time, and 20 ms acquisition time. Linear predictions were performed to remove noise, and the real FID was determined as previously described.[46,57,58] The data were processed with an exponential line broadening of 400-600 Hz using MestRe-C software.[59] The ^{207}Pb NMR shifts are reported as the observed signal plus ~2986 ppm, as reference by tetramethyllead (δ=0 ppm; toluene) using 1 M $Pb(NO_3)_2$ in D_2O (natural abundance salt, δ=-2986 ppm) as an external standard. The external standard was run after each experimental collection to adjust for any shifting of the magnetic field. All NMR samples containing Cu^{I} were prepared in an inert atmosphere glove box adding one equivalent of Cu^{I} followed by any necessary adjustment of pH.

X-ray Absorption Spectroscopy. Solutions of 1.0 mM Cu^{I}_S(3SCC) were prepared anaerobically with 30-50 mM HEPES buffer at pH 7.5. An excess (1.0 mM) of apo-3SCC was present to ensure the free Cu^{I} concentration was minimal (<0.01%). The samples were pH adjusted then mixed with 50% glycerol (glassing agent) and loaded into

a sample cell and frozen in liquid nitrogen for transport and analysis. All XAS measurements were performed at Stanford Synchrotron Radiation Lightsource, SSRL, (Beam line: 7-3). A Si(220) double crystal monochromator was utilized, with a flat Rh-coated vertically collimating harmonic rejection mirror. Data were collected with a beam size of 1 x 9 mm^2 and the x-ray energy was calibrated by collecting the absorption spectrum of a Cu foil as a reference, placed between two ionization chambers situated after the sample, at the same time as the fluorescence data were collected, with the first infection point assigned as 8980.3 eV. The samples during data acquisition were maintained at a temperature of ~7-9 K, and the data were measured in fluorescence mode with a 30-element energy resolving Ge detector. The data were collected using 0.25 eV steps in the XANES region (1 sec. integration time), and 0.05 $Å^{-1}$ increments for the extended X-ray absorption fine structure (EXAFS) region up to k=13.5 $Å^{-1}$, with an integration times of 1-20 s (k^3 weighted) in the EXAFS region for a total scan time of ~40 min. The raw data were examined for glitches and the fluorescence from the good channels was then utilized for averaging. The EXAFS data were analyzed using the EXAFSPAK[60] suite of programs, where the theoretical amplitude and phase parameters used were calculated using FEFF 9.[61] An initial E_0 value of 9,000 eV was used to convert data to *k*-space, and the background was removed using a 3-region cubic spline.

Results and Discussion

In Chapter 2, I determined that Cu^I will compete with Pb^{II} when only one metal binding site (Cys_3) is present in a **GR** or **TRI** peptide (Figure 4-1). In the presence of one equivalent of Cu^I, Pb^{II} titrated into **GR**L2WL16C (Table 4-1) resulted in an extinction coefficient of ~2000 $M^{-1}cm^{-1}$ at $\lambda_{345\ nm}$, approximately half of the maximal extinction coefficient observed for $Pb^{II}S_3$ in the absence of Cu^I. This lead me to believe that not only does Cu^I bind to the Cys_3 site provided within our **GR** and **TRI** peptides, but that Cu^I also binds with a relatively high association constant considering the competition observed with Pb^{II} for the site, and our previous knowledge that Pb^{II} binds with an affinity so high that we are not currently able to accurately measure $Pb^{II}Cys_3$ affinities. Therefore, I set out to characterize Cu^I binding to Cys_3 sites with the hope that I could eventually use the Cu^I and Pb^{II} competition to better characterize $Pb^{II}Cys_3$ binding.

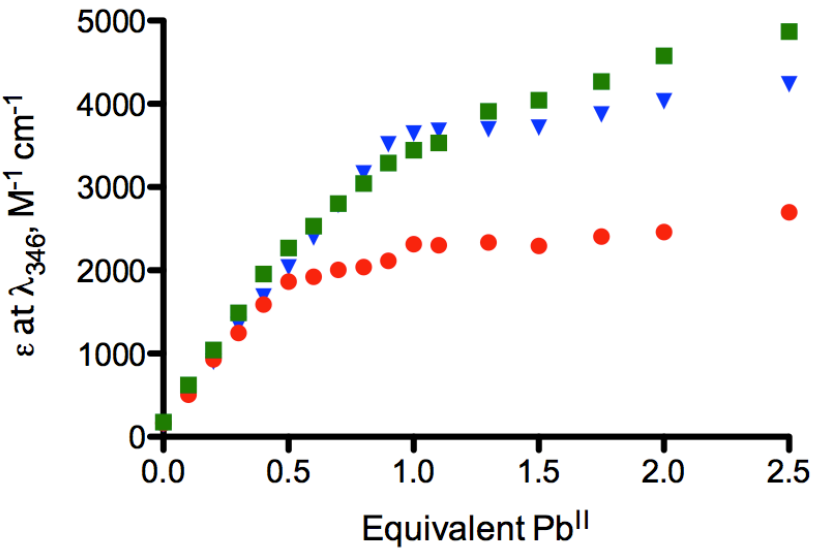

Figure 4-1. Titration curve of Pb^{II} into a solution of **GR**L2WL16C (blue inverted triangles), Cu^{I}(**GR**L2WL16C)$_3^{n+}$ (red circles) and Cu^{I}(**GR**L2WL16C)$_3^{n+}$ (green squares) shown as absorbance at 346 nm divided by concentration of Pb^{II} added (ε at λ_{346}) versus the equivalent of Pb^{II} added, with respect to the total concentration of 3SCC. Data collected at pH 8.5 in 100 mM Tris-HCl buffer.

Table 4-1. Peptide Sequences

Peptide	Sequence
	abcdefg
TRI	Ac-G LKALEEK LKALEEK LKALEEK LKALEEK G-NH_2
TRIL12AL16C	Ac-G LKALEEK LKA***A***EEK ***C***KALEEK LKALEEK G-NH_2
TRILWL12AL16C	Ac-G ***W***KALEEK LKA***A***EEK ***C***KALEEK LKALEEK G-NH_2
TRILWL12$_D$LL16C	Ac-G ***W***KALEEK LKA$_D$**L**EEK***C***KALEEK LKALEEK G-NH_2
TRIL2WL16C	Ac-G ***W***KALEEK LKALEEK ***C***KALEEK LKALEEK G-NH_2
GRAND	Ac-G LKALEEK LKALEEK LKALEEK LKALEEK LKALEEK G-NH_2
GRL2WL16C	Ac-G ***W***KALEEK LKALEEK ***C***KALEEK LKALEEK LKALEEK G-NH_2
GRL2WL16CL30H	Ac-G ***W***KALEEK LKALEEK ***C***KALEEK LKALEEK ***H***KALEEK G-NH_2
CoilSer	Ac-E WEALEKK LAALESK LQALEKK LEALEH G-NH_2
CSL9C	Ac-E WEALEKK ***C***AALESK LQALEKK LEALEH G-NH_2
GRANDCoilSer	Ac-E WEALEKK LAALESK LQALEKK LQALEKK LEALEH G-NH_2
GRCSL12DLL16C	Ac-E WEALEKK LAA$_D$**L**ESK***C***QALEKK LQALEKK LEALEH G-NH_2
GRCSL16CL30H	Ac-E WEALEKK LAALESK ***C***QALEKK LQALEKK ***H***EALEH G-NH_2

Spectroscopic Determination of Cu^I Binding Stoichiometry to Cys_3-Containing 3SCCs

Native copper metallochaperone studies revealed that Cu^ICys_3 centers provide a characteristic LMCT band at ~266 nm. Aliquots of Cu^I (stock $[Cu(CH_3CN)_4]BF_4$ dissolved in degassed acetonitrile and diluted in H_2O) were added in an inert atmosphere box to a solution of **TRI**L2WL16C (Table 4-1). As the peptide complexes Cu^I, an increase in absorbance is observed at 266 nm (Figure 4-2A). Plotting the change in absorbance at 266 nm, divided by the concentration of total Cu^I added (the effective extinction coefficient at 266 nm), versus the concentration of total Cu^I added provides a titration curve that shows a steep increase in absorbance to two equivalents of Cu^I added (with respect to 3SCC concentration) followed by a flattening out of the titration curve (Figure 4-2B). The $Cu^I_2Cys_3$ extinction coefficient at $\lambda_{266\ nm}$ is calculated to be 15,860 $M^{-1}cm^{-1}$. Interestingly, this data supports two equivalents of Cu^I binding to one equivalent of trimer.

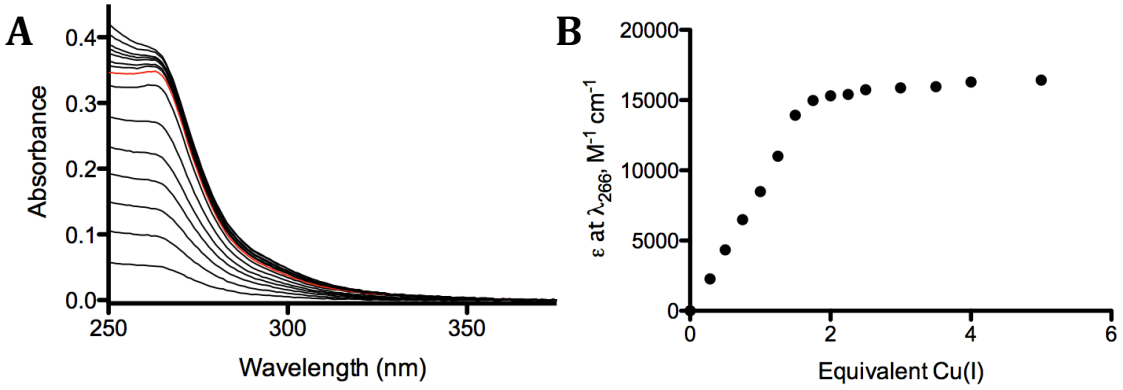

Figure 4-2. Titration spectra of Cu^I into a solution of **TRI**L2WL16C at pH 8.0 in 50 mM KPhos buffer (Panel A). Titration curve showing the 2:1 binding stoichiometry of Cu^I to 3SCC at 266 nm shown as absorbance at 266 nm divided by concentration of Cu^I added (ε at λ_{266}) versus the equivalent of Cu^I added, with respect to the total concentration of 3SCC (panel B).

The titration was repeated using the peptide **TRI**L2W (Table 4-1) to determine if Cu^{I} showed nonspecific binding to the exterior of the 3SCC, which might result in a contribution to the 266 nm band observed in the titration of Cu^{I} to **TRI**L2WL16C. Aliquots of Cu^{I} were added, in an inert atmosphere box, to a solution of **TRI**L2W (3SCC). No complexation of Cu^{I} is observed and virtually no change is seen in the UV spectra even after the addition of five equivalents of Cu^{I} have been added (Figure 4-3A). These results indicate that the 2:1 ratio of Cu^{I} to 3SCC corresponds to two Cu^{I} atoms binding to the Cys_3 binding site without the presence of non-specific binding to the exterior of the 3SCC (Figure 4-3B).

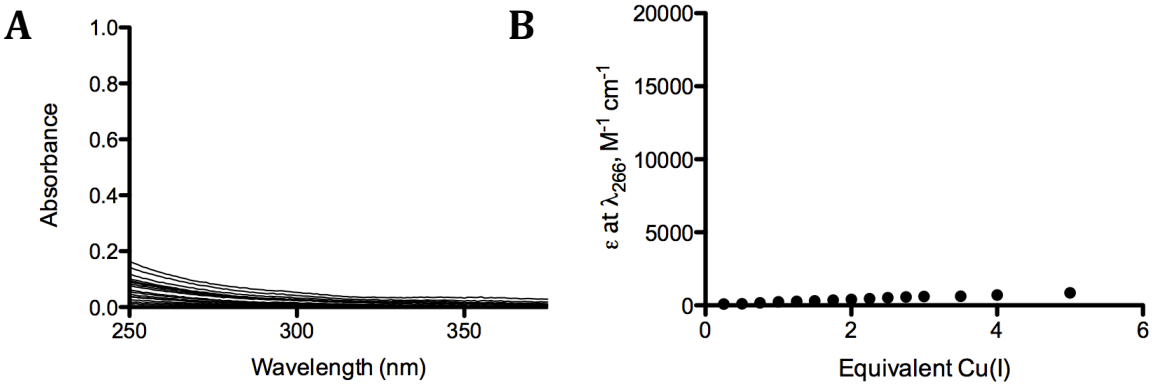

Figure 4-3. Titration spectra of Cu^{I} into a solution of **TRI**L2W at pH 8.0 in 50 mM KPhos buffer (Panel A). Titration curve showing the 2:1 binding stoichiometry of Cu^{I} to 3SCC at 266 nm shown as absorbance at 266 nm divided by concentration of Cu^{I} added (ε at λ_{266}) versus the equivalent of Cu^{I} added, with respect to the total concentration of 3SCC (panel B).

X-ray absorption spectroscopy (XAS) was used to obtain metrical parameters for the coordination environment when Cu^{I} is bound to **TRI**L2WL16C. Samples consisted of 1 mM Cu^{I}, 2 mM 3SCC, ~30-50 mM HEPES buffer, pH 7.5, and 50% glycerol. Examination of the X-Ray absorption near-edge structure (XANES) can give information about the coordination number and the oxidation state of the bound metal. The intensity of the pre-edge peak is particularly useful in this regard, as the height of the 1s→4p transition observed at 8,983 eV with respect to the edge peak (8,995 eV) is indicative of coordination number. For thiolate-rich Cu^{I} species, an intense peak with a ratio of ~0.9 or greater, when compared to the edge height, reflects a Cu^{I} coordination number of two (diagonal or linear geometry). A moderate peak height with a ratio of ~0.5-0.7 is

indicative of three-coordinate Cu^{I} binding, and an essentially non-existent pre-edge peak is observed for four-coordinate species.[62–65] The intense feature observed for Cu^{I}-bound **TRI**L2WL16 has a ratio of approximately 0.83, and falls in between the reported values for 2- and 3-coordinate Cu^{I} complexes (Figure 4-4).

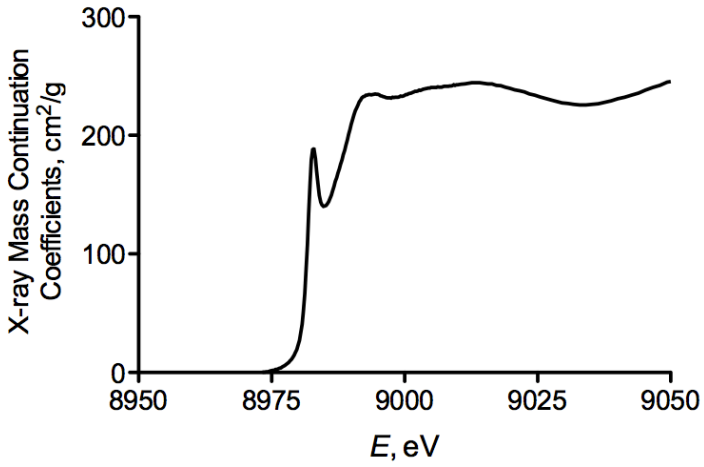

Figure 4-4. XANES of Cu^{I}_{2}(**TRI**L2WL16C)$_3^-$. Data collected at ~7K, pH 7.5 HEPES buffer.

Fitting of the extended X-Ray absorption fine structure (EXAFS) spectra can be used to determine Cu^{I} bond distances. A nearest-neighbor peak, typical of scattering observed by direct sulfur coordination, dominates the EXAFS spectrum at ~2.2 Å (Figure 4-5). There is a second unique peak observed at a longer distance (~2.65 Å) that is not consistent with ligands previously observed in our 3SCC, such as sulfur, nitrogen, or oxygen coordination. Due to the intensity of the pre-edge peak I used fitting models that included both two and three sulfur ligands, as well as varying numbers of oxygen ligands to fit the data. However, due to the out-of-phase components for sulfur and oxygen scatterers, it is difficult, using XAS spectroscopy, to elucidate if oxygen ligands are present in addition to the sulfur ligands. Fits with only two sulfur ligands consistently provided worse fits than three-sulfur fits (Table 4-2). No combination of sulfur, oxygen, and/or nitrogen provided a fit that accounted for the long distance scatterer at ~2.65 Å. Considering the UV-Vis spectroscopy data showing a 2:1 binding stoichiometry of Cu^{I}:3SCC, I also included a Cu-Cu interaction in the fits, which finally provided a fit that accounted for the second peak observed at ~2.65 Å.

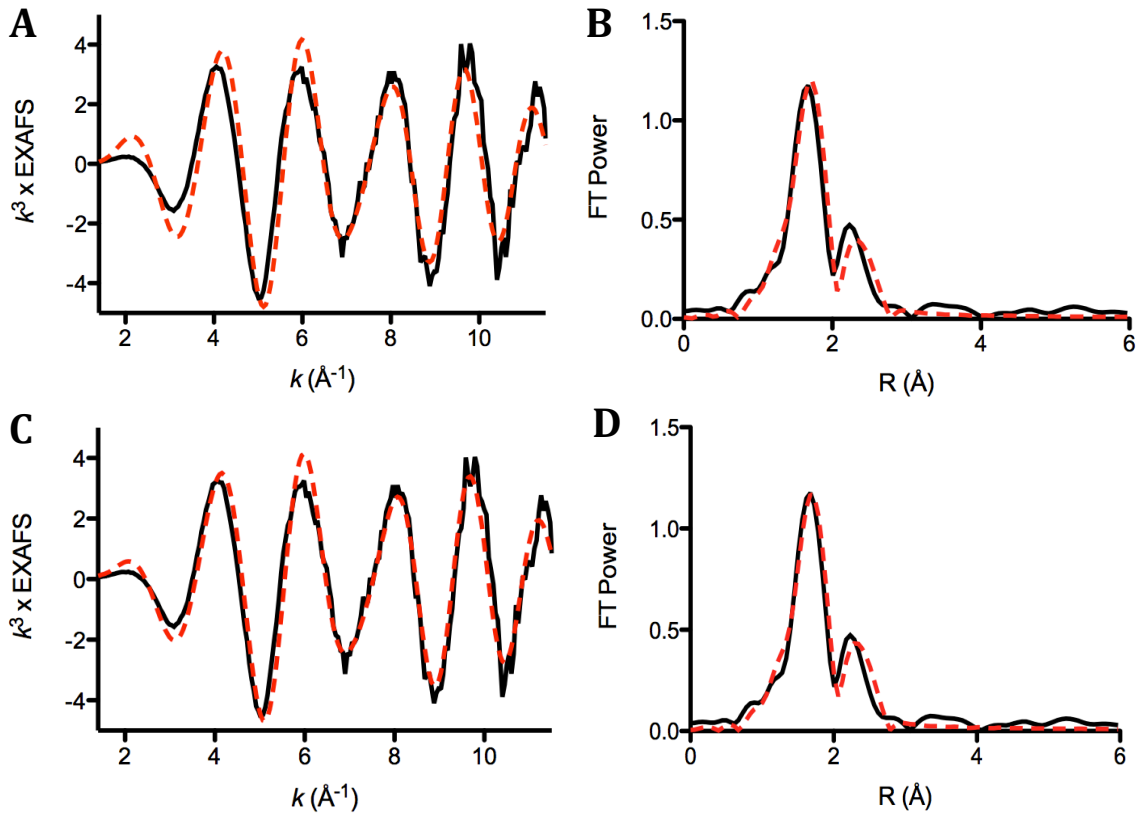

Figure 4-5. EXAFS and FT data (black) and fitting (red) for Cu^{I}_{2}(**TRI**L2WL16C)$_3^-$ with (A)(B) S_3Cu_1 and (C)(D) $S_3O_1Cu_1$ shells.

Table 4-2 and Figure 4-5 show the best EXAFS fits for Cu^{I}-bound **TRI**L2WL16C at pH 7.5. The fits support a model where two Cu^{I} ions are coordinated to three sulfur atoms at 2.20 Å and exhibit one Cu^{I}-Cu^{I} interaction at 2.66 Å. The addition of an oxygen parameter (Table 4-2), as seen in Figure 4-5, results in a slightly better fit with a Cu^{I}-O distance of 2.08 Å. The Cu^{I}-S distances of 2.20 Å falls in between reported two- and three-coordinate Cu^{I} centers (2.16 and 2.28 Å, respectively).[66]

At this particular point, Dr. Leela Ruckthong built models of a proposed binuclear Cu^{I} center in an **a** site Cys_3. Figure 4-6 shows a binuclear Cu^{I} center substituted for the As^{III} ion in As^{III}_{S}(**CS**L9C)$_3$, with the binuclear site laying directly on the three-fold axis of the 3SCC. Two water molecules were included, one above, and one below, the binuclear site to provide tetrahedral Cu^{I} coordination, as trigonal pyramidal Cu^{I} geometry is unprecedented. The Cu^{I}-OH_2 distances were set arbitrarily at 2.0 Å for modeling purposes. The Cu^{I}-Cu^{I} distance was fixed at 2.66 Å, with the Cu^{I} ion closer to the C-

termini of the 3SCC having to be moved slightly closer to the C-termini than the As^{III} ion. The Cu^{I}-S distances were optimized to satisfy all torsion angle requirements of the Cys_3 ligands. With the Cu^{I}-Cu^{I} distance fixed, the resulting Cu^{I}-S distances ranged from 2.44-2.46 Å. These distances are ~0.2 Å too long in comparison to the XAS fits. Conversely, fixing the Cu^{I}-S distances at 2.2 Å resulted in a Cu^{I}-Cu^{I} distance of 2.4-2.5 Å, too short in comparison to the XAS fits. Attempts at rotating the Cys_3 rotamers to provide a model consistent with both the Cu^{I}-S distances of 2.2 Å, while maintaining a Cu^{I}-Cu^{I} distance of 2.66 Å, were unsuccessful.

Table 4-2. EXAFS parameters of $Cu_2^{I}{}_S$(**TRI**L2WL16C)$_3^-$

Shell	Component	Fit Result
S_2Cu_1[a]	Cu-S	R =2.19 σ^2 = 0.00517
	Cu-Cu	R = 2.65 σ^2 = 0.0517 F = 141
S_3Cu_1	Cu-S	R =2.20 σ^2 = 0.00644
	Cu-Cu	R = 2.66 σ^2 = 0.00761 F = 129
$S_3O_1Cu_1$	Cu-S	R = 2.19 σ^2 = 0.00358
	Cu-O	R = 2.08 σ^2 = 0.00763
	Cu-Cu	R = 2.66 σ^2 = 0.00671 F = 79.0
$S_2S_1^*Cu_1$	Cu-S	R = 2.19 σ^2 =0.00358
	Cu-S*	R =2.37 σ^2 =0.011
	Cu-Cu	R = 2.66 σ^2 =0.0086 F = 98.0

R = distance in Å, σ^2 = Debeye Waller Factor in $Å^2$, ΔE_0 is fixed at -10. [a]Fit only converged when σ^2 values were linked.

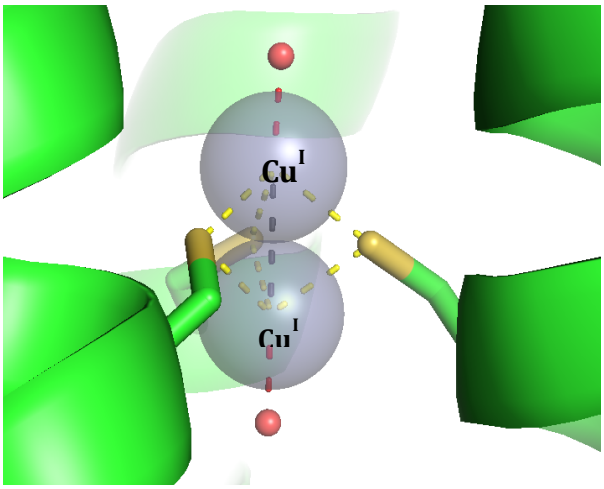

Figure 4-6. Side-on view of a pymol representation of a modeled symmetric binuclear Cu^I site bound to three sulfur atoms. Site is modeled from the $As^{III}_S(\mathbf{CS}L9C)_3$ structure (PDB: 2JGO).[44] Main chain atoms are shown in green, water molecules are shown in small red spheres, cysteine residues are shown as sticks with sulfur atoms highlighted in yellow and Cu^I ions are shown as grey spheres. The Cu^I-Cu^I distance is fixed at the EXAFS determined 2.67 Å and the water molecules are placed 2.0 Å either above the top Cu^I or below the lower Cu^I in the binuclear site. Resulting Cu^I-S distances are 2.33 Å (avg), which is approximately 0.12 Å longer than the EXAFS derived Cu-S distance.

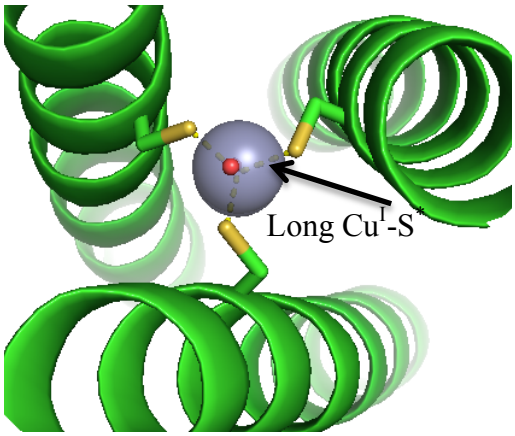

Figure 4-7. Top-down view of a pymol representation of a modeled binuclear Cu^I site bound to three sulfur atoms, shifted off of the helical axis toward the helical interface. The site is modeled from the $As^{III}_S(\mathbf{CS}L9C)_3$ structure (PDB: 2JGO).[44] Main chain atoms are shown in green, water molecules are shown in small red spheres, cysteine residues are shown as sticks with sulfur atoms highlighted in yellow and Cu^I ions are shown as grey spheres. The Cu^I-Cu^I distance is fixed at 2.67 Å and the water molecules are 2.0 Å above and below the Cu^I binuclear site. Resulting Cu^I-S distances are 2.21-2.22 Å (avg) and Cu^I-S^* distance is 2.5-2.6 Å (avg).

Since the above attempts did not provide Cu^{I}-S and Cu^{I}-Cu^{I} distances consistent with the XAS data, we then modeled the system where the Cu^{I}-Cu^{I} center was shifted off of the helical axis toward the helical interface of two of the helices (Figure 4-7). Again, arbitrary Cu^{I}-OH_2 distances were set at 2.0 Å to provide tetrahedral model geometry. The shifting of the binuclear site provided a model that could accommodate both a Cu^{I}-Cu^{I} distance of 2.66 Å and two Cu^{I}-S distances of 2.2 Å. However, to compensate for this adjustment, a longer third Cu^{I}-S* distance, denoted with an asterisk to differentiate it from the shorter thiolate, was measured at 2.47 – 2.56 Å (Figure 4-7). Re-fitting the EXAFS data with a $S_2S_1^{*}Cu_1$ coordination provided Cu^{I}-S distances and a Cu^{I}-Cu^{I} interaction at 2.19 Å and 2.66 Å, respectively, with a longer Cu^{I}-S^{*} distance of 2.37 Å (Table 4-2, Figure 4-8). Visually, the discrepancy between the raw data and the previous best fits observed at the long distance scatterer (~2.66 Å) has been adjusted for and the fit via inclusion of a longer distance Cu^{I}-S^{*} distance (Figure 4-8). The fitted Cu^{I}-S^{*} distance is still slightly shorter than the distance provided from the model (fit: 2.37 vs. model: 2.45 Å). It is possible that there is some phase interference in the XAS data between the Cu^{I}-Cu^{I} interaction and the Cu^{I}-S^{*} distance, resulting in the discrepancy in distances between the EXAFS fit and the model data.

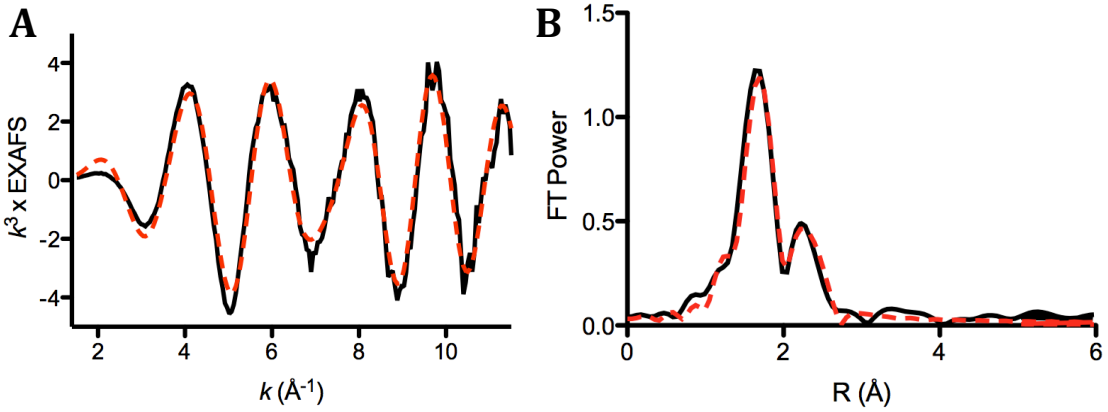

Figure 4-8. EXAFS (A) and FT (B) data (black) and fitting (red) for Cu^{I}_2(**TRI**L2WL16C)$_3^{-}$ with a $S_2S^{*}_1Cu_1$ shell.

In both of these models the location of the Cu^{I} ions, with respect to the sulfur ligands, provides a trigonal pyramidal Cu^{I} binding geometry. As mentioned above, trigonal pyramidal Cu^{I} sites are largely unprecedented. Previously, I accounted for this by

inclusion of a water molecule above, and below, the modeled binuclear $Cu^{I}_{2}Cys_{3}$ sites to provide a tetrahedral geometry for both copper ions. However, the XANES analysis of Cu^{I}_{2}(**TRI**L2WL16C)$_{3}^{-}$ does not support a tetrahedral Cu^{I} geometry. Therefore, I returned to the model to address the Cu^{I} ions moving in different directions while maintaining a 2.66 Å separation from one another (Figure 4-9). Shifting, asymmetrically, the binuclear site provided a model where each metal ion has two 2.2 Å Cu^{I}-S distances and one long Cu^{I}-S^{*} distance of 2.8-2.9 Å. In this scenario, the long distance Cu^{I}-S^{*} is to different helices. For example, if the "top" Cu^{I}, with respect to the N-terminal, is 2.2 Å from the sulfur ions of Cys residues of helices A and B, then the "bottom" Cu^{I} would be 2.2 Å from helices B and C. In this model the long Cu^{I}-S^{*} distance is still longer than the fit Cu^{I}-S^{*} distance (fit: 2.37 vs. model: 2.8-2.9 Å). It is possible that the Cu^{I}-S^{*} distance obtained from the EXAFS fit is convoluted due to the heavy Cu-Cu scatterer and at this time I believe that the models here offer three possibilities of how a binuclear Cu^{I} site is accommodated within a Cys_{3} site. Ultimately, a crystal structure is required to further elucidate the structure of such a binuclear site.

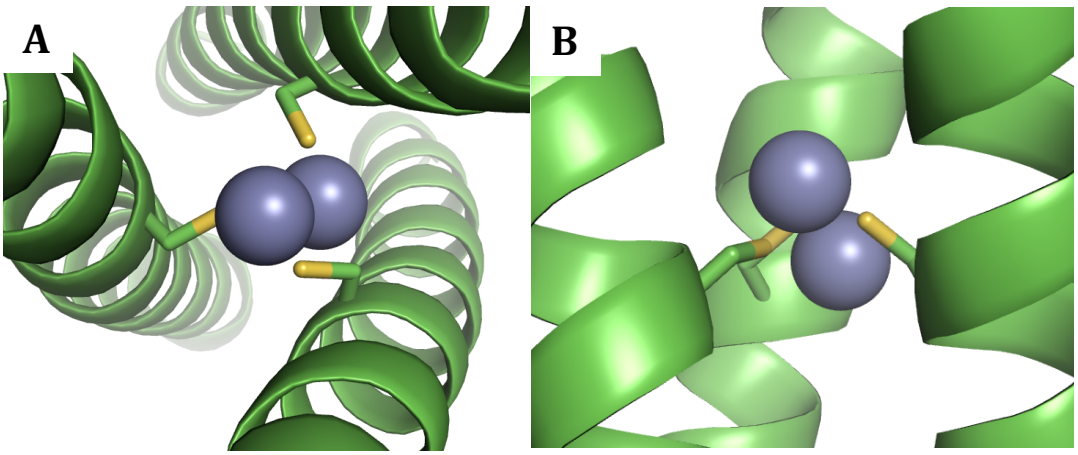

Figure 4-9. (A) Top-down and (B) side-on view of a Pymol representation of a modeled symmetric binuclear Cu^{I} site bound to three sulfur atoms. Site is modeled from the As^{III}_{S}(**CS**L9C)$_{3}$ structure (PDB: 2JGO).[44] Main chain atoms are shown in green, cysteine residues are shown as sticks with sulfur atoms highlighted in yellow and Cu^{I} ions are shown as grey spheres. The Cu^{I}-Cu^{I} distance is fixed at the EXAFS determined 2.67 Å. Resulting Cu^{I}-S distances are 2.2 Å, consistent with the EXAFS fits, and $Cu^{I}S^{*}$ distances are 2.8-2.9 Å, ~0.4 Å longer than the EXAFS derived Cu^{I}-S^{*} distance.

I next analyzed Cu^{I} binding to **TRI**L2WL12$_{D}$LL16C and **TRI**L2WL12AL16C to see if altering the sterics in the layer directly above the Cys_3 binding site, with respect to the N-termini, provided any differences in the UV spectroscopy or the titration data (Table 4-1, Figures 4-10A and 4-10C). Similarly to **TRI**L2WL16C, aliquots of Cu^{I} were added in an inert atmosphere box to a solution of **TRI**L2WL12DLL16C and **TRI**L2WL12AL16C. An increase at 266 nm was observed upon peptide complexation of Cu^{I}, for both peptides until two equivalents of Cu^{I} had been added, at which point the absorbance at 266 nm ceased to increase upon further additions of Cu^{I} (Figure 4-10C and 4-10D). In both cases the titration data plateau at two equivalents of Cu^{I} and the absorbance at two equivalents of Cu^{I} added correspond to extinction coefficients of 17,170 and 16,440 $M^{-1}cm^{-1}$. Preliminary XAS data analysis for both Cu^{I}-bound **TRI**L2WL12$_{D}$LL16C and **TRI**L2WL12AL16C indicates that both of these peptides behave similarly to Cu^{I}_{2}(**TRI**L2WL16C)$_3^{-}$.

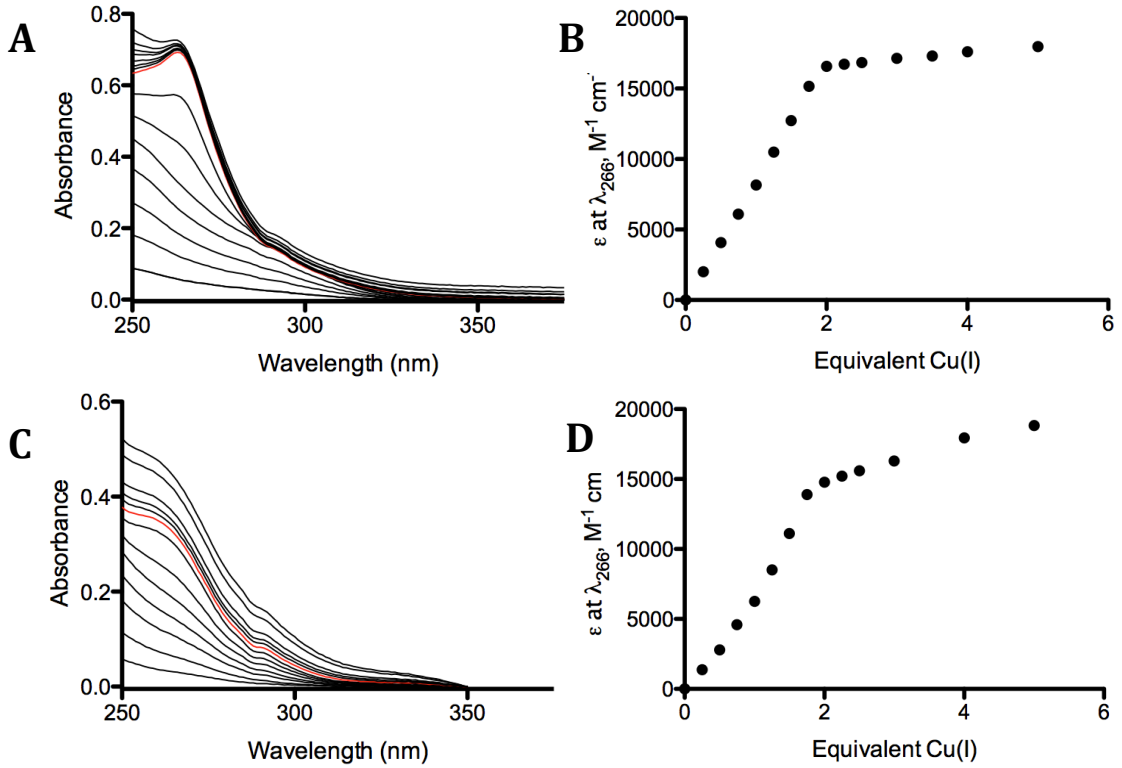

Figure 4-10. Titration spectra of Cu^{I} into a solution of (A) **TRI**L2WL12$_{D}$LL16C and (C) **TRI**L2WL12AL16C at pH 8.0 in 50 mM KPhos buffer. Titration curves showing the 2:1 binding stoichiometry of Cu^{I} to 3SCC for (B) **TRI**L2WL12$_{D}$LL16C and (D) **TRI**L2WL12AL16C at 266 nm shown as absorbance at 266 nm divided by concentration of Cu^{I} added (ε at λ_{266}) versus the equivalent of Cu^{I} added, with respect to the total concentration of 3SCC.

Preliminary XAS and UV-Vis analysis of Cu^I binding to **TRI** and **GR** peptides containing Cys_3 sites at pH 9.0 have shown different behavior when compared to the pH 7.5 data. The UV-Vis titration of Cu^I into **TRI**L2WL16C at pH 9.0 provides a similar increase in absorbance at 266 nm with a binding curve that shows slightly less linear character in the region of 0-2 eq. of Cu^I (Figure 4-11); however, saturation is still observed at two equivalents of Cu^I, supporting the formation of a binuclear site. XAS data at pH 9.0 adding one equivalent of Cu^I provides evidence for a mononuclear Cu^I site, while when two equivalents of Cu^I are present a Cu^I-Cu^I interaction is observed, supporting formation of the binuclear site at higher equivalents of Cu^I (data not included). At this point, more analysis is necessary but a model where the mononuclear site is formed at low concentrations of metal with formation of the binuclear site at higher metal concentrations is consistent with the biphasic nature observed via the UV-Vis titration. These differences between pH 7.5 and 9.0 indicate that the model of binding Cu^I to a Cys_3 site is pH dependent.

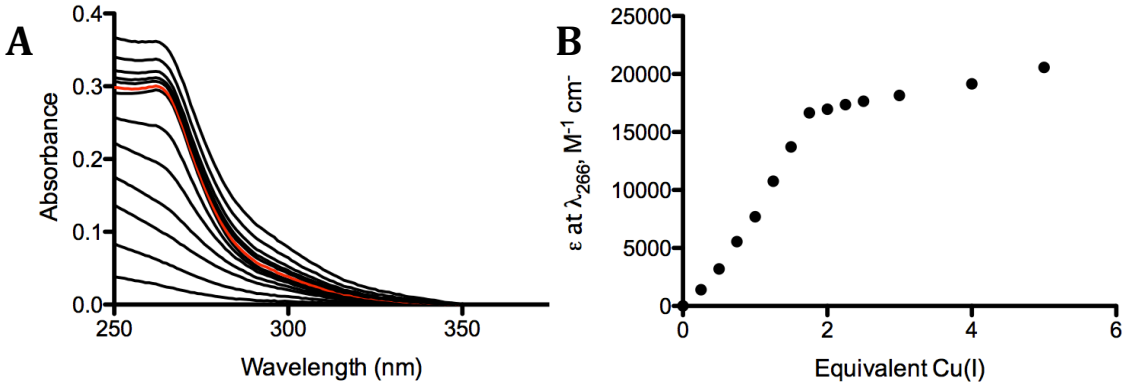

Figure 4-11. The titration spectra of Cu^I into a solution of **TRI**L2WL16C at pH 9.0 in 50 mM CHES buffer (Panel A). Titration curve showing the 2:1 binding stoichiometry of Cu^I to the 3SCC at 266 nm. The data are shown as absorbance at 266 nm divided by concentration of Cu^I added (ε at λ_{266}) versus the equivalent of Cu^I added with respect to the total concentration of 3SCC (panel B).

Comparison of Spectroscopic Features to Native Cu^I-Metallochaperones

I then looked to thiol-rich Cu^I native metalloproteins to compare the metrical and spectroscopic features observed in my binuclear $Cu^I_2Cys_3$ site. There are many Cu^I metallochaperones that share similar spectroscopic characteristics with

Cu^I_2(**TRI**L2WL16C)$_3^-$. AMT1 and ACE1 are Cu^I metalloregulatory proteins that share 50% sequence identity, contain 6-12 cysteine residues in the Cu^I binding domains, and bind 4-6 Cu^I ions *in vitro*.[67,68] EXAFS analysis supports trigonal coordination of Cu^IACE1 with a Cu^I-S distance of 2.26 Å and a Cu^I-Cu^I distance of 2.68 Å (Table 4-3) and UV-Vis titrations support a polynuclear Cu^I-thiolate center made up of six or seven metal ions.[66,68] Cu^IAMT1 showed a characteristic UV peak at 266 nm that saturates at four equivalents of Cu^I, and fits of the EXAFS data provide a Cu^I-S distance of 2.26 Å and a Cu^I-Cu^I distance of 2.75 Å (Table 4-3).[67] Pickering *et al*. determined a correlation between pure trigonal Cu^I coordination (Cu^I-S = 2.28 Å) and pure diagonal Cu^I coordination (2.16 Å), providing less than 20% diagonal coordination in the polynuclear Cu^I clusters of both AMT1 and ACE1 (Table 4-3). Cu^ICtr1, a membrane bound Cu^I transporter, contains six cysteine residues, binds four equivalents of metal with Cu^I-S distances of 2.248 Å and Cu^I-Cu^I distances of 2.706 Å (Table 4-3).[54] Interestingly, the Cu^I-S bond distances determined from the fits of my EXAFS data are 2.20 Å, which is an intermediate distance between the 2- and 3-coordinate extremes indicating that the Cu^I binuclear center may have some digonal coordination contribution, or that it has two short and one long Cu^I-S bonds resulting in an intermediate distance. A crystal structure is needed to elucidate further the structure of the proposed binuclear Cu^I center within the **TRI** peptides.

Table 4-3. EXAFS parameters of native Cu^I metallochaperones.

Protein	Cu-S	Cu-Cu	Reference
Cu^I_2(**TRI**L2WL16C)$_3^-$	2.20, 2.37*	2.66	This Work
ACE1	2.26	2.68	66
AMT1	2.26	2.75	67
Ctr1	2.248	2.706	54
CopZ	2.241	-	64
CopY	2.256	2.685	64
Cox19	2.261	2.664	74
Cox17	2.250	2.705	73
Cox11	2.245	2.706	72

The Cop and Cox families of metalloregulatory proteins are also largely involved in copper homeostasis.[69] CopZ, a Cu^I chaperone, binds one equivalent of Cu^I with a Cu^I-

S distance of 2.241 Å (Table 4-3).[64] CopZ delivers Cu^I to CopY, a copper-inducible repressor protein, which shows a 2:1 Cu^I:protein binding stoichiometry with Cu^I-S distance of 2.256 Å and a Cu^I-Cu^I distance of 2.685 Å (Table 4-3).[70,71] In both cases the Cu^I-S distance is slightly longer than what is observed in Cu^I_2(**TRI**L2WL16C)$_3^-$, but the Cu^I-Cu^I distance observed in CopY is very similar to what I have observed. Cox19, Cox17 and Cox11 show similar characteristics as well with Cu^I-S distances of 2.24-2.26 Å and a Cu^I-Cu^I distances of 2.66-2.71 Å (Table 4-3).[72–74]

In all of the cases of the above mentioned Cu^I metalloregulatory proteins, more than three cysteine residues are present in the Cu^I binding cavities, and generally at least four thiol ligands are utilized in forming the bi- or polynuclear Cu^I centers. Cox17 is an oligiomeric protein that binds three equivalents of Cu^I per monomer and contains seven cysteine residues, three of which are critical for functionality.[75] Single Cys→Ser mutations of the critical Cys or Ser substitutions of any of the non-essential cysteine residues do not inhibit Cu^I binding.[73] Additionally, proteins with Cys→Ser modification of up to three of the nonessential ligands ($Cys_{16,36,47}$Ser) still binds Cu^I and is functional. The single mutations of the critical Cys residues as well as the triple mutation all provide EXAFS fits that are comparable to the wild-type Cox17 with Cu^I-S distances of 2.242-2.253 Å and a Cu^I-Cu^I distances of 2.698-2.716 Å (Table 4-3). No manipulation of the As^{III}_S(**CS**L9C)$_3$ crystal structure allowed for a fourth proteinacious ligand to bind to the metal center, such as the external Lys and Glu residues that form salt bridges at the helical interface. The similarities observed between the bi- and polynuclear Cu^I centers of the native metalloregulatory proteins and the simplified $Cu^I_2Cys_3$ complexes obtained when binding Cu^I to the **TRI** peptides may in fact be due to exogenous solvent molecules that fill out the coordination sphere, as mentioned above and are included in the models as seen in Figures 4-6 and 4-7. However, the XAS data do not support additional solvent molecules directly coordinated to the Cu^I ions.

Due to the minimal crystallographic data for the Cu^I-metallochaperones and the essential lack of proposed polyhedral geometry of the native Cu^I clusters, it is difficult to make direct comparisons between the Cu^I_2 spectroscopic data and proposed models discussed in this work and the native systems. Crystal structures of Cu^I_2(**CS**L16C)$_3^-$ are

necessary to further elucidate the structure of the proposed binuclear Cu^I site (Table 4-1); however, at this point it is mostly likely, considering the XAS and UV-Vis data, in combination with the models described above, that Cu^I_2(**TRI**L2WL16C)$_3^-$ best support an intermediate 2- to 3-coordinate Cu^I environment with two short and one long Cu^I-S distance.

Cu^I-bound crystal structures are notoriously difficult to obtain due to the air sensitivity of the Cu^I center; however, Cu^I_2(**TRI**L2WL16C)$_3^-$ exposed to air shows no alteration in the 266 nm peak via UV spectroscopic analysis, even after 20 hours of continuous stirring while exposed to oxygen (Figure 4-12). Therefore, we are hopeful that crystal structures may be accessible.

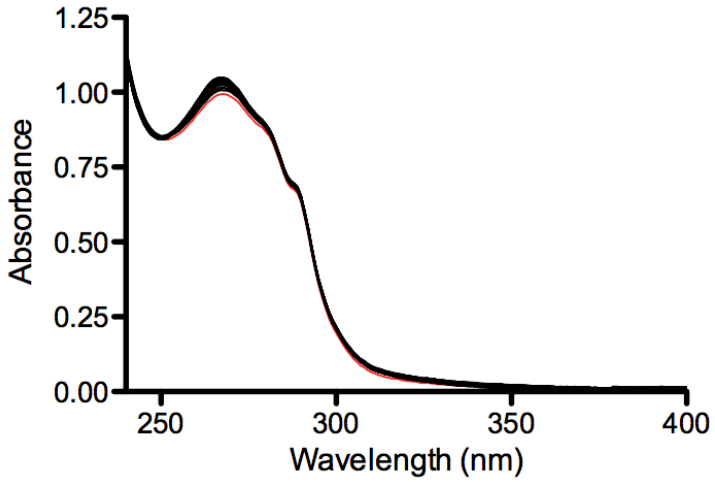

Figure 4-12. UV-Vis titration of Cu^I_2(**TRI**L2WL16C)$_3^-$, stirring while exposed to air, for 24 hours. Initial scan is shown in red.

One additional consideration for the slightly shorter Cu^I-S bond distances observed in **TRI**L2WL16C as compared to native systems is the very different topology in the secondary structure of the proteins. CopZ, CopA, Ccc2, Hah1 (also called Atox1), and Atx1 all contain varying numbers of similar ferredoxin-like βαββαβ-folds with MXCXXC motifs.[23] Solution structures have been solved for both apo- and Cu^I-bound Atx1 and Ccc2 (Figure 4-13).[26] In the case of Atx1, upon complexation of Cu^I, significant rearrangement of the alpha-helical region occurs; however, this rearrangement is not observed upon Cu^I binding to Ccc2. The only Cu^I-bound metallochaperone crystal

structure available is of Cu^{I}Hah1 (Figure 4-14).[18] Similar to the solution structures of Atx1 and Ccc2, the crystal structure of Hah1 shows Cu^{I} binding at the N-terminal end of the first alpha-helix to two cysteine residues from each dimer.

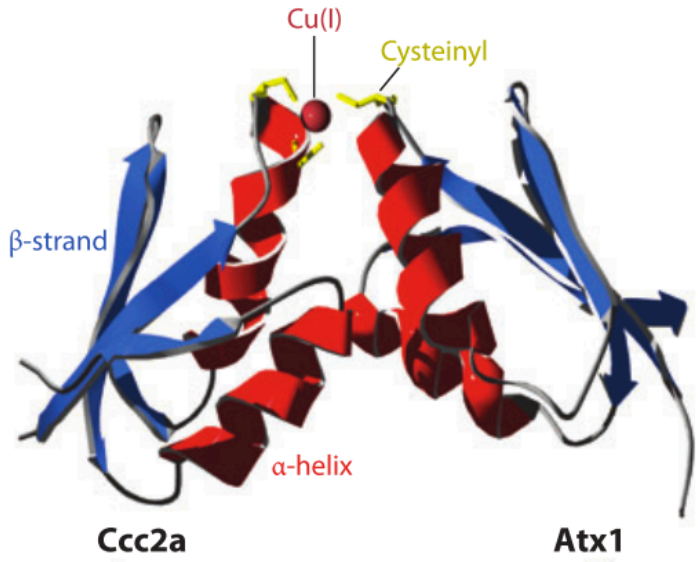

Figure 4-13. NMR solution structural model (PDB code: 2GGP) of a heterodimer of the *S. cerevisiae* copper metallochaperone Atx1 and one of two N-terminal cytosolic domains of its cognate P1-type copper-transporting ATPase Ccc2.[26] Cysteinyl (yellow) thiol coordinated Cu^{I} (red sphere) stabilizes a transient complex between similar βαββαβ (ferredoxin)-structural folds (red, α-helix; blue, β-strand). Figure adapted from Ref 23.

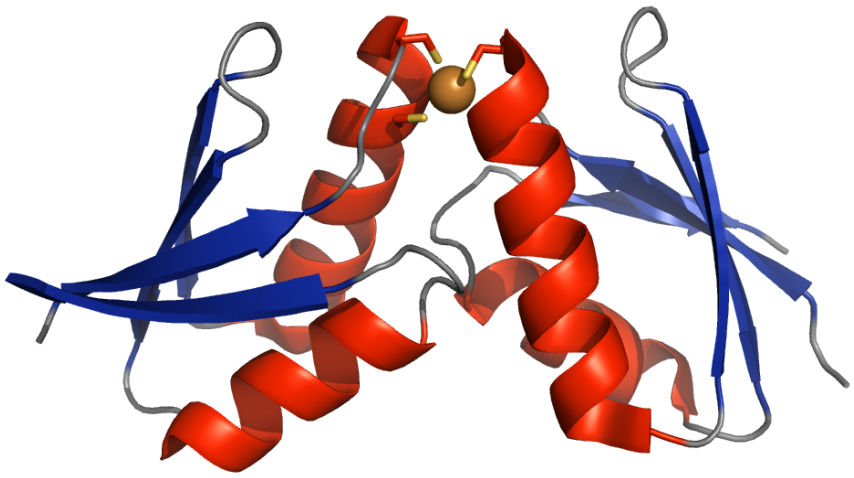

Figure 4-14. X-Ray crystal structure (PDB code: 1FEE) of the homodimer, Hah1.[18] Main chain atoms are shown in red (α-helix), blue (β-strand) and grey (loop regions), cysteine residues are shown as sticks with sulfur atoms highlighted in yellow and Cu^{I} ion is shown as an orange sphere.

CopZ, CopA, Ccc2, Hah1, and Atx1 all deliver Cu^{I} directly to their target molecule. Transport of Cu^{I} via metallochaperones Cox17 and Cox11 require accessory factors and, although the Cu^{I} binding sites share metrical parameters and spectroscopic features with CopZ, CopA, Ccc2, Hah1, and Atx1, their secondary structures vary dramatically.[23,76] Cox17, as mentioned above, is a eukaryotic copper metallochaperone for Sco1 and Cox11. Cox17 contains a CX_9C motif, that doesn't participate in Cu^{I} binding, but actually binds Cu^{I} at the helical hairpin of two alpha-helices (Figure 4-15).[77] This structural motif is also found in Cox19.[74] Conversely, Cox11, a Cu^{I} metallochaperone for the Cu_A site of cytochrome oxidase, is dominated by beta-sheets that form an immunoglobulin-like β-barrel fold with only one tethering trans-membrane alpha-helix (Figure 4-15).[78]

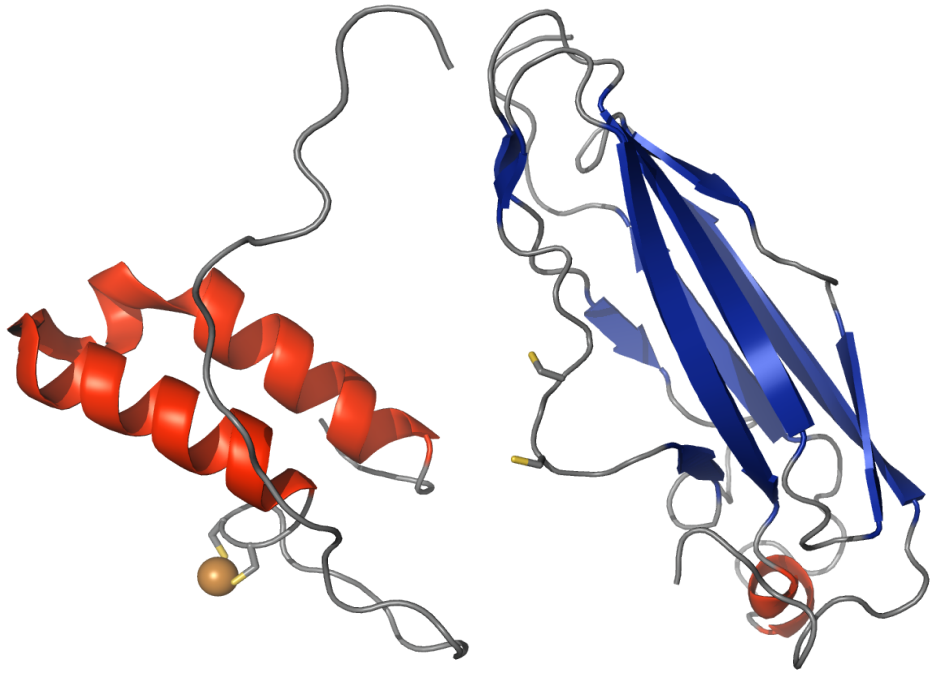

Figure 4-15. NMR solution structural models of Cox17 (PDB: 2RNB, left)[77] and Cox11 (PDB: 1SP0, right).[78] Main chain atoms are shown in red (α-helix), blue (β-strand) and grey (loop regions), cysteine residues are shown as sticks with sulfur atoms highlighted in yellow and Cu^{I} ion is shown as an orange sphere.

In all, Cu^{I} metallochaperones vary significantly in secondary and tertiary structures; yet provide very similar metrical parameters and spectroscopic features. From the various crystal structures collected by Dr. Leela Ruckthong we can say with some

certainty that we would not expect significant perturbations of the 3SCC as a whole when binding Cu^{I} as was observed in native proteins, particularly Atx1. Although the cysteine residues may rotate to accommodate predisposed metal binding (such is the case when binding Hg^{II} or Zn^{II}, see Chapters 1 and 2 for a discussion on predisposed vs. preorganized metal binding to Cys_3 sites), the overall protein shows little perturbation upon metal complexation. These differences could be a direct consequence of the many years of evolution behind native Cu^{I} metallochaperones and their ability to adapt appropriately upon Cu^{I} binding, whereas the Cys_3 site within our 3SCC has less flexibility due to the relatively rigid 3SCC motif resulting in slightly altered metrical parameters. A second, perhaps more likely scenario, is that the differences observed are a consequence of the necessity of native Cu^{I} metallochaperones to interact with other proteins in order to both obtain and, subsequently, deliver the Cu^{I} ion. Therefore the dynamics of the native proteins are probably a reflection of the recognition elements and uptake/transport requirements of copper homeostasis.

Ogawa and coworkers recently reported the first polynuclear metal binding site within a 3SCC, with a similar sequence compared to the **TRI** and **GR** peptides.[79,80] The peptide, AQ-C16C19 employs a heptad repeat of IAALENK with alternating Ile and Leu layers in the **a** and **d** sites. Substitution of the Ile16 and Leu19 layers with Cys residues provided a Cys_6 metal binding site that has been shown to bind four equivalents of Cd^{II} providing a $Cd^{II}_4S_6O_4$ multinuclear center within the 3SCC (Figure 4-16). Three of the four Cd^{II} ions bind to three sulfur ions each and to one Glu20 residue in **e** positions resulting in tetrahedral geometries for each metal ion. These three Cd^{II} ions bind in a plane in between the 16^{th} and 19^{th} Cys_3 layers with the fourth Cd^{II} ion directly above, toward the N-terminal, which binds exclusively to the Cys residues in the 16^{th} positions with a fourth, exogenous water molecule, again in a tetrahedral geometry. Upon binding of the Cd^{II} cluster a bulge in the peptide secondary structure occurs resulting in a break in the alpha helices. This break occurs at the 17Ala and 18Ala positions and allows for the Glu residues to rotate to a position that can coordinate directly to the Cd^{II} ions located at the helical interface. The Cd^{II}-S distances range from 2.34 – 2.73 Å (avg = 2.53 Å) and the Cd^{II}-O distances range from 1.91 – 2.49 Å (avg = 2.18 Å).

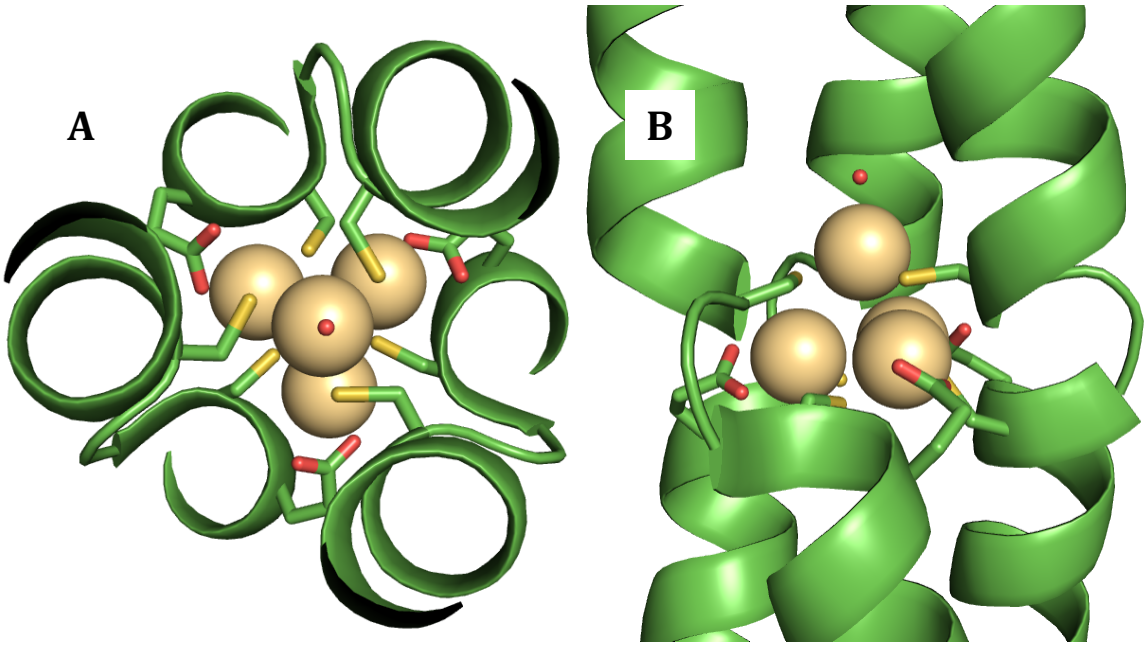

Figure 4-16. (A) Top-down and (B) side-on view of a pymol representation of the $Cd^{II}_4(AQ\text{-}C16C19)_3^{n+}$ complex based on the X-ray crystal structure (PBD: 4G1A).[79] Main chain atoms are shown in green, cysteine and glutamate residues are shown as sticks with sulfur atoms highlighted in yellow and oxygen atoms highlighted in red, and Cd^{II} ions are shown as peach spheres.

A change in the alpha-helical structure in **TRI** and **GR** upon metal binding is currently unprecedented but a crystal structure is required to completely rule out this possibility. However, the Cd^{II}-Cd^{II} distance is 4.0 Å, significantly longer than the 2.66 Å separation observed in my binuclear Cu^I site, and therefore this sort of arrangement is not likely within my system. When modeling the $Cu^I_2Cys_3$ site within the crystal structure of $As^{III}(\mathbf{CS}L9C)_3$ we did determine that significant structural perturbations would have to occur for the Glu residues to interact with the a metal bound to the interior of the **TRI** and **GR** peptides. Therefore, although a multinuclear site has been observed in a similar peptide scaffold to the **TRI** peptides, the polyhedral geometry observed for $Cd^{II}_4S_6O_4$ would not allow for the metrical parameters observed via XAS analysis of my $Cu^I_2Cys_3$ centers.

A crystal structure has been obtained for Cu^I binding to CopZ, an Atx-1 like copper chaperone from the Gram-positive bacterium *Bacillus subtilis*. XAS analysis of Cu^I-bound CopZ does not show evidence of a Cu^I-Cu^I interaction; however, the crystal

structure tells a different story. Under anaerobic conditions, a CopZ dimer crystal was obtained in the space group $P2_1$ at 1.5 Å refinement, where four Cu^I ions are found at the interface of the two monomers. The Cu^I ions have two different coordination environments, one of which shows trigonal coordination and the second of which shows distorted digonal coordination. The trigonal copper ions coordinate to two cysteine residues and one histidine residue and the digonal copper ions coordinate to only two cysteine residues. Upon closer inspection of the Cu^I coordination of one pair of Cu^I ions, with respect to the sulfur ions only, provided a short Cu^I-S distance of 2.2 Å, a longer Cu^I-S* distance of 2.5 Å and a Cu^I-Cu^I distance of 2.6 Å (Figure 4-17A). These values are very similar to those obtained for my binuclear Cu^I center in **TRI**L2WL16C via XAS analysis. Therefore, I re-visited the model of two Cu^I ions in a crystal structure of our trimers, where one copper ion is very close to a trigonal planar geometry in the center of the Cys_3 site and the second Cu^I ion is at the helical interface interacting with two of the sulfur ions (Figure 4-17B). This model provided a short Cu^I-S distance of 2.23 Å, a longer Cu^I-S* distance of 2.4 Å and a Cu^I-Cu^I distance of 2.7 Å, again, very similar to the experimental XAS distances. At this time, the best supported model for how two copper ions are binding to the same Cys_3 site within a 3CSS includes one trigonal planar Cu^I ion and one digonal-like Cu^I ion, similar to the crystal structure of CopZ.

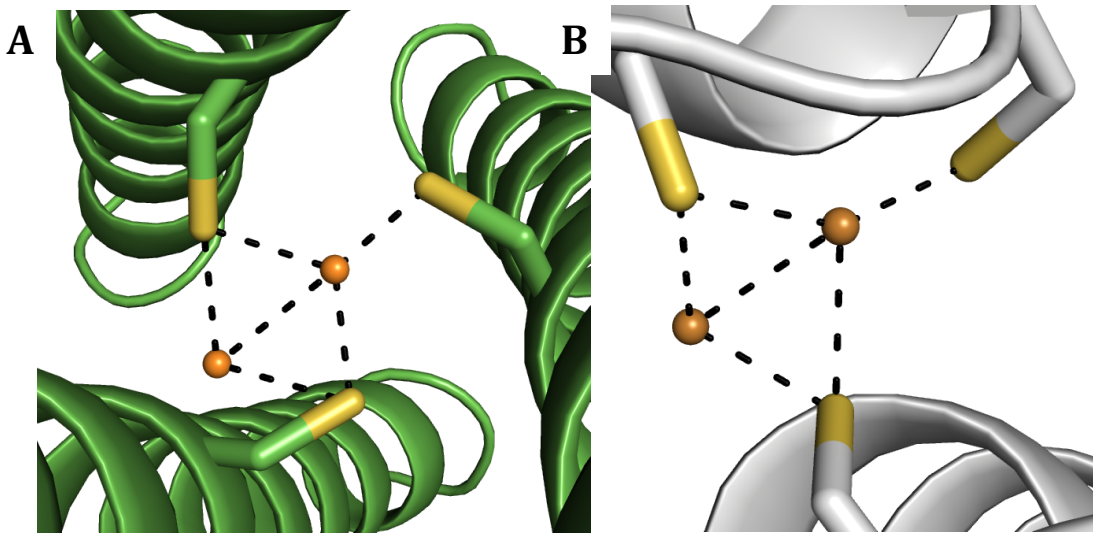

Figure 4-17. (A) Top-down view of a Pymol representation of a modeled binuclear Cu^I site bound to three sulfur atoms. Site is modeled from the $Zn^{II}_S(\mathbf{CS}L12AL16C)_3^-$ structure (PDB: not deposited). Main chain atoms are shown in green, cysteine residues are shown as sticks with sulfur atoms highlighted in yellow and Cu^I ions are shown as orange non-bonded spheres. The Cu^I-Cu^I distance is fixed at the EXAFS determined 2.67 Å. Resulting Cu^I-S distances are 2.23 Å, consistent with the EXAFS fits, and Cu^IS^* distances are 2.4 Å. (B) Top-down view of a Pymol representation of the binuclear Cu^I site from the X-ray crystal structure of the tetranuclear metal site of CopZ dimer bound to three cysteine ligands (PDB: 2QIF).[81] Main chain atoms are shown in grey, cysteine residues are shown as sticks with sulfur atoms highlighted in yellow and Cu^I ions are shown as orange non-bonded spheres. The Cu^I-Cu^I distance is measured at 2.6 Å, Cu^I-S and Cu^I-S* distances are 2.2Å and 2.5 Å, respectively.

Cu^I Binding Affinities for Cys_3-Containing 3SCCs

The affinity of Cu^I binding to **TRI**L2WL16C was determined by competitive chelation assay using a primary standard, bathocuproinedisulfonate, BCS^{2-}, as a chelator. Complexation of Cu^I by BCS^{2-} can be monitored with Visible spectroscopy as evidenced by the increase in absorption at 483 nm (Figure 4-18). Titrations were carried out in an inert atmosphere box where aliquots of BCS^{2-} were added to a solution of 40 μM Cu^I and 80 μM **TRI**L2WL16C with 50 mM buffer at various pH values. The data were analyzed in Prism 5 (GraphPad Software)[55] using multiple Cu^I binding models and ultimately fit with a nonlinear regression using Equations 10 and 23. Assumptions made in the model used to fit the data include that no mononuclear Cu^I species is formed, as supported by the linearity of the UV titration data. Attempts to fit the data using models corresponding

to one equivalent of Cu^{I} binding to 3SCC to form a mononuclear Cu^{I} center (Equation 9) or to a sequential binding pattern (where one additional equivalent of Cu^{I} binds to Cu^{I}-bound 3SCC, Equation 18) were unsuccessful due to non-convergence between the model and data sets. Additionally, the presence of the Cu^{I}-Cu^{I} peak in the EXAFS data, collected at significant excess of 3SCC, also supports essentially immediate formation of a $Cu_2^{I}S_3$ center. A second assumption is that there is no free Cu^{I} present due to the high affinity of Cu^{I} to the Cys_3 site, as evidenced by the sharpness observed in the Abs increase as observed in the UV-Vis titration data (Figure 4-2).

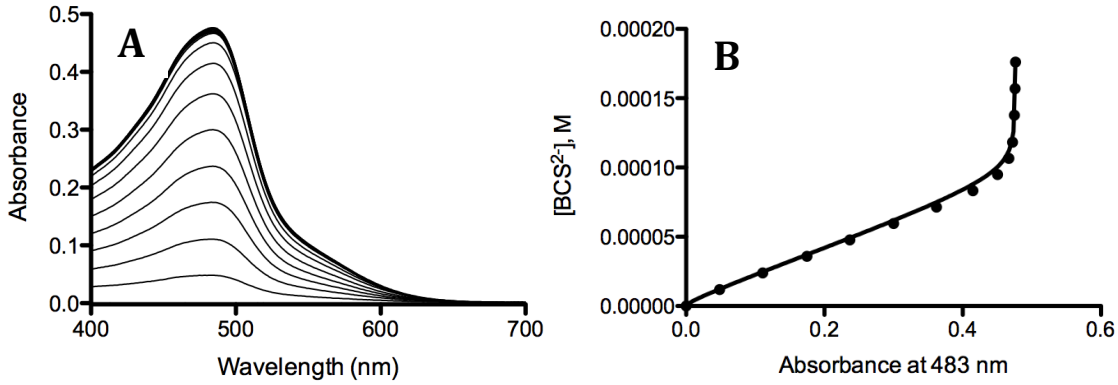

Figure 4-18. (A) Titration spectra of BCS^{2-} added to Cu^{I}_2(**TRI**L2WL16C)$_3^{-}$ at pH 7.5, HEPES buffer, showing an increase in absorbance at 483 nm, indicative of $[Cu^{I}(BCS)_2]^{3-}$ formation. (B) Titration curve of $[BCS^{2-}]$ versus Absorbance at 483 nm. Data is shown in black dots and fit is shown as a solid line.

Based on the BCS^{2-} competition, at both pH 6.5 and 7.5 the affinity ($K_{Cu2Cys3}$) for two Cu^{I} ions binding to **TRI**L2WL16C, for the binuclear site, were fitted to yield values of 6.6 ± 1.1 x 10^{28} and 3.2 ± 0.4 x 10^{28} M^{-2}, respectively (Figure 4-18, Table 4-4). Elongation of the peptide from **TRI**L2WL16C to **GR**L2WL16C results in a 2-fold tighter affinity, at pH 7.5, of 2.49 ± 0.3 x 10^{30} M^{-2} (Tables 4-1 and 4-4). Removal of hydrophobic packing in the layer directly above the Cys_3 site, **GR**L2WL12AL16C (Table 4-1), provides a comparable binding affinity to **GR**L2WL16C at 1.94 ± 0.2 x 10^{30} M^{-2} (Table 4-4). Analysis of two pH extreme values, 6.5 and 9.0, for **GRCS**L12$_D$LL16C shows an increase in binding affinity at higher pH from 4.90 ± 1.4 x 10^{28} M^{-2} to 2.38 ± 0.8 x 10^{31} M^{-2} (Table 4-4).

Table 4-4. Cu^I affinities to native Cu^I binding proteins and **TRI**/**GR** 3SCC

Protein	pH	K_a, M^{-2} or M^{-1}	Reference
TRIL2WL16C	6.5	$6.61 \pm 1.1 \times 10^{28}$	
	7.5	$3.17 \pm 0.4 \times 10^{28}$	
GRL2WL16C	7.5	$2.49 \pm 0.3 \times 10^{30}$	
GRL2WL12AL16C	7.5	$1.94 \pm 0.2 \times 10^{30}$	
GRCS$L12_DLL16C$	6.5	$4.90 \pm 1.4 \times 10^{28}$	
	9.0	$2.38 \pm 0.8 \times 10^{31}$	
Atx1	6.0	$\sim 10^{16}$	82
	8.0	$1.4 - 2.4 \times 10^{18}$	54
Ctr1	8.0	$2.1 - 7.1 \times 10^{18}$	54
Ccc2	8.0	$6.3 - 7.1 \times 10^{18}$	54
Hah1	7.0	$2.6 - 5.6 \times 10^{17}$	85
MNK1	7.0	3.6×10^{17}	85
CopZ	7.5	6.6×10^{14}	86
CopA	7.5	6.8×10^{11}	86
Wilson Protein*	6.5	$0.2 - 4.8 \times 10^{6}$	83
	7.5	$2.2 - 6.3 \times 10^{10}$	84

Interestingly, the binding affinities obtained for **GRCS**$L12_DLL16C$, **GR**L2WL12AL16C, and **GR**L2WL16C are similar, implying that the $Cu^I_2Cys_3$ sites are comparable in all three peptides (Tables 4-1 and 4-4). Comparison of the crystal structures of $Hg^{II}_SZn^{II}_{N/O}$(**GRCS**L16CL30H)$_3^+$ and apo-(**GRCS**L12DLL16C)$_3$ indicates that inclusion of a $_D$Leu layer directly above the Cys_3 site, with respect to the N-terminal, does not allow for a water molecule to occupy the space above the Cys_3 plane, as was observed for the $Hg^{II}Cys_3$ site in $Hg^{II}_SZn^{II}_{N/O}$(**GRCS**L16CL30H)$_3^+$ (as discussed in Chapter 1 and Chapter 2, Figure 4-19). This was determined by measuring the distance between the water molecule in $Hg^{II}_SZn^{II}_{N/O}$(**GRCS**L16CL30H)$_3^+$ and the plane of the δ-methyl group of the Leu layer of both of the Leu and $_D$Leu residues to be 3.80 and 1.33 Å, respectively (Figure 4-19).[82] The Cu^I affinity and crystal data, together, negate a possible water ligand to complete a tetrahedral coordination geometry as discussed above with respect to the binuclear models (Figures 4-6 and 4-7). These data instead support the third or fourth models (Figures 4-9 and 4-17) where the Cu^I ions move, asymmetrically, from the helical axis, with an intermediate two- and three-coordinate Cu^I environment provided by two short Cu^I-S and one long Cu^I-S^* ligands or where one Cu^I ion is trigonal planar at the helical axis with the second Cu^I ion at the helical interface.

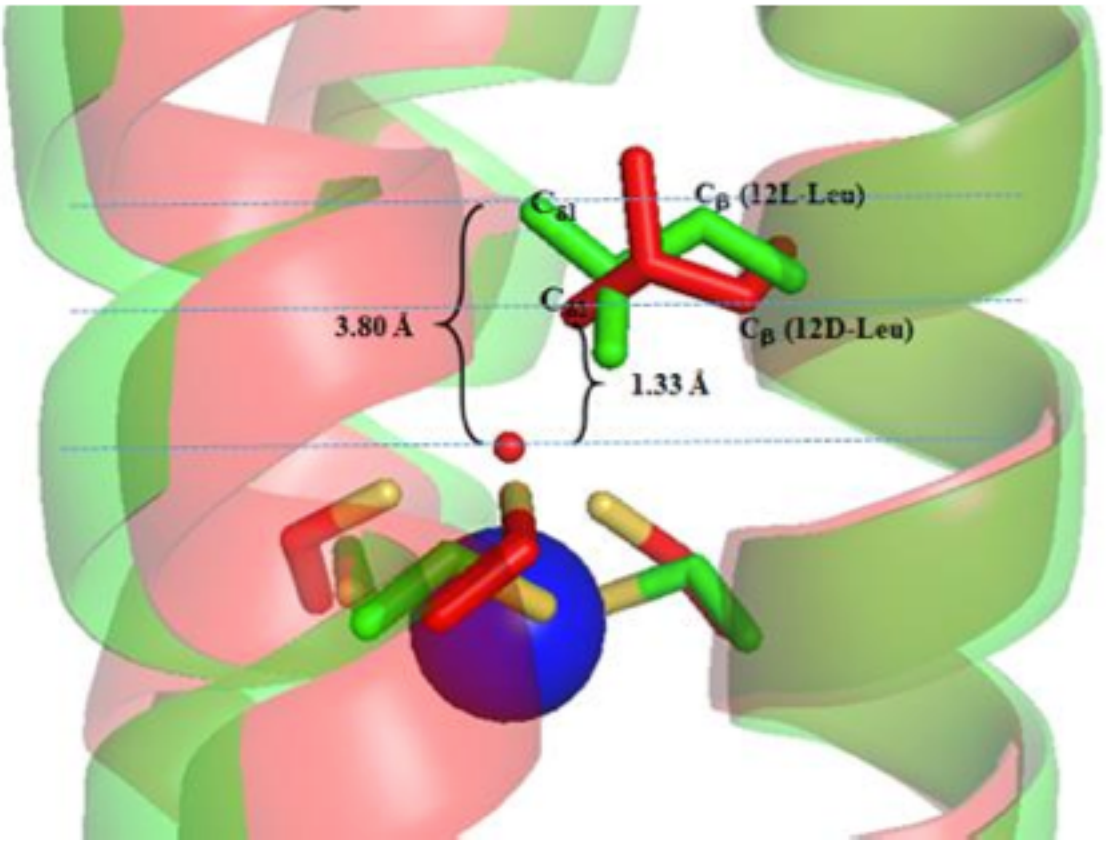

Figure 4-19. Pymol visualization representing the distances measured from the plane generated by the core δ-methyl carbon atom of the 12Leu residue to the water ion in $Hg^{II}_{S}Zn^{II}_{N}$(**GRCS**L16L30H)$_3^+$ compared to the related distance measured from the plane generated by the core δ-methyl carbon atom of the 12_DLeu residue in apo-(**GRCS**L12_DLL16C)$_3$ to the water of the opposite crystal structure. Main atoms of the apo-(**GRCS**L12_DLL16C)$_3$ are shown in red and $Hg^{II}_{S}Zn^{II}_{N}$(**GRCS**L16L30H)$_3^+$ in green. The Hg^{II} metal ion and the water molecule are shown as blue and red spheres, respectively. Cysteine residues and one Leu/$_D$Leu residue are shown as sticks with sulfur ions highlighted in yellow. Figure adapted from reference 81.

Measuring the binding affinities of Cu^I binding to various metallochaperones has proven to be a non-trivial task, largely due to the difficulty associated with measuring affinities for individual metal ions that make up the polynuclear sites that often form in these proteins; however, various Cu^I affinities for thiol-rich sites have been determined. Atx1 and Wilson Protein show an increase in binding affinity upon an increase of pH from 6.0 to 8.0 and 6.5 to 7.5, respectively,[54,83–85] similarly to the trend observed in **GRCS**L12_DLL16C from pH 6.5 to 9.0 (Table 4-4). High affinities are also reported for Atx1, Ctr1, and Ccc2, at pH 8, of 1.4 – 7.1 x 10^{18} M^{-1}, per each equivalent of Cu^I-bound (Table 4-4).[54] MNK1 and Hah1 (both of which bind one equivalent of Cu^I) provide

affinities one order of magnitude lower of 3.6 and 2.6 – 5.6 x 10^{17} M^{-1}, both measured at pH 7.0 (Table 4-4).[86] Wilson Protein, CopZ, and CopA bind Cu^{I} with lower affinities ranging from 10^{6} – 10^{14} M^{-1} (all of which bind one equivalent of Cu^{I}, Table 4-4).[84,85,87] With $K_{Cu2Cys3}$ values of 10^{28} – 10^{31} M^{-2}, for two equivalents of Cu^{I} binding to a single Cys_3 site in our **TRI** and **GR** peptides, it appears that Cu^{I} binds to our peptides with affinities that fall within the range of native Cu^{I} metallochaperones.

Previous work by Dr. Fangting Yu extensively characterized Cu^{I} binding to His_3 **TRI** peptides. Using the BCS^{2-} competition experiment, she determined a binding affinity for **TRI**L2WL23H of 5.0 x 10^{12} M^{-1}, which is approximately half of the value determined for the binuclear $Cu^{I}Cys_3$ sites as reported above.[48] Additionally, in Chapter 2, I determined that if a His_3 site is present in a peptide, such as **GR**L2WL16CL30H, Cu^{I} does not inhibit $Pb^{II}Cys_3$ binding. These data, considered together, led me to ask if Cu^{I} would compete for a His_3 or Cys_3 when the sites were present in the same peptide (in the absence of a second metal ion). There are three expected outcomes of this experiment, complete preference for the His_3 site, complete preference for the Cys_3 site, or a competition for Cu^{I} binding between both the His_3 and Cys_3 sites. If Cu^{I} binds exclusively to the His_3 site before binding to the Cys_3 site we would expect to see no change at 266 nm for the first one equivalent of Cu^{I} added. The opposite situation would occur if Cu^{I} binds exclusively to the Cys_3 site before binding to the His_3 site. In this case, we would see an increase in the 266 nm transition and a plateau at two equivalents, as observed in **TRI**L2WL16C. If competition occurs, we should see an increase at 266 nm from the beginning of the titration, but it should take more than two equivalents of Cu^{I} to fill the Cys_3 site.

Aliquots of Cu^{I} were added, in an inert atmosphere box, to a solution of **GR**L2WL16CL30H (Table 4-1), in 50 mM KPhos buffer at pH 8.0 (Figure 4-20). An immediate increase in absorbance at 266 nm upon the first addition of Cu^{I} negated the model for complete preference for Cu^{I} binding to the His_3 site. However, at two equivalents of Cu^{I} added the 266 nm peak was not saturated and an extinction coefficient of only ~8000 $M^{-1}cm^{-1}$ was observed at two equivalents, only about 50% of what is expected for a saturated $Cu_2^{I}Cys_3$ site (Figure 4-20B). After three equivalents of Cu^{I} were

added with respect to the concentration of 3SCC, we see a sharp transition in the titration curve and the band at 266 nm stops increasing upon further additions of Cu^{I} (Figure 4-20B). Therefore, it is obvious that the last of the three possibilities mentioned above exists, and when Cu^{I} is added to a peptide that contains both a Cys_3 and His_3 binding site, competition is observed for Cu^{I} binding.

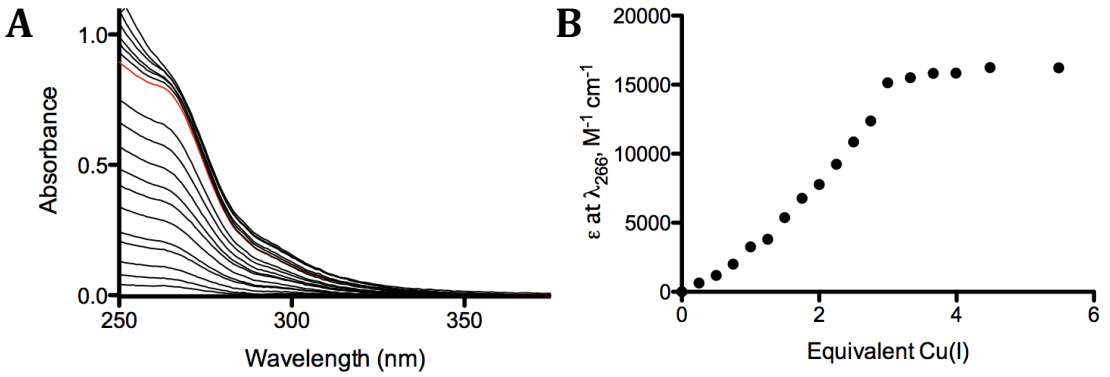

Figure 4-20. Titration spectra of Cu^{I} into a solution of (A) **GR**L2WL16CL30H at pH 8.0 in 50 mM KPhos buffer. Titration curve (B) showing a plateau at 3 equivalents of Cu^{I} as absorbance at 266 nm divided by concentration of Cu^{I} added (ε at λ_{266}) versus the equivalents of Cu^{I} added, with respect to the total concentration of 3SCC.

A new model can be derived to determine the Cu^{I} binding affinity for the Cys_3 site as a function of competition with the His_3 site. Additional assumptions must be considered in addition to those made when fitting the Cu^{I} affinity data with BCS^{2-}. Again, we assume that due to tight binding there is no free Cu^{I} in solution, every mole of Cu^{I} added to the sample solution is assumed to bind. Additionally, we assume that there is no mononuclear $Cu^{I}Cys_3$ site formed (the same model as for the BCS^{2-} titrations); therefore, when Cu^{I} binds to the Cys_3 site we get half the amount of binuclear metallated 3SCC. Lastly, and perhaps most important to note, is that I have assumed for the purposes of this model that the binding affinity of Cu^{I} to a His_3 site does not influence the affinity of Cu^{I} binding to a Cys_3 site in the same peptide scaffold, and vice versa.

The model as derived in Equations 27 and 28, considering the above-mentioned assumptions, cannot be simplified enough for fitting in Prism 5 (GraphPad Software)[55]. However, we can use the values of the measured parameters and those known based on initial values and measured parameters, $[Cu_2Cys_3]$, $[His_3]_f$, $[Cys_3]_f$, and $[CuHis_3]$, to

determine K_{comp} at each data point, which can then be used with K_a of $Cu^I(\mathbf{TRI}L2WL23H)_3^+$ to determine an estimated K_a for $Cu^I_2Cys_3$ binding. With the following mass balance equations for $[Cu]_T$, $[Cys_3]_T$ and $[His]_T$ we can rearrange to determine K_{comp} for each titration point (Table 4-5). Plotting K_{comp} versus $[Cu^I]_T$ results in a parabolic curve indicating that at very low and at very high concentrations of Cu^I the assumptions made during the derivation break down (Figure 4-21). Conversion of K_{comp} to K_a for $Cu_2^ICys_3$ reveals a similar parabolic curve with maximum K_a values at the beginning and at end of the titration with a range of K_a values from $8.0 \times 10^{22} - 2.3 \times 10^{25}$ M^{-2} (Figure 4-21). The discrepancy of 3-4 orders of magnitude observed between this technique and the BCS^{2-} competition experiment is likely due to the Cu^IHis_3 K_a being for a **TRI** peptide and, is probably related to the folding free energy of the peptide.[88] Considering the increase stability of **GR** compared to **TRI**, this difference could lead to an underestimation for a His_3 site in a **GR** peptide, and, in turn, an underestimated K_a calculated for the $Cu_2^ICys_3$ site.

Table 4-5. Measured K_{comp} and calculated $Cu_2^ICys_3$ K_a values for Cu^I competition in **GR**L2WL16CL30H

Cu, μM	K_{comp}	K_a, M^{-2}
12.50	2.000	5.00×10^{25}
25.00	0.558	$1.4.0 \times 10^{25}$
37.50	0.167	4.17×10^{24}
50.00	0.099	2.46×10^{24}
62.50	0.074	1.86×10^{24}
75.00	0.031	7.70×10^{23}
87.50	0.004	9.79×10^{22}
100.0	0.001	2.00×10^{22}
112.5	0.018	4.55×10^{23}
125.0	0.051	1.26×10^{24}
137.5	0.120	3.00×10^{24}
150.0	0.308	7.71×10^{24}
166.5	1.951	4.88×10^{25}

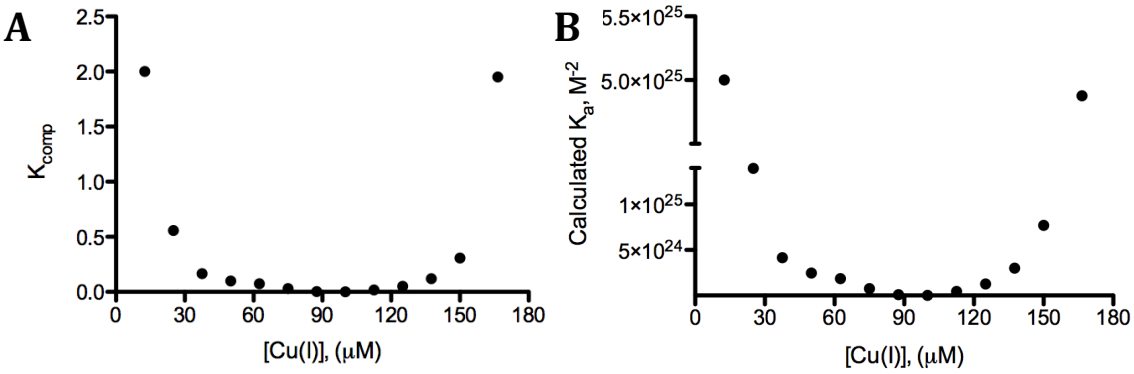

Figure 4-21. Plots showing (A) K_{comp} values and (B) calculated $K_{Cu2Cys3}$ values for $Cu^{I}_{2}Cys_3$ binding versus total concentration of Cu^{I} added to **GR**L2WL16CL30H as determined from the data in Figure 4-20 from 0-3 equivalents of Cu^{I} with respect to the concentration of 3SCC. The black circles represent the values calculated using Equation 28 as described in the Materials and Methods section.

Regardless, this method provides a second approach for determining the binding affinities of Cu^{I} to Cys_3 sites. The affinity of Cu^{I} to the His_3 site has been shown to vary when the sterics of the secondary coordination sphere and/or the electrostatics around the metal binding site are altered; therefore, one could imagine altering the His_3 site to either higher or lower affinity, based on the corresponding expected Cys_3 K_a, to tailor this experiment to varying affinities for the Cys_3 site.

Heterobinuclear Binding to Cys_3 sites in 3SCCs

As mentioned above, Pb^{II} and Cu^{I} compete for binding at a Cys_3 site within the **TRI** and **GR** peptides. This was first observed when titrating Pb^{II} into a solution of **GR**L2WL16C in the presence of one equivalent of Cu^{I}. In comparison to Pb^{II} binding to **GR**L2WL16C, in the absence of another metal, the extinction coefficient observed for the $Pb^{II}S_3$ species, in the presence of Cu^{I}, was approximately 2,000 $M^{-1}cm^{-1}$, about half of that observed in the absence of Cu^{I}. This observation suggested competition between Cu^{I} and Pb^{II} for the thiolate site. As discussed above, Cu^{I} may have high affinity both for His_3 and Cys_3 environments. In contrast, Pb^{II} strongly favors Cys_3 sites and has shown no affinity for the tris histidine region of the 3SCC. Therefore, I then analyzed the ability of Pb^{II} to complex to a Cys_3 site in the presence of Cu^{I}, but this time both a Cys_3 and a His_3 site were present in the peptide. Indeed, when Pb^{II} was titrated into

Cu^{I}(**GR**L2WL16CL30H)$_3^+$; no competition was observed between Pb^{II} and Cu^{I} at the cysteine site (Figure 4-1). This result indicated that when His_3 and Cys_3 sites were present, Pb^{II} binding to the Cys_3 site was not inhibited in the presence of Cu^{I}. Again, both $Pb^{II}Cys_3$ and $Cu^{I}Cys_3$ choromophores have features at 266 nm, so overlapping contributions make interpreting the changes at this wavelength non-trivial.

I could now apply the observations that Cu^{I} competed with Pb^{II} for Cys_3 binding in **GR**L2WL16C and that Cu^{I} formed a binuclear center with the three cysteine residues to interpret more clearly the Pb/Cu competition experiment. Given that there was one equivalent of Cu^{I} present in solution site prior to adding Pb^{II} and that this copper would form a binuclear structure, this meant that 50% of the Cys residues in **GR**L2WL16C were available for Pb^{II} binding. The strong binding observed from 0-0.5 equivalents of Pb^{II} added, the relatively sharp plateau observed from 0.5-2.5 equivalents of Pb^{II}, as well as the extinction coefficient of 50% the expected value supports this model. Therefore, we suspect that 50% of the Cys_3 sites are occupied by binuclear Cu^{I} binding leaving 50% open for Pb^{II} complexation.

I then looked at the reverse titration where aliquots of Cu^{I} were added to a solution of one equivalent Pb^{II} bound to **GR**L2WL16C (40 μM 3SCC), in an inert atmosphere box, 100 mM TRIS buffer at pH 7.5 (Figure 4-22). No change was observed at the LMCT $Pb^{II}S_3$ 346 nm peak upon addition of one equivalent of Cu^{I}, but an increase was observed at 266 nm (Figures 4-22B and 4-22C). Additionally, a closer analysis of the spectra that correlate to 0-1 equivalent Cu^{I} spectra yielded an isosbestic point at 330 nm (Figure 4-22C) indicating that two absorbing species were simultaneously present in solution. From 1-3 equivalents of Cu^{I} I saw a depletion of the 346 nm peak with a continuous increase in the 266 nm peak, and a new isosbestic point was observed at 270 nm (Figure 4-22D). After three total equivalents of Cu^{I} were added the entire $Pb^{II}S_3$ peak at 346 nm disappeared (Figures 4-22B and 4-22D). The combination of no decrease observed at 346 nm but an increase in absorbance at 346 nm indicated that Pb^{II} was not being displaced, but Cu^{I} was being complexed by the peptide at the Cys_3 site. This suggested that the *first equivalent* of Cu^{I} was binding in the presence of Pb^{II}, presumably forming a hetero-binuclear metal site of $Cu^{I}{}_S Pb^{II}{}_S$(**GR**L2WL16C)$_3$ complex. One should

recognize that if a Cu^{I}_{2} center was being formed under these conditions, it would require that Pb^{II} be removed, which would have diminished the 346 nm absorption band. I assign this isosbestic point at 330 nm as the conversion of a $Pb^{II}S_3$ center to $Cu^{I}Pb^{II}S_3$. Given the available x-ray structures for Pb^{II} bound to thiolate derived CS peptides, the simplest model would position the Pb^{II} below the sulfur plane towards the C-termini and the Cu^{I} would be found above the plane towards the N-termini. This is the first instance of a bi-nuclear site that contains one equivalent of Cu^{I} and one equivalent of Pb^{II}.

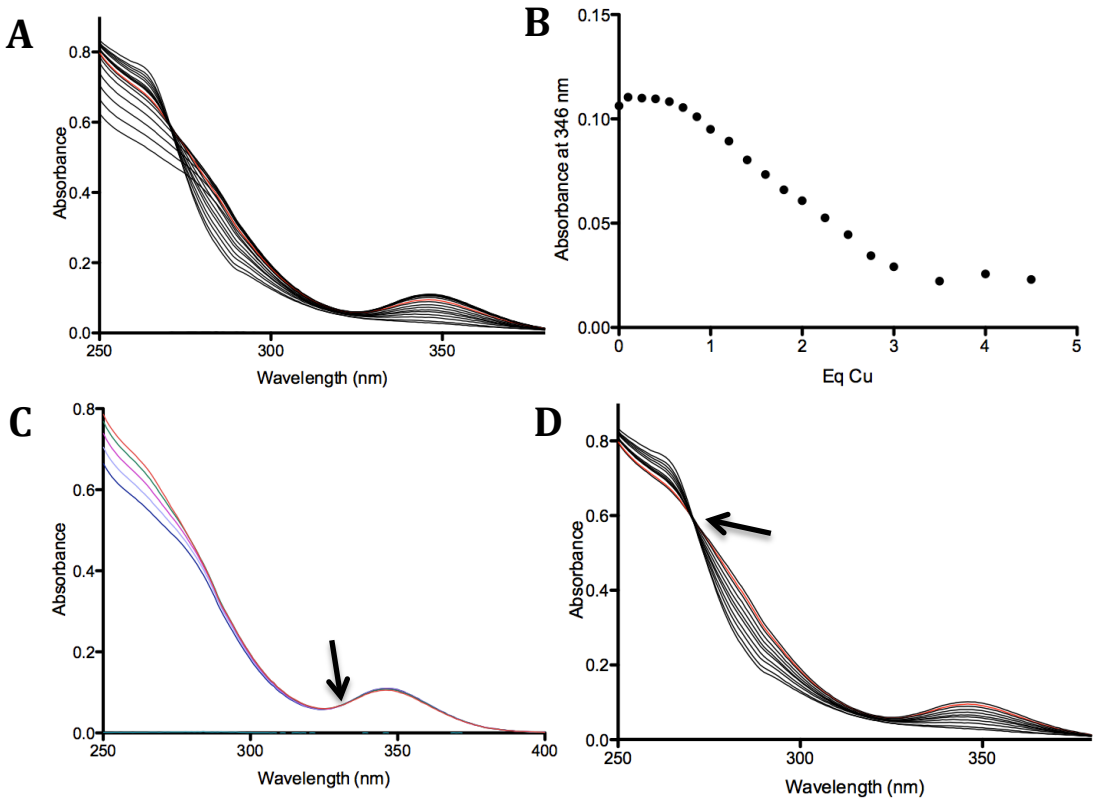

Figure 4-22. Titration spectra of Cu^{I} into a solution of (A) Pb^{II}(**GR**L2WL16C)$_3^-$ at pH 7.5 in 100 mM TRIS buffer. Titration curve (B) of absorbance at 346 nm as a function of total equivalents of Cu^{I} added with respect to the concentration of 3SCC. No change in the absorbance is observed for the first equivalent of Cu^{I} added, then a decrease is observed from 1-3 equivalents of Cu^{I} and a plateau is reached once three equivalents of Cu^{I} is reached. (C) Titration spectra of 0-1 equivalents of Cu^{I} added to Pb^{II}(**GR**L2WL16C)$_3^-$ with an isosbestic point at 330 nm. (D) Titration spectra of 1-3 equivalents of Cu^{I} added to Pb^{II}(**GR**L2WL16C)$_3^-$ with an isosbestic point at 270 nm. The final absorption spectrum is identical to that observed for Cu^{I}_{2}(**GR**L2WL16C)$_3^-$ alone.

The fact that three equivalents of Cu^{I} are required to displace one equivalent of Pb^{II} to form the binuclear Cu^{I} site indicates competition between Cu^{I} and Pb^{II} for the C-terminal side binding site. However, regardless of the direction of the titration (Cu^{I} added to $Pb^{II}{}_{S}(Pep)_3^-$ or Pb^{II} added to Pep_3 with one equivalent of Cu^{I} (presumably resulting in 0.5 equivalents of $Cu^{I}{}_2(Pep_3)^-$), an intermediate heterobinuclear site formed, preventing direct determination of the $Pb^{II}Cys_3$ affinities via competition with Cu^{I}.

Because Cu^{I} is diamagnetic, I reasoned that ^{207}Pb NMR spectroscopy would further probe the existence of the heterobinuclear site. First, I could directly probe the Pb^{II} ions presence at the Cys_3 site as displacement of a cysteine would cause a marked shift in the spectrum. Second, as detailed in Chapter 2, the ^{207}Pb NMR signal of Pb^{II}-bound **TRI** and **GR** peptides is very sensitive to perturbations of the secondary coordination sphere. Decreasing the sterics of the Leu layer directly above a $Pb^{II}Cys_3$ site via Leu→Ala substitution caused a 75 ppm upfield shift in the $Pb^{II}S_3$ spectrum.[46] Considering the close proximity expected between Cu^{I} and Pb^{II} ions that bind to the same Cys_3 site, I next wanted to determine if the presence of Cu^{I} resulted in a change in the chemical shift of $Pb^{II}{}_{S}(\mathbf{TRI}L2WL16C)_3^-$, which might reflect changing conformations of the cysteine side chains upon binding copper.

First, I re-analyzed a sample of 12 mM **TRI**L2WL16C, 4 mM 3SCC, dissolved in degassed 10% D_2O with 1 equivalent of ^{207}Pb (4 mM). The sample was prepared in an inert atmosphere box. As expected, a peak was observed at 5651 ppm, consistent with previously reported **a** site Cys_3 spectra with no additional mutations in the layers above or below the metal binding site (Figure 4-23). I then added one equivalent of Cu^{I}, anaerobically, to the sample and re-collected the ^{207}Pb NMR data. Interestingly, the ^{207}Pb NMR signal was observed at 5648 ppm, essentially unperturbed in signal intensity and chemical shift, (Figure 4-23). This data corroborates the UV-Vis titration in which the addition of one equivalent of Cu^{I} does not cause a decrease in the $Pb^{II}S_3$ peak observed at ~350 nm. However, this result is surprising in that the addition of another metal ion in close proximity to the $Pb^{II}Cys_3$ site did not perturb the chemical shift significantly. This could be due to the $Pb^{II}Cys_3$ bonding interactions dominating the chemistry when only one equivalent of Cu^{I} is added to a $Pb^{II}Cys_3$ site. In reference to the models above, it is

possible that the $Pb^{II}Cys_3$ site forms as previously observed and characterized in $Pb^{II}_{S}Zn^{II}_{N}$(**GRCS**L16CL30H)$_3^-$, where the Cys_3 site is pre-organized for Pb^{II} binding and the Cys rotamers require minimal changes to bind Pb^{II}. The addition of Cu^{I} results may then result in a distorted linear structure toward the helical interface. Most surprising is that neither the Pb^{II} nor the Cu^{I} electronic spectra are perturbed in the presence of one equivalent of the opposite metal.

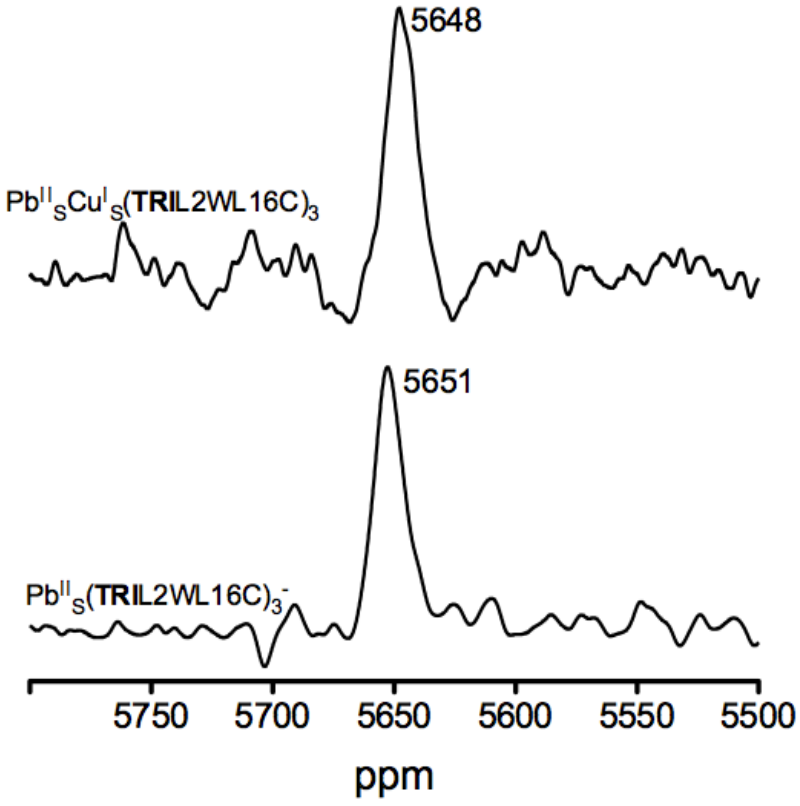

Figure 4-23. ^{207}Pb NMR spectra of Pb^{II}(**TRI**L2WL16C)$_3^-$ (bottom) and $Cu^{I}Pb^{II}$(**TRI**L2WL16C)$_3$ (top). All spectra were recorded at room temperature (25 °C) for 5 hr using isotopically enriched $Pb^{II}(NO_3)_2$, pH 7.5.

Initial models of a heterobinuclear site, provided from Dr. Leela Ruckthong, have been made by altering the crystal structure of Pb^{II}_{S}(**GRCS**L16CL30H)$_3^-$ (Table 4-1). Without altering the location of the Pb^{II} ion in the crystal structure, we added in a Cu^{I} ion at ~2.2 Å from the sulfur atoms of the cysteine ligands. The resulting model provided a Cu^{I}-Pb^{II} distance of only 2.66 Å, and an apparent overlap of the Cu^{I} and Pb^{II} ion spheres (Figure 4-24). Realizing that this distance is likely too short to allow formation of the

heterobinuclear center due to repulsion and that a Cu^{I}-Pb^{II} bond is highly unlikely, we then moved the Cu^{I} ion away from the Pb^{II} ion, towards the N-termini, to a distance where the Cu^{I} and Pb^{II} ion space filling spheres no longer overlapped, resulting in a more reasonable Cu^{I}-Pb^{II} distance of 3.23 Å (Figure 4-25). However, the Cu^{I}-S distances are now significantly elongated to 2.51 Å. This distance is much longer than the Cu^{I}-S distances in any of the above-mentioned Cu^{I} metalloregulatory proteins or for my Cu^{I}_{2} center; however, it is not unlikely that the geometry and/or the coordination number of the Cu^{I} ion change when forming an unprecedented $Cu^{I}Pb^{II}$ heterobinuclear site. Ultimately, XAS analysis and, ideally, a crystal structure are required to determine how Cu^{I} and Pb^{II} are interacting within the same Cys_3 binding site.

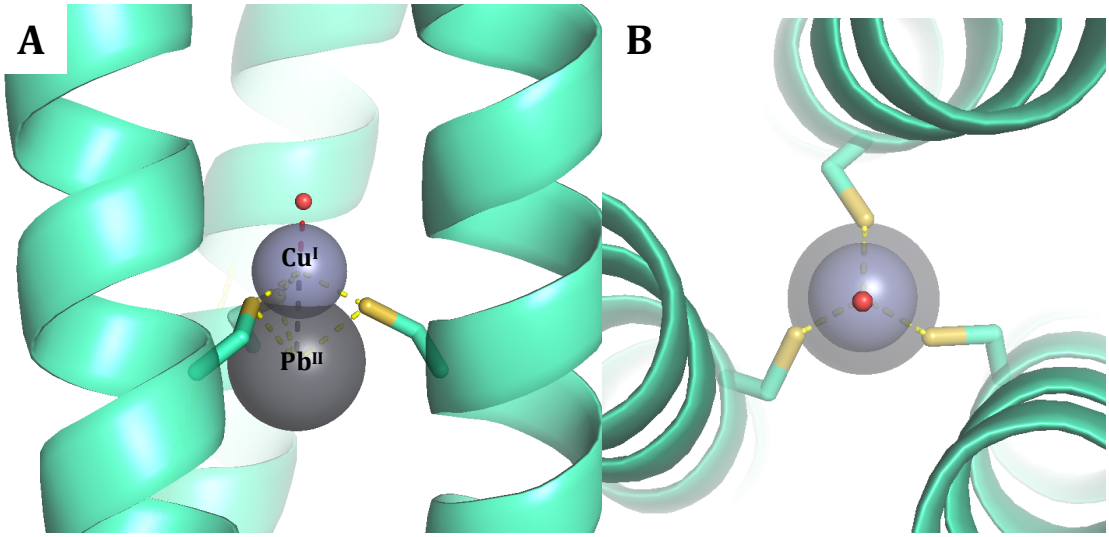

Figure 4-24. Side-on (A) and Top-down (B) views of a pymol representation of a modeled symmetric binuclear $Cu^{I}Pb^{II}$ site bound to three sulfur atoms. Site is modeled from the Pb^{II}_{S}(**GRCS**L16CL30H)$_3^-$ structure (PDB code not yet deposited).[82] Main chain atoms are shown in teal, water molecules are shown in small red spheres, cysteine residues are shown as sticks with sulfur atoms highlighted in yellow and Cu^{I} and Pb^{II} ions are shown as blue-grey and grey spheres, respectively. The Pb^{II} ion is not altered from the crystal structure and Pb^{II}-S distances are 2.65 Å. The Cu^{I}-S distances are fixed at 2.20 Å. Cu^{I}-Pb^{II} distance measures to 2.66 Å, the water molecule is 2.03 Å above the Cu^{I} ion.

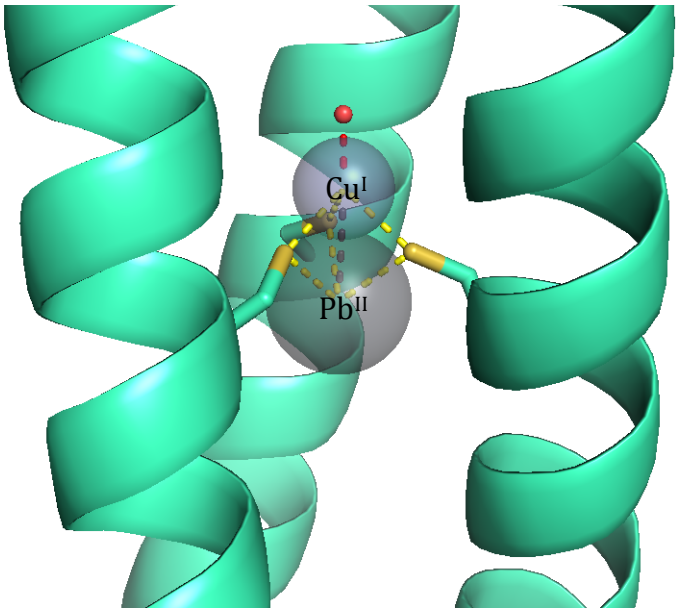

Figure 4-25. Side-on view of a Pymol representation of a modeled symmetric binuclear $Cu^{I}Pb^{II}$ site bound to three sulfur atoms. Site is modeled from the $Pb^{II}{}_{S}$(**GRCS**L16CL30H)$_3^-$ structure (PDB code not yet deposited).[82] Main chain atoms are shown in teal, water molecules are shown in small red spheres, cysteine residues are shown as sticks with sulfur atoms highlighted in yellow and Cu^{I} and Pb^{II} ions are shown as blue-grey and grey spheres, respectively. The Pb^{II} ion is not altered from the crystal structure and Pb^{II}-S distances are 2.65 Å. The water molecule is 2.00 Å above the Cu^{I} ion. The Cu^{I}-Pb^{II} distance has been elongated to 3.23 Å, which results in a Cu^{I}-S distance of 2.51 Å.

Knowing that Cu^{I} does not inhibit $Pb^{II}S_3$ binding **GR**L2WL16CL30H, and with data supporting a heterobinuclear $Cu^{I}Pb^{II}Cys_3$ site, I next wanted to analyze if Cu^{I} binding to $Pb^{II}{}_{s}$(**GR**L2WL16CL30H)$_3^-$ would provide evidence of $Cu^{I}Cys_3$ or $Cu^{I}His_3$ binding, exclusively. To a solution of $Pb^{II}{}_{S}$(**GR**L2WL16CL30H)$_3^-$, I added 0.5 equivalents of Cu^{I} (Figure 4-26). In the absence of Cu^{I} an extinction coefficient at 266 nm (determined by the absorbance divided by the concentration of Pb^{II}) was ~13,500 $M^{-1}cm^{-1}$, consistent with other $Pb^{II}Cys_3$ reports.[41,46,57] The increase in absorbance at 266 upon the addition of 0.5 equivalents of Cu^{I} provides an extinction coefficient for Cu^{I}-bound Cys_3 ($Cu^{I}Pb^{II}$(**GR**L2WL16CL30H)$_3$, since the $Pb^{II}Cys_3$ feature persists) of ~2,500 $M^{-1}cm^{-1}$ (determined by the increase in absorbance at 266 nm divided by the concentration of Cu^{I} added). The direct Cu^{I} titrations into Cys_3 peptides reported above provided $Cu^{I}{}_2Cys_3$ extinction coefficients at 266 nm of ~16,000 $M^{-1}cm^{-1}$, therefore, I would have expected ~4,000 $M^{-1}cm^{-1}$ if all of the added Cu^{I} (only 0.5 equivalent in this

case) bound exclusively to the Cys_3 site. Instead, it appears that when 0.5 equivalents of Cu^I is added to $Pb^{II}_S(\mathbf{GR}L2WL16CL30H)_3^-$ approximately 0.25 equivalents bind to the Cys_3 site presumable leading to the other 0.25 equivalents bind to His_3 site. These data indicate that the binding affinity of the second equivalent of Cu^I to the Cys_3 site is comparable to the binding affinity of Cu^I to a His_3 site, and also to the binding affinity of the Pb^{II} to the Cys_3 (supported by three equivalents of Cu^I required to displace one equivalent of Pb^{II} from a Cys_3 site).

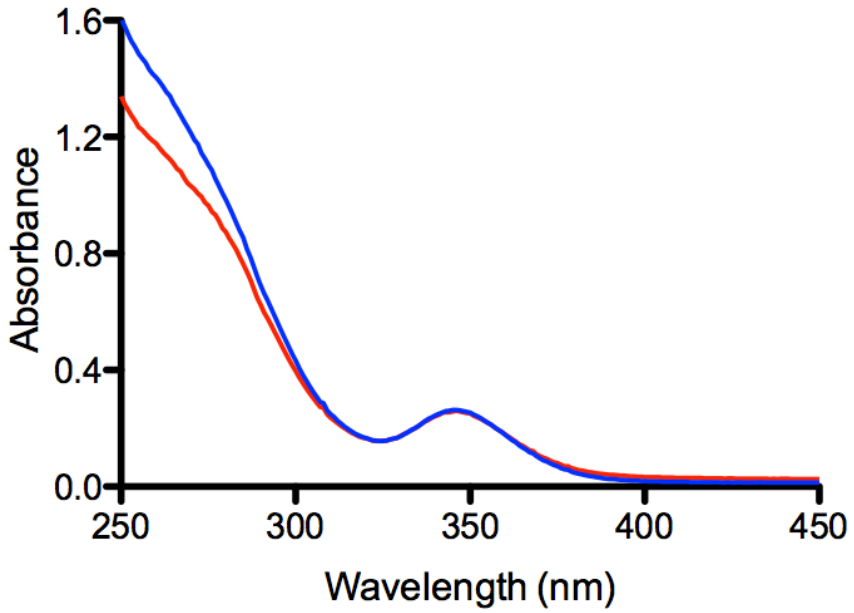

Figure 4-26. Overlay of titration spectra of 70 μM $Pb^{II}_S(\mathbf{GR}L2WL16CL30H)_3^-$ in the absence (red) and presence of 0.5 equivalents of Cu^I (blue) at pH 7.5 in 100 mM TRIS buffer.

Conclusions

In this chapter I have provided spectroscopic evidence that supports the first homobinuclear Cu^I_2 and heterobinuclear Cu^IPb^{II} centers obtained within the **TRI** and **GR** families of peptides. Previously, studies of metal binding single Cys_3 **a** sites in **TRI** and **GR** peptides have resulted in exclusively mononuclear metal centers. UV-Vis and XAS spectroscopies support this claim. Titrations of Cu^I into Cys_3 containing peptides provide 2:1 binding stoichiometry of metal:3SCC and a heavy long distance back scatterer is observed in the Fourier Transform of the collected EXAFS data, consistent with a Cu^I-

Cu^{I} interaction. Alteration of the sterics in the layer directly above the Cys_3 binding site, with respect to the N-termini of the 3SCC, of Leu12Ala or Leu12$_D$Leu show similar Cu^{I} binding stoichiometries indicating that the binuclear Cu_2^{I} site forms even when more (Leu12Ala) or less (Leu12$_D$Leu) space is available within the hydrophobic core of the scaffold. The similarities in the binding constants and spectroscopic data obtained, regardless of the steric bulk included in the layer above the Cys_3 binding site, best supports a model in which the Cu^{I} ions have two short Cu^{I}-S bonds and one longer Cu^{I}-S^{*} bond with a pseudo-linear/T-shaped coordination geometry. This stoichiometry is not observed with **TRI**L2W ruling out contributions to the spectroscopic features of non-specific Cu^{I} binding to exterior Glu or Lys residues. Primary standard competitive binding assays with BCS^{2-} provide $K_{aCu2Pep3}$ values of 10^{28} – 10^{31} M^{-2}. The binding affinities seem to be dependent on both pH and the length of the peptide analyzed (**TRI** or **GR**). Secondary competitive binding assays of Cu^{I} to two different sites (Cys_3 and His_3) within the same 3SCC provide comparable binding affinities to those obtained via BCS^{2-} competition. The binding affinities and stoichiometries as determined via UV-Vis spectroscopy of both **TRI** and **GR** Cys_3 containing peptides correlate well with native Cu^{I} metallochaperones. Additionally, bi- and polynuclear Cu^{I} complexes show similar characteristic XAS features with comparable Cu^{I}-S and Cu^{I}-Cu^{I} bond lengths. In general the measured bond lengths reported in this chapter are slightly shorter than those observed in native systems, perhaps due to the differences observed in secondary and tertiary structure between native metallochaperones and our *de novo* designed 3SCC; however, due to the lack of structural data or proposed polynuclear Cu^{I}-cluster geometry within metallochaperones, it is difficult to address the consistently shorter distances observed. Additionally, the binding constants obtained for the binuclear $Cu^{I}Cys_3$ sites in the **TRI** and **GR** peptides are approximately twice as tight as the mononuclear constants reported for native Cu^{I}-metallochaperones, providing assumed comparable binding affinities for single Cu^{I} ions.

With the initial hopes of obtaining $Pb^{II}Cys_3$ binding affinities via direct competition with Cu^{I} binding, spectroscopic analysis of peptides containing both Cu^{I} and Pb^{II} actually support the formation of an unprecedented $Cu^{I}Pb^{II}$ hetero-binuclear site. When one equivalent of Cu^{I} is present in a solution of peptide, which contains a Cys_3 site,

only 0.5 equivalents of $Pb^{II}Cys_3$ binding is observed, even upon addition of excess Pb^{II} supporting the notion that 0.5 equivalents of the Cys_3 site is already occupied by a $Cu^{I}Cys_3$ binuclear center. Conversely, when Cu^{I} is added to a Pb^{II}_{S}-bound peptide, the $Pb^{II}Cys_3$ site is not perturbed until greater than one equivalent of Cu^{I} is present, but evidence of Cu^{I}-Cys_3 coordination is observed. This supports that Cu^{I} is binding while Pb^{II} is not perturbed, supporting a $Cu^{I}Pb^{II}Cys_3$ heterobinuclear site. Additionally, analysis of $Pb^{II}Cys_3$ site via ^{207}Pb NMR shows no perturbation on the Pb^{II} coordination in the presence of one equivalent of Cu^{I}. Three total equivalents of Cu^{I} are required to completely displace the Pb^{II} ion, suggesting competition is observed between the binding of the second equivalent of Cu^{I} and the Pb^{II} ion. It appears that the order of metal addition matters with respect to competition observed between the binuclear Cu^{I} site and heterobinuclear $Cu^{I}Pb^{II}$ site indicating that there may be kinetic influences on the Cu^{I}/Pb^{II} Cys_3 competition. This is the first report of a mixed $Cu^{I}Pb^{II}$ binuclear complex. Additionally, it appears that the second equivalent of Cu^{I} that binds to the Cys_3 binuclear site is competitive with both $Pb^{II}Cys_3$ binding and $Cu^{I}His_3$ binding.

This study demonstrates the versatility of metal binding to a Cys_3 site within a highly simplified scaffold. The binding of other metals, such as Hg^{II}, Cd^{II}, Pb^{II}, and Zn^{II}, have been previously studied within Cys_3 substituted **GR** and **TRI** peptides. In the case of Hg^{II}, the metal preference for binding linearly can be utilized, stoichiometrically, to enforce formation of a 2SCC, but appropriate pH and 1:3 metal:monomer stoichiometry provides a model of a biologically relevant three-coordinate trigonal planar $Hg^{II}Cys_3$. The sterics around the Cys_3 site within **GR** and **TRI** peptide can be altered to enforce higher or lower coordination geometry of Cd^{II}. These steric changes also provide spectroscopic perturbations when Pb^{II} is bound to Cys_3 sites. However, in the case of Cu^{I} it appears that a high affinity binuclear site is produced, regardless of the sterics around the Cys_3 site. Additionally, it appears that the Cys_3 affinity is such that one equivalent will bind in the presence of Pb^{II} forming an unprecedented and very interesting heterobinuclear site.

References

(1) Klinman, J. P. *Chem. Rev.* **1996**, *96*, 2541–2562.
(2) Averill, B. A. *Chem. Rev.* **1996**, *96*, 2951–2964.
(3) Crichton, R. R.; Pierre, J. L. *Biometals* **2001**, *14*, 99–112.
(4) Solomon, E. I.; Szilagyi, R. K.; DeBeer George, S.; Basumallick, L. *Chem. Rev.* **2004**, *104*, 419–458.
(5) Rosenzweig, A. C.; Sazinsky, M. H. *Curr. Opin. Struct. Biol.* **2006**, *16*, 729–735.
(6) MacPherson, I. S.; Murphy, M. E. P. *Cell. Mol. Life Sci.* **2007**, *64*, 2887–2899.
(7) Solomon, E. I.; Sundaram, U. M.; Machonkin, T. E. *Chem. Rev.* **1996**, *96*, 2563–2606.
(8) Solomon, E. I.; Ginsbach, J. W.; Heppner, D. E.; Kieber-Emmons, M. T.; Kjaergaard, C. H.; Smeets, P. J.; Tian, L.; Woertink, J. S. *Faraday Discuss.* **2011**, *148*, 11–39.
(9) Solomon, E. I.; Hadt, R. G. *Coord. Chem. Rev.* **2011**, *255*, 774–789.
(10) Solomon, E. I.; Chen, P.; Metz, M.; Lee, S.-K.; Palmer, A. E. *Angew. Chem. Int. Ed. Engl.* **2001**, *40*, 4570–4590.
(11) Hannan, J. P.; Busch, J. L. H.; Breton, J.; James, R.; Thomson, A. J.; Moore, G. R.; Davy, S. L. *J. Biol. Inorg. Chem.* **2000**, *5*, 432–447.
(12) Halliwell, B.; Gutteridge, J. M. *Methods Enzymol.* **1990**, *186*, 1–85.
(13) Halliwell, B.; Gutteridge, J. M. *FEBS Lett.* **1992**, *307*, 108–112.
(14) Menkes, J. H.; Alter, M.; Steigleder, G. K.; Weakley, D. R.; Sung, J. H. *Pediatrics* **1962**, *29*, 764–779.
(15) Vulpe, C. D.; Packman, S. *Annu. Rev. Nutr.* **1995**, *15*, 293–322.
(16) Bull, P. C.; Cox, D. W. *Trends Genet.* **1994**, *10*, 246–252.
(17) Solioz, M.; Vulpe, C. *Trends Biochem. Sci.* **1996**, *21*, 237–241.
(18) Wernimont, A. K. K.; Huffman, D. L. L.; Lamb, A. L. L.; O'Halloran, T. V; Rosenzweig, A. C. C.; Halloran, T. V. O.; Rosenzweig, A. C. C. *Nat. Struct. Biol.* **2000**, *7*, 766–771.
(19) Gupta, A.; Lutsenko, S. *Future Med. Chem.* **2009**, *1*, 1125–1142.
(20) Dancis, A.; Yuan, D. S.; Haile, D.; Askwith, C.; Eide, D.; Moehle, C.; Kaplan, J.; Klausner, R. D. *Cell* **1994**, *76*, 393–402.
(21) O'Halloran, T. V; Culotta, V. C. *J. Biol. Chem.* **2000**, *275*, 25057–25060.
(22) Harrison, M. D.; Jones, C. E.; Solioz, M.; Dameron, C. T. *Trends Biochem. Sci.* **2000**, *25*, 29–32.
(23) Robinson, N. J.; Winge, D. R. *Annu. Rev. Biochem.* **2010**, *79*, 537–562.
(24) Pufahl, R. A.; Singer, C. P.; Peariso, K. L.; Lin, S.-J. J.; Schmidt, P. J.; Fahrni, C. J.; Culotta, V. C.; Penner-Hahn, J. E.; O'Halloran, T. V. *Science* **1997**, *278*, 853–856.
(25) Huffman, D. L.; O'Halloran, T. V. *J. Biol. Chem.* **2000**, *275*, 18611–18614.
(26) Banci, L.; Bertini, I.; Cantini, F.; Felli, I. C.; Gonnelli, L.; Hadjiliadis, N.; Pierattelli, R.; Rosato, A.; Voulgaris, P. *Nat. Chem. Biol.* **2006**, *2*, 367–368.
(27) Yu, F.; Cangelosi, V. M.; Zastrow, M. L.; Tegoni, M.; Plegaria, J. S.; Tebo, A. G.; Mocny, C. S.; Ruckthong, L.; Qayyum, H.; Pecoraro, V. L. *Chem. Rev.* **2014**, *114*, 3495–3578.
(28) Zastrow, M. L.; Pecoraro, V. L. *Biochemistry* **2014**, *53*, 957–978.
(29) Zastrow, M. L.; Pecoraro, V. L. *Coord. Chem. Rev.* **2013**, *257*, 2565–2588.

(30) DeGrado, W. F.; Summa, C. M.; Pavone, V.; Nastri, F.; Lombardi, A. *Annu. Rev. Biochem.* **1999**, *68*, 779–819.
(31) Hill, R. B.; Raleigh, D. P.; Lombardi, A.; DeGrado, W. F. *Acc. Chem. Res.* **2000**, *33*, 745–754.
(32) Ghosh, D.; Pecoraro, V. L. *Curr. Opin. Chem. Biol.* **2005**, *9*, 97–103.
(33) Dieckmann, G. R.; McRorie, D. K.; Tierney, D. L.; Utschig, L. M.; Singer, C. P.; O'Halloran, T. V.; Penner-Hahn, J. E.; DeGrado, W. F.; Pecoraro, V. L. *J. Am. Chem. Soc.* **1997**, *119*, 6195–6196.
(34) Dieckmann, G. R.; McRorie, D. K.; Lear, J. D.; Sharp, K. A.; DeGrado, W. F.; Pecoraro, V. L. *J. Mol. Biol.* **1998**, *280*, 897–912.
(35) Farrer, B. T.; McClure, C. P.; Penner-Hahn, J. E.; Pecoraro, V. L. *Inorg. Chem.* **2000**, *39*, 5422–5423.
(36) Farrer, B. T.; Harris, N. P.; Valchus, K. E.; Pecoraro, V. L. *Biochemistry* **2001**, *40*, 14696–14705.
(37) Matzapetakis, M.; Farrer, B. T.; Weng, T.-C.; Hemmingsen, L.; Penner-Hahn, J. E.; Pecoraro, V. L. *J. Am. Chem. Soc.* **2002**, *124*, 8042–8054.
(38) Farrer, B. T.; Pecoraro, V. L. *Proc. Natl. Acad. Sci. U. S. A.* **2003**, *100*, 3760–3765.
(39) Lee, K.-H.; Cabello, C.; Hemmingsen, L.; Marsh, E. N. G.; Pecoraro, V. L. *Angew. Chem. Int. Ed.* **2006**, *45*, 2864–2868.
(40) Iranzo, O.; Ghosh, D.; Pecoraro, V. L. *Inorg. Chem.* **2006**, *45*, 9959–9973.
(41) Matzapetakis, M.; Ghosh, D.; Weng, T.-C.; Penner-Hahn, J. E.; Pecoraro, V. L. *J. Biol. Inorg. Chem.* **2006**, *11*, 876–890.
(42) Iranzo, O.; Cabello, C.; Pecoraro, V. L. *Angew. Chem. Int. Ed.* **2007**, *46*, 6688–6691.
(43) Iranzo, O.; Thulstrup, P. W.; Ryu, S.-B.; Hemmingsen, L.; Pecoraro, V. L. *Chemistry* **2007**, *13*, 9178–9190.
(44) Touw, D. S.; Nordman, C. E.; Stuckey, J. A.; Pecoraro, V. L. *Proc. Natl. Acad. Sci. USA* **2007**, *104*, 11969–11974.
(45) Pecoraro, V. L.; Peacock, A. F. A.; Iranzo, O.; Luczkowski, M. In *ACS Symposium Series*; ACS Publications, 2009; pp. 183–197.
(46) Neupane, K. P.; Pecoraro, V. L. *Angew. Chem. Int. Ed.* **2010**, *49*, 8177–8180.
(47) Chakraborty, S.; Iranzo, O.; Zuiderweg, E. R. P.; Pecoraro, V. L. *J. Am. Chem. Soc.* **2012**, *134*, 6191–6203.
(48) Tegoni, M.; Yu, F.; Bersellini, M.; Penner-Hahn, J. E.; Pecoraro, V. L. *Proc. Natl. Acad. Sci. USA* **2012**, *109*, 21234–21239.
(49) Yu, F.; Penner-Hahn, J. E.; Pecoraro, V. L. *J. Am. Chem. Soc.* **2013**, *135*, 18096–18107.
(50) Yu, F. De novo designed metallopeptides with a type 2 copper center: a structural and functional model for copper nitrite reductase, Univeristy of Michigan, 2014.
(51) Meyer, M.; Albrecht-Gary, A.-M.; Dietrich-buchecker, C.; Sauvage, J.-P. *Inorg. Chem.* **1999**, *38*, 2279–2287.
(52) Chan, W. C.; White, P. D. *Fmoc Solid Phase Peptide Synthesis: A Practical Approach*; Chan, W.; White, P., Eds.; Oxford Univ Press, New York, 2000.
(53) *The Protein Protocols Handbook*; Walker, J. M., Ed.; 2nd ed.; Humana Press Inc.: Totowa, NJ, 2002.
(54) Xiao, Z.; Loughlin, F.; George, G. N.; Howlett, G. J.; Wedd, A. G. *J. Am. Chem.*

Soc. **2004**, *126*, 3081–3090.
(55) GraphPad Prism version 5.00 for Mac, GraphPad Software, San Diego California USA, www.graphpad.com.
(56) Tegoni, M.; Yu, F.; Bersellini, M.; Penner-Hahn, J. E.; Pecoraro, V. L. *Proc. Natl. Acad. Sci. U. S. A.* **2012**, *109*, 21234–21239.
(57) Neupane, K. P.; Pecoraro, V. L. *J. Inorg. Biochem.* **2011**, *105*, 1030–1034.
(58) Zampella, G.; Neupane, K. P.; De Gioia, L.; Pecoraro, V. L. *Chem. Eur. J.* **2012**, *18*, 2040–2050.
(59) Cobas, C.; Cruces, J.; Sardina, F.; MestRe-C version 2.3, Universidad de Santiago de Compostela, S. MestRe-C version 2.3, Universidad de Santiago de Compostela, Spain, 2000.
(60) George, G.N., Pickering, I. J. EXAFSPAK, 2000.
(61) Rehr, J. J.; Kas, J. J.; Vila, F. D.; Prange, M. P.; Jorissen, K. *Phys. Chem. Chem. Phys.* **2010**, *12*, 5503.
(62) Pushie, M. J.; Zhang, L.; Pickering, I. J.; George, G. N. *Biochim. Biophys. Acta* **2012**, *1817*, 938–947.
(63) Chen, K.; Yuldasheva, S.; Penner-Hahn, J. E.; O'Halloran, T. V. *J. Am. Chem. Soc.* **2003**, *125*, 12088–12089.
(64) Cobine, P. A.; George, G. N.; Jones, C. E.; Wickramasinghe, W. A.; Solioz, M.; Dameron, C. T. *Biochemistry* **2002**, *41*, 5822–5829.
(65) Ralle, M.; Lutsenko, S.; Blackburn, N. J. *J. Biol. Chem.* **2003**, *278*, 23163–23170.
(66) Pickering, I. J.; George, G. N.; Dameron, C. T.; Kurz, B.; Winge, D. R.; Dance, I. G. *J. Am. Chem. Soc.* **1993**, *115*, 9498–9505.
(67) Thorvaldsen, J. L.; Sewell, A. K.; Tanner, A. M.; Peltier, J. M.; Pickering, I. J.; George, G. N.; Winge, D. R. *Biochemistry* **1994**, *33*, 9566–9577.
(68) Dameron, C. T.; Winge, D. R. **1991**, *88*, 6127–6131.
(69) Odermatt, A.; Solioz, M. *J. Biol. Chem.* **1995**, *270*, 4349–4354.
(70) Cobine, P.; Wickramasinghe, W. A.; Harrison, M. D.; Weber, T.; Solioz, M.; Dameron, C. T. *FEBS Lett.* **1999**, *445*, 27–30.
(71) Strausak, D.; Solioz, M. *J. Biol. Chem.* **1997**, *272*, 8932–8936.
(72) Carr, H. S.; George, G. N.; Winge, D. R. *J. Biol. Chem.* **2002**, *277*, 31237–31242.
(73) Heaton, D. N.; George, G. N.; Garrison, G.; Winge, D. R. *Biochemistry* **2001**, *40*, 743–751.
(74) Rigby, K.; Zhang, L.; Cobine, P. A.; George, G. N.; Winge, D. R. *J. Biol. Chem.* **2007**, *282*, 10233–10242.
(75) Horvath, R.; Lochmüller, H.; Stucka, R.; Yao, J.; Shoubridge, E. A.; Kim, S. H.; Gerbitz, K. D.; Jaksch, M. *Biochem. Biophys. Res. Commun.* **2000**, *276*, 530–533.
(76) Huffman, D. L.; O'Halloran, T. V. *Annu. Rev. Biochem.* **2001**, *70*, 677–701.
(77) Banci, L.; Bertini, I.; Ciofi-Baffoni, S.; Janicka, A.; Martinelli, M.; Kozlowski, H.; Palumaa, P. *J. Biol. Chem.* **2008**, *283*, 7912–7920.
(78) Banci, L.; Bertini, I.; Cantini, F.; Ciofi-Baffoni, S.; Gonnelli, L.; Mangani, S. *J. Biol. Chem.* **2004**, *279*, 34833–34839.
(79) Zaytsev, D. V.; Morozov, V. A.; Fan, J.; Zhu, X.; Mukherjee, M.; Ni, S.; Kennedy, M. A.; Ogawa, M. Y. *J. Inorg. Biochem.* **2013**, *119*, 1–9.
(80) Mukherjee, M.; Zhu, X.; Ogawa, M. Y. *Inorg. Chem.* **2008**, *47*, 4430–4432.
(81) Hearnshaw, S.; West, C.; Singleton, C.; Zhou, L.; Kihlken, M. A.; Strange, R. W.;

Le Brun, N. E.; Hemmings, A. M. *Biochemistry* **2009**, *48*, 9324–9326.
(82) Ruckthong, L. Crystallographic Comparison of Tris-Thiolate Sites in Designed Proteins to Control Metal Geometries, University of Michigan, 2016.
(83) Miras, R.; Morin, I.; Jacquin, O.; Cuillel, M.; Guillain, F.; Mintz, E. *J. Biol. Inorg. Chem.* **2008**, *13*, 195–205.
(84) Wernimont, A. K.; Yatsunyk, L. A.; Rosenzweig, A. C. *J. Biol. Chem.* **2004**, *279*, 12269–12276.
(85) Yatsunyk, L. A.; Rosenzweig, A. C. *J. Biol. Chem.* **2007**, *282*, 8622–8631.
(86) Badarau, A.; Dennison, C. *J. Am. Chem. Soc.* **2011**, *133*, 2983–2988.
(87) González-Guerrero, M.; Argüello, J. M. *Proc. Natl. Acad. Sci. U. S. A.* **2008**, *105*, 5992–5997.
(88) Ghosh, D.; Lee, K.-H.; Demeler, B.; Pecoraro, V. L. *Biochemistry* **2005**, *44*, 10732–10740.

Chapter 5. Conclusions and Implications

De novo peptide design has offered a powerful approach to obtain redox- and catalytically active metal binding sites within simplified and symmetric protein environments allowing for the study of the structure-function relationship of native metalloenzymes. In the last five years, the Pecoraro laboratory has designed and characterized systems with the highest catalytic efficiency, in aqueous solutions, for CO_2 hydration, as inspired by the $Zn^{II}His_3$ site in Carbonic Anhydrase (CA), and for nitrite reduction, as inspired by the type two $Cu^{I/II}His_3$ site in Copper Nitrite Reductase (CuNiR).[1–4] While these systems are the fastest reported mimics for the native reactions of their corresponding metalloenzyme inspirations, the inherent symmetry of the three-stranded coiled coil (3SCC) motif restricts not only the type of sites that can be obtained (three-fold symmetric primary coordination ligands) but also limits any modifications to the binding sites (i.e. introduction of a acid-base catalyst would occur on each helix resulting in a three-fold modification near the metal binding site). Additionally, asymmetric primary coordination spheres were unattainable prior to this work. The primary goal of my thesis was to lift these symmetry-related restrictions by obtaining selectively asymmetric, heterotrimeric 3SCCs.

I have reported the first heterotrimeric 3SCCs obtained utilizing only natural amino acids that is not only metal-nucleated but that also only requires steric modifications in the layer directly above the nucleation site (Chapter 2). The requirement of only two corresponding layers to make selective heterotrimers results in space within the peptide scaffold to include a second metal binding site with potential catalytic redox or hydrolytic activity; therefore, resulting in the first report of a dual-site heterotrimeric 3SCC. The methodology to obtain selective heterotrimers employs mixing stoichiometrically two peptides, each containing Cys substitutions at the 16^{th} position of the sequence, where one peptide has a Leu residue at the 12^{th} position and the

complementary peptide contains an Ala substitution at the 12th position. These peptides are referred to as **TRI**-C and **TRI**-AC, respectively. Inclusion of a second metal binding site requires elongation of the peptide from 30 residues (the **TRI** peptides, sequence: Ac-G (LKALEEK)$_4$ G-NH$_2$) to 37 residues (the **GR** peptides, with five heptad repeats instead of four) resulting in sequences **GR**-ACH and **GR**-CH, respectively.

From pH 7.4 – 9.4, mixing Ala/Cys and Leu/Cys peptides (either **TRI** or **GR**) in a 2:1 ratio in the presence of Pb^{II} results in a pure heterotrimeric species as evidenced by a single ^{207}Pb NMR chemical shift (δ = 5600 ppm), which is unique compared to either Pb^{II}-bound homotrimeric peptide (δ = 5650 and 5575 for Pb^{II}_S(**GR**-CH)$_3^-$ and Pb^{II}_S(**GR**-ACH)$_3^-$, respectively). The presence of two chemical shifts, when Pb^{II}_S(**GR**-ACH)$_3^-$ and Pb^{II}[(**GR**-ACH)$_2$(**GR**-CH)$_1$]$^-$ are mixed, (correlating to the **GR**-ACH homotrimer and the Pb^{II}[(**GR**-ACH)$_2$(**GR**-CH)$_1$]$^-$ heterotrimer at δ = 5575 and 5600 ppm, respectively), indicates that a new species is indeed obtained and that coalescence is not the explanation for a single peak in the ^{207}Pb NMR spectra. Additionally, I analyzed the perturbed pK$_a$ of the thiol deprotonation in the presence of Pb^{II}, which can be analyzed via observation of the $Pb^{II}Cys_3$ LMCT band growing in with a fully deprotonated Cys_3 site is complexed with Pb^{II}. This analysis provided that the Pb^{II}[(**TRI**-AC)$_2$(**TRI**-C)$_1$]$^-$ thiol pK$_{a2}$ is acid shifted, significantly, to 10.47 ± 0.06, compared to Pb^{II}_S(**TRI**-AC)$_3^-$ and Pb^{II}_S(**TRI**-C)$_3^-$ homotrimers at 10.83 ± 0.04 and 11.72 ± 0.03, respectively. These results, corroborate the ^{207}Pb NMR data, and support the model that a new species is formed when two equivalents of the Ala/Cys peptide and one equivalent of the Leu/Cys peptide are mixed together in the presence of Pb^{II}.

^{207}Pb NMR analysis of the opposite peptide ratio, **GR**-ACH and **GR**-CH in a 1:2 stoichiometry, also provides a new chemical shift at 5625 ppm, suggestive of another heterotrimeric species but a small population of the 2:1 heterotrimer is also observed at 5600 ppm. These data support a model where 1:2 or 2:1 pairing of Ala/Leu residues in the layer directly above a $Pb^{II}Cys_3$ site provides heterotrimeric peptides, but only the 2:1 ratio yields a single species. The presence of Zn^{II} or Co^{II} does not perturb the $Pb^{II}Cys_3$ LMCT band observed via UV-Vis analysis or the ^{207}Pb NMR signals for either heterotrimer, supporting the contention that metal binding to a remote His_3 site does not

inhibit or prevent Pb^{II} binding and heterotrimer selectivity. Analysis of Co^{II} binding at the His_3 site of the homo- and heterotrimeric mixtures, in the absence of Pb^{II}, indicates that a statistical-like distribution is obtained, confirming the necessity of Pb^{II} to nucleate selective heterotrimer formation.

Analysis of the crystal structures of $Pb^{II}_{S}Zn^{II}_{N}$(**GRCS**L16CL30H)$_3^-$ and Pb^{II}_{S}(**GRCS**L12AL16C)$_3^-$, obtained by Dr. Leela Ruckthong, has allowed for a new hypothesis to been formulated addressing why the heterotrimers are selectively formed. The occupancy of water molecules within the 3SCC structures of $Pb^{II}_{S}Zn^{II}_{N}$(**GRCS**L16CL30H)$_3^-$ and Pb^{II}_{S}(**GRCS**L12AL16C)$_3^-$ is very different.[5] In the Ala/Cys structure three water molecules are observed at the helical interface, which hydrogen bond to the p-orbitals of the sulfur ions. Conversely, the Leu layer above the Cys_3 site prevents occupation of water molecules in similar locations in $Pb^{II}_{S}Zn^{II}_{N}$(**GRCS**L16CL30H)$_3^-$. Therefore, the heterotrimers, which would contain an intermediate number of Ala residues in the layer directly above the Cys_3 site, would presumably also allow for water occupancy in the space provided by said Ala substitutions. Therefore, one could imagine that an optimal combination of hydrogen packing (from the Leu residue) and hydrogen bonding (from waters included due to the Ala residues) would provide enhanced stability over the homotrimeric systems, which contain either only hydrogen-bonding (Pb^{II}_{S}(**GRCS**L12AL16C)$_3^-$) or only the hydrophobic packing ($Pb^{II}_{S}Zn^{II}_{N}$(**GRCS**L16CL30H)$_3^-$).

This stability-compromise model, considering a balance between hydrophobic packing and hydrogen bonding interactions, can also be applied to the lack of selectivity observed when Hg^{II} is used, instead of Pb^{II}, to nucleate heterotrimer formation. The ^{199}Hg NMR shows that heterotrimers are formed, but that selectivity is not observed. Hg^{II}[(**TRI**-AC)$_2$(**TRI**-C)$_1$]$^-$ and Hg^{II}[(**TRI**-AC)$_1$(**TRI**-C)$_2$]$^-$ provide intermediate chemical shifts (-210 and -193 ppm, respectively) compared to the Hg^{II}(**TRI**-AC)$_3^-$ and Hg^{II}(**TRI**-C)$_3^-$ homotrimers (-244 and -184 ppm), but peaks corresponding to both heterotrimers are present in either the 2:1 or 1:2 Ala:Leu mixture. In the corresponding homotrimeric Hg^{II} crystal structures, a central water molecule is observed.[5] In the heterotrimeric scaffolds, the presence of a central water molecule could function as a moderator in the hydrogen-

bonding network. This could result in a comparable number of hydrogen bonding interactions in both heterotrimer mixture, and thus providing comparable added stability to both heterotrimers and, therefore, removing discrimination between the 2:1 and 1:2 species. Of the heavy metals tested, only Pb^{II} leads to a single heterotrimeric species. Hg^{II} does bias toward heterotrimer formation, but mixtures appear for either mixture.

Attempts to obtain heterotrimers with the Ala/Leu pairing below the Cys_3 binding site have not yet been successful. This could be due to the preferred orientation of Pb^{II} when binding to a Cys_3 site, which has consistently proven to be in an *endo*-configuration pointing toward the C-terminus in both $Pb^{II}_{S}Zn^{II}_{N}$(**GRCS**L16CL30H)$_3^-$ and Pb^{II}_{S}(**GRCS**L12AL16C)$_3^-$ crystal structures. One could then imagine that introduction of the Ala below the Cys_3 site would not result in the introduction of water molecules (to date no water molecules have been observed below the metal binding sites when $_{L}$Leu layer is present). Therefore, the hydrogen-bonding/hydrophobic packing stabilization combination cannot occur, which seems to stabilize specific heterotrimer formation.

From a design aspect, future directions for this project include studies to determine if heterotrimer selectivity can be achieved if the Cys_3 site is moved to a **d** site with the Ala/Leu pairings in an **a** site, either above, or below, the metal binding site. A recent crystal structure of Pb^{II}_{S}(**CS**L12C)$_3^-$ provides an *endo*-configuration of Pb^{II}-binding, but the metal ion is actually pointing up toward the N-terminus. It is possible that the *endo*-confirmation of the Pb^{II} would prevent occupation of water molecules upon inclusion of an Ala layer above a **d** $Pb^{II}Cys_3$ site, resulting in no added stability of a hydrogen bonding network as previously discussed and eliminating selectivity for heterotrimer formation. On the other hand, if this is the case, introduction of the Ala/Leu pairing below a **d** $Pb^{II}Cys_3$ site may restore heterotrimer selectivity since the Ala residues are on the "opposite" side of the Cys_3 binding site where water molecules may be observed.

Additionally, one could address whether selective Pb^{II}-nucleated heterotrimer formation would be obtainable at different locations along the helical backbone. Above I mentioned moving from an a site to a d site, but one could also imagine moving from the middle of the 3SCC (12/16 positions) to the C-terminal end, say with Ala/Leu pairings in

the 26th position and a Cys_3 at the 30th position. Of course, being so close to the end of the helical scaffold would then lead to the question of whether the Ala residue should be more solvent exposed, compared to the Cys_3 site, resulting in inverting the mutations to a 26th position Cys_3 site and Ala/Leu pairing in the 30th position.

With the methodology in hand to obtain asymmetric 3SCC, I then addressed extending the asymmetry from the Ala/Leu Cys_3 site to a second, remote transition metal binding site (Chapter 3). To do so I included an Asp residue in the layer above the His_3 binding site, resulting in **GR**-CDH. One chemical shift at ~5600 ppm is observed when this peptide is mixed, 1:2, with **GR**-ACH in the presence of Pb^{II}. Spectroscopic analysis of both of the Co^{II}-bound homotrimeric peptides provided similar characteristics, including low extinction coefficients (~30 and ~80 $M^{-1}cm^{-1}$ for $Pb^{II}_{S}Co^{II}_{N/O}$(**GR**-ACH)$_3^{+}$ and $Pb^{II}_{S}Co^{II}_{N/O}$(**GR**-CDH)$_3^{n+}$, respectively), comparable axial EPR spectra, and average Co-L bond distances of 2.115 Å. The heterotrimeric mixtures, $Pb^{II}_{S}Co^{II}_{N/O}$[(**GR**-ACH)$_2$(**GR**-CDH)$_1$]$^{n+}$ and $Pb^{II}_{S}Co^{II}_{N/O}$[(**GR**-ACH)$_1$(**GR**-CDH)$_2$]$^{n+}$ provide Co^{II} spectroscopic fingerprints that are similar to each other but starkly different than the homotrimers. The heterotrimers provide extinction coefficient of ~150-200 $M^{-1}cm^{-1}$, significantly more rhombic-like EPR spectra and shorter average Co-L distances of 2.075-2.08 Å. Switching the location of the Asp residue from the Leu/Cys peptide to the Ala/Cys peptide (matching **GR**-CH and **GR**-ACDH) resulted in a similar trend in spectroscopic characteristics where the homotrimers, $Pb^{II}_{S}Co^{II}_{N/O}$(**GR**-ACDH)$_3^{+}$ and $Pb^{II}_{S}Co^{II}_{N/O}$(**GR**-CH)$_3^{n+}$, looked similar to each other and to those discussed above and the heterotrimers looked different than the homotrimers but comparable to $Pb^{II}_{S}Co^{II}_{N/O}$[(**GR**-ACH)$_2$(**GR**-CDH)$_1$]$^{n+}$ and $Pb^{II}_{S}Co^{II}_{N/O}$[(**GR**-ACH)$_1$(**GR**-CDH)$_2$]$^{n+}$. These similarities indicate that the location of the Asp with relation to the Ala or Leu substitution is perhaps irrelevant in terms for selective heterotrimer formation, but the peptide stability of **GR**-ACDH is significantly decreased.

All of the spectroscopic data support a 6-coordinate,[6,7] highly symmetric Co^{II} binding site in the homotrimers and a less symmetric, 5-coordinate[8] (perhaps closer to 4-coordinate in some cases) Co^{II} environment in the heterotrimers. These data also indicate that Co^{II} binds similarly to CA in the homotrimers and similarly to Co^{II}-substituted

carboxypeptidase A (CPA), thermolysin (TML), or VanX in the heterotrimers, in particularly $Pb^{II}_{S}Co^{II}_{N/O}[(\mathbf{GR}\text{-}ACH)_2(\mathbf{GR}\text{-}CDH)_1]^{n+}$ and $Pb^{II}_{S}Co^{II}_{N/O}[(\mathbf{GR}\text{-}ACDH)_2(\mathbf{GR}\text{-}CH)_1]^{n+}$.[9–14] Both of these heterotrimers provide pure $Pb^{II}S_3$ sites (via ^{207}Pb NMR analysis), and the EPR spectra look very similar; however, a slightly elevated extinction coefficient ($\varepsilon_{544\ nm}$ = 215 $M^{-1}cm^{-1}$ from 155 $M^{-1}cm^{-1}$) and slightly shorter bond distances (2.05 Å, single sphere fit) with elevated pre-edge area (10.3 from 5.8) and pre-edge:edge ratios (3.5 from 2.0) all support a more pure Co^{II} center in the for $Pb^{II}_{S}Co^{II}_{N/O}[(\mathbf{GR}\text{-}ACDH)_2(\mathbf{GR}\text{-}CH)_1]^{n+}$ heterotrimer. The spectroscopic data, in general for the heterotrimeric species, supports direct Asp coordination to the Co^{II} ion (resulting in the probable uncoordination of one His residue).

Further perturbations were made to the Co^{II} binding site including moving the Asp ligand below the His_3 site (resulting in 6-coordinate like spectral features), and inserting a $_{D}$Leu layer directly above the His_3 site (resulting in low extinction coefficients and an EPR spectrum indicative of a trigonal bipyramidal geometry in **TRI**-$_{D}$LH but resulted in non-specific binding in **GR**-C_{D}LH). All of the Co^{II} spectroscopic data combined support the success of the primary goal of Chapter 3, an asymmetric environment has indeed been obtained at a remote site within the heterotrimer systems. The initial goal of obtaining an asymmetric second coordination sphere to mimic CA is not supported via the Co^{II} spectroscopy; however, an asymmetric primary coordination sphere IS supported.

However, contrary to the Co^{II} spectroscopy, Zn^{II} XAS of $Pb^{II}_{S}Zn^{II}_{N/O}(\mathbf{GR}\text{-}ACH)_3^{n+}$, $Pb^{II}_{S}Zn^{II}_{N/O}(\mathbf{GR}\text{-}CDH)_3^{n+}$, and the corresponding heterotrimers provides consistent evidence for four-coordinate Zn^{II} environments in all of the homo- and heterotrimer samples at pH 7.5 and 9.5. This coordination number assignment is equivalent to the crystallographically determined values for the homotrimer lacking aspartate. These data suggest two things, first, that Zn^{II} binding to the heterotrimers does not coordinate the same as Co^{II} and, second, that, Co^{II} is, therefore, a non-innocent probe in the heterotrimeric systems. These observations suggest that perhaps the Zn^{II} coordination in my heterotrimers is not completely unlike the coordination of Zn^{II} in CA. Unfortunately, Zn^{II} XAS cannot readily distinguish between N_3O or N_2O_2 primary

coordination spheres, so the first coordination sphere environment around the Zn^{II} atom may indeed be asymmetric, even though the spectroscopy supports a 4-coordinate site. However, it is clear that even if the first coordination sphere is unperturbed, the second coordination sphere, as originally desired, must have asymmetric amino acid side chain disposition. An interesting experiment would be to analyze the Zn^{II} bound heterotrimers (and the corresponding $Pb^{I}_{IS}Zn^{II}_{N}$(**GR**-CTH)$_3^{n+}$ homotrimer) to determine how, or whether, the inclusion of a Thr residue, instead of an Asp residue, changes the Zn^{II} metrical parameters. Additional neutral analogues to address would be Asn or Gln residues in the layer above the His_3 site.

Taking together the results of Chapters 2 and 3, one could imagine a surplus of future directions for this project. First, I will address the possible hydrolytic avenues one could pursue. In Chapter 3, I determined the $Pb^{II}Cys_3$ site to be catalytically active toward *p*NPA hydrolysis; however, CO_2 hydration by $Pb^{II}_{S}Zn^{II}_{N/O}$(**GR**-ACH)$_3^{n+}$ is comparable to $Hg^{II}_{S}Zn^{II}_{N/O}$(**GR**-CH)$_3^{n+}$,[15] indicating that future direct comparison can be made for the CO_2 kinetic parameters. Therefore, one could imagine the vast possibilities for future kinetic studies using the heterotrimers reported here, new heterotrimers with varied acid/base or directly coordinating ligands, and even, perhaps, heterotrimers obtained with different nucleating metals.

Considering the results and conclusions of this thesis as a whole, a new avenue to analyze selective heterotrimer formation would be to use As^{III} as the nucleating metal. As mentioned in Chapters 1 and 2, Cys_3 sites are pre-organized for As^{III}, similarly to Pb^{II}, and As^{III} found in an *endo*-confirmation toward the C-terminus in As^{III}(**CS**L9C)$_3$, again similar to Pb^{II}.[16] As^{III} also has a lone pair and is very large, which could result in similar binding compared to Pb^{II}. Additionally, As^{III} has been shown to stay complexed to a Cys_3 site under extremely acidic conditions and even HPLC purification does not result in removal of As^{III} from a Cys_3 site.[17] These situations indicate very tight binding, tighter than both Pb^{II} and Hg^{II}, both of which are removed upon HPLC purification. Therefore, if As^{III} can nucleate heterotrimer formation the resulting peptide scaffold *may* be impervious to Cu^{I} competition and oxidative side effects from redox chemistry.

On one hand there are a plethora of studies to be completed using the presented Zn^{II}-bound Asp_XHis_3 systems with regards to CO_2 hydration. Analysis of improved hydrolytic activity with the introduction of a single Asp ligand could be addressed. Or, perhaps the inclusion of a charged residue near the Zn^{II} site perturbs the kinetic pK_a of the Zn^{II}-bound solvent molecule. Mentioned in Chapter 1, the previous CA mimic, $Hg^{II}{}_SZn^{II}{}_{N/O}$(**TRI**L9CL23H)$_3{}^{n+}$ has a catalytic pK_a of 8.8, two log units higher than that of HCAII.[18,19] All subsequent modifications made to Dr. Melissa Zastrow's mimic (inclusion of Thr_3 or Asp_3 residues) all resulted in elevated pK_a values.[15] Therefore an interesting question to ask is what is required, within our simplified construct, to provide a decrease in kinetic pK_a? A full pH profile of CO_2 hydration kinetics is necessary to determine if the simple inclusion of one Asp residue near a His_3 site results in the desired decrease in pK_a. The same analysis but with a single Thr residue would be a natural progression from the Asp_1His_3 pH profile.

In CA, substitution of the acid/base catalyst T199 with an Asp residue it has been shown that the protein rearranges to allow for direct Zn^{II}-coordination to the Asp, in addition to all 3His residues in the active site.[20] This results in abolishment of catalytic activity in CA. However, the Zn^{II} XAS data, in combination with the models provided in Chapter 3, strongly support the idea that the rigidity of the 3SCC prevents Zn^{II} coordination to all three His residues as well as direct coordination to the Asp residue. Therefore, the effect on catalytic activity due to coordination restrictions imposed on the metal binding site by the secondary structure is also an important question to ask.

Current work in the Pecoraro laboratory is also addressing the effects of Co^{II} coordination if a Glu residue is included in the layer above, or below, a His_3 binding site. Initial models, as described in Chapter 3, suggests that inclusion of a Glu residue in the 26th position would probably result in direct coordination of the carboxylic acid moiety directly to the metal ion, while still coordinated to the His_3 site. With the knowledge that a Co^{II} ion seems to prefer a chelation effect from an sequence containing L26DL30H, it would be very interesting to see if we see comparably Asp_XHis_2 binding or if indeed the Co^{II} ion coordinates to the Glu as well as the His_3 site. Zn^{II} analyses in these peptides would also be a natural progression.

Another exciting avenue to address would be adding different metals to the $Carboxylate_XHis_3$ site such as Fe or Mn. The Co^{II} data supports direct ligation of the Asp residue, but requires one His residue to uncoordinated from the metal. The combination of a Glu residue and addition of Fe or Mn could allow for analysis of a very different metalloenzyme, such as Fe- or Mn-superoxide dismustases.[21–23] These proteins have active sites in which the metal, Fe or Mn, binds to three His ligands and one carboxylate. If indeed the additional length offered from Glu compared to Asp can allow for direct carboxylate coordination and ligation to all three His residues, then this would provide another avenue to study asymmetric primary coordination spheres with our 3SCCs to mimic native metal binding sites.

The $CuHis_3$ secondary coordination sphere of CuNiR contains an acid/base Asp ligand;[24] however, the entirety of Chapter 4 indicates that utilizing a Pb^{II}-nucleated heterotrimer to study CuNIR activity will be non-trivial, at best. First to consider is the competition observed between Cu^{I} and Pb^{II} for the Cys_3 site. The data in Chapter 4 suggest that the addition of the Pb^{II} first, to form the heterotrimer at the Cys_3 site, and the presence of the His_3 site may prevent the Cu^{I} from binding to the Cys_3 site. Additionally, with the asymmetric addition of an Asp residue near the His_3 site, this may also help promote $Cu^{I}His_3$ binding. Additionally, the effects of a hetero-binuclear $Cu^{I}Pb^{II}Cys_3$ site on the formation of heterotrimers should be addressed, as it is possible that if heterotrimers can still be obtained, with Cu^{I} also present at the $Pb^{II}Cys_3$ site, albeit unlikely, that the site may not offer any redox activity and could actually offer stability to the heterotrimer formation. However, extensive controls considering the specificity of where Cu^{I} binds in such a heterotrimer would be required.

The next condition to consider is the optimal pH of 5.8, at which Dr. Fanting Yu observed CuNIR activity in the **TRI** peptides.[3,4,25] As discussed in Chapter 2, the pK_a of thiol deprotonation, presumably directly related to $Pb^{II}Cys_3$ binding, is very near to this pH, and the selectivity for heterotrimer formation at this pH would need to be investigated. Last, but certainly not least, thiol groups are prone to form disulfides under oxidative conditions. Therefore, the study of the redox-active site may only be analyzable under reductive conditions, potentially limiting the characterization of a CuNIR mimic.

With respect to both of these considerations, the $Cu^{I}Pb^{II}Cys_3$ site, and the sensitivity to oxidation of the Cys residues, this could be another situation in which using an As^{III}-nucleated 3SCC could be extremely beneficial. Of course, this project would be contingent on the characterization of As^{III}-nucleated heterotrimer formation. Studies to address the formation of a binuclear $Cu^{I}As^{III}Cys_3$ site would be required, as well as studies to address the Cys_3 sensitivity to oxidation while As^{III} is bound.

Of great personal interest would be the continuation of the potential hetero-binuclear $Pb^{II}Co^{II}$ site as evidenced by the change in spectra of $Pb^{II}_{S}Co^{II}_{N/O}$(**GR**-CDH)$_3^{n+}$ upon the addition of excess Pb^{II}. As discussed in Chapter 3, the addition of one additional equivalent of Pb^{II} to $Pb^{II}_{S}Co^{II}_{N/O}$(**GR**-CDH)$_3^{n+}$ resulted in a Co^{II} d-d band identical to that of $Pb^{II}_{S}Co^{II}_{N/O}$(**GR**-ACH)$_3^{n+}$. If the Pb^{II} ion is binding to the Asp residues a Pb^{II}-Co^{II} scatterer should be observed via XAS, which in turn would provide evidence of a 3SCC with two engineered metal binding sites, a Cys_3 and an Asp_3Hsi_3 site, that binds three equivalents of metal. If the selectivity of each site is properly addressed, one could imagine that three different metal ions could selectively bind to one 3SCC, such as a $Pb^{II}Cys_3$ site, a $Co^{II}His_3$ site and perhaps a $Ca^{II}Asp_3$ site (considering the affinity for Ca^{II} for oxygen rich metal binding sites).[26]

In Chapter 4, I reported evidence of the first binuclear metal site within the **TRI** and **GR** peptides observed when only one layer of metal binding ligands is included in the peptide sequence (**GR**-C and **TRI**-C). Both EXAFS and UV-Vis spectroscopies support a $Cu^{I}_2Cys_3$ center with a Cu-Cu interaction at 2.66 Å two or three Cu-S distances at 2.20 Å, and a UV transition at 266 nm. Modifications to the sterics in the layer directly above the Cys_3 (L12A or L12$_D$L) provide very similar spectroscopic characteristics indicating the formation of the binuclear site. Most likely the Cu^{I} ions are intermediate between 2- and 3-coordinate with two short Cu-S distances and a longer Cu-S interaction. This sort of binuclear Cu^{I} site is often seen in nature and ideally, Cu^{I} binding to ours systems could be used to understand better Cu^{I} metallochaperones, regulators and Cu^{I} homeostasis in general. Two different modes of competition, including a primary standard with BCS^{2-}, as well as a secondary competition with the His_3 site in the same construct, reveal binding affinities of $10^{28} – 10^{31}$ M^{-2}.

Ag^I has been shown to bind similarly to Cu^I in thiolate-rich environments; therefore, I have conducted initial studies on Ag^I binding to Cys_3 sites in 3SCCs. For both **TRI**-C and **TRI**-AC, UV analysis supports three equivalents of Ag^I binding per 3SCC. This stoichiometry, one metal ion per thiol residue, is comparable to that observed by Ogawa and coworkers.[27] Initial XAS analysis supports either a 2- or 3-coordinate Ag-S environment; however, further analysis is necessary to characterize the $Ag^I_SCys_3$ systems, primarily due to the previous samples having been prepared at a significant excess of 3SCC. The sample preparation could therefore be the reason a Ag^I-Ag^I interaction has not been observed at this time, even though the UV experiment provides evidence for multiple Ag^I ions in the binding site.

Drawing inspiration from Ogawa's reported structure of the $Cd^{II}_4S_6$ cluster, as discussed in Chapter 4, one could imagine that three silver ions could bind, each to two cysteine residues, at the helical interface.[28] This could also explain why a Ag^I-Ag^I interaction has not been observed via XAS analysis, since the Cd^{II}-Cd^{II} distance is too long, at 4 Å, and a comparable distance would not be unrealistic for Ag^I binding within such a similar scaffold. Once again, Ag^I binding could be offering a very different binding geometry compared to the binuclear Cu^I_2 site, or any of the previously analyzed heavy metals within a Cys_3 site. It is possible that in our 3SCCs the Ag^I ions bind to the sulfur ligands only, and no Glu residues as observed in the $Cd^{II}_4S_6$ cluster, therefore retaining the full α-helical structure of the 3SCC.

Arguably more interesting, and more convoluted, than the binuclear Cu^I site is what happens when both Pb^{II} and Cu^I are added to a peptide with a Cys_3 site. When one equivalent of Cu^I is present and Pb^{II} is titrated into the peptide, only half the expected $Pb^{II}Cys_3$ extinction coefficient is observed, supporting a model where 50% of the Cys_3 site is blocked from Pb^{II} binding – presumably due to 50% of the total peptide binding the Cu^I as a $Cu^I_2Cys_3$ site. The addition of excess Pb^{II} does not displace the Cu^I from the Cys_3 site. If Pb^{II} is added to the peptide first, then one equivalent of Cu^I does not perturb the Pb^{II} spectroscopy (UV-Vis or ^{207}Pb NMR), but evidence for Cu^ICys_3 binding is observed, supporting Cu^I and Pb^{II} binding simultaneously to the Cys_3 site. Two more equivalents of Cu^I (three equivalents total) are required to completely remove Pb^{II} from the Cys_3 site.

These data, combined, indicate that one equivalent of Pb^{II} and the second equivalent of Cu^{I} compete for binding to the Cys_3 site.

However, if a His_3 site is also present in the sequence, such at **GR**-CH, with one equivalent of Cu^{I} present, Pb^{II} binding is not inhibited at the Cys_3 site. This indicates that the $Cu^{I}_2Cys_3$ site is not formed, because the above experiments show that Pb^{II} cannot disrupt the binuclear Cu^{I} site. Therefore, the Cu^{I} is probably partially occupying the His_3 site and partially occupying the Cys_3 site, with no formation of the binuclear $Cu^{I}_2Cys_3$ site. All of these data together support the view that there are kinetic implications in the binding of Cu^{I} and Pb^{II} to the Cys_3 site, and that the order of metal addition directly influences the formation of the $Cu^{I}_2Cys_3$ or $Cu^{I}Pb^{II}Cys_3$ site.

References

(1) Zastrow, M. L.; Pecoraro, V. L. *J. Am. Chem. Soc.* **2013**, *135*, 5895–5903.
(2) Zastrow, M. L.; Peacock, A. F. A.; Stuckey, J. A.; Pecoraro, V. L. *Nat. Chem.* **2012**, *4*, 118–123.
(3) Tegoni, M.; Yu, F.; Bersellini, M.; Penner-Hahn, J. E.; Pecoraro, V. L. *Proc. Natl. Acad. Sci. U. S. A.* **2012**, *109*, 21234–21239.
(4) Yu, F.; Penner-Hahn, J. E.; Pecoraro, V. L. *J. Am. Chem. Soc.* **2013**, *135*, 18096–18107.
(5) Ruckthong, L. Crystallographic Comparison of Tris-Thiolate Sites in Designed Proteins to Control Metal Geometries, University of Michigan, 2016.
(6) Coleman, J. E. *Annu. Rev. Biochem.* **1992**, *61*, 897–946.
(7) Bertini, I.; Luchinat, C. *Ann. N.Y. Acad.* **1984**, *429*, 89–98.
(8) Maret, W.; Vallee, B. L. *Methods Enzym.* **1993**, *226*, 52–71.
(9) Bencini, A.; Bertini, I.; Canti, G.; Gatteschi, D.; Luchinat, C. *J. Inorg. Biochem.* **1981**, *14*, 81–93.
(10) Grell, E.; Bray, R. C. *Biochim. Biophys. Acta* **1971**, *236*, 503–506.
(11) Horrocks, W. D.; Ishley, J. N.; Holmquist, B.; Thompson, J. S. *J. Inorg. Biochem.* **1980**, *12*, 131–141.
(12) Kaden, T. A.; Holmquist, B.; Vallee, B. L. *Inorg. Chem.* **1974**, *13*, 2585–2590.
(13) Martinelli, R. A.; Hanson, G. R.; Thompson, J. S.; Holmquist, B.; Pilbrow, J. R.; Auld, D. S.; Vallee, B. L. *Biochemistry* **1989**, *28*, 2251–2258.
(14) Breece, R. M.; Costello, A.; Bennett, B.; Sigdel, T. K.; Matthews, M. L.; Tierney, D. L.; Crowder, M. W. *J. Biol. Chem.* **2005**, *280*, 11074–11081.
(15) Zastrow, M. De novo designed metalloenzymes: structural stabilization and hydrolytic catalysis in a family of α-helical coiled coils, University of Michigan, 2013.
(16) Touw, D. S.; Nordman, C. E.; Stuckey, J. A.; Pecoraro, V. L. *Proc. Natl. Acad. Sci. USA* **2007**, *104*, 11969–11974.
(17) Farrer, B. T.; McClure, C. P.; Penner-Hahn, J. E.; Pecoraro, V. L. *Inorg. Chem.* **2000**, *39*, 5422–5423.
(18) Lindskog, S. *Biochemistry* **1966**, *5*, 2641–2646.
(19) Fierke, C.; Calderone, T.; Krebs, J. F. *Biochemistry* **1991**, *30*, 11054–11063.
(20) Ippolito, J. A.; Baird, T. T.; McGee, S. A.; Christianson, D. W.; Fierke, C. A. *Proc. Natl. Acad. Sci. U. S. A.* **1995**, *92*, 5017–5021.
(21) Maliekal, J.; Karapetian, A.; Vance, C.; Yikilmaz, E.; Wu, Q.; Jackson, T.; Brunold, T. C.; Spiro, T. G.; Miller, A.-F. *J. Am. Chem. Soc.* **2002**, *124*, 15064–15075.
(22) Jackson, T. a; Gutman, C. T.; Maliekal, J.; Miller, A.-F.; Brunold, T. C. *Inorg. Chem.* **2013**, *52*, 3356–3367.
(23) Sugio, S.; Hiraoka, B. Y.; Yamakura, F. *Eur. J. Biochem.* **2000**, *267*, 3487–3495.
(24) Averill, B. A. *Chem. Rev.* **1996**, *96*, 2951–2964.
(25) Yu, F. De novo designed metallopeptides with a type 2 copper center: a structural and functional model for copper nitrite reductase, Univeristy of Michigan, 2014.
(26) Ouyang, H.; Vogel, H. J. *BioMetals* **1998**, *11*, 213–222.
(27) Morozov, V. A.; Ogawa, M. Y. *Inorg. Chem.* **2013**, *52*, 9166–9168.

(28) Zaytsev, D. V.; Morozov, V. A.; Fan, J.; Zhu, X.; Mukherjee, M.; Ni, S.; Kennedy, M. A.; Ogawa, M. Y. *J. Inorg. Biochem.* **2013**, *119*, 1–9.